Title
Mass Transport of Condensed Species in Aerodynamic Fallout Glass from a Near-Surface Nuclear Test

Author
Weisz, David Gabriel

Publication Date
2016

Peer reviewed|Thesis/dissertation

Mass Transport of Condensed Species in Aerodynamic Fallout Glass from a Near-Surface Nuclear Test

by

David Gabriel Weisz

A dissertation submitted in partial satisfaction of the

requirements for the degree of

Doctor of Philosophy

in

Engineering – Nuclear Engineering

in the

Graduate Division

of the

University of California, Berkeley

Committee in charge:

Professor Karl van Bibber, Chair
Professor Eric Norman
Professor Michael Nacht
Dr. Kim Knight

Summer 2016

Mass Transport of Condensed Species in Aerodynamic Fallout Glass from a Near-Surface Nuclear Test

Abstract

Mass Transport of Condensed Species in Aerodynamic Fallout Glass from a Near-Surface Nuclear Test

by

David Gabriel Weisz

Doctor of Philosophy in Engineering – Nuclear Engineering

University of California, Berkeley

Professor Karl van Bibber, Chair

In a near-surface nuclear explosion, vaporized device materials are incorporated into molten soil and other carrier materials, forming glassy fallout upon quenching. Mechanisms by which device materials mix with carrier materials have been proposed, however, the specific mechanisms and physical conditions by which soil and other carrier materials interact in the fireball, as well as the subsequent incorporation of device materials with carrier materials, are not well constrained. A surface deposition layer was observed preserved at interfaces where two aerodynamic fallout glasses agglomerated and fused. Eleven such boundaries were studied using spatially resolved analyses to better understand the vaporization and condensation behavior of species in the fireball. Using nano-scale secondary ion mass spectrometry (NanoSIMS), we identified higher concentrations of uranium from the device in 7 of the interface layers, as well as isotopic enrichment (>75% ^{235}U) in 9 of the interface layers. Major element analysis of the interfaces revealed the deposition layer to be chemically enriched in Fe-, Ca- and Na-bearing species and depleted in Ti- and Al-bearing species. The concentration profiles of the enriched species at the interface are characteristic of diffusion. Three of the uranium concentration profiles were fit with a modified Gaussian function, representative of 1-D diffusion from a planar source, to determine time and temperature parameters of mass transport. By using a historical model of fireball temperature to simulate the cooling rate at the interface, the temperature of deposition was estimated to be ∼2200 K, with 1σ uncertainties in excess of 140 K. The presence of Na-species in the layers at this estimated temperature of deposition is indicative of an oxygen rich fireball. The notable depletion of Al-species, a refractory oxide that is highly abundant in the soil, together with the enrichment of Ca-, Fe-, and ^{235}U-species, suggests an anthropogenic source of the enriched species, together with a continuous chemical fractionation process as these species condensed.

This dissertation is dedicated to the memory of Dr. Ian D. Hutcheon and of Professor Stanley G. Prussin

Their passion and knowledge truly set the bar for scientific excellence. Their friendship and mentorship will be deeply missed.

Contents

List of Figures

List of Tables

Acknowledgments

First I would like to thank my late advisors Stanley Prussin and Ian Hutcheon. Both pillars of their respective fields, Stan and Ian were like minded in their idealism for the scientific process – they taught me that no work is worth doing unless done properly. Even in the face of grave illness, they remained dedicated to their work and their students to the very end. I will be forever grateful for their mentorship.

I would next like to thank my current technical advisor, Kim Knight. Despite her already enormous work load, she took on the responsibilities of advising me. She held me to the same standards that Stan and Ian would have expected, and I am sure they would have immense pride seeing her fill this role. I would also like to thank my current academic advisor, Karl van Bibber, for his support through this process; his encouragement during a time of uncertainty was integral to the completion of this work. I would like to thank my other committee members Rick Norman and Michael Nacht for their time and insight.

Without the numerous collaborators at Lawrence Livermore National Laboratory, this work would have been impossible. Rick Ryerson provided critical guidance in both the planning and execution of diffusion couple experiments. Brett Isselhardt spent hours editing this dissertation and still more hours sitting through meetings and discussion regarding this work. Ben Jacobsen spent months helping me put this work in publishable form, and came in on weekends to help me collect NanoSIMS data. Naomi Marks endured much harassment showing me how to operate the EPMA. Jenny Matzel and Peter Weber provided technical guidance and discussion, particularly regarding the NanoSIMS. Christy and Erick Ramon, Gary Eppich, Josh Wimpenny, and many others in the Nuclear and Chemical Sciences group at LLNL, provided invaluable support.

The other members of Stan's research group – Laurence Lewis, Patricia Shuster, Eva Uribe, Araina Hansen, and Brian Quiter – dedicated much time and effort helping me get through this process during our weekly group meetings. My officemates at LLNL Marc Fitzgerald and Laurence both entertained endless, and oftentimes questionable, discussion regarding this work.

Lastly, I would not be here without the support of my friends and family. I would like to thank my parents and my brother, who encouraged my scientific curiosity from the beginning. I also thank my children, Aria and Aiden, for being my very favorite diversions. Most of all, I would like to thank my loving wife Jess, whose support over the years it took to get to this point is so appreciated.

Chapter 1

Introduction

1.1 Studying glassy fallout debris to understand post-detonation fallout formation

The hazardous effects of nuclear weapons have been apparent since the Trinity test in 1945, which marked the beginning of the Atomic Era. The immediate destructive effects of a nuclear explosion manifest as a shockwave, thermal radiation, and nuclear radiation in the form of gamma rays and neutrons [1]. In addition to these initial effects, the production of radioactive fallout is of critical concern to the exposed population and emergency response personnel, and further forms a record for post-detonation nuclear forensics [2]. In the intervening decades, the arms race between the United States and the Soviet Union resulted in the development and testing of sophisticated weapon designs and delivery systems, as well as the proliferation of nuclear weapons technology to countries around the world. Today, the threat posed by nuclear weapons still exists, whether it is an exchange between potential regional rivals [3], or a smuggled nuclear device by non-state actors into a major city [4].

Radioactivity in a post-detonation environment is primarily a result of the short-lived products from the fissioning of nuclear fuel (usually as either ^{235}U or ^{239}Pu), although neutron activation products also have an effect [1]. Many of these products, which are in the vapor phase immediately post-detonation, can incorporate into carriers, such as water, molten soil, or other nearby materials, forming fallout which is then dispersed based on size and local weather conditions. For example, when a nuclear bomb is detonated in a near-surface explosion, materials from structures and nearby surfaces (environmental debris) are swept up into the ensuing fireball and can interact with vaporized device material. As the fireball rises, the entrained environmental debris, can melt, incorporate bomb debris, then quench, producing micron- to mm and greater sized fallout glasses of various morphologies [1, 5, 6]. Fallout glass morphologies depend on the emplacement of the device and the local geology. For example, in near-surface shots in silicate soil, observed fallout objects included large irregular objects of partially melted soil (mm-scale and larger) as well as smaller, spherical glassy objects (sub-mm to mm-scale). Higher radioactivity associated with the glassy regions

(rather than unmelted regions) indicates that radionuclides must have mixed into molten carrier material, which then quenched quickly, without significant recrystallization [7, 8, 9]. Aerodynamic glass objects consisting of multiple agglomerated spheroidal glasses have been observed in numerous near-surface testing environments [7]. These objects, which formed in the fireball and quenched prior to hitting the ground, would have had the highest probability of interaction and incorporation of vaporized device material.

Fallout has been a subject of study over several decades to understand how radionuclides are incorporated into fallout, and determine how radionuclides would be distributed over a geographic area following a nuclear event [6, 10, 11, 12]. Understanding how radionuclides are distributed around ground zero is essential to public safety and strategic deployment of emergency personnel in the event of a nuclear detonation [2]. As the dose-rate to emergency personnel dictates where and for how long they can be deployed following a nuclear explosion, predictive dispersion modeling coupled with real-time radiation measurements is necessary to determine the radiation field. Further, predictive dispersion modeling is used to dictate the potential evacuation of down-wind population centers [13].

To determine the hazard from fallout in terms of radiation dose, dispersion codes [14] incorporate historical fallout formation models explaining the variation in chemical behavior of radionuclides observed in fallout from aboveground tests [15, 16]. Such types of codes are currently in use by the Interagency Modeling and Atmospheric Assessment Center (IMAAC) to model nuclear incidents (*e.g.,* the detonation of an improvised nuclear device) [17]. While models for how radionuclides interact with carrier materials differ, there is consensus that fission products, unfissioned actinides, and vaporized inert materials are incorporated into molten carriers via some combination of condensation, convective mixing, and agglomeration [15, 18, 19] (Figure 1.1). These models capture a general picture of fallout formation, but the processes controlling how environmental debris and device material interact in the vapor phase and combine with carrier materials remain relatively unexplored. The physical and chemical processes through which device material and environmental debris interact to form fallout glass are not well constrained, yet are essential for advancing the understanding of chemistry of fallout formation. Because of these issues, if a nuclear explosion were to occur in an urban environment, fallout formation models used to inform dispersion models may be inaccurate, as these models are based on observations from above ground nuclear testing in non-urban environments [15, 16]. It is possible that the tons of structural material incorporated into the fireball would interact with vaporized fission products and device materials in ways not observed in previous testing environments, which would subsequently affect the resultant prediction of fallout formation and dispersion. Any inaccuracies in the predicted radiation hazard may hamper the efforts of emergency responders, and further endanger lives in an already chaotic environment.

Understanding how device materials incorporate into fallout is also integral to post-detonation nuclear forensic analysis, as these materials preserve a record of device signatures that have been altered by the physical and chemical processes of fallout formation [20]. The setting in which a detonation occurs, such as height of burst and geology, can have an effect on the interdependent processes that control how device materials interact with the environ-

ment, and are subsequently interpreted. In the event of a nuclear detonation by an unknown perpetrator in a metropolitan area, decision makers handling post-event response will require answers expeditiously. Interpreting signatures for the purposes of attribution after they have been altered in a nuclear explosion is complicated and time consuming [2], and is reliant on an understanding of the chemical processes (*e.g.,* fractionation) that occurred post-detonation [20]. Inaccurate assumptions regarding chemistry in the fireball could potentially muddle or delay the attribution process. However, by studying the chemical variation observed in fallout glasses, we can gain critical insight into fallout formation chemistry, which can better inform these types of nuclear forensic analyses particularly if faced with nuclear explosions in untested environments.

Historically, chemical distributions of actinides were explored via autoradiography, a technique used to spatially determine the distribution of gamma and beta-emitters in samples characterized shortly after formation. The autoradiographs revealed patterns of radionuclide incorporation which were used to develop fallout formation models [15, 16]. For example, studies commonly reported a relative increase in the radionuclide activity at the surface of fallout objects, which suggested a fractionation sequence based on condensation temperature, wherein more refractory (higher vaporization temperature) species condensed early, while the more volatile species condensed later, at cooler fireball temperatures [6, 12]. Autoradiography, however, cannot determine the identity of these radionuclides, and the spatial resolution of this technique is typically limited to 10's of microns.

While many of the high activity species observed in these original studies have decayed away in the intervening decades, historical fallout still retains a record of the chemical interactions that control fallout formation. These interactions can be revealed through the study of unfissioned actinides as well as major element compositional variation, including investigation of surface layers preserved in fallout today. By using modern, spatially resolved analytical techniques (*e.g.,* nano-scale secondary ion mass spectrometry (NanoSIMS)), the species, such as residual actinides, that are preserved in these surface layers of glassy fallout can be observed, and subsequently interpreted through the lens of historical fallout formation models (as shown in Lewis et al. (2015)).

In this study, it is observed for the first time that a surface deposition layer is preserved at the interfaces between fused molten objects, where vaporized species deposited on the surface of either object prior to collision and quenching. This thesis investigates the interfaces of agglomerated glassy fallout objects from a near-surface, uranium-fueled test, in order to test formation models and further investigate the chemical processes that control the incorporation of device materials into glassy fallout objects. A combination of qualitative (scanning electron microscopy), semi-quantitative (energy dispersive X-ray spectroscopy), and quantitative analytical techniques (electron probe microanalysis and NanoSIMS) is used to characterize the compositional variation of major elements and uranium isotopes at these interfaces. Preserved interfaces in agglomerated fallout glasses appear to retain a record of the interaction of device material and environmental debris as a distinctive chemical layer that was originally deposited on the surface of fallout objects prior to agglomeration. Additionally, a record of diffusive mass transport from these interfaces into the agglomerated

objects is preserved as distinct concentration profiles. Here, these observations are used to estimate thermal and temporal conditions applying a model of one-dimensional planar diffusion and yield-dependent fireball cooling curves. This thesis uses the unique relationships at agglomerate interfaces to characterize the vapor component in the fireball, interpret how key chemical species interacted with molten environmental debris to form fallout glasses, and deduce the time and temperature conditions over which these species diffuse into agglomerated objects.

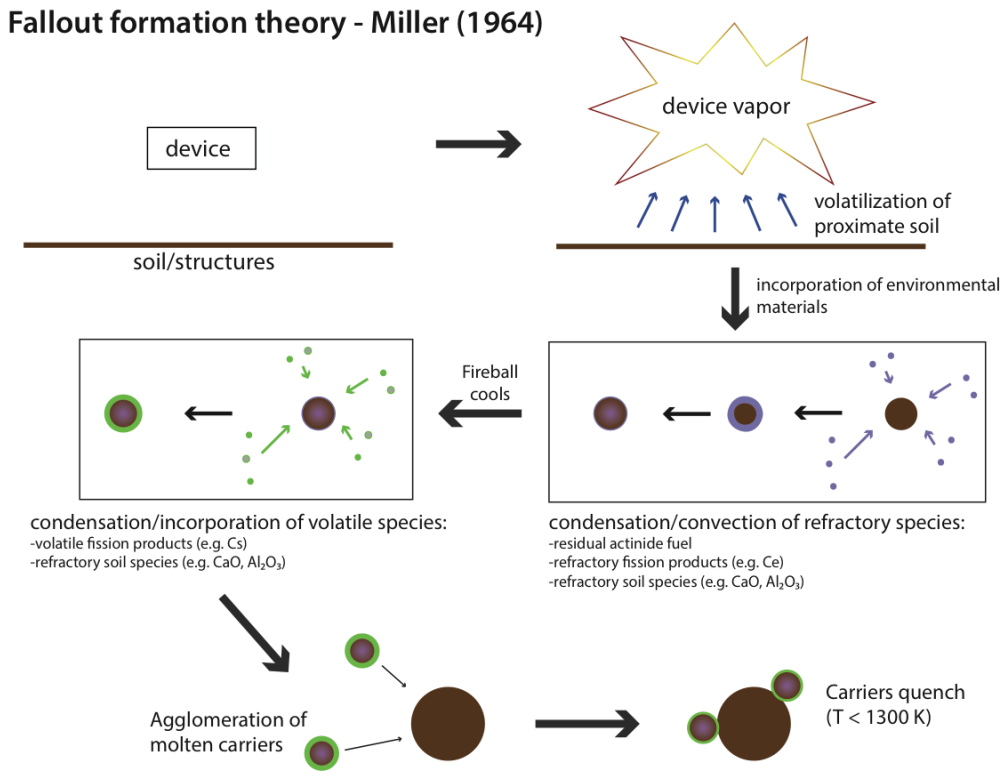

Figure 1.1: This diagram illustrates the interaction of the fireball with environmental debris and the subsequent condensation process onto carrier materials. According to the Miller model [15], refractory species will distribute volumetrically in molten carriers, while more volatile species will accumulate on the surface of already frozen carriers. In this study, it is hypothesized that a deposition layer on the surface of molten carriers agglomerated onto larger host objects prior to quenching is preserved at the interface of where the objects fused together. This interface is the main object of study for this thesis.

1.2 Historical Models of Fallout Formation

In order to understand how fallout forms and how fission products and device material incorporate into fallout, it is necessary to understand the progression of a nuclear explosion to the subsequent fireball of bomb vapor that is produced, and then cools. When a nuclear weapon detonates, the initial energies produce temperatures on order 10^7 K, vaporizing the device. At approximately 1 microsecond, these materials radiate heat as soft X-rays (a few eV), which are absorbed by the surrounding air [1]. The volume of air that absorbs this energy is highly dependent on yield and initial temperature conditions (Figure 1.2) [21]. As this parcel increases in temperature, it becomes increasingly transparent to the emitted radiation, while the cooler air surrounding it is opaque. The hot air reradiates in the visible spectrum, leading to the rapid, isotropic heating of the surrounding air, resulting in a luminous fireball [22]. The fireball rapidly expands within a millisecond, leading to an adiabatic decrease in average temperature of the fireball. The fireball, which is much less dense than the surrounding air, quickly rises, and continues to expand and cool as it incorporates more air [1, 21].

In the case of an air-burst, where the fireball does not interact with the ground, macroscale fallout is not formed. This is because in the absence of carrier materials, fallout is formed as micron-scale (and smaller) condensates, which distribute over thousands of kilometers [1]. In contrast, in a near-surface nuclear explosion, environmental material and debris from structures may be incorporated into the fireball, the extent of which is controlled by the yield and height of burst. The reflection of the blast wave and rising fireball off the surface of the earth brings soil or structural materials into the fireball, which can melt and/or vaporize depending on the fireball temperature. For example, in a surface-burst, it is estimated that approximately 5000 tons of soil are displaced per kiloton of yield, about 25 tons are vaporized [23]. As vaporized materials in the fireball cool, they may condense onto the surface of molten carrier materials – about 200 tons of soil are melted per kiloton of yield in a surface-burst. When the molten materials mixed with the bomb vapor quench (either when the fireball is cool enough, or if they are ballistically ejected from the fireball), they encapsulate the incorporated fission products and/or other vaporized device and environmental materials, that condensed onto carrier surfaces and diffused or otherwise mixed into these molten precursors. The materials that fall to the surface over the first 24 hours are known as 'local' fallout, and can range in size from a few microns to a few cm, distributing geographically based on size [24, 25].

Analyses of fallout and melt products, and theories on fallout glass formation, first emerged following the detonation of the Trinity device. In 1948, Ross made observations of the glass, known as trinitite, that formed as a result of that test. While his analysis was limited to the optical properties of the glass, he inferred details about formation temperature (much greater than 1470 ^{o}C), as well as the potential addition of anthropogenic copper to the glass while molten [5]. This information, along with the geographic spread of radioactivity following detonation, provided the first evidence of the extent to which device materials and radioactive fission products interacted with, and dispersed through, the environment

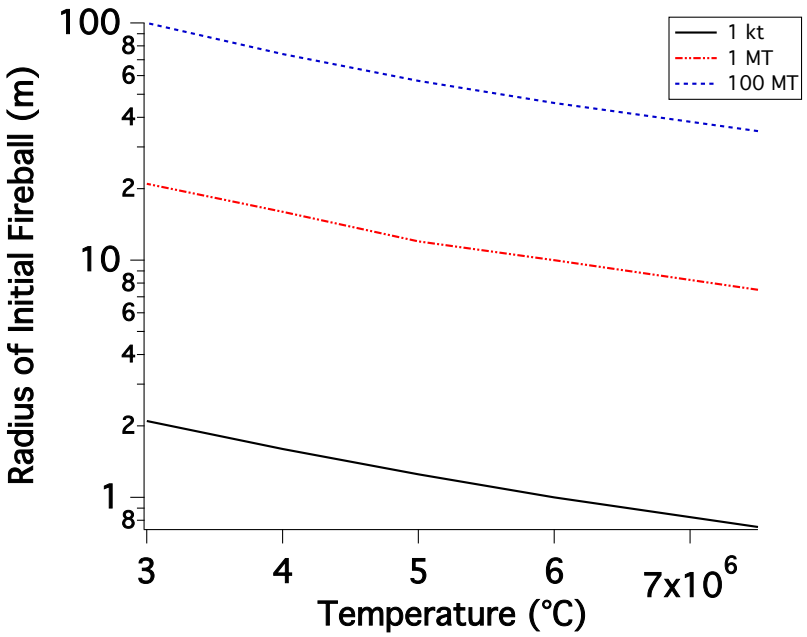

Figure 1.2: The required size of a spherical parcel of air that would be necessary to absorb the amount of X-ray energy initially produced from the given yield for a range of initial temperature conditions (adapted from [21])

post-detonation.

One of the first mathematical approaches to the formation of fallout, published in 1956 by Stewart, described the mechanisms of condensation and coagulation [26]. In this model, the nucleation of condensates formed from the cooling vapor depends on the saturation vapor pressure of metal or metal-oxide species in the fireball, as well as the potential cooling rate and thermal variation within the fireball. These calculations provide a prediction of the size distribution of particles expected to result from either a near-surface explosion or an air-burst. The model is also based, in part, on empirical observations of fireball temperature and estimates of vaporization of materials in the fireball (*i.e.,* ∼100 tons of SiO_2 for a surface burst). The study predicts an average particle size of less than 1 micron assuming a pure condensation process, but acknowledges that non-vaporized materials could effect the particle size distribution, and that more information is required to derive a comprehensive formation model. This information was acquired in a series of subsequent studies, including determination of the particle size distribution [27], spatial distribution of radionuclides within individual fallout objects [10], and the gross radioactivity of fallout objects [28, 29].

The environment and height of burst of the detonation have an effect on key parameters of fallout formation models, including the size distribution, the degree of chemical fractionation, and morphology of the subsequent fallout [27]. As reported by Heft, surface-bursts and sub-surface bursts (Figure 1.3A) produce glassy particles in sizes ranging from tens to thousands

of microns. In the Heft study, chemical fractionation of radionuclides in these particles is approximated as a linear relationship between the ratio of a given radionuclide to refractory species, and the ratio of specified volatile and refractory species. Fallout formation in tower shots displays a similar pattern of fractionation to surface bursts, but also includes metallic spheres up to a few hundred microns in diameter, presumably the result of molten tower components. Air bursts are observed to produce metal oxide particles from the sub-micron size up to 20 microns in diameter. The Heft study thus categorized fallout into two broad particle populations: one that is comprised of environmental debris that was melted (or partially melted), and another that is comprised of metal oxide spheres that formed from a condensation and/or agglomeration process. The observation of sub-micron particle sizes from air-bursts is in line with the Stewart model of condensation ($\sim$1 micron) [26]; however, the largest particles ($>$10 microns) are not explainable by that model, and were asserted to be a result of the agglomeration of material that was not completely vaporized.

Further studies exploing fallout found that different types of particulates had different radionuclide compositions [28, 29]. Fallout from a high-yield test in the Eniwetok Proving Grounds was characterized by two classes of environmental debris-based fallout: the 'altered' fallout, which comprised partially or wholly melted coral particulates, or 'unaltered' particulates [28]. The primary difference in the associated radionuclide composition was that the 'altered' particles were measured to have 100-fold higher fissions/g than the 'unaltered' particles, and appeared to be depleted in the more volatile radionuclides. This observation suggests that these volatile species may have condensed at later times late, thus the 'altered' molten particles incorporated disproportionately more of the less volatile radionuclides. This finding was not observed in the Small Boy test, however, a lower-yield near-surface test, where these two sample populations showed comparable radionuclide fractionation patterns [29]. In that event, the spheroidal, or 'altered', particles were shown to have higher specific activities. In Figure 1.3B for example, a fallout object from an unidentified moderate yield, near-surface shot with a silicate glass core is shown, with an exterior layer having high radioactivity [12]. The surface is coated with iron oxide-rich glass which, with the activity distribution, is consistent with a condensed layer incorporating into the interior of the object via diffusive mass transport.

Another study from an unidentified test in the Eniwetok Proving Grounds characterized three types of fallout, with varying amounts of tower material and environmental material [10, 12]. The composition of the first type of fallout was a combination of calcium carbonate, calcium hydroxide, and iron oxide. In this fallout, radioactivity is primarily associated with iron oxide rich regions, as observed by autoradiography, and was thought to have resulted from vapor phase condensation of fission products and tower components. The second type of fallout was characterized as sub-mm black spheroids of mixed iron oxides, that were homogeneous in their radioactivity distributions. The third type of fallout from this test was found in the form of unaltered coral grains that had approximately 10 micron radioactive black spheroids fused to the surface. These black spheroids are interpreted to be the result of vapor condensation of fission products that collided with other vapor condensed particles, such as the iron support structure. While the observed chemistry in fallout from various

testing environments differed, the empirically derived size and activity relationships from these studies form the basis for general fallout formation codes that are relied upon today [14].

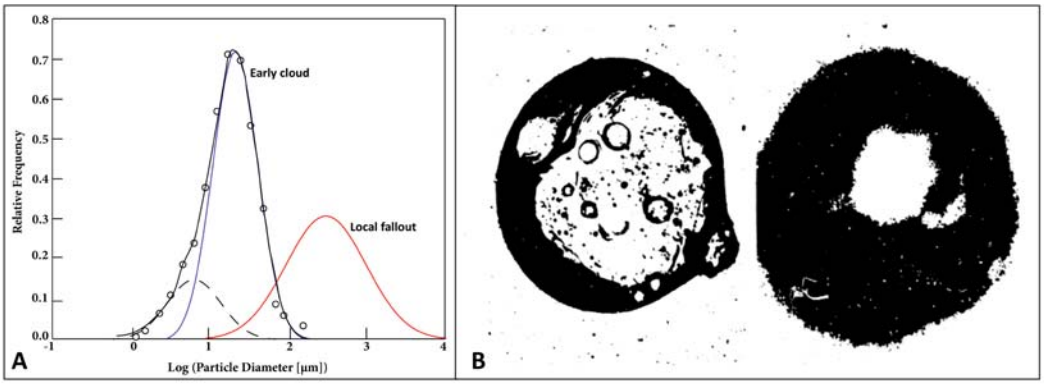

Figure 1.3: (A) A graph of the size distribution of fallout from an unidentified test. The 'early cloud' peak indicates the fallout size distribution from air filter samples collected early in the cloud, while the 'local fallout' peak indicates the size distribution from glassy samples collected proximate to ground zero (adapted from [27]). (B) Thin section and autoradiograph (left and right, respectively) from a tower shot at the Nevada Test Site [12]. The activity is seen deposited around the outside of the fallout object, and appears to have mixed inward.

Fallout formation and distribution models by Miller [15], Freiling [30], and Norman [31] were developed using observations from nuclear testing, and were based on both physico-chemical principles and empirical relationships determined from tests. These models explored how fallout formed in a wide range of environments, including details such as how the local geology, height of burst, incorporation of structures (*e.g.,* support tower), and yield, affects the formation of fallout and the resultant distribution of fission products (and other radionuclides).

In the 1960's, a more comprehensive set of models of fallout formation were published by Miller, for the first time combining both condensation theory and empirical relationships of fireball parameters derived from nuclear testing [7, 12, 15, 32]. Miller's models, specified for near-surface explosions, provide a mathematical treatment to fractionation, condensation thermodynamics, and the effect of carrier size. One key component of his model involves the invocation of a two-stage condensation sequence. In the first stage, refractory materials condense onto the surface of liquid-state carrier materials. Some of these larger carriers fall out of the fireball early, proximate to ground zero, and contain comparatively little in the way of volatile radioisotopes. During the second stage, after the fireball has cooled, the more volatile species condense onto the surfaces of particles that have quenched (Figure 1.1A). Some of these particles constitute 'global' fallout, or fallout particulates that travel thousands of kilometers away from ground zero.

At its root, the Miller model bases fractionation of vaporized species in the fireball on their vapor pressures, as determined by Raoult's law (1),

$$P_{v1} = N_1 P \tag{1.1}$$

where P_{v1} is the vapor pressure of the species of interest, N_1 is the mole fraction in the vapor phase, and P is total pressure of the vapor. This model also makes use of empirical scaling equations (2) and (3), as determined by fireball light output,

$$W = 0.65\rho_0(2R)^5/t^2 \tag{1.2}$$

$$H = 3.75W^{0.51}t_*^{-1.45e^{-9e^{-2.73t_*}}}e^{-93^{-12Wt_*}} \tag{1.3}$$

where W is total weapon yield in kt, H is the power output (kilotons/second), ρ_0 is the air density, R is the radius of the main shock front, and t_* is the ratio of time to the time of the final maximum (based on light output).

Freiling expanded upon the approach of Miller [16, 18, 30, 33], incorporating physical principles such as gas-phase diffusion of species in the fireball, condensation onto carriers, diffusion within carriers, as well as re-evaporation of deposited species into a model based on fluid dynamics and equilibrium thermodynamics (Figure 1.4A). In Freiling's model, the incorporation of radionuclides is ruled by the continuous, temperature-dependent competition between each of these processes as given by

$$J_n = J_v \times \alpha_c - J_c \times \alpha_e \tag{1.4}$$

where J_n is the total inward flux of a given radionuclide, J_v is the flux from condensation of a vaporized radionuclide species, α_c is the probability that a vapor-phase radionuclide sticks to the surface, J_c is the flux of a radionuclide species within a molten carrier, and α_e is the probability that a radionuclide species within a molten carrier escapes back into the vapor phase.

The notable addition of diffusion and re-evaporation of species is of particular interest, as this formulation addresses the competition between the amount of radionuclide addition versus radionuclide loss in carriers. Furthermore, the effect of heat transfer in a cooling fireball affects the rate of diffusion, which is based on the Arrhenius relationship

$$D = D_0 e^{-E_a/RT} \tag{1.5}$$

where D is the diffusivity of the species of interest, D_0 is the pre-exponential constant, E_a is the activation energy of diffusion, R is the gas constant, and T is the instant temperature. This was taken into account in Freiling's model by integrating over the change of temperature over time [16].

Another early publication [31] disputed the model presented by Miller, particularly what was perceived as a simplification of the condensation and diffusion processes as a "go/no-go"

model of two stages based on the physical state of the carrier material. This study, by Norman and Winchell, instead proposed a continuous condensation/diffusion process that occurs throughout a carrier's residence time in the fireball, even below the freezing temperature of the carrier material – in this particular study, a silicate. While acknowledging the effect the changing temperature has on diffusivity, this study presented the diffusivity of radionuclides of interest at 1450 ^{o}C in a molten silicate, characterizing radioantimony as a function of SiO_2 content. Most pertinent to this thesis, concentration gradients measured by electron probe microanalysis were characteristic of diffusion of Pb and Fe from the surface to interior of a fallout object, supporting a model of condensation, diffusion, and thermodynamic radionuclide absorption onto the surfaces of fallout objects (Figure 1.4B).

After above-ground testing effectively ended in 1963 with the Limited Test Ban Treaty [1], computational models became a primary resource for understanding fallout aerial distribution and dispersion. By the 1970's, the study of fallout formation became dominated by the development of computational fallout dispersion models. For example, the details from earlier formation models were used in the development of a computational model known as the Defense Land Fallout Interpretive Code (DELFIC). The DELFIC model [14] incorporates variables of atmospheric conditions, particulate diffusion through a gaseous medium, fireball evolution, activity distribution in particles, assumptions of the chemical properties of entrained materials, and the height of burst to predict the aerial distribution of fallout and radioactivity after a nuclear explosion. Of interest to fallout formation, DELFIC uses a generalized version of the model Freiling established for activity incorporation for different particle-size distributions [14, 34, 35]. More specifically, the DELFIC model calculates the activity distribution in fallout based on the size of the particle (the volume of fission products potentially incorporated), the volatility of species in a fission mass chain (assuming oxide form), and the particle-size distribution.

Today, there are several well-known particle dispersion and distribution models in addition to DELFIC, including the Hazard Prediction and Assessment Capability (HPAC) [36, 37] and the Hybrid Single-Particle Langrangian Integrated Trajectory Model (HYSPLIT) [38, 39, 40]. The HPAC model, developed by the Defense Threat Reduction Agency, is a dispersion and plume model for weapons of mass destruction, including but not limited to nuclear explosions and radiological releases [36, 37]. HYSPLIT is a plume and deposition model for a general pollutant or dispersant [38]. Given the broader application of these two models (*e.g.,* chemical and biological agent dispersion), neither HPAC nor HYSPLIT directly account for incorporation of radionuclides into a liquid phase carrier.

In all of these models, which combine mathematical treatments with empirical relations derived from test data, the understanding of how radionuclides and residual actinides incorporate into carrier materials is largely based on empirical relationships derived from a few early atmospheric tests. Further, the physicochemical parameters that are incorporated into computational models utilize experimentally derived chemical properties of materials (*i.e.,* the vaporization properties of radionuclides and carrier materials which control fractionation [34, 14]), which may be carrier-material dependent and/or dramatically variable in different fireball conditions. Two parameters that are not adequately addressed in fallout formation

models, but are critical to understanding formation chemistry, are 1) condensation sequence and speciation of vaporized species and 2) the mechanism of mixing of species into carrier materials after condensation. More specifically, the presence of oxidizing or reducing environments may affect the speciation of vaporizing or condensing materials [41], which affects temperature-dependent fractionation. Finally, the rate at which material volumetrically incorporates into molten hosts will affect the rate of re-evaporation of condensed species, which is essential for determining the amounts of various species present in molten hosts. The rate of bomb vapor incorporation into molten carrier material is controlled by diffusion and mechanical mixing, is dictated by the diffusivity of species in the molten carriers as well as the viscosity of the molten carrier materials, both of which are temperature dependent [11, 42]. Clearly, further study is required to address these parameters to establish a more comprehensive model of fallout formation.

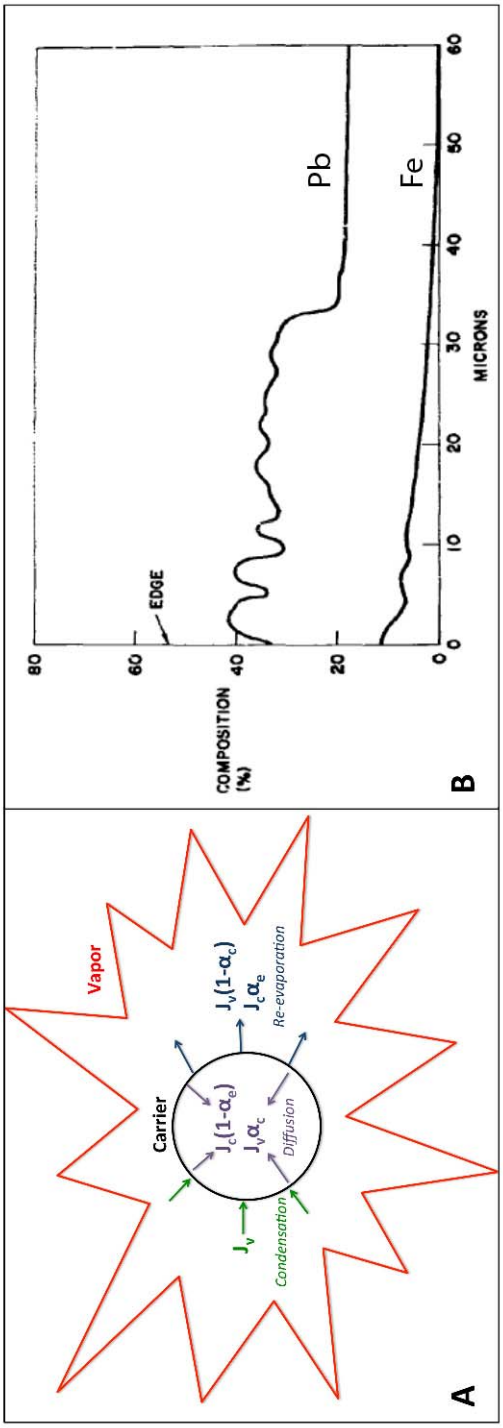

Figure 1.4: (A) The effect of condensation, diffusion within the carrier, and re-evaporation from the carrier given in Equation 1.4 (derived from [18]). (b) Concentration profiles in fallout from the Norman and Winchell study (after Figure 18 in [31]), illustrating the diffusion behavior of Pb (top line) and Fe (bottom line).

1.3 Contemporary Fallout Research

Over the past decade, there has been renewed interest in fallout research. In contrast to Cold War era research focused on the distribution and dispersion of radioactive fallout particulates, these studies are typically motivated by renewed interest in interpreting details and signatures of a device having a potentially unknown origin [43, 44, 45, 46]. For example, a study of trinitite (fallout formed in the Trinity explosion) published in 2006 measured several activation products and fission products via gamma spectroscopy in the glass, from which device characteristics were hypothesized [43]. These studies show copper and iron inclusions, as well as variable lead isotopic compositions, which the authors suggest are indicative of device components, such as wiring and the tamper [44, 45]. Such studies have motivated further interest in improving the understanding of mixing relationships between device materials and soil using modern analytical techniques including scanning electron microscopy, X-ray spectroscopy, mass spectrometry [47, 48, 49, 50, 51, 52, 53].

Several recent studies of trinitite have focused on formation, specifically in terms of how the device material mixed with local soil [46, 51, 50]. One model of trinitite glass formation was put forth by Belloni, based on gamma spectroscopy and autoradiography. This model suggested that as the fireball cooled, vaporized sand, fission products, activation products, and non-fissioned actinides mixed together and coalesced, into droplets. These droplets then rained down onto the molten surface of sand on the ground, forming the observed high-activity top layer. This model states that still more sand was incorporated into the fireball due to the subsequent vacuum and afterwinds, followed by the instantaneous freezing of entrained material at approximately 10 seconds after the explosion was initiated, as cold air infiltrated the fireball [46], thus increasing the inventory of trinitite. However, this accounting of the formation of trinitite contradicts early formation theories put forth by Stewart and Heft, where primary condensates either deposit on the surface of entrained molten soil, or disperse as 'global' fallout [12, 26, 27], and would instead explain trinitite formation wholly by the gravitational settling of entrained soil onto a molten layer of soil on the ground.

Other work, using autoradiography, electron probe microanalysis (EPMA) and laser ablation inductively-coupled plasma mass spectrometry (LA-ICP-MS), identify the distribution of actinides, major elements, and trace elements in trinitite to deduce how the device material mixed with soil [50, 51]. Through such analyses, a series of correlations between soil-based and anthropogenic species were established using bivariate plots and three-isotope plots of analyzed species, as well as multivariate statistical techniques [50, 51], to explain the incorporation of device materials into molten soil. For example, one study used a series of bivariate plots of major element oxides against FeO to differentiate minerals found at the Trinity test site from potential anthropogenic species, and Principal Component Analysis (PCA) including trace elements and actinides to make determinations of alleged anthropogenic end-members (*i.e.,* device associated materials) [51]. However, the model proposed in that study is based on condensation temperatures derived from a solar system composition gas condensation process [41], which is markedly different than the environment of a nuclear fireball, and would have a notable effect on the speciation of condensing materials. While

these studies indicate that device-related material mixed with molten soil, and propose techniques for nuclear forensic analysis, such recent studies do little to address the deficiencies in historical fallout formation models.

Recent work analyzing fallout from other nuclear tests focus on determining formation conditions and how device materials incorporated into glassy fallout [54, 55, 56]. The characterization of stable noble gasses has confirmed that historical fallout preserves a record of the relative volatilities of some fission products, though the distribution was not spatially determined in this study [54]. By looking at the stable xenon isotope ratios preserved in aerodynamic fallout glass, this study was able to estimate the surface closure time of selected fallout samples from a near-surface test, as well as characterize the volatility of the xenon isotope precursors in the fireball as they incorporated into the carrier materials. These parameters suggest a residence time of the characterized fallout in the fireball of <3 seconds, under potentially reducing conditions. These parameters can be used to, in part, address the oxidation state and subsequent speciation of materials interacting with carriers lacking in historical formation models.

In another publication, bulk chemical and isotopic data from a uranium-fueled test were acquired, indicating two-component mixing of unfissioned fuel with molten soil in a population of mm-scale fallout debris [55]. *In situ* secondary ion mass spectrometry (SIMS) analyses of samples from the same test reveal some degree of isotopic enrichment of uranium (residual nuclear fuel) throughout the volume of such fallout glasses [56]. Together, these analyses characterize the degree of heterogeneity observed in actinide distributions between fallout objects and within individual fallout objects (the $^{235}U/^{238}U$ ratio ranges from 0.02 to 11.84 [56]). When interpreted in the context of fallout formation models such as the Miller's, the presence of device uranium in the fallout samples is expected, as refractory materials were theorized to condense first and mix volumetrically into molten carriers. However, the observed heterogeneity in uranium isotopic composition through the samples is indicative of a more complex physicochemical mixing processes between host objects and a vapor phase containing an unfissioned fuel component, and point away from simple fractionation models proposed by historical fallout studies.

Thus, despite new research into glassy fallout formation and signature incorporation, current models still do not adequately describe formation chemistry, particularly the processes of condensation and diffusion that are important to how vaporized species interact with carriers. Further, recent studies focused on constraining fallout formation parameters illustrate that the approaches taken by historical fallout formation models may be oversimplified, and that the parameters that control fractionation, condensation, and incorporation of vaporized species into carrier materials used in fallout dispersion models are still inadequate. By determining the composition of the surfaces of glassy fallout objects, this thesis seeks to reveal key details of chemical fractionation, condensation/deposition, and incorporation, and provide a test of the validity of historical fallout formation models.

1.4 Samples

Sample isolation and selection

To understand the chemical and isotopic variation on the surfaces of fallout objects, agglomerated fallout objects having multiple adhered spherules on the surfaces were selected. It was hypothesized that at the interfaces where glassy objects have fused together, a surface layer would be best preserved and protected from any subsequent effects of weathering or other alteration. In this thesis, observations at the interfaces of agglomerated fallout samples are used to test established formation models, identify short their comings, and suggest alternative formation sequences. Additionally, this study seeks to estimate the time and temperature of mass transport from composition profiles at these interfaces, further constraining fallout formation conditions. In order to explore these interfaces, agglomerated fallout glass samples from a uranium-fueled, near-surface nuclear test were selected, provided from the same anonymous event studied by Eppich et al. (2014) and Lewis et al. (2015) [55, 56].

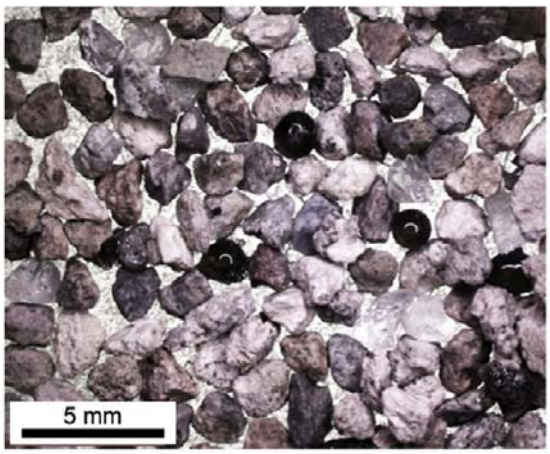

Figure 1.5: Aerodynamic fallout glass and soil grains. The fallout glass is seen as mm-scale, black, spherical objects.

The Eppich et al. (2014) study characterizes the typical samples from this test to be opaque and greenish-black, with no observable crystallinity and often containing visible vesicles. As seen in Figure 1.5, the aerodynamic fallout glasses from this event are often black, highly symmetric glasses of approximately mm-scale. For this study, aerodynamic fallout glasses from this test were separated by sieve size (down to 0.30 mm mesh size), and were shown to have a range of aerodynamic morphologies. The sizes of these objects range from sub-mm to cm-scale, while the shapes range from nearly perfectly spherical to irregular rounded objects (*e.g.,* Figure 1.6). Five samples of agglomerated fallout glasses from a region close to ground zero were acquired for this study. The samples were specifically chosen for their preservation of secondary objects fused to the host glass surfaces. All samples

were mm-sized, highly symmetric, aerodynamic glassy objects with multiple adhered smaller spheroids.

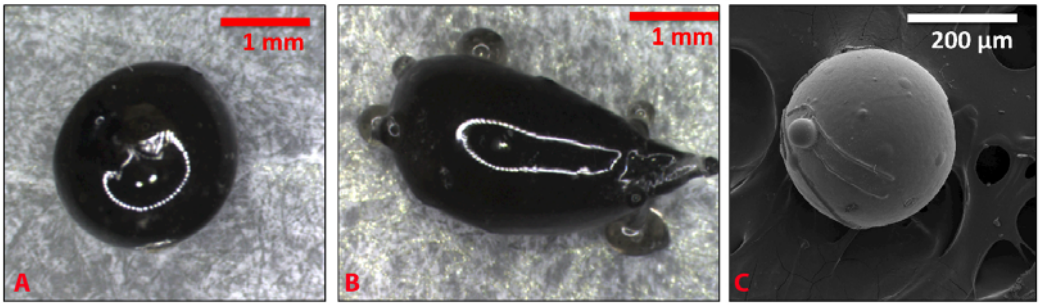

Figure 1.6: Examples of glassy fallout objects. (A) A larger spheroidal glassy object, approximately 3 mm in diameter. The irregular white line at the center of the object is the reflection of the optical microscope light. (B) A large aerodynamic glassy fallout object having smaller glassy objects agglomerated onto it. (C) A secondary electron image (showing sample topography, explained in detail in Chapter 2) of fallout glass from the smallest sampled sieve size, showing a much smaller (approximately 20 micron) sphere attached to its surface.

Sample Descriptions

In sample A, tens of secondary objects ranging in size from 5 to 500 microns can be observed fused to the larger host object (Figure 1.7). In the other 4 samples selected for this study, fewer than five secondary objects (100 micron-scale) were observed fused to each larger host sample (Figure 1.8). On sample B, several sub-mm scale spheroidal objects are seen fused to the surface, with the central two also fused to each other. This sample is approximately 0.4 cm long, although it appears to have fractured on both ends. Sample C shows a tapered and curved fallout object with at least 6 secondary objects agglomerated onto the surface. The agglomerated spherules labeled C1 and C2 are adjacent to one another, and the agglomerated object labeled C3 is isolated and more fully incorporated into the larger host object. Sample D shows a larger, oblong host having two spheroidal objects, adjacent to one another, fused to the surface. The two fused peripheral objects are approximately the same size, each between 200 and 300 microns in diameter. Sample E shows an oblong host object having a number of objects agglomerated to its surface. The agglomerated objects where interfaces were studied are labeled E1 and E2, where E1 is largely independent from the rest of the host object, while E2 is fully incorporated into the host and does not appear as an agglomerated object in optical imaging.

A collection of local soil proximate to the test ground zero was also collected to study the likely protolith to the aerodynamic glassy fallout. The soil at this test site was a combination of fine grained sand and small pebbles [55], which were separated by size fraction and picked

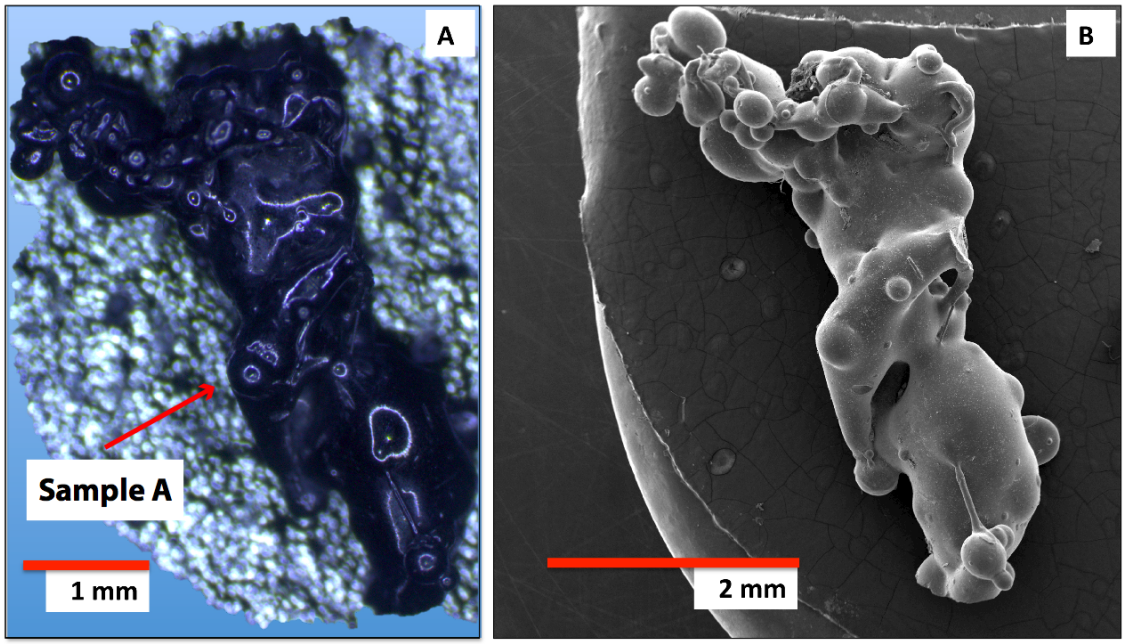

Figure 1.7: Optical and secondary electron image of Sample A. (A) Optical image of Sample A, which is an agglomeration of numerous sub-mm-scale spheroids. (B) Secondary electron image of Sample A, coated in iridium, showing the topography of the sample surface.

clean of remnant fallout glass. These soil samples were selected from the size 12 sieve separation (approximately 1.68 mm), and grains were typically between 1 and 2 mm in size. Approximately 50 of these soil grains (of the same size fraction shown in Figure 1.5, ∼1 mm) were randomly selected and mounted in a 1-inch (2.54 cm) epoxy puck.

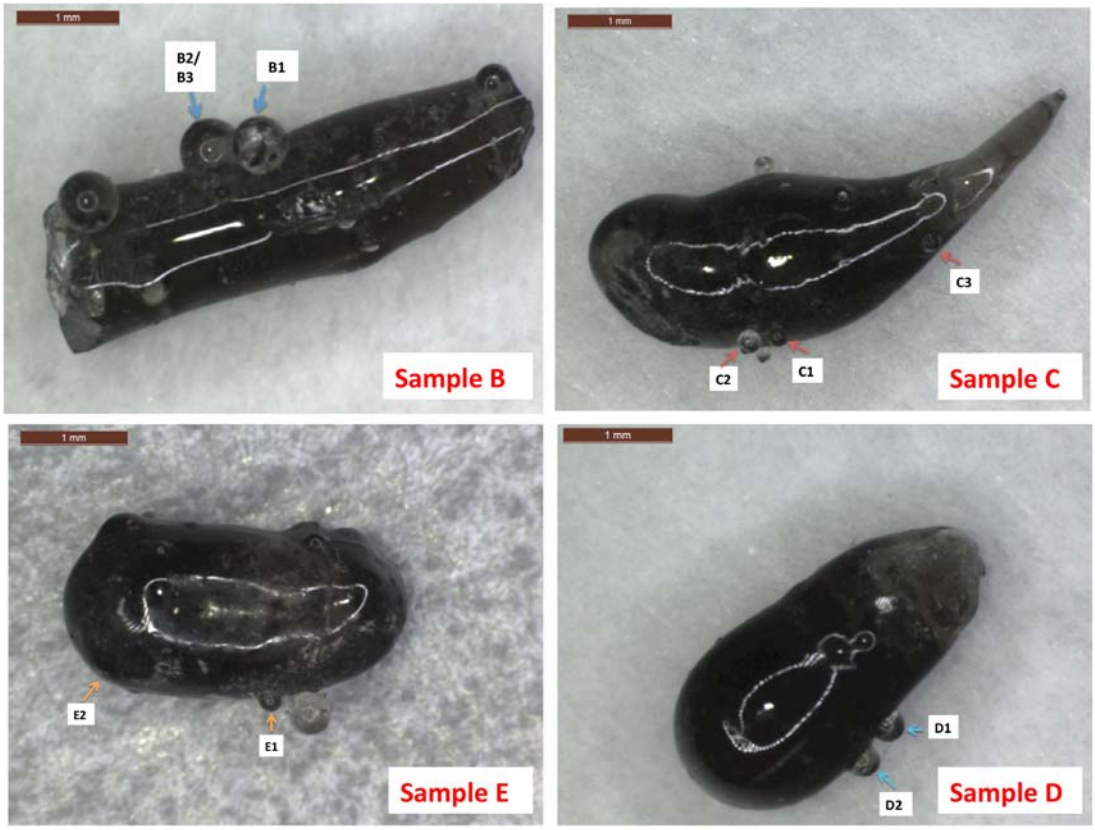

Figure 1.8: Optical images of Samples B-E. The top left frame shows sample B, where attached objects B1, B2, and B3 are labeled. Object B2 is fully incorporated into B3, and cannot be seen optically. The top right frame shows sample C, with fused objects C1, C2, and C3 labeled. The bottom left frame shows sample D, with attached objects D1 and D2 labeled. The bottom right frame shows sample E, with attached objects E1 and E2 labeled. Object E2 is fully incorporated into larger sample E, and cannot be distinguished by optical microscopy.

1.5 Thesis Outline

All prepared samples were characterized using multiple analytical techniques (as discussed in Chapter 2), including scanning electron microscopy (SEM) and electron probe microanalysis (EPMA) on both fallout and environmental debris samples, and NanoSIMS (nanoscale secondary ion mass spectrometry) on fallout samples.

The following Chapter (2) summarizes all analytical techniques used, including scanning electron microscopy, energy dispersive and wavelength dispersive X-ray spectroscopy, and nano-scale secondary ion mass spectrometry. The summary includes the basic theory behind instrument operation, as well as the conditions and operating parameters used to conduct the

analyses for each instrument. This chapter also includes a description of sample preparation for fallout and soil samples.

In Chapters 3 and 4, the results of the analytical techniques are presented. More specifically, the results of qualitative and semi-quantitative techniques (*i.e.,* scanning electron microscopy, energy dispersive X-ray spectroscopy, and X-ray mapping) are presented in Chapter 3, while the results of quantitative analytical techniques (*i.e.,* wavelength dispersive X-ray spectroscopy and nano-scale secondary ion mass spectrometry) are given in Chapter 4. Also in Chapter 4, the results of the analytical techniques are interpreted in terms of the compositions that are observed at the interfaces, and applied to models of vaporization and condensation processes of device materials and environmental materials in the fireball. In Chapter 5, a model of diffusive mass transport from the deposition layer into glassy fallout is defined and applied to observed profiles of compositional variation in selected fallout samples.

In Chapter 6, the limitations of current literature values used in the diffusive mass transport models are discussed, and preliminary results of diffusion studies conducted in manufactured materials similar to those of the studied fallout glasses are shown. Finally, in Chapter 7, summarized conclusions are given, along with discussion of promising avenues of future research to refine fallout formation modeling in terms of condensation and diffusion incorporation parameters. The full dataset for each analytical technique is provided in the appendices.

Chapter 2

Analytical Methods: Theory and Application

To characterize the compositional variation at the interfaces of agglomerated fallout glasses, a series of analytical techniques is applied, including scanning electron microscopy (SEM), energy dispersive X-ray spectroscopy (EDS), electron probe microanalysis (EPMA), and nano-scale secondary ion mass spectrometry (NanoSIMS). Each of these techniques is used to make a unique measurement in the samples: SEM utilized both backscatter and secondary electron modes to qualitatively understand compositional variation, as well as topography of intact samples and polished sample surfaces. EDS and EPMA qualitatively and quantitatively characterized major element compositional variation across sample interfaces, and NanoSIMS was used to characterized uranium isotopic variation across interfaces, in combination with select isotopes of Si, Fe, and Ca. Table 2.1 provides a list of the samples and the analytical techniques applied to each one.

Sample preparation

In order to apply the above surface characterization techniques, all samples had to be polished flat. To achieve this, individual fallout glasses (and soil grains) were embedded in epoxy mounts, cured, and polished flat through a sequence of polishing grits, until a 1 micron surface roughness was achieved. Selected polished fallout glasses (sample B, C, and D) are shown in Figure 2.1. Polishing reduces the effects of surface topography, which can locally change the penetration depth of an incident beam, and result in image artifacts not representative of the sample composition. As the samples are non-conductive fallout glasses (or soil grains), a 5 nm conductive carbon coating was applied to their surfaces, to reduced the effects of localized charge buildup, which can distort the resultant images.

Table 2.1: Analytical techniques applied to fallout and soil samples

Sample ID	Optical	SEM	EDS	EPMA	NanoSIMS	Diameter (major axis)
A1	x	x	x		x	144 μm
B1	x	x		x	x	398 μm
B2		x		x	x	50 μm
B3	x	x	x	x	x	560 μm
C1	x	x	x	x	x	142 μm
C2	x	x	x	x	x	138 μm
C3	x	x	x	x		90 μm
D1	x	x	x		x	165 μm
D2	x	x		x	x	173 μm
E1	x	x	x	x	x	157 μm
E2		x	x	x		86 μm
Soil	x		x			

Figure 2.1: Optical image of polished, flat Samples B, C, and D, with attached objects indicated by yellow arrows. The scale is the same across all images. Large vesicles, ranging in size from ∼10-100 microns, can be observed in all of these samples.

2.1 Scanning Electron Microscopy

Introduction

Scanning electron microscopy has been used for over 70 years as a technique for micron and sub-micron scale imaging [57, 58]. The basic principle of operation of the scanning electron microscopy relies on the irradiation of a sample surface by a focused electron beam that is rastered over a surface. This irradiation results in electron interactions within the sample,

producing detectable signals in the form of secondary electrons, backscattered electrons, and X-rays, which can be detected, and used to characterize sample topography and composition [58].

For this study, an FEI Inspect-F Scanning Electron Microscope was used to acquire secondary-electron images (SE) and backscatter electron (BSE) images. SE images were acquired to observe topographical features on the intact sample prior to polishing, while BSE images were used to characterize the compositional variations in all the fallout samples and interfaces. The mineral compositions and characteristic heterogeneity of the local soil was also characterized through BSE imaging of polished grain mounts.

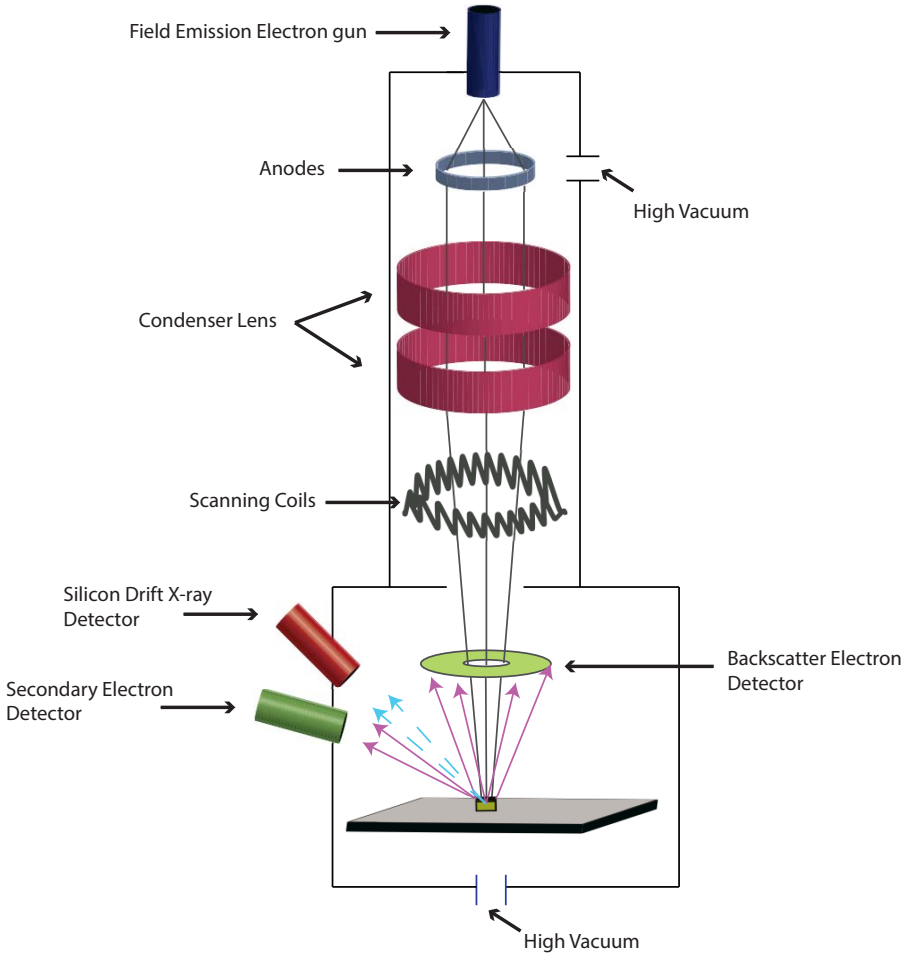

Figure 2.2: General schematic of a FEI Inspect-F SEM, the scanning electron microscope setup used for the analyses in this study, including secondary electron detector, backscatter electron detector, and energy dispersive X-ray detector.

The Scanning Electron Microscope

A basic schematic of a scanning electron microscopy is given in Figure 2.2. The incident electron beam source, or the electron gun, is used to generate electrons and is typically thermionically emitted from a tungsten filament [57]. For the SEM used in this study, electrons are generating using a field emission gun. In this type of electron source, a high voltage is applied to the tip of a tungsten needle approximately 100 nm in diameter. This produces a field in excess of 10 V/nm, lowering the potential barrier for electron emission. The advantage of a field emission source is that it increases electron emission (up to 1000× compared to conventional tungsten filaments) and decreases energy spread of emitted electrons, which improves resolution. However, this source requires high vacuum to prevent gas deposition at the tip, which would detrimentally affect electron emission [58]. The potential difference between the source and the anode determines both the field strength for electron emission as well as the accelerating voltage of the electrons to the sample. The accelerating voltage applied in these analyses were 5 kV and 15 kV for SE and BSE images, respectively.

The initial electron beam exiting the anode is defocused. In the case of a field emission source, a demagnification of over 100x is required to produce a small probe size (approximately 1 nm) (*ibid.*). In order to produce a small probe size, a series of electromagnetic lenses is necessary to focus the incident beam. These lenses, known as condensing lenses, are made of iron cylinders filled with wire windings, that focus the beam as determined geometrically by

$$m = p/q \tag{2.1}$$

where m is demagnification, p is the distance to the lens midpoint from the source, and q is the distance from the lens midpoint to the image (*ibid.*).

Scanning coils raster the beam across the sample surface via the Lorentz force. The beam is moved sequentially across the sample in two dimensions as the current in the scanning coils changes continuously over time. The beam location (*i.e.,* the current in the coils) corresponds to a specific location on the sample, so the detected signal emitted by the sample (*i.e.,* backscatter electrons, secondary electrons, or X-rays) after the beam interacts can be displayed digitally as either an electron micrograph or a compositional X-ray map (further described below).

Secondary Electron Detection

Secondary electrons originate in the sample itself, as outer shell electrons with low binding energy. Electrons from the incident beam that inelastically scatter in the sample strip these outer shell electrons as they travel into the sample. The probability of escape decreases exponentially with depth

$$p \approx e^{-z/\lambda} \tag{2.2}$$

where z is depth into the sample, λ is the mean free path [58]. Due to their very low energies, only electrons at the very surface (a depth of <10 nm) will be emitted. More than 90% of emitted secondary electrons have energies less than 10 eV. This makes SE detection ideal for surface characterization, as illustrated in Figure 2.3. In this image, variation in surface topography for intact sample A is illustrated.

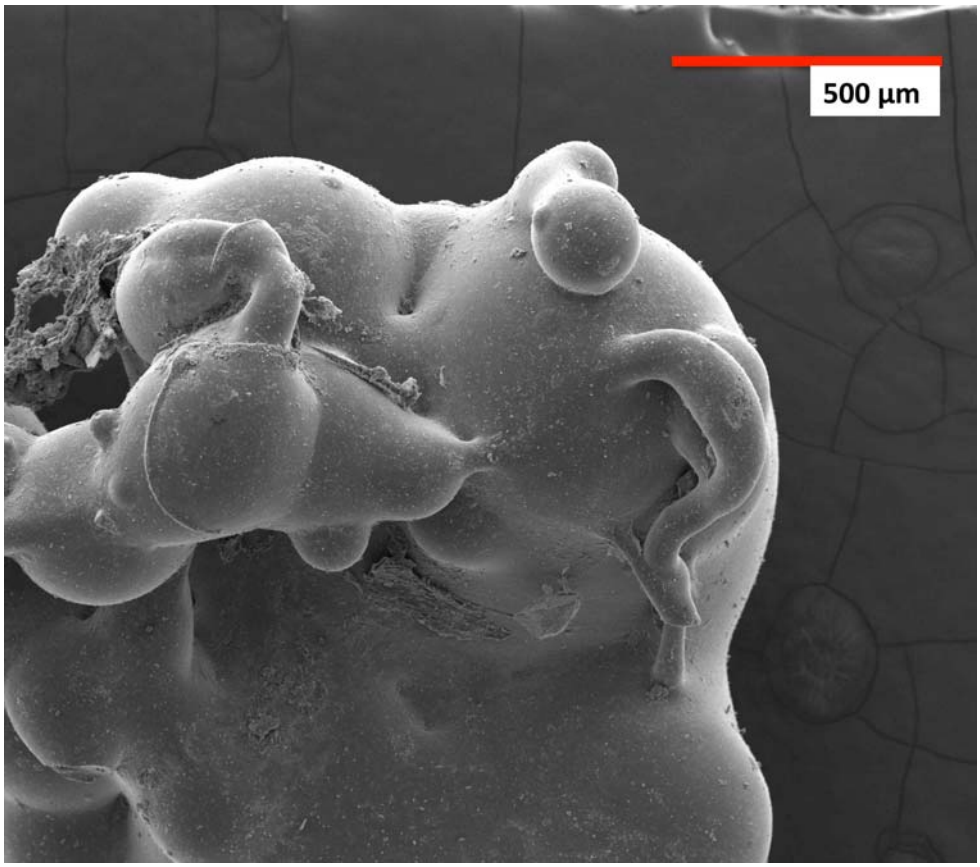

Figure 2.3: Example of a SE micrograph, shown for sample A. This image shows micron-scale topographical features that are difficult to resolve with optical microscopy.

The most common type of secondary electron detector, the Everhart-Thornley detector (used in this study), comprises a scintillator and a Faraday cage having a low positive voltage. This low voltage attracts the low energy secondary electrons emitted from the surface of the sample, liberated by the incident beam, while backscatter electrons are virtually unaffected [59]. The only backscatter electrons that are detected are those that impinge directly onto the detector, thus , the secondary electron detector is situated away from regions of high backscatter emission to minimize this effect.

Backscatter Electron Detection

When the electron beam interacts with the sample, the incident electrons also elastically scatter in the sample. These electrons have a probability of leaving the sample after multiple scattering events; the electrons that escape the sample are known as backscattered electrons. This process is dependent on atomic number and electron energy by

$$Q = 1.62 \times 10^{-20}(Z^2/E^2)\cot^2(\phi_0/2) \tag{2.3}$$

where Q is the cross-section of elastic scattering above the threshold angle for backscatter (ϕ_0), Z is the atomic number of the sample atom, and E is the incident electron energy [58]. The dependence of the probability of backscatter on sample atomic number allows for relative compositional variations (based on average Z) to be characterized through changes in the relative intensity of backscatter electrons detected. This is exemplified in Figure 2.4, which is a BSE micrograph of object D2. In this image, the brightness corresponds to BSE electron density, which is in turn related to average atomic number, as dictated by equation 2.2.

For BSE imaging, samples were prepared by polishing flat, and coated with conductive carbon. As the backscatter electrons can be emitted from depths of up to 1 micron from the sample surface, the samples were prepared by polishing flat to 1-micron surface roughness.

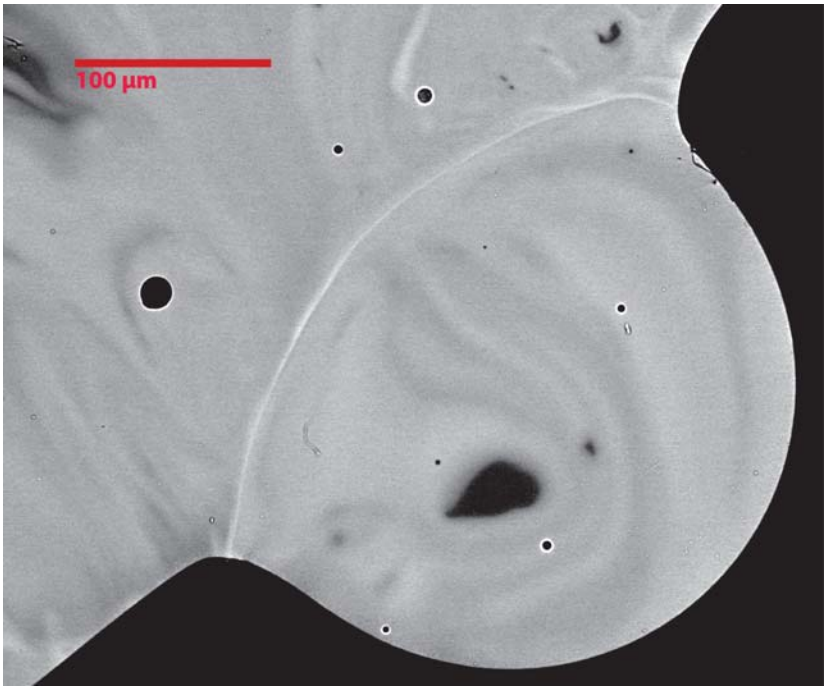

Figure 2.4: Example of a BSE micrograph, shown for object D2, illustrating composition as contrast variation, with brighter areas corresponding to higher average atomic number.

Backscatter electrons are emitted by the sample in a distribution approximately following the form of

$$\eta(\phi) = \eta_n \cos(\phi) \tag{2.4}$$

where η is the fraction of electrons emitted at angle ϕ from the sample, and η_n is the number of backscatter electrons emitted back towards the incident beam [57]. Because of this emission distribution, the backscatter electron detector is a ring-shaped, solid-state silicon diode situated above the sample (and around the incident beam).

Energy Dispersive X-ray Spectroscopy

As the incident beam interacts with the sample material, electrons can be inelastically scattered by an inner shell electron in a sample atom. This process ejects inner shell electrons or excite them into a higher energy level, leaving the atom in an excited state. The hole in the inner shell is rapidly filled by de-excitation of an electron in a higher energy level into the lower energy level, along with the release of energy in the form of a characteristic X-ray, as illustrated in Figure 2.5. The energy release of these X-rays is based on the starting energy level of the electron that is moving into the hole, as well as the energy level of the inner shell where the hole is. The emitted photon energy E is given by

$$E = RZ^2(\frac{1}{n_l^2} - \frac{1}{n_u^2}) \tag{2.5}$$

where R is the Rydberg constant (13.6 eV), Z is the atomic number, n_l is the lower energy level, and n_u is the upper energy level [57]. These characteristic X-ray energies are representative of the atoms from which they are emitted; thus, the detection of these X-ray energies can be used to characterize the composition of the sample material. In energy dispersive X-ray spectroscopy (EDS), these characteristic X-rays are detected in a single crystal semiconductor diode. The EDS detector in the SEM used in this study was an AMETEK EDAX Apollo XL silicon drift detector, which is advantageous in that it does not require liquid nitrogen cooling, accepts high input count rates, and is capable of a larger detector area relative to older EDS detector technologies. The energy resolution for this detector is on order 100-200 eV, depending on the X-ray energy and count rate conditions. However, X-ray production and detection has several complicating factors, including continuum X-ray production, the path of incident electron penetration scattering in the sample, X-ray absorption within the sample, as well as X-ray fluorescence effects, each of which are described below.

As incident electrons penetrate into a sample, they undergo Coulombic deceleration as they interact with the fields of charge carriers in the sample. This deceleration results in incident electron energy loss in the form of X-ray emission known as Bremsstrahlung. Because deceleration events may cause an electron to lose any amount of energy up to its initial energy, a continuum of X-ray energies are emitted, which are detected along with the characteristic X-rays. Therefore, in order to determine the composition from X-ray emissions, the characteristic X-ray peaks have to be distinguishable from this background of

Bremsstrahlung. This can be achieved using an incident electron energy that is sufficiently high in comparison to the excitation energy of the atom of interest. As incident electron energy increases, the depth of penetration and scattering into the sample increase. Not only does this cause a degradation in spatial resolution, but it also increases the absorption of produced X-rays in the sample [58]. Thus, a balance between spatial resolution and X-ray production must be determined for individual sample analyses.

The production of X-rays in the sample does not only depend on the initial electron beam energy, but also the electron density of the material. This X-ray production range is given by the empirically determined Anderson-Hasler range equation

$$R = \frac{0.064}{\rho}(E_0^{1.68} - E_c^{1.68}) \tag{2.6}$$

where ρ is the material density, E_0 is the incident electron energy, and E_c is the excitation energy for a specified element and energy level [60]. For a given electron beam energy, the interaction volume varies depending on the characteristic X-ray of interest. In this thesis, a 15 keV incident electron beam was used; thus, the range of Al K_α X-rays was 2.2 microns, while the range of Fe K_α X-rays was 1.7 microns.

As X-rays are produced, they interact within the sample and may be absorbed, such that the total number of emitted X-rays are attenuated by the sample itself. The intensity of emitted X-rays in comparison to the initial intensity of produced X-rays also depends on the depth at which they were produced and the density of the sample through the relationship

$$I = I_0 e^{-\mu x} \tag{2.7}$$

where I is the emitted X-ray intensity, I_0 is the initial intensity, x is the path length of the X-ray through the sample, and μ is attenuation coefficient of the X-ray for a specific energy and material. Given the above equation, the effect of X-ray absorbance in the sample is highly dependent on the depth of X-ray production, the material in which it is produced, and the energy of the X-ray.

Finally, the effect of secondary fluorescence has to be taken into account when using emitted X-ray energies to determine sample composition. This secondary fluorescence effect is present when characteristic X-rays from one element has a have enough energy to excite an inner shell electron of other elements in the sample to a higher energy level, which de-excites by emitting its own characteristic X-ray. This effect can cause an overestimate of the amount of the other elements in the sample, if not corrected for. This is well illustrated in samples with Ni and Fe, where the Ni K_α X-rays are strongly absorbed by Fe in the sample and re-emitted as Fe K_α X-rays, which not only decreases the observable signal from Ni, but erroneously increases the signal from Fe.

In compositional analysis by EDS, the above effects are accounted for using what is known as the ZAF correction, encompassing sample atomic number (Z), X-ray absorpotion (A), and X-ray fluorescence (F) [58]. The correction can be applied either using standards or without standards. When standards are used to determine the ZAF correction, matrix effects, X-ray

absorption, and X-ray fluorescence are accounted for by comparing the measured spectrum in the unknown sample with a spectrum from a known material using the same operating procedures. In standards-based ZAF, mathematical models are combined with empirical test data for scattering, absorption, and ionization potential, which are then used to define the correction factor for a species of interest (*ibid.*). In standardless ZAF, models of X-ray production and propagation are used in combination with a library of experimentally acquired values on pure-element standards [61]. In both cases, the correction is applied iteratively, based on an initial guess of element concentrations.

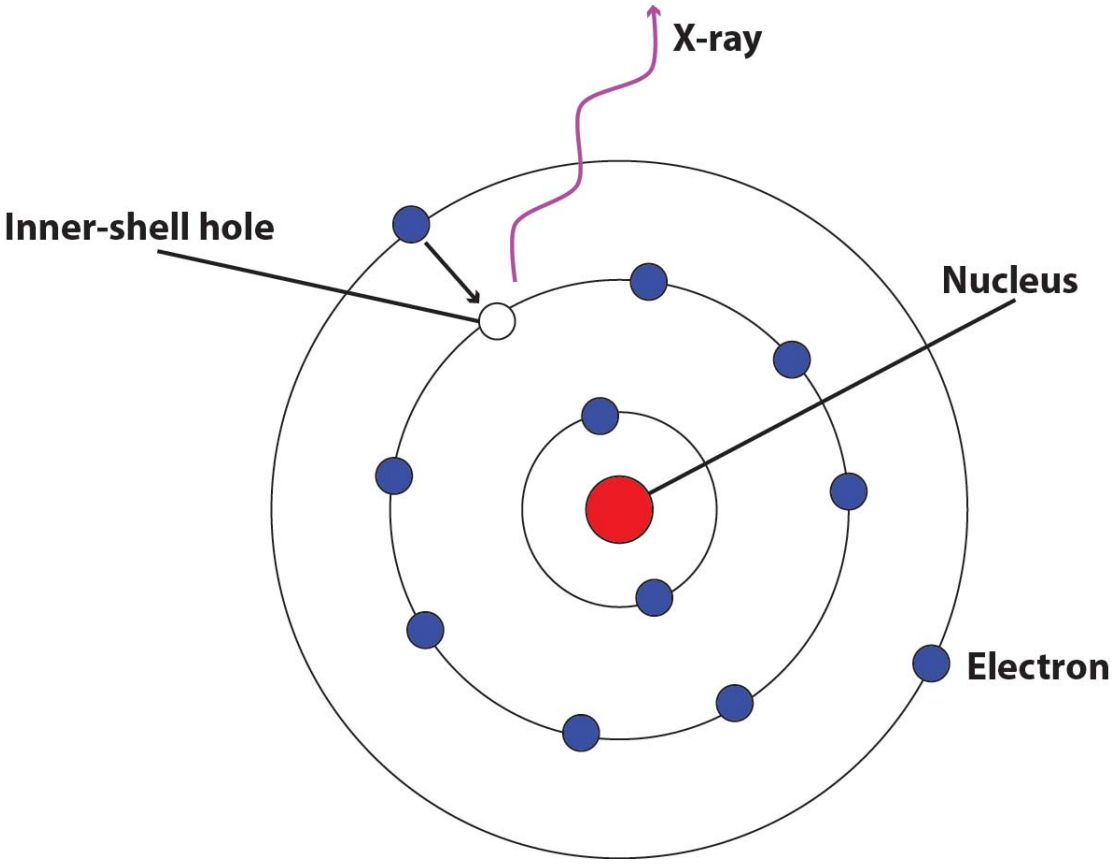

Figure 2.5: Illustration of the de-excitation of an atom as a higher energy level electron (blue) moves into an inner-shell hole (white), with emission of a characteristic X-ray (purple)

In this study, a standardless ZAF correction was applied to X-ray spectra acquired by EDS to determine compositional variation for Si, Al, Fe, Mg, Ti, Na, K, Ca, and O, as EDS was used for rapid and semi-quantitative understanding of composition across the interfaces. The ZAF correction was determined using the TEAM EDS software suite (by EDAX, Inc.). In Figure 2.6, an X-ray spectrum of an EDS spot taken on a Sample A is given, along with the composition as determined by standardless ZAF correction (Table 2.2). Here, a standardless ZAF correction was applied to counts from specific characteristic X-ray peaks

(*e.g.,* Al K_α X-ray peak) to determine composition. The uncertainties are based on counting statistics and peak convolution.

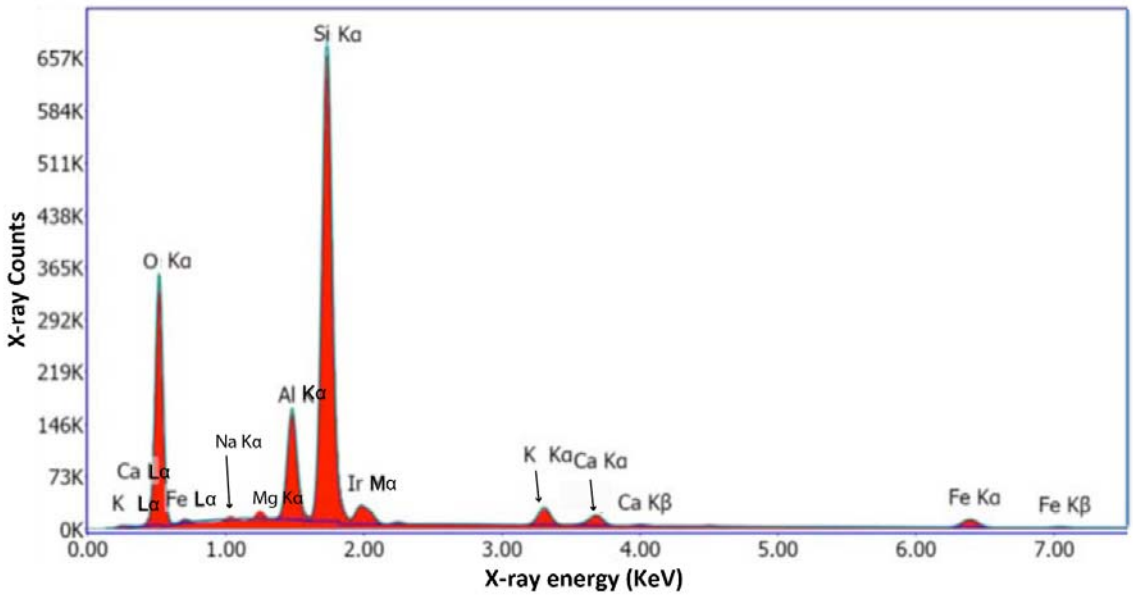

Figure 2.6: X-ray spectrum from an EDS spot taken on Sample A. Iridium peaks are due to the conductive iridium coating.

Table 2.2: ZAF correction from the TEAM EDS Software Suite (EDAX, Inc.), showing composition by element weight percent as determined by the spectrum in Figure 2.6.

Element	Weight (%)	Error (%)
O K_α	39.37%	7.52%
Al K_α	8.00%	3.59%
Si K_α	36.96%	3.27%
Ir M_α	4.57%	2.21%
K K_α	2.97%	2.81%
Ca K_α	2.23%	2.85%
Fe K_α	5.91%	2.73%

As seen from the X-ray spectrum, the ZAF correction can be complicated by several factors, including (1) when the signal of the characteristic X-ray of the element of interest is too low in comparison to the continuum X-rays, or (2) if the elements in the sample produce characteristic X-ray peaks that cannot be resolved (*i.e.,* too close in energy) [58]. For example, in Figure 2.6, several peaks can be seen that have very low signal to background ratio (*e.g.,* $Mg_{K\alpha}$).

As can be seen in Figure 2.7, an EDS spectrum taken at another spot on the same sample identified a phosphorus K_α (2.01 KeV) X-ray peak, where an iridium M_α (1.99 KeV) X-ray peak was in Figure 2.6, such that it measured 1.39 wt.% phosphorus, but did not detect iridium. As the sample was initially iridium coated for conductivity, the peak is misidentified as phosphorus and the ZAF correction is improperly applied. The assertion that this peak is misidentified is further supported by the measured X-ray intensities, as the predicted phosphorus K_α/M_α intensity ratio is ∼100 [62], compared with a measured value of ∼7. To avoid this specific issue, the samples were coated with carbon, which does not interfere with peak identification for species of interest. However, low signal-to-background ratios still affected some peak identification in this study, and spectra were reviewed manually prior to acceptance.

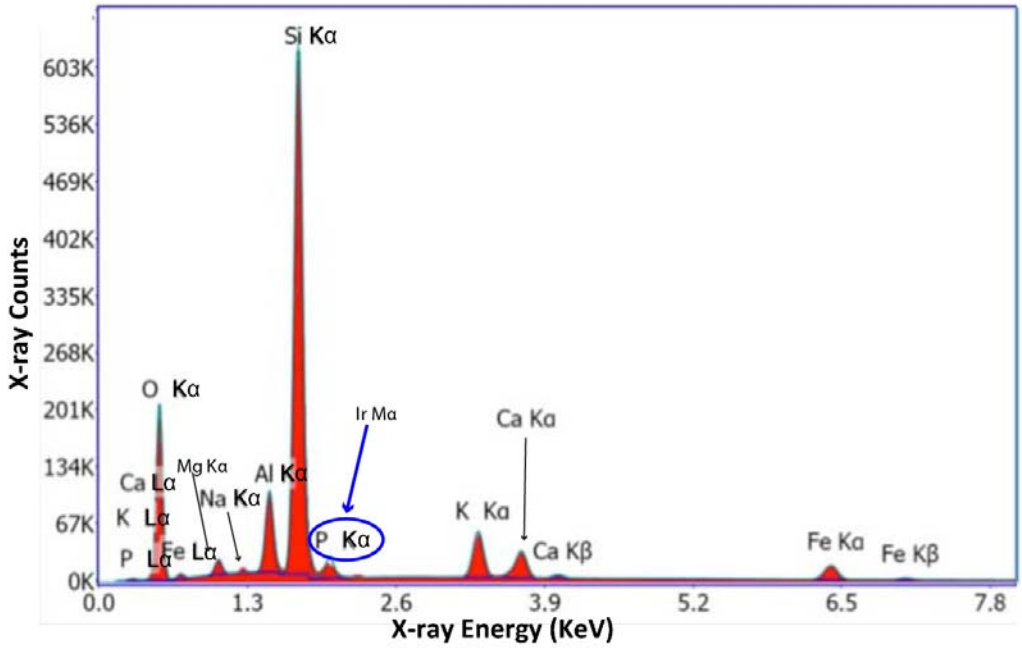

Figure 2.7: X-ray spectrum from an EDS spot taken on a second location on Sample A. A phosphorus peak is incorrectly identified where the iridium M X-ray peak is seen in Figure 2.4, with which it completely overlaps.

Thus, in this study, energy dispersive X-ray spectroscopy was used as a semi-quantitative analysis method to rapidly characterize compositional variation across the interfaces. The EDS data was used to understand general variations of each species of interest in terms of their change in X-ray counts, and thus did not quantify the data in terms of element concentrations. Profiles across the diameter of attached objects and the interfaces where the fused onto the host objects were acquired as a series of 1 micron diameter analysis spots, spaced approximately 1 micron apart, with elemental variation reported as total X-ray counts per spot for each element. A total of 7 interfaces were characterized in this way (see Table

2.1). This is exemplified for object C3, where the Fe variation is shown across the attached object and its respective interface, in Figure 2.8.

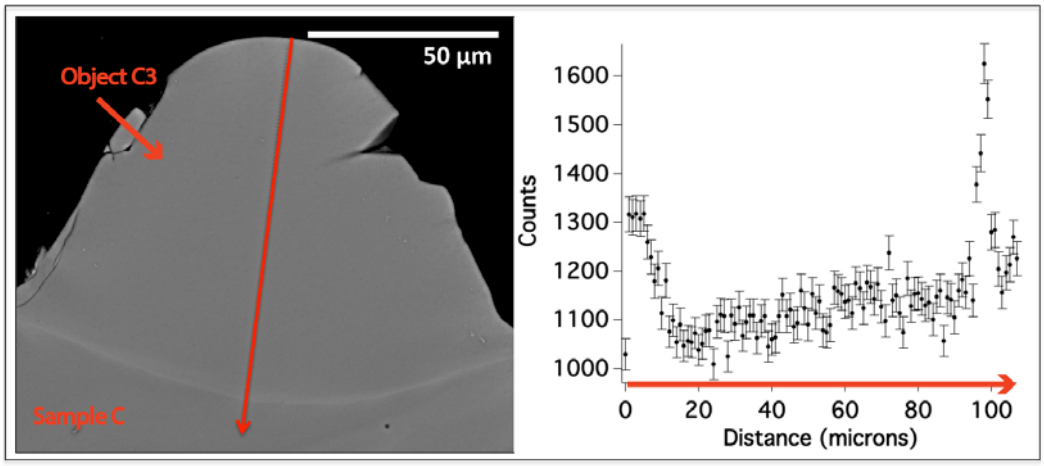

Figure 2.8: The left frame shows the BSE image of object C3, with the red line showing the traverse along which EDS spot analyses were taken. The right frame shows the variation of Fe K_α X-ray counts acquired per spot across object C3 and its corresponding interface, exemplifying qualitative EDS sample analysis. The error bars represent the 1σ uncertainty, which is based solely on counting statistics.

2.2 Electron Probe Microanalysis

To quantitatively determine sample compositions, an electron probe microanalyzer (EPMA) was utilized. As the incident electron beam, optics, and electron detection techniques are, in principal, the same as an SEM, an EPMA is capable of acquiring backscatter and secondary electron micrographs in the same manner [57]. While X-rays are also generated in the same way (electron interactions in the sample, see Section 2.1), the X-ray detection technique that was used via EPMA for this study was wavelength dispersive X-ray spectroscopy (WDS), rather than EDS. Compositional maps of major elements (Si, Al, Fe, Ca, K, Mg, Mn, Ti, and Na) and quantitative analyses of major elements (Si, Al, Fe, Ca, K, Na, Mg, Mn, and Ti, as oxides) were acquired using WDS for both soil samples and fallout samples.

In WDS, diffraction crystals are used to select specific wavelengths from the X-rays emitted by the sample and reflect them into a detector. This crystal-detector system improves energy resolutions 10-fold over typical EDS detectors, and allows for quantitative analysis of species present in concentrations down to 0.1 weight % [58]. The EPMA used for this study, a JEOL JXA-8200 electron microprobe, has 5 wavelength-dispersive spectrometers, each having a different crystal configuration. In WDS, the crystal diverts X-rays following Bragg's law:

$$n\lambda = 2d\sin(\theta) \tag{2.8}$$

where n is an integer, λ is the wavelength of the incident X-ray, d is the lattice spacing of the crystal, and θ is the scattering angle. Bragg's law of diffraction of X-rays from a crystal, such as those used in WDS detectors, is given in Equation 2.8, where the incident X-ray beam shown going to the lower level in the lattice travels a path $2d\sin\theta$ longer than the beam incident on the top level of the lattice (see Figure 2.9).

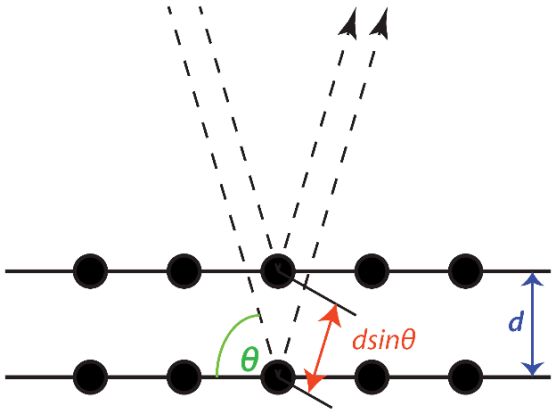

Figure 2.9: The incident and scattering angle are identical for two incident X-ray beams on a lattice, with levels spaced d apart, illustrating Bragg's law of diffraction.

The diffraction crystals used in WDS detectors are manufactured having a curvature, such that all incident X-rays are scattered at the same angle. This is because in a perfectly flat diffraction crystal, the incident X-rays emitted from the sample would impinge on the diffraction crystal at different angles and subsequently be scattered at different angles, dramatically reducing X-ray collection efficiency. Individual detectors and diffraction crystals are bound to a circle that is defined by the radius of curvature of the diffraction crystal, which is known as a Rowland circle [57].

As no single crystal is capable of diffracting all X-ray wavelengths of interest to a detector bound by the Rowland circle, WDS detectors are typically equipped with several crystals having varying lattice spacings. This EPMA instrument is equipped with multiple detectors, each of which are bound by distinct Rowland circles offset by angle or radius, as exemplified in Figure 2.10 [58, 57]. Having this system of multiple detectors, each having multiple diffraction crystals, the EPMA was capable of quantitatively analyzing multiple elements in a single sample simultaneously across the spectral range of potential X-ray emissions. The diffraction crystals used in this study were thallium acid phthalate (TAP), pentanerythritol (PET), and lithium fluoride (LIF). The detected major elements, their corresponding detection energies, and crystal energy detection ranges [63] are given in Table 2.3.

In the WDS spectrometers used in this study, the detectors used were gas proportional counters. In these gas proportional counters, the fill gas is xenon and P10 (which is a

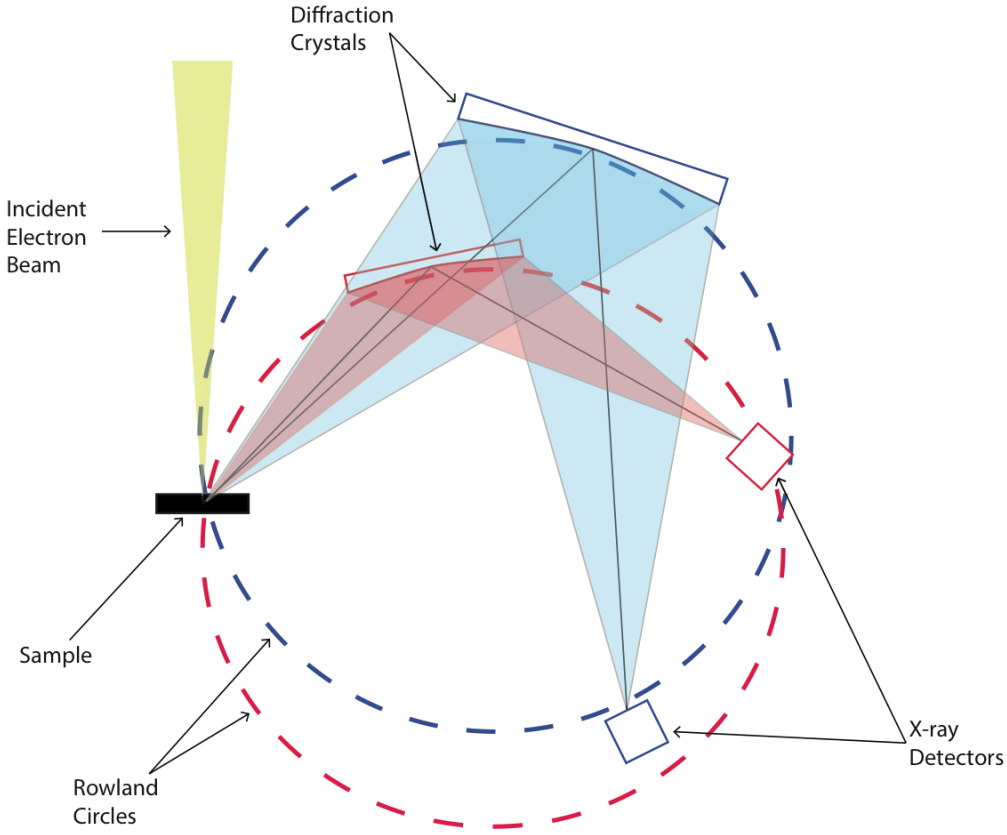

Figure 2.10: Example of two detector-crystal pairs bound to individual Rowland circles, each of which is specific to an individual X-ray wavelength (shown in blue and red) [57].

combination of 10 % methane and 90 % argon). The X-rays incident on these detectors pass through a window into the gas, creating electron-ion pairs by photoelectric interaction. These electrons are collected by a positively charged tungsten wire, which generates a measurable pulse [58]. The applied potential is on order 1 kV in these detectors, which is sufficient to generate a discrete discharge pulse from each collected ion pair. Thus, the number of ion-pairs, and the pulse generated, is proportional to the energy of the incident X-ray.

In addition to using WDS for X-ray detection, the other distinct feature of the EPMA used in this study (in comparison to the EDS) is the incorporation of standards, with which the EPMA calibrated all spectrometers for each analysis. For standards-based analyses, mineral standards were selected to most closely match the suspected composition of the sample (which was estimated using EDS). In samples such as fallout, which comprise multiple oxide species, there was not a single standard containing all the elements of interest. In this case, several standards were used to calibrate each characteristic X-ray wavelength to be used for compositional quantification. For quantitative standardization, mineral stan-

Table 2.3: EPMA crystal settings and detected X-ray energies for major elements

Element	Crystal	Energy Range (KeV)	$E_{K\alpha}$ (KeV)
Al	TAP	0.521 - 1.695	1.486
Na	TAP	0.521 - 1.695	1.041
Mg	TAP	0.521 - 1.695	1.254
K	PET	1.535 - 4.994	3.314
Si	PET	1.535 - 4.994	1.739
Ca	PET	1.535 - 4.994	3.692
Ti	PET	1.535 - 4.994	4.511
Mn	LIF	3.332 - 15.330	5.899
Fe	LIF	3.332 - 15.330	6.404

dards comprising the oxide species of interest were analyzed using the same spectrometer and goniometer crystal settings used in sample analysis. The standards were K-Feldspar ($KAlSi_3O_8$) for K_2O, Al_2O_3 and Si; hematite (Fe_2O_3) for FeO; spessartine ($Mn_3^{2+}Al_2(SiO_4)_3$) for MnO; rutile (TiO_2) for TiO_2; diopside ($MgCaSi_2O_6$) for CaO; albite ($NaAlSi_3O_8$) for Na_2O; and magnesium oxide (MgO) for MgO. The composition was quantified applying a standard-based ZAF correction, which was calculated by comparing the measured spectra to the standard spectra, with individual elements calibrated corresponding their specified standard. For this study, the ZAF correction program used for quantitative EPMA was *CITZAF*, developed by the National Institute of Standards and Technology [64].

Quantitative composition profiles of major elements (presented here as the oxides SiO_2, Al_2O_3, FeO, CaO, K_2O, Na_2O, MgO, MnO, TiO_2) were acquired via WDS in traverses across the diameter of each analyzed fallout spherule along a path normal to the interface between fused objects, as well as across the interface into the larger host objects. The traverses consisted of 1 micron diameter analysis spots spaced 1.5 microns apart, with a total of 9 interfaces characterized this way, exemplified in Figure 2.11 for FeO variation in sample C1. Each spot was acquired with an accelerating voltage of 15 kV and a current of 10 nA. Quantitative analyses were collected as element weight percent totals and converted to their corresponding oxide species using stoichiometric oxide conversion. In order to avoid topographical edge effects near the boundary between the sample material and the epoxy, only points more than 3 microns away from the edge were considered.

Spot analyses in fallout samples were categorized regarding their proximity to the interface. Spots with local concentration maxima or minima observed co-located with the relatively high-Z interface region identified by BSE images are designated as 'interface points', while all points not co-located with the high-Z interface are designated 'interior points', for the purposes of data discussion. Individual spot analyses were also acquired by WDS on the soil grain mounts in order to characterize the composition of the constituent phases of the soil material.

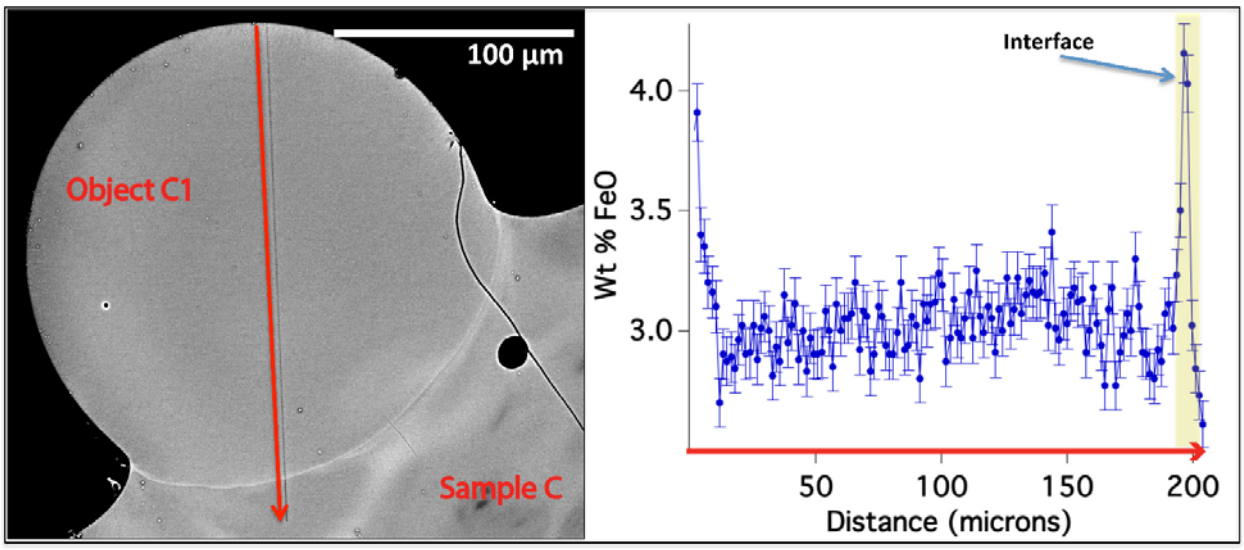

Figure 2.11: The left frame shows the BSE image of object C1, with the red line showing the traverse along which EPMA spot analyses were acquired. The right frame exemplifies the results of EPMA spot analyses along the red line, showing the variation of FeO across object C1 and its corresponding interface in weight %, with the interface points highlighted in yellow. The error bars show 1σ uncertainty determined by counting statistics and the applied CITZAF correction. The traverse of EDS spot analyses can be seen as a gray line immediately adjacent to the red arrow.

Qualitative compositional maps were also acquired via WDS in the areas around the interfaces where the smaller objects were fused to the large host object in each sample. A total of 10 interface areas were characterized this way for Si, Al, Fe, Ca, K, Mg, Mn, Ti, and Na. This is exemplified for sample D (Figure 2.12), where the Ca WDS map shows the elemental variation, reflective of what is also seen in backscatter. The maps of K, Mg, Mn, and Ti are not reported, as variation in these elements is not observable. This is due to the very low count rate for Mn (found to be $\sim$1 cps in spot analyses). For Mg and Ti, the signal-to-noise ratio was found to be very low, approaching $\sim$1 in most cases. The maps of K do not show variation, despite high count rates found in spot analyses (>900 cps) and very high signal-to-noise (>40); however, this could indicate that there is either minimal variation in K in these samples (which is not the case, see section 4.1), or that the analysis time was not sufficient to resolve compositional variation. The characterization of K and Na, two volatile elements, is explored in the next section.

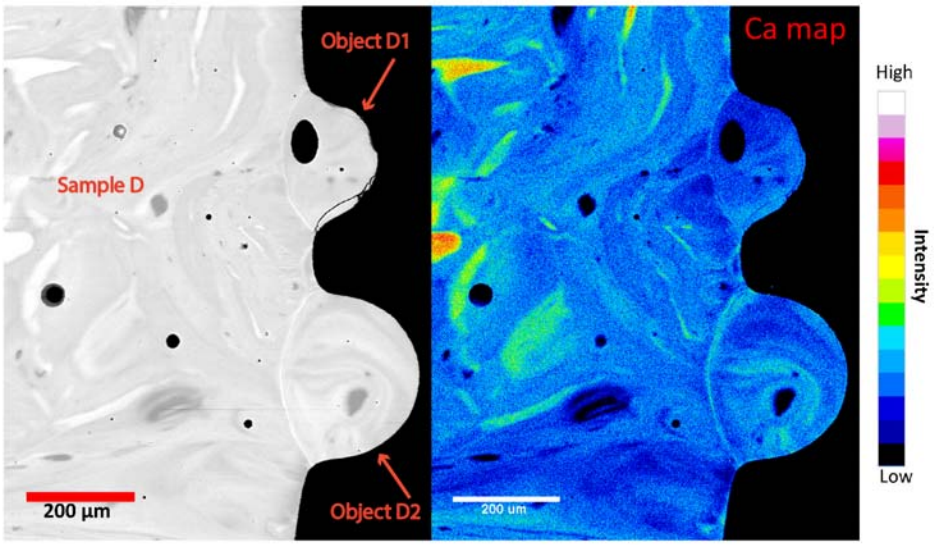

Figure 2.12: The left frame shows the BSE image of Sample D, where contrast variation represents change in average atomic number. The right frame exemplifies the results of WDS mapping, showing the variation of Ca across the mapped region of Sample D. As seen in this image, the variation in contrast often corresponds to variation in a particular element, in this case Ca.

Volatilization of Sodium and Potassium

As shown in the EPMA analyses on the fallout samples (Section 4.1), the Na_2O and K_2O concentration appears to have a high degree of uncertainty in comparison to the other measured major elements, given its concentration in the samples, and in comparison to the EDS analyses (see Section 3.4). This uncertainty may have been an effect of volatilization of Na_2O, as well as K_2O, due to electron beam interaction with the glass matrix of the samples. This effect is a well known phenomenon in electron probe microanalysis, and is attributed to a localized rise in temperature at the analysis site [65]. This change in temperature is dependent on the beam conditions, and can be calculated as follows

$$\Delta T = 1.14\frac{VI}{kd} \tag{2.9}$$

where ΔT is the change in temperature in Celsius, V is the accelerating voltage in kV, I is the current in μA, k is the thermal conductivity, and d is the spot size in microns. As suggested by Equation 2.9, the localized change in temperature increases as the spot size decreases. The study by Siivola [65] demonstrated that this volatilization effect was most profound in the alkali metals Na, K, and Cs, and was particularly apparent for Na in all of the analyzed samples (which included crystalline and amorphous samples).

In order to study the effect of alkali volatilization in the fallout samples due to electron

probe beam interactions, a series of analyses were acquired on Lake County obsidian glass, which has a composition very similar to the fallout glass that was the subject of study for this thesis [66] (further detailed in Chapter 6). A series of 10 WDS analyses were acquired for each of 5 different spot sizes, ranging from the focused probe diameter up to a 20 microns spot size, under otherwise identical conditions. The average concentration for Na_2O from 10 spots is plotted for each probe diameter, as well as the standard deviation, in Figure 2.13A. As seen in the plot, there is approximately a 15% relative depletion from the highest to the lowest probe diameter, with measured concentration systematically decreasing as the probe diameter is increasingly focused. This trend was not observed in the K_2O concentration (Figure 2.13B), consistent with the study by Siivola [65], which found that Na generally volatilizes more readily. Thus, the EPMA measurements of Na_2O made on the fallout samples may be depleted, or incorporate a degree of uncertainty in each individual measurement of more than 15%. While it is unclear to what extent this effect is present in the EDS analyses, the smaller relative variation of the spot analyses acquired by semi-quantitative EDS (rather than EPMA) suggests that these data may be more reliable for illustrating relative compositional variation of Na in the fallout samples.

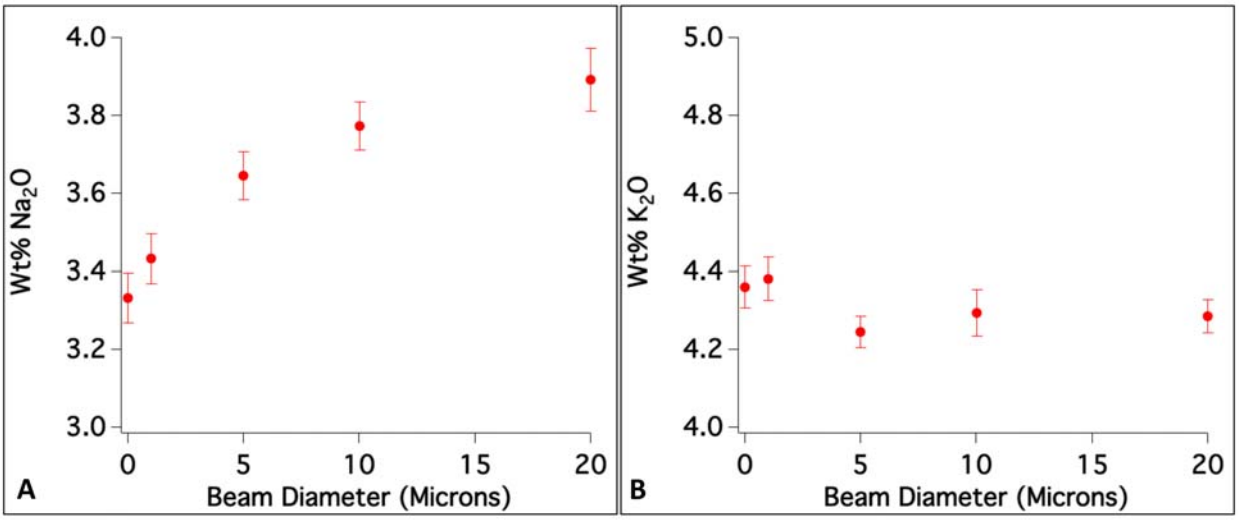

Figure 2.13: Na and K concentration in Lake County Obsidian as a function of EPMA beam size. (A) EPMA analyses for Na_2O on homogenized Lake County obsidian glass for spot sizes ranging from 20 microns down to the focused probe diameter (<<1 micron), showing a systematic decrease in concentration with increasing probe diameter. (B) EPMA analyses for K_2O using the same parameters, showing no discernible volatilization trend.

2.3 Nano-scale Secondary Ion Mass Spectrometry

Secondary ion mass spectrometry (SIMS) is a mass spectrometric technique used for acquiring spatially resolved analyses in a sample to determine isotopic composition of a species. SIMS is ideal in that a wide range of isotopes can be separated and analyzed, it is capable of measuring species in trace amounts, and has very high lateral spatial resolution [67]. In this study, a Cameca NanoSIMS 50, which is capable of sub-micron lateral spatial resolution, was used to measure secondary ions of $^{30}Si^+$, $^{54}Fe^+$, $^{44}Ca^+$, $^{235}U^+$, $^{238}U^+$, $^{235}U^{16}O^+$, and $^{238}U^{16}O^+$ across agglomerate interfaces, with a spot size of 750 nm.

In secondary ion mass spectrometry, a primary beam of ions is used to sputter material from the surface of a sample, some of which are emitted in the form of secondary ions (Figure 2.14a). SIMS instruments fundamentally comprise of a primary ion source, a primary column through which the primary beam travels and is focused on the sample, a secondary column through which the sputtered secondary ions are directed, a mass spectrometer where the ions are separated by mass and charge, and a detector (or series of detectors) to measure species of interest (Figure 2.14b).

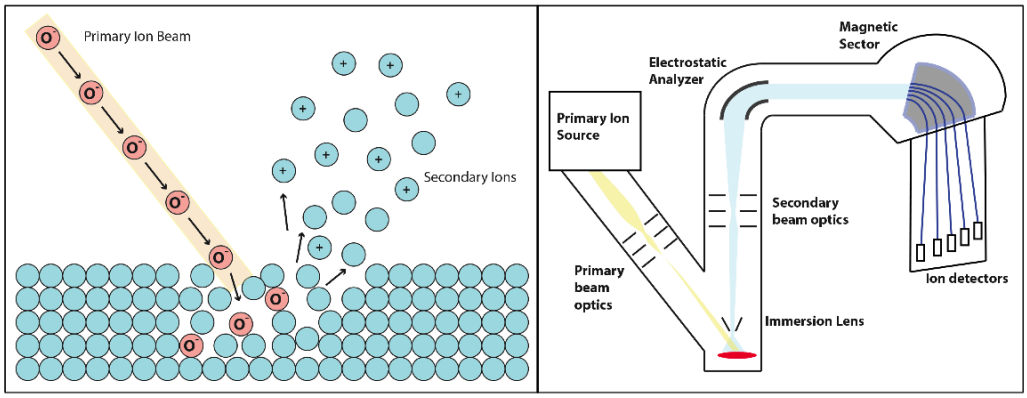

Figure 2.14: (a) illustration of primary ion beam sputtering ions and neutral species form the surface of a sample. (b) general schematic of a double-focusing SIMS instrument.

The primary ion beam can be one of numerous species, and the ions used are dependent on the sample and analytical conditions, including ion yield for the species of interest, resolution, sample conductivity, and other factors. Commonly, O_2^+, Cs^+, and O^- are used, with each species more favorable for particular analytes and sample conditions [68]. For instance, in samples where positive ions are of interest, oxygen primary ions produce a secondary ion yield enhancement, whereas cesium primary ions enhance yields of secondary negative ions. In non-conductive samples, using a negative primary ion beam is favorable to reduce charge localization effects, which can negatively affect ion yields and/or deflect the incident beam [68].

For this study, as uranium was the species of interest in the sample, an oxygen primary beam was utilized. More specifically, an O^- primary beam was used to charging effects on

the non-conductive glassy fallout samples. For oxygen ions, the most commonly used ion generation source is a duoplasmatron. However, in this study, we used a Hyperion II ion source, which has superior brightness to duoplasmatron sources [69]. The Hyperion II is an inductively coupled plasma ion source, where a tunable RF power source is coupled to a number of induction coils around a chamber. This in turn supplies energy to oxygen (or another gas) in the chamber and ionizes it. An ion beam is extracted via an aperture in the anode and accelerated down the primary column [70]. The sample is held at a voltage opposite of the anode, which attracts primary ions to the surface and repels secondary ions. The primary beam is subsequently shaped by a series of electrostatic condenser lenses known as einzel lenses, which comprises three cylindrical electrodes designed to focus the ion beam onto the sample.

As secondary ions are sputtered from the surface of the sample, they are accelerated down the secondary column through an aperture in a grounded metallic plate known as the immersion lens. In the NanoSIMS instrument, the primary and secondary ion beams are coaxial, which allows the immersion lens to be as close to the sample as possible, which increases the efficiency of secondary ion collection. In the secondary column, another series of electrostatic lenses and deflectors are used to direct the secondary ion into the mass spectrometry system [67]. This system is a double focusing mass spectrometer, comprising both an electrostatic analyzer (ESA) and a magnetic sector. The electrostatic analyzer is comprised of two curved plates held at different potentials [71]. This works to improve mass resolution by narrowing the spread of ion energies following

$$R = \frac{2V}{E} \tag{2.10}$$

where R is the radius of curvature of the deflection of the secondary beam, V is the potential between the two plates, and E is the energy of the secondary ion.

Upon exiting the ESA, the focused secondary ion beam is directed into the magnetic sector, which separates the ions by mass following Lorentz law

$$R = \frac{mv}{qB} \tag{2.11}$$

where m is ion mass, v is velocity, q is charge, and B is the applied magnetic field. This separates the incident ions in the secondary beam by their mass onto different radial trajectories. These ions are then directed towards the detection system.

In the NanoSIMS instrument, there are two types of detectors used to measure ions: a faraday cup or an electron multiplier. In a faraday cup, ions are collected in a metal cup producing a deposited charge. The current from this deposited charge is converted to voltage by measuring the signal across a resistor. This voltage signal can be used to calibrate the number of counts per second detected on the faraday cup. A faraday cup is particularly useful for measuring very high count rates ($>1\times10^6$ cps) [67].

In this study, electron multipliers were used as the ion detectors. In an electron multiplier, a conversion electrode produces electrons upon collision of the secondary ions. These

electrons are accelerated onto acceleration electrodes known as dynodes, each of which produce multiple electrons for every electron impact. Thus, for each detected ion, up to 10^9 electrons are generated, with the number of electrons and the subsequent current produced a function of the impact energy and acceleration voltage of the ions [67]. This type of detector has much higher sensitivity than the faraday cup detector, but cannot accommodate high count rates (the maximum count rate in this study was for ^{30}Si at ~100000 cps). The NanoSIMS instrument has 5 electron multipliers, which can be moved to detect magnetically separated ions on different radial trajectories (as dictated by equation 2.11) without having to change the B-field in the magnetic sector. Secondary ions of $^{30}Si^+$, $^{54}Fe^+$, $^{44}Ca^+$, $^{235}U^+$, and $^{235}U^{16}O^+$ were collected simultaneously, at a magnetic field of 3791 mT. The secondary ions $^{238}U^+$ and $^{238}U^{16}O^+$ were collected simultaneously, at a magnetic field of 3815 mT.

In order to acquire quantitative measurements using secondary ion mass spectrometry, a constant concentration of primary ions must be present in the surface, as changes in the sample matrix can affect ion yields [72]. This steady state, known as sputtering equilibrium, was determined in these analyses by looking at the yield of ^{235}U in each measurement cycle, and removing those cycles that fell below the steady state count rate (exemplified in Figure 2.15). Sample analyses were acquired as secondary ion images of 20×20 μm^2 areas (*e.g.,* Figure 2.16a), with each image constructed from a series of 75-100 cycles of 256×256 pixel rasters (except Sample A1, which was constructed from a 10×10 μm^2, 128×128 pixel raster).

To quantify the variation of ^{54}Fe, ^{44}Ca, and ^{235}U across the interface on fallout samples, the ion images were normalized to ^{30}Si, which was found to be relatively constant (<10% variation in the image). This is exemplified in Figure 2.16, where the ^{30}Si ion image is shown at the interface of object C1 (Figure 2.16a), as well as the variation across the interface (Figure 2.16b).

Thus, isotope ratio images of $^{54}Fe/^{30}Si$ (except Sample A1, which used $^{56}Fe/^{30}Si$), $^{44}Ca/^{30}Si$, $^{235}U/^{30}Si$, and $^{235}U/^{238}U$ were then generated from the ion images, wherein the ratio image is an intensity map of an isotope ratio at each interface. Isotope ratio images were constructed using L'Image software [73]. Each ratio image was smoothed using a 9-pixel smoothing function (which approximated the NanoSIMS spot size used in this study, 750 nm). This is exemplified in Figure 2.17, where the ratio image of $^{235}U/^{30}Si$ at the interface of object D2 is shown (Figure 2.17a) as well as its relative position in BSE imaging (Figure 2.17b).

In order to construct isotope ratio profiles, a 15-pixel wide line was drawn normal to and across the interface between the two fused objects in each isotope image. The width of the line was selected to minimize the uncertainties in regions where count rates were low, while still accurately representing the variation of the isotope ratio across the interface. The 1σ measurement uncertainties for isotope ratios derived from the profiles (as determined from counting statistics) were <1% for $^{44}Ca/^{30}Si$, $^{54}Fe/^{30}Si$, and $^{56}Fe/^{30}Si$, <5% for $^{235}U/^{30}Si$, and <10% for $^{235}U/^{238}U$ (the full data set is given in Appendix C).

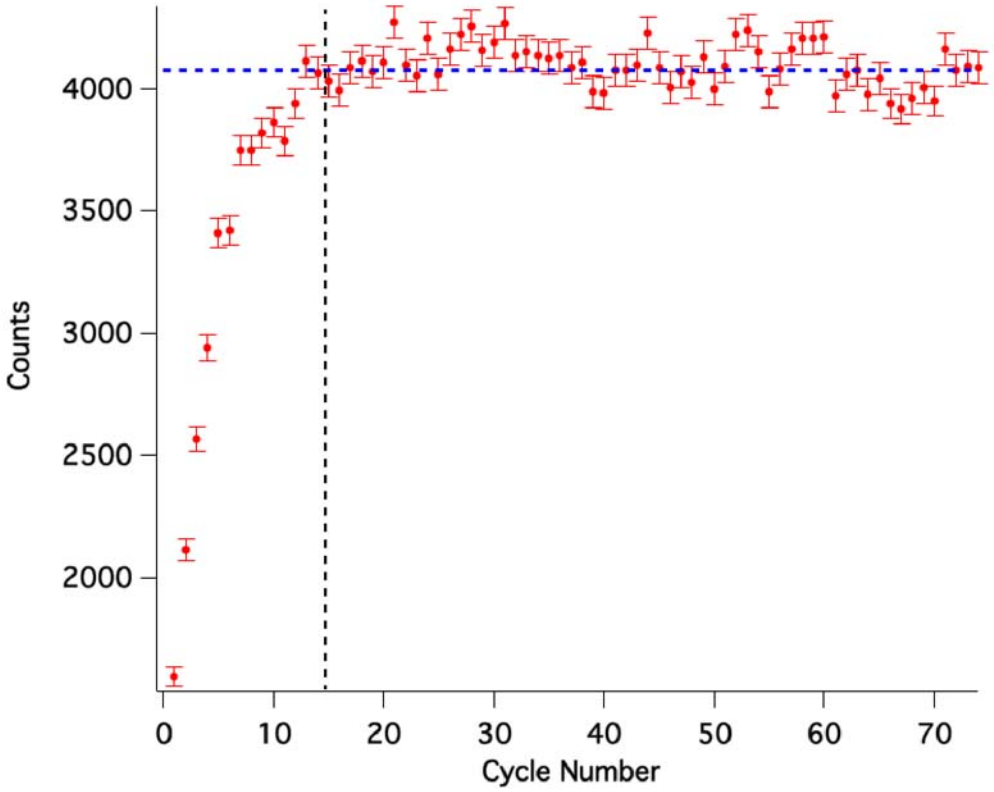

Figure 2.15: Sputtering equilibrium determined for NanoSIMS analysis of object C1, based on counts/cycle of ^{235}U. The blue line represents the average of the last 30 cycles, and was used as a determination of equilibrium counts/cycle, and the black line indicates where equilibrium was acquired at cycle 15. Uncertainties are 1σ.

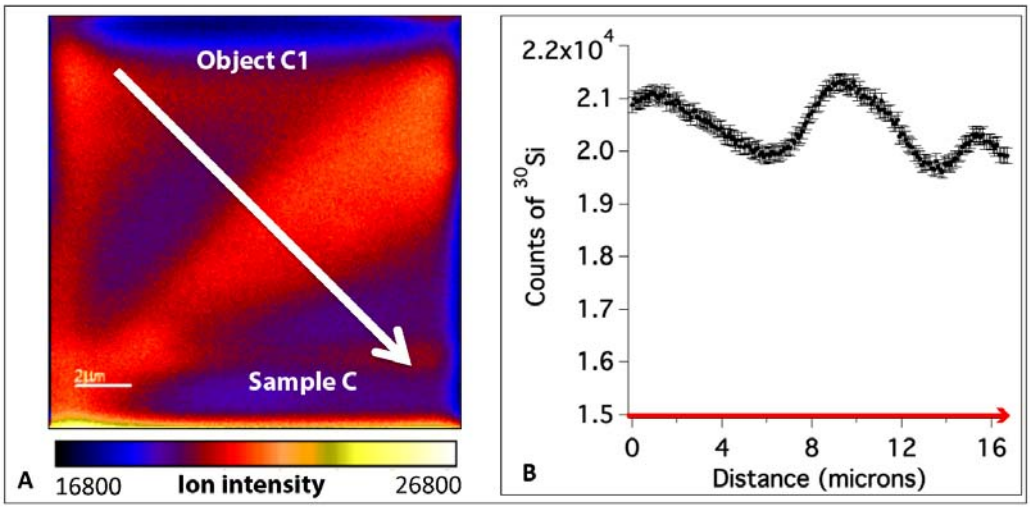

Figure 2.16: (A) Ion image acquired by NanoSIMS of ^{30}Si at the interface of object C1, where variation is shown an intensity map (the color bar is in total counts per pixel), with red and yellow depicting the highest intensity and blue and black depicting the lowest intensity. The white arrow indicates the path of the traverse shown in (B), from object C1, across the interface, and into the larger host object. (b) Plot of counts of ^{30}Si along the white arrow shown in (a), which has an average value of 20463±483 counts (representing a 2.4% standard deviation). The variation in Si does not exceed 10% for any interface.

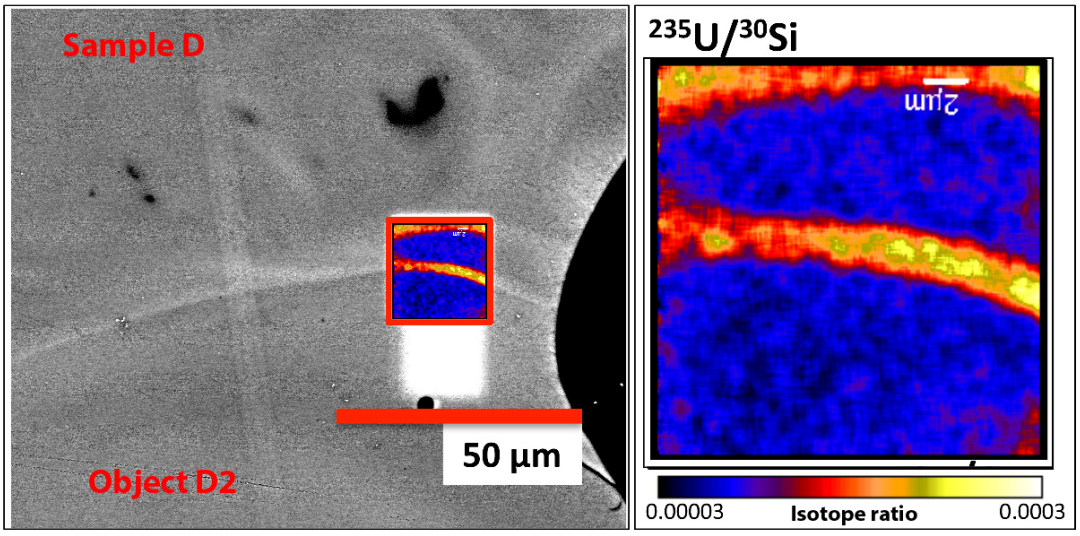

Figure 2.17: The left frame shows a BSE image of sample D, showing the relative position of the ratio image. The right frame shows the isotope ratio image of ^{235}U/^{30}Si at the interface of Object D2 and Sample D.

Analyses of Standards

Due to the the variable ionization properties of different species in different matrices, quantitative analysis by SIMS is only possible with the use of standards. Quantitative determination of concentrtation requires the use of relative sensitivity factors (RSF) as determined from standards. These relative sensitivity factors are acquired for species of interest in a specific matrix, and concentration can be determined following

$$\frac{I_R}{C_R} = RSF_E \frac{I_E}{C_E}\,, \tag{2.12}$$

where I_R and I_E are the secondary ion intensities of the reference element and element of interest, respectively, C_R and C_E are the concentrations of the reference element and element of interest, respectively, and RSF_E is the relative sensitivity factor for the species of interest. The RSF values are typically derived from calibrated standards [68].

The standards used in this study included both a matrix-matched glass standard (to measure concentration and uranium isotope ratio), as well as a U_3O_8 standard (as a second measurement of isotope ratio, for comparison). The ^{235}U-enriched glass standard was created at LLNL by fusing 5% by weight of the CRM U100 U_3O_8 standard into a matrix of approximately 32% SiO_2, 37% Al_2O_3, and 31% CaO. The RSF was determined for the ratio of (^{235}U+^{238}U) / ^{30}Si to be 0.07 ± 0.04. This value is comparable to the RSF ratio of U/Si of 0.12 in a silicon matrix, as determined by Wilson using an oxygen primary beam [74]. The uncertainty on the measured RSF ratio was attributed to compositional heterogeneity in the glass. The absolute concentration of uranium in these samples was determined by

$$C_U = A \cdot C_{^{30}Si} \cdot RSF_{U/Si}(1 + \frac{1}{B})\,, \tag{2.13}$$

where A is the ^{235}U/^{30}Si ratio, B is the ^{235}U/^{238}U ratio, and $C_{^{30}Si}$ is the concentration of ^{30}Si determined by EPMA (and the natural abundance of ^{30}Si).

Measurements on standards were conducted to calibrate the ^{235}U/^{238}U values. This calibration takes into account the instrumental mass fractionation of uranium isotopes over the course of the analyses, and were conducted on both a matrix-matched glass standard (U100) and a U_3O_8 particle standard (U200) as described above [75, 76]. The U100 analyses were acquired as ion images (12×12 μm^2). Analyses on the U200 particle standard were acquired as 10×10 μm^2, 64×64 pixel rasters, not measured as ion images, but instead as ion sum totals.

As seen in Figure 2.18, the isotope ratios images of ^{54}Fe/^{30}Si, ^{44}Ca/^{30}Si, ^{235}U/^{30}Si, ^{235}U/^{238}U are presented for the U100 glass standard (the same isotope ratio images presented for fallout samples). From the images, it is clear that there is compositional heterogeneity in the sample for Fe, Ca, and U, which have maximum variations of >300%, 140%, 240%, and 180% respectively. This heterogeneity is likely due to the manufacturing process of the glass standards (which were produced in house at LLNL [77]). The ratio image of ^{235}U/^{238}U does, however, show a relative homogeneity in comparison to the other isotope ratio images.

As only the relative chemical variation of Fe, Ca, and U was necessary for the study, and the $^{235}U/^{238}U$ ratio image indicates isotopic homogeneity, the U100 glass standard was found to be appropriate for $^{235}U/^{238}U$ calibration.

In order to minimize potential edge effects, the edge of the rasters were excluded by using a region central to the ion image. This is shown in Figure 2.19, where there is a clear region of high signal intensity around the periphery of the image, which is likely an analytical artifact. These edge effects are likely due to crater formation from sputtering via the incident beam, which can affect sample topography (see Figure 2.20, which shows the crater formed from ion imaging by the NanoSIMS in SE imaging). To avoid this effect, a region of interest was acquired for each ion image, defined as a 10×10 micron box in the center of each image to avoid edge artifacts (Figure 2.19). The counts of ^{235}U and ^{238}U within this box were summed, and used to acquire the $^{235}U/^{238}U$ ratio for each U100 standard analysis, which are presented in Table 2.4.

Also shown in Figure 2.18 (rightmost image) is the relative error image. In this image, the yellow region represents regions of high relative error, and the black/blue regions represent regions of low relative error as calculated by

$$\delta R = \frac{\sigma R}{R} \tag{2.14}$$

where δR is the relative error, σR is the uncertainty on the ratio at a given pixel, and R is the ratio of interest (in this case $^{44}Ca/^{30}Si$). As seen in the relative error image, the region of interest (white box) was chosen to avoid the region of highest relative error (at the top) and mitigates the influence of edge effects.

In Table 2.4, the results from both the U100 and U200 standard analyses are presented, as well as their certified reference values. The measurements for both standards shows a minimal degree of isotopic variation between each analysis, regardless of whether they were acquired as ion images (in the case of U100) or simply as rasters (in the case of U200). The deviations from the certified value for each analysis are also presented. As indicated in Table 2.4, there is little deviation from the certified $^{235}U/^{238}U$ value in any single measurement for either U100 glass or U200 (as a particle), illustrative of the accuracy and precision of the uranium isotope ratio measurements acquired in this study. The average deviation was 1.5%. As shown in Table 2.4, the U100-doped glass has a $^{235}U/^{238}U$ ratio of 0.1136 ± 0.0001 (measured at LLNL by ICP-MS), and 20% ^{235}U enriched U_3O_8 particle standard (CRM U200, certified $^{235}U/^{238}U$ ratio $= 0.2512 \pm 0.0003$) was also used. The glass and U_3O_8 particle standards yielded measured percent deviations from the certified $^{235}U/^{238}U$ ratios of 1.5% and 2.5%, respectively.

Even with the use of calibrated standards, interferences can produce inaccurate results in SIMS (and mass spectrometry, generally). These interferences come in the form of molecular species that have masses close to that of the species of interest, isotopes of different elements having the same mass number, or even other isotopes of the same element if the mass number is sufficiently high. The interferences of interest for this study were $^{208}Pb^{27}Al$, which interferes with ^{235}U measurements, and $^{29}Si^{1}H$, which interferes with ^{30}Si measurements. These

interferences were resolved by using the above described double-focusing mass spectrometer in combination with a physical barrier in the form of a slit. Wider slits allow a wider range of ion masses through, while narrow slits have higher mass resolving power, which comes at the cost of signal intensity. Mass resolving power, a factor that is often used to ensure that interferences are satisfactorily resolved, can be calculated by

$$R = \frac{M}{\delta M} \tag{2.15}$$

where R is the required mass resolving power, M is the mass of the species of interest, and δM is the mass difference between the species of interest and the potential interference mass. For this study, a mass resolving power (M/δM) of 4000 was used, which was sufficient to resolve both ^{208}Pb^{27}Al (required M/δM = 2741) and ^{29}Si^{1}H (required M/δM = 2841).

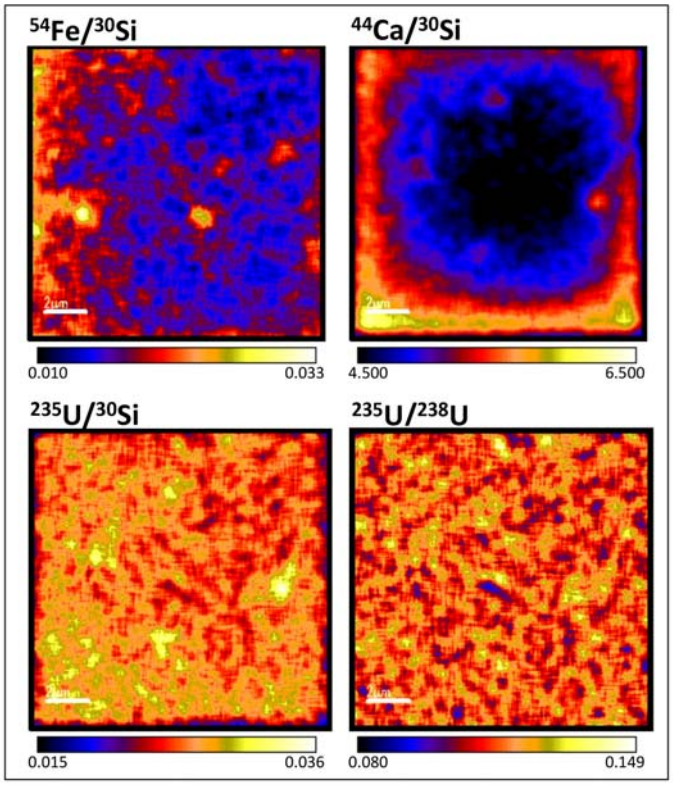

Figure 2.18: Isotope ratio images for ^{54}Fe/^{30}Si, ^{44}Ca/^{30}Si, ^{235}U/^{30}Si, ^{235}U/^{238}U acquired from one analysis raster (12×12 μm^2) on the U100 glass standard (pixel size is ∼90 nm). The color bar shows the value of each isotope ratio at each pixel.

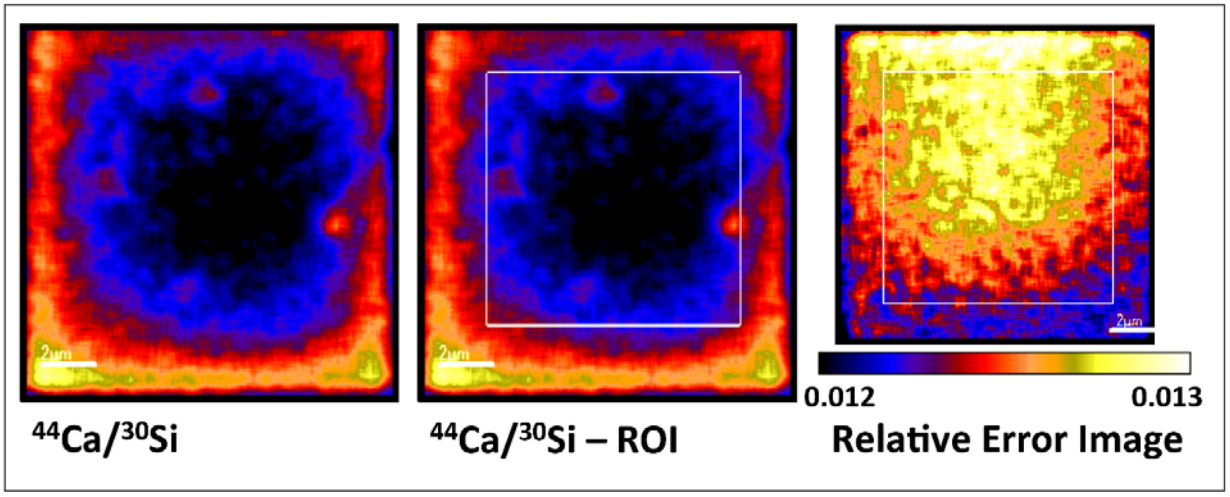

Figure 2.19: The left image shows the isotope ratio image (12×12 μm^2) of ^{44}Ca/^{30}Si from Figure 2.18 (same color scale, pixel size ∼90 nm). The middle frame shows the isotope ratio image of ^{44}Ca/^{30}Si from Figure 2.18, with the region of interest used for standard analysis shown as a white box (10×10 μm^2) in the center of the image. The right frame shows the relative error image, where yellow represents regions of high relative error, and the black represent regions of low relative error. The color scale here represents the value of the 1σ uncertainty on the ^{44}Ca/^{30}Si ratio at each pixel.

Table 2.4: Summary of standard analysis results for ^{235}U/^{238}U ratio acquired from both the U100 and U200 standards. Uncertainties are 1σ on both the isotope ratios and the % deviation.

Sample ID	^{235}U/^{238}U	% Deviation
U100	0.1167±0.0016	2.18±0.67
U100	0.1148±0.0015	0.53±0.66
U100	0.1145±0.0023	0.29±1.56
U100	0.1153±0.0002	0.99±0.10
U100	0.1158±0.0003	1.46±0.13
U200	0.2428±0.0031	3.37±0.62
U200	0.2479±0.0030	1.34±0.60
U200	0.2464±0.0032	1.93±0.64
U100 reference value	0.1142±0.0001 [75]	
U200 reference value	0.2513±0.0003 [76]	

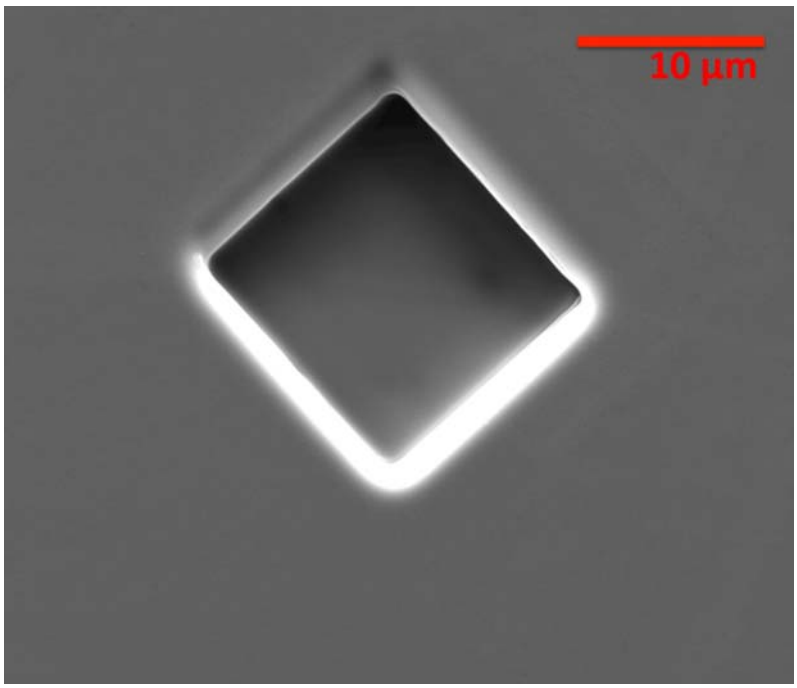

Figure 2.20: SE image of a NanoSIMS crater on Sample B3, the borders of which can give rise to edge effects which can locally affect ion image intensities, as shown in Figure 2.19. The bright, saturated regions are where the primary ion beam sputtered away the conductive carbon coating, causing sample charging.

Chapter 3

Qualitative Compositional Analysis

3.1 Backscatter Electron Imaging

After polishing the samples to expose their interiors and interfaces, samples were imaged in backscatter electron imaging (Table 2.1). This imaging shows the spatial distribution of average atomic number variation across the sample and the interface, and is used to qualitatively characterize the composition. In backscatter electron imaging, the interface in every sample appears as a bright, white boundary, separating the attached spherule from the larger host object, indicating higher average atomic number.

In Sample A, the interface appears diffuse, and is approximately 10 microns at its widest point (Figure 3.1). The edge of object A1 where the sample meets the epoxy also appears bright in backscatter electron imaging, and looks continuous with the interface. However, it is unclear if the brightness along the edge is due to an actual higher atomic number feature, or if it is simply an edge effect. The effect of charging is most obvious in the large central crack, where irregular regions of high brightness are present. Cracking in these samples is very common after polishing, as the glasses are likely under high internal stress due to rapid quenching, as well as the expansion of the epoxy as it cures. Also seen in Figure 3.1 is what appears to be another interface that extends to the bottom righthand side of the image. This is likely another agglomerated object that fully incorporated into the larger host object, a feature that is commonly found throughout the sample set.

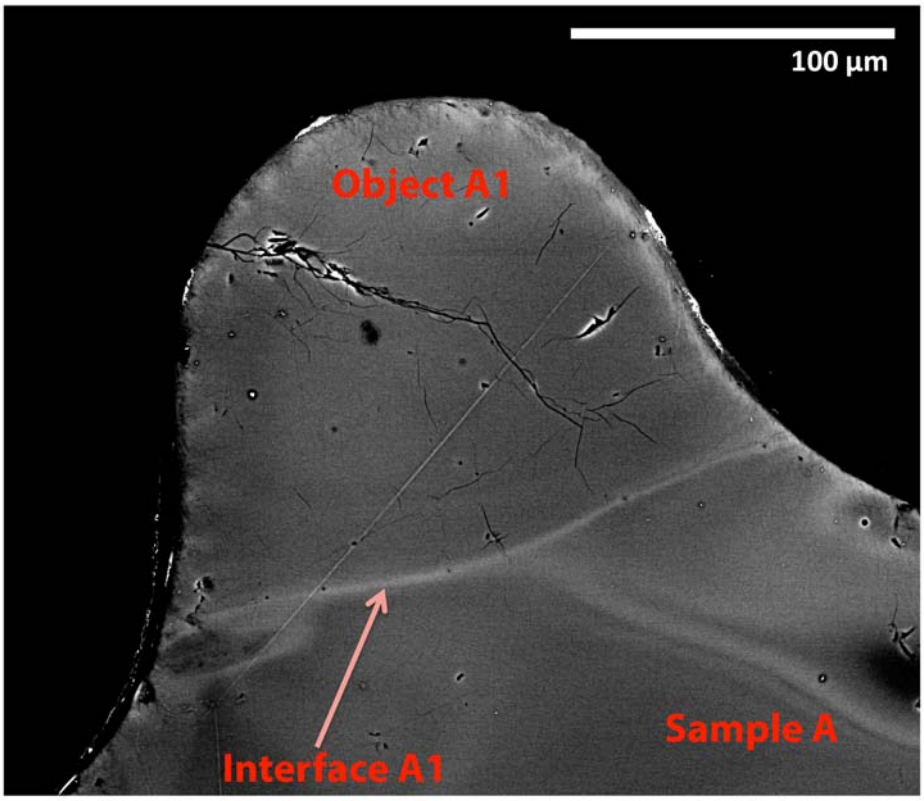

Figure 3.1: Backscatter electron micrograph of object A1 on Sample A, with the interface indicated by the red arrow. The effects of charging is apparent around the perimeter of Object A1 as bright white regions, which are also seen around the large central crack.

In Figure 3.2, the backscatter micrograph of Sample B shows the interface of where the two attached spherules are fused (interface B1), as well as the interface of where the one of these spherules is attached to the larger host object (interface B3). Next to and intersecting interface B1, there is another interface (interface B2), which outlines an object that is fully incorporated into the larger object central to Figure 3.2. The contrast variation within this sample shows a number of interesting features present in the sample. First, there appear to be several compositionally distinct agglomerated objects around the perimeter of the large central object (which is fused at interface B3), that have fully incorporated into B3. Additionally, there is considerable compositional banding across the object, which is indicative of flow while the carrier was still molten. There are also several voids of varying size (micron-scale to tens of microns in diameter), which appear as black circles in the body of the sample. These voids are likely the result of degassing of the molten material. Finally, diffuse, dark regions (*i.e.,* low average atomic number) are present throughout this sample and the sample set as a whole, and are indicative of relict (incompletely melted/mixed) minerals in the carrier, presumably from the original mineral/soil host object.

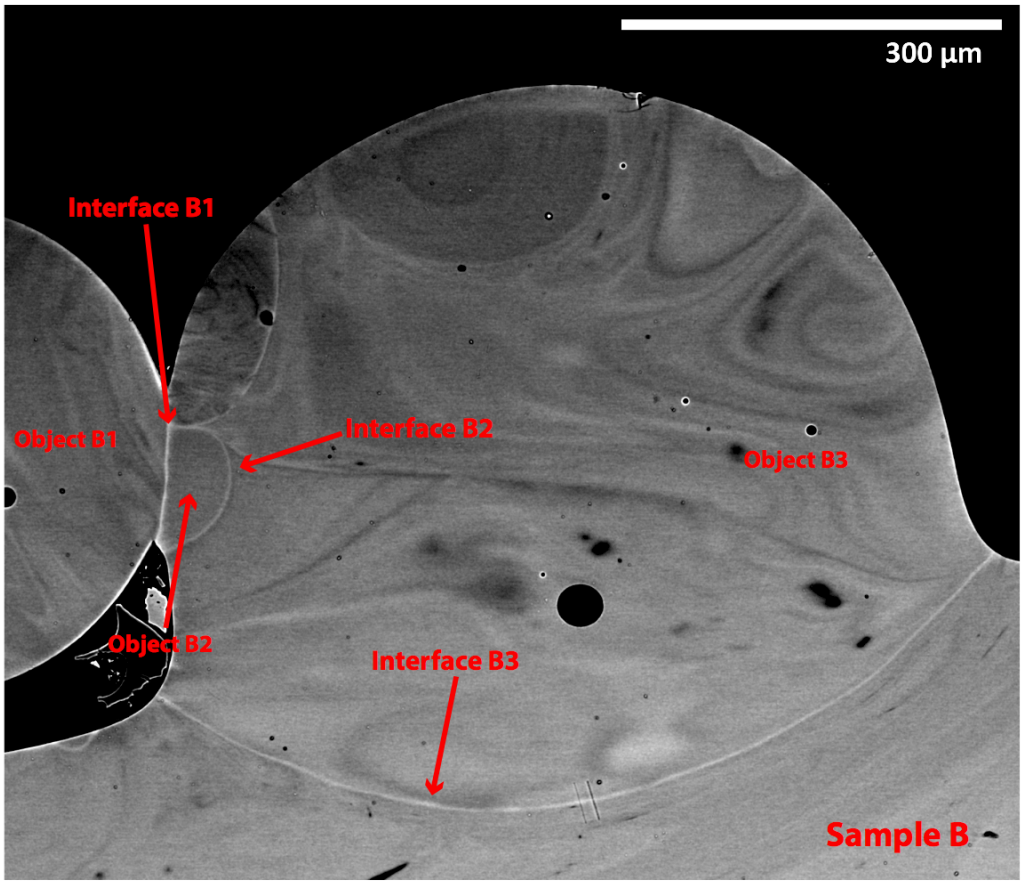

Figure 3.2: Backscatter electron image showing objects B1, B2, and B3, with each object and interface indicated by a corresponding red arrow. Flow banding is evident throughout the objects, particularly in Object B3, which features relict mineral grains and numerous small voids.

The backscatter electron image of Sample C (Figure 3.3) is shown inverted relative to its corresponding optical image (see Figure 1.8), with the agglomerated objects of interest at the top of the image. The entire sample is shown in the backscatter image. The contrast variation in the image shows what appears to be a heterogeneous host, with relatively homogeneous spheroidal objects fused to its surface (sample heterogeneity is further discussed in Section 3.2). In the larger host object, there appear to be numerous relict minerals of distinct composition, observable as regions of varying brightness. As with the previous Sample B, there are a number of voids, as well as evidence of flow banding. The fused objects themselves show little relative compositional variation under the contrast and brightness conditions provided in this backscatter image. Further, each agglomerated object (from left to right) shows an increasing degree of incorporation into the larger host object.

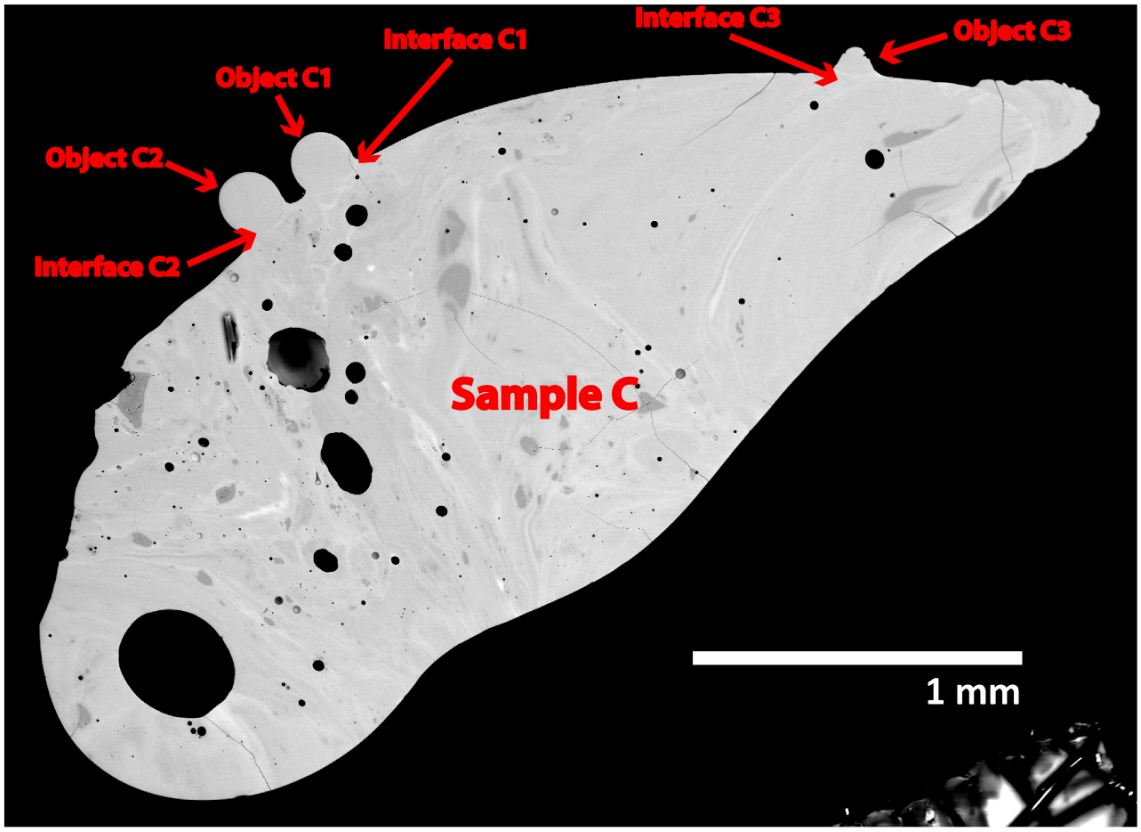

Figure 3.3: Backscatter electron image of Sample C, with Objects C1, C2 and C3 (and their interfaces) indicated by red arrows. Objects C1, C2, and C3 appear relatively homogeneous in comparison to the larger Sample C, which has numerous relict minerals and several large interior voids (as well as many smaller voids).

The backscatter image of Sample D (Figure 3.4) shows that the large object and the smaller fused objects are compositionally heterogeneous. There is obvious compositional banding, indicative of liquid phase flow, that continues from the large object into either of the smaller fused objects shown in the electron micrograph. The object on the left (Object D1) hosts a large void within its volume, which appears to be deformed directionally against the host, and appears to have chipped and cracked where the surface of the object meets with the epoxy. Such defects in the surface of Object D1 may be the result of environmental exposure effects or, more likely, a result of polishing. The righthand object (D2) hosts an apparent relict mineral grain, which can be seen as a diffuse, dark bleb. Interestingly, the flow banding in Object D2 appears to follow the contours of the relict grain, suggesting flow as a result of rotation of the relict grain within the volume of the object while molten.

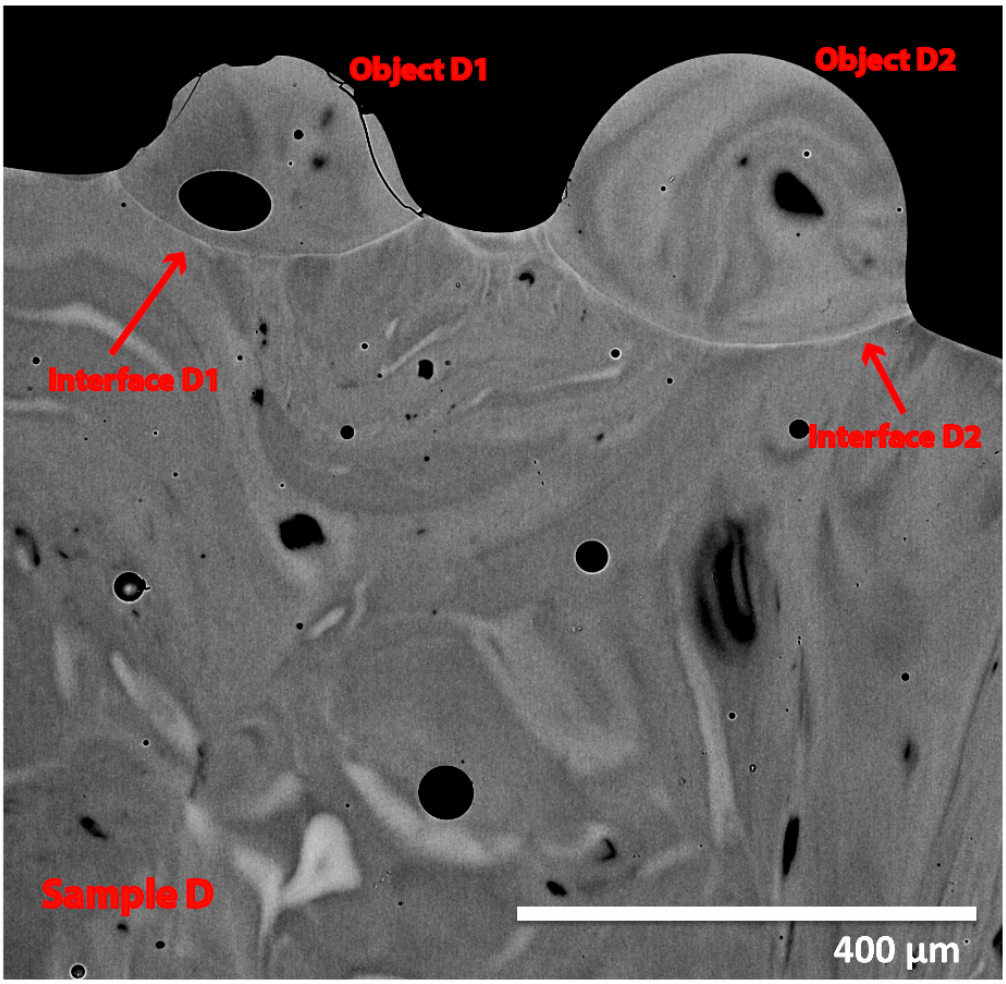

Figure 3.4: Backscatter electron image of Sample D, with Objects D1 and D2 (and their interfaces) indicated in red. The larger Sample D appears to host both lower and higher relative atomic number relict mineral, as well as several obvious voids. Object D1 hosts a large central void, while Object D2 hosts a lower atomic number relict mineral.

Upon polishing, the interfaces of Object E1 and included Object E2 were exposed, as shown in backscatter electron imaging (Figure 3.5), and found to be approximately co-planar. The most striking feature shown here is the very large (approximately 1 mm in diameter) central void in the host. The exposed region to the top-right of the host that appears detached from the rest of the sample is the large spherical object that is barely fused to the surface. It appears detached by virtue of where it fused to the host; it would required further polishing to reveal the interface of this object (it is not co-planar with E1 and E2). The attached Objects E1 and E2 do not appear to have the level of heterogeneity illustrated by the rest of the host sample, although Object E2 does have two relict mineral

grains embedded in its volume.

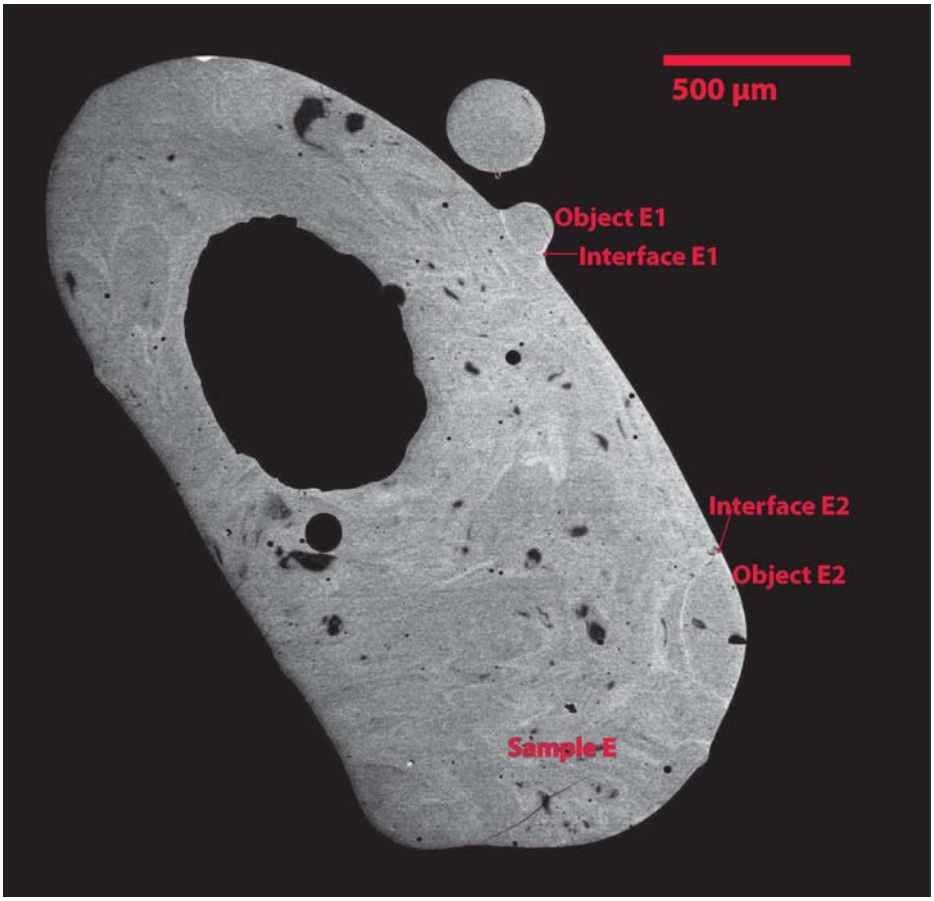

Figure 3.5: Backscatter electron image of Sample E, with Objects E1 and E2 (and their interfaces) indicated by red arrows. While Object E1 is spheroidal and fused to the surface, Object E2 is flattened and almost fully incorporated into the larger host. The larger host object of Sample E appears relatively heterogeneous, and hosts a mm-scale central void. A third object (top right), which appears detached, is indeed fused to Sample E, but the interface is not co-planar with the other objects and is therefore not visible in this image.

The backscatter electron images of soil (exemplified in Figure 3.6) reveal that individual soil grains consist of numerous mineral compositions of varying sizes. The observed grains are consistent with previous analyses of soil from this test [55] in that they were characteristic of granitic and rhyolitic clasts, containing porous and microcrystalline features. As seen in the electron micrograph (Figure 3.6), there are a range of mineral compositions from relatively high average atomic number (an iron rich mineral, later identified by EPMA as ilmenite in Chapter 4) to relatively low atomic number (an SiO_2 rich mineral, later identified by EPMA as quartz in Chapter 4) within a single soil grain. The black regions are epoxy which, within the sample, highlights the microcrystalline structures characteristic of clay

minerals, which predominate. As has been shown, the fallout is comprised of molten and partially homogenized soil grains such as those shown in Figure 3.6, and is commonly found to host relict mineral grains, which are likely the result of larger minerals in the soil that did not have time to fully diffuse or otherwise mix into the rest of the melt prior to quenching.

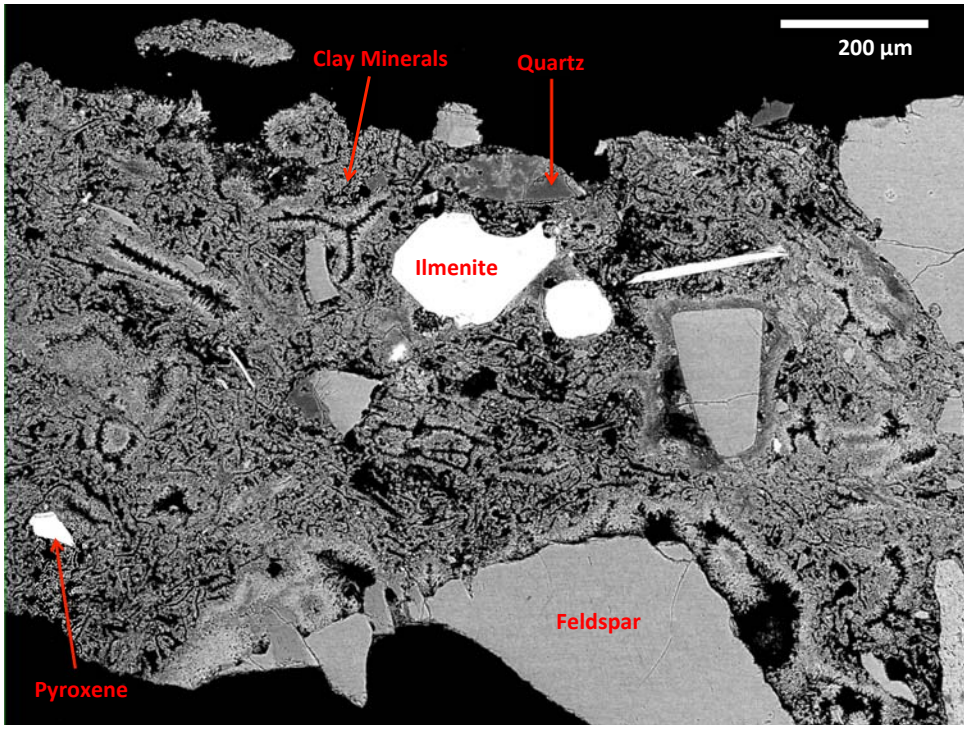

Figure 3.6: Backscatter electron image of a soil grain, illustrating the general heterogeneity of the soil. Key minerals were later identified (by EPMA, see Chapter 4), on the basis of composition.

3.2 Relative heterogeneity and morphology of fused glassy objects

Sample heterogeneity was characterized by examining the contrast variation in backscatter electron imaging between the larger host object (Samples A, B, C, D, and E) and select agglomerated objects (Objects A1, B1, B2, B3, C1, D1, D2, and E1). The degree of heterogeneity represented by the relative grayscale intensities does not translate from image to image, as the brightness and contrast was not kept consistent between the images, but instead maximized to highlight local compositional variation. However, the difference in contrast variation within images of single samples can be used as a qualitative metric for understanding the extent of mixing and homogenization within the analyzed fallout glasses.

The relative brightness distributions of each object was determined in *ImageJ* image processing software by acquiring a histogram of gray-scale intensity (256 intensities) for all pixels in each object, from BSE images. The brightness and intensity of objects within a single image were normalized to accentuate the contrast variation such that objects would be comparable within each BSE image. Voids and epoxy, which had the lowest relative brightness of any feature, were excluded by thresholding.

Contrast Variation Plots

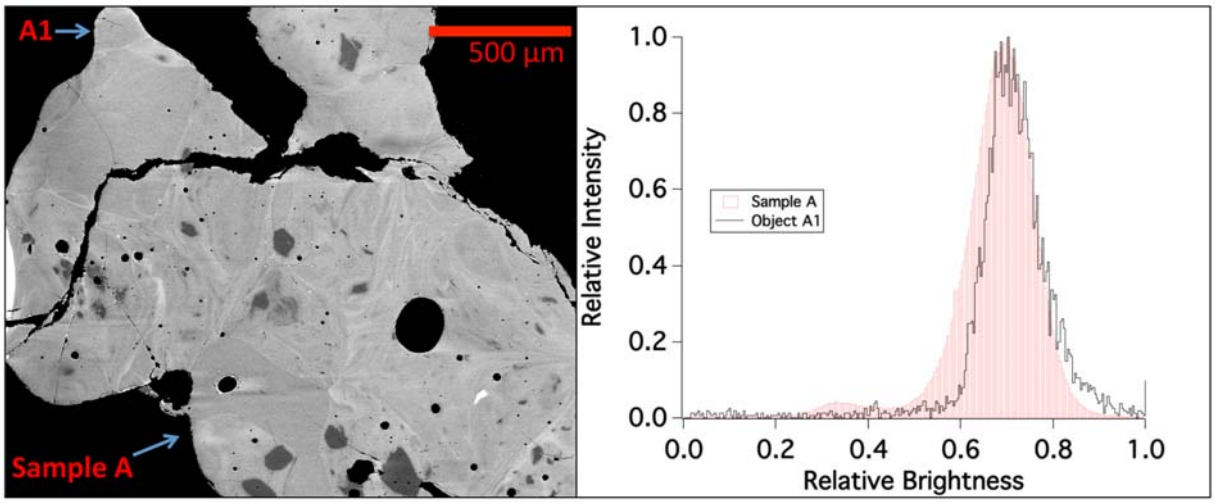

Figure 3.7: Left, backscatter electron image of part of Sample A from which contrast variation was measured. Right, histograms of Object A1 as well as Sample A are plotted, normalized to maximum frequency. The histogram of relative brightness of Object A1 reveals relative homogeneity in comparison to Sample A.

In Figure 3.7, the contrast variation shows the relative heterogeneity between the smaller fused object (A1) and the host (Sample A). As seen in Figure 3.7 (right frame), the primary peak of the host object has a slightly larger spread in contrast than the smaller fused object (A1). Further, the larger host object has a secondary peak at a relative brightness of 0.3. Based on the contrast variation, the larger object shows a slightly greater degree of heterogeneity at relatively lower Z when compared to the smaller fused Object A1.

In Figure 3.8, the contrast variation was acquired for Sample B, in the same manner as described for Sample A, above. The BSE image shown in Figure 3.8 (left frame) shows attached Objects B1, B2, and B3 (B2 is fully integrated into B3, see Figure 3.2). As shown in Figure 3.8 (right frame), the host object shows a range of contrast variation that is substantially broader than either attached Objects B1 or B2 and B3, which are combined into a single contrast variation curve. However, this could be due to a systematic decrease in brightness from the right side of the object to the left side of the object, as can be seen

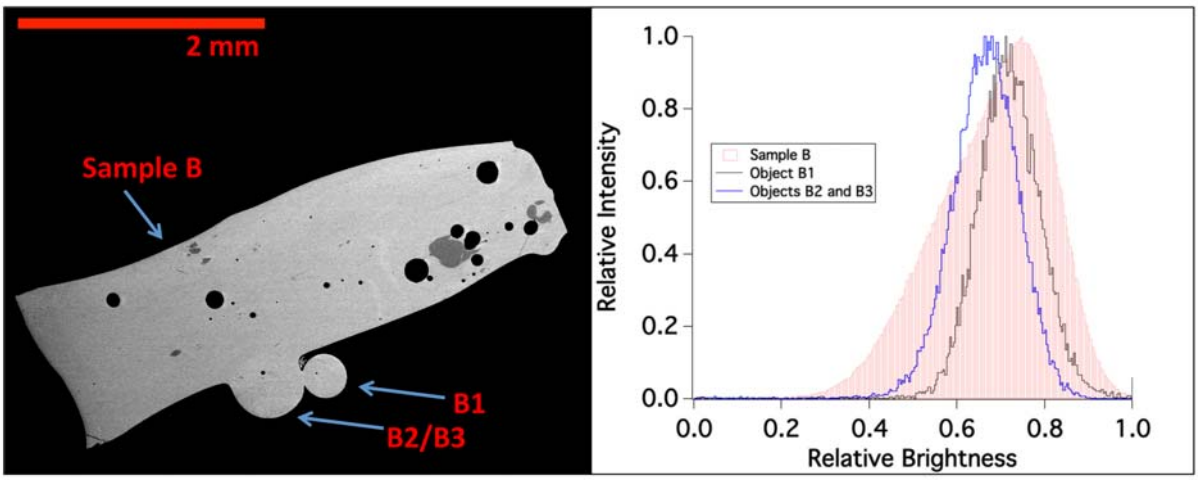

Figure 3.8: Left, backscatter electron image of the entirety of Sample B, including attached objects B1, B2, and B3. Right, histograms of the relative brightness for B1, and B2/B3 together, as well as the larger host object are plotted, showing similar relative heterogeneity in Objects B1, B2, and B3. The width of the relative brightness histogram of Sample B may be due to misalignment of the sample during analysis.

in the BSE image (Figure 3.8, left frame). The systematic variation observed may be due to misalignment of the sample during analysis. The attached objects, while offset from one another in terms of their relative brightness variation, have approximately the same peak width, indicating similar degrees of compositional heterogeneity at these boundaries.

In Sample C, the large object is host to a numerous relict mineral grains, as apparent in BSE imaging (Figure 3.9, left frame). The smaller adhered objects are generally homogeneous when compared to the larger host object, as exemplified by the contrast variation plots of both the adhered Object C1 along with the larger host object, as shown in Figure 3.9 (right frame). The contrast variation plot for Sample C shows a convolution of two peaks in relative brightness (one at approximately 0.55, and another at approximately 0.62 relative brightness). The contrast variation of attached Object C1 has a single quasi-Gaussian brightness distribution, with a peak at approximately 0.6 relative brightness. The distribution of Object C1 is notably narrower than the extent of the distribution of the larger host object, indicating that C1 is relatively more homogeneous.

In Sample D, BSE imaging (Figure 3.10, left frame) of this fallout object shows visible heterogeneity in the form of numerous relict mineral grains. The smaller adhered Objects D1 and D2 display a degree of visible heterogeneity that was not obvious in Object C1. Flow banding can be seen extending from the larger host into the interior of Object D2. The resultant heterogeneity of all of these objects is shown in Figure 3.10 (right frame). In this figure, the normalized contrast variation for all of the objects gives a brightness distribution that is approximately the same for both attached Objects D1 and D2, as well

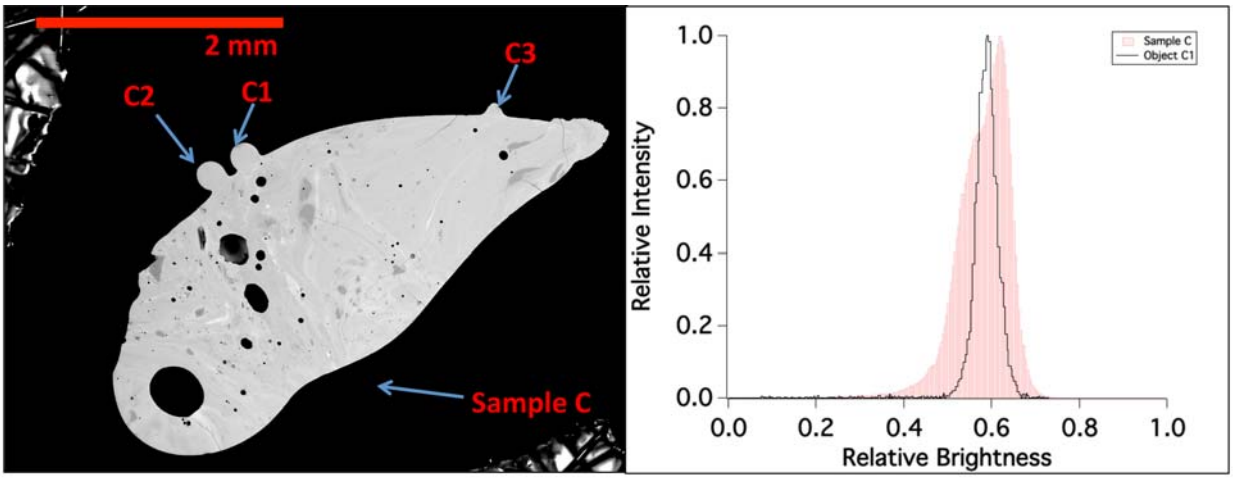

Figure 3.9: Left, backscatter electron image of the entirety of Sample C, including attached Objects C1, C2, and C3. Right, histograms of the relative brightness for C1 as well as the larger Sample C are plotted, showing the relative homogeneity of Object C1 compared with Sample C.

as the larger host object. There is a slight offset in brightness between each of the objects, potentially indicating a gross compositional difference. However, given the similarity in width of each of the relative brightness distributions, it can be ascertained that a similar degree of heterogeneity is present not only between the smaller Objects D1 and D2, but also of the larger host.

In Sample E, BSE imaging (Figure 3.11, left frame) depicts a largely heterogeneous host object with a mm-scale central void. Object E1 is adhered to the surface, while Object E2 is shown integrated into the body of the host object. The large host shows compositional flow banding as well as multiple relict mineral grains. The contrast variation of object E1 as well as the larger host object is shown in Figure 3.11 (right frame). In this plot, the relative brightness distribution of the host object appears as a convolution of at least two peaks, similar to that of the larger host object in Sample C. The slight intensity increase near the origin is likely due to voids, which were unable to be excluded from the measurement based on size. The relative brightness distribution of the smaller fused Object E1 is substantially narrower than the host, indicating a much higher degree of homogeneity. The single-peak distribution is in approximately the same location as the higher-maximum second peak of the larger host.

Summary

Backscatter electron images of polished fallout samples show a range of morphological and compositional characteristics in mm-scale host objects and smaller, adhered fallout spherules. The 5 larger (mm-scale) host objects, to which the smaller objects are attached, commonly

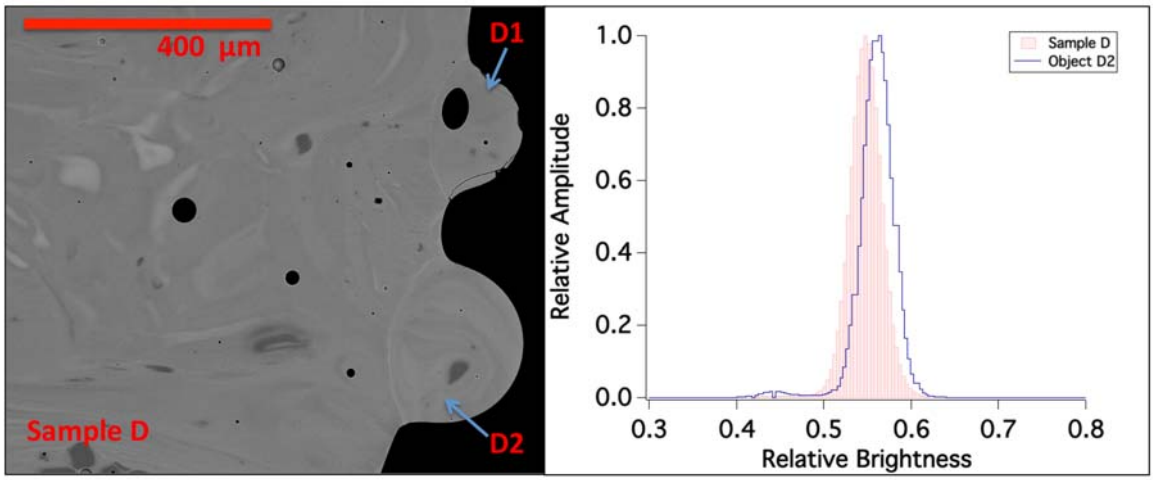

Figure 3.10: Left, backscatter electron image of Sample D, including attached Objects D1 and D2. Right, histograms of the relative brightness for D1 and D2, as well as the larger host object, are plotted, showing the same relative heterogeneity between D1, D2 and larger Sample D.

have large vesicles (up to 1 mm in diameter), as well as inclusions of what appear to be relict soil grains with diffuse boundaries based on major element composition (*e.g.,* Object D2). The internal composition of the small, attached, glassy objects ranges from relatively chemically homogeneous (Objects C1-3, E1) to distinctly heterogeneous (Objects B3, D1, and D2). Vesicles (seen as dark black circles or ovals) were most commonly observed in the samples showing the greatest degree of heterogeneity in major element composition. Small patches, approximately tens of microns in diameter (*e.g.,*, Sample D2), were identified by EDS, as nearly pure SiO_2 in composition and were commonly observed throughout the sample suite.

The extent to which the smaller objects have been incorporated into larger objects varies. For example, Objects C1 and C2 are two fused objects that have retained a highly spherical geometry, with the ratio of major and minor axes being 1.07 in both cases. Object C3, on the other hand, appears flattened against the host object, having a ratio of major to minor axis of 1.44, with the major axis measured at the widest point of the sample. This is further exemplified in objects B1-3, where multiple stages of incorporation appear to be preserved; Object B3 has a flattened interface and has merged into the larger host, while Object B1 has only slightly merged with the central object. Between these two agglomerates, Object B2 is a smaller (50 micron) object that is sandwiched between B1 and B3, and appears to have merged fully into the surface of B3.

As described in section 3.1, the distinct feature present in all samples, and of particular relevance to this study, is seen at the interfaces of where the small glassy spheres (<1 mm) are attached to the larger objects. These interfaces appear as a thin bright boundary line, and

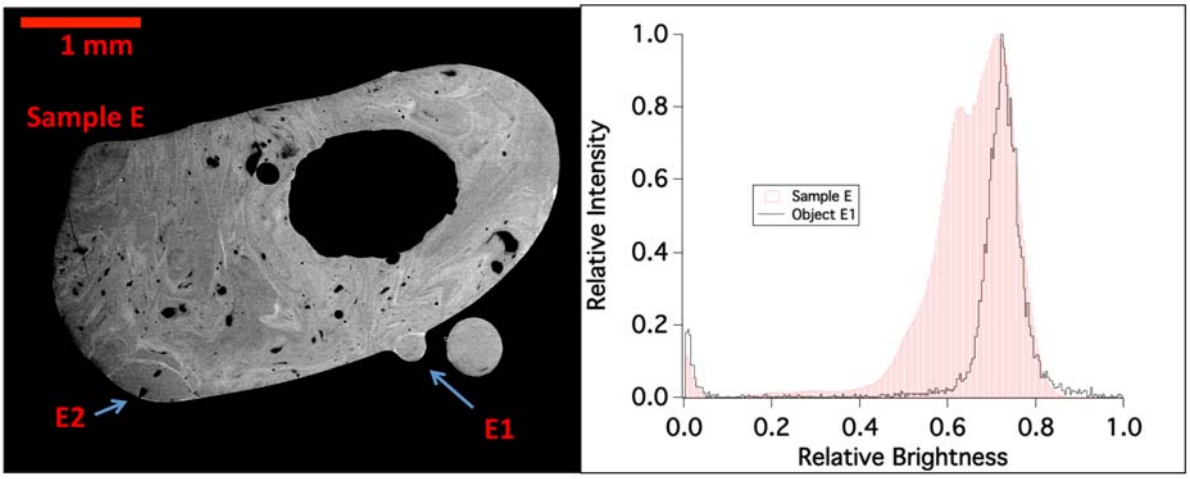

Figure 3.11: Left, backscatter electron image of the entirety of Sample E, including attached Objects E1 and E2 (which appears fully integrated into the larger host object). Right, histograms of the relative brightness for E1 as well as the larger host object are plotted, showing the relative homogeneity of Object E1 compared with larger Sample E.

are regions of relatively higher average atomic number (Z) than the surrounding material. Despite the range of morphologies and compositional variation observed in the agglomerated glassy fallout presented in this study, this high Z boundary feature is observed at every interface where the objects have fused together, and has not been previously documented in the fallout literature.

3.3 X-ray Mapping

Sample Maps

At the interface where Object A1 is attached to the larger host, energy dispersive X-ray spectroscopy was used to acquire maps for Al, Ca, Fe, and Na (Figure 3.12). This was the only sample in which electron probe microanalysis was not used to acquire maps, as the sample was damaged before this technique could be employed. In the EDS map for Al, there is a consistent depletion at the interface, with relatively higher concentration in attached object A1, and even higher concentration in the larger host. Both Ca and Fe are enriched at the interface and the edge of the sample, though this is most evident for Fe. The regions of enrichment of Fe, in particular, spatially correspond to the regions of Al depletion. In the EDS map of Na, the smaller attached object appears volumetrically enriched with Na relative to the larger host, and there is enrichment of Na at the interface or the edge.

In Figure 3.13, X-ray maps of Objects B1, B2, and B3 are shown for Al, Ca, Fe, and Na, as acquired by EPMA. These maps show a similar pattern of Al depletion co-located

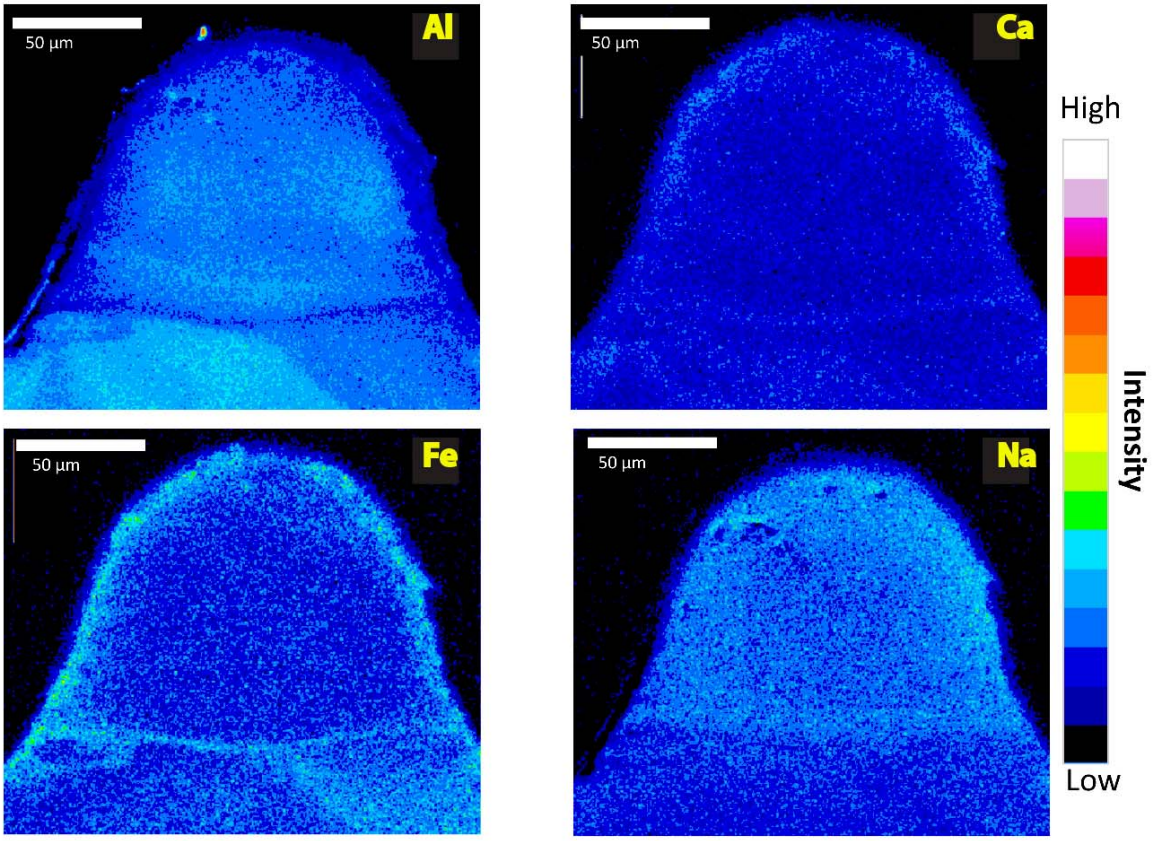

Figure 3.12: Qualitative compositional map of Object A1 (see Figure 3.1 for BSE image) acquired by energy dispersive X-ray spectroscopy for aluminum, calcium, iron, sodium. There is depletion of Al at the interface, with relative enrichments of Ca and Fe. Attached Object A1 appears relatively more enriched in Na in comparison to larger Sample A.

with Fe and Ca enrichment. This is most evident at the interface of where attached object B1 is fused to B2 and B3, although this pattern is observed at all interfaces on this sample. Both the Al and Ca maps show evidence of compositional flow banding, and the Ca map shows evidence of agglomeration of multiple objects. The Na map shows enrichment of Na around the surface of object B3 where it meets the epoxy (shown in black). The interface of where object B1 meets objects B2 and B3 shows enrichment of Na, though enrichment is not immediately apparent at any of the other interfaces on this object, as observable in X-ray mapping.

The EPMA map for Objects C1 and C2 show differing patterns of compositional variation (Figure 3.14). While both Objects show enrichment of Fe and depletion of Al at their respective interfaces, the Ca and Na maps of objects C1 and C2 show distinct differences. Object C2 shows relatively higher volumetric Ca enrichment than object C1. Further, while

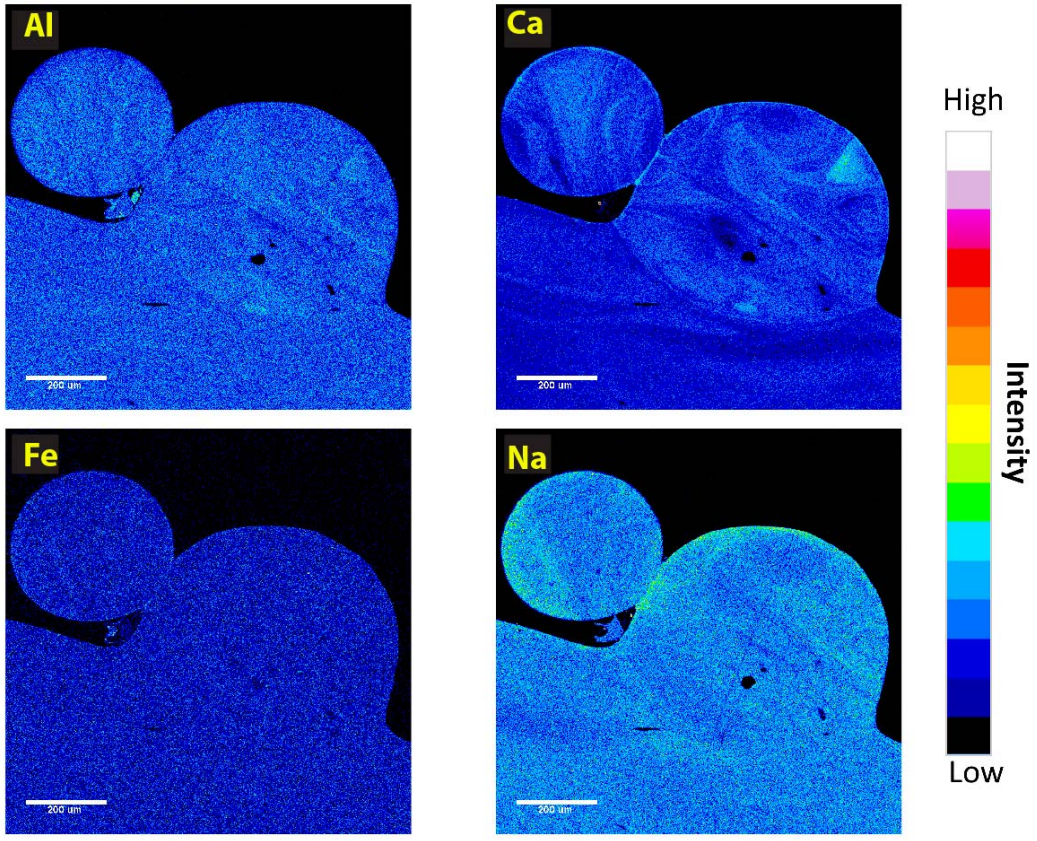

Figure 3.13: Qualitative compositional map of Objects B1, B2, and B3 (see Figure 3.2 for BSE image), acquired by wavelength dispersive X-ray spectroscopy for aluminum, calcium, iron, sodium. The interfaces of attached objects are depleted in Al and enriched in both Ca and Fe, relative to the interior composition of either the attached objects or the host sample. The edge of the attached objects adjacent to the epoxy are discontinuously enriched in Na.

both Objects C1 and C2 show enrichment of Ca around their edges and interfaces, C2 shows a distinct double ring feature, wherein a ring of high Ca enrichment encircles a ring of low enrichment around the surface of the object and at the interface. In the Na X-ray map, object C1 appears to be volumetrically more enriched in Na than C2. In Object C1, the Na variation appears diffuse, having a higher relative Na concentration at the edge and interface than its interior. In C2, however, the Na map indicates that Na did not appreciably penetrate into the volume of the object from the exterior. The EPMA map of Object C3 (Figure 3.15) shows a similar pattern of Al, Ca, and Fe composition to that seen in Object C1, although the composition at the edge of the object is difficult to discern due to chipping of the sample (likely due to polishing). As was observed in Object C1, the Na map of Object C3 shows a higher volumetric Na concentration, relative to a diffuse pattern of Na

compositional variation from the exterior to the interior of the object.

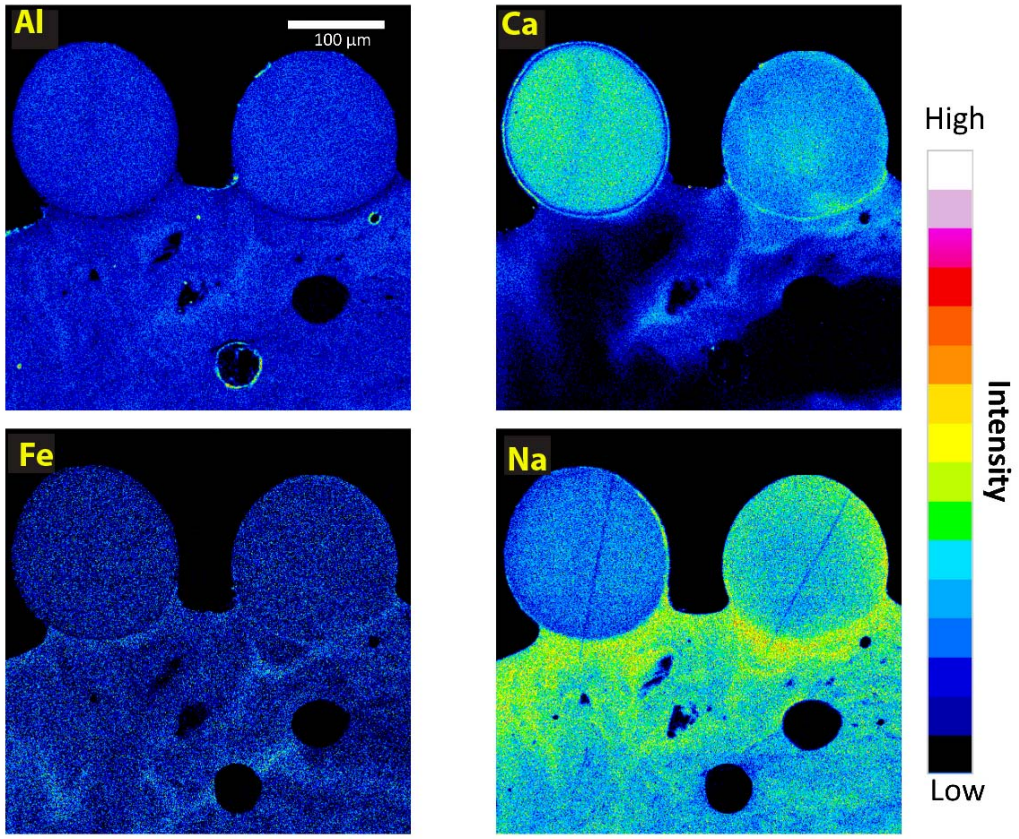

Figure 3.14: Qualitative compositional map acquired of Objects C1 (right) and C2 (left, see Figure 3.3 for BSE image), by wavelength dispersive X-ray spectroscopy for aluminum, calcium, iron, sodium. Object C1 has an interface depleted in aluminum and enriched in Ca and Fe. Object C2 has an interface depleted in Al and enriched in Fe; however, the interface exhibits a unique double ring feature in the Ca compositional map that extends through the interface all the way around the object. Larger Sample C is enriched in Na at the edge close to the epoxy and both attached objects.

In Figure 3.16, EPMA maps reveal the compositional variation for both Objects D1 and D2, as well as the adjacent region of the larger object of Sample D, for Al, Ca, Fe, and Na. At the interfaces of D1 and D2, the maps of Al, Ca, and Fe same relative depletion and enrichment patterns observed in the previous samples. The interface of object D2 shows a distinct enrichment of Na, which is not obvious, and may be absent, at the interface of Object D1. The Ca map is illustrative of the heterogeneity of the large host object in Sample D, as well as in the smaller attached Objects D1 and D2, where compositional banding and relict mineral inclusions are present. In the Na map, the larger object shows a higher relative

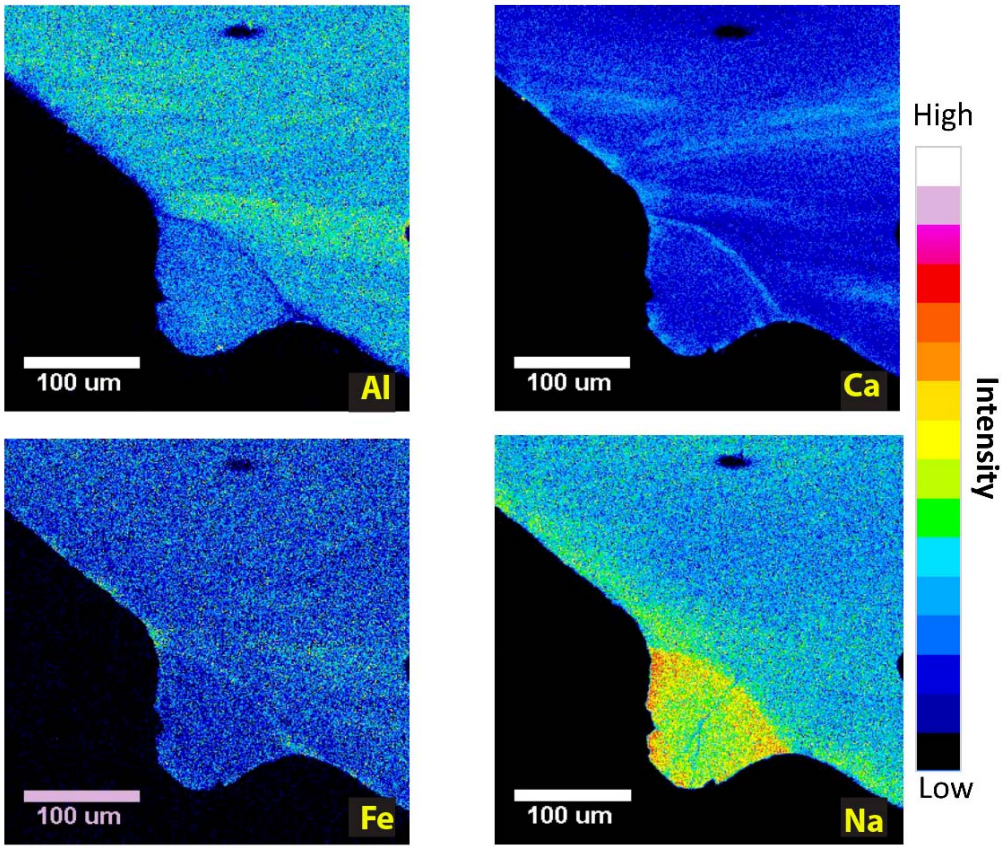

Figure 3.15: Qualitative compositional map acquired of Object C3 (see Figure 3.3 for BSE image) by wavelength dispersive X-ray spectroscopy for aluminum, calcium, iron, sodium. The interface of Object C3 is depleted in Al and enriched in both Ca and Fe. The Na compositional map indicates chemical enrichment of Na around the edge of attached Object C3.

concentration of Na at the surface of the sample where it meets the epoxy compared to its interior.

The EPMA X-ray maps in Figure 3.17 show the compositional variation of Al, Ca, Fe, and Na in Object E1. The edge and interface composition shown in the X-ray maps for this object are exemplary of the pattern of enrichment of Ca, Fe, and Na shown in other samples, as well as the distinct depletion of Al at the interface. The Na map shows a diffuse, continuous layer of Na all the way around the surface of Object E1, as well as at the interface (as further shown in Figure 3.26). In Figure 3.18, the EPMA X-ray maps are shown for Object E2. This object, which is fully integrated into the larger host, is most clearly outlined in the Na X-ray map (upper right side). As with the previous samples, there is a distinct depletion of Al, and relative enrichment of Ca and Fe, at the interface. As with

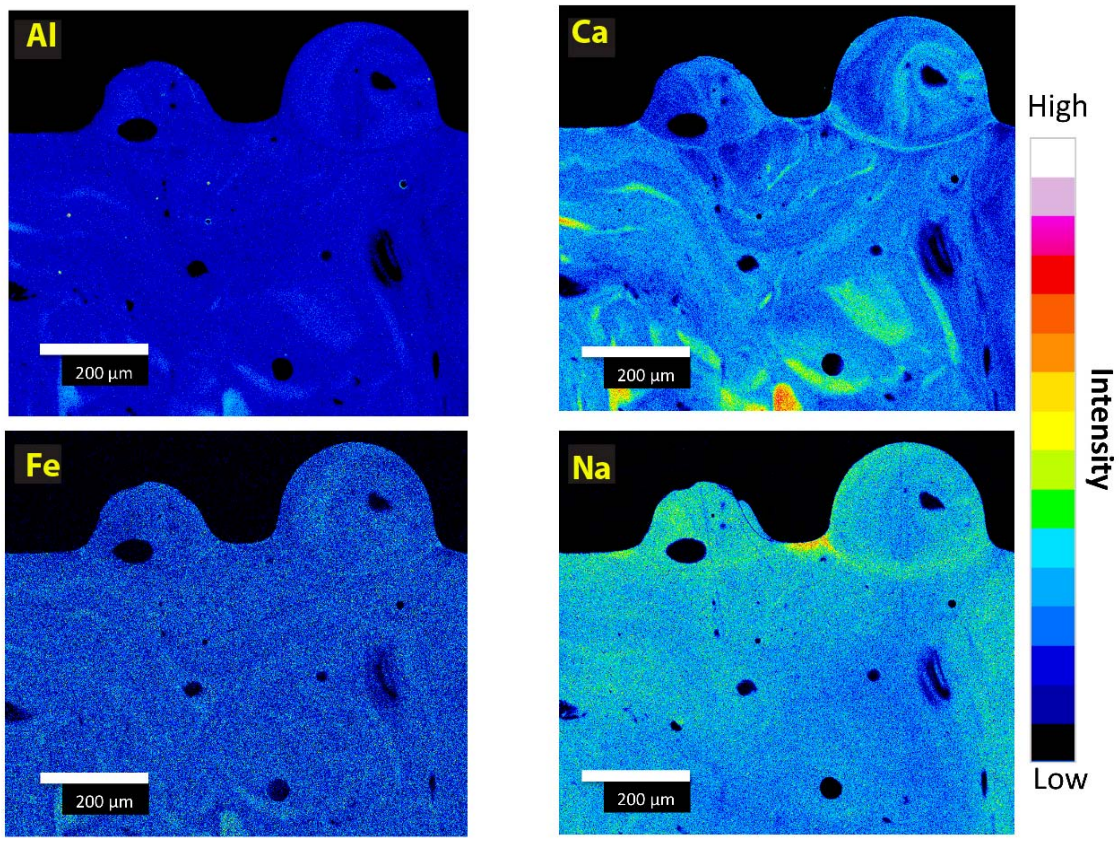

Figure 3.16: Qualitative compositional map acquired of Objects D1 (left) and D2 (right, see Figure 3.4 for BSE image) by wavelength dispersive X-ray spectroscopy for aluminum, calcium, iron, sodium. The Al compositional map shows depletion of Al at the interfaces of both attached objects. The interface is enriched in Ca, Fe, and Na, as shown in their corresponding compositional maps. The Ca map suggests distinct heterogeneity within larger Sample D in comparison to Objects D1 and D2.

E1, the Na map shows a continuous, diffuse, layer of Na all the way around the object and at the interface. In the Ca map, another smaller object adjacent to E2 is present, and also fully incorporated into the larger host.

Summary

X-ray intensity maps show that the high Z interfaces observed in the BSE images are part of a continuous layer that surrounds the smaller, attached objects, and is enriched in Ca and Fe and depleted in Al relative to the average composition of the interiors of the smaller objects. The edges of objects adjacent to epoxy also are enriched in Ca and Fe relative to the interiors. Although this enrichment at the sample edges could result from an artifact due

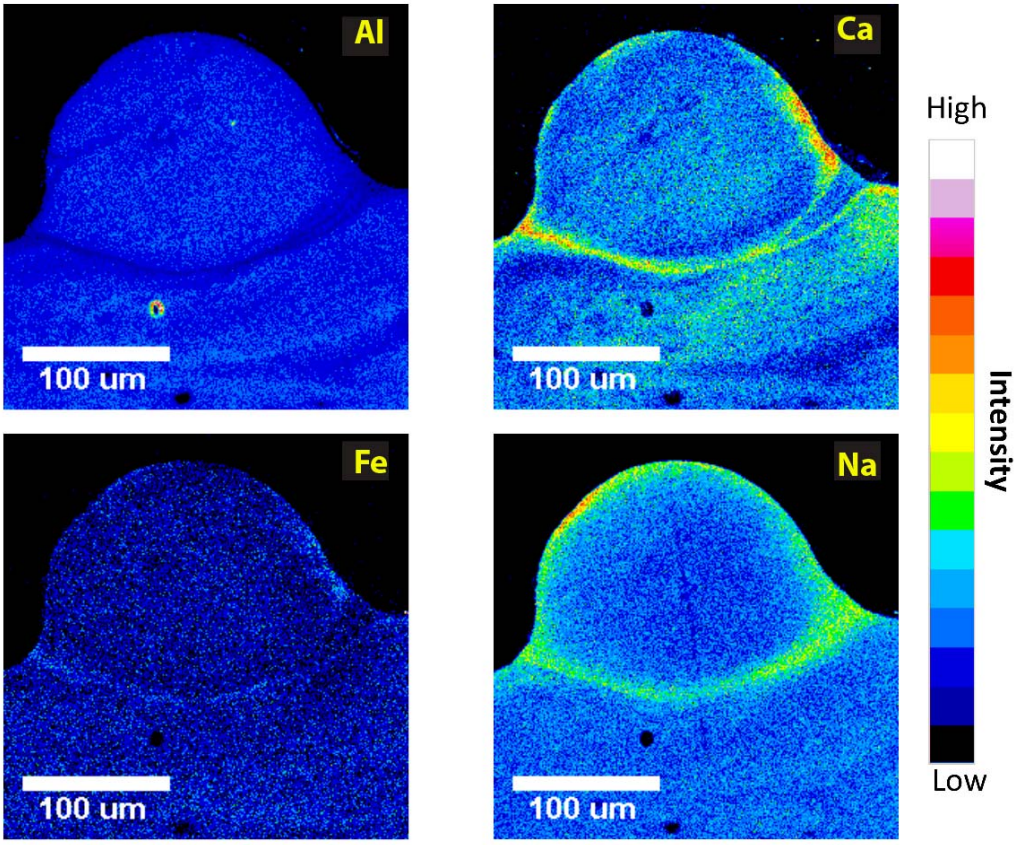

Figure 3.17: Qualitative compositional map acquired of Object E1 (see Figure 3.5 for BSE image) by wavelength dispersive X-ray spectroscopy for aluminum, calcium, iron, sodium. The interface of Object E1 is depleted in Al and enriched in Fe and Ca. The Na compositional map shows a diffuse Na layer all the way around the attached object.

to topographical edge effects, the continuity of this feature along agglomeration boundaries away from edges is strong evidence that the feature is intrinsic to the adhered objects. Sample C2 in particular shows a continuous, uniformly thick layer of Ca around the entire object, and is adjacent a region depleted in Ca. In 9 of the studied objects, the interface and exterior edge of the adhered objects is also enriched in Na, appearing as a thicker, more diffuse region when compared to the areas of Ca and Fe enrichment. Objects with observable enrichment in Na at the interface and/or outer edge (as seen in X-ray intensity maps and EDS traverses) include A1, B1, B2, C1, C2, C3, D2, E1 and E2.

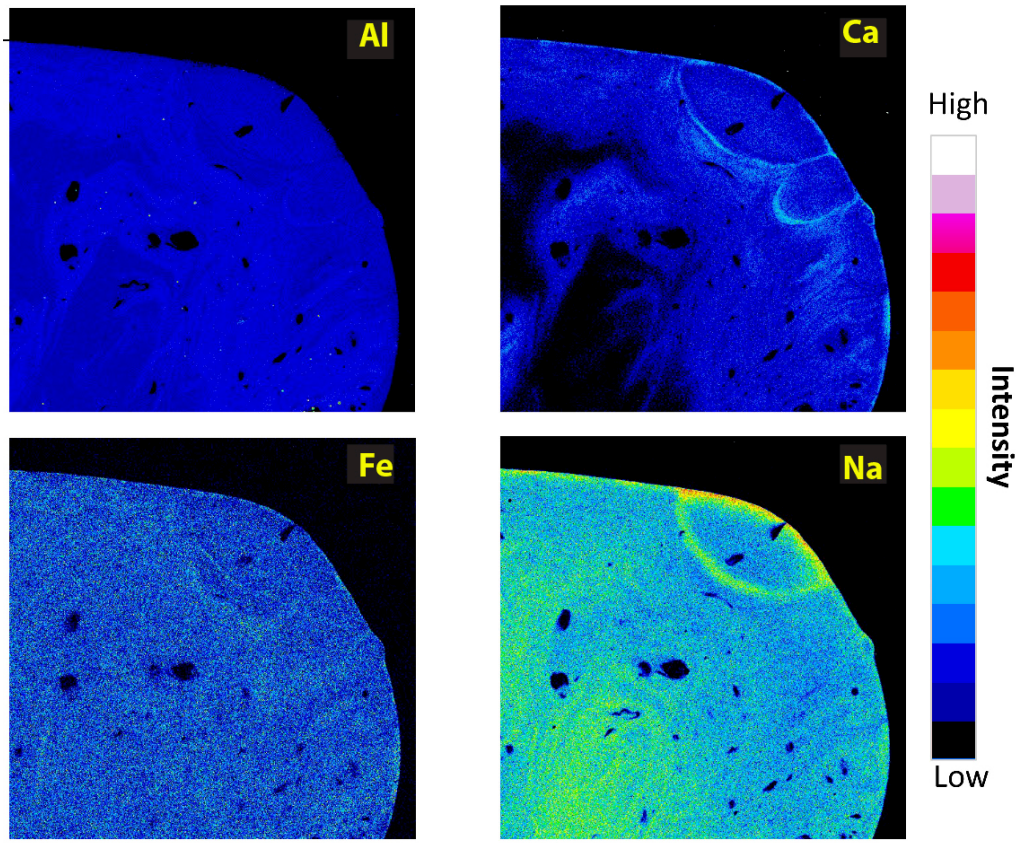

Figure 3.18: Qualitative compositional map acquired of Object E2 (see Figure 3.5 for BSE image) by wavelength dispersive X-ray spectroscopy for aluminum, calcium, iron, sodium. The interface of Object E2 is relatively depleted in Al and enriched in Ca and Fe. The Na compositional map indicates that, like Object E1, there is a diffuse Na layer all the way around the object.

3.4 Semi-quantitative Compositional Variation

EDS Spot Analyses

For selected samples and interfaces (see Table 2.1), energy dispersive X-ray spectroscopy was utilized to acquire a series of one-micron spot analyses across the interfaces of attached objects to rapidly capture compositional variation for major elements. The output of these spot analyses were in total X-ray counts for each major element of interest, including Al, Si, Fe, Ca, Mg, Na, and K, which provided a metric for semi-quantitative, relative compositional variation between samples (see Appendix A).

In Figure 3.19, a backscatter electron image of Object A1 is shown in the upper frame, with the location and direction of the spot analyses shown by the red arrow. The major

element variation as X-ray counts for Al, Ca, Fe, and Na are shown in the right hand frames. The output for each EDS analyzed interface is presented in the same format below. For Object A1, approximately 40 spots were acquired across the interface into the larger host object. As seen in the major element plots, the patterns observed in the qualitative EDS maps for Object A1 match with the semi-quantitative compositional variation for these major elements. The corresponding depletion of Al for A1 was found to be approximately 30%, and the corresponding enrichments for Ca, Fe, and Na were approximately 50%. The major element plots also show the difference in composition between the attached objects and the large host object in each sample. Here, for example, the Al and Ca content is notably higher (22% and 9%, respectively) in Sample A compared to Object A1, while the Fe content is approximately the same between the two. The Na content, on the other hand, is shown to be slightly lower (approximately 14%) in Sample A.

From Object B3, 32 spot analyses were acquired by EDS across the interface into Sample B (red arrow, Figure 3.20). At the interface of Object B3, the compositional variation trends in Al, Ca, and Fe (right frames, Figure 3.20) are consistent with the results of EPMA maps, and conform to the pattern observed in other samples. The variation in Na, however, does not show a discernible enrichment at the interface. Unlike Sample A, Sample B has a lower Al and Ca content than the attached Object B3 (2% and 13%, respectively), while Fe content is still approximately the same between the two (<1% difference). Again, the variation in Na at the interface and on either side of it does not yield any discernible pattern of enrichment or depletion.

In Sample C, spot analyses were acquired by EDS across the major diameters of attached Objects C1, C2, and C3 and through their respective interfaces into Sample C (Figures 3.21-3.23). These analyses revealed major element variation at the edge as well as at the interface. In Object C1 (Figure 3.21), the Al, Ca, and Fe major element plots show the characteristic depletion and enrichment at the interface (located at 200 microns, Figure 3.21) observed in other samples, with 45% relative depletion of Al, and relative enrichments of 19% and 45% for Ca and Fe, respectively. Further, the major element variation at the edge (located at 0 microns, Figure 3.21), show the same pattern as at the interface for Al, Ca, and Fe, wherein there is a depletion of Al (21%) and a enrichment of Fe and Ca (8% and 4%, respectively), though not to the same extent as observed at the interface. The Na variation in this sample shows an enrichment at both the edge and the interface, with a gradient of decreasing concentration towards the interior of the object, as observed in EPMA mapping (Figure 3.14). The sharp rise in Ca in the interior of the object observed in the major element plot (Figure 3.21) is also apparent in the EPMA map (Figure 3.14).

Object C2 (Figure 3.22) shows major element variation that is distinct from all of the other samples for Fe and Ca. The double-ring structure shown for Ca in the EPMA map (Figure 3.14) is also evident from the spot analyses at the interface (see Ca plot, 200 microns, Figure 3.22), where a 34% depletion in Ca is adjacent to a 47% enrichment. In the semi-quantitative EDS plots, there is a depletion of Ca followed by a narrow region of enrichment; this pattern is also observed for Fe at the interface. While evident in EPMA mapping at the edge, this feature was not observed in the semi-quantitative EDS spot analyses at the edge

(at 0 microns, Figure 3.22), likely due to its proximity to the epoxy. For Al, Ca, Fe, and Na, the composition within the interior of the object is relatively homogeneous in comparison to the other measured samples.

In Figure 3.23, the major element variation is shown for Object C3. The interface where Object C3 is fused to Sample C (at approximately 95 microns, Figure 3.23) shows the characteristic enrichment of Fe and Ca, and depletion of Al, as seen at the other interfaces (with the exception of Object C2). Of particular interest, the degree of enrichment of Ca and Fe (and depletion of Al) at the edge of the sample (at 0 microns, Figure 3.23) is similar to what is observed at the interface. The Na plot also shows an enrichment at both the edge and the interface, though the edge appears to be substantially more enriched (20% relatively more enriched than the interface). The observed drop at the very edge in all the plots (at 0 microns, Figure 3.23) is likely due to spot overlap on the epoxy.

Sample D1 (Figure 3.24) shows the greatest degree of variation for the plotted major elements. It is unclear to what extent the proximity of the spots to the large central void in the object affected the analyses (due to topographical variation). However, the interface (at 175 microns, Figure 3.24), shows a depletion in Al. There is also a sharp local maximum for both Ca and Fe at the interface. The spots at the edge are difficult to interpret, and may be affected by potential chipping or cracking at the very edge of Object D1 (at 0 microns, Figure 3.24). The Na plot does show a very distinct enrichment at the edge (35% relative to the interior), with a slight but distinguishable enrichment at the interface. Unique to this sample, approximately 100 EDS analyses were take within Sample D. The degree of compositional variation for Al, Ca, and Fe within the large host is comparable to that observed within attached object D1, although the larger host is relatively depleted in Na (12%, relative to the interior of the attached object).

Finally, Object E1 (Figure 3.25) shows the characteristic patterns enrichments and depletions of the major elements that were established in almost all of the samples. The degree of depletion of Al (30%), and enrichment of Ca and Na (35% and 70%, respectively), at the edge is almost identical to what is observed at the interface. The variation observed within the sample itself is relatively minimal (% standard deviations of 3%, 4%, 5%, and 8%, for Al, Ca, Fe, and Na, respectively), with larger fluctuations attributable to spots taken on cracks within the sample.

Given the chemical similarities of Na and K (as alkali metals, they have very similar bonding, ionization, oxidation properties, and mineral sources), it was expected that the variation of K will reflect the variation in Na. The patterns of K measured by EDS, though not shown in the above plots (see Appendix A), were observed to be comparable to Na in 5 of the measured objects. This is exemplified in Figure 3.26, where the K and Na variation across object E1 are plotted together, and the patterns of variation are almost identical.

Other measured elements included Mg, Ti, and Si. Due to the low count rates (*i.e.,* low concentrations of <1 wt.% element) of Mg and Ti, the semi-quantitative analyses of these elements did not reveal obvious patterns of variation that could be distinguished from the uncertainty on the individual measurements. The EDS spot analyses reveal a Si variation of less than 10% of the maximum value for every measured interface, with no discernible

pattern of enrichment or depletion at the interface. The entire EDS data set is given in Appendix A.

Summary

A total of 7 interfaces were characterized for compositional variation via EDS spot analyses (see Table 2.1). Compositional variation was determined as a series of EDS spot analyses along traverses from within adhered objects into the host samples. At every interface characterized by EDS spot analyses, there is a relative increase in Fe and Ca (up to 50% relative enrichment) at the interface compared to within the attached objects and samples themselves. All of the interfaces characterized by EDS also present a relative depletion of Al (up to 45% relative depletion), which also spatially correspond to enrichments of Ca and Fe. In 6 of the 7 interfaces, there was also an enrichment of Na (up to 70% relative enrichment) that spatially corresponds to Fe and Ca. This consistent and distinct pattern of enrichment and depletion at the interfaces is associated with the same pattern of enrichment and depletion present at the edges in 5 of the objects, although these edges are more difficult to characterize using EDS spot analyses due to edge effects. These observations are indicative of a distinct chemical layer around the adhered spheroidal glassy objects, which is further characterized for quantitative major element composition in the following Chapter (4).

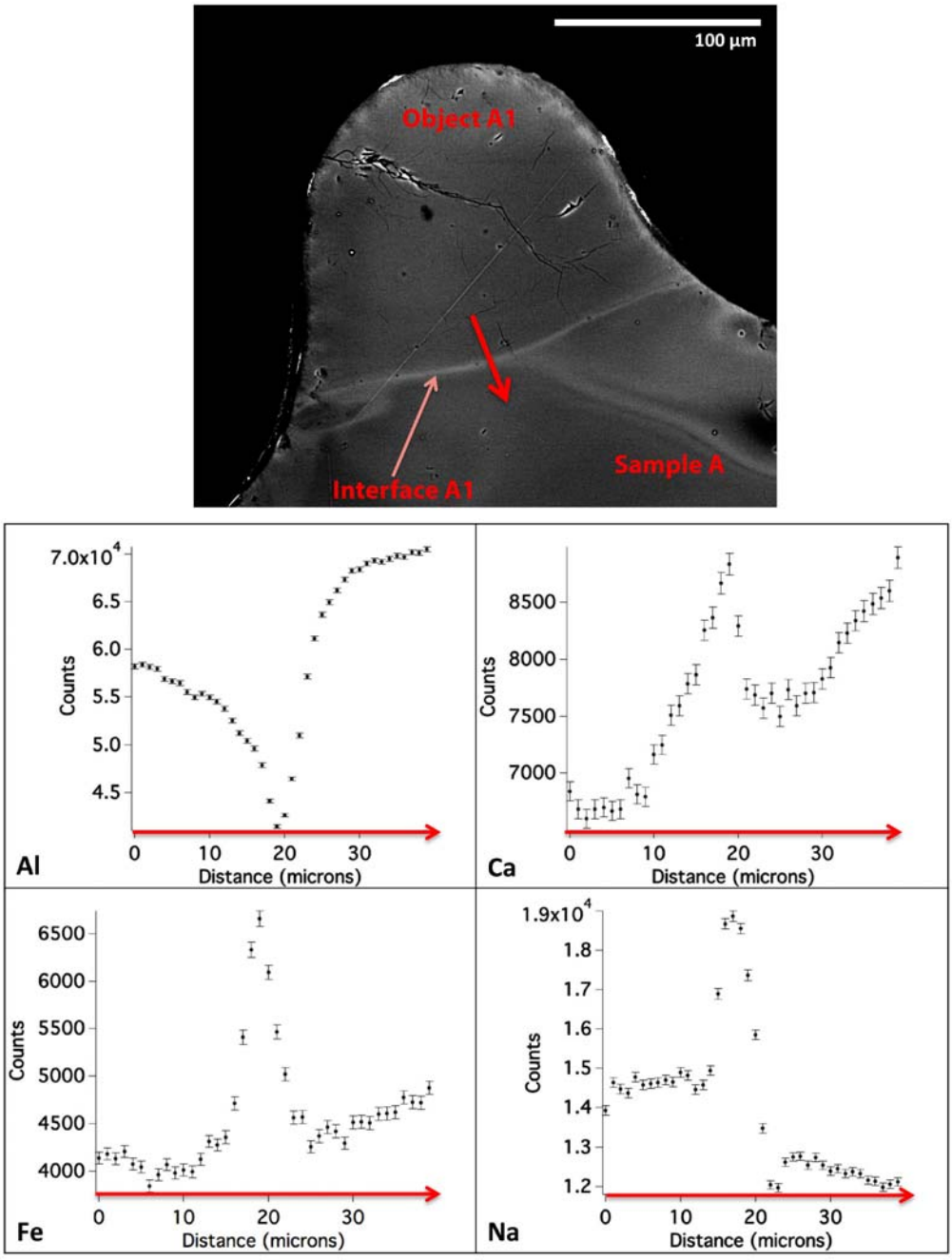

Figure 3.19: EDS spot analyses along the red line across the interface of Object A1 for aluminum, calcium, iron, and sodium. The variation of Al indicates a depletion at the interface relative to the interior regions on either side, while the variation of Ca, Fe, and Na indicates relative enrichment of each of these species at the interface.

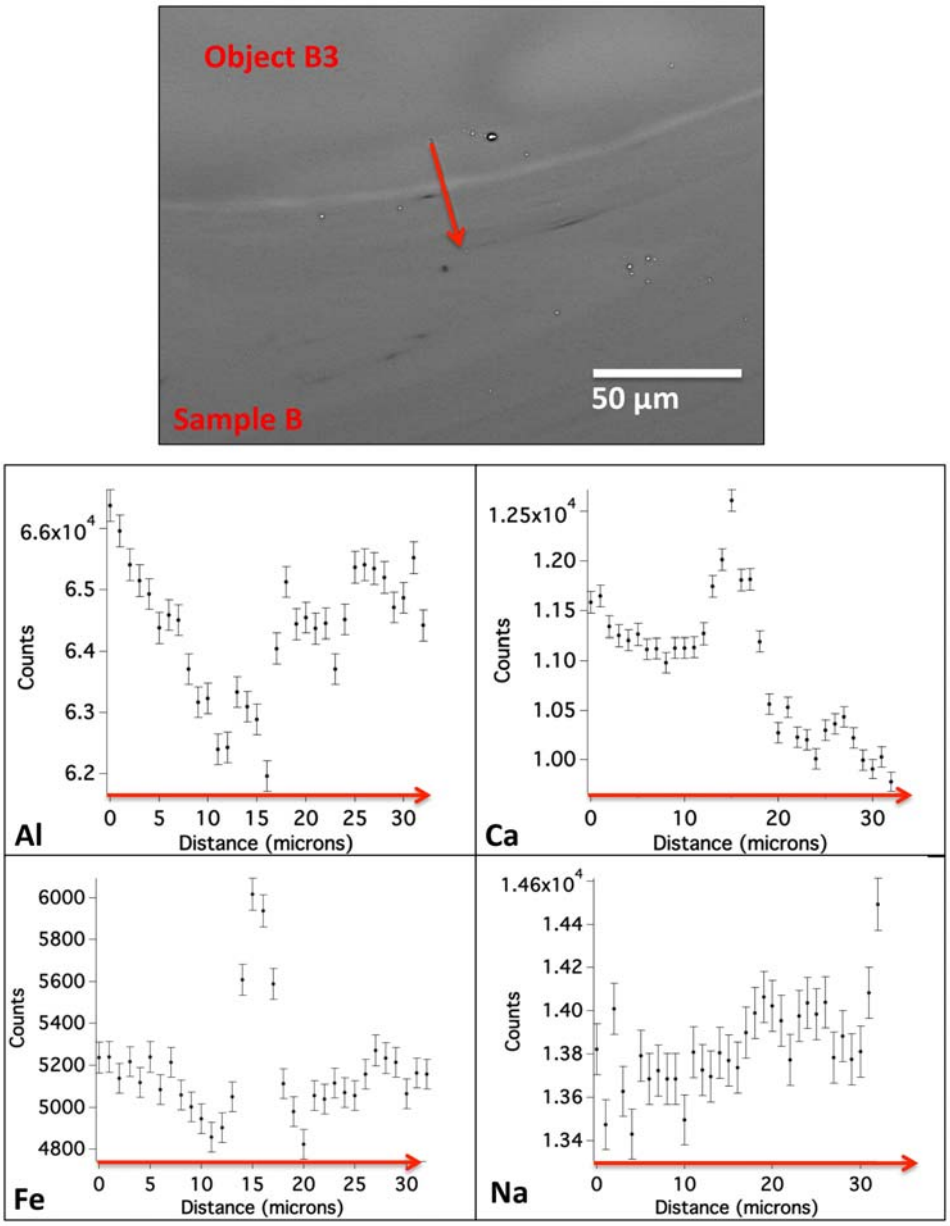

Figure 3.20: EDS spot analyses along a line across the interface of Object B3 for aluminum, calcium, iron, and sodium. The variation of Al indicates a depletion at the interface relative to the interior regions on either side of it, while the variation of Ca and Fe indicates relative enrichment of each of these species at the interface. The variation of Na across the interface does not correspond, spatially, with any other observed enrichment or depletion.

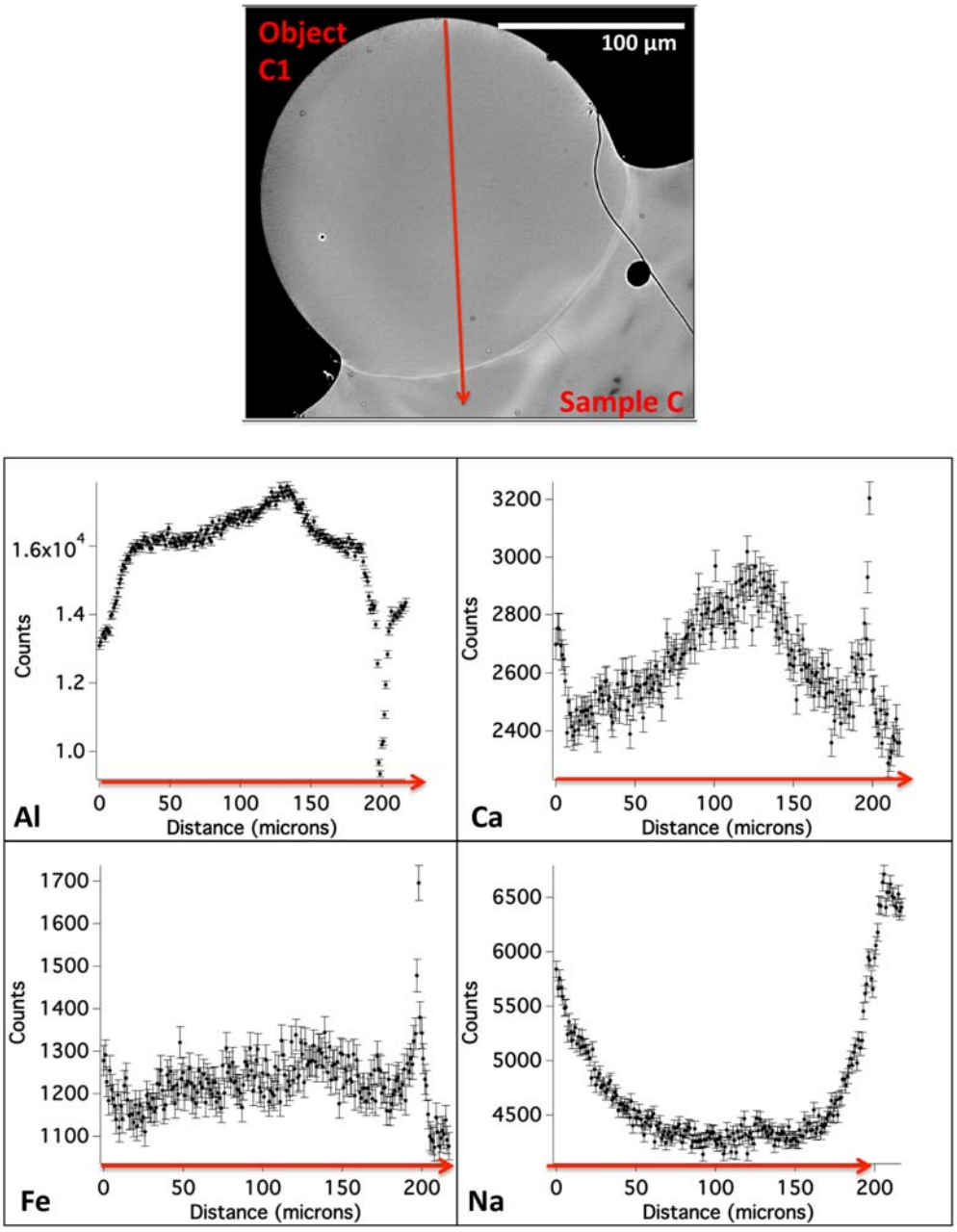

Figure 3.21: EDS spot analyses along a line from the edge of Object C1 across the interface into the larger object for aluminum, calcium, iron, sodium. In these plots, the edge is noted as 0 microns, and the interface is located at approximately 200 microns from the edge. The edge and the interface are both depleted in Al, and enriched in Ca, Fe, and Na, relative to the interior of the attached object and Sample C.

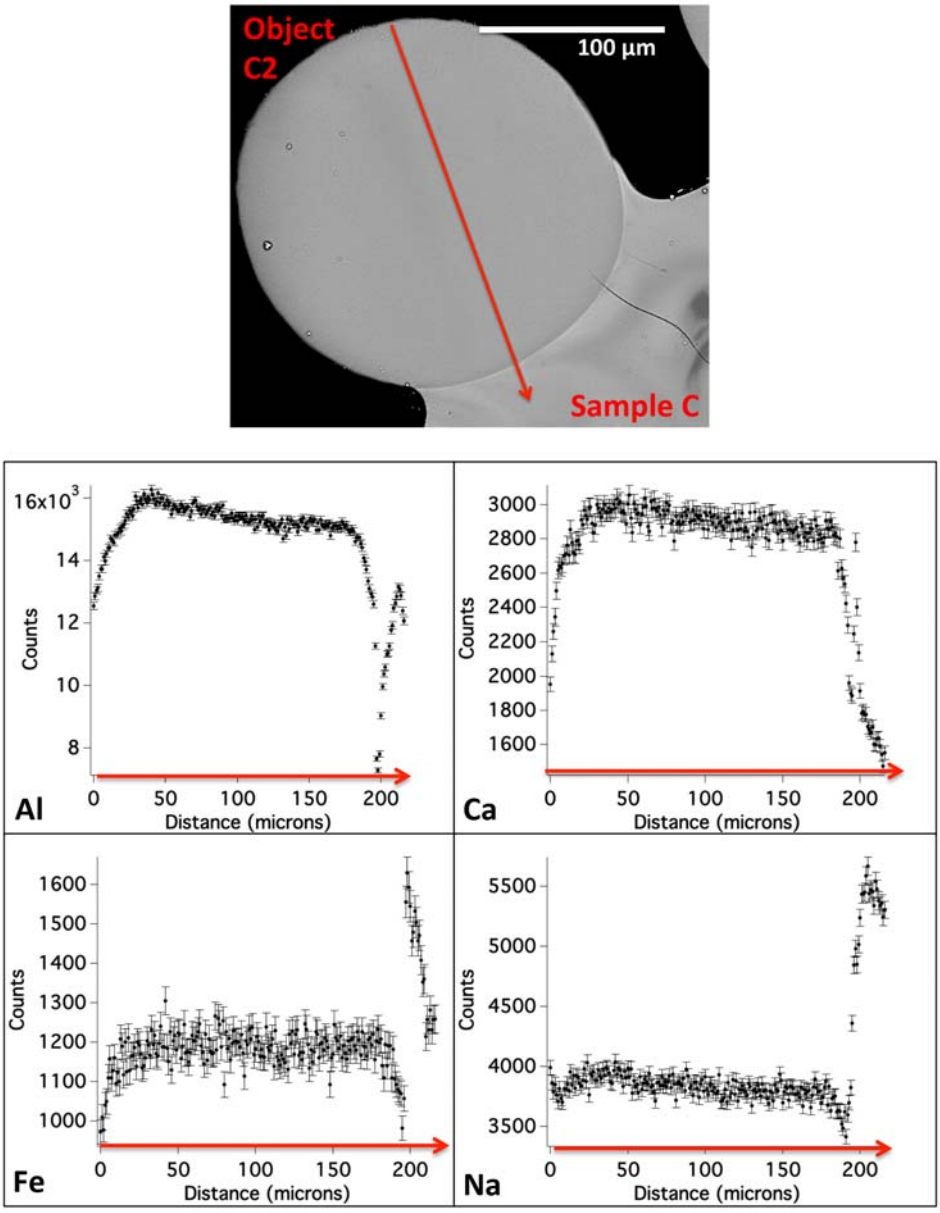

Figure 3.22: EDS spot analyses along a line from the edge of Object C2 across the interface into Sample C for aluminum, calcium, iron, sodium. The edge is noted as 0 microns, and the interface is located at approximately 200 microns from the edge. The edge and the interface are both depleted in Al. The edge is depleted in Fe and Ca, while the interface shows a region of relative depletion compared to the interior of Object C2, adjacent to a region of relative enrichment of both Fe and Ca. It is unclear if Na is enriched at the interface, or if the increase in Na is due to a higher Na concentration in Sample C.

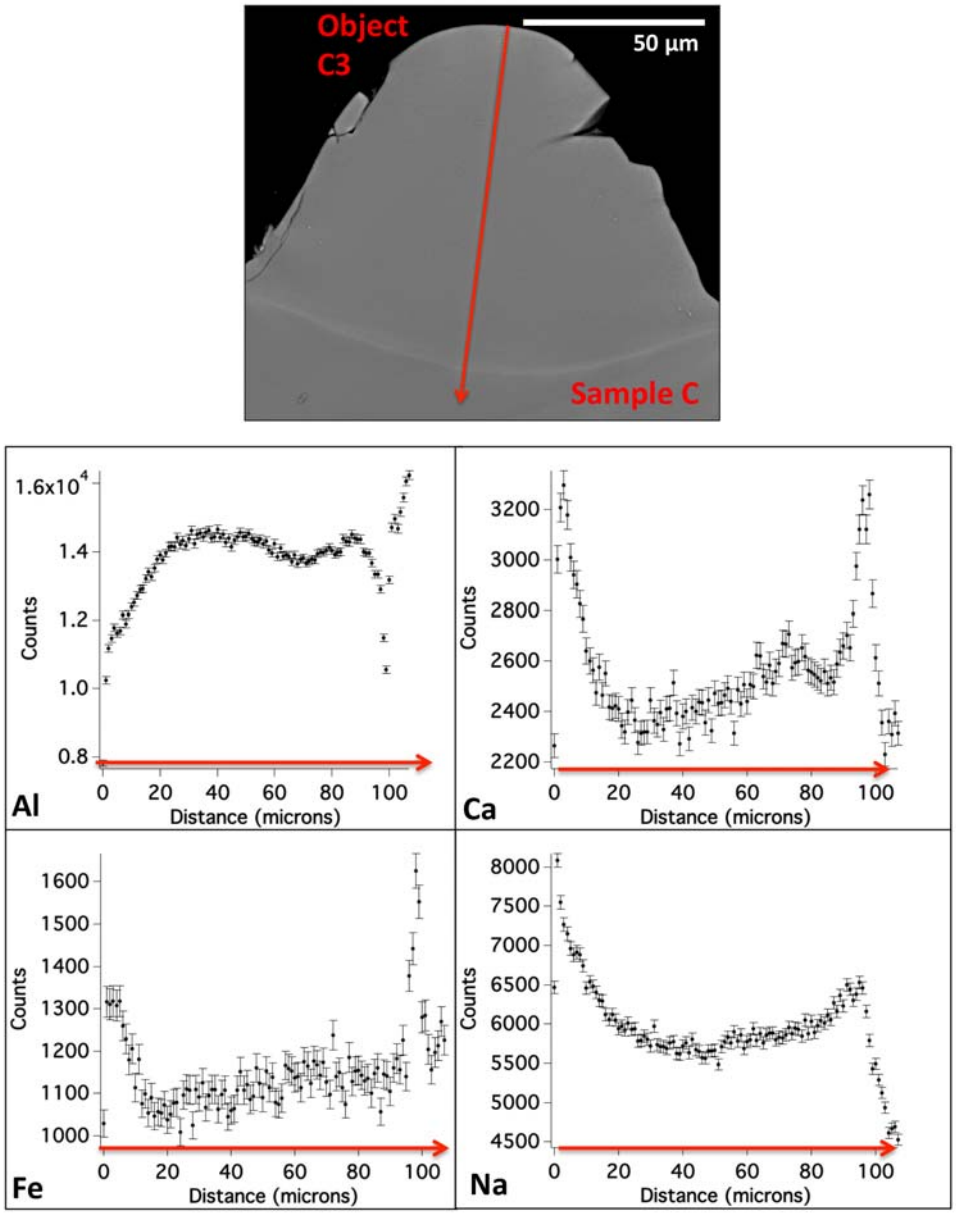

Figure 3.23: EDS spot analyses along a line from the edge of Object C3 across the interface into Sample C for aluminum, calcium, iron, sodium. The edge is noted as 0 microns, and the interface is located at approximately 95 microns from the edge. The edge and interface are relatively depleted in Al, and enriched in Ca, Fe, and Na, compared with the interior of Object C3.

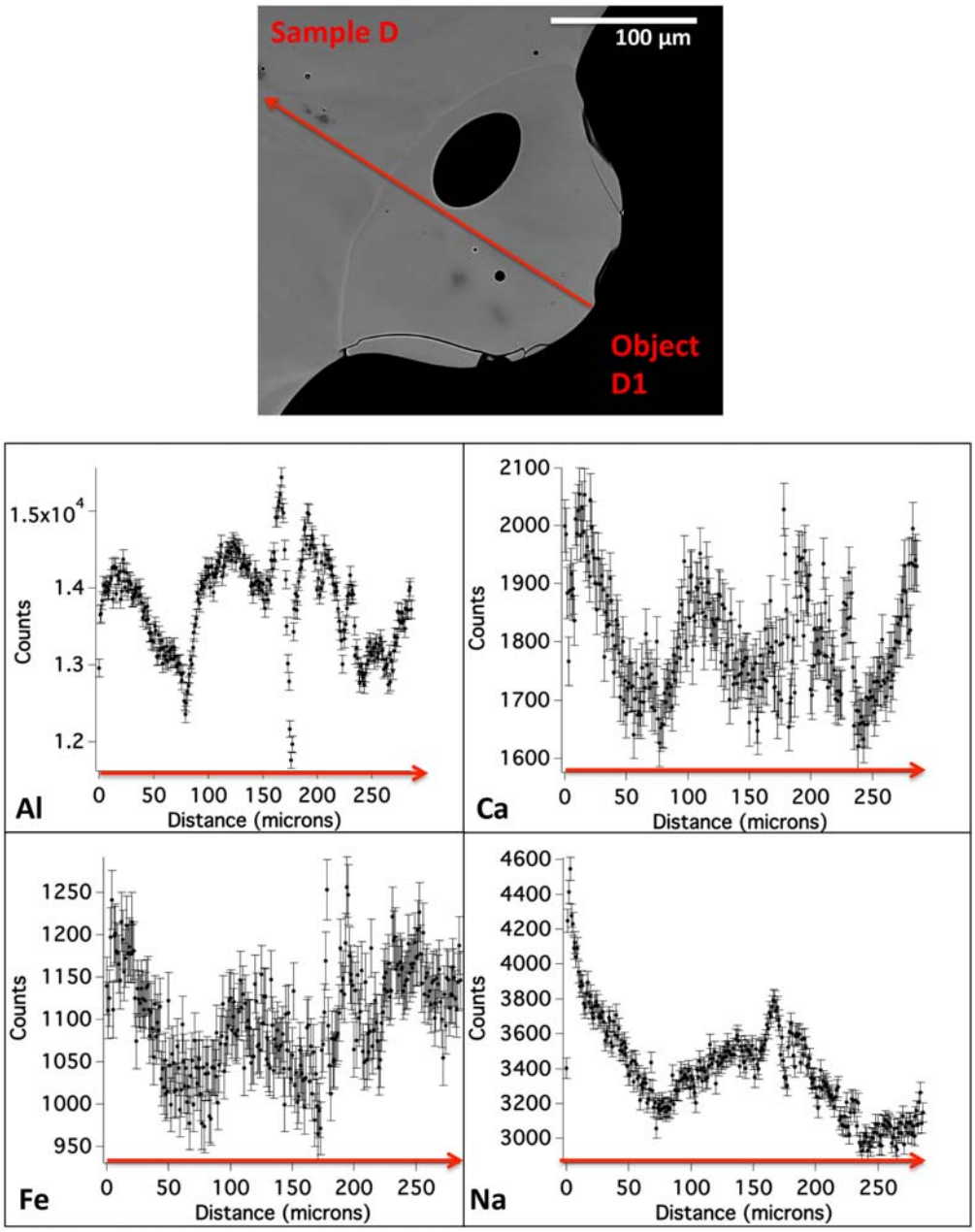

Figure 3.24: EDS spot analyses along a line from the edge of Object D1 across the interface into Sample D for aluminum, calcium, iron, sodium. The edge is noted as 0 microns, and the interface is located at approximately 175 microns from the edge. The heterogeneity of Object D1 is shown by the variation in each species. Despite this variation, there is a distinct depletion of Al at the interface relative to the interior composition of Object D2, and a corresponding relative enrichment of Ca, Fe, and Na.

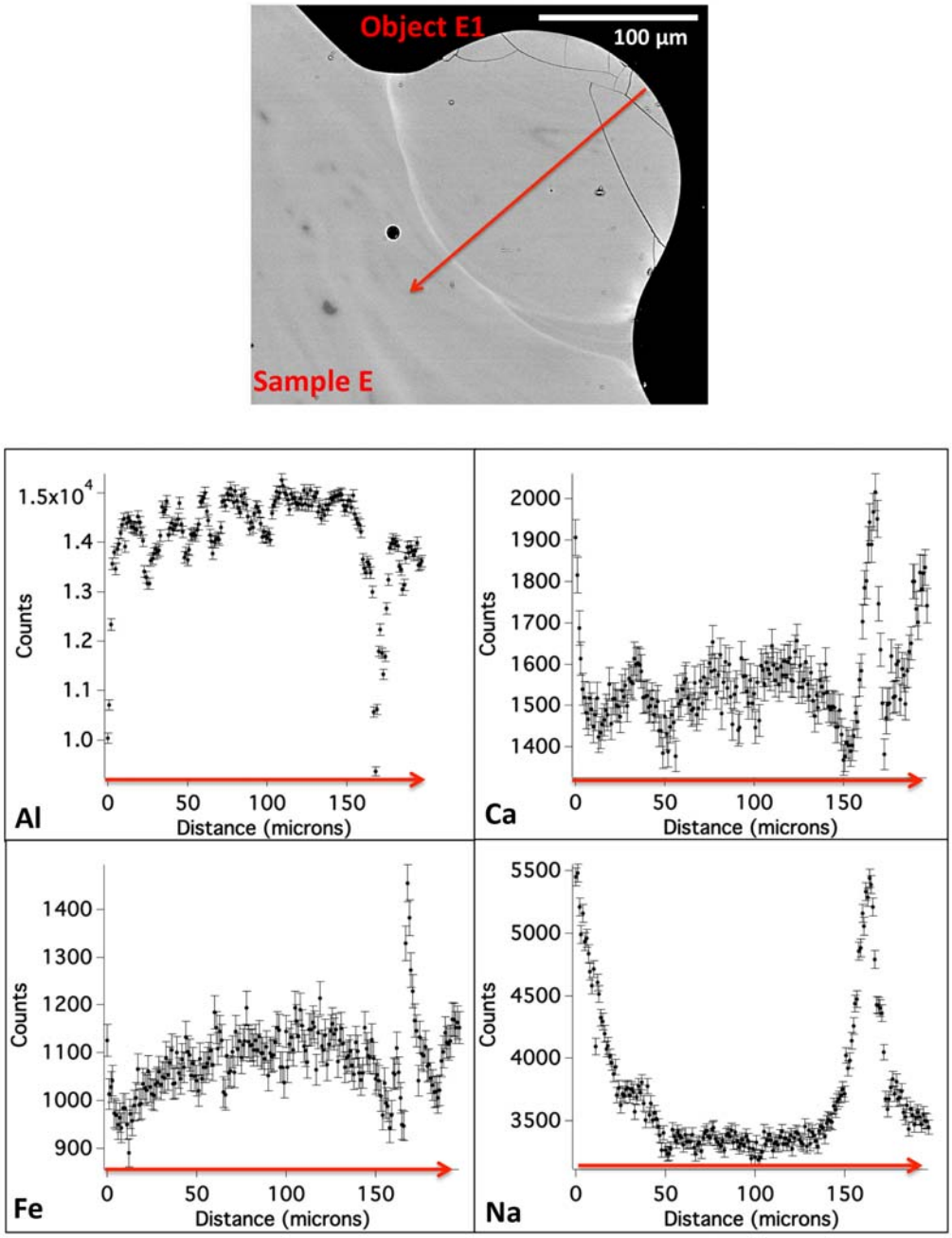

Figure 3.25: EDS spot analyses along a line from the edge of Object E1 across the interface into Sample E for aluminum, calcium, iron, sodium. The edge is noted as 0 microns, and the interface is located at approximately 170 microns from the edge. The edge and interface are relatively depleted in Al, and relatively enriched in Ca, Fe, and Na, compared with the interior of Object E1.

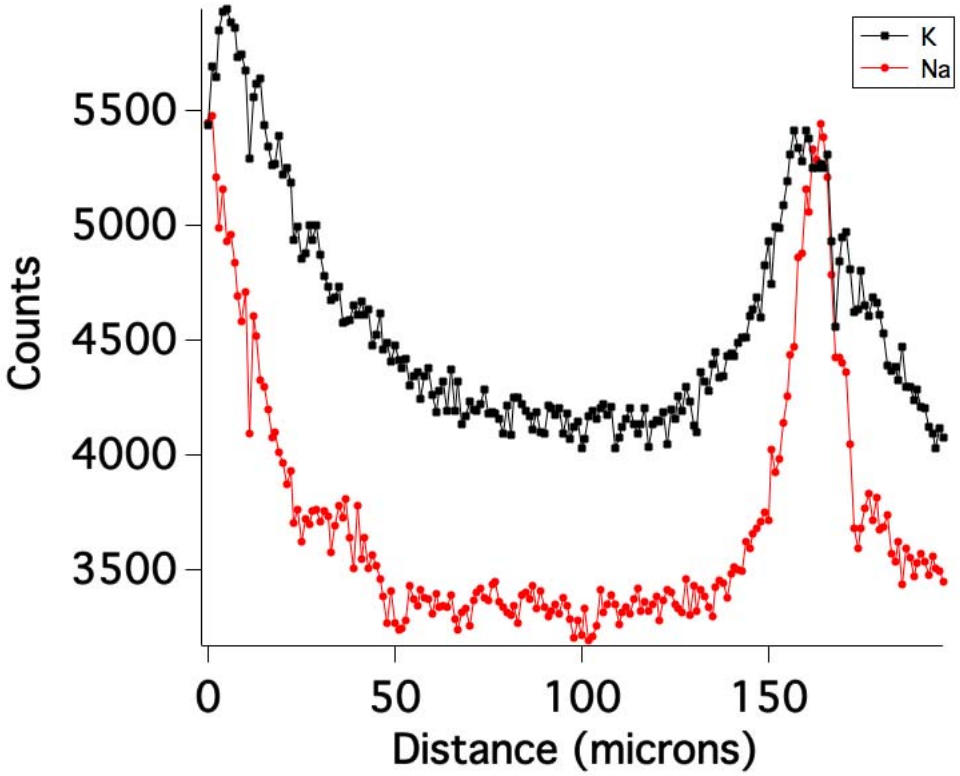

Figure 3.26: EDS spot analyses across object E1 for Na and K, showing relative enrichment of both Na and K at the edge and interface and the similarity of these patterns between these two elements.

Chapter 4

Quantitative Compositional Analysis

To quantitatively understand the variation of species within agglomerated fallout objects and at the interfaces where they fused onto the surfaces of larger hosts, quantitative analytical techniques are used, including electron probe microanalysis (EPMA) and nano-scale secondary ion mass spectrometry (NanoSIMS). Specifically, EPMA is used to measure the major element variation through agglomerated fallout objects and across their interfaces, as well as measure the major element composition of selected soil samples, which served as the carrier precursors to the fallout objects in this test. In order to understand the contribution of device uranium to the agglomerate interface layer, NanoSIMS is used to measure ^{235}U and ^{238}U variation, and estimate the uranium concentration at the interfaces.

4.1 EPMA Analyses

Electron probe microanalysis (EPMA) was used to acquire wavelength dispersive x-ray spectroscopy (WDS) analyses across selected attached objects (See Table 2.1) and their interfaces to quantitatively assess the compositional variation of major elements. The analyses were acquired as a series of 1 micron spots spaced 1 micron apart, following the analytical conditions set forth in Section 2.2. The WDS analyses were acquired for Si, K, Mn, Al, Fe, Ca, Na, Mg, and Ti, and the results are presented in stoichiometrically oxide corrected form for Al_2O_3, FeO, CaO, Na_2O, MgO, and TiO_2 (unlike element X-ray counts, as given in the EDS spot analyses, Figures 3.19-3.26). As these species are likely present as oxides in these samples, the WDS data are presented in oxide form, although the precise speciation is unknown. Further, as discussed in Section 2.2, the values for Na_2O may be underestimated by up to 15%, due to beam volatilization effects. The edges and interfaces of agglomerated objects were compared to the average interior composition (Figure 4.1) of the objects to determine the extent of compositional variation in the deposition layer shown in Chapter 3. For the purposes of comparison, the edges are defined as regions of chemical enrichment or depletion within 10 microns from the edge of an agglomerated object adjacent to the epoxy, and the interfaces are defined as regions of chemical enrichment or depletion 5-10 microns

wide where agglomerated objects fused to the surface of larger hosts. The interior average composition (as shown in Figure 4.1), is defined as the average value of all data points within agglomerated objects, excluding points defined as edge or interface points.

The average major element oxide composition of the interiors of agglomerated fallout objects exhibit a different compositional range than the values found in mm-scale objects [55, 56]. For example, the average Al_2O_3 and SiO_2 concentrations range from 12.78 - 16.96 wt.% and 68.15 - 74.92 wt.% respectively (Figure 4.1, top left), while the values acquired by Lewis et al. (2015) have respective ranges of 13.5 - 14.6 wt.% and 71.4 - 72.4 wt.%. The average MgO and TiO_2 concentrations range from 0.46 - 0.91 wt.% and 0.23 - 0.46 wt.% respectively (Figure 4.1, bottom left), while the values acquired by Lewis et al. (2015) have respective ranges of 0.4 - 0.6 wt.% and 0.2 - 0.3 wt.%. The average Na_2O concentrations in the agglomerated objects (ranging from 1.05 - 2.29 wt.%, Figure 4.1, bottom right), fall below the range found by Eppich et al. (2014) and Lewis et al. (2015), which are 3.0 - 3.6 wt.% and 3.0 - 3.7 wt.%, respectively. However, the average K_2O concentrations (3.44 - 5.78 wt.%) are similar to those found by Eppich et al. (2014) and Lewis et al. (2015), (3.9 - 5.5 wt.%, and 3.5 - 4.9 wt.%, respectively). The average CaO and FeO concentrations (1.19 - 2.49% and 2.13 - 3.52% respectively, Figure 4.1, top right) have approximately the same ranges of both Lewis et al. (2015) and Eppich et al. (2014).

In the following section, the Si data are not presented, as the Si content across the interfaces and the samples themselves is not highly variable (<2.9% standard deviation for the entire dataset). The K data are also not presented, given their similarity to the Na data (as shown by EDS, Figure 3.26). Finally, the Mn data are not plotted, as the count rate was very low ($\sim$1 cps), and often indistinguishable from background ($\sim$2 cps).

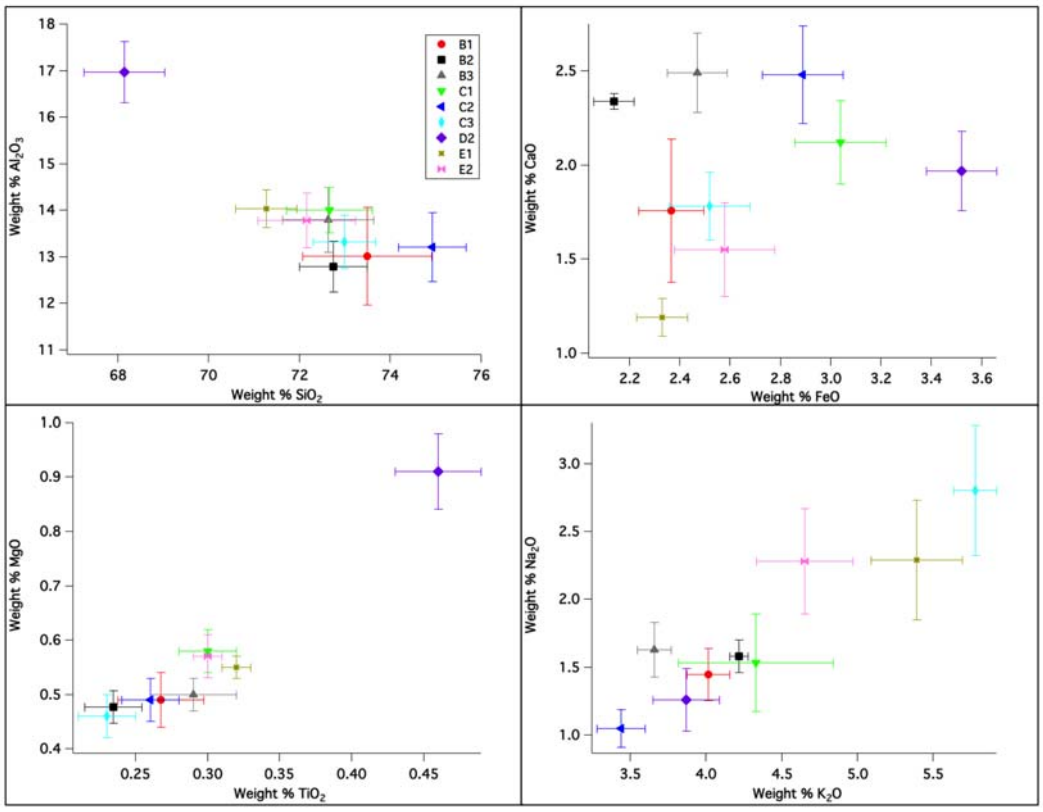

Figure 4.1: Average major element oxide composition of the interiors of agglomerated fallout objects B1, B2, B3, C1, C2, C3, D2, E1, and E2, with 1σ uncertainties. The top left plot shows the average Al_2O_3 and SiO_2 concentrations (ranging from 12.78 - 16.96 wt.% and 68.15 - 74.92 wt.% respectively), the top right plot shows the average CaO and FeO concentrations (ranging from 1.19 - 2.49 wt.% and 2.13 - 3.52 wt.% respectively), the bottom left plot shows the average MgO and TiO_2 concentrations (ranging from 0.46 - 0.91 wt.% and 0.23 - 0.46 wt.% respectively), and the bottom right plot shows the average Na_2O and K_2O concentrations (ranging from 1.05 - 2.29 wt.% and 3.44 - 5.78 wt.% respectively). In the top left and bottom right plots, Object D2 can be seen apart from the concentration cluster of the other objects, indicating similar concentrations in the rest of the objects for these species.

Trends and characterization of major element relationships at agglomerate interfaces

The spot analyses across Objects B1 and B2 were taken along a single joined traverse, as they were both agglomerated onto Object B3, which is fused to Sample B (Figure 3.2). The spot analyses for Object B1 and its interface are presented in Figure 4.2, where the interface points are highlighted in blue. The interface is 4.5 microns wide, as characterized by the FeO

variation (extending from within Object B1 across the interface into Object B2). This plot shows a local maxima for CaO, MgO, and FeO at the interface, which are 74%, 44%, and 32% enriched, respectively, relative to their average interior compositions (1.76 ± 0.38%, 0.49 ± 0.05%, and 2.37 ± 0.13% by weight, respectively). There is also a local minima of Al_2O_3 at the interface (11.62 ± 0.06% by weight, relative to the average interior concentration of 13.02 ± 1.05%), although it is difficult to distinguish from the variation of Al_2O_3 through the object itself (which spans a relative range of ∼40%). The Na_2O plot shows an increase at the interface, although it is not clear if this illustrates an enrichment at the interface, or simply a higher relative Na_2O content in Object B2. The TiO_2 content at this interface is difficult to distinguish from the variation through the sample itself. This could be due to the low concentration TiO_2 (∼0.25 weight %) in these fallout samples, which approaches the limit of detection by EPMA.

The spot analyses for Object B2 traverse the diameter of the entire object (∼50 microns). This dataset is a continuation of the dataset given for Object B1, where the data at 200 microns in Figure 4.2 corresponds to the data at 0 microns in Figure 4.3, also shown in the BSE image of Figures 4.2 and 4.3. The major element composition in the interior of Object B2 is more homogeneous than in Object B1, which corresponds to what is observed qualitatively in BSE; this is most apparent for Al_2O_3 and CaO (Figure 4.3). The concentration of Al_2O_3 at the interface is 11.27 ± 0.07% by weight, representing a 12% depletion relative to the average composition of 12.79 ± 0.54% by weight in Figure 4.1. Again, the FeO, MgO, and CaO plots show increased concentration at the interface (2.55 ± 0.08%, 0.55 ± 0.01%, 2.90 ± 0.03 by weight, respectively) relative to the interior concentrations of these species (2.14 ± 0.08%, 0.48 ± 0.03, and 2.34 ± 0.04% by weight, respectively). The interface, as characterized by the FeO variation, is 3 microns wide. The TiO_2 plot shows a depletion of 24% at the interface relative to the interior concentration (0.23 ± 0.02% by weight). Object B2 does not show an observable pattern of enrichment or depletion in Na_2O through the object, or at the interface itself. However, there is greater than 20% relative variation in Na_2O within the interior of the sample from spot to spot, which is indicative of Na heterogeneity in the sample.

In Object B3, spot analyses were acquired across the interface (Figure 4.4), and approximately 60 microns into the large host object of sample B. As shown in the BSE image, there is significant chemical heterogeneity. The major element composition at the interface follows a similar pattern as seen in objects B1 and B2, where local minima are observed co-located for Al_2O_3 and TiO_2, and local maxima are observed co-located for CaO, FeO, and MgO. The interface is 6 microns wide, as measured by the FeO variation. Again, there is >20% spot to spot variation in the Na_2O analyses. There is relative depletion of Al_2O_3 at the interface (12.67 ± 0.07% by weight) relative to the average interior composition (13.80 ± 0.70% by weight). There is also an observed relative depletion of TiO_2 at the interface (0.25 ± 0.01% by weight) in comparison to its average interior concentration (0.29 ± 0.03% by weight), although this depletion falls within the range of the observed spot-to-spot variation in the interior concentration dataset (which spans a relative range of 17%). These local minima of Al_2O_3 and TiO_2 at the interface are co-located with enrichments in CaO, MgO,

and FeO concentration (29%, 33%, and 32%, respectively), relative to the average interior concentrations (2.49 ± 0.21%, 0.50 ± 0.03%, and 2.47 ± 0.12% by weight, respectively).

Object C1 illustrates a pattern of enrichment and depletion of the major elements typically observed in most samples for this study (Figure 4.5). The spot analyses were acquired from the outer edge of the object, through its major diameter, and across the interface, capturing the major element variation at the edge and the interface. The composition of the interior points is homogeneous for Al_2O_3, FeO, MgO, and Na_2O (Figure 4.1). There is depletion of Al_2O_3 concentration at the outer edge of the object, and a depletion at the interface (5.37 ± 0.05% by weight, compared to 14.00 ± 0.49% by weight at the interface). While it is difficult to distinguish a depletion of TiO_2 at the edge within the measurement uncertainties, TiO_2 shows strong depletion at the interface (0.19 ± 0.02% by weight compared to 0.30 ± 0.02). The compositional variation of CaO, MgO, and FeO at the edge and the interface show enrichment in both places, co-located with the depletion of Al_2O_3. The enrichments of CaO, MgO, and FeO are significant also at the interface, with enrichments of 54%, 12%, and 41%, respectively, relative to their interior concentrations of 2.12 ± 0.22%, 0.58 ± 0.04%, and 3.04 ± 0.18% by weight. The interface, as measured by the FeO variation, is 9 microns wide. There is also enrichment of Na_2O at the interface (2.24 ± 0.04% by weight, compared to 1.53 ± 0.36% by weight at the interface).

In attached object C2, there is a unique pattern of compositional variation at both the edge and the interface (Figure 4.6) where the object is fused to the large host of Sample C. The interior points for all the major elements show minimal variation in comparison to the other samples (Figures 4.1 and 4.6). This observation of homogeneity is in line with the qualitative results of X-ray mapping, which also show relative homogeneity in Al, Ca, Fe, and Na concentrations (Figure 3.14). At the edge and the interface, there is a depletion of Al_2O_3 and TiO_2. Specifically, the Al_2O_3 concentration at the interface is 7.05 ± 0.06% by weight, compared to 13.21 ± 0.74% by weight on the interior of the object, while the TiO_2 concentration at the interface is 0.15 ± 0.02% by weight, compared to an average concentration of 0.26 ± 0.02% by weight on the interior of the object. Unlike all of the other analyzed interfaces, there is also a depletion of MgO at the edge and the interface (29% relative to the average interior concentration). The CaO, FeO, and Na_2O composition at the edge and the interface show an unusual pattern of enrichment and depletion. This is most visible at the interface, where there is a relative depletion of ∼60% and ∼30% in CaO and FeO concentration, respectively, compared to the interior average concentrations (2.48 ± 0.26% and 2.89 ± 0.16%, respectively) immediately followed by a relative enrichment of CaO and FeO (∼50% and ∼100%, respectively, compared to the aforementioned region of relative depletion) moving from the interior of the object, across the interface into the large host object. The Na_2O plot shows the inverse pattern: a relative enrichment (∼100%) followed by a relative depletion (∼50%) at the interface. The interface, as characterized by the FeO variation, is 9 microns wide. At the edge, there is relative depletion of CaO and FeO (∼50% and ∼30%, respectively), which is not discernible in the X-ray map (Figure 3.14). The X-ray map shows that the enrichment pattern observed at the interface (particularly for CaO) continues all the way around the object as concentric rings of enrichment and

depletion. The absence of this pattern at the edge of the plot of the spot analyses (Figure 4.5) is likely due to the elimination of the points at the very edge which overlapped with the epoxy.

Object C3 shows the more typical pattern of chemical variation at its edge and interface for Al_2O_3, CaO, MgO, and FeO (Figure 4.7). There is a depletion of Al_2O_3 at the interface (9.19 ± 0.12 wt.% in comparison to an average interior concentration of 13.32 ± 0.57 wt.%), followed by an increase in concentration in the host sample C (>18 wt%). The CaO, MgO, and FeO composition at the edge and interface indicates an enrichment of each species, with relative enrichments of 57%, 30%, and 55%, respectively, at the interface (relative to interior average concentrations of 1.78 ± 0.18 wt.%, 0.46 ± 0.04 wt.%, and 2.52 ± 0.16 wt.%, respectively). There is no observable depletion of TiO_2 at the interface, although there is a slight depletion at the edge (17% relative to the interior). The Na_2O composition across the object does not show any discernible variation, with the exception of a relative decrease in concentration of 31% in host Sample C. The interface, as characterized by the FeO concentration variation, is 7.5 microns wide.

Compositional flow structures within object D2 and the large host object (Figure 4.8), are reflected in the major element concentration plots. Despite the extent of the compositional variation observed in Object D2 (>50% relative variation for the Al_2O_3, CaO, MgO, and TiO_2 and datasets) a discernible compositional change at the interface outside of this variation is captured in the data, reflecting the depletion of Al_2O_3 (12.57 ± 0.14 wt%, compared to an average interior concentration of 16.96 ± 0.66 wt.%) and enrichment of CaO (2.21 ± 0.04 wt.% compared to an interior concentration of 1.97 ± 0.21 wt.%) and FeO (4.24 ± 0.13 wt.% compared to an interior concentration of 3.52 ± 0.14 wt.%) at the interface. The interface, as characterized by the FeO concentration variation, is 9 microns wide. The MgO concentration variation does not reflect an enrichment at the interface due to the variation within the sample itself; there is a concentration of 0.82 ± 0.03 wt.% at the interface, compared to the average interior concentration of 0.91 ± 0.07 wt.%. There is a decrease in TiO_2 concentration at the interface, however, there is no observable local minima. It is difficult to distinguish a unique TiO_2 concentration at the interface from the change in concentration between object D2 and the large host object of Sample D due to the uncertainties on each spot analysis. There is no distinguishable Na_2O variation at the interface relative to the Na_2O concentration on either side of it.

Perhaps the most illustrative example of the major element enrichment and depletion trends that appear to be characteristic of interfaces is preserved in object E1 (Figure 4.9). The interface where object E1 is fused to the larger host of sample E shows relative depletions of Al_2O_3 and TiO_2, as well as relative enrichments of CaO, MgO, FeO, and Na_2O. The depletions of Al_2O_3 and TiO_2 are 42% and 32%, respectively, relative to the respective average interior concentrations of 13.78 ± 0.59 wt.% and 0.30 ± 0.01 wt.%. The relative enrichments of MgO and FeO were both 55% compared to their respective average interior concentrations of 0.57 ± 0.04 wt.% and 2.58 ± 0.20 wt.%. The relative enrichment of CaO is 199% compared to the average interior concentration of 1.19 ± 0.10 wt.%. The interface, as characterized by the FeO concentration variation, is 7.5 microns wide.

The interface where object E2 is fused to the larger host object E shows the same trend of depletion and enrichment for all of the major elements observed in Samples A, B, C, and D, with the exception of TiO_2, which does not show a clear pattern of enrichment or depletion at the interface (Figure 4.10). There is a depletion of Al_2O_3 (11.39 ± 0.06 wt.%, compared to an average interior concentration of 13.78 ± 0.59 wt.%) and enrichments of CaO (3.11 ± 0.03 wt.% compared to an average interior concentration of 1.55 ± 0.25 wt.%), MgO (0.93 ± 0.02 wt.% compared to an average interior concentration of 0.57 ± 0.04 wt.%), and FeO (3.71 ± 0.11 wt.% compared to an average interior concentration of 2.58 ± 0.20 wt.%). There is also an enrichment of Na_2O at the interface (3.02 ± 0.04 wt.% compared to an average interior concentration of 2.28 ± 0.39 wt.%), observable in the X-ray map of Na for object E2 (see Figure 3.18), where a layer of relatively higher Na concentration surrounds the entire object. The peak width for interface E2 (as defined by the FeO variation) is 12 microns, is the widest of all of the measured interfaces.

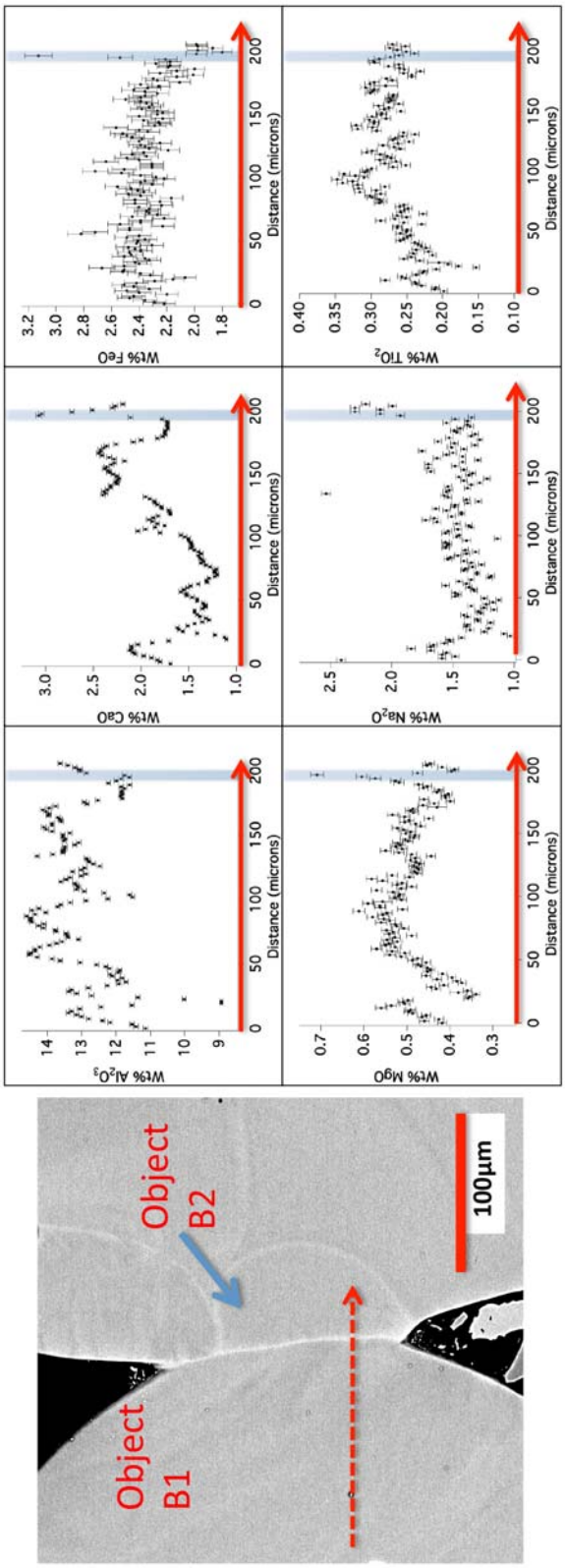

Figure 4.2: EPMA spot analyses across Object B1 (see Figure 3.2 for the full BSE image) showing variation of Al, Ca, Fe, Mg, Na, and Ti oxide concentrations. The location of the analyses is shown in the BSE image as a red-dashed line, along which a series of 1 micron spot analyses were acquired. The interface points, defined by the FeO local maximum, are shaded in blue, and is 4.5 microns wide. Local maxima for CaO, MgO, and FeO at the interface, show enrichment of 74%, 44%, and 32% enriched, respectively, relative to their average interior compositions. Na_2O is increased at the interface, although it is offset by 3 microns. There is ∼40% relative variation through the interior of the object, and a local minima of Al_2O_3 at the interface is apparent. The TiO_2 does not show any trend at the interface.

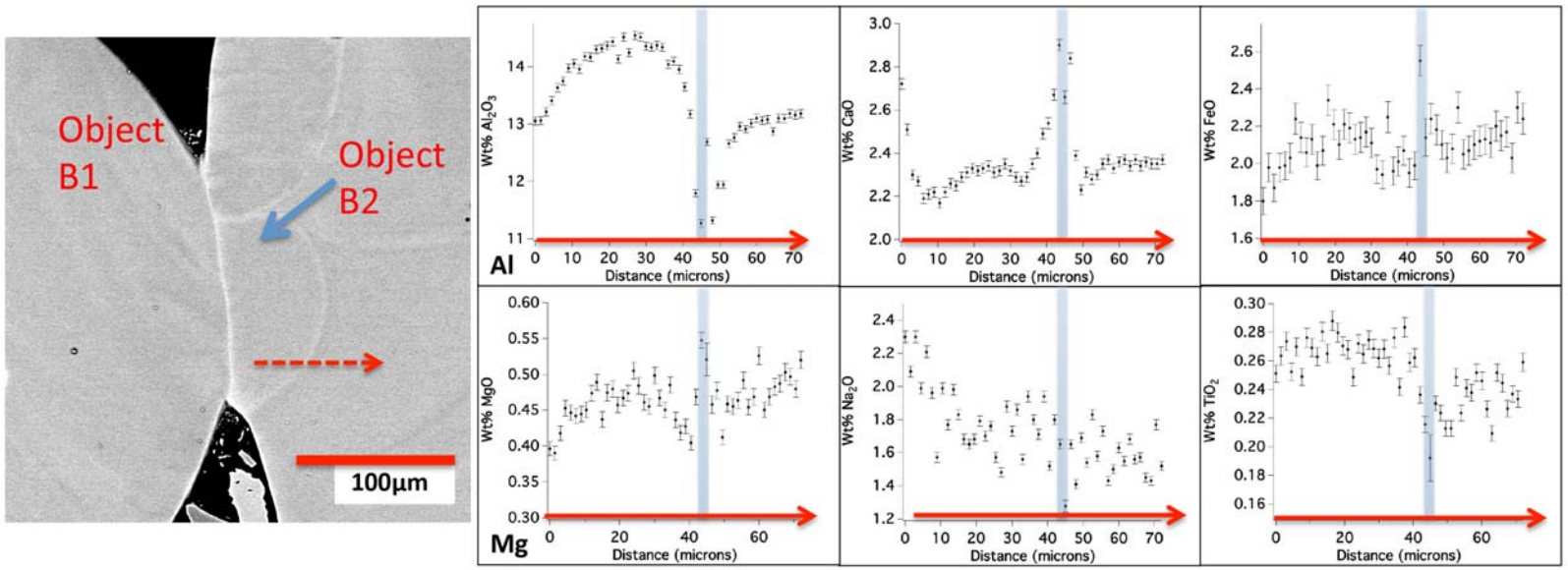

Figure 4.3: EPMA spot analyses across object B2 (along the same traverse shown in Figure 4.1) showing variation of Al, Ca, Fe, Mg, Na, and Ti oxide concentrations. The location of the analyses is shown in the BSE image as a red-dashed line, along which a series of 1 micron spot analyses were acquired. The interface points, defined by the FeO local maximum, are shaded in blue, and is 3 microns wide. This dataset is a continuation of the dataset given for Object B1, where the data at 200 microns in Figure 4.2 correspond to the data at 0 microns in Figure 4.3. The Al_2O_3 plot reveals a depletion at the interface, while the FeO, MgO, and CaO plots show a co-location of increased concentration at the interface relative to the interior concentrations of these species. The TiO_2 plot shows a depletion of 24% at the interface relative to the interior concentration. There is no observable pattern of enrichment or depletion in Na_2O through the object, or at the interface itself.

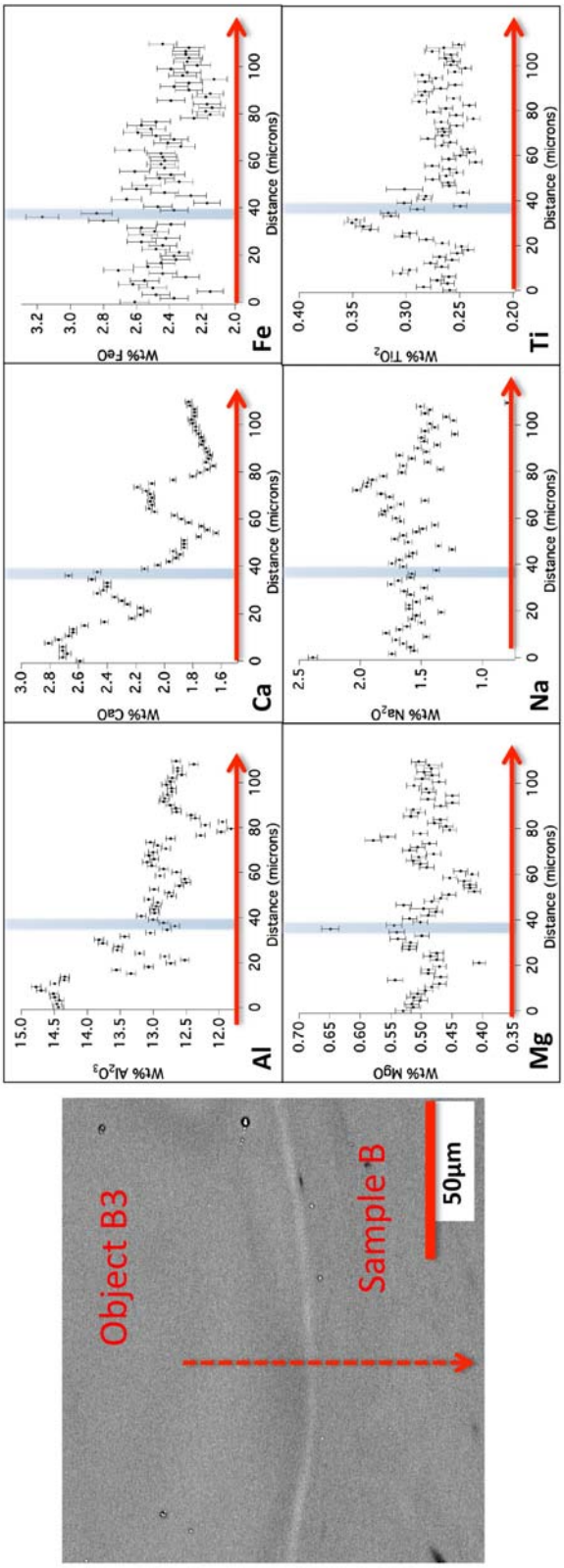

Figure 4.4: EPMA spot analyses across object B3 showing variation of Al, Ca, Fe, Mg, Na, and Ti oxide concentrations. The location of the analyses is shown in the BSE image as a red-dashed line, along which a series of 1 micron spot analyses were acquired. The interface points, defined by the FeO local maximum, are shaded in blue, and is 6 microns wide. Local minima are observed for Al_2O_3 and TiO_2, and local maxima are observed for CaO, FeO, and MgO at the interface. Na_2O does not show an obvious trend of enrichment or depletion at the interface.

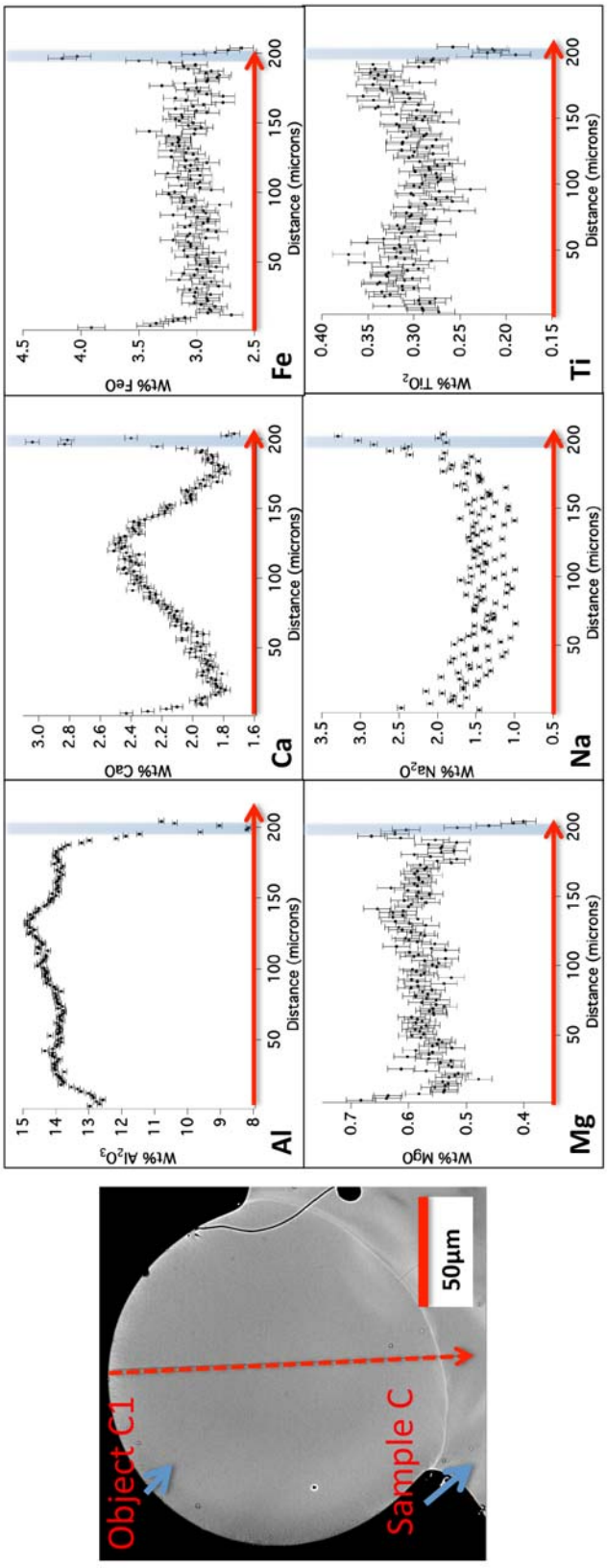

Figure 4.5: EPMA spot analyses across object C1 showing variation of Al, Ca, Fe, Mg, Na, and Ti oxide concentrations. The location of the analyses is shown in the BSE image as a red-dashed line, along which a series of 1 micron spot analyses were acquired. The interface points, defined by the FeO local maximum, are shaded in blue, and is 9 microns wide. Al_2O_3 and TiO_2 are depleted at the interface, while CaO, FeO, MgO, and Na_2O are enriched relative to the interior concentrations. The Na_2O and MgO maxima are 3 microns offset from the FeO maxima.

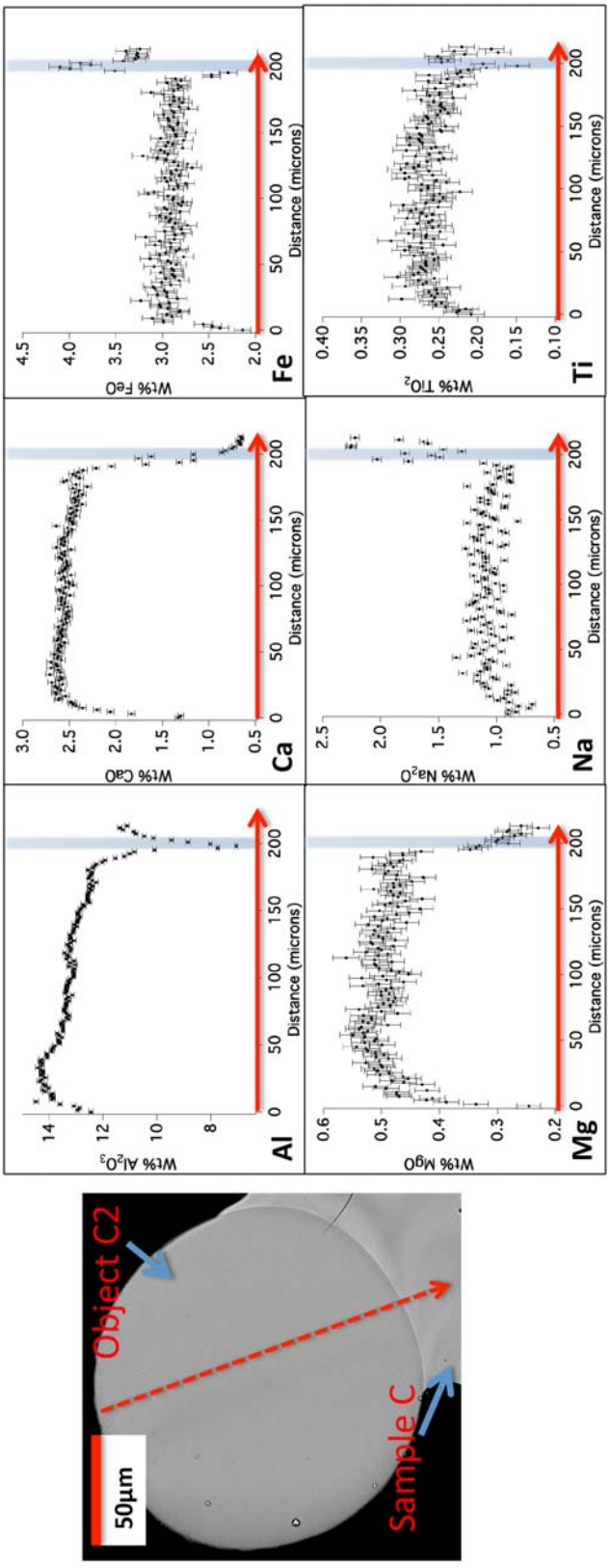

Figure 4.6: EPMA spot analyses across object C2 showing variation of Al, Ca, Fe, Mg, Na, and Ti oxide concentrations. The location of the analyses is shown in the BSE image as a red-dashed line, along which a series of 1 micron spot analyses were acquired. The interface points, defined by the FeO local maximum, are shaded in blue, and is 9 microns wide. The interior points for all the major elements show a relatively homogeneous composition. There is a unique pattern of compositional variation at both the edge and the interface in CaO, FeO, and Na_2O. This is most visible at the interface, where there is a relative depletion of CaO and FeO concentration immediately followed by a relative enrichment of CaO and FeO, and an inverse pattern in Na_2O. At the edge, EPMA data show relative depletion of CaO and FeO, and X-ray mapping shows that this enrichment pattern (particularly for CaO) continues all the way around the object as concentric rings (Figure 3.14).

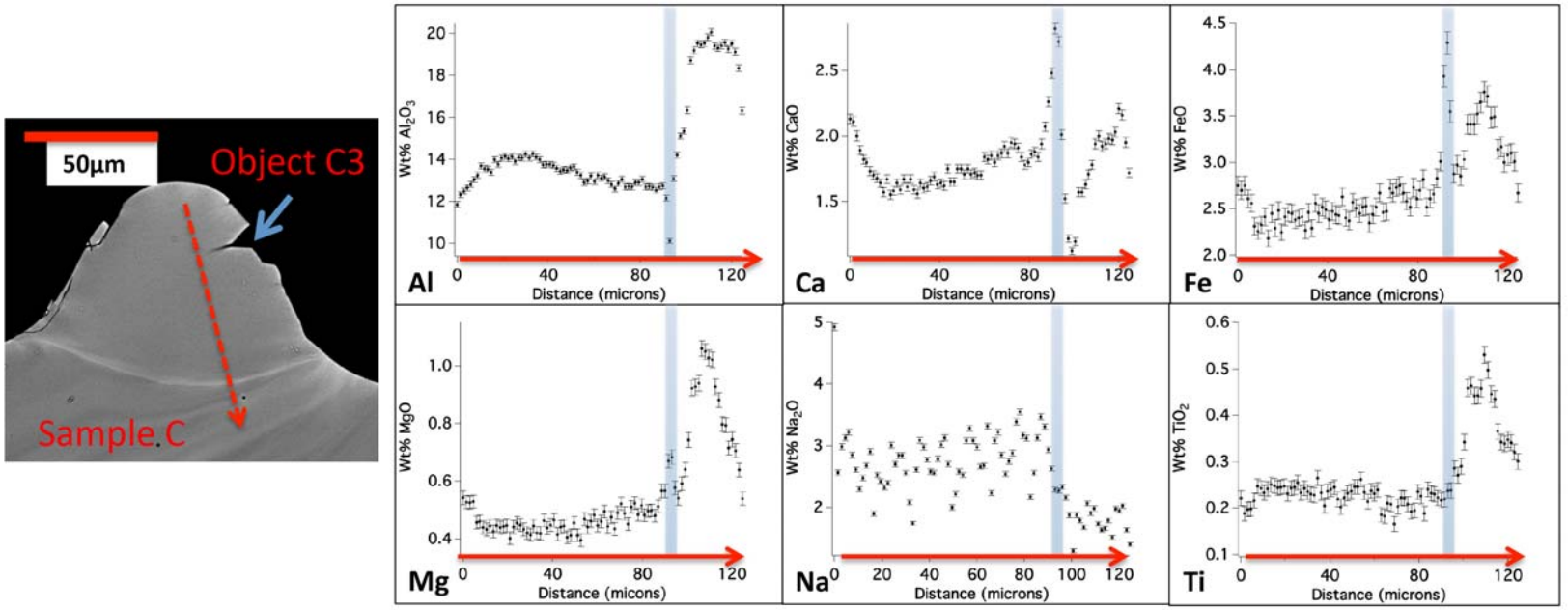

Figure 4.7: EPMA spot analyses across object C3 showing variation of Al, Ca, Fe, Mg, Na, and Ti oxide concentrations. The location of the analyses is shown in the BSE image as a red-dashed line, along which a series of 1 micron spot analyses were acquired. The interface points, defined by the FeO local maximum, are shaded in blue, and is 7.5 microns wide. This object shows the more typical pattern of chemical variation at its edge and interface for Al_2O_3, CaO, MgO, and FeO. There is a depletion of Al_2O_3 at the interface in comparison to its average interior concentration, followed by increase in concentration in host sample C. The CaO, MgO, and FeO composition at the edge and interface indicate enrichment of each species relative to the interior. There is no observable depletion of TiO_2 at the interface. The Na_2O composition across the object or interface does not show any discernible variation, and there is a relative depletion of Na_2O in the larger host of Sample C.

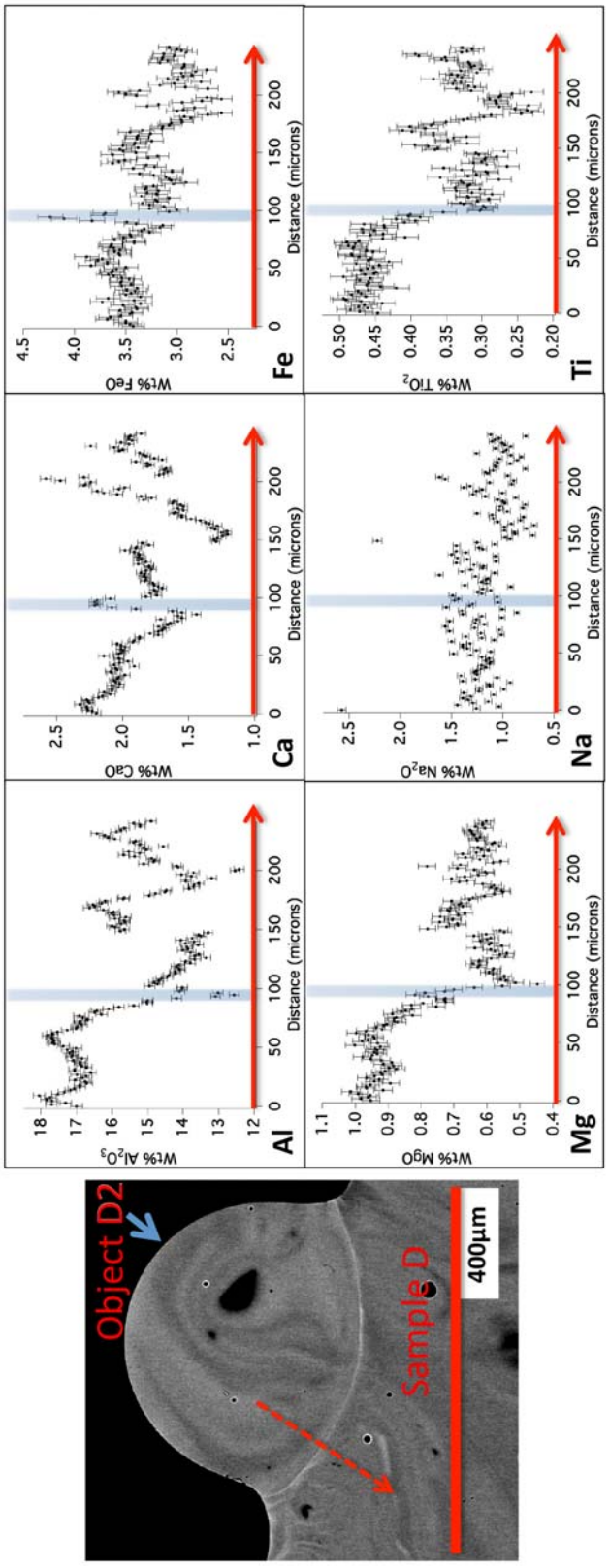

Figure 4.8: EPMA spot analyses across object D2 showing variation of Al, Ca, Fe, Mg, Na, and Ti oxide concentrations. The location of the analyses is shown in the BSE image as a red-dashed line, along which a series of 1 micron spot analyses were acquired. The interface points, defined by the FeO local maximum, are shaded in blue, and is 9 microns wide. As seen in the BSE image, there are visible compositional flow structures within object D2 which are reflected in the major element concentration plots. There is a depletion of Al_2O_3 and TiO_2 at the interface, and a corresponding enrichment of CaO, FeO, and MgO relative to the values on either side of the interface. There is no distinguishable Na_2O variation at the interface relative to the Na_2O concentration on either side of it.

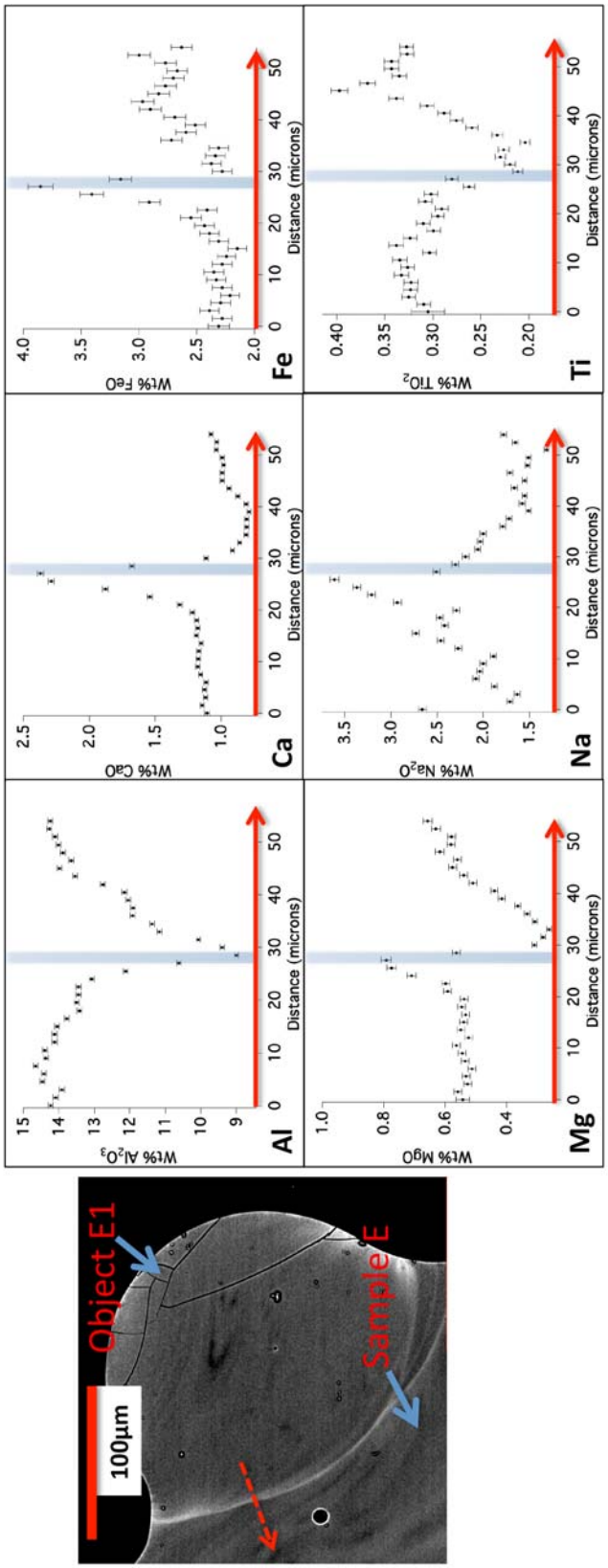

Figure 4.9: EPMA spot analyses across object E1 showing variation of Al, Ca, Fe, Mg, Na, and Ti oxide concentrations. The location of the analyses is shown in the BSE image as a red-dashed line, along which a series of 1 micron spot analyses were acquired. The interface points, defined by the FeO local maximum, are shaded in blue, and is 7.5 microns wide.The interface where object E1 is fused to the larger host of sample E shows relative depletions of Al_2O_3 and TiO_2, as well as relative enrichments of CaO, MgO, FeO, and Na_2O. The relative enrichment of CaO is the largest relative increase of any interface (199%) compared to the average interior concentration.

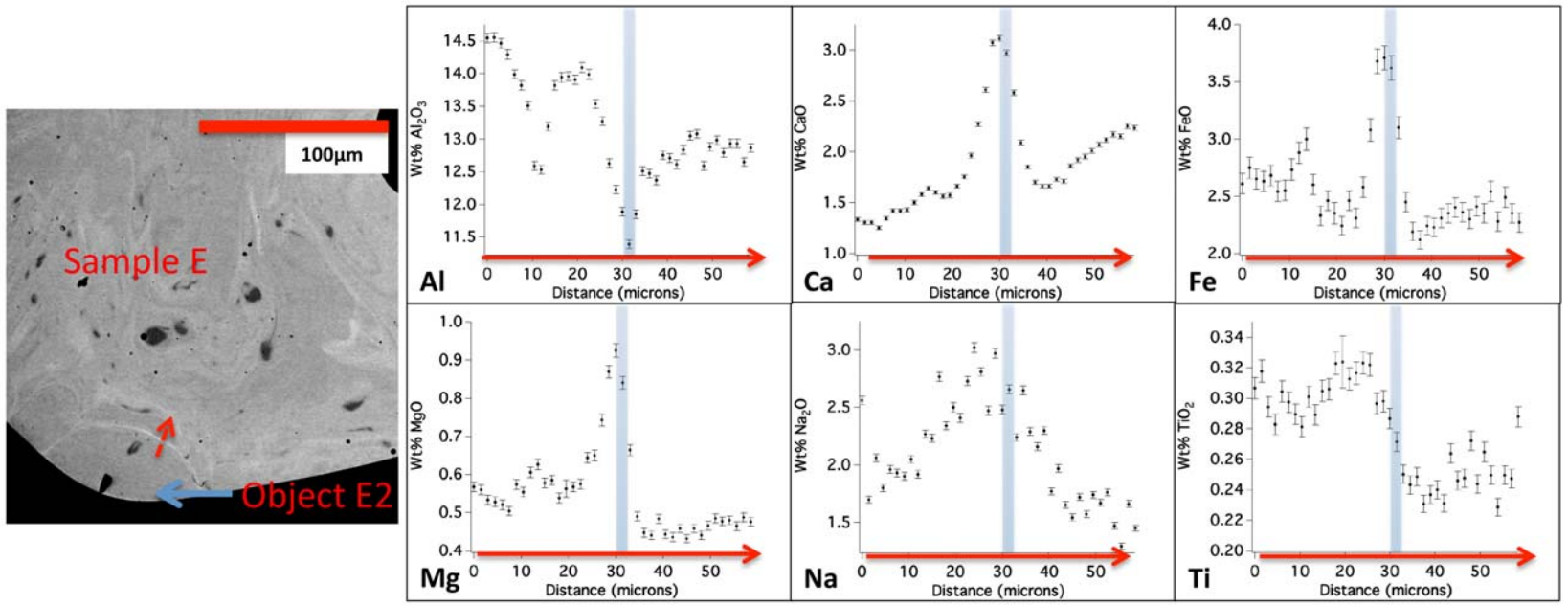

Figure 4.10: EPMA spot analyses across object E2 showing variation of Al, Ca, Fe, Mg, Na, and Ti oxide concentrations. The location of the analyses is shown in the BSE image as a red-dashed line, along which a series of 1 micron spot analyses were acquired. The interface points, defined by the FeO local maximum, are shaded in blue, and is 12 microns wide, which is the widest of all of the measured interfaces.There is a depletion of Al_2O_3 at the interface, and a corresponding enrichment of CaO, FeO, and MgO relative to the values on either side of the interface. TiO_2 does not show a clear pattern of enrichment or depletion at the interface. There is also an enrichment of Na_2O at the interface, which appears diffuse and is offset from the FeO maxima by 4.5 microns (also observable in the X-ray map of Na for object E2, see Figure 3.18).

Summary of quantitative major element fallout glass analyses

The major element traverses show a chemical enrichment of Fe and Ca observed at every interface, along with a corresponding depletion of Al and Ti, relative to the interiors of agglomerated objects. While the interface values do not show a pattern of enrichment or depletion in comparison to the interface values for SiO_2 (Figure 4.11, top left), all of the interface values (ranging from 5.37 - 12.67 wt.%) are depleted in Al_2O3 relative to their respective average values (ranging from 12.78 - 16.96 wt.%). All of the interface values for CaO (ranging from 2.55 - 4.49 wt.%) and FeO (ranging from 1.76 - 3.11 wt.%, Figure 4.11, top right) are enriched compared to their interior average values (ranging from 1.19 - 2.49 wt.% and 2.13 - 3.52 wt.% respectively), with the exception of B2 and C2. The TiO_2 concentration at the interface (ranging from 0.15-0.29 wt.%) is depleted relative to the interior average (ranging from 0.46 - 0.91 wt.%, Figure 4.11, bottom left) in all the objects except B1 and B3. Neither the K_2O nor the Na_2O concentrations show a discernible pattern of enrichment or depletion at the interface relative to the interior averages (Figure 4.11, bottom right).

The compositional and spatial data for 9 measured interfaces are presented in Table 4.1. Localized enrichments of Fe, Ca, and Mg (converted to oxides) are observed at all 9 measured interfaces (Table 4.1). As the concentration of each measured element varies considerably on either side of the interface, nominal values are described here as the average value of three points on either side of the peak for each oxide of interest, exemplifying the increase in concentration of these species due to a deposition layer. Both Fe and Ca interface enrichments are observed to be $\sim$50% relative to their corresponding nominal values observed on either side of each interface. A corresponding depletion at the interface of Al and Ti is also observed at all 9 interfaces measured with EPMA, with both elements depleted $\sim$20% relative to the nominal values on either side of the minima for each interface (Table 4.1). Six of the 9 interfaces are shown to have a relative enrichment of Na_2O compared to the nominal values on either side of the interface (Table 4.1). A schematic characterizing this observed trend in compositional variation at the outer edges and interfaces of agglomerated fallout objects is given in Figure 4.12.

Table 4.1: Summary of WDS analyses at interfaces characterizing the relative enrichment and depletion in comparison to nominal values on either side of the interface. The uncertainties on the maxima/minima are the 1σ uncertainties on the measurement. The Na_2O data may be underestimated due to the volatilization effect described in Section 2.2. The uncertainties on the nominal values are the 1σ standard deviation of 6 spot analyses on either side of the interface.

	Al_2O_3		Na_2O		FeO	
	Local Min (wt%)	Nominal (wt%)	Local Max (wt%)	Nominal (wt%)	Local Max (wt%)	Nominal (wt%)
B1	11.62 ± 0.06	13.02 ± 1.05	2.30 ± 0.04	1.67 ± 0.30	3.13 ± 0.10	2.37 ± 0.13
B2	11.27 ± 0.07	13.53 ± 0.77	1.65 ± 0.03	1.67 ± 0.19	2.55 ± 0.08	2.10 ± 0.12
B3	12.67 ± 0.07	13.06 ± 0.69	1.75 ± 0.01	1.67 ± 0.10	3.17 ± 0.10	2.40 ± 0.14
C1	5.37 ± 0.05	11.73 ± 0.90	2.24 ± 0.04	1.58 ± 0.14	4.21 ± 0.11	2.98 ± 0.22
C2	7.05 ± 0.06	13.09 ± 0.90	2.03 ± 0.04	1.64 ± 0.55	4.10 ± 0.12	2.91 ± 0.18
C3	9.19 ± 0.12	14.93 ± 1.15	3.00 ± 0.05	2.21 ± 0.62	4.49 ± 0.12	2.90 ± 0.25
D2	12.57 ± 0.14	15.60 ± 1.39	1.32 ± 0.03	1.32 ± 0.23	4.24 ± 0.13	3.29 ± 0.28
E1	9.00 ± 0.06	15.60 ± 1.39	3.61 ± 0.04	2.45 ± 0.50	3.85 ± 0.11	2.49 ± 0.24
E2	11.39 ± 0.06	13.30 ± 1.32	3.02 ± 0.04	2.40 ± 0.20	3.71 ± 0.11	2.46 ± 0.20

	MgO		CaO		TiO_2	
	Local Max (wt%)	Nominal (wt%)	Local Max (wt%)	Nominal (wt%)	Local Min (wt%)	Nominal (wt%)
B1	0.71 ± 0.01	0.49 ± 0.05	3.07 ± 0.03	1.76 ± 0.38	0.24 ± 0.01	0.27 ± 0.03
B2	0.55 ± 0.01	0.46 ± 0.03	2.90 ± 0.03	2.35 ± 0.13	0.19 ± 0.01	0.25 ± 0.02
B3	0.65 ± 0.01	0.49 ± 0.03	2.67 ± 0.03	2.07 ± 0.34	0.25 ± 0.01	0.27 ± 0.02
C1	0.73 ± 0.03	0.65 ± 0.12	2.93 ± 0.04	1.90 ± 0.28	0.19 ± 0.02	0.30 ± 0.04
C2	0.34 ± 0.02	0.48 ± 0.06	1.76 ± 0.04	2.39 ± 0.47	0.15 ± 0.02	0.26 ± 0.02
C3	0.73 ± 0.03	0.56 ± 0.06	2.74 ± 0.04	1.74 ± 0.26	0.23 ± 0.02	0.29 ± 0.05
D2	0.82 ± 0.03	0.73 ± 0.15	2.21 ± 0.04	1.86 ± 0.27	0.29 ± 0.02	0.37 ± 0.08
E1	0.79 ± 0.02	0.51 ± 0.11	2.37 ± 0.02	1.06 ± 0.17	0.21 ± 0.01	0.31 ± 0.04
E2	0.93 ± 0.02	0.52 ± 0.06	3.11 ± 0.03	1.74 ± 0.31	0.25 ± 0.01	0.28 ± 0.03

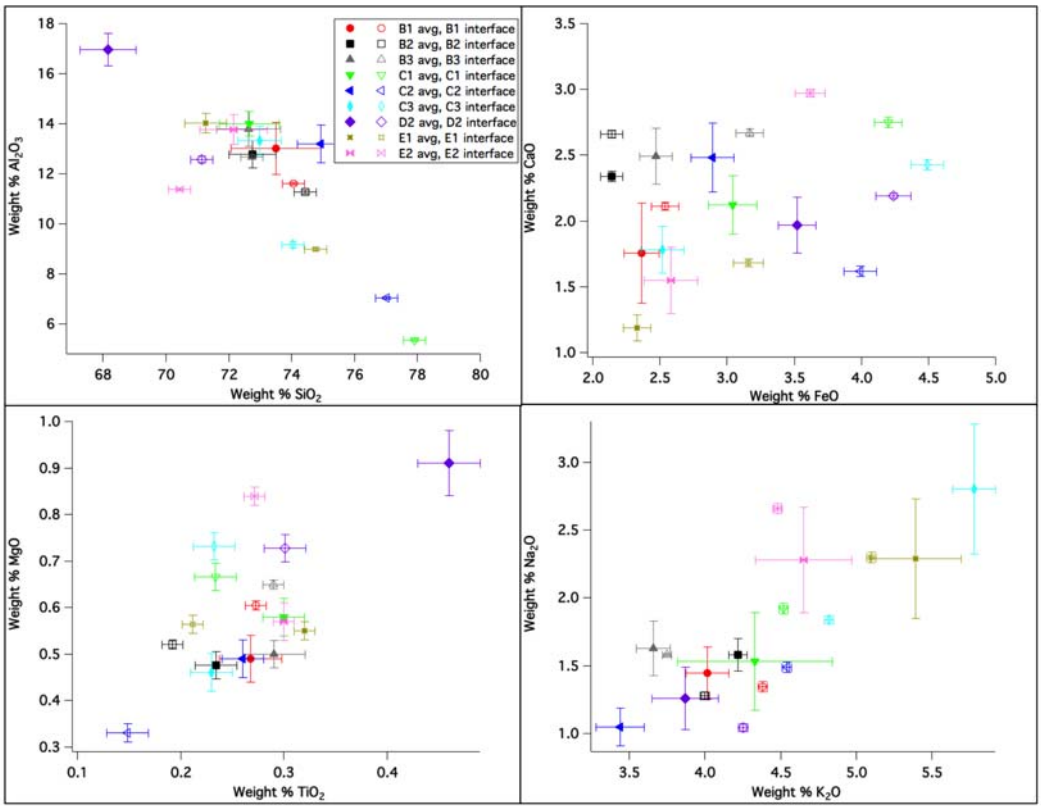

Figure 4.11: Average major element oxide composition of the interiors of agglomerated fallout objects B1, B2, B3, C1, C2, C3, D2, E1, and E2, with their corresponding interface values (1σ uncertainties). While the interface values do not show a pattern of enrichment or depletion in comparison to the interface values for SiO_2 (top left), all of the interface values are depleted in Al_2O3 relative to their respective average values. All of the interface values for CaO and FeO (top right) are enriched compared to their interior average values, with the exception of B2 and C2. The MgO concentration (bottom left) at the interface is enriched relative to the interior average value in all objects except C2 and D2, while the TiO_2 concentration at the interface is depleted relative to the interior average in all the objects except B1 and B3. Neither the K_2O nor the Na_2O concentrations show a discernible pattern of enrichment or depletion at the interface relative to the interior averages.

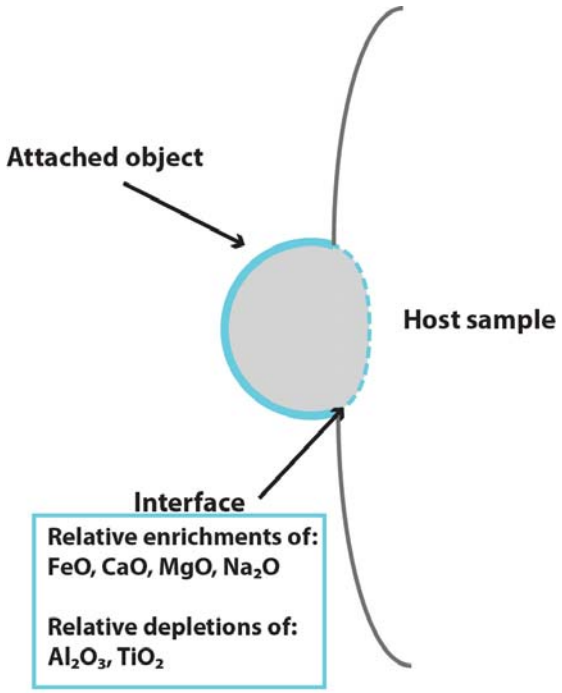

Figure 4.12: Diagram of the most commonly observed compositional variation observed at the edges and interfaces of agglomerated fallout objects.

Quantitative major element soil analyses

Quantitative compositional analyses of soil were acquired by EPMA on polished grains from soil acquired proximate to ground zero. These analyses provide a general understanding of the composition of the soil, which served as the carrier material precursor for fallout glass from this test. While these analyses do not provide a comprehensive mineralogical survey of the soil, they do provide a context through which to understand the possible combinations of mineral compositions that combined to form the dominant glass compositions in the resultant fallout. To a first order, the contribution from non-soil sources to major element concentrations in these glasses is considered negligible. Qualitatively, backscatter electron imaging (*e.g.,* Figure 3.6) reveals that the soil is primarily comprised of fine-grained granitic and rhyolitic clasts (<1 mm). The mineralogy is dominated by clay, as well as roughly equal amounts of feldspar minerals and quartz, with lesser amounts of pyroxene and ilmenite. All spot analyses made on the darkest regions (Figure 3.6) revealed a >98% SiO_2 composition, and were compositionally consistent with quartz.

A series of 18 WDS spot analyses were acquired on suspected feldspar minerals observed in the soil, which are presented in Table 4.2. The major element composition reveals a range of compositions, which were then used to determine the fraction of feldspar components contributing to each analysis, presented in Table 4.3, (illustrated in Figure 4.13), where representative analyses are shown on corresponding minerals in BSE imaging. The feldspar component mole fractions show that the feldspar minerals observed in the soil include plagioclase and alkali feldspars.These compositions were plotted as a ternary diagram in Figure 4.14, with the designated feldspar mineral ranges superimposed on the plotted data. From this plot, it is clear that the analyzed feldspar minerals fall predominantly in the ranges defined for andesine and sanidine (Figure 4.13). As shown in Figure 4.14, the sanidine compositions have roughly equal concentrations of Na and K, and the andesine concentrations have a Ca:Na ratio of ∼2:3. This is similar the concentrations of these species observed in the soil analyses of Eppich et al. (2014) from the same test [55], indicating that these feldspar minerals may be the dominant contributors of Na, K, and Ca to the soil, which served as the carrier materials precursors for the fallout objects in this study. Further, the analyzed feldspar minerals have high concentrations of Al_2O_3 (>17%, Table 4.2), and are one of the predominant sources of Al in the soil (which serves as a carrier for glassy fallout), which has a concentration of ∼10 wt % Al_2O_3 [55].

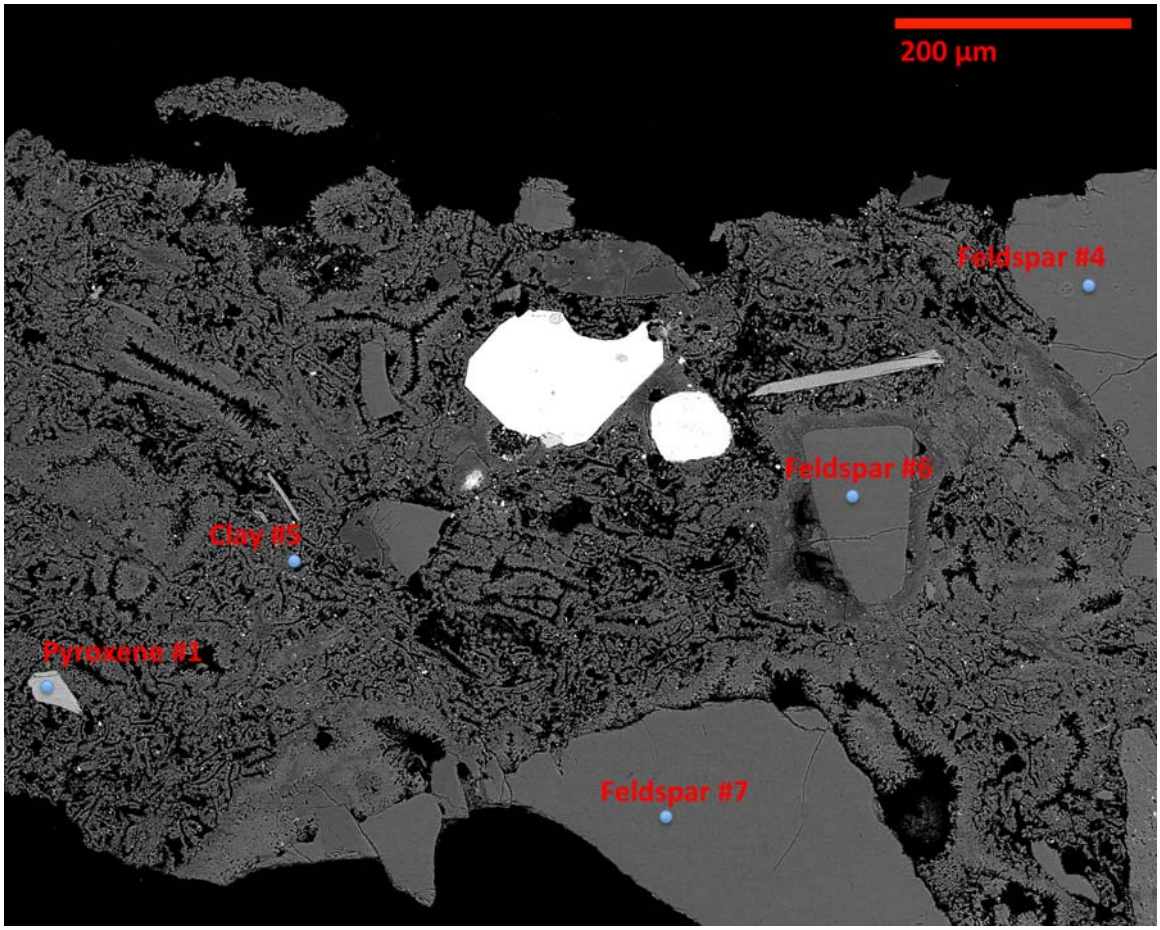

Figure 4.13: Three representative soil analyses on feldspar minerals from a soil grain acquired proximate to ground zero of this test, as shown in BSE imaging. These spots correspond to feldspar analyses #4, 6, and 18 in Tables 4.2 and 4.3, corresponding to andesine (spots 4 and 6) and sanidine (spot 18) as shown in Figure 4.14. Also shown in this figure is a representative pyroxene, corresponding to pyroxene analysis #1 in Table 4.4, characterized as clinoenstatite in Figure 4.15.

Table 4.2: Major element composition of feldspar minerals in soil samples proximate to ground zero acquired by EPMA spot analyses. Uncertainties are 1σ.

Analysis #	SiO_2	TiO_2	Al_2O_3	FeO	MnO	MgO	CaO	Na_2O	K_2O	Total
1	63.36±0.48	0.10±0.04	20.69±0.12	0.29±0.06	0.10±0.05	0.00±0.00	1.09±0.03	4.65±0.07	8.46±0.04	98.74
2	61.43±0.47	0.13±0.04	20.73±0.12	0.25±0.06	0.01±0.04	0.00±0.00	1.12±0.03	4.73±0.08	8.3±0.04	96.7
3	58.20±0.50	0.07±0.03	24.48±0.13	0.84±0.09	0.06±0.05	0.09±0.02	6.26±0.06	6.00±0.08	2.11±0.02	98.12
4	58.09±0.46	0.00±0.03	26.00±0.14	0.38±0.07	0.02±0.05	0.02±0.02	7.13±0.06	6.53±0.09	1.39±0.02	99.56
5	66.43±0.48	0.00±0.00	18.95±0.12	1.03±0.09	0.00±0.00	0.00±0.00	0.01±0.01	6.73±0.09	6.68±0.04	99.83
6	59.29±0.46	0.09±0.03	24.69±0.13	0.34±0.06	0.00±0.00	0.00±0.00	6.01±0.06	6.92±0.09	1.75±0.02	99.09
7	59.86±0.47	0.08±0.03	24.58±0.13	0.37±0.07	0.00±0.00	0.00±0.00	5.60±0.06	7.18±0.09	1.65±0.02	99.32
8	59.63±0.47	0.04±0.03	25.01±0.13	0.30±0.07	0.06±0.05	0.02±0.02	6.15±0.06	6.77±0.09	1.66±0.02	99.63
9	64.28±0.48	0.04±0.03	20.34±0.12	0.19±0.06	0.04±0.05	0.00±0.00	0.90±0.03	5.67±0.08	7.87±0.04	99.33
10	66.07±0.48	0.02±0.03	20.03±0.12	0.10±0.06	0.00±0.00	0.00±0.00	0.33±0.02	6.88±0.09	6.77±0.04	100.2
11	66.99±0.48	0.05±0.03	20.00±0.12	0.11±0.06	0.00±0.00	0.01±0.02	0.44±0.02	7.24±0.09	6.06±0.04	100.9
12	57.33±0.45	0.06±0.04	26.54±0.14	0.59±0.07	0.00±0.00	0.03±0.02	8.32±0.07	5.75±0.08	1.55±0.02	100.17
13	64.14±0.48	0.00±0.00	22.26±0.12	0.17±0.05	0.00±0.00	0.00±0.00	3.00±0.04	8.83±0.10	1.31±0.02	99.71
14	64.71±0.48	0.05±0.03	19.91±0.12	0.27±0.06	0.00±0.00	0.00±0.00	0.51±0.02	4.01±0.07	10.39±0.05	99.84
15	64.22±0.48	0.00±0.00	22.65±0.13	0.17±0.05	0.00±0.00	0.00±0.00	3.06±0.04	8.86±0.10	1.33±0.02	100.29
16	62.36±0.47	0.01±0.03	22.99±0.13	0.14±0.06	0.02±0.04	0.01±0.02	3.30±0.04	8.81±0.10	1.23±0.02	98.87
17	65.63±0.48	0.00±0.00	19.69±0.12	0.09±0.05	0.00±0.00	0.00±0.00	0.22±0.02	4.01±0.07	11.04±0.05	100.68
18	68.49±0.49	0.07±0.04	17.49±0.11	2.22±0.13	0.01±0.05	0.00±0.00	0.00±0.00	6.33±0.09	7.29±0.04	101.9

Table 4.3: Feldspar component mole % derived from major element compositions of feldspar minerals in soil samples, as calculated by major element composition [78].

Analysis #	Anorthite ($CaAl_2Si_2O_8$)	Albite ($NaAlSi_3O_8$)	Orthoclase ($KAlSi_3O_8$)
1	5.54	42.99	51.46
2	5.71	43.76	50.53
3	31.89	55.31	12.80
4	34.61	57.36	8.03
5	0.05	60.46	39.49
6	29.15	60.74	10.11
7	27.24	63.20	9.56
8	30.18	60.12	9.70
9	4.39	49.97	45.64
10	1.58	59.74	38.68
11	2.13	63.11	34.76
12	40.45	50.58	8.97
13	14.61	77.80	7.59
14	2.51	36.04	61.45
15	14.80	77.54	7.66
16	15.94	76.99	7.07
17	1.05	35.20	63.76
18	0.00	56.89	43.11

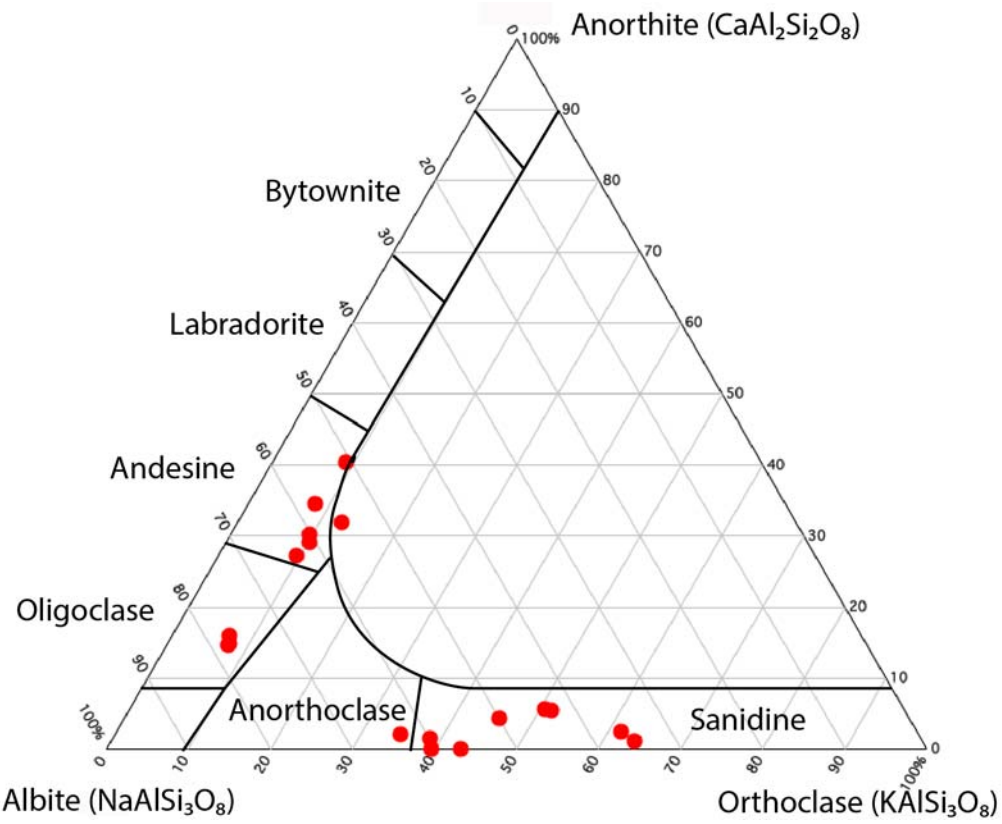

Figure 4.14: Ternary diagram of feldspar components, with EPMA spot analyses of feldspar minerals in selected soil samples overlaid based on their component mole fraction. The analyzed feldspar minerals fall predominantly in the ranges defined for andesine and sanidine. The sanidine compositions have roughly equal concentrations of Na and K, and the andesine concentrations have a Ca:Na ratio of ∼2:3.

To a lesser extent, various minerals of relatively higher average atomic number were also observed in backscatter imaging of the soil samples (approximately 10% of the observed non-clay minerals). EPMA spot analyses of the brightest regions acquired by WDS identified most of these minerals as ilmenite ($FeTiO_3$, see Figure 3.6), with a composition approximately equal parts FeO and TiO_2 (42% and 48% by weight, respectively, with approximately 1% of both MgO and MnO). Other high-Z minerals were identified as pyroxene of various composition (Table 4.4). The major element analyses were used to determine the pyroxene component fractions of each of the 3 analyses. The components fractions show that the pyroxene minerals observed in the soil include at least two distinct pyroxene compositions.These component fractions were plotted as a ternary diagram in Figure 4.14, with the designated pyroxene mineral ranges superimposed on the plotted data. From this plot, it is clear that the analyzed pyroxene minerals fall in the range defined for clinoenstatite ($Mg_2Si_2O_6$) and diopside ($CaMgSi_2O_6$) (Figure 4.15), and are the predominant source of Mg observed in the soil samples. Further, diopside (along with andesine, Table 4.2) may also serve as a significant source of Ca in these fallout glasses (which have a Ca concentration ranging from 1.19 - 2.49 wt.%, Figure 4.1), although it was relatively rare. The clay minerals which predominate the soil samples were also characterized by EPMA. However, the effect of volatilization on clay minerals makes data acquisition by EPMA difficult, often producing major element sum totals <96%. A total of 6 spot analyses on clay minerals (*e.g.,* Analysis #5, Figure 4.13) were acquired with adequate sum totals (>96%), and are presented in Table 4.6. These minerals have significant SiO_2 (77.26 ± 6.66 wt.%), Al_2O_3 (11.81 ± 3.08 wt.%), K_2O (4.76 ± 0.98 wt.%), Na_2O (4.02 ± 0.91 wt.%), and FeO (1.94 ± 0.86 wt.%) concentrations, and likely serve as a significant source of these species in the fallout glasses, which have similar concentrations of these species (Figure 4.1).

Although data was not acquired on all of the observed minerals, there is assuredly a broader range of pyroxene, ilmenite, and feldspar compositions in the soil than represented by the above dataset. Other less common minerals, such as zircons, were also rarely observed; these were only cursorily analyzed in real-time by EDS, and quantitative data were not acquired.

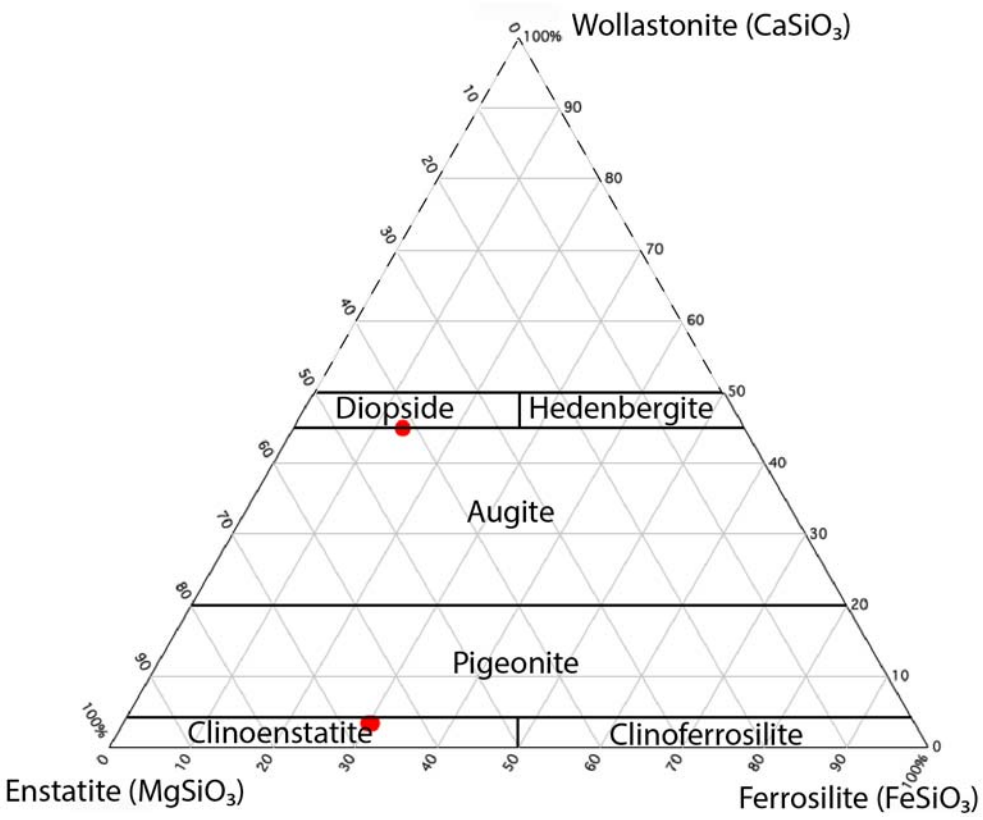

Figure 4.15: Ternary diagram of pyroxene components, with EPMA spot analyses of pyroxene minerals in selected soil samples overlaid based on their component mole fraction, showing a predominance of Mg-rich pyroxenes.

Table 4.4: Major element composition of pyroxene minerals in soil samples proximate to ground zero acquired by EPMA spot analyses. Uncertainties are 1σ.

Analysis #	SiO_2	TiO_2	Al_2O_3	FeO	MnO	MgO	CaO	Na_2O	Total
1	52.89±0.44	0.35±0.04	0.76±0.03	18.72±0.34	0.69±0.08	23.49±0.15	1.68±0.03	0.07±0.00	98.68
2	48.03±0.41	1.56±0.06	5.91±0.07	8.18±0.23	0.12±0.06	14.30±0.12	21.51±0.11	0.35±0.01	100.42
3	53.09±0.45	0.31±0.04	0.76±0.03	18.66±0.35	0.72±0.09	22.81±0.15	1.61±0.03	0.00±0.00	97.98

Table 4.5: Pyroxene component mole % derived from major element compositions of pyroxene minerals in soil samples as calculated from major element composition [79]

Analysis #	Wollastonite ($CaSiO_3$)	Enstatite ($MgSiO_3$)	Ferrosilite ($FeSiO_3$)
1	3.43	66.73	29.83
2	45.01	41.63	13.36
3	3.36	66.24	30.40

Table 4.6: Major element composition of clay minerals in soil samples proximate to ground zero acquired by EPMA spot analyses. Uncertainties are 1σ.

Analysis #	Al_2O_3	FeO	MnO	Na_2O	MgO	K_2O	CaO	SiO_2	TiO_2	Total
1	11.88±0.09	1.55±0.11	0.03±0.04	4.21±0.07	0.01±0.02	4.84±0.03	0.25±0.02	78.56±0.51	0.06±0.03	101.40
2	12.54±0.10	2.54±0.13	0.11±0.05	4.89±0.08	0.02±0.02	5.54±0.03	0.04±0.01	74.84±0.50	0.07±0.04	100.60
3	10.22±0.09	1.21±0.10	0.03±0.05	3.25±0.06	0.00±0.00	4.52±0.03	0.04±0.01	80.51±0.52	0.04±0.03	99.85
4	7.04±0.07	1.10±0.09	0.00±0.00	2.61±0.06	0.00±0.00	2.94±0.03	0.02±0.01	86.61±0.53	0.07±0.04	100.45
5	16.35 ±0.11	3.34±0.15	0.15±0.06	4.45±0.07	0.05±0.02	5.62±0.03	0.09±0.01	66.49±0.48	0.05±0.04	96.59
6	12.82±0.10	1.91±0.12	0.00±0.00	4.76±0.08	0.00±0.00	5.08±0.03	0.03±0.01	76.56±0.51	0.00±0.00	101.33

In Figure 4.16, the Al_2O_3 data is plotted against the SiO_2 data for the feldspar analyses, clay analyses, as well as the analyses acquired by EPMA within the attached glassy fallout objects and their interfaces. In this figure, the data closest to the local maximum at the interfaces of each agglomerated fallout object is represented by red hexagons, the analyses acquired within the attached objects is shown as gray triangles, the feldspar analyses are shown as black diamonds, and the clay analyses are shown as blue triangles. The black line is a linear fit of the feldspar data with a pure quartz (100% SiO_2) data point, which approximates a first order mixing relationship between the measured feldspar and observed quartz in the soil data. The clay data fall into the same compositional region as the analyses on the interiors of attached glassy fallout objects, and 4 of the 6 data points fall along the line representing simple mixing between quartz and feldspar. This indicates that the major element (*i.e.,* Si, Al) composition of the attached objects can be described, to a first order, as a mixture between these major soil components (*i.e.,* clay, feldspar minerals, and quartz). The dashed gray line represents a linear fit of the interface data points, showing a similar relationship between Al_2O_3 and SiO_2, but offset from the composition of both soil and the interiors of the agglomerated fallout objects. This is indicative of the contribution of another component that significantly altered the major element composition of the interface.

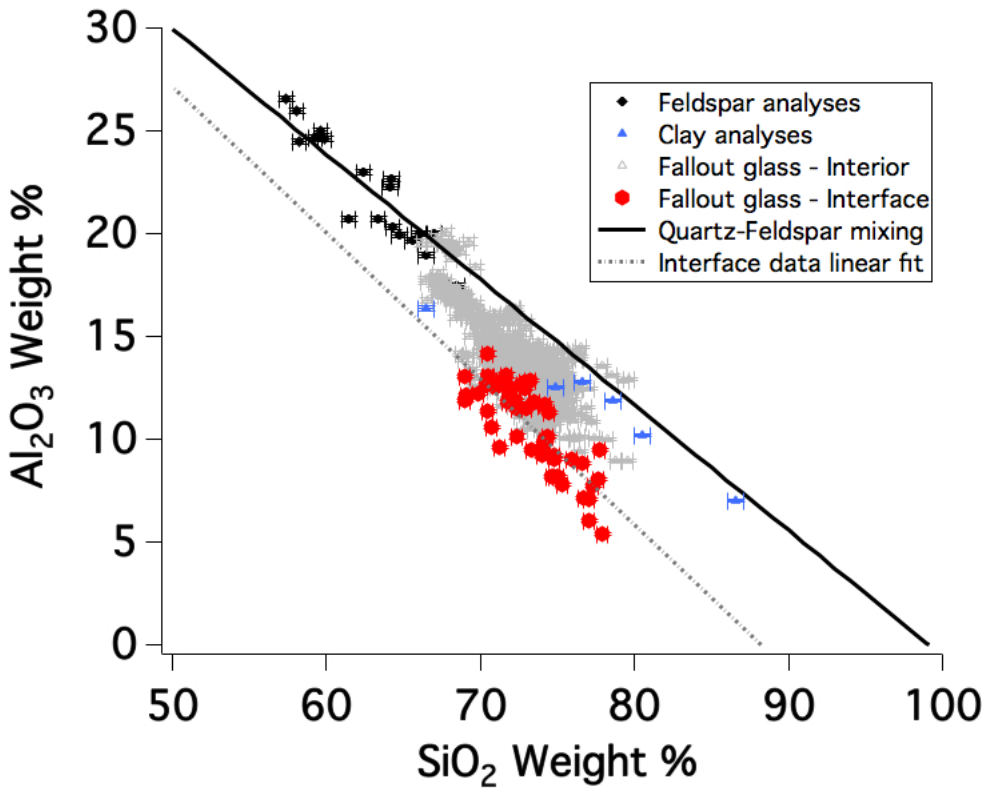

Figure 4.16: The Al_2O_3 vs. SiO_2 data for feldspar, clay and fallout glasses. The interface data is shown as red hexagons (representing points at the interface proximate to the local maxima/minima), and the interior data is shown as gray triangles. Feldspar analyses are shown as black diamonds, all uncertainties are given as 1σ. Blue triangles represent the EPMA analyses acquired on clay-dominated regions in the soil (See Figure 4.13). The black line is a linear fit of the feldspar data with a pure quartz (100% SiO_2) data point, and the dashed gray line represents a linear fit of the interface data points of the glassy agglomerated fallout. The data points interior to attached fallout objects as well as the clay compositions are bound by these two lines. This shows that the major element (*i.e.,* Al, Si) composition of the attached objects can be described as a mixture between major soil components (clay, feldspar minerals, and quartz). The interface data points show a similar relationship between Al_2O_3 and SiO_2, but offset from the composition of both soil and the interiors of the agglomerated fallout objects. This is indicative of the contribution of another component that significantly altered the major element composition of the interface.

4.2 NanoSIMS Analyses

Nano-scale secondary ion mass spectrometry (NanoSIMS) was used to determine the relative variation of uranium isotopes (^{235}U and ^{238}U) across selected interfaces (specified in Table 2.1) where the attached glassy objects were fused to the larger fallout samples. NanoSIMS is better suited for these samples given its ability to measure the relative variation of individual uranium isotopes (^{235}U and ^{238}U in this study), high lateral spatial resolution (sub-micron scale, compared to micron-scale for EPMA), and its superior detection limit of trace species (the detection limit for U in EPMA is >40 ppm in the most ideal case, versus sub-ppm for NanoSIMS [80]). To determine the spatial relationship between of uranium isotope variation at the interface, and the local enrichment and depletion trends of major elements (as presented in Section 4.1), isotopes of Ca (^{44}Ca) and Fe (^{54}Fe or ^{56}Fe) were also acquired by NanoSIMS at the same locations.

To address condensation and deposition of vaporized species onto agglomerated fallout objects, determining the absolute concentration of species across the interface was not necessary. The relative compositional variation, however, may be illustrative of how carriers incorporate species to form fallout. This was exemplified by Lewis et al. (2015), where the relative variation in isotope ratio of ^{235}U/^{238}U was used to understand the relative variation of uranium concentration within fallout objects [56]. Here, the relative variation of uranium concentration was determined by normalizing the uranium isotopic measurements to ^{30}Si, as Si content was shown to be relatively invariable across the interfaces (never exceeding 10% relative variation, see Section 2.3). Ion images and the data plots (presented in Figures 4.17 - 4.26) show the relative compositional variation of Fe, Ca, and U as isotope ratios of ^{54}Fe/^{30}Si, ^{44}Ca/^{30}Si, and ^{235}U/^{30}Si (with the exception of object A1, which uses ^{56}Fe/^{30}Si). To assess the degree of isotopic enrichment of uranium at these interfaces, ion images and data plots for ^{235}U/^{238}U are also presented for each analyzed interface. These values were calibrated using uranium doped glass and uranium oxide particle standards (detailed in 'Analyses of Standards', Section 2.3), and the maximum concentration of uranium was estimated at each interface using the calculated RSF (see Section 2.3, Equation 2.12).

The NanoSIMS ion image data acquired at the interface of object A1 (Figure 4.17) and the larger host object show the expected pattern of Fe and Ca chemical enrichment, as observed in the EDS analyses. This is seen clearly in the isotope ratio images of ^{56}Fe/^{30}Si and ^{44}Ca/^{30}Si, where higher isotope ratios are shown in orange and yellow, and lower isotope ratios are shown in blue and black. The relative variation is illustrated (right hand side) as traverses across the interface following the white arrow in the upper-left isotope ratio image. In these plots, the ^{56}Fe/^{30}Si and ^{44}Ca/^{30}Si peaks (relative enrichments of 61% and 11%, respectively) are co-located (within 1.5 microns, at 5.7 microns in the plots). The width of the interface, as characterized by the width of the base of the ^{56}Fe/^{30}Si peak, is ∼7 microns. Unique to object A1, the compositional variation of U (as represented by ^{235}U/^{30}Si) shows a region of relative depletion co-located with the enrichments of Fe and Ca at the interface. There is a local maximum of ^{235}U/^{30}Si adjacent to this region of depletion, seen at approximately 3.6 microns; however, it is difficult to distinguish this local maximum from

compositional variation around the interface. The BSE image (far left, Figure 4.17), with the $^{235}U/^{30}Si$ isotope ratio image superimposed on it, shows that the region of depletion is indeed co-located with interface. As seen in the $^{235}U/^{238}U$ data plot (Figure 4.17), the uranium at the interface, and on either side of it, is predominantly ^{235}U. The $^{235}U/^{238}U$ isotope ratio exceeds 7 across the isotope ratio image, and reaches a ratio as high as 9.58 ± 0.34, which corresponds to an isotopic enrichment of $90.5 \pm 0.3\%$. While the lowest $^{235}U/^{238}U$ point (7.13 ± 0.30) corresponds to the region of depletion in the $^{235}U/^{30}Si$ (0.000121 ± 0.000003 at 5.7 microns), the isotopic variation of uranium ($^{235}U/^{238}U$ ratio) does not correspond to the uranium concentration (as represented by $^{235}U/^{30}Si$). All isotope ratios on either side of the interface are roughly the same in both Object A1 and host Sample A.

As was observed in Object A1, the isotope ratio data for Object B1 (Figure 4.18) shows a pattern of relative $^{54}Fe/^{30}Si$ and $^{44}Ca/^{30}Si$ enrichment (100% and 93%, respectively), which is also observed in the EPMA data (Figure 4.2) across the interface of where object B1 fuses to the larger Sample B. For this object, and all of the subsequent NanoSIMS analyses for this thesis, ^{54}Fe was measured rather than ^{56}Fe (as was measured in Object A1). The width of the interface as characterized by the width of the base of the $^{54}Fe/^{30}Si$ peak is $\sim$7 microns, compared with 4.5 microns, as measured by EPMA. The data calculated as a traverse across the acquired isotope ratio image of the interface (Figure 4.18) along the white arrow, show that the enrichment of Fe and Ca are co-located. At this interface, the uranium compositional variation (as represented by the $^{235}U/^{30}Si$ ratio) shows a distinct enrichment that is co-located with the Fe and Ca enrichment. Contrary to what is shown in object A1, the BSE image with the $^{235}U/^{30}Si$ ratio image superimposed on it shows that the region of uranium enrichment is approximately continuous with the bright, diffuse interface region shown in BSE (see Figure 3.2). The $^{235}U/^{238}U$ image and plot show a distinct isotopic enrichment in object B1 relative to the object to which it is attached (a ratio of 6.30 ± 1.23 compared with a ratio of 4.12 ± 0.36). In both cases, the average isotopic enrichment away from the boundary is very high (>80% in both objects). As seen in Object A1, there is no observable increase of isotope ratio at the interface, where the $^{235}U/^{30}Si$ maxima ($2.02 \pm 0.05 \times 10^{-4}$, corresponding to a uranium concentration of 36 ± 21 ppm by weight, calculated as shown in Section 2.3) is located.

The ion image data acquired for object B2 shows another unique pattern (with this data set) of chemical and isotopic variation in uranium (Figure 4.19). The $^{54}Fe/^{30}Si$ and $^{44}Ca/^{30}Si$ ratio images and plots show peak enrichment (22% and 45%, respectively, relative to the values on either side of the interface) co-located with the interface (as observed in the EPMA analyses), with a width of $\sim$7 microns, compared with 3 microns as determined by EPMA, which is attributable to the spatial uncertainties in the EPMA spot analyses ($\pm$1.5 microns) or, more likely, spatial variations in interface width. There is no relative enrichment of uranium concentration at the interface. There is, however, an increase in uranium concentration and uranium isotopic enrichment in the object to which B2 is fused (Object B3) relative to Object B2 itself. Also, there is a gradient of decreasing concentration from Object B3 to Object B2 (Figure 4.19) rather than a local minimum or maximum (as seen in objects A1 and B1, respectively). Of further note, the $^{235}U/^{238}U$ variation across

the interface appears to closely mirror the $^{235}U/^{30}Si$ variation. The $^{235}U/^{238}U$ ratio within Object B2 is on average 4.36 ± 0.52 (which corresponds with what was observed in Object B1, Figure 4.18), while in the larger object to which it is fused, the $^{235}U/^{238}U$ is 6.20 ± 0.20 (86.1 ± 0.4% enriched in ^{235}U).

The ion image data acquired for object B3 (Figure 4.20) shows relative enrichment of Fe, Ca, and U at the interface (as seen in the ratio images and plots of $^{54}Fe/^{30}Si$, $^{44}Ca/^{30}Si$, $^{235}U/^{30}Si$). While the $^{54}Fe/^{30}Si$ variation shows the same pattern of local enrichment at the interface that has been observed in the previous samples (a distinct maximum above an approximately constant baseline, in this case 33%, with a width of ∼6 microns), this is not the case for $^{44}Ca/^{30}Si$ variation. Despite an enrichment of $^{44}Ca/^{30}Si$ at the interface, Object B3 has a substantially lower $^{44}Ca/^{30}Si$ ratio than Sample B (36% lower $^{44}Ca/^{30}Si$ ratio relative to Sample B), making a local maximum difficult to distinguish. As seen in the EPMA plot (Figure 4.5) at the same interface, there is significant variation in Ca concentration (17% standard deviation), and the BSE image (Figure 4.2) shows a high degree of chemical heterogeneity, generally. This heterogeneity in both Sample B and Object B3 is also reflected in the image and plot of $^{235}U/^{30}Si$ (26% standard deviation). While there is a distinct region of enrichment seen at the interface, it is adjacent to two regions of relative depletion of $^{235}U/^{30}Si$ ratio within both object B3 and the large host object. Further, the local maximum of $^{235}U/^{30}Si$ near the interface ($0.75 \pm 0.03 \times 10^{-4}$, corresponding to a uranium concentration of 14 ± 8 ppm by weight) is offset from the local maximum of $^{54}Fe/^{30}Si$ by 3.8 microns. The local maximum of $^{235}U/^{238}U$ is approximately co-located with the $^{235}U/^{30}Si$ near the interface (4.17 ± 0.35). Object B3 has an average $^{235}U/^{238}U$ ratio of 3.23 ± 0.83, consistent with what was observed in Object B2 (Figure 4.19).

The ion image data of object C1 show the characteristic relative enrichments of Fe, Ca, and U (as seen in the ratio images and plots of $^{54}Fe/^{30}Si$, $^{44}Ca/^{30}Si$, $^{235}U/^{30}Si$, Figure 4.21) observed at most of the analyzed interfaces. The ratio images and the data plots show that the peaks of $^{54}Fe/^{30}Si$ (0.1910 ± 0.0001, a relative enrichment of 72%, with a width of ∼7 microns), $^{44}Ca/^{30}Si$ (0.1251 ± 0.0001), and $^{235}U/^{30}Si$ ($9.43 \pm 0.09 \times 10^{-4}$, corresponding to a uranium concentration of 154 ± 88 ppm by weight) are the global maxima for each image, and are co-located (at 8.6 microns, Figure 4.21). The $^{235}U/^{238}U$ image captures an isotopic enrichment of uranium at the interface (7.73 ± 0.15), and the $^{235}U/^{238}U$ plot shows that this enrichment is co-located with the $^{235}U/^{30}Si$ peak, indicating a relationship between isotopic enrichment and concentration, spatially, which have been previously reported by Eppich et al. (2014) and Lewis et al. (2015), but in contrast to other objects (like A1 and C2, see below). While host Sample C has a similar $^{235}U/^{30}Si$ ratio as Object C1, the $^{54}Fe/^{30}Si$ and $^{44}Ca/^{30}Si$ ratios are slightly depleted relative to Object C1 (23% and 30% relative depletion, respectively).

The isotope ratios for $^{54}Fe/^{30}Si$ and $^{44}Ca/^{30}Si$ in Object C2 (Figure 4.22) show a pattern of enrichment and depletion as observed in the X-ray maps (Figure 3.14) and the WDS dataset (Figure 4.5) for Fe and Ca. The pattern of variation in the isotope ratio images of $^{54}Fe/^{30}Si$ and $^{44}Ca/^{30}Si$ consists of a region of depletion (24% and 53% relative depletion for $^{54}Fe/^{30}Si$ and $^{44}Ca/^{30}Si$, respectively, to the interior values) adjacent to a region of relative

enrichment at the interface (225% and 246% relative to the local minima for $^{54}Fe/^{30}Si$ and $^{44}Ca/^{30}Si$, respectively). There is a gradual decrease in relative concentration for both Fe and Ca moving away from the interface into the large host object of Sample C, suggestive of a diffusive boundary. This same pattern is observed in the plot of $^{235}U/^{30}Si$, where a distinct maximum at the interface ($4.50 \pm 0.05 \times 10^{-4}$, corresponding to a uranium concentration of 82 ± 47 ppm by weight) is co-located with the relative enrichment of $^{54}Fe/^{30}Si$ and $^{44}Ca/^{30}Si$ ratios. Because of the substantially lower $^{235}U/^{30}Si$ ratio within attached object C2, it is difficult to distinguish if a region of relative depletion at the interface (at 4.5 microns) exists. The data acquired from the traverse across the interface (along the white arrow), do not yield an observable pattern of $^{235}U/^{238}Si$ ratio variation (6.52 ± 1.04 in Object C2, and 6.81 $\pm$ 0.21 in Sample C adjacent to the interface), contrary to what was observed in Object C1, and what has been described in previous studies [55, 56]. Of further note, the regions of high $^{235}U/^{30}Si$ in the ion image (seen superimposed on the BSE image in Figure 4.22) are continuous with the wide, bright region on the BSE image (which was found by EPMA to be enriched in Fe and Ca, Figure 4.6), forming a continuation of the boundary of agglomerated Object C2.

The ion image data acquired for object D1 (Figure 4.23) reveals relative enrichments of $^{54}Fe/^{30}Si$, $^{44}Ca/^{30}Si$, and $^{235}U/^{30}Si$ co-located at the interface (30%, 44%, and 28%, respectively). The width of the interface, as characterized by the width of the base of the $^{54}Fe/^{30}Si$ peak, is $\sim$8 microns. Unique to this interface, and most clearly seen in the upper-right of the $^{44}Ca/^{30}Si$ ratio image, there appears to be a discontinuity at the interface. In this region, the average number of counts per pixel increases by 17%, 8%, and 37% for ^{30}Si, ^{54}Fe, and ^{235}U relative to the regions on either side of the interface, while exhibiting a relative decrease of 55% in ^{44}Ca. In BSE imaging (Figure 4.24), this region is seen as a dark bleb at the interface, indicating lower average atomic number. The increase in ^{30}Si indicates that this region is a SiO_2 inclusion, that accumulated Fe and ^{235}U as a result of being located at the interface between Object D1 and Sample D. Uranium concentration could not be calculated, as Si concentration was not acquired by EPMA for this interface.

In object D2 (Figure 4.25), there is relative enrichment of $^{54}Fe/^{30}Si$, $^{44}Ca/^{30}Si$, and $^{235}U/^{30}Si$ co-located at the interface (55%, 86%, and 219%, respectively, compared with the regions on either side of the interface). The width of the interface as characterized by the width of the base of the $^{54}Fe/^{30}Si$ peak is $\sim$5 microns. The acquired ion images appear to overlap another region of relatively higher atomic number, as shown in the BSE image. In the ion image, this second region can be seen as an area at the bottom, with high $^{54}Fe/^{30}Si$ and $^{235}U/^{30}Si$ ratios of similar value to the central interface (7.5×10^{-2} and 1.2×10^{-4}, respectively). The local $^{235}U/^{238}U$ maximum (5.74 ± 0.18) is co-located with the local maximum of $^{235}U/^{30}Si$ (at $\sim$11 microns), which corresponds to a uranium concentration of 29 ± 17 ppm by weight.

The ion image data acquired for object E1 (Figure 4.26) show enrichment for $^{54}Fe/^{30}Si$, $^{44}Ca/^{30}Si$, $^{235}U/^{30}Si$, and $^{235}U/^{238}U$ that are approximately co-located (at 9.0 microns, Figure 4.26), although the $^{235}U/^{30}Si$ ratio maximum is slightly shifted (at 7.2 microns). At this interface, as also seen in the EPMA spot analyses (Figure 4.8), the region of relative enrich-

ment is substantially wider (>12 microns) than in the other measured interfaces (between 5 and 10 microns in width). As seen in most of the measured interfaces, the $^{235}U/^{238}U$ ratio data plot shows a local maximum (8.91 ± 0.30) at approximately the same place as the local maximum for $^{235}U/^{30}Si$ ($3.13 \pm 0.03 \times 10^{-4}$), corresponding to a uranium concentration of 50 ± 29 ppm by weight.

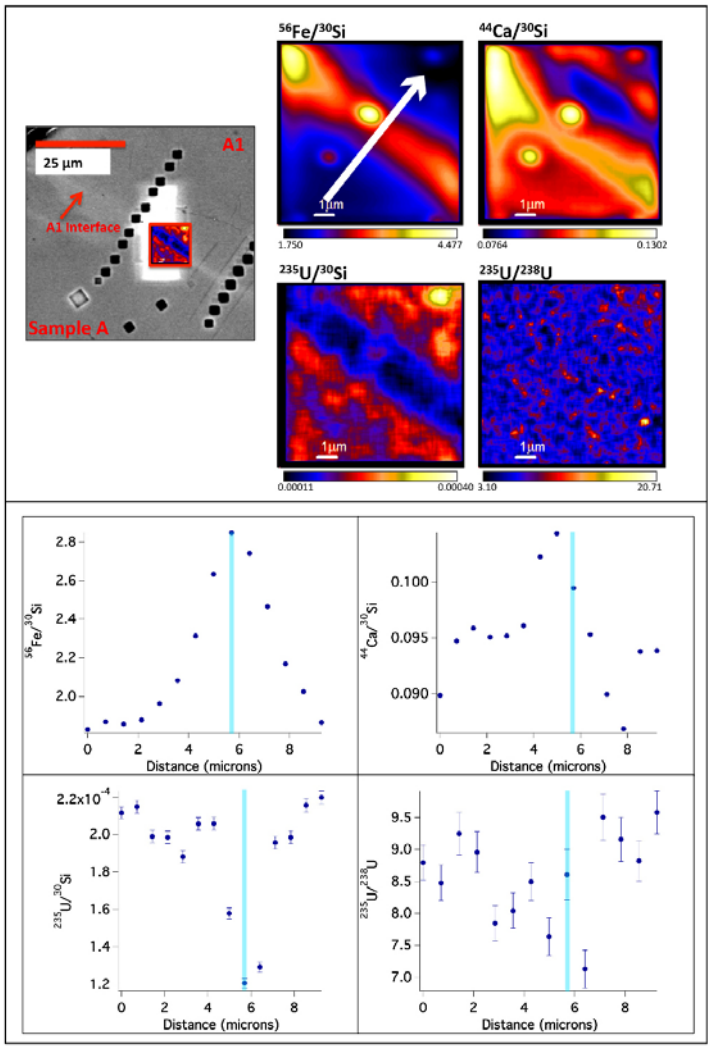

Figure 4.17: In the top frames, a BSE image showing the location of ion image acquisition at the interface of object A1, as well as the isotope ratio images for ^{56}Fe/^{30}Si, ^{44}Ca/^{30}Si, ^{235}U/^{30}Si, ^{235}U/^{238}U, are shown. The black squares in the BSE image are locations of NanoSIMS analysis craters not acquired as images. In the bottom frames, isotope ratio variations along the white arrow across the interface (shown in the ^{56}Fe/^{30}Si ratio image) for ^{56}Fe/^{30}Si, ^{44}Ca/^{30}Si, ^{235}U/^{30}Si, ^{235}U/^{238}U are shown, with the location of the local ^{56}Fe/^{30}Si maximum indicated by the blue line in each frame. There are enrichments of both ^{56}Fe/^{30}Si and ^{44}Ca/^{30}Si, co-located (within 1.5 microns) with a depletion of ^{235}U/^{30}Si at the interface relative to the regions adjacent to the interface. The ^{235}U/^{238}U ratio does not show a discernible pattern, but indicates a high isotopic enrichment (>87% ^{235}U). The uncertainties in the lower panels are 1σ.

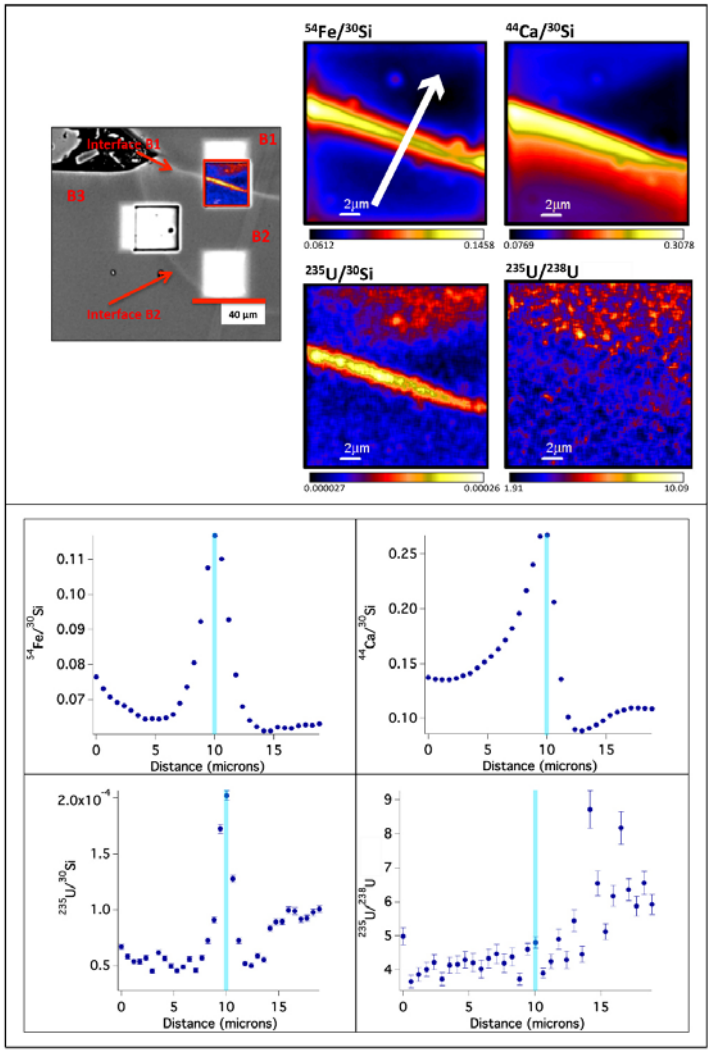

Figure 4.18: In the top frames, a BSE image showing the location of ion image acquisition at the interface of object B1, as well as the isotope ratio images for $^{54}Fe/^{30}Si$, $^{44}Ca/^{30}Si$, $^{235}U/^{30}Si$, $^{235}U/^{238}U$, are shown. In the bottom frames, isotope ratio variations along the white arrow across the interface (shown in the $^{54}Fe/^{30}Si$ ratio image) for $^{54}Fe/^{30}Si$, $^{44}Ca/^{30}Si$, $^{235}U/^{30}Si$, $^{235}U/^{238}U$ are shown, with the location of the local $^{54}Fe/^{30}Si$ maximum indicated by the blue line in each frame. The white squares seen in the BSE image show where the coating has been sputtered away during NanoSIMS analysis: the white square on the right is where the ion images of object B2 were made (Figure 4.19), the white square at the top is simply where the coating was sputtered away when searching for the interface with the instrument. There are enrichments of $^{54}Fe/^{30}Si$, $^{44}Ca/^{30}Si$, and $^{235}U/^{30}Si$ precisely co-located at the interface. The $^{235}U/^{238}U$ ratio variation does not show a discernible pattern at the interface, but increases in Object B1, relative to Object B2. The uncertainties in the lower panels are 1σ.

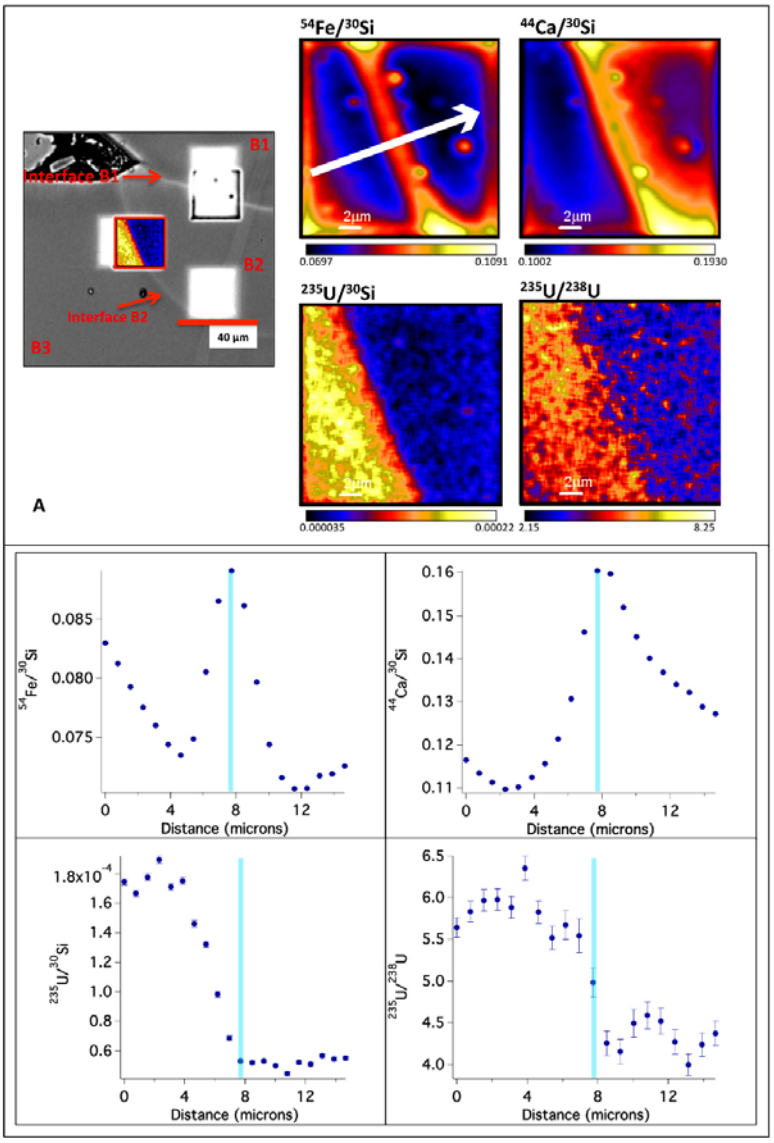

Figure 4.19: In the top frames, a BSE image showing the location of ion image acquisition at the interface of object B2, as well as the isotope ratio images for $^{54}Fe/^{30}Si$, $^{44}Ca/^{30}Si$, $^{235}U/^{30}Si$, $^{235}U/^{238}U$, are presented. In the bottom frames, the isotope ratio variations along the white arrow across the interface (shown in the $^{54}Fe/^{30}Si$ ratio image) for $^{54}Fe/^{30}Si$, $^{44}Ca/^{30}Si$, $^{235}U/^{30}Si$, $^{235}U/^{238}U$, are presented, with the location of the local $^{54}Fe/^{30}Si$ maximum indicated by the blue line in each frame. While there is relative enrichment of $^{54}Fe/^{30}Si$ and $^{44}Ca/^{30}Si$ ratio at the interface, this pattern is not observed for the $^{235}U/^{30}Si$ ratio. Instead, there is a gradient of decreasing concentration from Object B3 to Object B2, which is also observed in the $^{235}U/^{238}U$ ratio variation. The uncertainties in the lower panels are 1σ.

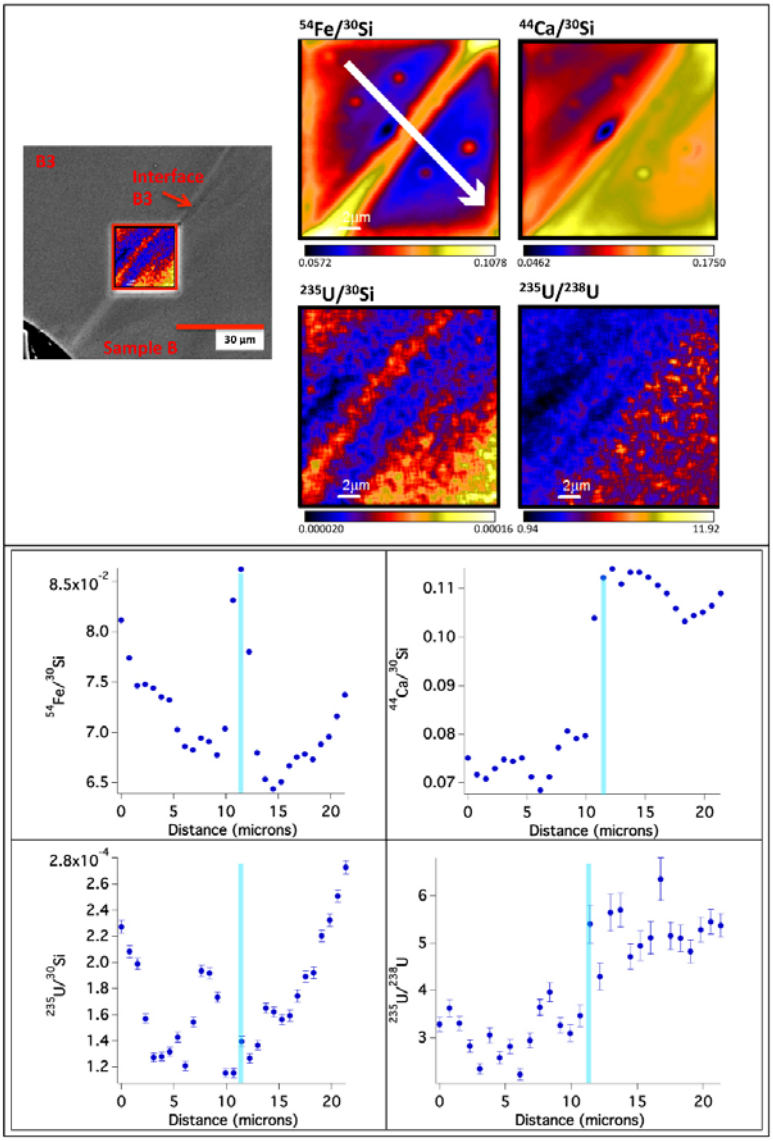

Figure 4.20: In the top frames, a BSE image showing the location of ion image acquisition at the interface of object B3, as well as the isotope ratio images for $^{54}Fe/^{30}Si$, $^{44}Ca/^{30}Si$, $^{235}U/^{30}Si$, $^{235}U/^{238}U$, are presented. In the bottom frames, the isotope ratio variations along the white arrow across the interface (shown in the $^{54}Fe/^{30}Si$ ratio image) for $^{54}Fe/^{30}Si$, $^{44}Ca/^{30}Si$, $^{235}U/^{30}Si$, $^{235}U/^{238}U$, are shown, with the location of the local $^{54}Fe/^{30}Si$ maximum indicated by the blue line in each frame. The $^{54}Fe/^{30}Si$ variation reveals local enrichment at the interface. There is an enrichment of $^{44}Ca/^{30}Si$ at the interface, however, Object B3 has a substantially higher $^{44}Ca/^{30}Si$ ratio than Sample B, making a local maximum difficult to distinguish. There is a region of enrichment of $^{235}U/^{30}Si$ ratio seen at the interface, adjacent to two regions of relative depletion. The uncertainties in the lower panels are 1σ.

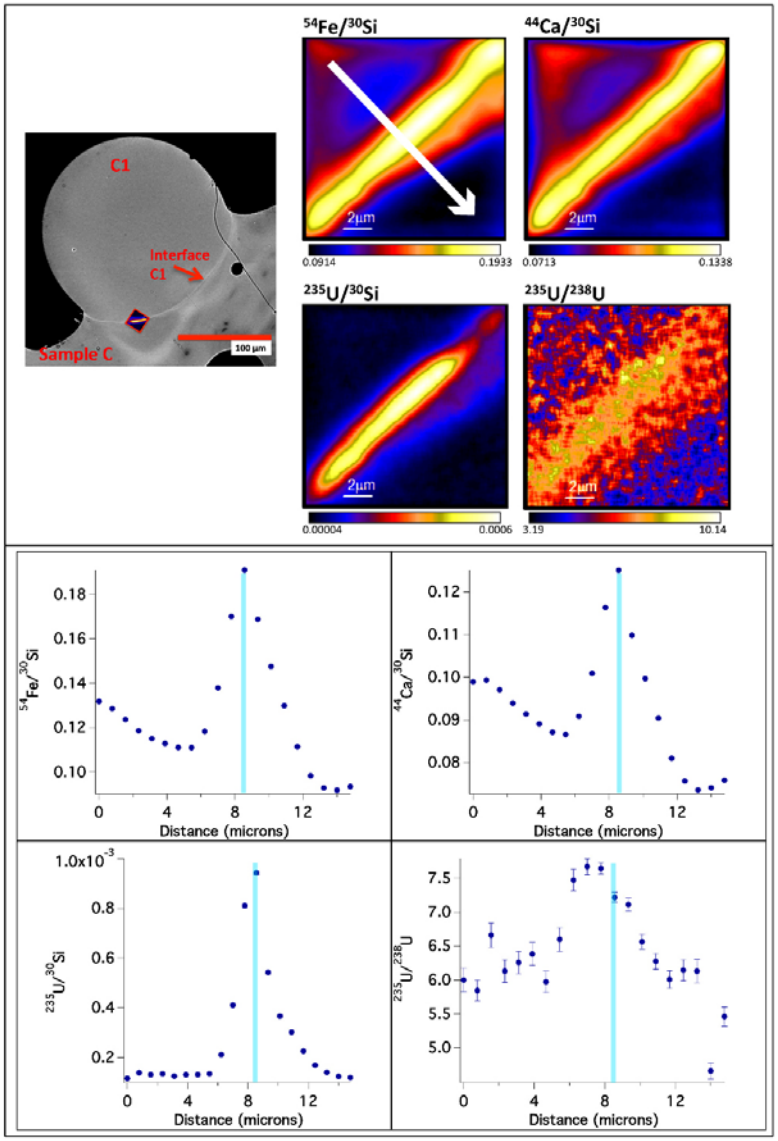

Figure 4.21: In the top frames, a BSE image showing the location of ion image acquisition at the interface of object C1, as well as the isotope ratio images for $^{54}Fe/^{30}Si$, $^{44}Ca/^{30}Si$, $^{235}U/^{30}Si$, $^{235}U/^{238}U$, are presented. In the bottom frames, the isotope ratio variations along the white arrow across the interface (shown in the $^{54}Fe/^{30}Si$ ratio image) for $^{54}Fe/^{30}Si$, $^{44}Ca/^{30}Si$, $^{235}U/^{30}Si$, $^{235}U/^{238}U$, are presented, with the location of the local $^{54}Fe/^{30}Si$ maximum indicated by the blue line in each frame. There are characteristic relative enrichments of $^{54}Fe/^{30}Si$, $^{44}Ca/^{30}Si$, $^{235}U/^{30}Si$. The $^{235}U/^{238}U$ plot shows relative enrichment that is co-located (within 1.5 microns) with the $^{235}U/^{30}Si$ maxima. The uncertainties in the lower panels are 1σ.

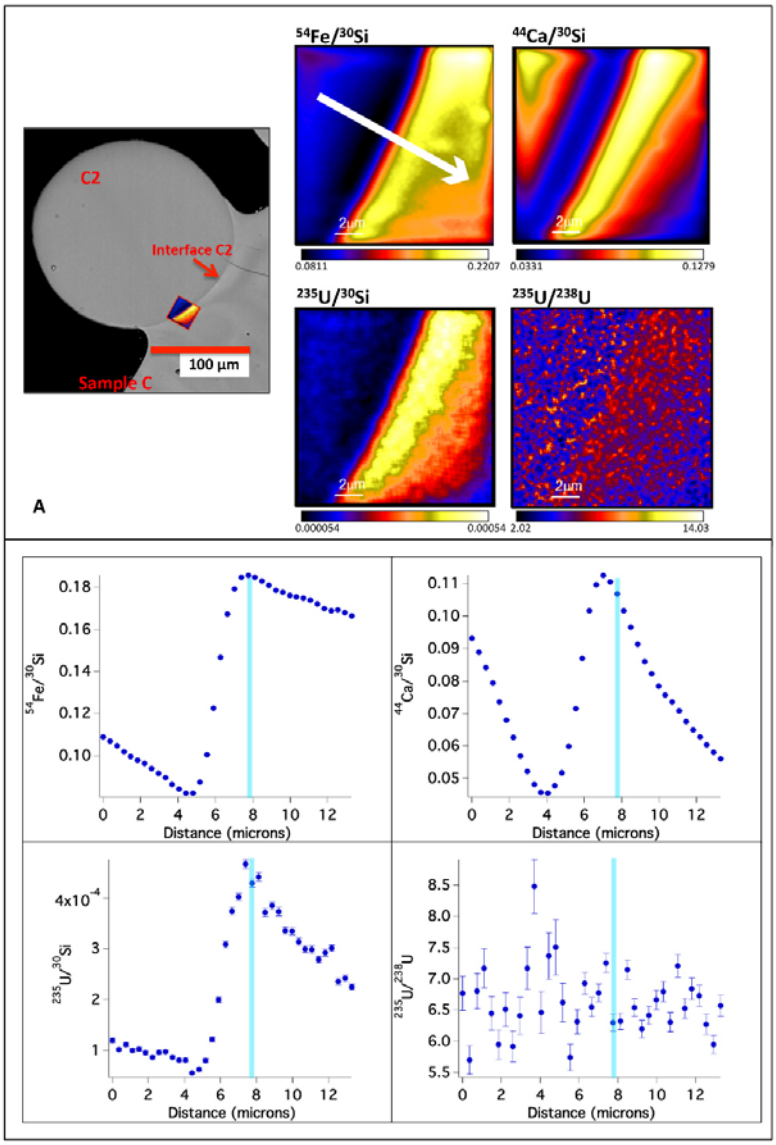

Figure 4.22: In the top frames, a BSE image showing the location of ion image acquisition at the interface of object C2, as well as the isotope ratio images for $^{54}Fe/^{30}Si$, $^{44}Ca/^{30}Si$, $^{235}U/^{30}Si$, $^{235}U/^{238}U$, are presented. In the bottom frames, the isotope ratio variations along the white arrow across the interface (shown in the $^{54}Fe/^{30}Si$ ratio image) for $^{54}Fe/^{30}Si$, $^{44}Ca/^{30}Si$, $^{235}U/^{30}Si$, $^{235}U/^{238}U$, are presented, with the location of the local $^{54}Fe/^{30}Si$ maximum indicated by the blue line in each frame. The isotope ratio images of $^{54}Fe/^{30}Si$ and $^{44}Ca/^{30}Si$ show of a region of depletion adjacent to a region of relative enrichment at the interface. There is a decrease in relative concentration for both Fe and Ca moving away from the interface into the large host object of Sample C, suggestive of diffusion. The data acquired from the traverse across the interface (along the white arrow), do not yield an observable pattern of $^{235}U/^{30}Si$ ratio variation. The uncertainties in the lower panels are 1σ.

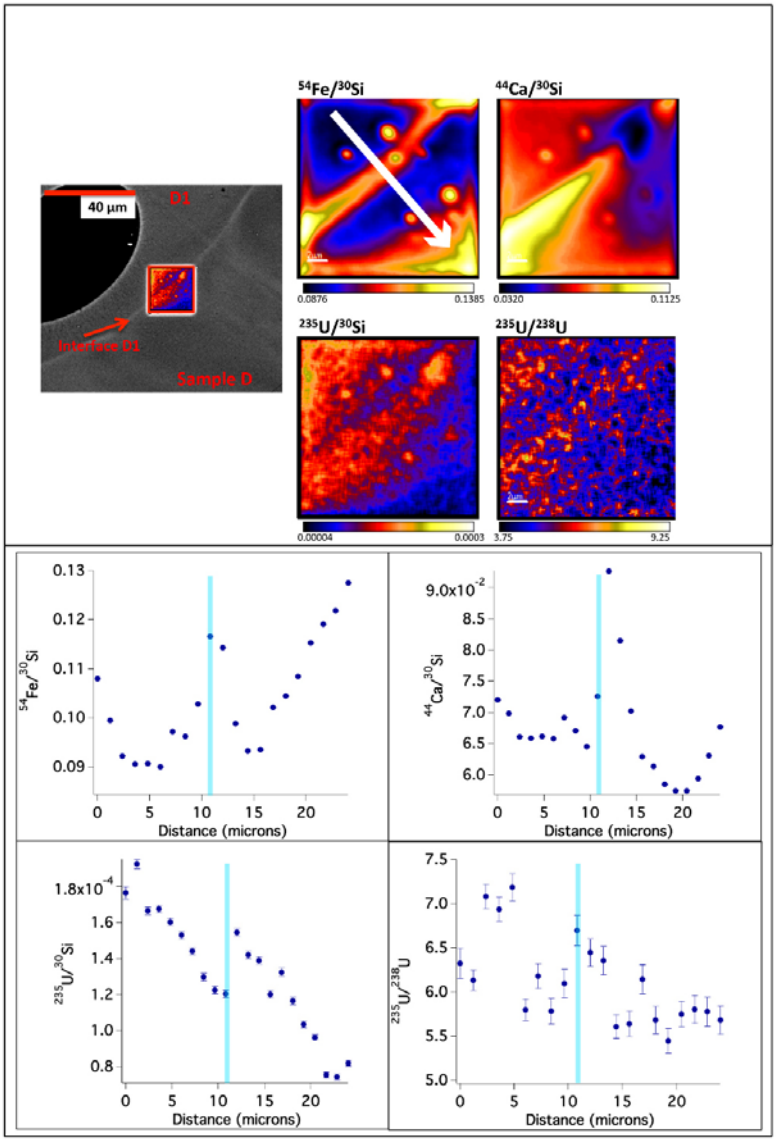

Figure 4.23: In the top frames, a BSE image showing the location of ion image acquisition at the interface of object D1, as well as the isotope ratio images for $^{54}Fe/^{30}Si$, $^{44}Ca/^{30}Si$, $^{235}U/^{30}Si$, $^{235}U/^{238}U$, are shown. In the bottom frames, the isotope ratio variations along the white arrow across the interface (shown in the $^{54}Fe/^{30}Si$ ratio image) for $^{54}Fe/^{30}Si$, $^{44}Ca/^{30}Si$, $^{235}U/^{30}Si$, $^{235}U/^{238}U$, are shown, with the location of the local $^{54}Fe/^{30}Si$ maximum indicated by the blue line in each frame. Unique to this interface, and most clearly seen as a region of depletion in the upper-right of the $^{44}Ca/^{30}Si$ ratio image, there is a discontinuity at the interface. This feature is characterized in more detail in Figure 4.24. The uncertainties in the lower frames are 1σ.

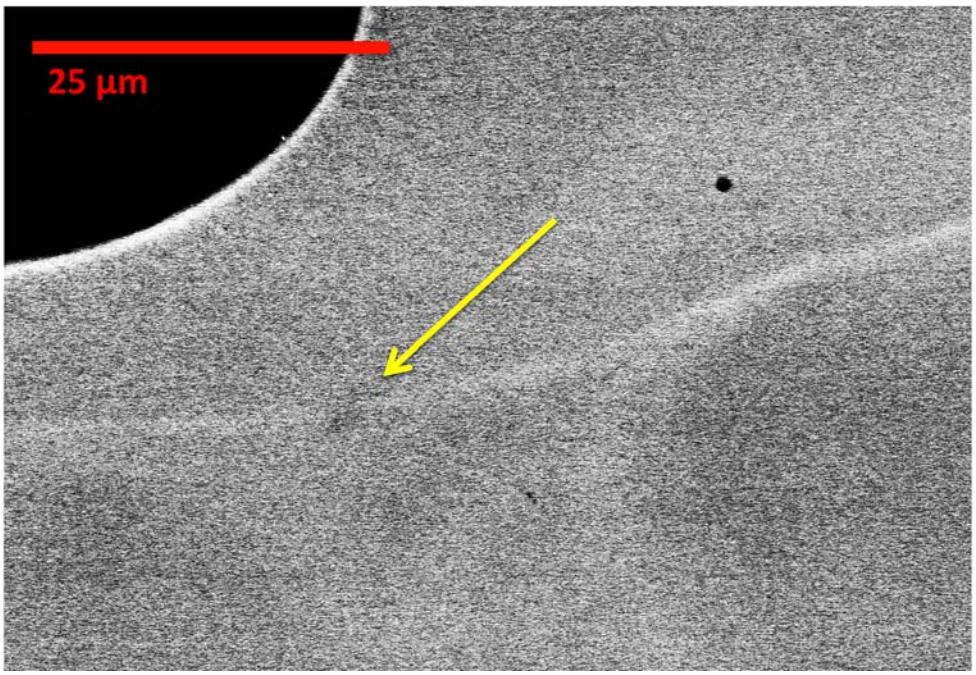

Figure 4.24: The discontinuity in the $^{44}Ca/^{30}Si$ seen in Figure 4.22 is shown in BSE imaging, which is seen as a dark bleb (yellow arrow) indicating relatively lower average atomic number (but not a void). This region corresponds to a 20% increase in ^{30}Si counts, indicating that this region is likely an SiO_2 inclusion. In this region, the average number of counts per pixel increases by 17%, 8%, and 37% for ^{30}Si, ^{54}Fe, and ^{235}U relative to the regions on either side of the interface. The increase in ^{30}Si indicates that this region is a SiO_2 inclusion, that accumulated Fe and ^{235}U as a result of being located at the interface between Object D1 and Sample D.

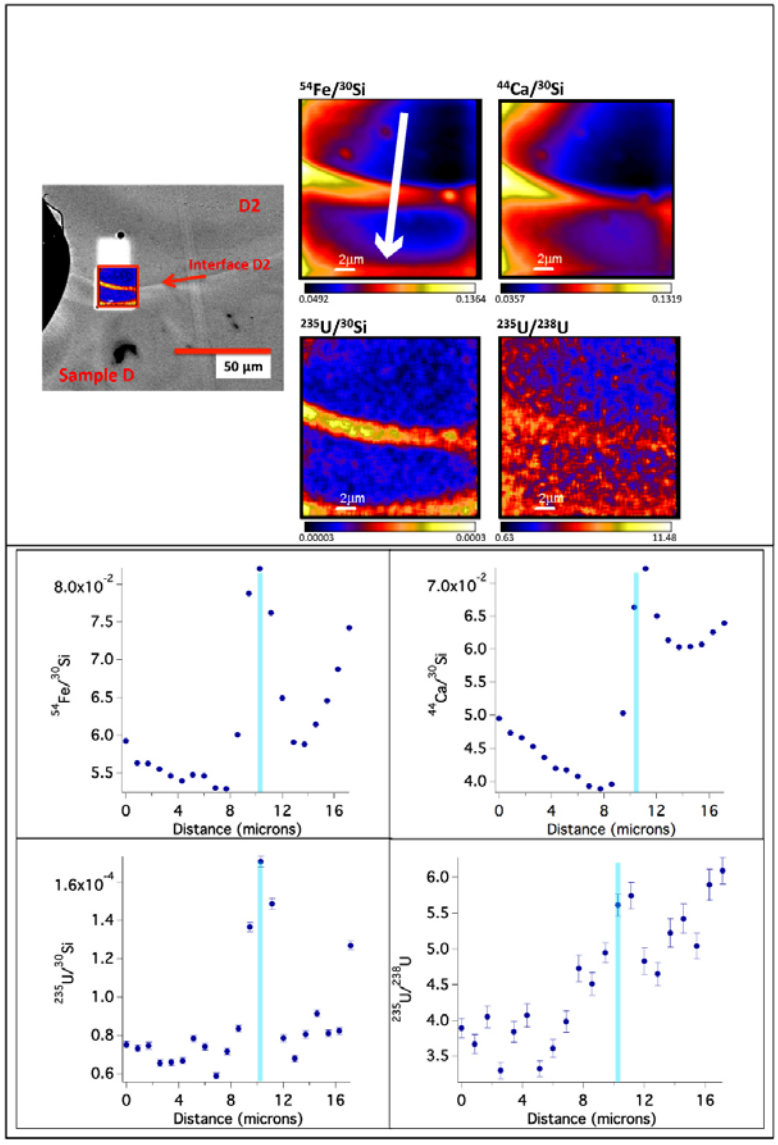

Figure 4.25: In the top frames, a BSE image showing the location of ion image acquisition at the interface of object D2, as well as the isotope ratio images for $^{54}Fe/^{30}Si$, $^{44}Ca/^{30}Si$, $^{235}U/^{30}Si$, $^{235}U/^{238}U$, are presented. In the bottom frames, the isotope ratio variations along the white arrow across the interface (shown in the $^{54}Fe/^{30}Si$ ratio image) for $^{54}Fe/^{30}Si$, $^{44}Ca/^{30}Si$, $^{235}U/^{30}Si$, $^{235}U/^{238}U$, are presented, with the location of the local $^{54}Fe/^{30}Si$ maximum indicated by the blue line in each frame. There is relative enrichment of $^{54}Fe/^{30}Si$, $^{44}Ca/^{30}Si$, and $^{235}U/^{30}Si$ co-located (within 1.5 microns) at the interface. The local $^{235}U/^{238}U$ maximum is co-located with the local maximum of $^{235}U/^{30}Si$. The uncertainties in the lower panels are 1σ.

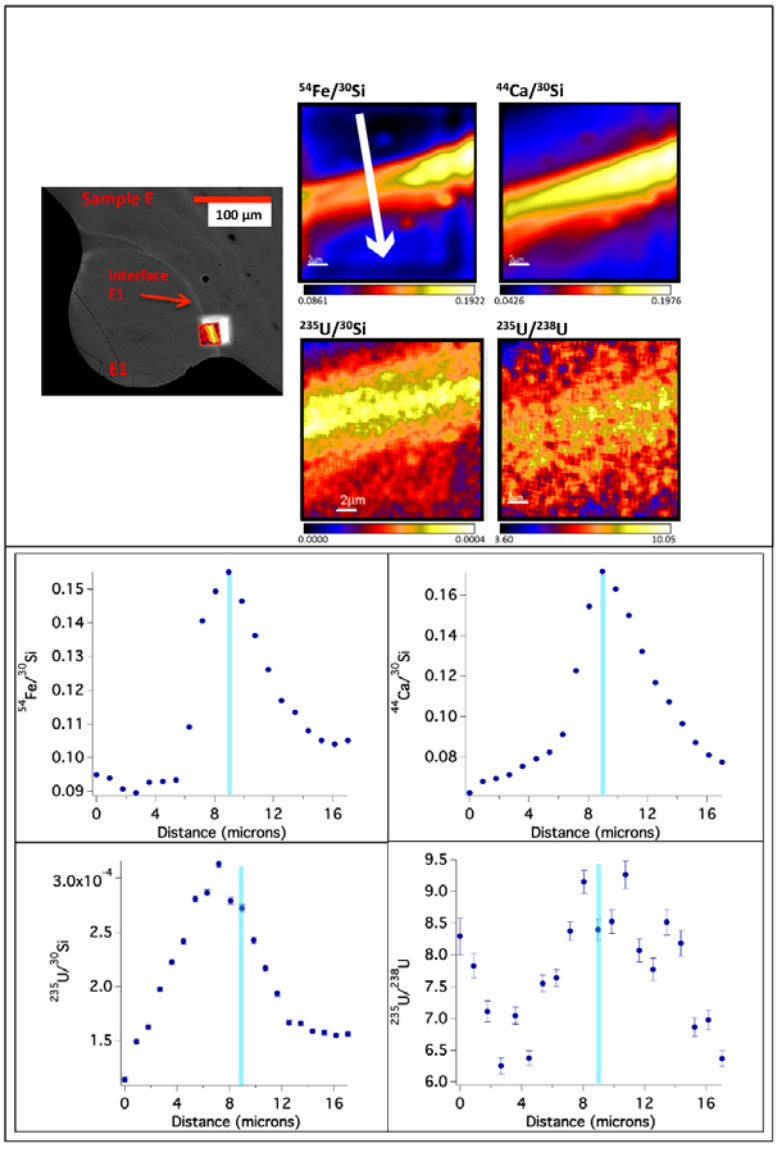

Figure 4.26: In the top frames, a BSE image showing the location of ion image acquisition at the interface of object E1, as well as the isotope ratio images for ^{54}Fe/^{30}Si, ^{44}Ca/^{30}Si, ^{235}U/^{30}Si, ^{235}U/^{238}U, are presented. In the bottom frames, the isotope ratio variations along the white arrow across the interface (shown in the ^{54}Fe/^{30}Si ratio image) for ^{54}Fe/^{30}Si, ^{44}Ca/^{30}Si, ^{235}U/^{30}Si, ^{235}U/^{238}U, are presented, with the location of the local ^{54}Fe/^{30}Si maximum indicated by the blue line in each frame. There is enrichment of ^{54}Fe/^{30}Si, ^{44}Ca/^{30}Si, ^{235}U/^{30}Si, and ^{235}U/^{238}U approximately co-located at the interface. The local maximum of ^{235}U/^{238}U ratio is approximately co-located (within 1.5 microns) with the local maximum for ^{235}U/^{30}Si. The uncertainties in the lower panels are 1σ.

Summary

The isotope ratio images of $^{54}Fe/^{30}Si$, $^{44}Ca/^{30}Si$, $^{235}U/^{30}Si$, $^{235}U/^{238}U$, and the ratio variation profiles acquired from them, show a relative enrichment of $^{54}Fe/^{30}Si$ and $^{44}Ca/^{30}Si$ ratio at the interface (relative to the regions on either side of the interface) for all 9 of the analyzed interfaces (Table 4.7). This is consistent with what is observed by EPMA at these interfaces (with the exception of Interface A1 and D1, which were not analyzed with EPMA). The $^{235}U/^{30}Si$ ratio was used to understand the variation of uranium concentration across the interface (assuming Si is relatively invariable, as previously supported in Section 4.1). The $^{235}U/^{30}Si$ ratio is relatively enriched at the interface in 7 of the 9 analyzed interfaces, with the exception of A1 and B2 (Table 4.7). The relative increase in $^{235}U/^{30}Si$ ratio at interfaces, in comparison to the regions on either side of the interface, varied between the analyzed interfaces from a minimum relative enrichment at Interface D1 of 28% to a maximum relative enrichment of 900% at Interface C1. At only 5 of these interfaces, the increase in $^{235}U/^{30}Si$ ratio spatially corresponds to an increase in the $^{235}U/^{238}U$ ratio (Interfaces B3, C1, D1, D2, and E1). At all all of the measured interfaces, there was an enrichment in $^{235}U/^{238}U$ ratio relative to natural (0.0073). The minimum measured $^{235}U/^{238}U$ ratio was 2.21 ± 0.12 (corresponding to an enrichment of $68.8 \pm 1.1\%$, at Interface D3) and the maximum measured ratio was 9.73 ± 0.43 (corresponding to an enrichment of $90.7 \pm 0.4\%$, at Interface A1, Table 4.7).

In previous studies [55, 56], the absolute concentration of uranium was also measured within fallout glasses from this test. In the Eppich et al. (2014) study, which measured uranium concentration via bulk dissolution mass spectrometry, the concentration of uranium was reported to be between 14.7 and 32.9 ppm, whereas soil from the test site was found to have a measured uranium concentration from 2.7 to 4.3 ppm. In the Lewis et al. (2015) study, which estimated uranium concentration from SIMS spots taken within similar glassy objects, the uranium concentration was found to range from 3.5 to 19.4 ppm across objects. In this study, however, the interface U concentrations (calculated as described in Section 2.3) were considerably higher: the minimum measured concentration at an interface was 14 ± 8 ppm (Interface B3), and the highest concentration was found to be 154 ± 88 ppm (Interface C1, Table 4.7). Given the high $^{235}U/^{238}U$ ratios at every interface (>80% enriched in ^{235}U), this constitutes a higher contribution of device material at these surfaces of these objects prior to agglomeration than has ever been previously reported. However, unlike the studies by Eppich et al. (2014) and Lewis et al. (2015), the $^{235}U/^{238}U$ isotope ratio does not exhibit an obvious correlation with uranium concentration in this data set (Figure 4.27). This could be the effect of heterogeneous mixing of uranium from vaporized soil with uranium from the device.

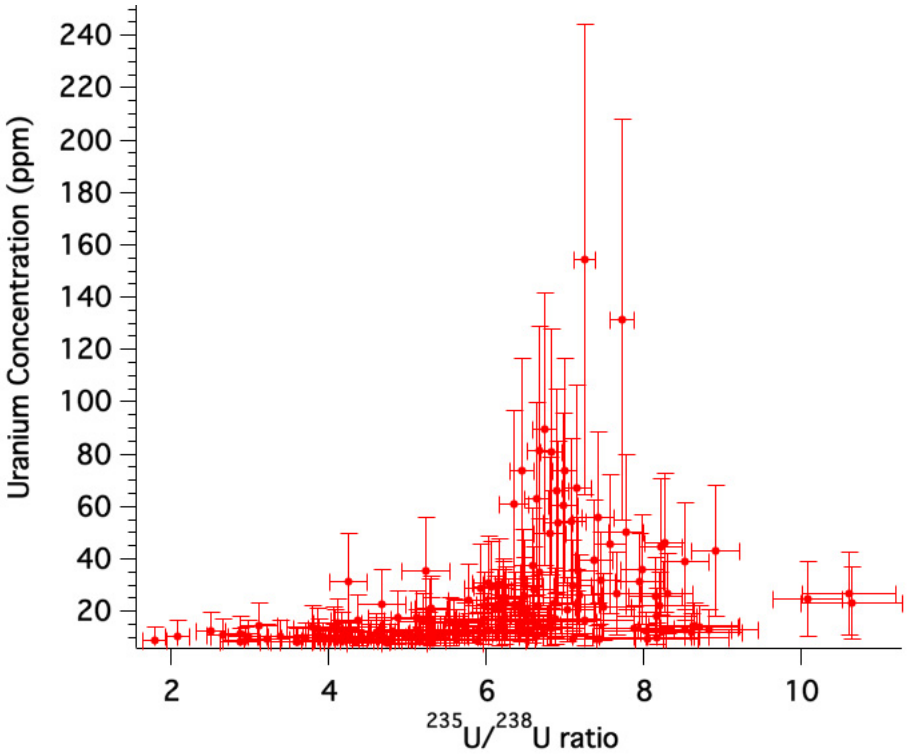

Figure 4.27: The $^{235}U/^{238}U$ ratio as derived from the NanoSIMS ion image traverses is plotted against uranium concentration calculated from the $^{235}U/^{30}Si$ ratio for the entire NanoSIMS ion image traverse data set (Interfaces A1 and D1 are excluded, as the uranium concentration could not be calculated, as the Si concentration was not determined via EPMA). As seen here, there is no correlation between the uranium isotope ratio and concentration. This may be due to heterogeneity in vaporized uranium components (*i.e.,* from the soil and device) in the fireball.

Table 4.7: NanoSIMS analyses at the interface for $^{54}Fe/^{30}Si$, $^{44}Ca/^{30}Si$, $^{235}U/^{30}Si$, and $^{235}U/^{238}U$, along with the calculated U concentration at the interface. Uncertainties are 1σ.

Interface	$^{44}Ca/^{30}Si$		$^{54}Fe/^{30}Si$		$^{235}U/^{30}Si$		$^{235}U/^{238}U$	U conc (ppm)
	Max	Min	Max	Min	Max	Min		
A1	0.1043±0.0001	0.0868±0.0001	2.8486±0.0008*	1.8267±0.0005	0.000206±0.000003	0.000121±0.000003	8.49±0.30	N/A**
B1	0.2668±0.0002	0.0889±0.0001	0.1168±0.0001	0.0611±0.0001	0.000202±0.000005	0.000045±0.000002	5.23±0.30	35±20
B2†	0.1604±0.0001	0.1096±0.0001	0.0891±0.0001	0.0707±0.0000	0.000190±0.000002	0.000045±0.000001	6.47±0.23	32±18
B3	0.1140±0.0001	0.0683±0.0001	0.0862±0.0001	0.0643±0.0001	0.000075±0.000003	0.000039±0.000002	4.07±0.33	14±8
C1	0.1251±0.0001	0.0736±0.0001	0.1910±0.0001	0.0918±0.0001	0.000943±0.000009	0.000117±0.000003	7.25±0.13	154±88
C2	0.1138±0.0001	0.0462±0.0001	0.1873±0.0001	0.0831±0.0001	0.000453±0.000005	0.000071±0.000002	6.68±0.15	82±47
D1	0.0927±0.0001	0.0574±0.0000	0.1166±0.0001	0.0906±0.0001	0.000154±0.000002	0.000074±0.000001	6.39±0.25	N/A**
D2	0.0722±0.0001	0.0388±0.0000	0.0821±0.0001	0.0529±0.0000	0.000171±0.000003	0.000059±0.000002	5.61±0.15	29±17
E1	0.1714±0.0001	0.0624±0.0001	0.1551±0.0001	0.0896±0.0001	0.000313±0.000003	0.000114±0.000002	7.78±0.22	50±29

*A1 actually used the $^{56}Fe/^{30}Si$ ratio

**A1 and D1 did not have EPMA data for SiO_2 so concentration could not be calculated

†B2 did not have a local maximum at the interface for $^{235}U/^{30}Si$, so the global maximum was used

4.3 Interpreting qualitative and quantitative observations

The results of each analytical technique yield observations of distinct chemical and/or isotopic variation at the interface of where small, glassy fallout objects are fused to the surface of larger host objects, as well as the outer edge of these objects, compared to the interiors of agglomerated fallout objects. The compositional variation at the edge follows the same general compositional pattern as what is observed at the interfaces, and shown to be continuous in X-ray mapping. Clearly, the distinct compositional region at the interface is a layer that is continuous around the surface of at least the attached objects. This layer must have deposited in the fireball while the carrier was still molten, and likely constitutes a late-stage deposition, as it is preserved where two glassy objects are fused together. The composition of this deposited layer provides insight into the environment in which species vaporized post-detonation, how these materials may have interacted in the vapor phase, and how they condensed and mixed into molten carrier materials.

Thermal histories preserved in agglomerated fallout glasses and their implications

The bulk composition of fallout glass is compositionally similar to local environmental materials [55] (see also, Figure 4.16); however, at the sub-mm-scale, fallout glasses reveal significant compositional heterogeneities (*e.g.,* Figure 3.4). Larger (mm-scale) host objects preserve evidence of mechanical mixing (such as flow banding, Figure 3.4), variable degrees of vesiculation (*e.g.,* Figure 3.5), eccentric (non-spherical) shapes (*e.g.,* Figure 3.3), and inclusion of vitrified relict grains (in these samples, typically SiO_2 with diffuse boundaries, *e.g.,* Figure 3.4). Among the studied population of agglomerated objects examined here, several are quite homogeneous in average chemical composition compared to their larger hosts (Figures 3.7-3.11, and 4.1). This observation suggests that these smaller objects were not only molten long enough to acquire a spherical shape through surface tension, but also heated to sufficient temperature long enough to allow for relative homogenization of multi-mineralic soil grains through advection and diffusion.

There also exists varying degrees of homogeneity between the small adhered objects in this sample set. For example, Object D2 is the among the most compositionally heterogeneous in the sample set, while sample C1 is relatively homogeneous (Figure 4.28). As shown in Figure 4.28, D2 and C1 are approximately the same size ($\sim$250 and $\sim$200 microns in diameter, respectively). While a comparable level of homogeneity would be expected assuming identical starting composition and temperature history, C1 is compositionally homogeneous in major elements, while D2 is not (relative to their respective host objects). Further, Sample D2 shows evidence of relict quartz, and has preserved compositional flow banding, suggesting internal advection or mechanical mixing. The difference in the degree of chemical heterogeneity between the two objects indicates that these individual objects have

distinct thermal histories. That is, they were exposed to variable degrees of heating and/or a variable duration of heating.

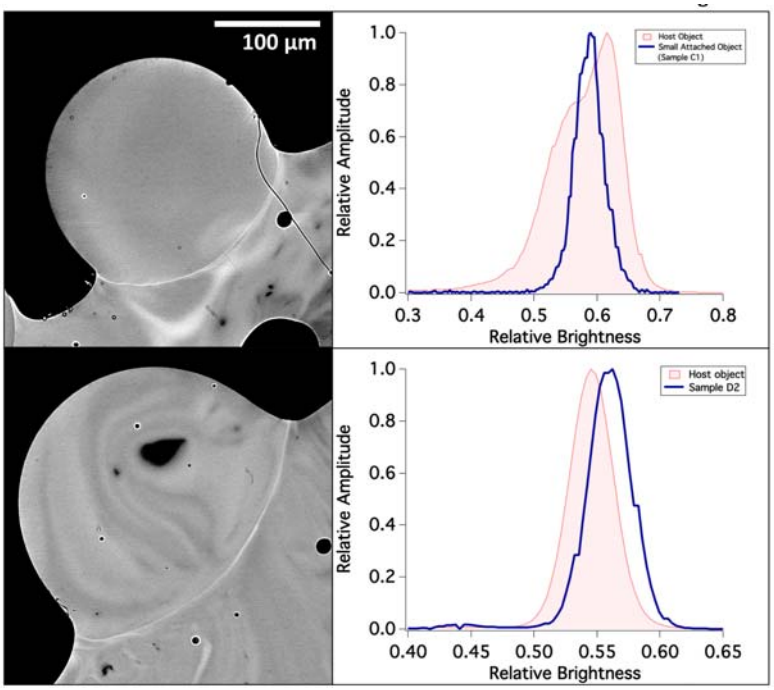

Figure 4.28: BSE images of C1 and D2 along with their contrast variation plots, juxtaposed to show the range in heterogeneity in similarly-sized agglomerated objects.

The degree of deformation and coalescence of small objects after collision with larger objects is also indicative of a variable record of the thermal history of glassy fallout agglomerates. In Objects C1-3 for instance (Figure 3.3), C1 and C2 experienced little deformation from sphericity upon collision with the larger object, while C3 has coalesced with the larger object. In sample C2, the larger host object appears to wrap around the exterior of the smaller object to some extent (see Figure 3.14, Na X-ray map). This suggests that the smaller object was more viscous than the host object, though surface tension and collisional velocity also affect the outcomes of liquid droplet collisions [81]. While droplet interaction parameters were not quantified in this study, viscosity increases more than 1000-fold for glass compositions similar to fallout from 2000K to 1500K [42], and the degree of deformation and coalescence may reflect the thermal dissimilarity between objects.

The timescales at which surface closure to mass transfer occurs in glasses of these compositions (∼1500 K) has been quantified by Cassata et al. (2014) in mm-scale objects to be from <0.1 to 2.9 seconds, a range that is attributed to both thermal variation in the fireball and the trajectory of entrained material through the fireball [54]. Thus, as the collisions between agglomerated objects occurred in the fireball, the range of thermal histories experienced by similarly-sized fallout objects also indicates thermal heterogeneity in the fireball

and/or a difference in duration of heating for individual objects. In either or both cases, the presence of a deposition layer at every observed interface suggests that condensation processes, or deposition of condensates onto the surfaces of molten carrier materials, occurs over a range of times and/or temperatures, during which the molten environmental debris is entrained in the fireball. Further, given the diffusive nature of the composition profiles, the deposition at the interface was likely continuous (*i.e.,* not a result of re-entrainment).

Interpreting enrichments of device material at interfaces

Using NanoSIMS to probe the interfaces of agglomerated fallout glasses, an increase in ^{235}U was observed relative to the interior of these objects. The ubiquitous presence of enriched levels of ^{235}U (Table 4.7) in these fallout glasses confirms that there is significant mixing of device material with environmental debris during formation, as seen in previous studies of larger objects [55, 56]. The bulk uranium concentration in aerodynamic fallout glasses form this test calculated by previous studies indicates that condensation of device material and subsequent deposition onto molten carriers occurred early enough to mix (by advection, diffusion, or both) into the interior of the carrier. However, the substantial increase in concentration of uranium (Table 4.7) at the interfaces of agglomerated fallout glasses indicates that this deposition was, in fact, highly favored immediately prior to quenching of carrier materials. Historical autoradiography studies also show that the mixture of device material into fallout is indeed not a uniform process - in particular, an enrichment of active beta emitters (such as ^{90}Sr and other fission products) has been observed as a surface layer on fallout objects [8, 10]. While we can no longer directly characterize high-activity nuclide distributions in these aged materials due to their decay, this historically observed feature is likely the same surface layer preserved at the interface of agglomerated objects.

It is expected that a fraction of other local material proximate to the device (such as soil and structures) would have also been vaporized in the initial explosion, and is probably the source of the other observed chemical enrichments in the interface layers. In these analyses, local enrichments of ^{235}U are correlated with increased iron and calcium concentration at 7 of 9 interfaces (as shown by the isotope ratios in Figures 4.17 - 4.26), suggesting that these species co-condensed, and were deposited together. This is exemplified in Figure 4.29, which shows the peak-normalized variation of ^{44}Ca/^{30}Si, ^{54}Fe/^{30}Si, and ^{235}U/^{30}Si at the interface of Object C1. This figure illustrates the precise co-location of ^{44}Ca/^{30}Si, ^{54}Fe/^{30}Si, and ^{235}U/^{30}Si enrichments at the interface which is observed in most samples. These patterns of enrichments are likely the result of Fe and Ca from the soil or anthropogenic components vaporizing together with the device, and subsequently forming either a direct condensate from the vapor state or depositing onto the carrier materials as a condensed species. In the case of object C1 (and other interfaces exhibiting the co-location of enriched species), these species were likely well mixed in the vapor phase prior to condensation, and co-deposited onto the surface of the object prior to its fusing to the host with no significant re-evaporation of any of the deposited species.

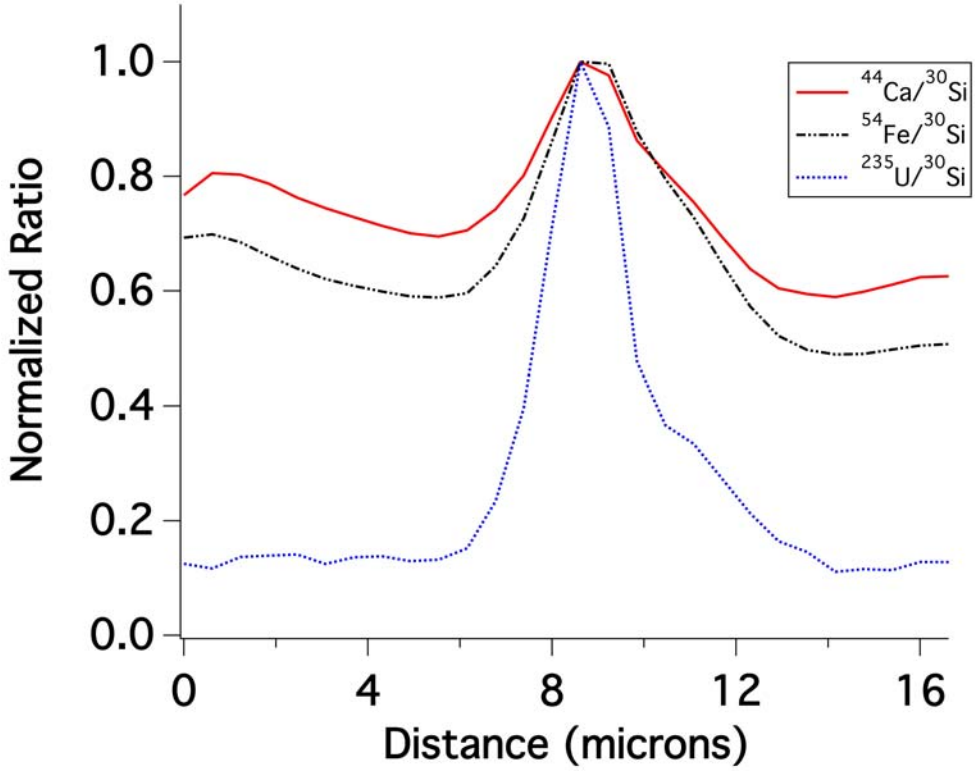

Figure 4.29: Peak-normalized variation of $^{44}Ca/^{30}Si$, $^{54}Fe/^{30}Si$, and $^{235}U/^{30}Si$ at the interface of object C1 plotted together to show co-location of local maxima.

4.4 Interpreting chemical variation at the interface

In Figure 4.30, the comparison of the interface values with the average object compositions reveal that the observed concentration enrichments and depletions cannot be explained by compositional variation of the host objects. This is exemplified by the major element oxide plot of CaO vs. Al_2O_3 (Figure 4.30A); the interior data points vary by approximately 10 wt.% in Al_2O_3 and 2 wt.% in CaO, however, the interface data points are all lower in Al_2O_3 composition. While some interface data points do fall within the compositional range of the interior points, they are still depleted in Al when compared to the interior data points of their corresponding host object (Table 4.6). The Ca content of interface data points is also generally enriched compared to interior points; however, samples C2 and E1 appear to have a lower concentration of Ca at the agglomerate interface. When compared to the corresponding interior points, however, the interface of sample E1 is still substantially enriched in Ca (41% enriched, Figure 4.11). In the plot of FeO vs. TiO_2 (Figure 4.30B), the interface data points show a clear trend of enrichment in Fe relative (by as much as 55%) to the interior points of the corresponding host samples, with the exception of samples B1 and B2. In 6 of the 9

measured interfaces, there is evidence of Ti depletion relative to the interior data points by >25%.

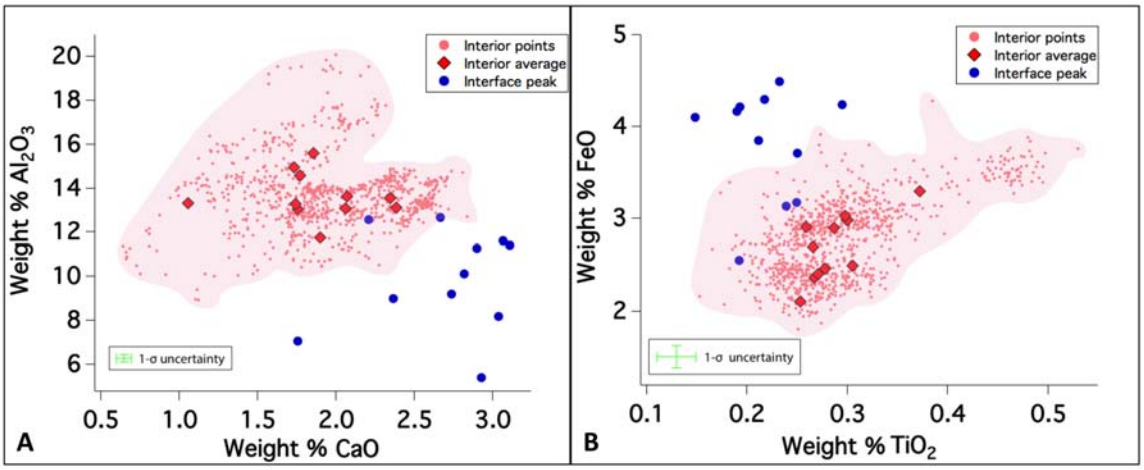

Figure 4.30: (A) Major element oxide plot of CaO vs. Al_2O_3 taken from quantitative WDS data from across the agglomerated spheroidal glassy objects, and across the interface where they fused to larger objects. The interior data represent 903 data points taken in the interior of the spheroidal objects; the gray shaded region shows the compositional range of the dataset. The interface points, indicated in blue, represent data points taken at the Al_2O_3 trough of relative Al depletion in concentration (the same spatial location of the local FeO maxima at each interface). The interface data points are depleted in Al_2O_3 for all samples, and the CaO content at the interface is enriched in 8 of the 9 samples. (B) Major element oxide plot of FeO vs TiO_2 from the same dataset, with the shaded region depicting the range of the interior dataset. Here, FeO is observed to be enriched at the interface with a corresponding depletion of TiO_2 for 6 of the 9 sample interfaces.

Al_2O_3 and TiO_2 are relatively refractory oxides which are abundant in the soil material from which such fallout is derived. Given the similarity in boiling points of FeO, TiO_2, CaO, and Al_2O_3 (2785K, 3273K, 3100K, and 3250K respectively [82, 83, 84, 85]) and the occurrence of FeO with TiO_2 and CaO with Al_2O_3 in major mineral phases (*i.e.*,, ilmenite and andesine, respectively, see Section 4.1), it might be expected that these species would enter the vapor phase together, and condense proportionally onto molten hosts. However, it was observed that the agglomerate interface layers are consistently depleted in Al and Ti, alongside relative enrichment of Fe and Ca (Figure 4.30).

Recent studies of fallout debris from the Trinity test (trinitite) identify unusual chemical and isotopic enrichments as signatures from the support structure, unfissioned fuel, and non-fuel device components [44, 51, 52, 53]. Thus, one possible explanation of the fractionation of Al from Ca may be that the Ca enrichments observed at the interface reflect the role of an anthropogenic source. This source could be a support structure, such as common

cement (having >60% CaO), proximate to the device prior to detonation, rather than simple derivation from local soil material (which is ∼1.5 wt% CaO [55]). While Al_2O_3 is also a common constituent of concrete aggregates, the relative aluminum content of potential anthropogenic structures can vary considerably, and for this anonymous event, is unknown. The excess Fe-bearing species observed at the interfaces in these samples would also support an origin from vaporization of a substantial Fe-bearing component (*i.e.,* steel) possibly in the form of associated structural materials. The observed pattern of enrichments and depletions may therefore result from contributions of proximate structural materials, creating an apparent fractionation of aluminum-bearing species from the iron, calcium, and uranium-bearing species.

Another possible explanation for the observation of depletion of Al and Ti at the interfaces, however, is that Al and Ti did not enter the vapor phase with Fe and Ca as might be expected based on their boiling points and co-occurrences in their respective common mineral phases (Al, Ca in andesine and Fe, Ti in ilmenite), and thus, were not available for interaction with molten hosts in the fireball. While boiling point data gives a general metric for relative volatility, it may in this case be a poor proxy for estimating vaporization behavior, as it is typically calculated for pure compounds. It is possible that Fe and Ca (as well as the other locally enriched species) could disproportionately enter the vapor phase relative to Al and Ti in multicomponent carriers. This interpretation is complicated, however, by the observation that CaO is approximately as refractory as Al_2O_3 in a molten silicate system similar to that which is found in the fallout samples [86]. However, fractionation between these species may instead be dictated by the condensation behavior of these species in the fireball, which is dependent on speciation of vaporized constituents. The speciation in the vapor phase depends on the oxygen fugacity of the environment and the interactions between vaporized constituents. For example, condensation temperatures for Ca, Ti, and Al are calculated by Lodders et al. (2003) [41] to be within ∼100 K of each other. However, these values are calculated for elements condensing out of a solar composition gas in equilibrium rather than for fireball conditions, which is dramatically different.

The study by Lamoreaux et al. (1987), which presents vapor pressure data for major element oxides, exemplifies the effect environment can have on vapor phase constituents [87]. For example, in that study, Ca is shown to have the highest vapor pressure of any Ca-species between 1300K and 2200K in reducing environments. In oxygen-rich environments, on the other hand, CaO has the highest vapor pressure, and is over 5 orders of magnitude lower than Ca in the reducing environment over the same temperature range. Further, compared to any Al-species in oxygen-rich environments, the CaO vapor pressure is roughly 2 orders of magnitude higher in vapor pressure, while Al-species in reducing environments have the same vapor pressure as Ca. The effect of speciation is further complicated in oxygen-rich environments for Al-species in that AlO has a higher vapor pressure in one temperature regime (>2000 K), and Al has a higher vapor pressure in another (<2000 K). Based on this data, changes in oxygen fugacity will change the proportions of how species vaporize, and changes in temperature can change the speciation of vapor phase constituents, which will affect the rate and temperature of condensation. Although the data in this thesis are

reported as oxides (for EPMA data) and ions (for NanoSIMS), the speciation of the deposited constituents is unknown.

Continuous fractionation and fireball heterogeneity

Historical models of fallout formation argue that refractory species (including uranium) are expected to condense early and distribute volumetrically into molten host materials, while more volatile species are expected to condense later and deposit on the surface of already solidified hosts [15, 18, 88]. In a silicate system of composition similar to that of the fallout objects, Al_2O_3 and CaO would be considered the most refractory species, while K_2O, SiO_2, and Na_2O are the most volatile [86]. Thus, if the condensation was dictated by the relative volatility of individual vaporized species, one would expect to see a distinct separation of refractory oxides from volatile oxides. Consequently, this would lead to a higher relative concentration of refractory species (*e.g.,* Ca and Al from the environmental debris, ^{235}U from the device) volumetrically distributed inside of the glassy fallout objects, and a post-quenching surface-deposited layer of volatile species (*e.g.,* Na_2O, K_2O from the environmental debris). Instead, as observed at these interfaces, both refractory (Fe, Ca, and ^{235}U) and volatile species (Na) are observed to be co-located at the interfaces in more than half of the observed samples, while there is a notable depletion of Al in all the interfaces.

The presence of a layer enriched in both refractory and volatile species deposited onto molten soils that have already encountered and incorporated a device-material bearing vapor phase does not fit well into a two-stage interaction model such as that proposed by Miller (1960) [15]. Two possible explanations can account for the presence of such a layer: 1) The presence of a continuous condensation and mixing process based on the volatility of species and the cooling of the fireball that resulted in the deposition of a condensation layer on cooling fallout objects, and/or 2) molten fallout interacting with a compositionally and thermally heterogeneous fireball. Norman and Winchell (1966) [31] first proposed a model of continuous condensation and diffusion to explain the incorporation of fission products, in contrast with the model of Miller (1960) where refractory species would condense early and mix volumetrically, while volatile species would deposit onto an already frozen particle without being appreciably incorporated into the object. However, continuous profiles of condensed species were not observed at *every* interface in our study. As shown in the ^{235}U/^{30}Si ion ratio images of the agglomerate interfaces of samples A1 and B3 (Figures 4.17 and 4.20, respectively), as well as the qualitative EPMA map of the Ca distribution in sample C2 (Figure 3.14), continuous concentration profiles of every species are not present in all samples. This observation is exemplified in Figure 4.20, where the ^{235}U/^{30}Si isotope ratio image shows a distinct layer of ^{235}U at the interface between two objects. Two zones of relative ^{235}U depletion can be seen on either side of the interface, one of which hosts a local maxima for ^{54}Fe/^{30}Si, separating it from the higher ^{235}U/^{30}Si ratio in the two objects (Figure 4.20, top left and bottom right).

The presence of a relatively high ^{235}U/^{30}Si region adjacent to a relatively low ^{235}U/^{30}Si (but high ^{54}Fe/^{30}Si) region can only be explained by a discontinuous evaporation and con-

densation process. For example, if the molten carrier objects passed through a vapor in the fireball having a negligible uranium concentration (*i.e.,* not well-mixed with device material) but significant iron concentration, the partial pressure of U would then favor an evaporative process, resulting U loss from the environmental host material, but permitting significant deposition of Fe. Subsequently, if debris then passed through a vapor having high uranium concentration (*i.e.,* well-mixed with vaporized device material), the partial pressure of U would favor a condensation process, depositing a layer of higher relative ^{235}U. If the trajectory of the fallout debris brought it through a relatively cooler region of the fireball that was more concentrated in volatile species, it is possible that these species could also condense onto and diffuse into a still-molten fallout object. Given the variation in relative enrichment and depletion of species observed at the interfaces, this study suggests that a combination of these processes is likely to be occurring.

The scenarios that describe the pattern of chemical variation at the interface are summarized in Figure 4.31. As illustrated in Figure 4.31A, the presence of both volatile and refractory species at the interface is suggestive of a semi-continuous process of condensation, deposition, and mixing. This continuous process would also account for the potential chemical fractionation caused by unexpected speciation due to chemical interactions within the fireball environment. The range of chemical behaviors observed at the interface, such as the relative enrichment of volatile species only at selected interfaces, also suggests a heterogeneous temperature distribution and/or unmixed vaporized species in the fireball. Further, as illustrated in Figure 4.31B, the depletion of refractory Al and Ti oxides at the interface co-located with similarly refractory Ca oxide could suggest the presence of a non-soil source, such as anthropogenic structural material. Given the observed patterns of compositional variation described above, it seems likely that all of these processes are occurring to some extent. To further understand speciation in the fireball, constraints on the time and temperature of deposition of the observed layer at agglomerated interfaces were derived (see Chapter 5).

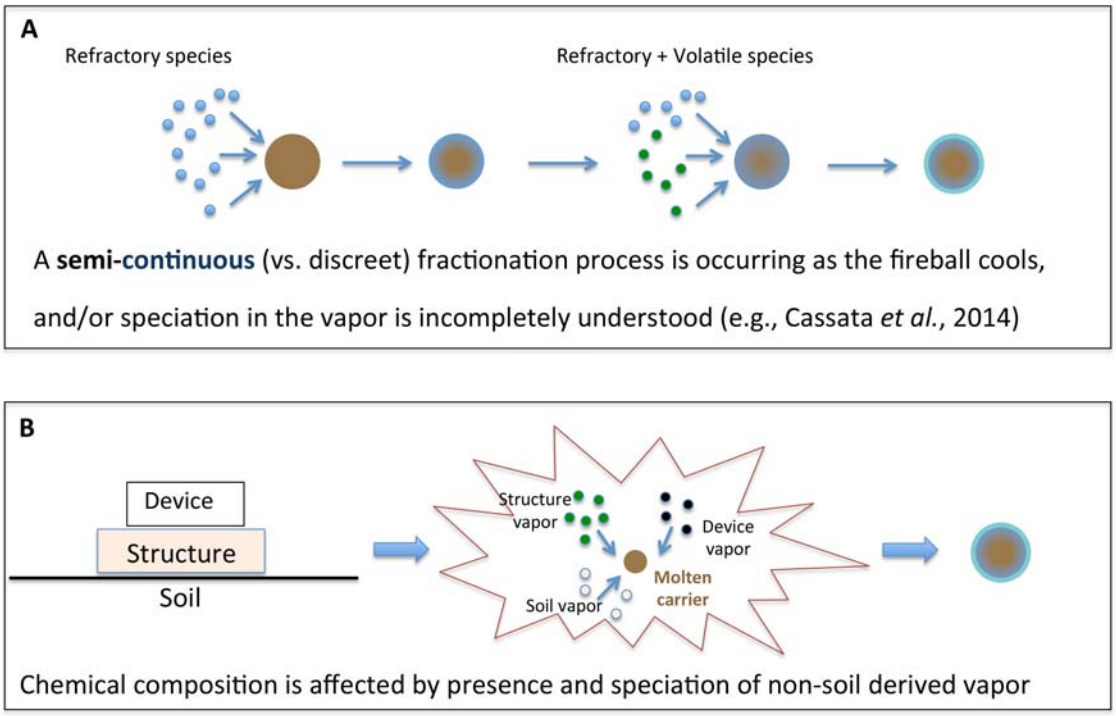

Figure 4.31: (A) A semi-continuous fractionation process describes the presence of volatile and refractory species co-located at interfaces. (B) The depletion of Al and Ti, and enrichment of Ca, Fe, and ^{235}U, suggests the presence of a non-soil derived vapor source.

Chapter 5

Diffusive mass transport in agglomerates from a deposition layer

5.1 Introduction

The conditions and chemical processes through which device material and soil interact to form glassy fallout objects are not well understood, particularly the effects of fireball temperature and composition on speciation and condensation. However, these details are critical to our understanding of the distribution of radionuclides post-detonation, and improving sample interpretation for nuclear forensic analysis. One goal of this study was to constrain the time scales and temperature ranges that control mass transport in aerodynamic fallout glasses by studying and modeling the compositional variation profiles at the interfaces of agglomerated glassy objects. By constraining these parameters, the temperature of deposition of species onto agglomerated fallout objects can also be constrained, and then be used to interpret speciation of vaporized constituents in the fireball. As previously shown, the interfaces between the small objects and the larger host objects are consistently enriched in iron, calcium, magnesium, and uranium. The quasi-Gaussian concentration profiles of these elements suggest chemical diffusion, from which time and temperature parameters can be derived.

In this study, a model of diffusive mass transport was applied to the observed uranium concentration variation (as $^{235}U/^{30}Si$ isotope ratio profiles) in the observed deposition layer found at the interfaces of agglomerated fallout objects. This chapter describes the relationship of fireball cooling rates (modeled yields ranged from 0.1 kt to 10 kt), soil residence time, and temperature, on the diffusion of ^{235}U in a deposited layer from the surface of aerodynamic fallout objects. By applying a one-dimensional planar diffusion model to observed $^{235}U/^{30}Si$ profiles at the interfaces where two fallout objects have fused, one can estimate the cooling time and temperature range over which diffusion occurs post-deposition.

5.2 Model

Diffusive mass transport from a planar source

In the case of a thin layer of condensed species deposited on the surface of a molten soil host that subsequently fuses with a larger molten object the deposited layer is expected to diffuse into both objects, assuming that there is a chemical potential gradient between the layer and the molten objects. In the idealized case that the layer comprises a single species, is infinitesimally thin, and is between two homogeneous objects of equal composition, we expect a concentration distribution to evolve from the layer between two objects of equal temperature over time, following the form of Equation 5.1

$$C(x,t) = C_0 e^{\frac{-x^2}{4Dt}}\,, \tag{5.1}$$

where C is concentration, C_0 is the initial concentration of the species in the layer, D is the diffusivity, t is time, and x is the dimension of diffusion [89].

Equation 5.1 is derived from Fick's second law of diffusion, which describes diffusive flux of a species through a medium. In this model, Fick's second law is applied to a system of a dilute, planar source diffusing into a liquid-phase medium (*i.e.,* molten soil). However, in order to apply Fick's second law of diffusion to a model of planar diffusion from a deposition layer in molten carrier material for the purposes of fallout formation modeling, a basic understanding of binary diffusion must be established (illustrated in Figure 5.1).

Fick's second law can be derived [90] from the change in mass of a species through a volume

$$\Delta M = m_1 - m_2\,, \tag{5.2}$$

where ΔM is the change in mass of the diffusing species, m_1 is the mass of the species entering the volume, and m_2 is the mass of the species exiting the volume. This equation can be rewritten as

$$V\frac{\Delta M}{V} = A\frac{m_1}{A} - A\frac{m_2}{A}\,, \tag{5.3}$$

where V is volume, and A is the cross sectional area of the volume through which the species is diffusing to derive a relationship between change in concentration and fluence of the species. By substituting concentration ($C = \frac{\Delta M}{V}$) and fluence ($\phi = \frac{m}{A}$), this equation becomes

$$V\Delta C = A\phi_1 - A\phi_2\,, \tag{5.4}$$

where ΔC represents the change in concentration of the species through the volume. As diffusivity is a time-dependent process, both sides of the equation are divided by Δt, giving

$$V\frac{\Delta C}{\Delta t} = A\frac{\phi_1}{\Delta t} - A\frac{\phi_2}{\Delta t} = A(J_1 - J_2)\,, \tag{5.5}$$

where J is the flux of the species through cross sectional area A. Dividing both sides by V, and considering $J_2 = J_1 + \Delta J$, where ΔJ is the change in flux over the volume,

$$\frac{\Delta C}{\Delta t} = \frac{A}{V}(J_1 - (J_1 + \Delta J)) \,. \tag{5.6}$$

As the concentration and flux through the volume change instantaneously with time, then for one-dimensional diffusion the above equation is better represented as

$$\frac{\delta C}{\delta t} = \frac{A}{V}(J_1 - (J_1 + \frac{\delta J}{\delta x}\Delta x)) \,, \tag{5.7}$$

where Δx represents the length of the volume in the direction of diffusion, following the relationship $\Delta x = \frac{V}{A}$. Thus, the above equation can be rewritten as

$$\frac{\delta C}{\delta t} = \frac{1}{\Delta x}(J_1 - (J_1 + \frac{\delta J}{\delta x}\Delta x)) \,, \tag{5.8}$$

which reduces to

$$\frac{\delta C}{\delta t} = -\frac{\delta J}{\delta x} \,. \tag{5.9}$$

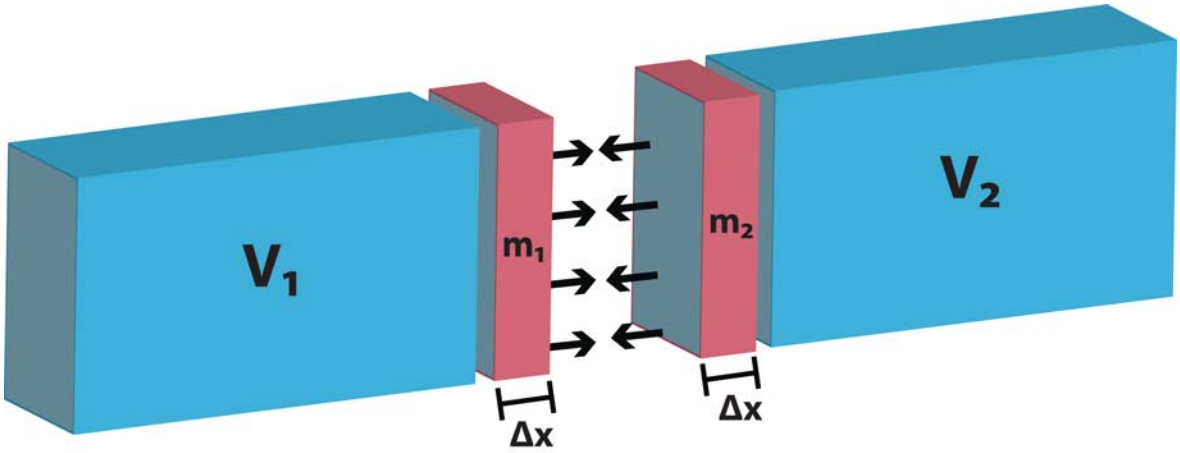

Figure 5.1: Mass transport between two semi-infinite volumes of different concentration, illustrative of one dimensional diffusive mass transport in a diffusion couple.

When studying diffusive mass transport of a species between regions of varying concentrations, one can consider the probabilistic transfer of mass between two adjacent, semi-infinite volumes (*i.e.,* a diffusion couple). This is illustrated in Figure 5.1; the left-hand volume (V_1) has a concentration C_1, and a species with mass m_1 has equal probability of moving towards V_1 or V_2. This process is the same for species in V_2 (which has concentration C_2); these species, having mass m_2, have equal probability of moving towards V_2 and V_1. Using these definitions,

$$m_{1\to2} = 0.5 \cdot C_1 \cdot A \cdot \Delta x\,, \tag{5.10}$$

and

$$m_{2\to1} = 0.5 \cdot C_2 \cdot A \cdot \Delta x\,, \tag{5.11}$$

where $m_{1\to2}$ is the mass moving from V_1 to V_2, and $m_{2\to1}$ is the mass moving from V_2 to V_1. In this case, Δx represents the distance of the concentration gradient ($\frac{\delta C}{\delta x}$) between the two volumes. Thus, the total mass transferred between V_1 and V_2 is still ΔM, given as

$$\Delta M = m_{1\to2} - m_{2\to1} = 0.5 \cdot A \cdot \Delta x(C_1 - C_2)\,. \tag{5.12}$$

Again, as diffusive mass transport is a time-dependent process, the above equation is rewritten as

$$\frac{\Delta M}{\Delta t} = \frac{0.5 \cdot A \cdot \Delta x(C_1 - C_2)}{\Delta t}\,, \tag{5.13}$$

which represents the change in total mass transferred between the two volumes over time in the diffusion couple shown in Figure 5.1.

The difference in concentration between V_1 and V_2 can be represented as

$$C_2 = C_1 + \frac{\delta C}{\delta x} \cdot \Delta x\,, \tag{5.14}$$

which simply states that the concentration in V_2 is equal to to the concentration in V_1 plus the concentration gradient induced by the mass transfer between the two halves of the diffusion couple.

Thus, equation 5.13 can be rewritten as

$$\frac{\Delta M}{\Delta t \cdot A} = \frac{0.5 \cdot \Delta x(C_1 - (C_1 + \frac{\delta C}{\delta x} \cdot \Delta x))}{\Delta t}\,, \tag{5.15}$$

where diffusive flux between the two halves of the diffusion couple is represented by

$$J = \frac{\Delta M}{\Delta t \cdot A}\,. \tag{5.16}$$

Equation 5.15 can simply be reduced to

$$J = -\frac{0.5 \cdot (\Delta x)^2}{\Delta t}\frac{\delta C}{\delta x} = -D\frac{\delta C}{\delta x} \tag{5.17}$$

where $\frac{0.5\cdot(\Delta x)^2}{\Delta t}$ is defined as a coefficient, D, known as the diffusivity.

Combining equations 5.9 and 5.17, we arrive at Fick's second law

$$\frac{\delta C}{\delta t} = D\frac{\delta^2 C}{\delta x^2}\,, \tag{5.18}$$

which states that the time-dependent change in concentration is equal to the rate of change of the concentration gradient in one dimension, given a proportionality constant D (*i.e.,* the diffusivity). Thus, using this equation, the functional form of a concentration profile can be determined for 1-dimension mass transport problems, such as the above described planar diffusion model [91].

Assuming the deposition layer is infinitesimally thin in comparison to the carrier objects, we can represent the deposition layer as a delta function. This is illustrated in Figure 5.2, where the deposition layer at Interface D2 is shown to be very thin (<5 microns) in comparison to either Object D2 or Sample D (also shown in Figure 3.4).

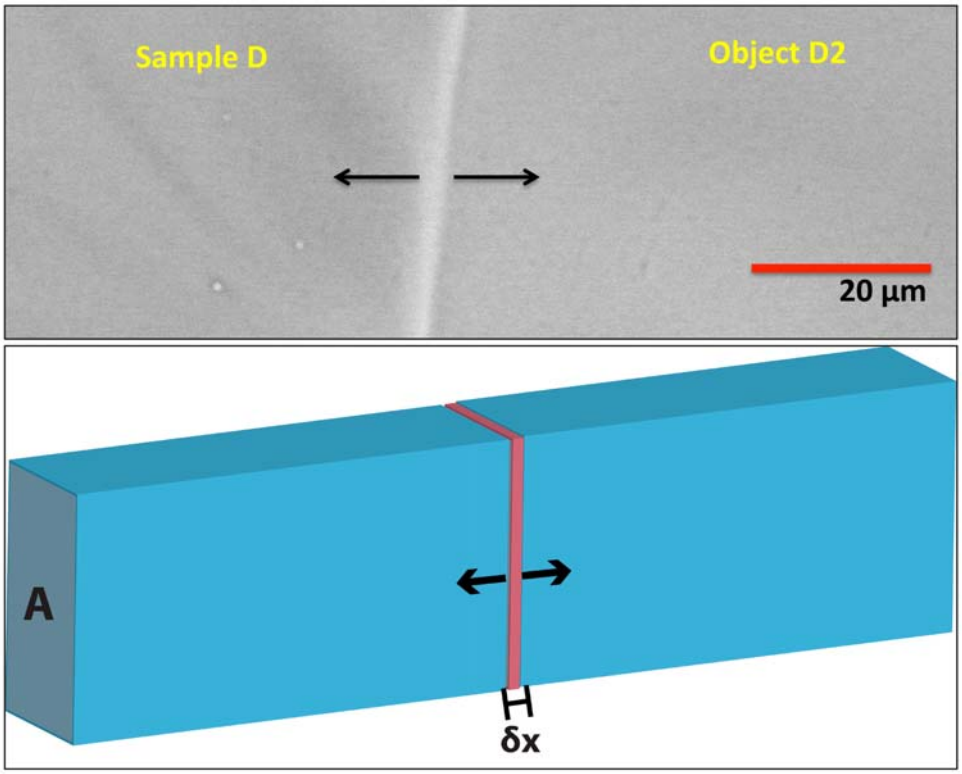

Figure 5.2: Top, BSE image of the interface between Sample D and Object D2. The interface region is very thin (<5 microns) in comparison to the larger objects. Bottom, schematic of mass transport from an infinitesimal planar source (red) through a volume (blue) having cross sectional area A, which was used to model deposition layers as shown at Interface D2 (above).

The initial concentration of the layer is given as

$$C(x) = M\delta(x) \tag{5.19}$$

where M is the mass of the diffusant. The variables that control mass transport can be organized into dimensionless parameters via the Buckingham Pi theorem [91]:

$$\pi_1 = \frac{C}{M/A\sqrt{Dt}}\,, \tag{5.20}$$

and

$$\pi_2 = \frac{x}{\sqrt{Dt}}\,, \tag{5.21}$$

such that, through dimensional analysis, π_1 is equal to some function of π_2:

$$\pi_1 = f(\pi_2)\,, \tag{5.22}$$

where A is the cross sectional area, D is the diffusivity, t is time, and x is the direction of diffusion.

Equation 5.22 can be reorganized to present concentration as a function of time and distance,

$$C(x,t) = \frac{M}{A\sqrt{Dt}} f(\frac{x}{\sqrt{Dt}})\,. \tag{5.23}$$

Using a series of substitution steps, Equation 5.23 can be combined with Equation 5.18 to determine the functional form of f, from which we arrive at the equation representing a concentration distribution from diffusion of a planar source

$$C(x,t) = \frac{M}{A\sqrt{4\pi Dt}} e^{(\frac{-x^2}{\sqrt{4Dt}})}\,, \tag{5.24}$$

which is identical to Equation 5.1, where the pre-exponential fraction can be defined as C_0. In the idealized case described above, one would expect the concentration distribution of the diffusing species to spread in a Gaussian shape from a delta function over time, as shown in Figure 5.3.

Thus, when considering a deposited layer of material at the interface of agglomerated glassy fallout objects, concentration profiles should approximate a Gaussian distribution from the interface, particularly if the still-molten material did not have considerable pre-existing concentration or thermal gradients prior to deposition and agglomeration (addressed in Section 5.3). In such a scenario, the concentration profile of a species of interest can be fit by a Gaussian distribution,

$$G = \frac{A}{\sigma\sqrt{2\pi}} e^{-\frac{(x-\mu)^2}{2\sigma^2}}\,, \tag{5.25}$$

where A is the amplitude of the peak, σ is the standard deviation of the distribution, and μ is the average. In non-linear least squares regression analysis, each of these variables are fitting parameters and are determined from the fit. Using Equation 5.25 to fit the

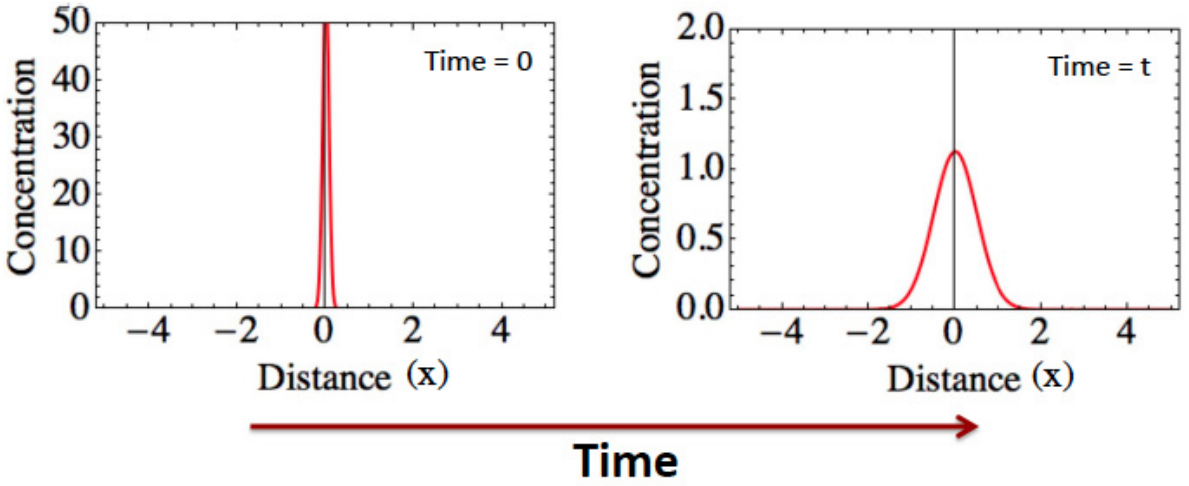

Figure 5.3: Model of a concentration distribution from 1-dimensional diffusion from an infinitesimal planar source, taking the form of a Gaussian distribution at arbitrary time t. The concentration is presented in relative units, as the area under both curves is the same.

concentration distribution of a species observed at a given interface, a value of σ can be acquired, which has the following relation according to Equation 5.1

$$\sigma = \sqrt{2Dt}\,, \tag{5.26}$$

where D is the diffusivity of a species of interest and t is the time over which it diffused. Thus, from the concentration distribution observed for a species at the interface, parameters of diffusivity and time can be acquired.

However, diffusivity is temperature dependent according to the Arrhenius equation (Equation 1.5), which is uniquely defined for a single species diffusing through a specific medium over a temperature range. Thus, equation 5.26 is more accurately written as

$$\sigma = \sqrt{2D(T)t}\,, \tag{5.27}$$

and, from the σ derived from the concentration distribution of a species of interest, a convolved parameter of time and temperature can be determined if the Arrhenius relationship for the species of interest was known.

When considering that fallout is formed in a cooling fireball environment [92], the derived σ value is actually more accurately represented as

$$\sigma = \sqrt{2D_{avg}t}\,, \tag{5.28}$$

where D_{avg} is the average diffusivity over a specific temperature interval in the medium, where D_{avg} is defined as

$$D_{avg} = \frac{1}{b-a}\int_a^b D_0 e^{-\frac{E_a}{RT}}\,dT\,, \tag{5.29}$$

where the interval a to b represents the temperature range over which diffusion occurs.

In the context of a carrier in a cooling fireball environment, the parameter of T is the temperature of the molten soil through which the deposited material is diffusing. This temperature decreases according to the environment in which the droplet is entrained (*i.e.,* the fireball), which is a time dependent process. Thus, Equation 5.29 can be rewritten as

$$D_{avg} = \frac{1}{t}\int_0^t D_0 e^{-\frac{E_a}{RT(t)}}\,dt\,, \tag{5.30}$$

where $T(t)$ is the cooling rate of the molten material as dictated by the cooling of the fireball, and t is the time interval over which diffusion is able to occur. By combining Equations 5.28 and 5.30, the following relationship is derived

$$\frac{\sigma^2}{2} = D_{avg}t = \int_0^t D_0 e^{-\frac{E_a}{RT(t)}}\,dt\,. \tag{5.31}$$

Therefore, by determining the σ value from fitting the concentration distribution of a species that diffused from the interface, the time of mass transport can be deconvolved from the temperature interval, if the parameters E_a, D_0, and $T(t)$ are defined. As illustrated in the subsequent sections, the parameters E_a and D_0 can be acquired from studies conducted in similar materials (which are available in the literature), and the cooling rate $T(t)$ can be modeled using empirical relationships from historical studies of fireballs from atmospheric testing.

Effective binary diffusion of uranium

While the above treatment of diffusive mass transport is applicable for a 1-dimensional planar diffusion model, the rate of mass transport is not directly acknowledged. Diffusive mass transport is dictated by thermally induced random motion experienced by particles in a medium, which can be solid, liquid, or gas-phase (or some combination). As shown above, a concentration difference between two regions leads to mass transport of species between these regions, the rate of which is controlled by the state of the medium, the size of the diffusing species, and the chemical interactions between the diffusing species and the medium. This rate is directly related the diffusivity, D, of the species in a medium.

The simplest form of diffusion is binary diffusion, or diffusion in a system having two components. For example, in a layer having only a single species deposited onto the surface of a homogeneous molten medium, a model of binary diffusion could be applied to describe the rate of diffusion of the species into the medium. In that case, there is only one relationship (*i.e.,* one diffusivity) describing the mass transport of the species through the medium.

In this study, however, the deposited layer comprises multiple species, which are diffusing through a molten (liquid-phase or otherwise amorphous) glass constituent having multiple compositional components. To most accurately describe such a system, a series of flux relationships must be established describing the effect that the concentration gradient of each species has on the diffusion of each other species present in the system [89]. These relationships are defined as

$$J_1 = -D_{11}\nabla C_1 - D_{12}\nabla C_2 ... - D_{1n}\nabla C_n \,, \tag{5.32}$$

$$J_2 = -D_{21}\nabla C_1 - D_{22}\nabla C_2 ... - D_{2n}\nabla C_n \,, \tag{5.33}$$

and continuing for each of n species, until

$$J_n = -D_{n1}\nabla C_1 - D_{n2}\nabla C_2 ... - D_{nn}\nabla C_n \,, \tag{5.34}$$

where each D is the diffusion coefficient that contributes to mass transport of a species as it is affected by another species in the system.

In multicomponent systems, the above system of equations is typically solved in matrix notation, where the diffusion coefficients make up an $n \times n$ matrix known as the diffusivity matrix, which is uniquely defined for each multicomponent system [89]. For the silicate-based system observed in the glassy fallout in this study, however, there is no solution to the diffusivity matrix available in the literature. This is complicated further when considering diffusion of the species from a distinct deposition layer into the multicomponent soil composition.

In order to model diffusion in such complex systems, I use a simplified approach, known as effectively binary diffusion (EBD), to the multicomponent diffusion problem. In EBD, species of interest in a multicomponent systems can be treated as a series of approximately binary diffusion systems, where the diffusivity relates to the rate of mass transfer of a single species through the rest of the species combined. This method has been widely applied to mineral melts in the field of geochemistry, and has been used to understand multicomponent silicate systems similar to those found in the glassy fallout material in this study [89, 93].

For the EBD approach to be appropriate for a given multicomponent system, one of several distinct scenarios must be applicable [89]. In the first scenario, the concentration gradients in the multicomponent system are due to dilution caused by an increased concentration of a single minor component. In the second scenario, there is an interdependent compositional difference between two components in the system. in the third scenario EBD is used for diffusion couples of different composition for species having very large concentration changes between each end of the couple. In the last scenario, there are large gradients in multiple components in the same direction that have consistent relative magnitudes. In this case, an EBD approach is appropriate for the species with the largest gradient.

For this study, the fourth scenario is the most applicable – the observed layer being explained is enriched in multiple species (*e.g.,* Fe, Ca, and ^{235}U). The species in this layer

diffuse from the interface into both adjacent objects, which are typically very similar in major element composition (see Section 4.1). As observed in Table 4.7, the relative concentration increase is clearly the greatest in ^{235}U. That is, the maximum concentration increased over 900% relative to the concentration in either adjacent glassy object. To derive the time and temperature of deposition the layer, as well as the time of mass transport from the layer, I found it most appropriate to apply a model of EBD of uranium in a molten system of rhyolitic composition.

The most pertinent study available regarding diffusion of uranium in a composition similar to fallout glass is by Mungall and Dingwell (1997) [93], where uranium diffusivity was determined in a haplogranitic melt (79% SiO_2, 12% Al_2O_3). While the valence state of uranium in the fallout glass during deposition and diffusion is unknown, [93] suggests uranium is present in the hexavalent state in environments of high oxygen fugacity, which is assumed for this study at the temperature and pressure ranges of interest (< 2500 K and ~ 1 atm, respectively). Further, recent work using x-ray absorption near edge structures (XANES) on melt glass from a uranium-fueled test determined that the uranium predominantly existed in the hexavalent state (*i.e.,* UO_2^{2+}) [94].

As expected, the equation dictating the temperature dependence of uranium diffusion in this system was found by Mungall to be Arrhenian,

$$D_u = 12.27e^{-\frac{-363.8}{RT}}\,, \tag{5.35}$$

with the pre-exponential diffusivity given in cm^2s^{-1}, and the activation energy given in $KJ{\cdot}mol^{-1}$. These parameters were used with Equation 5.31 to determine the time and temperature parameters controlling the diffusion of uranium from the deposition layer in selected samples.

Average temperature of tropospheric nuclear fireball

It is theorized that fallout debris is a mixture of liquid phase soil and vaporized or condensed device materials [15, 18, 23]. As the glass objects in this study are aerodynamic in shape, it is likely that these objects solidified before coming in contact with the ground. In order to acquire a layer of Fe, Ca, and U at the interface of two fused objects, at least their surfaces were in the liquid state when the layer was deposited and before the objects collided, subsequently solidifying before significant ground interaction. It follows that the cooling rate of the interfaces (where the still molten objects collided), $T(t)$, would be dictated by the cooling rate of the fireball. As the temperature history of the objects in the fireball is unknown, the average cooling rate of the fireball was used to determine the approximate cooling rate of the fallout objects.

As described in Section 1.3, historical fallout formation models make use of fireball temperatures as derived from empirical scaling equations, such as Hillendahl's equations from light output curves [92]:

$$T = 7000W^{-0.07}(\frac{1}{t_{fmax}})^{-0.34}\,, \tag{5.36}$$

where T is temperature in K, W is the yield in kt, and t_{fmax} is the time (in seconds) of the second fireball light output maximum,

$$t_{fmax} = 0.037W^{0.49}\,. \tag{5.37}$$

These two equations were combined and differentiated to derive a yield-dependent fireball cooling rate after t_{fmax}:

$$-\frac{dT}{dt} = 776W^{0.10}t^{-1.34} \cong (3 \times 10^{-11})W^{-0.3}T^4\,. \tag{5.38}$$

Equation 5.38 is used as the ambient thermal environment input for modeling the cooling of fallout. As the event in question is anonymous, in Figure 5.4, the cooling curves for 0.1 kt, 1 kt, and 10 kt yields are given, as determined from Equation 5.38. The initial temperature was selected to be 2500 K, which is the boiling point of SiO_2 [95], and for this study is considered the maximum temperature at which a deposition layer could have formed on the surface of molten soil carriers (deposition is unlikely to occur on a boiling surface). As seen in Figure 5.4, cooling becomes more gradual as yield increases: a 0.1 kt fireball cools to below 1500 K in approximately 1 second, while a 10 kt fireball takes almost 5-fold longer to cool to 1500 K. The cooling rates used for this diffusion study were modeled to be 0.1 kt, 1 kt and 10 kt, to show the effect of yield on the thermal environment dictating diffusion over a range of magnitudes.

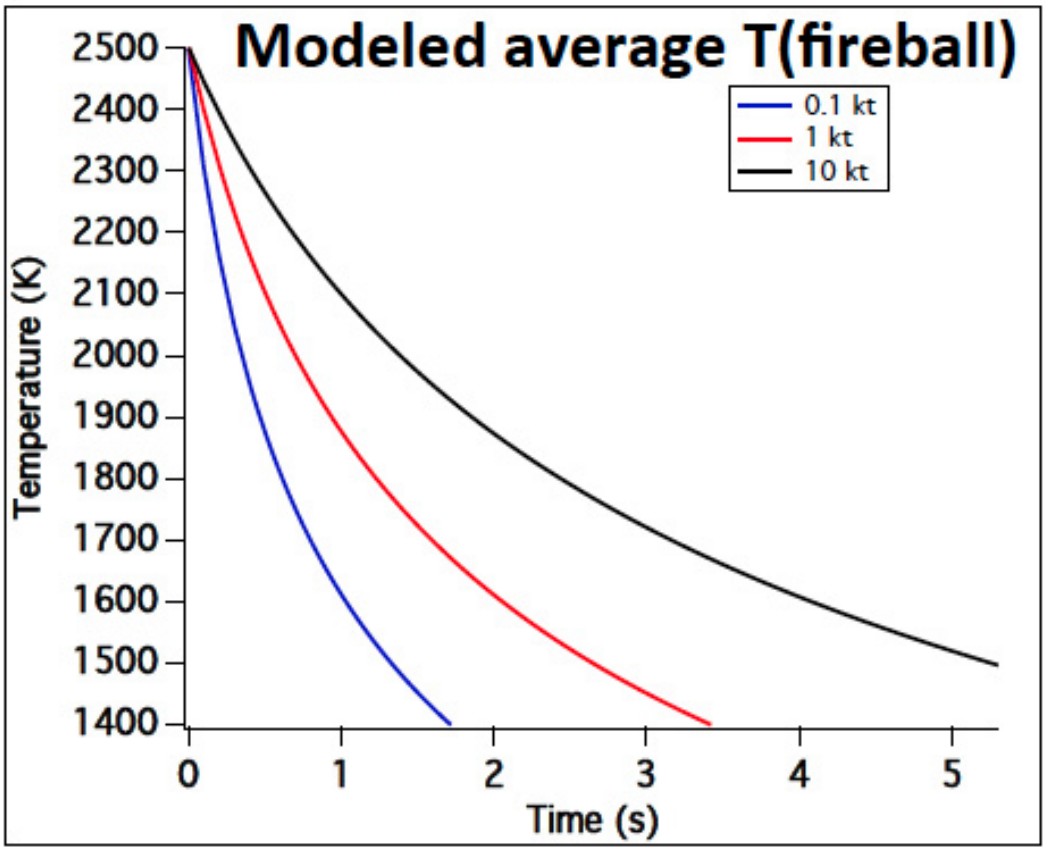

Figure 5.4: The fireball cooling curves determined from Equation 5.38 for 0.1 kt, 1 kt, and 10 kt near-surface nuclear explosions for temperatures below 2500 K based empirical scaling equations derived from light output curves [92].

Modeling cooling rate at selected interfaces

The temperature variation at the interface of agglomerated fallout objects was modeled using COMSOL Multiphysics Modeling Software, a finite element analysis solver based on coupled series of partial differential equations designed to simulate physical systems. Finite element analysis is a computational method for approximating the effect of a physical process on a geometric domain that cannot be directly solved otherwise. In finite element analysis, the geometry of a system is divided into a series of discrete polyhedra of predefined size (known as meshing) from which a series of interrelated partial differential equation boundary problems can be solved simultaneously.

In order to model the temperature variation at the interface, a three-dimensional model was constructed in COMSOL as shown in Figure 5.5a. This model simulated two spherical objects that fused together, with the larger object having a diameter of 1.5 mm, and the smaller object having a diameter of 0.4 mm. As shown in the 3-dimensional model, the

Table 5.1: Literature values of some material properties of a rhyolite melt

Property	Value	Reference
thermal conductivity k	0.5 $W/(m \cdot K)$	Murase et al. (1973) [96]
density ρ	2300 kg/m^3	Collier et al. (2006) [97]
ratio of specific heats γ	1.33	Collier et al. (2006) [97]
heat capacity at constant pressure C_p	1200 $J/(kg \cdot K)$	Romine et al. (2012) [98]
emissivity ϵ	0.8	Harris, A. (2013) [99]

smaller object is partially embedded in the larger object. In this model, the 'interface' was defined as the outer edge of the larger sphere that lay within the smaller sphere. Meshing of this model used tetrahedra, which could be automatically generated by COMSOL to mesh the unusual geometry of the modeled agglomerated objects. The tetrahedra ranged in size from 1 micron to 25 microns, such that features of interest could be approximated most accurately while minimizing computational time. Figure 5.5b shows a 3-D wireframe image of the meshing tetrahedra that made up the volume of the modeled geometry.

The heat transfer model applied to this system included conductive, convective, and radiative heat transfer. Conduction was used to model heat transfer within the object itself, while convective and radiative heat transfer was used to model the external effect of the cooling fireball environment on change in temperature within the modeled fallout object. In order to most accurately model these modes of heat transfer, the model was imbued with key material properties of molten rhyolite. Specifically, these properties included the thermal conductivity k, density ρ, ratio of specific heats γ, the heat capacity at constant pressure C_p), and emissivity ϵ (see Table 5.1) for a rhyolitic melt.

The differential equations that were used to simulate boundary conduction, convection, and radiative heat transfer between each discrete volume were

$$\rho C_p \frac{\delta T}{\delta t} + \rho C_p \vec{n} \cdot \nabla T = \nabla \cdot (k \nabla T) + Q \,, \tag{5.39}$$

$$-\vec{n} \cdot (-k \nabla T) = h \cdot (T_{ext} - T) \,, \tag{5.40}$$

and

$$-\vec{n} \cdot (-k \nabla T) = \epsilon \sigma (T_{ext}^4 - T^4) \,, \tag{5.41}$$

respectively, where $\vec{n}$ is the unit vector, T_{ext} is the ambient temperature (as determined by Equation 6.38), T is the temperature of the discrete volume within the object, t is time, h is the heat transfer coefficient of air, and Q is the heat energy.

To simultaneously solve these equations over the entire system, COMSOL used an interative minimization routine known as Generalized Minimal Residual algorithm (GMRES)

[100]. Using this minimization routine, COMSOL approximated the solution for each discrete volume in the defined geometry over a series of 50 iterations for each time step, which was 0.1 seconds over a period of 5 to 10 seconds for this simulation, depending on the modeled yield. Thus, for each time step, the temperature at each defined tetrahedra in the object could be determined and a temperature profile could be acquired.

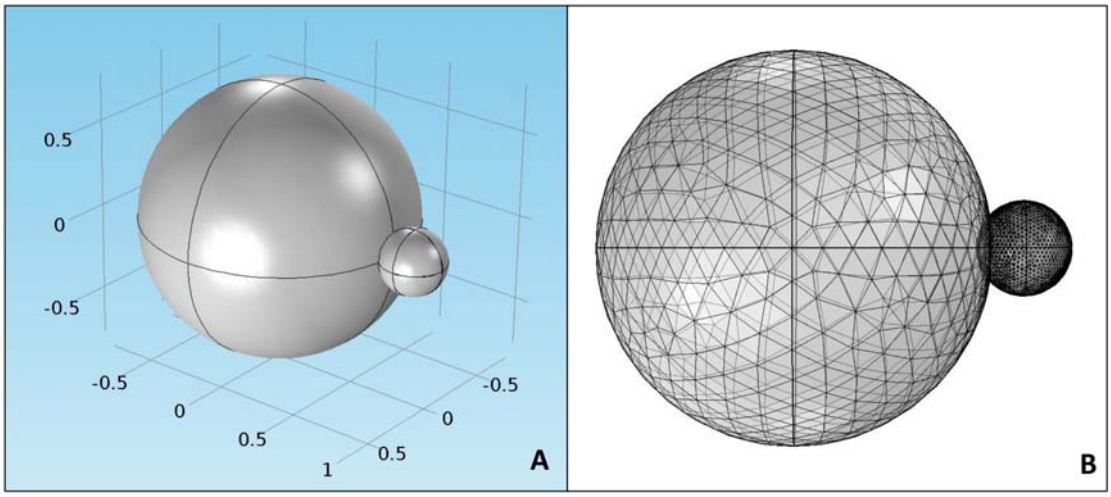

Figure 5.5: (A) COMSOL 3-D mockup of aerodynamic fallout glass where two objects have fused together, where the grid scale is in millimeters. The large object is 1.5 mm in diameter, and the smaller attached object is 0.4 mm in diameter. (B) Wire frame of the meshed geometry, using tetrahedra from 1 micron to 25 microns, to model the geometry.

In Figure 5.6, the temperature profile of the object is shown at 1.0 seconds for the modeled object, with an ambient cooling rate defined by the average temperature of a fireball from a 1 kt near-surface nuclear explosion as defined by Equation 5.38 (see Figure 5.4 for the cooling curve). For these models, an initial temperature of 2500 K was selected (the approximate boiling point of SiO_2 [95]) for the fallout material. The models were run until the interface had cooled to approximately 1500 K (well below the solidification temperature posited by Freiling [16]). As seen in the temperature profile shown in Figure 5.6, there is a modeled temperature gradient of approximately 300 K across the object, with the interface (indicated by the black arrow) lying within the cooler temperature regime relative to the center of the larger object. Within the smaller attached object, there exists little thermal variation relative to the larger object. This difference is due to the large surface-to-volume ratio of the smaller object. As the modeled ambient temperature approaches 1500 K, cooling within the object is dominated by convective cooling, and the thermal gradient within the object effectively disappears.

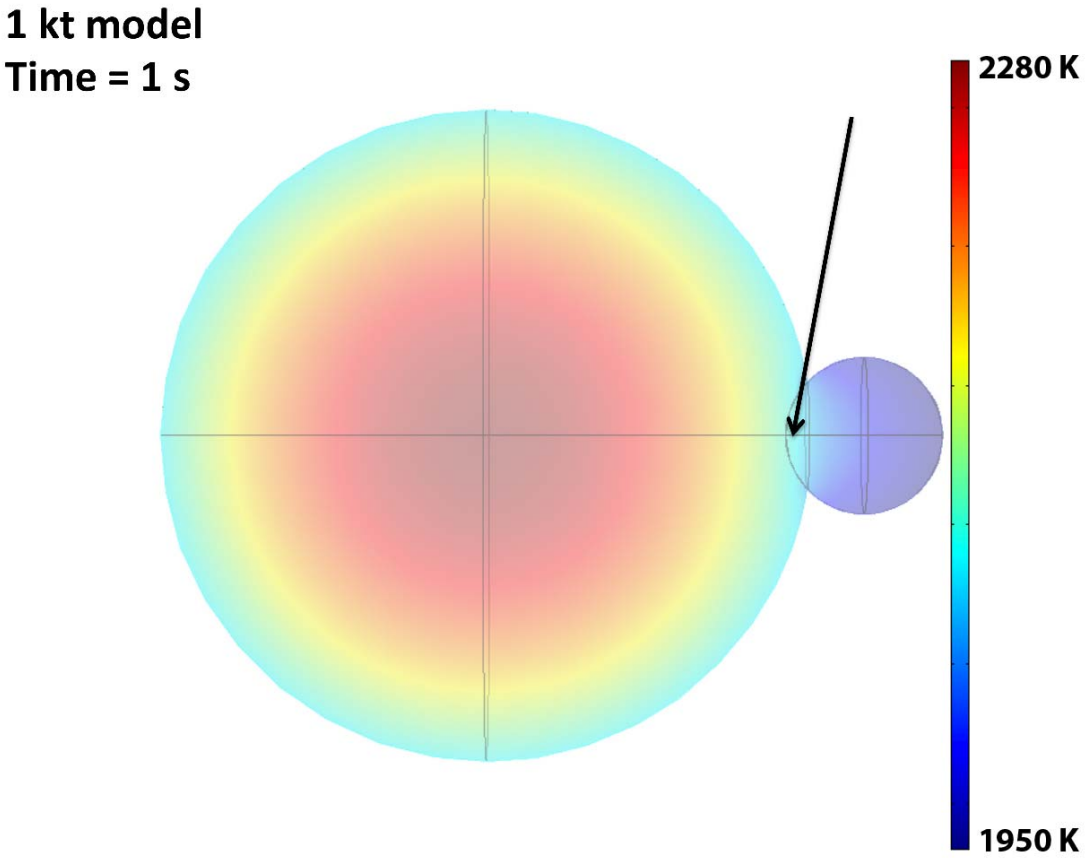

Figure 5.6: Temperature profile of the 3-D fallout mockup acquired by finite element analysis after 1.0 s of cooling in a 1 kt fireball from 2500 K. This model incorporates conductive and radiative thermal transport with the external environment and within the object. The black arrow indicates the interface point, where the cooling rate equation of the interface was determined for the yield series.

Most critical to this study, however, was the temperature change at the interface over time, which controls the rate of mass transport from the interface into either object. In order to understand the effect (if any) the thermal gradient had on mass transport as species diffused from the interface, the temperature difference at each time step was acquired across the interface (over ∼5 microns, consistent with the width of the interfaces, *e.g.,* Figure 5.2). In Figure 5.7, the thermal gradient is shown across the interface at $t = 1.0$ seconds (as shown in Figure 5.6). As seen from this image, the temperature difference over 5 microns is less than 5 degrees K, which has a negligible effect on the rate of diffusion from the interface. At

any time step for an assumed yield from 0.1-10 kt, the temperature gradient did not exceed 10 degrees K. Thus, the cooling rate at the instantaneous interface point was used as the estimated cooling rate over the entire interface region.

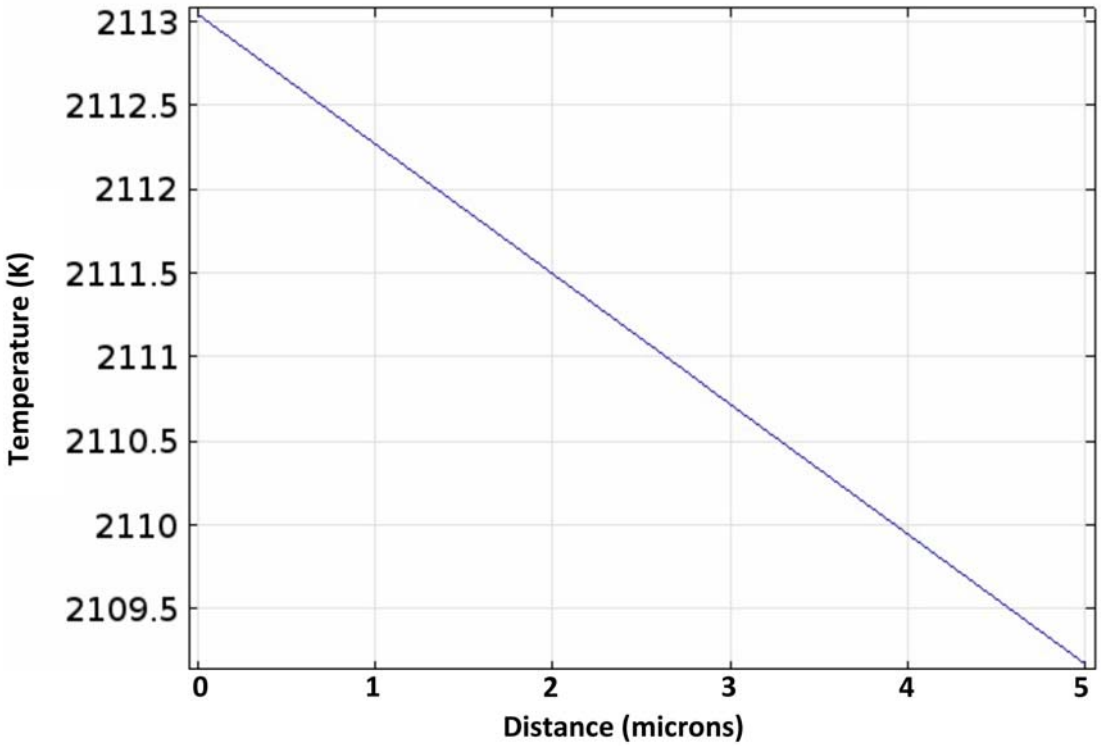

Figure 5.7: The temperature gradient across the modeled interface over 5 microns. The temperature gradient is negligible (<5 degrees K) across the interface after 1.0 seconds in a 1 kt fireball cooling from 2500 K.

The cooling curves at the interface point were acquired for the yield series 0.1 kt, 1 kt, and 10 kt from 2500 K to 1500 K, generated as described above. As described above, these curves were generated from a series of 0.1 s time steps and are reported over the time-scale necessary to reach 1500 K. Using non-linear least squares regression fitting of each point in the time series, the cooling rates for each yield were most accurately approximated as simple exponential functions. This is shown in Figure 5.8, where the temperature at the interface is shown over 2500 K to 1500 K for the 10 kt yield for each 0.1 s time step. The black line represents the exponential fit function (Equation 5.44).

For 0.1 kt, the interface cooling rate (in degrees K) was expressed as

$$T(t) = 1289 + 1242e^{-0.67t}\,, \tag{5.42}$$

for 1 kt, the interface cooling rate was expressed as

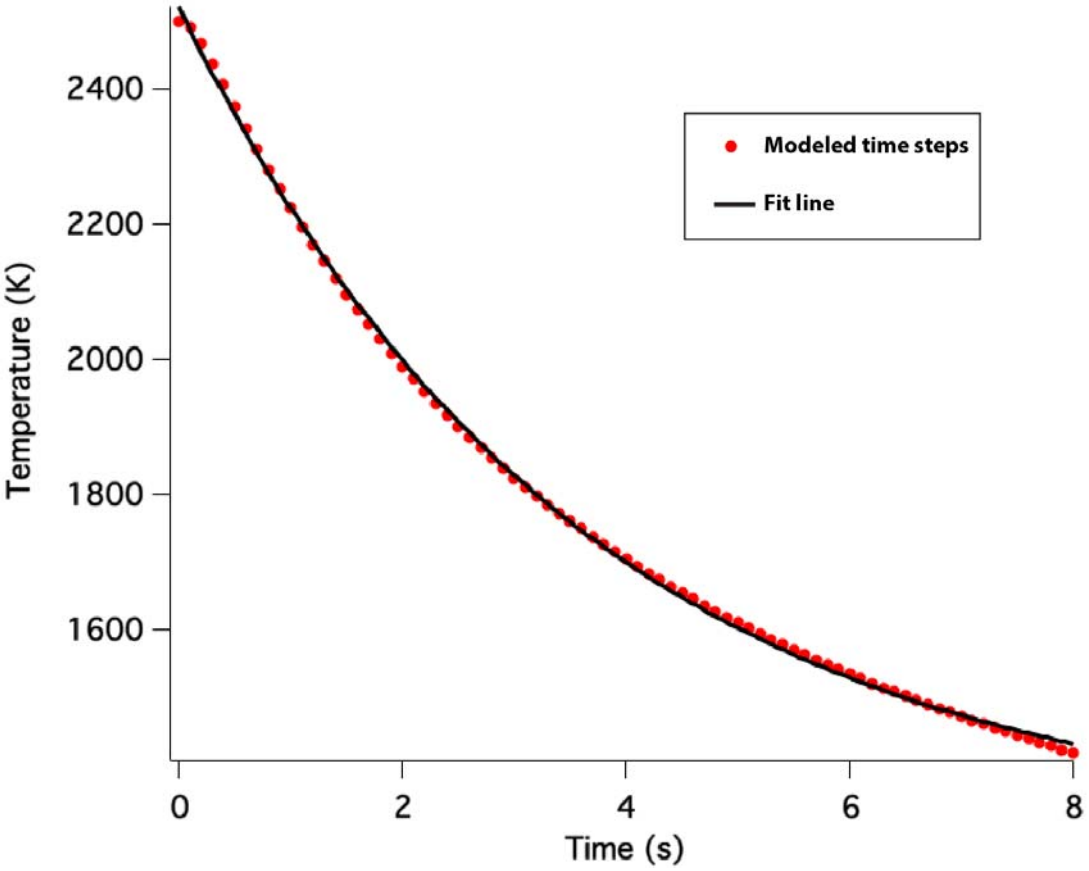

Figure 5.8: The temperature at the modeled interface from 2500 K to 1500 K for 10 kt fireball cooling rate environment (Equation 5.44) for each 0.1 s time-step. Mass transport would effectively stop (<1500 K) after approximately 8 seconds.

$$T(t) = 1306 + 1226e^{-0.46t}\,, \tag{5.43}$$

and for 10 kt, the interface cooling rate was expressed as

$$T(t) = 1300 + 1222e^{-0.28t}\,. \tag{5.44}$$

These cooling equations are presented in Figure 5.9, showing the cooling rate for each yield in the series. As expected, lower yield fireball environments corresponded to steeper temperature decreases, and higher yield fireball environments corresponded to a more gradual temperature decline at the interface.

The cooling rates represented by these curves and equations were incorporated into Equation 5.31 as $T(t)$ for each yield in the series for the purposes of deriving time and temperature parameters of mass transport from measured diffusion profiles at agglomerate interfaces.

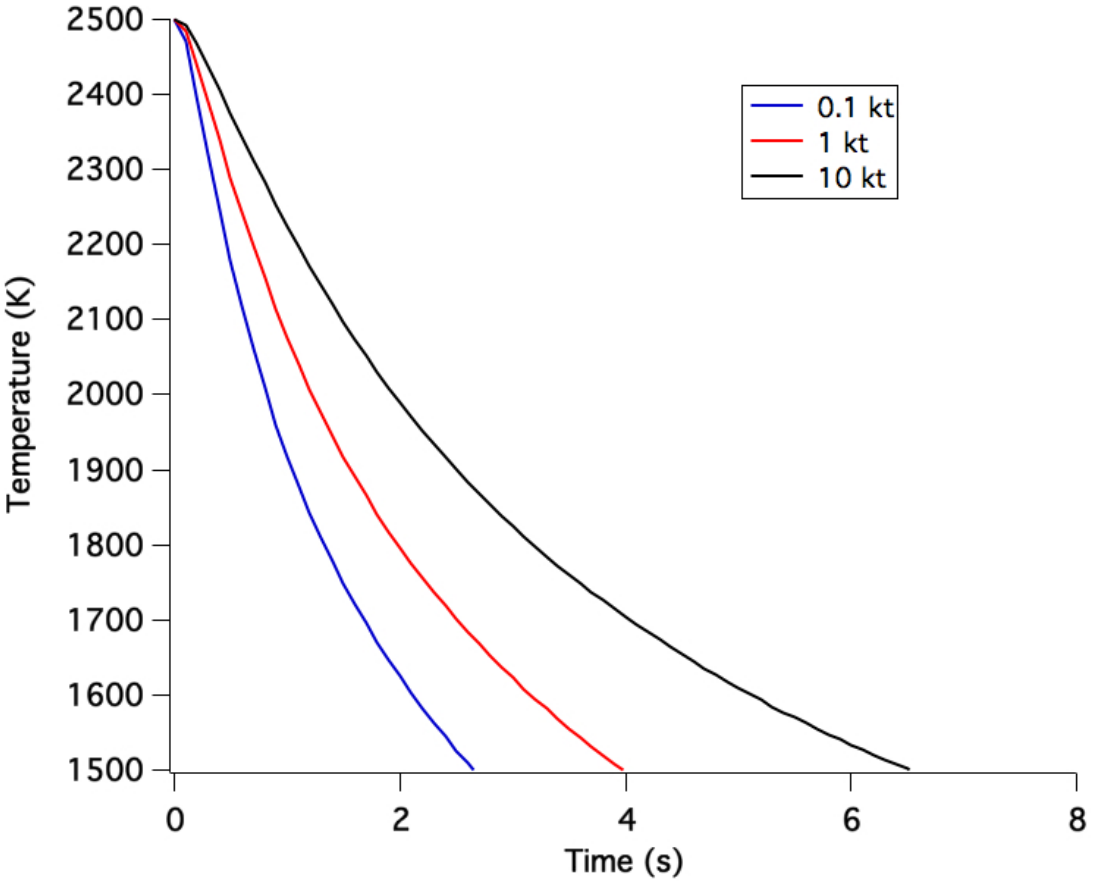

Figure 5.9: The cooling curves at the modeled interface from 2500 K to 1500 K for 0.1 kt, 1 kt, and 10 kt fireball cooling rates derived from Equation 5.38 from 2500 K. Equation 5.42 is shown by the blue line, Equation 5.43 is shown by the red line, and Equation 5.44 is shown by the black line.

Without knowing the time of deposition along a given cooling curve, the interval over which mass transport occurred, as defined in Equation 5.31, cannot be bounded. Instead, by combining 5.31, 5.35, and any of 5.42-5.44, an expression that defines mass transport over any given interval along the cooling curves of 5.42-5.44 can be constructed:

$$\frac{\sigma^2}{2} = D_{avg}t = \int_{t_1}^{t_2} D_{0U} e^{-\frac{E_{aU}}{RT(t)}} dt\,, \tag{5.45}$$

where D_{0U} is the pre-exponential diffusivity of uranium ($10^{1.09\pm0.15} cm^2/s$), and E_{aU} is the activation energy of uranium ($363.8 \pm 24.0 kJ/mol$) in molten rhyolite [93].

By setting a pre-defined maximum time (t_2) as the time at which the interface reaches 1500 K (and mass transport effectively stops), we can solve for t_1, or the time of deposition along the cooling curve for a given yield in the series. This is illustrated in Figure 5.10 for

the 1 kt yield environment. As shown in the figure, t_2 is defined for the given cooling curve to be the time at which the interface is at 1500 K, approximately 4 seconds. By knowing the rate of mass transport of a species, in this case uranium as defined by Equation 5.35, and the σ values for uranium from experimental measurements as defined by Equation 5.28, the time of deposition t_1 can be approximated for along the cooling curve of a given yield for each applicable interface.

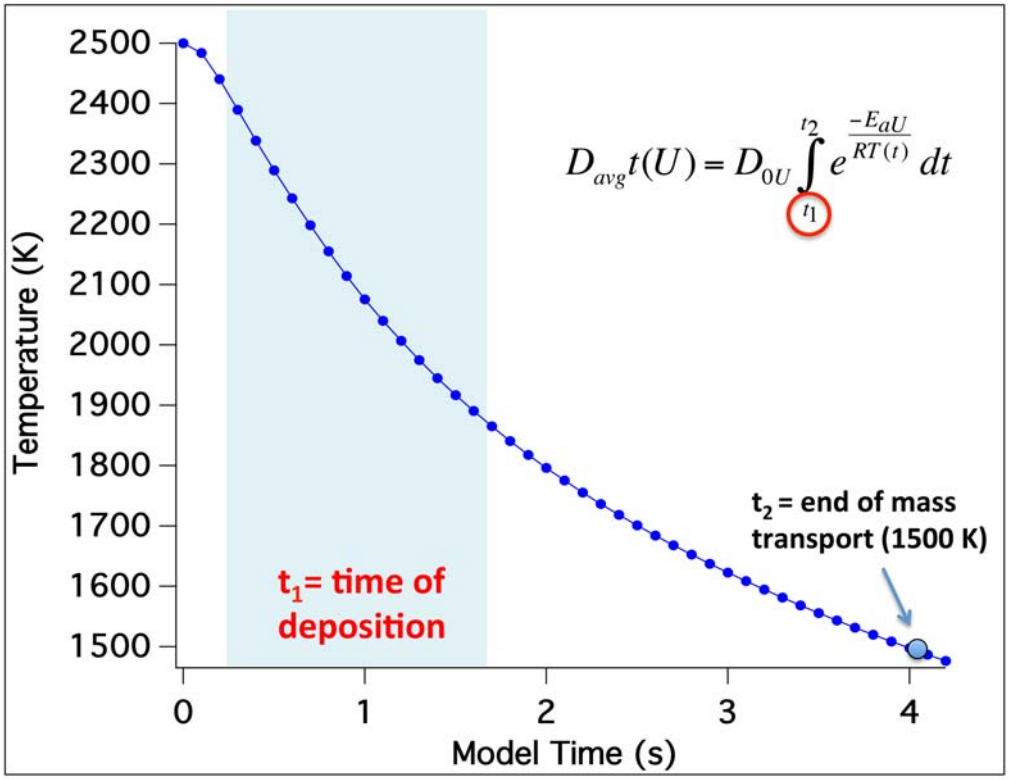

Figure 5.10: In order to bound the time of deposition (t_1) along a cooling curve, we can solve Equation 5.45, if the time mass transport effectively stops, the diffusivity of a given species, and the extent of diffusion of a given species from the interface is known.

5.3 Results

Gaussian fits of the $^{235}U/^{30}Si$ ratio data at interfaces B1, C1, and D2

While enrichments of $^{235}U/^{30}Si$ ratio were observed at nearly every interface, the pattern of variation was not always simply fit with Equation 5.25. Often, there was substantial skewing of the profile (Figure 4.19), sharp increases of $^{235}U/^{30}Si$ ratio on either side of the interface

(Figures 4.17 and 4.20), or unclear patterns of variation (Figures 4.14 and 4.16). Thus, only samples illustrating distinct Gaussian peaks of $^{235}U/^{30}Si$ ratio at the interface were ideal for applying this model.

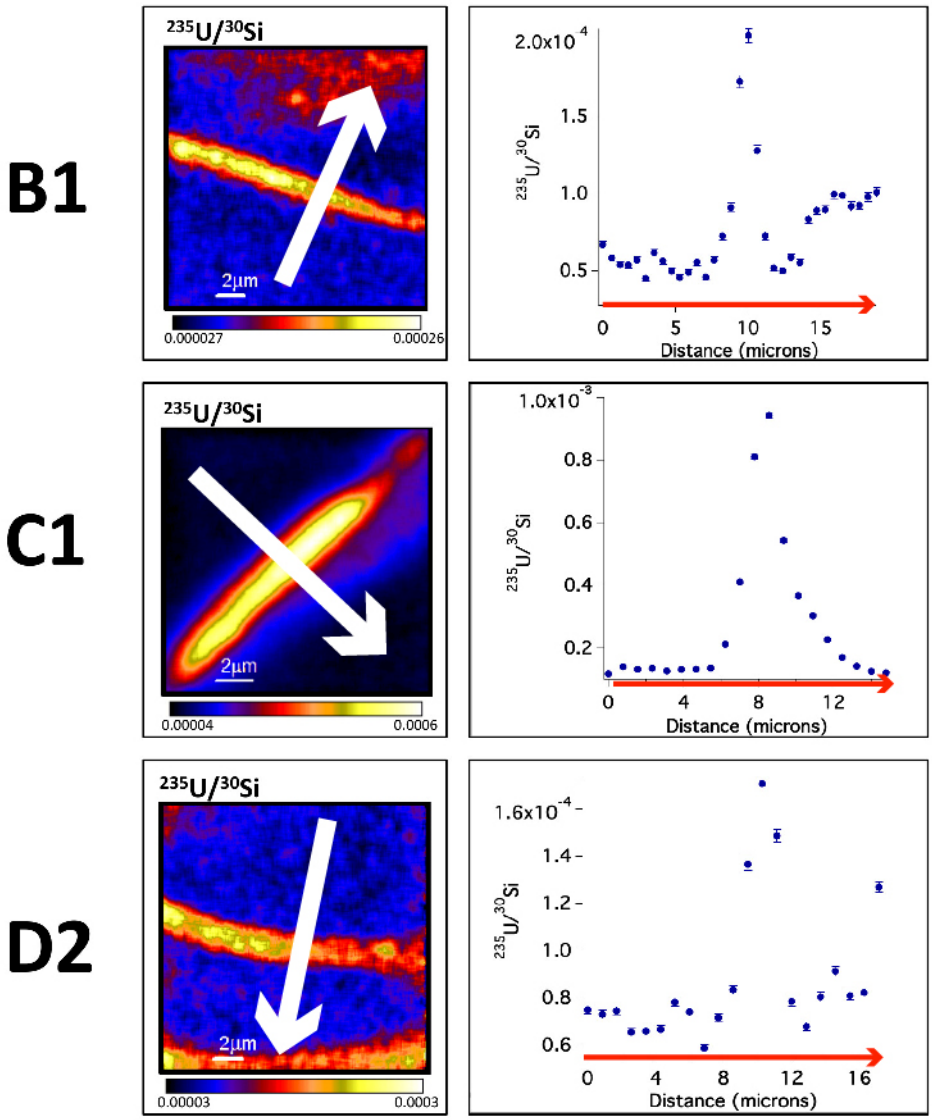

Figure 5.11: NanoSIMS ion images and isotope ratio variation profiles across the interface for $^{235}U/^{30}Si$ for samples B1, C1, and D2 (see Figures 4.15, 4.18, 4.22). The isotope ratio profiles for these interfaces were the ones best fit with the modified Gaussian distribution of Equation 5.46 out of the sample set, with minimal variation on either side of the interface.

Interfaces of B1, C1, and D2 were selected to study mass transport given the minimal variation found on either side of these interfaces (Figure 5.11). At Interface B1, there is an

Table 5.2: $D_{avg}t$ values from fits of B1, C1, and D2 $^{235}U/^{30}Si$ ratio using Equation 5.46.

Sample ID	$D_{avg}t(\mu m^2)$
B1	0.33 ± 0.03
C1	0.40 ± 0.06
D2	0.44 ± 0.10

approximately symmetric peak, with a slight increase in the $^{235}U/^{30}Si$ ratio towards the top of the image. At Interface C1, there is a slight skewing across the interface, but was found to be approximately Gaussian. At Interface D2, there is a symmetrical peak at the interface, with a sharp increase in the $^{235}U/^{30}Si$ ratio towards the bottom of the image. The aberrant points in both B1 and D2, however, were sufficiently far from the interface so that they did not interfere with the Gaussian fit.

The $^{235}U/^{30}Si$ ratio data acquired from NanoSIMS ion imaging (see Section 4.2) was fit in IGOR Pro software using non-linear least squares regression analysis with a modified version of Equation 5.25:

$$G = A + Bx + Cx^2 + \frac{D}{\sigma\sqrt{2\pi}} e^{-\frac{(x-\mu)^2}{2\sigma^2}}, \tag{5.46}$$

where the quadratic expression is added to allow for minor variation on either side of the interface and still acquire a Gaussian fit of the peak. The interface data for B1, C1, and D2 are shown with fit Equation 5.46 in Figures 5.12 - 5.14. The $D_{ave}t$ values are given in Table 5.2, as derived from Equation 5.28 and the acquired σ values of the fits.

As seen in Figures 5.12 - 5.14, the peak widths are all approximately the same for the three studied interfaces ($\sim$7 microns). The addition of the quadratic expression to Equation 5.25 visually appears to properly fit the variation on either side of the peak in B1, C1, and D2, without interfering with the peak width.

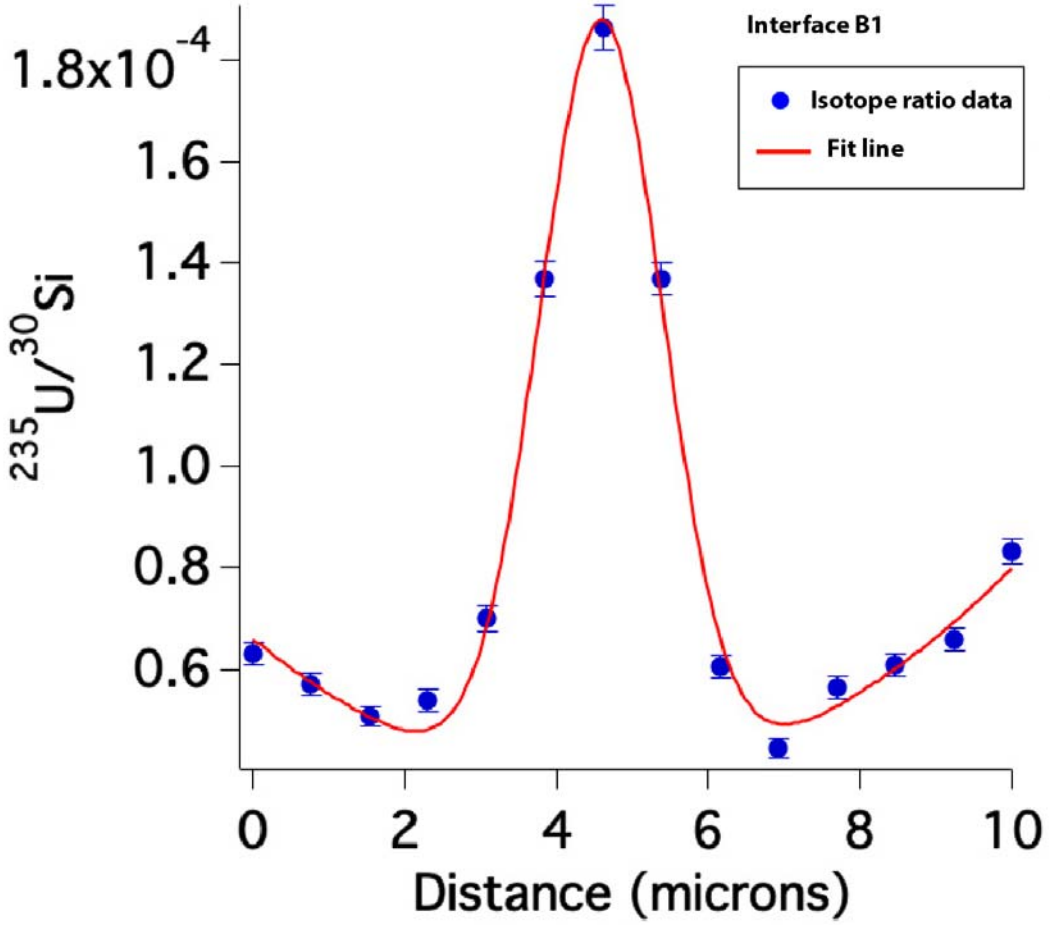

Figure 5.12: $^{235}U/^{30}Si$ Isotope ratio profile for sample B1 fit with Equation 5.46, $D_{avg}t = 0.33 \pm 0.03\ \mu m^2$). The fit intersects with every data point in the fit, and is within 1 σ of all but 2 of the data points.

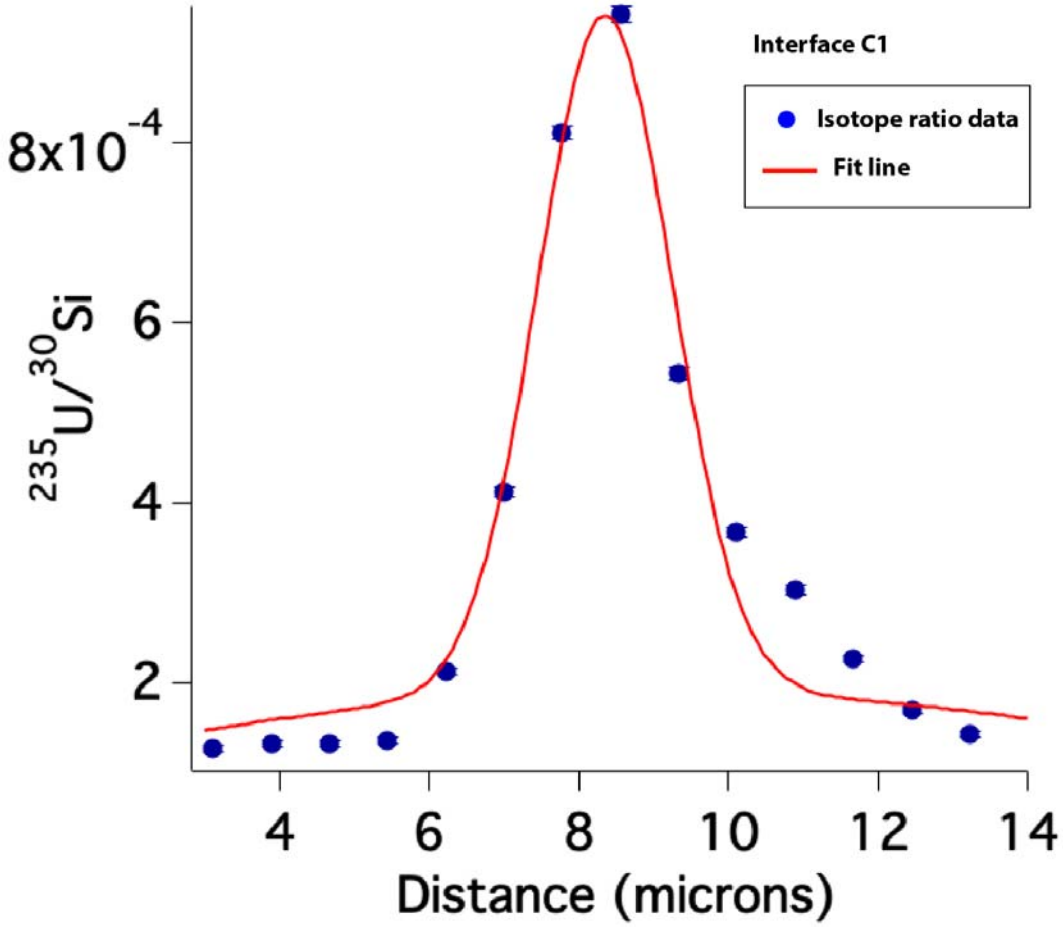

Figure 5.13: $^{235}U/^{30}Si$ Isotope ratio profile for sample C1 fit with Equation 5.46, $D_{avg}t = 0.40 \pm 0.06\ \mu m^2$). Despite the slight skewing of the data, 7 of the 10 peak data points are within 1 σ of the fit.

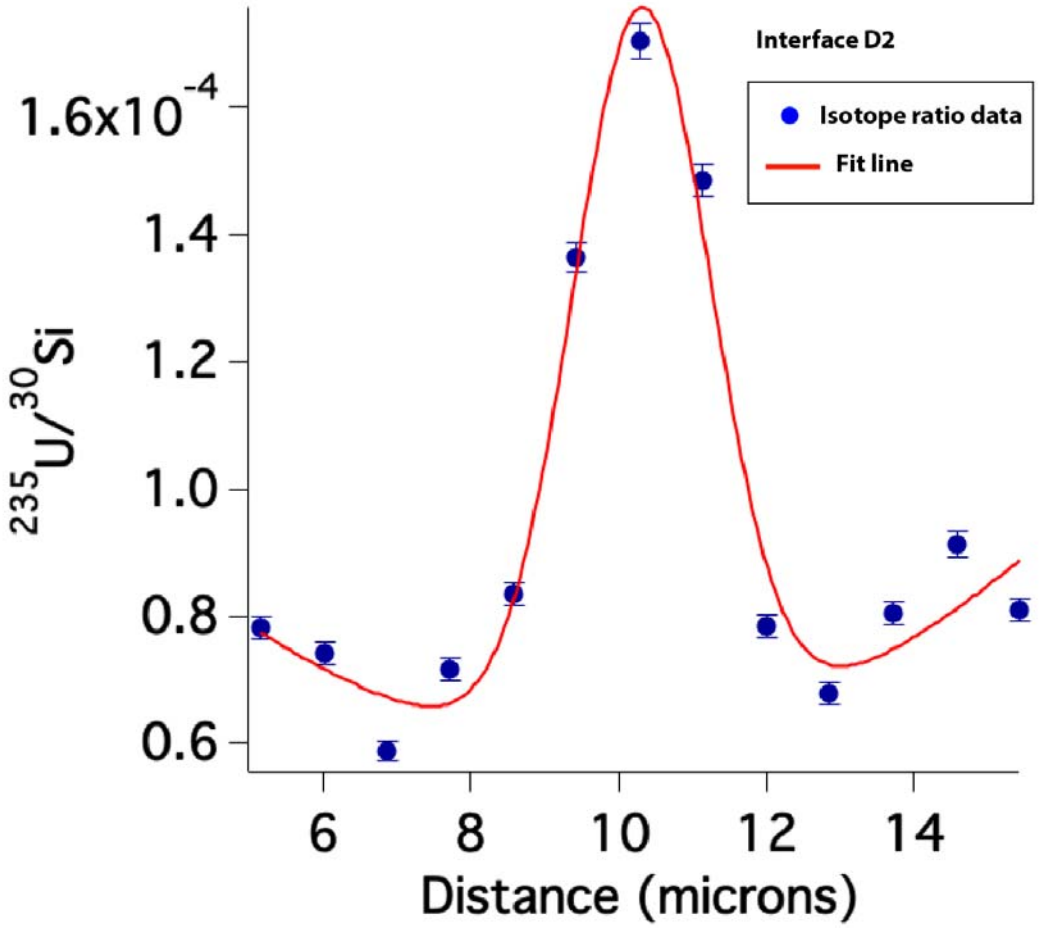

Figure 5.14: $^{235}U/^{30}Si$ Isotope ratio profile for sample D2 fit with Equation 5.46, $D_{avg}t = 0.44 \pm 0.10\ \mu m^2$). Despite the variation on either side of the peak, the fit intersects with 60% of the peak data points and provides a good approximation of the peak shape.

Probability distributions for the time of deposition

The $D_{avg}t$ parameters given in Table 5.2, in combination with Equation 5.45 and the cooling equations $T(t)$ for the interfaces at each yield, allow for the determination of the time of deposition t_1 along each given interface cooling curve for B1, C1, and D2. As Equation 5.45 cannot be solved analytically for t_1, and there are uncertainties on the values of D_{0U}, E_{aU}, and $D_{avg}t$, probability distributions of the time of deposition t_1 were solved numerically in MATLAB software.

A maximum value of t_2 of 3 seconds, 4 seconds, and 8 seconds were used for the 0.1, 1, and 10 kt interface cooling curves, respectively. These values were used to ensure that the temperature would have dropped to below 1500 K (as shown in Figure 5.9), ending diffusive mass transport. All of the parameters for Equation 5.45 that went into the MATLAB numerical determination of t_1 probability distributions are defined in Table 5.3. Thus, a total of 9 probability distributions for the value of t_1 were calculated (3 interfaces, 3 different yields).

Probability distributions were calculated by generating 1000 values at each of 100 predefined t_1 values for each cooling curve. Each of these 100 t_1 values are equal time steps between $t_1 = 0$ (where the interface temperature is 2500 K), and $t_1 = t_2$, thus effectively solving for t_1 within the range of possible values. At each time-step, the 1000 values represent the difference between the integral in Equation 5.45 and the $D_{avg}t$ value for a randomly selected value from normal distributions of D_{0U}, E_{aU}, and $D_{avg}t$ based on their given value and uncertainties. The probability at each time-step was determined based on the number of values out of the 1000 randomly generated values for each time-step produced a negative value for the following relationship:

Table 5.3: Parameters used in $D_{avg}t = \int_{t_1}^{t_2} D_{0U} e^{-\frac{E_{aU}}{RT(t)}} dt$ to solve for t_1 for each interface, at the corresponding cooling curve for each yield.

Sample ID	$D_{avg}t(\mu m^2)$	t_2 (seconds)
B1 - 0.1 kt	0.33 ± 0.03	3
B1 - 1 kt	0.33 ± 0.03	4
B1 - 10 kt	0.33 ± 0.03	8
C1 - 0.1 kt	0.40 ± 0.06	3
C1 - 1 kt	0.40 ± 0.06	4
C1 - 10 kt	0.40 ± 0.06	8
D2 - 0.1 kt	0.44 ± 0.10	3
D2 - 1 kt	0.44 ± 0.10	4
D2 - 10 kt	0.44 ± 0.10	8

*$D_{0U} = 10^{1.09 \pm 0.15} cm^2/s$

**$E_{aU} = 363.8 \pm 24.0$ kJ/mol

$$\int_{t_1}^{t_2} D_{0U} e^{-\frac{E_{aU}}{RT(t)}} dt - D_{avg} t = Z \,, \tag{5.47}$$

where, if Z was negative, the time of deposition t_1 did not correspond to a cooling interval sufficiently long enough to allow for mass transport of uranium from the interface that would produce the observed $D_{avg}t$ value. By calculating the probability for each time-step in this fashion, a probability distribution representing a complimentary error function was calculated for each interface-yield combination. This is illustrated in Figure 5.10, which shows the number of negative values of Z for each time-step for the B1 interface with the 1 kt cooling curve. The blue line is the complimentary error function fit of the generated dataset based on

$$a + b \cdot ErfC(\frac{\mu_{t1} - x}{|2 \cdot c|}) \,, \tag{5.48}$$

where a is the background value (approximately zero in this case), b is the magnitude of the function (approximately 500 in this case), μ_{t1} is the average value of t_1, and c is the width of the error function.

Given that

$$erf(x) = \frac{1}{\sqrt{\pi}} \int_{-x}^{x} e^{-t^2} dt \,, \tag{5.49}$$

we can derive a Gaussian probability distribution from Equations 5.25 and 5.48, where

$$c = \frac{\sigma_{t1}\sqrt{2}}{2} \,, \tag{5.50}$$

when σ_{t1} is the standard deviation of the probability distribution of t_1.

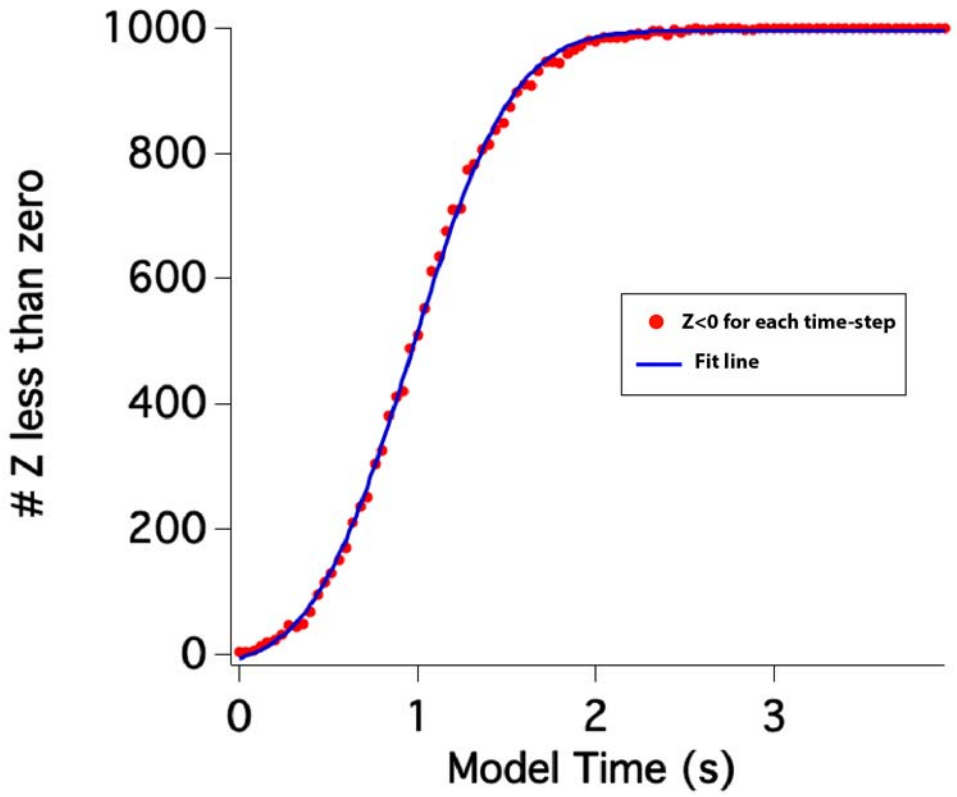

Figure 5.15: Illustrated here is the cumulative probability distribution function of deposition times for interface B1 in a 1 kt cooling environment. Number of $Z = negative$ values based on Equation 5.47 for each time-step (shown as red points) for the B1, 1kt model (Table 5.3). The blue line represents the error function fit of the dataset, which was used to derive uncertainties on the time of deposition (Table 5.4)

Time and temperature of deposition

Using Equation 5.48, μ_{t1} and σ_{t1} were determined for each of the interface-yield combinations (Table 5.4). Using these values, the temperature of deposition T_{dep} was determined for each interface-yield combination using Equations 5.42-5.44, the respective cooling curves for each yield. Note that only the values for t_1 have normally distributed uncertainties (σ = standard deviation). As the cooling curves are exponential functions, the uncertainties on T_{dep} simply represent the temperature interval that corresponds to 1σ uncertainty on t_1. As seen in Table 5.4, there is little variation between the time and temperature of deposition between the interfaces at each corresponding yield. There is substantial relative time variation between each yield in the series, however, ranging from about 0.5 seconds at 0.1 kt to about 1.65 seconds at 10 kt. From 0.1 kt to 10 kt, there is approximately 100 K difference in the temperature of deposition for each studied interface.

Table 5.4: Time and temperatures of deposition as modeled for B1, C1, and D2 at 0.1, 1, and 10 kt yield scenarios.

Sample ID	time of deposition t_1 (seconds)	T_{dep} (degrees K)
B1 - 0.1 kt	0.56 ± 0.27*	$2144\pm^{169}_{140}$
B1 - 1 kt	0.97 ± 0.43	$2093\pm^{171}_{141}$
B1 - 10 kt	1.75 ± 0.74	$2049\pm^{173}_{140}$
C1 - 0.1 kt	0.50 ± 0.30	$2179\pm^{197}_{161}$
C1 - 1 kt	0.87 ± 0.45	$2130\pm^{188}_{154}$
C1 - 10 kt	1.63 ± 0.75	$2075\pm^{181}_{147}$
D2 - 0.1 kt	0.49 ± 0.31	$2185\pm^{206}_{167}$
D2 - 1 kt	0.83 ± 0.47	$2145\pm^{201}_{162}$
D2 - 10 kt	1.59 ± 0.76	$2084\pm^{185}_{150}$

*uncertainties are 1σ

5.4 Implications of diffusive mass transport from agglomerated interfaces

$^{235}U/^{30}Si$ profiles at interfaces indicate different formation environments

Agglomerated aerodynamic fallout glasses preserve a record of the thermal histories experienced prior to quenching in the fireball. The patterns of $^{235}U/^{30}Si$ variation seen at the studied interfaces are indicative of a range of formation environments experienced by the objects. The most symmetrical profiles, as shown in Figure 5.11 indicate that, upon collision of the small droplet and large droplet in the fireball, the temperature difference between these two objects was negligible at their surfaces. In an environment where both objects were approximately the same temperature, species would not preferentially diffuse into either object from the interface, forming a more symmetrical profile. This suggests that in the sample with the most symmetrical profiles, the fallout droplets were in a similar temperature regime of the fireball prior to collision.

Interfaces B1, C1, and D2 (Figure 5.11) all have similar $D_{avg}t$ values (Table 5.2). As this parameter is directly related to the extent of diffusion from the interface, and they are similarly sized objects, it is likely that these objects also experienced similar formation environments (*i.e.,* fireball temperature regimes). However, as previously stated, Interface E1 (Figure 4.23) shows a much broader peak width ($\sim$12 microns, versus $\sim$7 microns for B1, C1, and D2). This width corresponds to either a longer duration in the same temperature regime as the other samples, or the droplets that formed Interface E1 experienced a higher temperature, creating a broader diffusion profile.

Substantial skewing of the profile in one direction is indicative of either a distinct com-

positional difference or a temperature difference. As the composition of these fallout objects are approximately the same, skewing in this case suggests a temperature difference between molten objects prior to collision. The most obvious example of this observed in the sample set is illustrated in Figure 4.19, which shows the $^{235}U/^{30}Si$ variation at the interface of Object C2. At this interface, the $^{235}U/^{30}Si$ profile is sharply skewed towards Sample C, indicating that diffusion occurred essentially unidirectionally from the interface. As discussed in Section 4.3, the sphericity and the relative compositional homogeneity of Object C2 itself is indicative of a relatively lower temperature when compared to the larger host object of Sample C. The evidence of preferential diffusive transport into Sample C bolsters this observation. Thus, it is clear that Object C2 had an opportunity to cool to a greater extent than the larger host. While the bulk temperature would be expected to be different in a cooling environment between the objects given the larger surface-to-volume ratio of the smaller object, the immediate surface temperatures of both objects would be expected to be similar prior to collision. Thus, the skewed $^{235}U/^{30}Si$ profile suggests that the the smaller object may have originated from a cooler temperature regime in the fireball itself.

Historical fallout formation theories, such as Miller's [15], model condensation and incorporation of radionuclides, as well as the subsequent fractionation of radionuclides, using fireball scaling equations. These models are reliant on average fireball temperatures, which can be determined from empirical light output observations, but do not address potential temperature gradients that exist within the fireball itself [1]. However, it is clear from this limited sample set that similarly sized fallout objects may experience a different time-temperature history based on composition profiles found at agglomerated interfaces. Thus, localized fireball temperature heterogeneity is likely to have an effect on the rate of incorporation of radionuclides and other vaporized species into carriers, particularly via the condensation-diffusion process.

Constraining the timescale of mass transport and temperature of deposition

The modeled time of deposition shown in Table 5.4 for the interface-yield combinations, compared to the modeled times that the interfaces reach 1500 K based on the yield-dependent fireball cooling rate (Figure 5.9), indicate a maximum time of mass transport of ∼2 seconds, ∼3 seconds, and ∼4.5 seconds for the 0.1 kt, 1 kt, and 10 kt yield models, respectively. These values are comparable to the time of surface closure of fallout as determined by Cassata et al. (2014) (<2.9 s, [54]). While neither the yield of the test for this study, nor the yield of the test in the Cassata et al. study are known to the author, the overlapping timeframes of mass transport strongly suggest that incorporation of fission products, unfissioned device materials, and other vaporized constituents into aerodynamic glassy fallout objects occurred over the course of a few seconds. As discussed in Chapter 4, the Cassata et al. study posits two possible scenarios explaining this rapid closure time: that either the location in the fireball where the fallout formed cooled to 1500 K within that timeframe, or that the

fallout glasses were ejected from the fireball and rapidly quenched within the given timeframe (<2.9 seconds) [54]. The cooling rate modeling for the yield series shown in Figure 5.9 is entirely consistent with average fireball temperatures reaching quenching temperatures within seconds of reaching the vaporization temperature of SiO_2 (2500 K).

As also shown in Table 5.4, the temperature of deposition derived from fireball modeling by yield for each interface of interest increases as the yield increases. This observation is not unexpected - the smaller yield fireball cools more quickly, thus in order to acquire the same diffusion profile as observed at larger modeled yields, the temperature would have to be higher. In this study, 0.1, 1, and 10 kt yields were modeled to not only observe the effect of varying fireball environments, but to constrain a maximum temperature of deposition. The lowest modeled yield, 0.1 kt, is on the lower end of US nuclear weapons test yields, as published by the US Department of Energy [101]. Thus, while the yield of the test from which these samples were acquired is unknown, it is unlikely that the temperature of deposition would greatly exceed the values reported for the 0.1 kt model for the studied interfaces from this test.

Even using 0.1 kt as a yield limit, the temperature of deposition did not substantially vary when the modeled yield was increased by two orders of magnitude. Specifically, for each of the modeled interfaces, the temperature of deposition only changed by ∼100 K between the 0.1 kt and 10 kt models, which is well within the uncertainty determined from the 1σ on the time of deposition (Table 5.4). For the three roughly symmetrical interfaces B1, C1, and D2, that were used as model inputs, the most likely maximum temperature of deposition is 2185 K. The temperatures of deposition for each interface at each yield are shown in Figure 5.16 and fit by linear least squares regression. According to the model (as illustrated in Figure 5.16) the temperature of deposition changes by ∼200 K over 5 orders of magnitude of modeled yield.

There are large uncertainties on the derived T_{dep} for each studied interface at each yield in the series. As shown in Figure 5.16, the 1σ uncertainties on each value exceed 140 K. While this model provides a ballpark estimate of the temperature at which condensation processes may be occurring for these species, constraining these uncertainties is critical to understanding the speciation of vaporized constituents, which can change depending on the temperature (further detailed in Chapter 6).

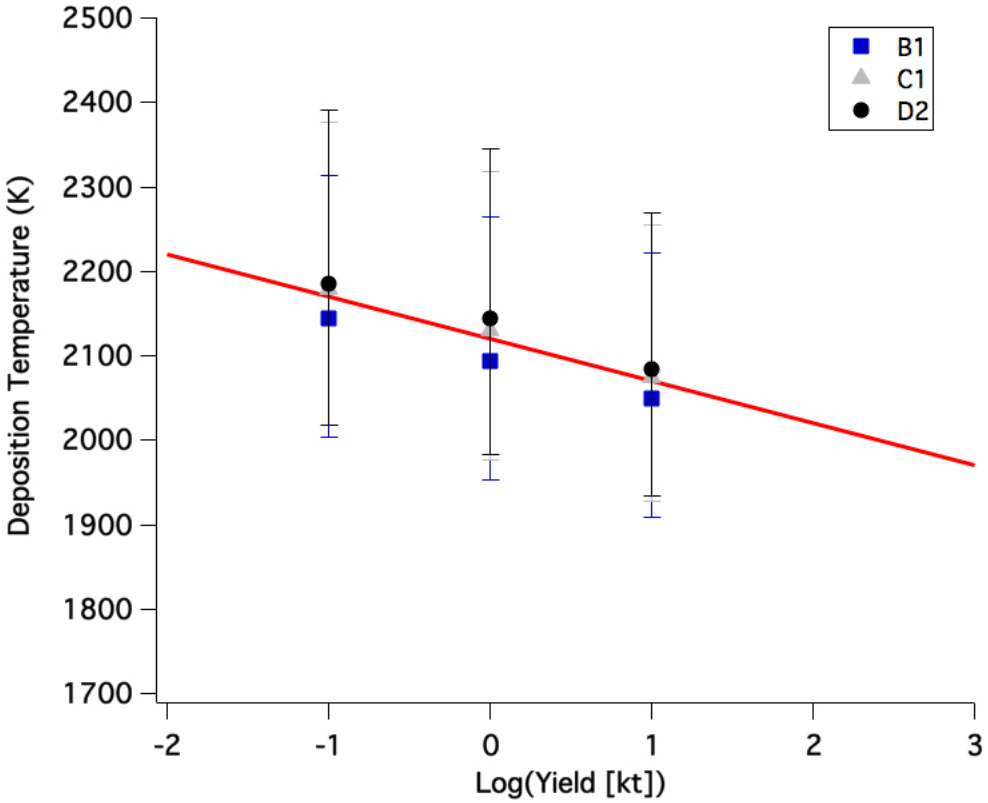

Figure 5.16: Temperature of deposition for each interface vs the log of the modeled yield, with 1σ uncertainties. The red line is a linear fit, from which the approximate temperature of deposition can be extrapolated for varying yields. While the fit line is applied to the data points only, the uncertainties in T_{dep} at each yield are systematic (*i.e.,* each is dependent on the uncertainties of the diffusivity parameters of uranium), thus the slope of the fit line would remain the same taking into account the uncertainties. As shown here, the estimated maximum deposition temperature is 2200 K, with uncertainties of roughly 200 K.

Temperature of deposition and the speciation of vaporized constituents

When considering deposition of species onto molten fallout objects from the perspective of condensation sequence of vapor phase constituents, the temperature regime under consideration based on the model output is roughly 2000 K to 2200 K over a broad range in yields (Figure 5.16). Fallout formation models dictate that refractory species will condense first and incorporate into molten carriers while volatile species will deposit onto the surface of already quenched carriers [15]. As shown in Chapter 4, the interfaces of agglomerated fallout objects reveal enrichments of some refractory species (*i.e.,* calcium, iron, and uranium) and depletion in others (*i.e.,* aluminum and titanium). Based on boiling point data, both FeO

and CaO, which were likely derived in large part from the soil (see Section 4.1), though may have had additional anthropogenic contributions (see Section 4.3) vaporize around 3000K, and are considered refractory [82, 83, 84, 85]. Uranium metal and UO_2 (from the device) are generally even more refractory, with boiling points of 4000 K and 3800 K, respectively [102]. As seen in Figure 5.17, the maximum calculated T_{dep} has a lower temperature than the boiling point of any of the species present at the interface, as well as certain species present in the soil that were found to be depleted at the interface (*i.e.,* Al_2O_3 and TiO_2). Thus, all of the rock forming species would be expected to condense out of the vapor phase based on boiling point data alone.

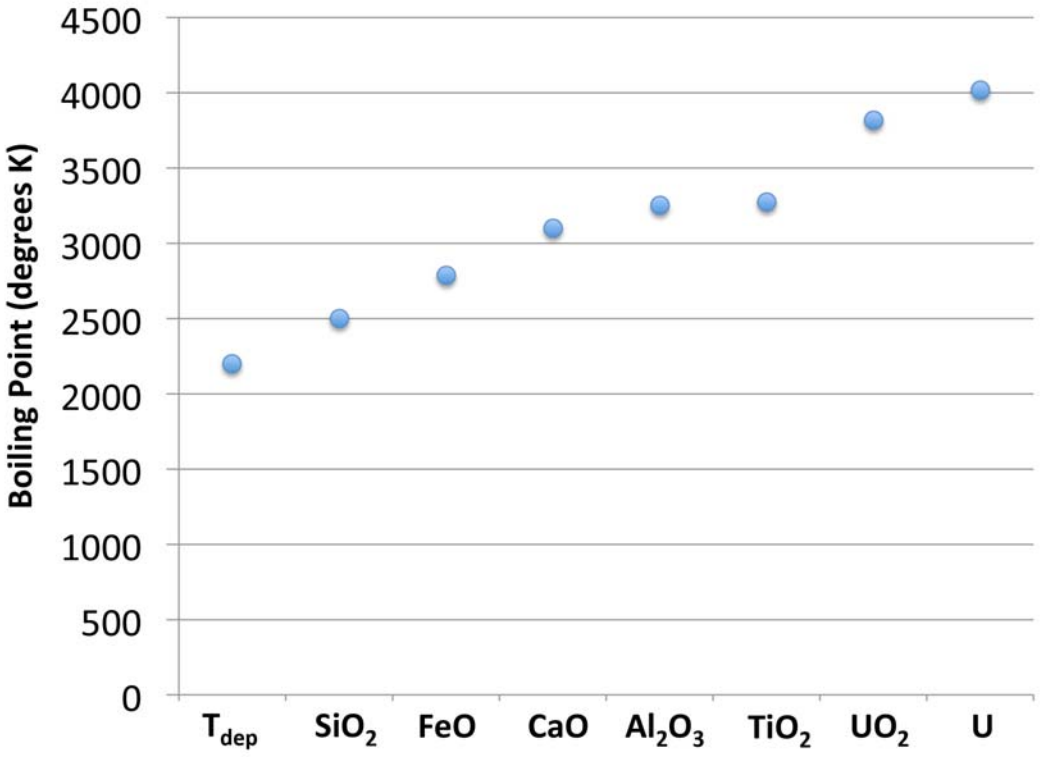

Figure 5.17: Boiling points of selected species of interest at the interface (section 4.1). Boiling point can serve as one potential metric of the relative volatility of these species relative to each other.

As already stated in Section 4.3, the boiling point may be a poor metric for the relative volatility of species in fireball environments with multiple vapor-phase constituents. The condensation behavior of each species, which is dictated by temperature-dependent vapor pressures, depends on the relative concentration of vaporized constituents as dictated by Raoult's law (Equation 1.1). The vapor pressure of the Al-species in atmospheric conditions is approximately two orders of magnitude lower than for the Ca-species at ~2200 K, and they are approximately the same in reducing conditions at that temperature ([87]). Given this

observation, and the fact that Al_2O_3 has a much higher concentration in soil compared to CaO (see Section 4.2), a higher concentration of Al_2O_3 in the vapor would be expected, and thus, a higher vapor pressure based on Raoult's law, if both of these species were derived from the soil. Therefore a source of Ca in addition to that found in the soil may have been present, such as a cement structure (Section 4.3), that dramatically increased the concentration of CaO in the vapor, and subsequently increase vapor pressure of CaO, relative to Al_2O_3, at ∼2200 K.

The co-location of Na_2O and CaO at most interfaces is also at odds with current understanding of relative volatilities of species. Assuming equilibrium conditions, at ∼2200 K, the vapor pressure of CaO is over 7 orders of magnitude lower than Na (the constituent with the highest vapor pressure of the Na-oxide species) in an oxygen-rich environment [103, 87]. In a reducing environment, the vapor pressure of Ca (the constituent with the highest vapor pressure in reducing environments) is 11 orders of magnitude lower than Na at ∼2200 K. Thus, in either environment, Ca-species and Na-species would be expected to experience considerable chemical fractionation, particularly given that Na_2O is more than 2 fold more abundant in the soil than CaO. However, in an oxygen-rich environment, the vapor pressure of Na approaches atmospheric pressure at around 2200 K [103]; this does not happen until temperatures cool to 1400 K in reducing conditions. Thus, co-location of Na- and Ca-species would be possible in an oxygen-rich environment (which the fireball is theorized to be during fallout formation [6, 15]), where there was substantial contribution of Ca to the vapor from an additional source undergoing continuous fractionation (as described in Section 4.3).

The assertion that sodium deposition is the result of an oxygenated fireball is in apparent contrast to what was shown by Cassata et al. (2014), where measurements of volumetric xenon isotope concentrations indicate that the fireball was in a reducing state [54]. However, as shown in the recent XANES study of melt glass from near-surface nuclear tests [94], the cooling rate of the fireball (and the carriers entrained in the fireball) can affect the final redox state of the glasses. Thus, the incorporation of xenon isotope precursors (the decay products of fission products) into the volume of molten fallout glasses may have occurred in an earlier, anoxic state, while the deposition layers observed in the agglomerated fallout objects in this study are likely the result of late stage addition in a more oxygenated fireball. This is the first definitive evidence of a transition from anoxic to oxidized conditions in a fireball.

Further, while Raoult's law, and studies such as those by Lamoreaux et al. (1984, 1987), can be used to estimate the vapor pressure and condensation behavior of individual species in a multi-component vapor, they are only accurate for ideal solutions. This interpretation is further complicated when taking into account the effect of oxidation on a multicomponent vapor, resultant condensates, and the multicomponent carrier materials in a high temperature environment. These effects are evident by the fact that uranium fractionation studies have observed both refractory and volatile behavior of uranium in post-detonation environments [20]. As illustrated above, the boiling point of both U and UO_2 are around 4000 K; as such both species are considered highly refractory. There are several potential species of gaseous uranium oxide that may exist, each having different thermochemical properties, including

but not limited to UO, UO_2, and UO_3 [104]. Further, the interaction of uranium with other constituents in a multicomponent vapor could form numerous other complex species, each with a distinct condensation behavior that could effect fractionation, and explain a temperature of deposition much lower than what is anticipated by the boiling points of uranium metal or UO_2. This complex behavior is not limited to uranium. In vaporization experiments comprising multiple oxides, such as those found in the soil (*e.g.,* CaO, MgO, Al_2O_3, TiO_2, and SiO_2), complex gaseous oxides such as CaAlO, $CaSiO_3$, MgAlO, AlSiO, and $CaTiO_3$ have been observed [105].

In summary, by constraining the temperature of deposition (∼2000-2200 K), there is evidence that the Ca, Fe, and ^{235}U species in these interface layers originated, at least in part, from anthropogenic sources. Further, the presence of Na_2O co-located with these species at some interfaces indicates that the fireball was likely oxygenated at the time and temperature of deposition. The co-location of Na_2O with Ca, Fe, and ^{235}U, along with the volumetric incorporation of at least ^{235}U as shown in previous studies [55, 56], show that these species underwent a continuous chemical fractionation process as these species condensed, and are suggestive of an oxygenated fireball during deposition. However, in order to more completely understand these processes and their effect on fallout formation, the speciation of the vaporized constituents under fireball conditions needs to be studied in-depth.

Chapter 6

Uranium diffusivity in rhyolitic melts

6.1 Background

Diffusion literature

While there is extensive literature on diffusion in molten silicate material of varying composition for numerous species [106], there is comparatively little on diffusive mass transport of uranium. The literature on mass transport of uranium in molten silicates has traditionally focused on geochemical study as well as fabrication and stability of nuclear waste vitrification glasses [107, 108, 109, 93]. Each of these studies addresses a specific scenario under which uranium diffuses, including a range of temperatures, concentrations, and melt compositions. For example, in one study addressing nuclear waste glass, the composition was a borosilicate material of approximately 60% SiO_2 and 17% B_2O_3 [109], while another study addressed diffusion in a haplobasaltic SiO_2-Al_2O_3-MgO-CaO composition (48%, 16%, 17%, and 19%, respectively) [108]. These studies show that the activation energy of uranium diffusion changes dramatically based on compositional changes: diffusion in the borosilicate composition had an activation energy of ∼300 kJ/mol, versus ∼214 kJ/mol in the haplobasaltic composition (representing a 40% increase in activation energy).

The most pertinent diffusion study to the model defined in Chapter 5 is by Mungall et al. (1997) [93]. In that study, the composition of the melt is very similar to that of the fallout glass in this study. Specifically, a U-doped and undoped haplogranitic melt glass was prepared as a mixture of 79.1% SiO_2, 12.1% Al_2O_3, 4.6% Na_2O, and 4.2% K_2O. The doped haplogranitic material had 0.1% U by weight. These materials were homogenized by heating at 1600 °C and stirring for several days. Diffusion couples were assembled by polishing cored sections of the resultant doped and undoped glass, and heating adjacent cored sections in both high pressure and atmospheric conditions. The high pressure experiments were conducted in a piston cylinder at pressures between 1.0 and 3.5 GPa, while the 1 atm experiments were conducted in a open platinum cylinder within a box furnace.

The pressure regime of interest to the modeling described in Chapter 5 is ∼1 atm - the approximate pressure of the fireball when the temperature is below 2500 K [1]. Thus, from

the Mungall et al. (1997) study, the 1 atm experimental data is of particular interest. The values of E_a and D_0 derived from these experiments were incorporated into the diffusion model (see Table 5.3). As shown in Section 5.4, however, the uncertainties on these values are large, with the uncertainties on E_a exceeding 6%, and the uncertainties on D_0 >40% [93]. In Figure 6.1, with these uncertainties incorporated into Equation 5.35, the 1σ uncertainty in the diffusivity at any given temperature spans roughly two orders of magnitude

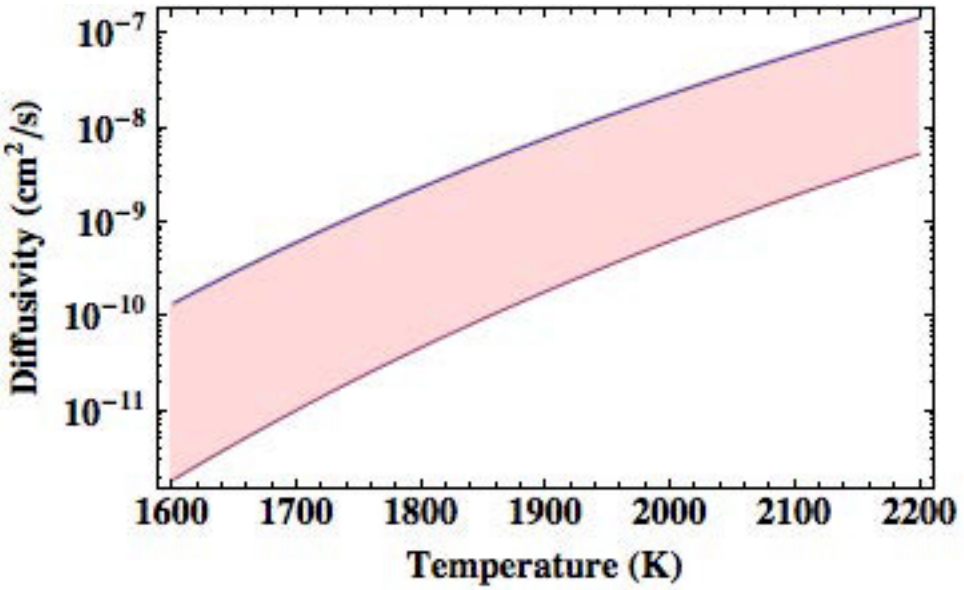

Figure 6.1: The 1σ uncertainty band of the temperature-dependent diffusivity (Equation 5.35) from the study of Mungall et al. (1997) spans two orders of magnitude at any given temperature.

In [93], the diffusivity was determined by diffusion couple experiments conducted at a series (1200 - 1600°C) of temperatures. In such experiments, the expected concentration distribution takes the functional form of an error function over time at constant temperature

$$C(x,t) = C_0 - \frac{\Delta C}{2} Erf(\frac{x}{\sqrt{(4Dt)}}), \tag{6.1}$$

where C_0 is the initial concentration, ΔC is the difference in concentration between the halves of the diffusion couple, D is the diffusivity at a constant temperature, and t is the time of diffusion. To derive the diffusivity from the resultant concentration profile, two approaches can be taken. The first approach uses non-linear least squares regression fitting using an equation of the form of Equation 6.1. The second method, elected by Mungall et al. (1997), is to transform the dataset into values of $Erf^{-1}(C)$ versus $x/\sqrt{2t}$, effectively linearizing Equation 6.1, allowing one to derive D from linear regression analysis [93]. In this manner, the diffusivity was acquired from the diffusion couple experiments at each temperature, and was used to derive E_a and D_0 from the Arrhenius equation, which can be rewritten as

$$Ln(D) = \frac{-E_a}{R} \cdot \frac{1}{T} + Ln(D_0) \tag{6.2}$$

from linear regression analysis, with $-E_a/R$ and $Ln(D_0)$ as fitting parameters.

Motivation to improve uranium diffusivity parameters

The data from Mungall et al. (1997) was sufficient to produce an approximation for the maximum temperature of deposition [93]; however, the uncertainties on the acquired T_{dep} were very large (>140 K) due to the aforementioned uncertainties on the 1 atm diffusion parameters. The uncertainties on these data are hypothesized to be controlled by two major contributing factors. The first factor, and likely the one most influencing the uncertainties, is the limited number of diffusion couple runs acquired at 1 atm. The second factor is the uncertainties on the acquired D values for each individual experiment. Regarding the first factor, there were only 4 runs reported under atmospheric conditions: one at 1200 °C, one at 1400 °C, and two at 1600 °C. Thus, only three temperatures over a 400 degree range were used to construct the Arrhenius plot from which E_a and D_0 were derived [93]. Regarding the second factor, the study reports uncertainties on each acquired diffusivity as 50% and 80% confidence intervals. Notably, even at the 50% confidence interval, there is up to 20% variability in the acquired value of the diffusivity at a given temperature (*ibid.*). This could be attributed to either the inverse error function data transformation cited above that was used by the authors in the study, or to the uncertainty based on the data acquisition method (*i.e.,* uncertainty derived from the analytical conditions of electron probe microanalysis).

By halving the literature uncertainty values, the precision on the temperature of deposition could be improved by ∼50%, as illustrated in Figure 6.2. This improvement has the potential to improve the understanding of speciation of vapor phase constituents in the fireball based on the temperature of deposition, as exemplified in Figure 6.3. Figure 6.3 shows the vapor pressure of gaseous aluminum species as a function of temperature, described in Section 4.3 [87]. As illustrated in the figure, the evaporation of Al_2O_3 favors Al in one temperature regime (<2200 K) and Al_2O in the higher temperature regime (>2200 K). Thus, if the temperature of deposition on the surface of agglomerated fallout objects is ∼2200 K with uncertainties in excess of 140 K, it is unclear which species would be favored in a condensation re-evaporation process based on this vapor pressure data. However, if the uncertainties were cut in half, the process would clearly favor Al_2O evaporation.

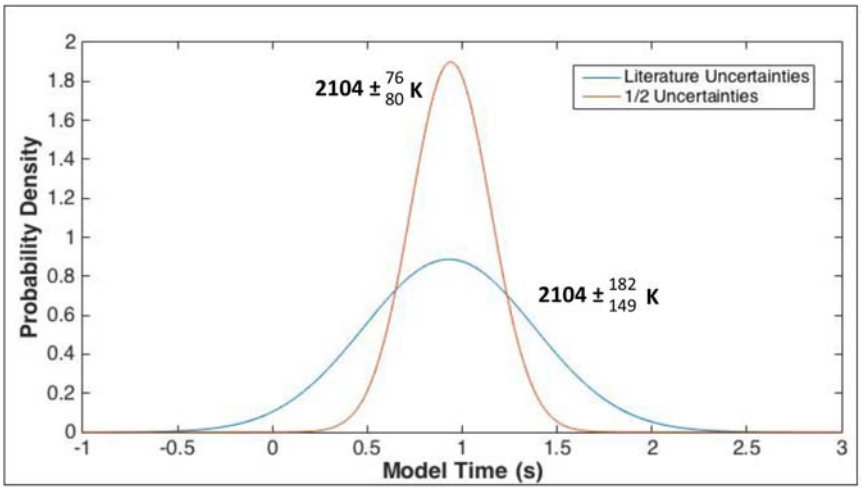

Figure 6.2: Probability distribution of the time of deposition for sample B1 in a 1 kt cooling environment based on the Mungall et al. (1997) values (Table 5.3) compared to a hypothesized distribution if these uncertainties were halved.

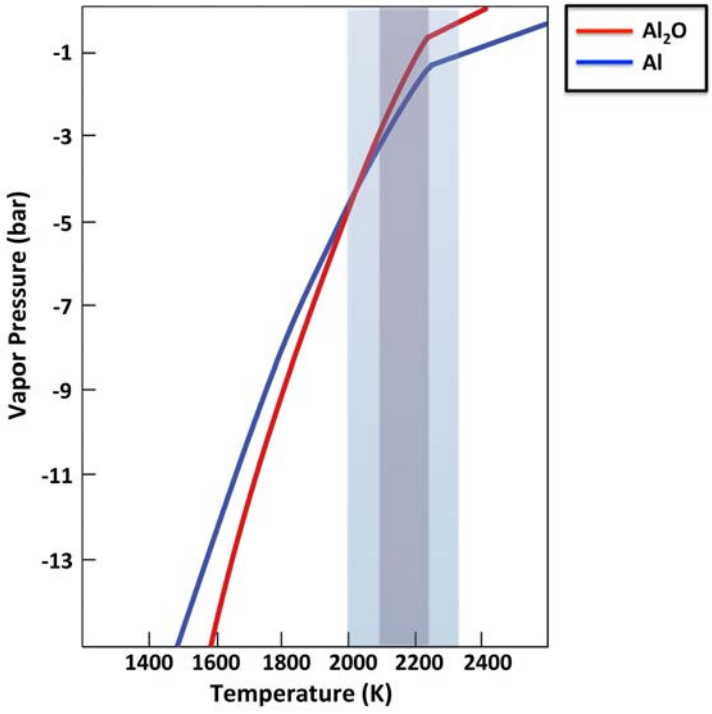

Figure 6.3: Vapor pressure of gaseous aluminum species Al vs. Al_2O over Al_2O_3 in vacuum, derived from Lamoreaux et al. (1987) [87]. The light shaded region is the maximum modeled T_{dep} uncertainty, while the dark region is T_{dep} with uncertainties, if halved.

By increasing the number of incremental temperature measurements in a series of diffusion couple experiments, a higher precision can be acquired for the diffusivity parameters for use in the model described in Chapter 5. Further, by using modern data acquisition techniques with non-linear least squares regression analysis, subsequent diffusion couple concentration profiles can yield diffusivities having lower uncertainties. Thus, in this chapter, a series of diffusion couple experiments are described, designed to improve the uncertainties on E_a and D_0 in order to further constrain the temperature of deposition acquired from the modeling described in Chapter 5. Additionally, preliminary results of high-pressure experiments (2 GPa) are presented, along with the derived E_a and D_0 from these experiments.

6.2 Experimental setup

In this study, Lake County obsidian (LCO), which is a rhyolitic volcanic glass, was used for diffusion couple experiments. This material closely matches the fallout glass composition for this study (see Table 6.1), and was used to create diffusion couples (see Figure 5.1) comprised of both uranium-doped and pure LCO. To produce uranium-doped LCO, the obsidian was ground in an agate mortar and pestle under ethanol, fused in air at 1450 °C, then reground for 60 minutes. Depleted uranium (<0.72% ^{235}U) was then added as a nitrate solution, reground in ethanol, and fused at 1450 °C. The resultant material was a homogeneous rhyolitic powder, and, in the case of the doped material, contained ∼1000 ppm of depleted uranium (sufficiently high concentration to be detectable by EPMA).

The diffusion couples were assembled in graphite cylinders, where equal masses of doped and undoped LCO were added sequentially, then compressed in the cylinder, forming the setup depicted in Figure 6.4. Before heating, the concentration profile across assemblies is a step-function (as shown to the right of the top illustration). After heating at constant pressure and temperature, the resultant diffusion profile in the diffusion couple is expected to follow an error function (Equation 6.1), as illustrated in Figure 6.4 (bottom illustration).

Table 6.1: Oxide composition (wt.%) of Lake County obsidian [66] versus fallout glass composition from this test [55].

Oxide	LCO	Fallout Glass
SiO_2	76.1	72.0-75.0
Al_2O_3	13.0	10.0-12.0
FeO	0.7	3.0
CaO	0.5	1.0-2.0
MgO	0.1	0.5
Na_2O	3.7	3.0-3.5
K_2O	4.8	4.0-5.0

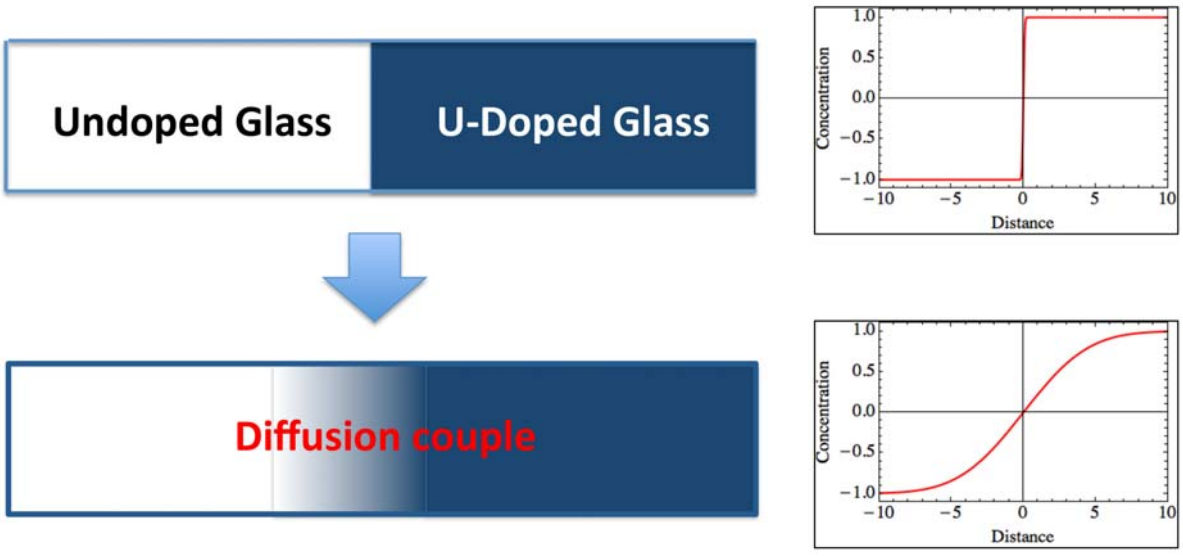

Figure 6.4: Diagram of diffusion couple experiments using U doped and undoped LCO, with the theorized form of the concentration profile before and after heating.

The graphite furnaces containing the LCO powder were contained within a larger assembly, as shown in Figure 6.5. The assembly was constructed of a combination of highly refractory ceramic parts, including MgO spacers to position the graphite chamber in the middle of the assembly to limit the effects of potential thermal gradients through the assembly during heating. The top MgO spacers have ∼1 mm diameter slots to accommodate the thermocouple wires (type S) used to monitor the temperature of the assembly. As this diffusion assembly is heated resistively, a graphite sleeve and base plug surrounds the assembly, contained within a plexiglass sleeve. The entire diffusion assembly was inserted into salt cells, which deform under high pressure such that the applied experimental pressure approaches equilibrium conditions. The cylindrical assembly was designed to be 0.5" (∼1.25 cm) in diameter.

A McNutt hydraulic piston press was used for the high pressure experiments. The piston press setup for the high pressure experiments is shown in Figure 6.6. The piston press assembly comprises a stack of steel spacing members supporting a large steel pressure vessel between the top of the chamber and the piston. A 0.5" steel piston adapter was used in conjunction with a hollow steel support bridge to compress the diffusion assembly to 2 GPa. A slotted steel plate was situated above the pressure vessel to accommodate the thermocouple wires for temperature modulation and monitoring. The diffusion assembly was resistively heated by applying a current through the assembly via terminals on the slotted steel plate and the bridge. Temperature ramping was set at 100 °C/min, at an input power of 18 W.

After compression and heating, assemblies were quenched via cold water circulation through the piston press setup (<60 s). The graphite furnace was extracted from the as-

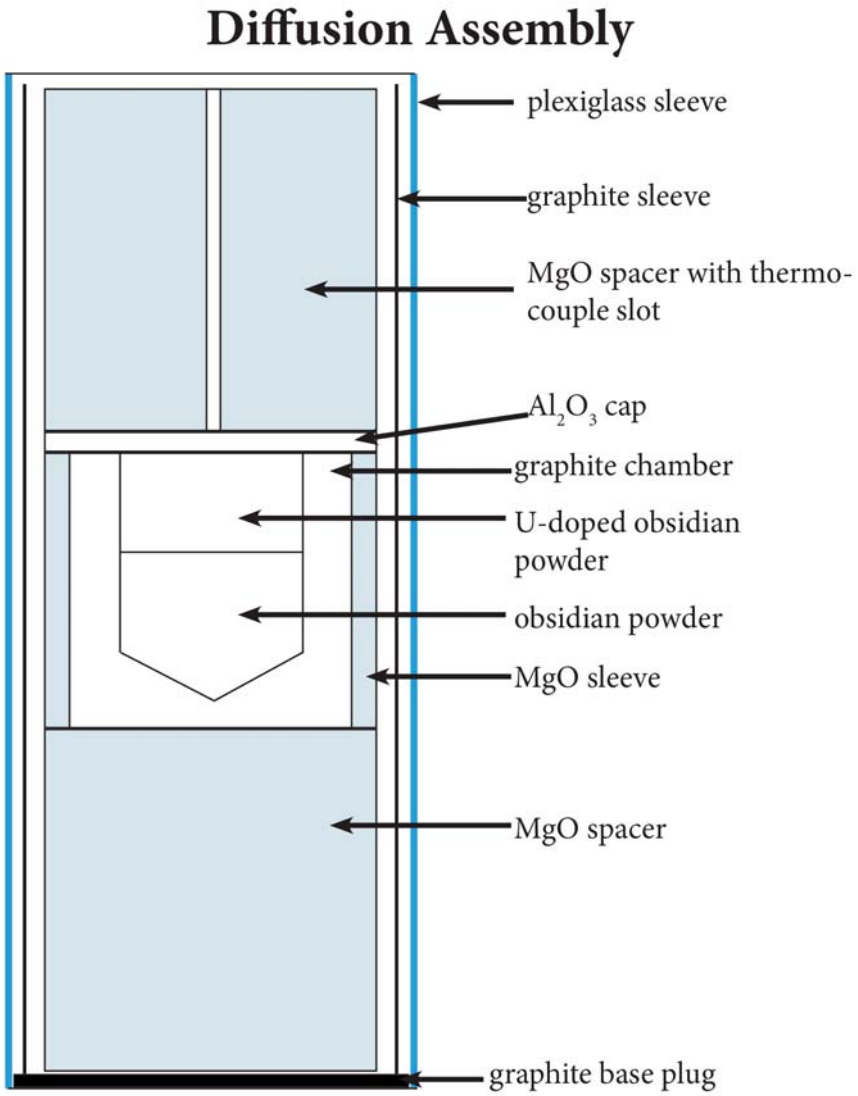

Figure 6.5: Schematic of the graphite furnace assembly containing the doped and undoped LCO.

sembly, and was bisected to expose the fused glass diffusion couple. The exposed glass was polished to 1 micron surface roughness and coated with a 5 nm layer of carbon for conductivity. Each couple was measured across its entire length for uranium concentration using electron probe microanalysis, as described in Chapter 2. The electron probe analyses were conducted with an accelerating voltage of 15 kV at a current of 10×10^{-8} A. The traverse across the length of the diffusion couple consisted of a series of 10 micron spots, spaced $\sim$10 microns apart. Uranium M_a x-rays were acquired on a PETH crystal for 60 seconds, acquiring a maximum count rate of >200 cps.

Table 6.2: Preliminary diffusion couple experiments conducted at 2 GPa

Run	Temperature (degrees K)	Time (s)
1	2023	14400
2	1923	28800
3	1823	86400
4	1723	100800

Four preliminary diffusion couple experiments were carried out at 2 GPa to assess the reproducibility of the experiments of Mungall et al. (1997) (see Table 6.2). These preliminary assemblies were approximately 2.5 mm in length, such that >100 EPMA spots would be acquired for each resultant glass diffusion couple (see Appendix D for full data set). The resultant glassy diffusion couples had obvious cracks and fractures within them (*e.g.,* Figure 6.7), as rapid quenching results in high internal sample stress. Electron probe analyses acquired on or near such fractures were ignored, and subtracted from the total length of the sample such that the diffusion length would not be obscured by count rate fluctuations caused by surface topography.

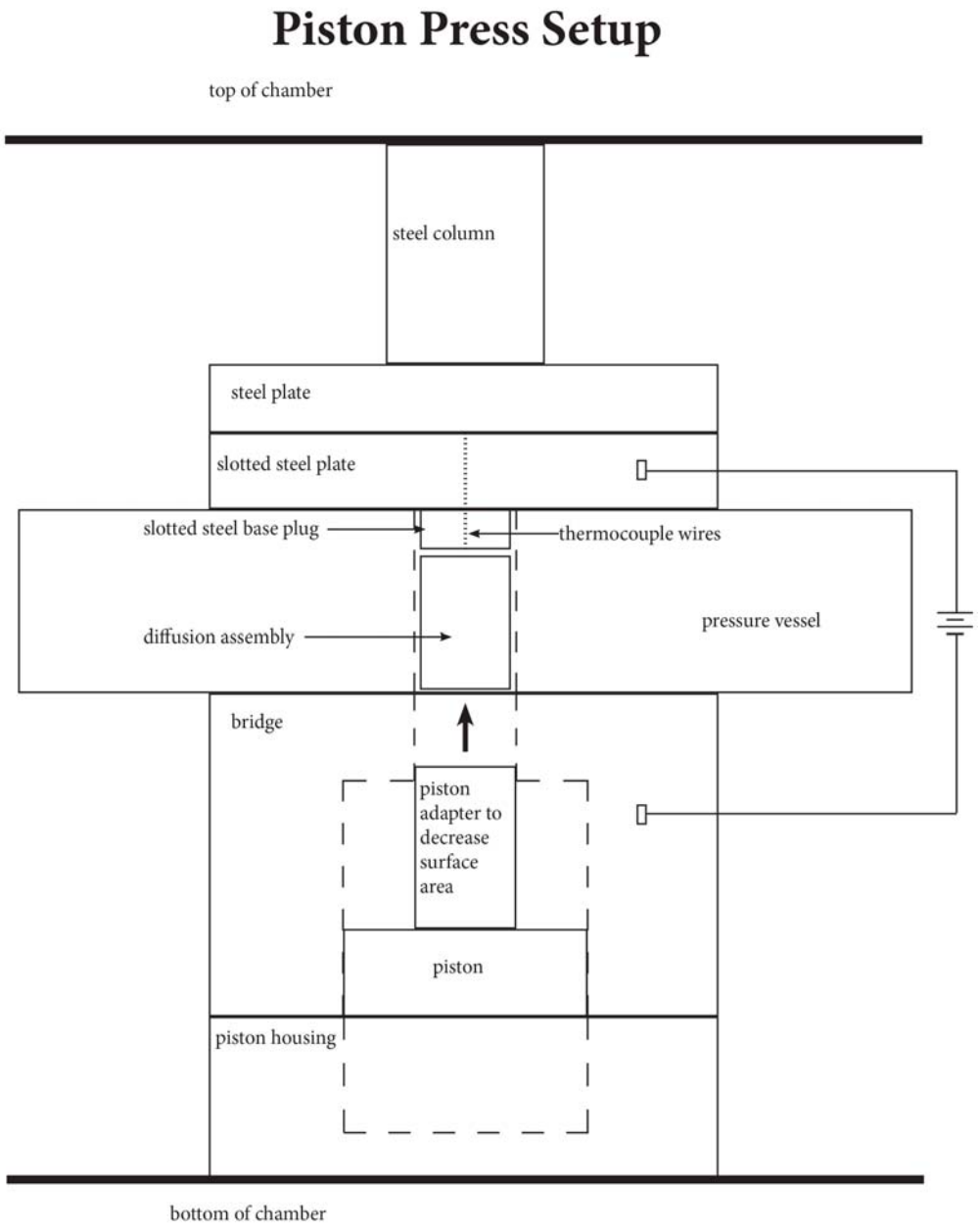

Figure 6.6: Schematic of the piston cylinder apparatus used for the diffusion couple experiments.

6.3 Initial results and discussion

Preliminary results were acquired as standardless analyses, and concentration is presented as raw counts of uranium x-rays. The concentration profiles across the measured diffusion couples were fit with non-linear least squares regression, using Equation 6.1 to derive a parameter $\sqrt{Dt}$, as shown in Figure 6.8. The measured variation in uranium concentration at either end of the diffusion couples was 4-8% for each of the measured diffusion couples in the preliminary dataset. However, the 1σ uncertainty on the diffusivity values acquired from the preliminary results illustrated in Figure 6.8 were generally around 10% (see Table 6.3).

When compared to the previously acquired literature values, the 1σ uncertainty on the diffusivity values acquired here were substantially lower (<10%) than the 50% confidence interval established in previous experiments under similar conditions (∼30% at 1.9 GPa; see Table 1 of [93]). While the Mungall et al. (1997) reference does not provide the dataset from which the diffusivity values were acquired, the improvement in the diffusivity value is either due to the fitting methodology and/or due to smaller analytical uncertainties.

The diffusivity values presented in Table 6.3 were used to construct an Arrhenius plot using Equation 6.2, where the Ln of the diffusivity values were plotted against the given inverse temperatures (in degrees K). The Arrhenius plot for the preliminary 2 GPa dataset is shown in Figure 6.9. The blue fit line is a linear least squares regression fit of the data from the 4 preliminary runs, weighted by the uncertainty on each diffusivity, which had an r^2 of 0.99. The linear regression fit parameters were E_a/R and $Ln(D_0)$; E_a was calculated to be 308 ± 10 kJ/mol, and $Ln(D_0)$ was 0.85 ± 0.66, respectively.

The uncertainty on the activation energy in this dataset was improved >2-fold over those in the study by Mungall et al. (1997). Specifically, the % uncertainty on E_a was 3%, versus 7% determined by Mungall et al. from their 1 atm experiments. While the same number of runs were used to calculate E_a in this study, they were spread over 4 different temperatures, rather than 3 in the Mungall et al. (1997) study. The value for $Ln(D_0)$ acquired by this preliminary dataset had much larger uncertainties than those reported in the literature: the uncertainty acquired by Mungall et al. was approximately 14%, compared to 78% as determined here. As the value with the most influence over the uncertainty on temperature-

Table 6.3: Diffusivity and 1σ uncertainty derived from preliminary diffusion couple experiments conducted at 2 GPa.

Run	Temperature (degrees K)	Diffusivity (cm^2/s)
1	2023	$(2.20 \pm 0.20) \times 10^{-8}$
2	1923	$(1.15 \pm 0.10) \times 10^{-8}$
3	1823	$(3.95 \pm 0.19) \times 10^{-9}$
4	1723	$(9.49 \pm 0.71) \times 10^{-10}$

dependent diffusivity is the activation energy, it is encouraging that the value determined by this preliminary dataset was substantially improved in comparison to that by Mungall et al. (1997). To determine if the uncertainties can be further improved upon, more runs at smaller temperature intervals are required.

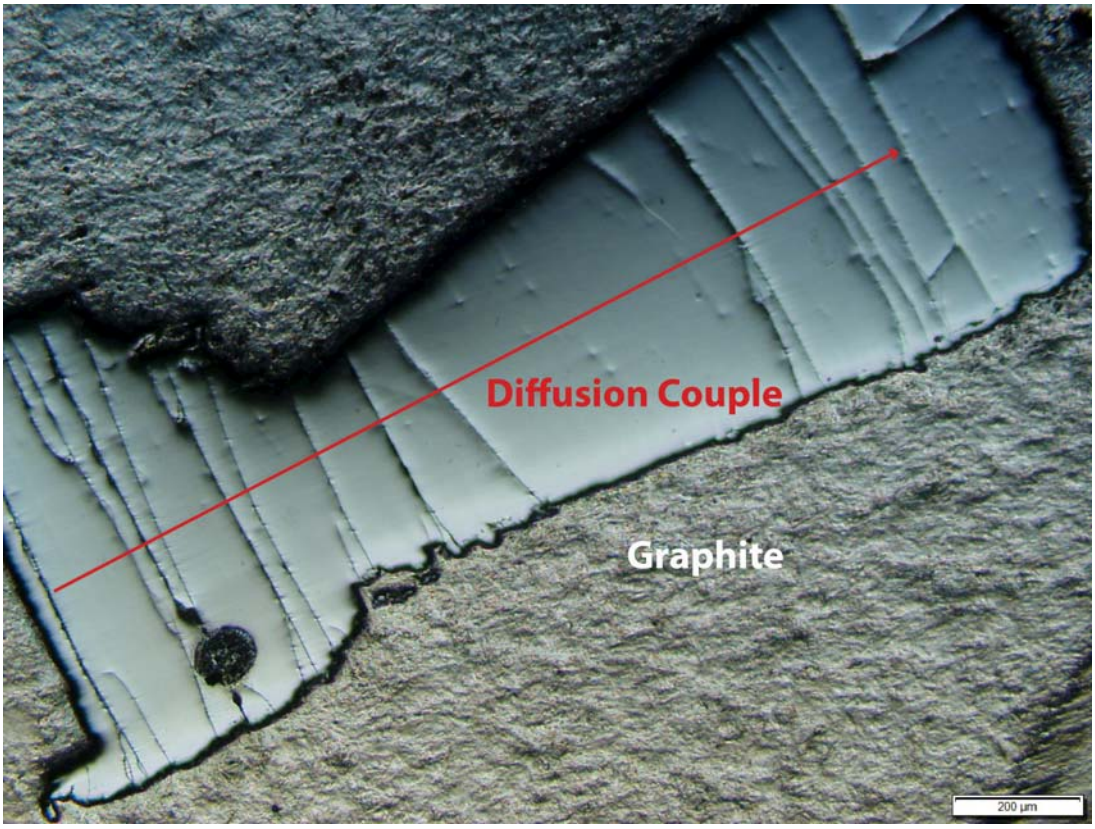

Figure 6.7: Optical image of a polished diffusion couple within the graphite furnace. The location of sequential EPMA spot analyses is indicated by the red arrow.

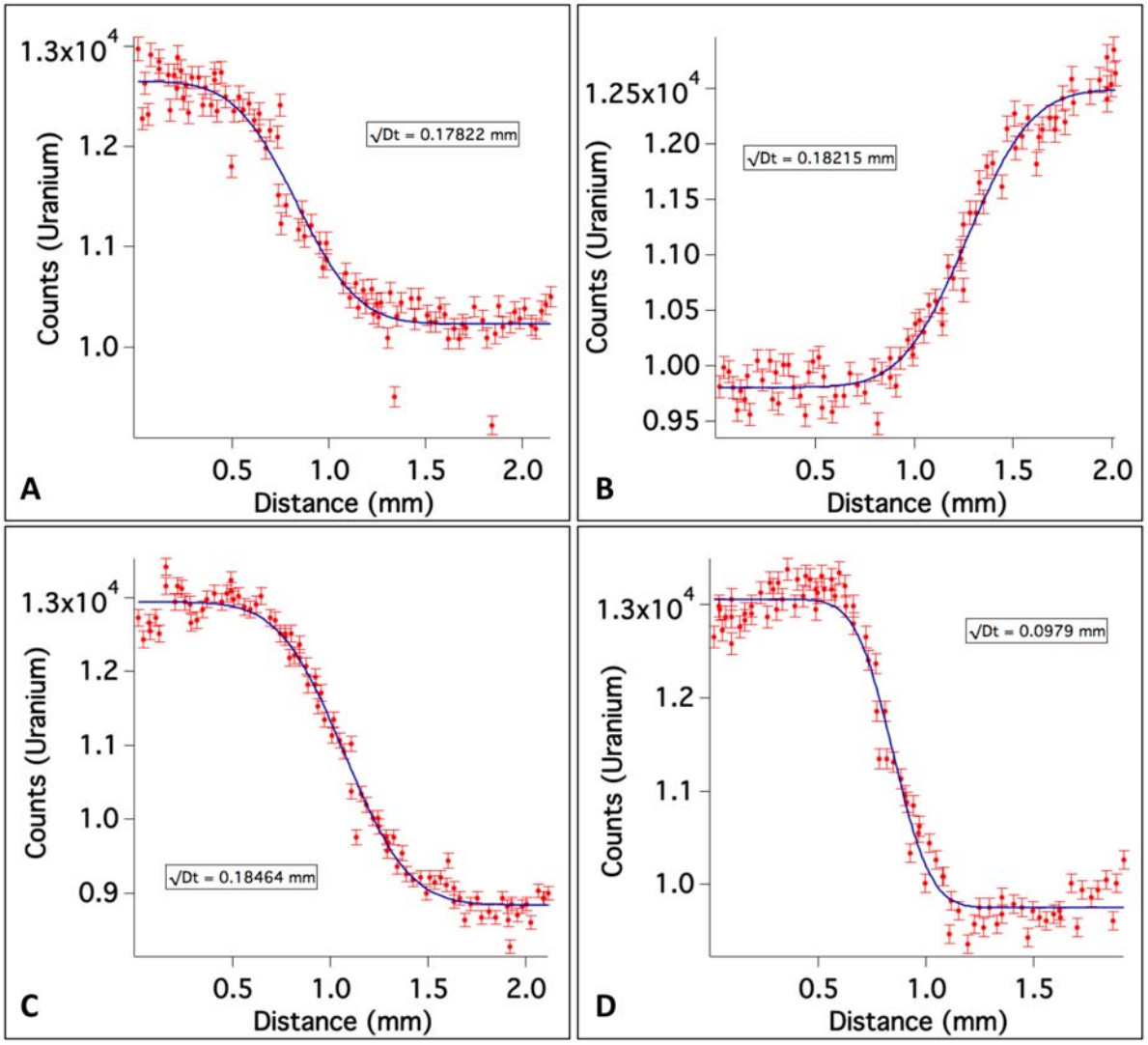

Figure 6.8: Uranium variation data from diffusion couples at 2 GPa for various times and temperatures: (a) 2023 K, 14400 s; (b) 1923 K, 28800 s; (c) 1823 K, 86400 s; (d) 1723 K, 100800 s. Each dataset was fit with Equation 7.1 to determine the $\sqrt{Dt}$ from which the diffusivity D was determined (Table 6.3.

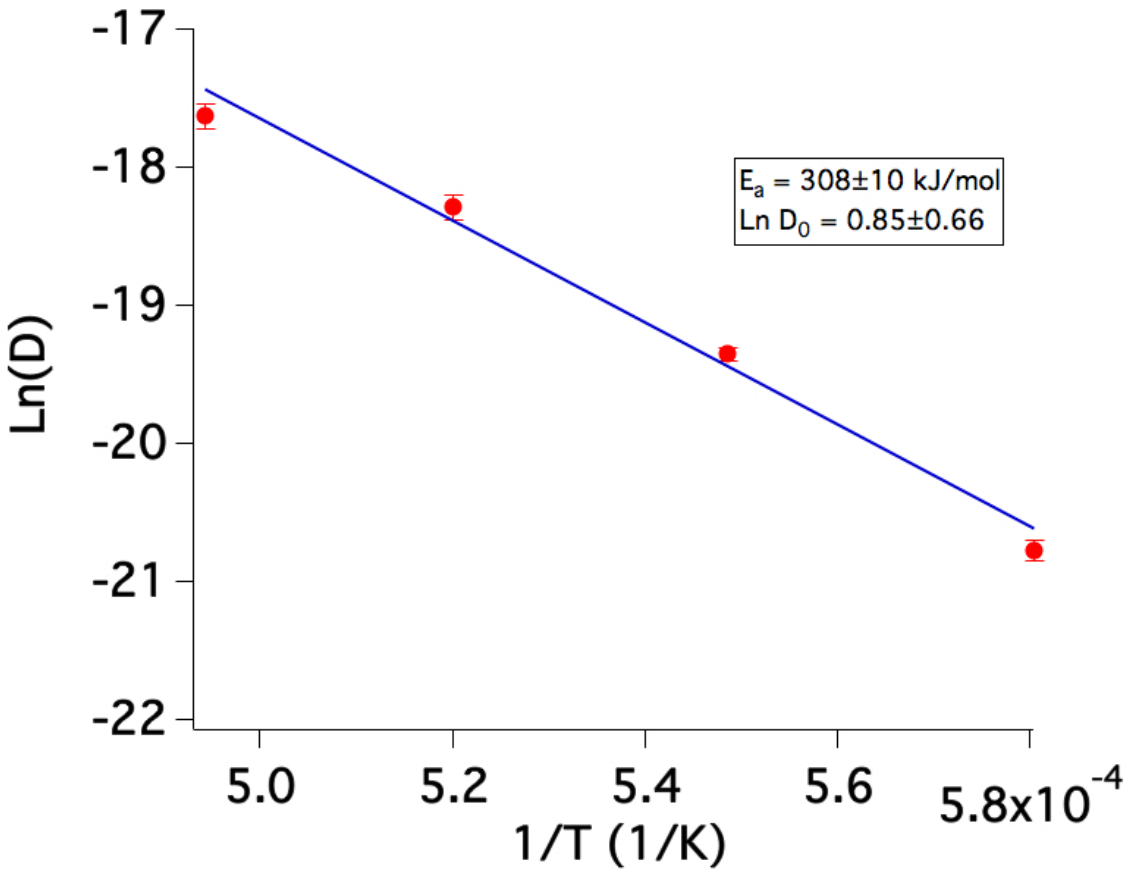

Figure 6.9: Arrhenius plot of the 2 GPa diffusivity data set. The activation energy and pre-exponential diffusivity was derived from the linear fit. Uncertainties are 1σ.

6.4 Planned diffusion experiments

While the preliminary results of 2 GPa diffusion couples illustrated the value of expanding upon the diffusion experiments designed by Mungall et al. (1997), further experimentation is needed to further limit the uncertainties on the temperature-dependent diffusivity, particularly in the ∼1 atm pressure regime, which is more in line with the theorized pressure in the fireball at the temperatures of interest (∼2000-2200 K), as described above.

New diffusion couple experiments are proposed to improve the E_a uncertainty and $Ln(D_0)$ determined at 2 GPa. The proposed diffusion couple experiments would include reproducing runs already taken at 1723, 1823, 1923, and 2023 K, and adding diffusion couple experiments in 50 K increments between them. I further propose to expand the temperature range down to 1523 K, as well as increase the range up to 2123 K if the required input power does not exceed the safety tolerance of the power supply (<24 W). By acquiring multiple diffusivity measurements at each temperature, for an increased and more continuous temperature range, it is anticipated that a much more precise value of the E_a can be determined.

To acquire the diffusivity parameters in the 1 atm pressure regime, two approaches may be considered for further diffusion couple experimentation. The first approach follows the method set forth by Mungall et al. (1997), where diffusion couples are assembled in open cylinders made of a material having high thermal conductivity and melting temperature (*e.g.,* platinum), and heated in a box furnace. While this approach was sufficient in the study of Mungall et al. (1997) to acquire diffusivity parameters, there are intrinsic uncertainties associated with this method. These uncertainties are associated primarily with the ramping time for the diffusion couples to reach the temperature of interest, and the cooling times associated with open-air cooling. As these values are not presented in the Mungall et al. (1997) study, a simple preliminary experiment will be performed to understand the ramping/cooling times, and to determine if they affect the subsequent diffusion length. The second approach is to acquire a full dataset over a range of pressures to establish a pressure-dependence for E_a and D_0. This approach has two primary disadvantages: 1) it will require a much more extensive dataset (*i.e.,* many more diffusion couple runs) to cover a range of pressures from which it would be possible to extrapolate the 1 atm diffusivity parameters; and 2) the diffusivity may have unexpected, non-Arrhenian behavior over differing pressure regimes, such that a pressure-dependence could not be established. However, studies have shown that under these melt conditions, Arrhenian behavior would be expected [93, 110]. Ideally, both approaches to understanding the 1 atm temperature-dependent diffusivity parameters and limiting their uncertainties will be taken for comparison. Thus, the ideal outcome of the proposed experiments is improved uncertainties on the temperature-dependent diffusivity parameters at 1 atm, as well as a pressure-dependent relationship determined from experiments over a range of pressures. The diffusion couple runs for these proposed experiments are outlined in Table 6.4.

Table 6.4: Proposed diffusion couple runs over a range of temperatures and pressures to further constrain the uncertainty in uranium diffusivity parameters.

Experiment	Temperature (degrees K)	Pressure (Pa)	Time (s)	# of runs
1	2023	0.1 MPa; 1, 2, 3 GPa	14400	2 at 2 GPa, 3 at each other pressure
2	1973	0.1 MPa; 1, 2, 3 GPa	14400	3 at each pressure
3	1923	0.1 MPa; 1, 2, 3 GPa	28800	2 at 2 GPa, 3 at each other pressure
4	1873	0.1 MPa; 1, 2, 3 GPa	28800	3 at each pressure
5	1823	0.1 MPa; 1, 2, 3 GPa	86400	2 at 2 GPa, 3 at each other pressure
6	1773	0.1 MPa; 1, 2, 3 GPa	86400	3 at each pressure
7	1723	0.1 MPa; 1, 2, 3 GPa	100800	2 at 2 GPa, 3 at each other pressure
8	1673	0.1 MPa; 1, 2, 3 GPa	100800	3 at each pressure
9	1623	0.1 MPa; 1, 2, 3 GPa	172800	3 at each pressure
10	1573	0.1 MPa; 1, 2, 3 GPa	172800	3 at each pressure
11	1523	0.1 MPa; 1, 2, 3 GPa	345600	3 at each pressure

Chapter 7

Conclusion

7.1 Summary and Conclusions

Understanding fallout formation is critical to fallout dispersion modeling and post-detonation sample analysis; however, the processes that control formation are not adequately understood. This dissertation explored the interdependent processes of vaporization, condensation, and diffusion in fallout through the study of a distinct compositional layer, identified in agglomerated fallout glass from a near-surface nuclear test. Specifically, the layer was identified at the interface of where smaller, spheroidal glassy objects fused to the surface of a larger piece of aerodynamic fallout glass, using modern analytical techniques. This interface layer was found to be continuous around the surface of the smaller attached objects, and was used to probe the composition of a suspected deposition layer of condensed material, originating as vaporized constituents within the fireball.

The composition of the interface layer revealed enrichments and depletions of major elements relative to the interior composition of the glassy objects. Relative enrichments of Fe and Ca were distinctly observed at every interface that was analyzed, while enrichments of Na were apparent but not ubiquitous. Depletions of Al and Ti were also noted at every interface that was measured, relative to the interior composition. The enrichments and depletions of each of these measured major elements were found to be approximately co-located (within 1.5 microns). Trace element analysis by NanoSIMS also revealed relative chemical enrichment of uranium (as $^{235}U/^{30}Si$ ratio) in 7 of the 9 measured interfaces. This pattern of enrichment and depletion was unexpected from the perspective of fractionation as dictated by historical fallout models, which anticipate refractory species to condense first and incorporate into molten carriers, while more volatile species condense later onto the surfaces of already frozen carriers. As Al_2O_3 and CaO have very similar volatilization behaviors in silicates, and are generally much more refractory than Na_2O according to vapor pressure studies, these observations are at odds with what was expected.

To further understand this unusual behavior, an estimate of time and temperature of mass transport was derived from the concentration profiles of uranium at the interface, which was

consistent with diffusion from a planar source. By modeling uranium diffusion using the cooling rates of fireballs of varying yields, a maximum temperature at which this layer was deposited was found to be roughly 2200 K. According to vapor pressure studies of pure Na_2O, Na-species in oxidizing conditions may begin condensing around this temperature, while reducing conditions would require much lower temperatures ($\sim$1400 K). Thus, the presence of Na-species on the surfaces of agglomerated fallout objects at this temperature is suggestive of an oxygen-rich fireball.

This temperature is substantially lower than the boiling points of the refractory species of interest (Al, Ca, Fe, and U, which were all assumed to be in oxide form). As the vapor pressure of Al-species and Ca-species are both negligible at 2200 K, condensation would be expected to occur at a much higher temperature. Further, the vapor pressures of Al-species are generally higher than Ca-species (both negligible at 2200 K), and fractionation between Al- and Ca-species would not be expected at this temperature. Two possibilities are proposed to explain this discrepancy. The first possibility is that unknown anthropogenic sources contributed additional Ca to the vapor-phase. As Ca is co-located with Fe and U, which likely originated as vaporized device material, it is possible that a source adjacent to the device, such as a concrete support structure, may have contributed excess Ca to the vapor-phase. This material, would not only increase the vapor pressure of Ca-species, but potentially dilute any remaining Al-species in the vapor phase, and subsequently extending the duration over which Ca-species could condense as the fireball cooled. Given the refractory nature of CaO, it is likely that this was a continuous process over the cooling period. The second possibility is that the condensation and re-evaporation process of vaporized material and carrier material is dictated by the speciation of these constituents, and the behavior of these species in the vapor phase. As speciation of these constituents under these conditions is largely unknown, it is likely that unexpected oxides or complexes form in the vapor phase which subsequently control their corresponding condensation behavior. There is some evidence suggesting that this is possible, given that uranium (which is typically understood to be refractory) has been observed to behave as a volatile species (as discussed in Section 5.4). Given the above observations, it is likely that both of these processes occurred together to form these fallout objects.

In summary, the co-location of Na- and Ca-species would be possible in an oxygen-rich environment (which the fireball is theorized to be during fallout formation [6, 15]), where there was substantial contribution of Ca to the vapor from an additional source undergoing continuous fractionation (as described in Section 4.3). The assertion that sodium deposition is the result of an oxygenated fireball is in apparent contrast to what was shown by Cassata et al. (2014), where measurements of volumetric xenon isotope concentrations indicate that the fireball was in a reducing state [54]. However, as shown in the recent XANES study of melt glass from near-surface nuclear tests [94], the cooling rate of the fireball (and the carriers entrained in the fireball) can affect the final redox state of the glasses. Thus, the incorporation of xenon isotope precursors (the decay products of fission products) into the volume of molten fallout glasses may have occurred in an earlier, anoxic state, while the deposition layers observed in the agglomerated fallout objects in this study are likely the

result of late stage addition in a more oxygenated fireball. This is the first definitive evidence of a transition from anoxic to oxidized conditions in a fireball. This is supported by the evidence that this layer must have deposited in the fireball while the carrier was still molten, and likely constitutes a late-stage deposition, as it is preserved where two glassy objects are fused together. Further still, the substantial increase in concentration of uranium at the interfaces of agglomerated fallout glasses indicates that this deposition was, in fact, highly favored immediately prior to quenching of carrier materials.

While the above observations and constraints improve our understanding of these processes and provide insight into the fallout formation environment, they raise more questions than they answer. For example, the extent of temperature and compositional heterogeneities in the fireball are largely unknown, though both of these factors can affect fallout formation, as shown in this dissertation. Further, it is still unclear how vapor phase soil constituents interact with fission products and device materials in the fireball, and how the resultant speciation affects the incorporation of radionuclides into molten carriers. It is clear from this study that much more work is required to produce a comprehensive fallout formation model.

7.2 Future Work

Constraining uranium diffusion to improve model accuracy

Current vapor pressure data could provide insight into how speciation affects the deposition of at least the major elements observed at the interface. However, the uncertainties acquired on the maximum temperature of deposition are too high to properly compare the vapor pressure data between individual constituents (with 1σ uncertainties >140 K, see Section 6.1). The modeled uncertainties could be narrowed by improving the uncertainties on literature values of uranium diffusivity parameters. Preliminary diffusivity experiments have provided promising results that these parameters can be determined with greater precision. By conducting further experiments to narrow the diffusivity parameters, I hope to constrain the maximum temperature of deposition such that existing vapor pressure data could provide insight into the question of speciation.

While the experiments set forth in Table 6.4 are likely to improve the uncertainties on uranium diffusion parameters in rhyolitic material, they could be further expanded by measuring uranium diffusion in a range of melt compositions. By studying diffusion in melt compositions having a range of SiO_2 concentrations, for example, the effect of polymerization on diffusivity could be better understood. Such data would also allow for uranium diffusion modeling between compositionally distinct zones within individual fallout objects, as well as expand the uranium diffusion model to fallout from different testing environments (*i.e.,* different geologies). This could be extended even further by varying the composition of other minor and major elements in diffusion couples, to better understand their effects on the diffusivity of uranium through a multicomponent system such as fallout.

Determining the relative volatilities of species in a multicomponent system

In order to truly understand the effect of vapor composition on fallout formation, experiments should be conducted to determine which vapor-phase constituents would be present in the fireball. More specifically, scaled heating experiments (*e.g.,* by laser heating or box-furnace) on soil material of varying composition would reveal the relative volatilities of major and minor soil components, and how the initial composition of the melt would affect vaporization behaviors. Experiments could be conducted over a range of temperatures (*e.g.,* 1500 K to 3000 K), such that the relative volatility of these species was understood as a function of temperature. Species could either be measured in real-time (*e.g.,* by using Knudsen effusion mass spectrometry to measure vapor pressures), or by measuring the remaining material post-heating using bulk dissolution mass spectrometric techniques (*e.g.,* inductively coupled plasma mass spectrometry).

These experiments could also be used to understand the speciation of vapor-phase constituents during volatilization. Experiments have been conducted to determine the speciation and concentration of vapor-phase constituents from multicomponent systems, including silicates [111, 112], though these compositions diverge substantially, and are thus not relevant, to fallout glasses from this study. However, a similar technique (*i.e.,* Knudsen effusion mass spectrometry) could be applied, along with high-temperature vaporization experiments, to a multicomponent system reflecting fallout glass composition.

Further confounding vaporization and condensation behavior is the conflicting understanding of the fireball oxygen content – this study, and historical fallout studies [6, 15] present evidence that the fireball was in an oxidized state, while another study presents evidence of a reducing fireball environment [54]. Thus, the effect of oxygen fugacity on relative volatility could be established by conducting these experiments in both atmospheric and anoxic conditions. By understanding each of these effects, the relative volatilities and condensation rates of vaporized materials could be used to inform a more comprehensive fallout formation model.

Bibliography

[1] S. Glasstone and P. J. Dolan. *The Effects of Nuclear Weapons.* Tech. rep. O-213-794. US DOD and US DOE, 1977.

[2] M. May et al. "Nuclear forensics: role, state of the art, and program needs". In: *American Association for the Advancement of Science and the American Physical Society, Washington, DC* (2008).

[3] D. J. Karl. "Pakistan's Evolving Nuclear Weapon Posture: Implications for Deterrence Stability". In: *The Nonproliferation Review* 21.3-4 (2014), pp. 317–336.

[4] G. Michael. "Surveying the Contemporary Nuclear Landscape". In: *Democracy and Security* 11.1 (2015), pp. 83–92.

[5] C. S. Ross. "Optical Properties of Glass from Alamogordo, New Mexico." In: *American Mineralogist* 33 (1948), pp. 360–362.

[6] C. E. Adams, N. H. Farlow, and W. R Schell. "The compositions, structures and origins of radioactive fall-out particles." In: *Geochimica et Cosmochimica Acta* 18 (1960), pp. 42–56.

[7] C. F. Miller. *Fallout and Radiological Countermeasures Volume 1.* Tech. rep. DTIC Document, 1963.

[8] G. R. Crocker, J. D. O'Connor, and E. C. Freiling. *Physical and Radiochemical Properties of Fallout Particles.* Tech. rep. USNRDL-TR-899. US Naval Radiological Defense Laboratory, 1965.

[9] G. R. Crocker, J. D. O'Connor, and E. C. Freiling. "Physical and radiochemical properties of fallout particles." In: *Health Physics* 12.8 (1966), pp. 1099–1104.

[10] C. E. Adams and J. D. O'Connor. *The Nature of Individual Radioactive Particles VI. Fallout Particles from a Tower Shot, Operation Redwing.* Dec. 1957.

[11] E. C. Freiling. "Radionuclide Fractionation in Bomb Debris". In: *Science* 133 (1961), pp. 1991–1998.

[12] C. F. Miller. *Biological and Radiological Effects of Fallout from Nuclear Explosions.* Tech. rep. IMU-4536. Menlo Park, CA: Stanford Research Institute, 1964.

[13] *Nuclear Detonation-specific Emergency Response Recommendations*. Tech. rep. Interagency Policy Coordination Subcommittee for Preparedness, Response to Radiological, and Nuclear Threats, 2010.

[14] H. G. Norment. *DELFIC: Department of Defense Fallout Prediction System. Volume I-Fundamentals*. Tech. rep. DTIC Document, 1979.

[15] C. F. Miller. *A Theory of Formation of Fallout from Land-surface Nuclear Detonations and Decay of the Fission Products*. Tech. rep. Naval Radiological Defense Lab., San Francisco, 1960.

[16] E. C. Freiling, G. R. Crocker, and C. E. Adams. "Nuclear debris formation. Radioactive fallout from nuclear weapons tests". In: *Proceedings of an USAEC Conference*. 1965, pp. 1–41.

[17] S. Blonski et al. *Evaluation of a potential for enhancing the decision support system of the Interagency Modeling and Atmospheric Assessment Center with NASA Earth Science Research results*. Tech. rep. NASA, John C. Stennis Space Center, 2007.

[18] E. C. Freiling. "Mass-Transfer Mechanisms in Source-Term Definition". In: *Radionuclides in the Environment* (1970), pp. 1–12.

[19] Y. A. Izrael and E. D. Stukin. "Production of Radioactive Fallout." In: *The Gamma Emission of Radioactive Fallout* (1967).

[20] K. J. Moody, P. M. Grant, and I. D. Hutcheon. *Nuclear Forensic Analysis, Second Edition*. CRC Press, 2014. ISBN: 9781439880623. URL: https://books.google.com/books?id=DwrSBQAAQBAJ.

[21] H. L. Brode. *Fireball Phenomenology*. Santa Monica, CA: Rand Corporation, 1964.

[22] S. Zhang. *Movies of Cold War Bomb Tests Hold Nuclear Secrets*. Dec. 2015. URL: www.wired.com/2015/12/nuclear-films/.

[23] Y. A. Izrael. *Radioactive fallout after nuclear explosions and accidents*. Vol. 3. Elsevier, 2002.

[24] S. Glasstone. *The effects of nuclear weapons*. Tech. rep. US Department of Defense, 1964.

[25] R. S. Clark et al. "Time interval between nuclear detonation and formation of single fallout particles". In: *Journal of Geophysical Research* 72.6 (1967), pp. 1793–1796.

[26] K. Stewart. "The condensation of a vapour to an assembly of droplets or particles". In: *Trans. Faraday Soc.* 52 (1956), pp. 161–173. DOI: 10.1039/TF9565200161. URL: http://dx.doi.org/10.1039/TF9565200161.

[27] R. E. Heft. "Characterization of radioactive particles from nuclear weapons tests." In: *Advan. Chem. Ser. No. 93, 254-81 (1970).* (Jan. 1970).

[28] J. Mackin et al. "Radiochemical analysis of individual fall-out particles". In: *Journal of Inorganic and Nuclear Chemistry* 15.1 (1960), pp. 20–36.

[29] J. N. Pascual and E. C. Freiling. *Fractionation Versus Particle Type in Nuclear Surface Shot Small Boy. Differences in Radiochemical Composition Between Fritted and Spheroidal Particles*. Tech. rep. DTIC Document, 1967.

[30] Edward C Freiling. "Fractionation in surface bursts". In: *Radioactive fallout from nuclear weapons tests. Washington, DC: US Atomic Energy Commission* (1962), pp. 25–46.

[31] J. Norman and P. Winchell. "Cloud Chemistry of Fallout Formation". In: *Proceedings of the Fallout Phenomena Symposium Part I. Monterey, CA: Defense Atomic Support Agency* (1966).

[32] C. F. Miller. *Fallout Models and Radiological Countermeasure Evaluations*. Tech. rep. DTIC Document, 1965.

[33] E. C. Freiling and M. A. Kay. "Radionuclide Fractionation in Air-Burst Debris". In: *Nature* 209.5020 (Jan. 15, 1966), pp. 236–238. URL: http://dx.doi.org/10.1038/209236a0.

[34] E. C. Freiling. *Fractionation I. High-yield Surface Burst Correlation*. Tech. rep. Naval Radiological Defense Lab., San Francisco, 1959.

[35] E. C. Freiling. *Fractionation 3. Estimation of Degree of Fractionation and Radionuclide Partition for Nuclear Debris*. Tech. rep. DTIC Document, 1963.

[36] C. A. Biltoft. *Phase 1 of Defense Special Weapons Agency Transport and Dispersion Model Validation*. Tech. rep. DTIC Document, 1997.

[37] D. S. Haslip. *Prediction of Radiological Hazard Areas with HPAC*. Tech. rep. DTIC Document, 1999.

[38] R. R. Draxler and G. D. Hess. "An overview of the HYSPLIT_4 modelling system for trajectories". In: *Australian meteorological magazine* 47.4 (1998), pp. 295–308.

[39] B. E. Moroz et al. "Predictions of dispersion and deposition of fallout from nuclear testing using the NOAA-HYSPLIT meteorological model". In: *Health physics* 99.2 (2010).

[40] A. F. Stein et al. "NOAA's HYSPLIT atmospheric transport and dispersion modeling system". In: *Bulletin of the American Meteorological Society* 96.12 (2015), pp. 2059–2077.

[41] K. Lodders. "Solar system abundances and condensation temperatures of the elements". In: *The Astrophysical Journal* 591.2 (2003), p. 1220.

[42] D. Giordano, J. K. Russell, and D. B. Dingwell. "Viscosity of magmatic liquids: a model". In: *Earth and Planetary Science Letters* 271.1 (2008), pp. 123–134.

[43] P. P. Parekh et al. "Radioactivity in Trinitite six decades later". In: *Journal of environmental radioactivity* 85.1 (2006), pp. 103–120.

[44] A. J. Fahey et al. "Post-detonation nuclear debris for attribution". In: *Proceedings of the National Academy of Science* 107.47 (2010), pp. 20207–20212.

[45] N. Eby et al. "Trinitite: the atomic rock". In: *Geology Today* 26.5 (2010), pp. 180–185.

[46] F. Belloni et al. "Investigating incorporation and distribution of radionuclides in trinitite". In: *Journal of environmental radioactivity* 102.9 (2011), pp. 852–862.

[47] J. J. Bellucci et al. "Distribution and behavior of some radionuclides associated with the Trinity nuclear test". In: *Journal of Radioanalytical and Nuclear Chemistry* 295.3 (2013), pp. 2049–2057.

[48] J. J. Bellucci et al. "Lead isotopic composition of trinitite melt glass: evidence for the presence of Canadian industrial lead in the first atomic weapon test". In: *Analytical chemistry* 85.15 (2013), pp. 7588–7593.

[49] E. C. Koeman et al. "Oxygen isotope composition of trinitite postdetonation materials". In: *Analytical chemistry* 85.24 (2013), pp. 11913–11919.

[50] C. Wallace et al. "A multi-method approach for determination of radionuclide distribution in trinitite". In: *Journal of Radioanalytical and Nuclear Chemistry* 298.2 (2013), pp. 993–1003.

[51] J. J. Bellucci et al. "A detailed geochemical investigation of post-nuclear detonation trinitite glass at high spatial resolution: delineating anthropogenic vs. natural components". In: *Chemical Geology* 365 (2014), pp. 69–86.

[52] P. H. Donohue et al. "Nuclear forensic applications involving high spatial resolution analysis of Trinitite cross-sections". In: *Journal of Radioanalytical and Nuclear Chemistry* 306.2 (2015), pp. 457–467.

[53] G E. G. N. Eby et al. "Trinitite redux: Mineralogy and petrology". In: *American Mineralogist* 100.2-3 (2015), pp. 427–441.

[54] W. S. Cassata et al. "When the dust settles: stable xenon isotope constraints on the formation of nuclear fallout". In: *Journal of environmental radioactivity* 137 (2014), pp. 88–95.

[55] G. R. Eppich et al. "Constraints on fallout melt glass formation from a near-surface nuclear test". In: *Journal of Radioanalytical and Nuclear Chemistry* 302 (2014), pp. 593–609.

[56] L. A. Lewis et al. "Spatially-resolved analyses of aerodynamic fallout from a uranium-fueled nuclear test". In: *Journal of environmental radioactivity* 148 (2015), pp. 183–195.

[57] R. Egerton. *Physical principles of electron microscopy: an introduction to TEM, SEM, and AEM*. Springer Science & Business Media, 2006.

[58] J. Goldstein et al. *Scanning electron microscopy and X-ray microanalysis: a text for biologists, materials scientists, and geologists*. Springer Science & Business Media, 2012.

[59] T. E. Everhart and R. F. M. Thornley. "Wide-band detector for micro-microampere low-energy electron currents". In: *Journal of Scientific Instruments* 37.7 (1960), p. 246. URL: http://stacks.iop.org/0950-7671/37/i=7/a=307.

[60] C. A. Anderson and M. F. Hasler. "Extension of electron microprobe techniques to biochemistry by the use of long wavelength X-rays". In: *Proceedings of the Fourth International Conference on X-ray Optics and Microanalysis*. 1966, pp. 310–327.

[61] D. E. Newbury, C. R. Swyt, and R. L. Myklebust. "Standardless Quantitative Electron Probe Microanalysis with Energy-Dispersive X-ray Spectrometry: Is It Worth the Risk?" In: *Analytical Chemistry* 67.11 (1995), pp. 1866–1871. DOI: 10.1021/ac00107a017. eprint: http://dx.doi.org/10.1021/ac00107a017. URL: http://dx.doi.org/10.1021/ac00107a017.

[62] M. O. Krause. "Atomic radiative and radiationless yields for K and L shells". In: *Journal of physical and chemical reference data* 8.2 (1979), pp. 307–327.

[63] *Wavelength Dispersive X-ray Microanalysis Explained*. Tech. rep. OIA/011/B/0502. Oxford Instruments, 2002.

[64] J. T. Armstrong. "Citzaf-a package of correction programs for the quantitative Electron Microbeam X-Ray-Analysis of thick polished materials, thin-films, and particles". In: *Microbeam Analysis* 4.3 (1995), pp. 177–200.

[65] J. Siivola. "On the evaporation of some alkali metals during the electron microprobe analysis". In: *Bull. Geol. Soc. Finland* 41 (1969), pp. 85–91.

[66] E. B. Watson and T. M. Harrison. "Zircon saturation revisited: temperature and composition effects in a variety of crustal magma types". In: *Earth and Planetary Science Letters* 64.2 (1983), pp. 295–304.

[67] P. Van der Heide. *Secondary Ion Mass Spectrometry: An Introduction to Principles and Practices*. John Wiley & Sons, 2014.

[68] R. G. Wilson, F. A. Stevie, and C. W. Magee. *Secondary ion mass spectrometry: a practical handbook for depth profiling and bulk impurity analysis*. Wiley-Interscience, 1989.

[69] 2016. URL: http://www.oregon-physics.com/hyperion2.php.

[70] R. W. Boswell et al. *Rf system, magnetic filter, and high voltage isolation for an inductively coupled plasma ion source*. US Patent App. 14/028,305. Sept. 2013.

[71] W. J. Rink and J. W. Thompson. *Encyclopedia of Scientific Dating Methods*. Dordrecht: Springer Netherlands, 2015.

[72] U. Breuer et al. "Comparative studies of SIMS and SNMS analyses during the build up of sputter equilibrium under oxygen and rare gas ion bombardment". In: *Fresenius' journal of analytical chemistry* 358.1-2 (1997), pp. 47–50.

[73] L. R. Nittler. *L'image Interactive Processing of SIMS Images*. 1997.

[74] R. G. Wilson. "SIMS quantification in Si, GaAs, and diamond-an update". In: *International journal of mass spectrometry and ion processes* 143 (1995), pp. 43–49.

[75] New Brunswick Laboratory - Department of Energy. *Certificate of Analysis CRM U100*. Mar. 2008.

[76] New Brunswick Laboratory - Department of Energy. *Certificate of Analysis CRM U200*. Mar. 2008.

[77] G. R. Eppich et al. *Characterization of low concentration uranium glass working materials*. Tech. rep. Lawrence Livermore National Laboratory (LLNL), Livermore, CA, 2013.

[78] *Mineralogical Spreadsheet*. 2015. URL: `www.gabbrosoft.org`.

[79] R. O. Sack and M. S. Ghiorso. "Thermodynamics of multicomponent pyroxenes: I. Formulation of a general model". In: *Contributions to Mineralogy and Petrology* 116.3 (1994), pp. 277–286.

[80] M. Bose et al. "Secondary Ion Mass Spectrometry at Arizona State University". In: *Lunar and Planetary Science Conference*. Vol. 47. 2016, p. 1452.

[81] J. Qian and C. K. Law. "Regimes of coalescence and separation in droplet collision". In: *Journal of Fluid Mechanics* 331 (1997), pp. 59–80.

[82] R. M. Cornell and U. Schwertmann. *The iron oxides: structure, properties, reactions, occurrences and uses*. John Wiley & Sons, 2003.

[83] W. M. Haynes. *CRC handbook of chemistry and physics*. CRC press, 2014.

[84] D. R. Lide. *CRC Handbook of Chemistry and Physics 2004-2005: A Ready-Reference Book of Chemical and Physical Data*. 2004.

[85] P. Patnaik. *Handbook of inorganic chemicals*. Vol. 1. McGraw-Hill New York, 2003.

[86] L. S. Walter and J. E. Giutronich. "Vapor fractionation of silicate melts at high temperatures and atmospheric pressures". In: *Solar Energy* 11.3 (1967), pp. 163–169.

[87] R. H. Lamoreaux, D. L. Hildenbrand, and L. Brewer. "High-Temperature Vaporization Behavior of Oxides II. Oxides of Be, Mg, Ca, Sr, Ba, B, Al, Ga, In, Tl, Si, Ge, Sn, Pb, Zn, Cd, and Hg". In: *Journal of physical and chemical reference data* 16.3 (1987), pp. 419–443.

[88] Y. A. Izrael. *Gamma emission of radioactive fallout.* Dewey, 1970.

[89] Y. Zhang. "Diffusion in minerals and melts: theoretical background". In: *Reviews in Mineralogy and Geochemistry* 72.1 (2010), pp. 5–59.

[90] A. Erturk. *Derivation of Basic Transport Equation*. Power Point slides.

[91] S. A. Socolofsky and G. H. Jirka. *Environmental Fluid Mechanics Part I: Mass Transfer and Diffusion*. Institut fur Hydromechanik, 2002.

[92] A. W. Klement Jr. *Radioactive Fallout From Nuclear Weapons Tests. Proceedings of the Second Conference, Germantown, Maryland, November 3-6, 1964. AEC Symposium Series No. 5*. Tech. rep. Division of Biology and Medicine (AEC), Washington, DC, 1965.

[93] J. E. Mungall and D. B. Dingwell. "Actinide diffusion in a haplogranitic melt: Effects of temperature, water content, and pressure". In: *Geochimica et cosmochimica acta* 61.11 (1997), pp. 2237–2246.

[94] J. I. Pacold et al. "Chemical speciation of U, Fe, and Pu in melt glass from nuclear weapons testing". In: *Journal of Applied Physics* 119.19 (2016), p. 195102.

[95] H. L. Schick. "A Thermodynamic Analysis of the High-temperature Vaporization Properties of Silica." In: *Chemical Reviews* 60.4 (1960), pp. 331–362.

[96] T. Murase and A. R. McBirney. "Properties of some common igneous rocks and their melts at high temperatures". In: *Geological Society of America Bulletin* 84.11 (1973), pp. 3563–3592.

[97] L. Collier et al. "Attenuation in gas-charged magma". In: *Journal of volcanology and geothermal research* 153.1 (2006), pp. 21–36.

[98] W. L. Romine et al. "Thermal diffusivity of rhyolitic glasses and melts: effects of temperature, crystals and dissolved water". In: *Bulletin of volcanology* 74.10 (2012), pp. 2273–2287.

[99] A. Harris. *Thermal Remote Sensing of Active Volcanoes: A User's Manual*. Cambridge University Press, 2013.

[100] Y. Saad and M. H. Schultz. "GMRES: A generalized minimal residual algorithm for solving nonsymmetric linear systems". In: *SIAM Journal on scientific and statistical computing* 7.3 (1986), pp. 856–869.

[101] *United States Nuclear Tests: July 1945 through September 1992*. Tech. rep. DOE/NV–209-REV 16. US Department of Energy, National Nuclear Security Administration Nevada Field Office, Sept. 2015.

[102] *Thermophysical Properties of Materials for Nuclear Engineering: A Tutorial and Collection of Data*. Tech. rep. IAEA-THPH. International Atomic Energy Agency, 2008.

[103] R. H. Lamoreaux and D. L. Hildenbrand. "High temperature vaporization behavior of oxides. I. Alkali metal binary oxides". In: *Journal of physical and chemical reference data* 13.1 (1984), pp. 151–173.

[104] I. Grenthe, H. Wanner, and I. Forest. *Chemical thermodynamics of uranium*. Vol. 1. North-Holland Amsterdam, 1992.

[105] S. I. Shornikov and O. I. Yakovlev. "A Study of Complex Gaseous Oxides over the CaO-MgO-Al_2O_3-TiO_2-SiO_2 Melts". In: *Lunar and Planetary Science Conference*. Vol. 45. 2014, p. 1624.

[106] Y. Zhang and D. J. Cherniak, eds. *Diffusion in minerals and melts*. Mineral Soc America, 2010.

[107] H. J. Matzke and E. Vernaz. "Thermal and physicochemical properties important for the long term behavior of nuclear waste glasses". In: *Journal of nuclear materials* 201 (1993), pp. 295–309.

[108] T. La Tourrette and G. J. Wasserburg. "Self diffusion of europium, neodymium, thorium, and uranium in haplobasaltic melt: The effect of oxygen fugacity and the relationship to melt structure". In: *Geochimica et cosmochimica acta* 61.4 (1997), pp. 755–764.

[109] T. Dunn. "Uranium (VI) diffusion in a supercooled borosilicate melt". In: *Journal of non-crystalline solids* 92.1 (1987), pp. 1–10.

[110] J. E. Mungall. "Empirical models relating viscosity and tracer diffusion in magmatic silicate melts". In: *Geochimica et Cosmochimica Acta* 66.1 (2002), pp. 125–143.

[111] J. Björkvall and V. L. Stolyarova. "A mass spectrometric study of Al_2O_3-SiO_2 melts using a Knudsen cell". In: *Rapid Communications in Mass Spectrometry* 15.10 (2001), pp. 836–842.

[112] V. Stolyarova, I. Archakov, and M. Shultz. "High temperature mass spectrometric study of the thermodynamic properties of borosilicate systems". In: *High temperature science* 28 (1988), pp. 79–86.

Appendix A

EDS dataset

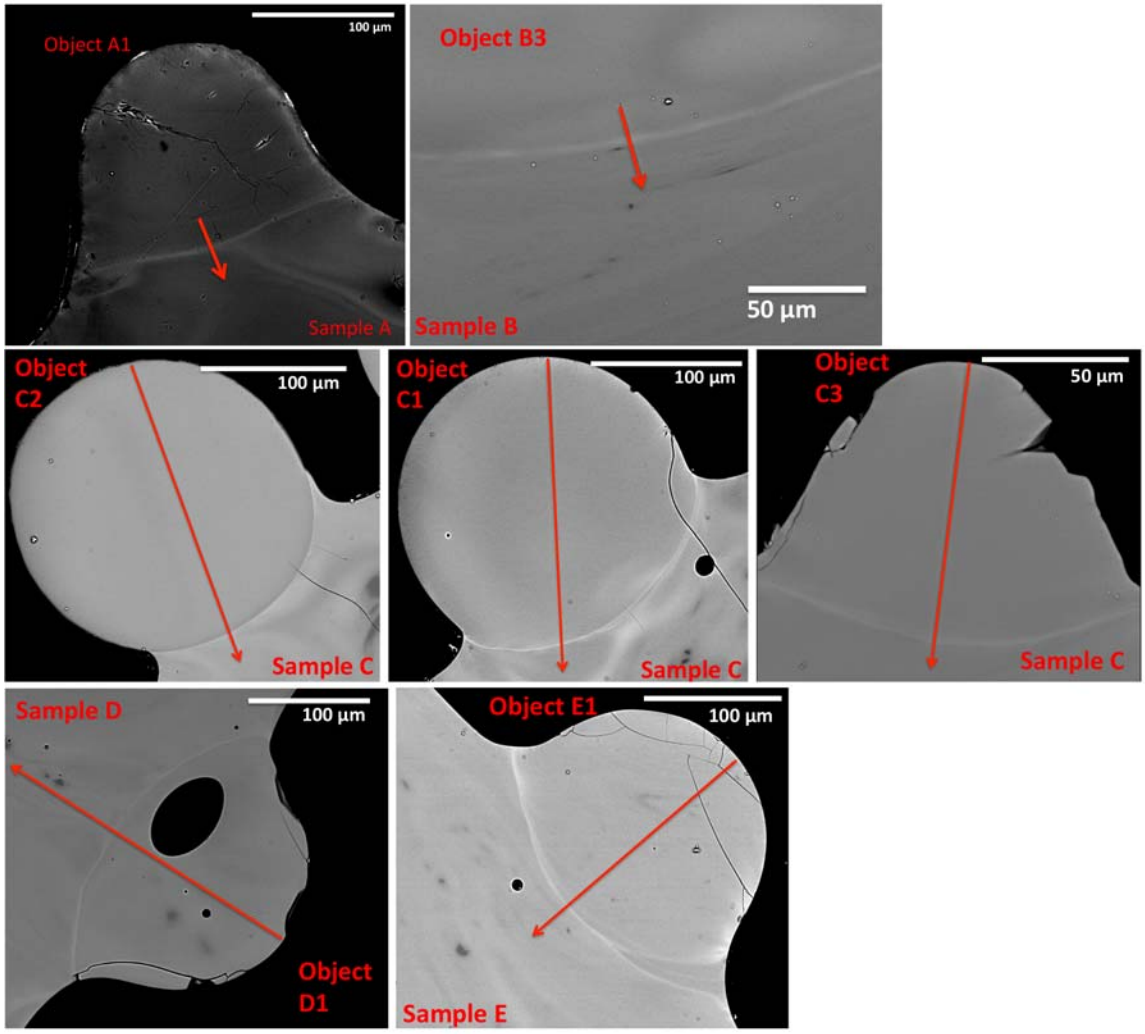

Figure A.1: BSE images of samples and objects, with red arrows indicating the location of sequential EDS spot analyses.

Table A.1: EDS analyses for 7 aerodynamic fallout glass samples

Sample	Spot	Na	1σ	Mg	1σ	Al	1σ	Si	1σ	K	1σ	Ca	1σ	Fe	1σ
A-1	1	13930	118	6708	82	58184	241	228217	478	17183	131	6839	83	4135	64
A-1	2	14648	121	6955	83	58383	242	231205	481	17216	131	6683	82	4178	65
A-1	3	14477	120	6995	84	58160	241	231307	481	17312	132	6597	81	4133	64
A-1	4	14368	120	6828	83	57969	241	231970	482	17288	131	6684	82	4206	65
A-1	5	14782	122	6671	82	56882	239	231850	482	17209	131	6697	82	4071	64
A-1	6	14578	121	6918	83	56631	238	233408	483	17369	132	6668	82	4043	64
A-1	7	14610	121	6593	81	56473	238	233690	483	17395	132	6681	82	3841	62
A-1	8	14636	121	6690	82	55487	236	234449	484	17203	131	6956	83	3961	63
A-1	9	14702	121	6668	82	54967	234	234853	485	17438	132	6814	83	4070	64
A-1	10	14657	121	6749	82	55326	235	234801	485	17095	131	6791	82	3980	63
A-1	11	14896	122	6952	83	54949	234	234802	485	16891	130	7165	85	4009	63
A-1	12	14822	122	6932	83	54546	234	234417	484	16868	130	7245	85	3995	63

A-1	13	14461	120	6926	83	53755	232	235492	485	16967	130	7511	87	4121	64
A-1	14	14583	121	7033	84	52515	229	236600	486	16539	129	7592	87	4312	66
A-1	15	14950	122	7156	85	51192	226	235740	486	16697	129	7786	88	4271	65
A-1	16	16883	130	7042	84	50434	225	235078	485	16589	129	7866	89	4356	66
A-1	17	18670	137	7234	85	49614	223	232952	483	16322	128	8254	91	4713	69
A-1	18	18867	137	7202	85	47850	219	231541	481	16086	127	8366	91	5406	74
A-1	19	18556	136	7719	88	44141	210	233217	483	15687	125	8670	93	6328	80
A-1	20	17355	132	7794	88	41450	204	236982	487	15329	124	8838	94	6661	82
A-1	21	15848	126	7409	86	42639	206	239338	489	15193	123	8290	91	6093	78
A-1	22	13480	116	7495	87	46431	215	239751	490	15227	123	7737	88	5463	74
A-1	23	12049	110	7121	84	50988	226	236777	487	15372	124	7686	88	5022	71
A-1	24	11972	109	7451	86	57158	239	233107	483	15706	125	7569	87	4561	68
A-1	25	12614	112	7347	86	61105	247	228454	478	15967	126	7704	88	4566	68
A-1	26	12749	113	7245	85	63618	252	225868	475	15789	126	7496	87	4256	65
A-1	27	12773	113	7450	86	64947	255	224946	474	15827	126	7731	88	4367	66
A-1	28	12541	112	7365	86	66192	257	224780	474	15667	125	7592	87	4464	67
A-1	29	12738	113	7459	86	67290	259	222830	472	15569	125	7701	88	4418	66
A-1	30	12535	112	7530	87	68254	261	221880	471	15159	123	7706	88	4293	66
A-1	31	12384	111	7792	88	68357	261	221310	470	14959	122	7829	88	4512	67
A-1	32	12444	112	7789	88	68968	263	221004	470	14866	122	7928	89	4521	67
A-1	33	12333	111	7915	89	69315	263	221296	470	14601	121	8147	90	4505	67
A-1	34	12374	111	7892	89	69164	263	219662	469	14777	122	8230	91	4602	68
A-1	35	12337	111	8047	90	69499	264	219408	468	14529	121	8339	91	4603	68
A-1	36	12172	110	8086	90	69804	264	219465	468	14289	120	8424	92	4621	68
A-1	37	12134	110	8001	89	69650	264	219928	469	14471	120	8484	92	4778	69
A-1	38	11985	109	8104	90	70178	265	219384	468	14115	119	8539	92	4728	69
A-1	39	12059	110	8119	90	70079	265	219251	468	13953	118	8599	93	4721	69
A-1	40	12121	110	8008	89	70453	265	218235	467	14199	119	8893	94	4874	70
B-3	1	2803	53	1049	32	7519	87	30684	175	2569	51	1246	35	555	24
B-3	2	2865	54	1042	32	7464	86	31393	177	2474	50	1233	35	534	23
B-3	3	2778	53	1029	32	7624	87	30980	176	2573	51	1216	35	553	24
B-3	4	2667	52	1021	32	7705	88	31217	177	2449	49	1322	36	547	23
B-3	5	2871	54	1050	32	7924	89	31313	177	2494	50	1241	35	591	24
B-3	6	2726	52	1046	32	7814	88	31247	177	2449	49	1364	37	615	25
B-3	7	2771	53	1068	33	7694	88	31394	177	2395	49	1352	37	603	25
B-3	8	2722	52	1043	32	7878	89	31222	177	2386	49	1296	36	576	24
B-3	9	2708	52	1099	33	7543	87	31364	177	2449	49	1294	36	600	24
B-3	10	2618	51	1051	32	7428	86	31825	178	2342	48	1316	36	590	24
B-3	11	2493	50	1024	32	7357	86	32387	180	2414	49	1213	35	598	24
B-3	12	2490	50	1010	32	7284	85	32367	180	2447	49	1297	36	580	24
B-3	13	2445	49	1095	33	7212	85	32443	180	2422	49	1196	35	605	25
B-3	14	2366	49	959	31	7042	84	32768	181	2374	49	1149	34	567	24
B-3	15	2355	49	959	31	7104	84	32718	181	2377	49	1174	34	561	24
B-3	16	2348	48	991	31	7278	85	32956	182	2316	48	1169	34	575	24
B-3	17	2325	48	1012	32	7335	86	32646	181	2239	47	1180	34	563	24
B-3	18	2389	49	1018	32	7266	85	32785	181	2285	48	1121	33	535	23
B-3	19	2411	49	1039	32	7149	85	32984	182	2291	48	1165	34	583	24
B-3	20	2327	48	1046	32	7216	85	32656	181	2215	47	1137	34	550	23
B-3	21	2439	49	1026	32	7364	86	32606	181	2250	47	1159	34	561	24
B-3	22	2324	48	997	32	7549	87	32928	181	2338	48	1169	34	564	24
B-3	23	2345	48	992	32	7492	87	32699	181	2255	47	1134	34	577	24
B-3	24	2395	49	1008	32	7583	87	33034	182	2224	47	1111	33	596	24
B-3	25	2270	48	991	31	7424	86	32770	181	2193	47	1180	34	593	24
B-3	26	2305	48	1012	32	7481	86	32765	181	2339	48	1141	34	574	24
B-3	27	2355	49	1028	32	7500	87	33086	182	2350	48	1212	35	598	24
B-3	28	2293	48	1009	32	7529	87	32868	181	2331	48	1226	35	577	24
B-3	29	2296	48	973	31	7473	86	32924	181	2173	47	1163	34	574	24
B-3	30	2326	48	1003	32	7510	87	32857	181	2273	48	1156	34	562	24
B-3	31	2343	48	1011	32	7426	86	32815	181	2156	46	1152	34	562	24
B-3	32	2279	48	1039	32	7551	87	33123	182	2137	46	1146	34	535	23
B-3	33	2227	47	1016	32	7432	86	33030	182	2188	47	1106	33	563	24
B-3	34	2273	48	1032	32	7577	87	32875	181	2249	47	1163	34	529	23
B-3	35	2265	48	1014	32	7418	86	33140	182	2240	47	1153	34	552	23

B-3	36	2222	47	946	31	7432	86	33151	182	2069	45	1164	34	515	23
B-3	37	2264	48	999	32	7396	86	33139	182	2157	46	1127	34	593	24
B-3	38	2198	47	1033	32	7590	87	33062	182	2204	47	1211	35	538	23
B-3	39	2244	47	968	31	7394	86	33053	182	2211	47	1217	35	600	24
B-3	40	2185	47	974	31	7426	86	33314	183	2175	47	1150	34	546	23
B-3	41	2302	48	995	32	7327	86	33534	183	2157	46	1227	35	518	23
B-3	42	2112	46	959	31	7333	86	33407	183	2240	47	1206	35	580	24
B-3	43	2283	48	971	31	7167	85	33311	183	2121	46	1216	35	566	24
B-3	44	2094	46	1034	32	7392	86	33364	183	2058	45	1208	35	601	25
B-3	45	2245	47	999	32	7293	85	33459	183	2024	45	1225	35	614	25
B-3	46	2150	46	1030	32	7303	85	33401	183	2056	45	1213	35	584	24
B-3	47	2196	47	955	31	7403	86	33400	183	2028	45	1162	34	611	25
B-3	48	2142	46	1049	32	7140	85	33521	183	2150	46	1226	35	563	24
B-3	49	2184	47	988	31	7328	86	33790	184	2125	46	1211	35	573	24
B-3	50	2195	47	957	31	7341	86	33671	184	2134	46	1233	35	538	23
B-3	51	2155	46	998	32	7395	86	33884	184	2069	45	1279	36	538	23
B-3	52	2173	47	990	31	7339	86	33256	182	2146	46	1192	35	593	24
B-3	53	2098	46	1032	32	7153	85	33602	183	2063	45	1194	35	624	25
B-3	54	2094	46	904	30	7195	85	33617	183	2107	46	1208	35	601	25
B-3	55	2139	46	940	31	7202	85	33868	184	2043	45	1189	34	591	24
B-3	56	2204	47	983	31	7481	86	33558	183	2061	45	1223	35	606	25
B-3	57	2183	47	920	30	7343	86	33286	182	2065	45	1221	35	600	24
B-3	58	2137	46	1002	32	7284	85	33079	182	2089	46	1218	35	535	23
B-3	59	2088	46	1007	32	7383	86	33669	183	2057	45	1218	35	560	24
B-3	60	2132	46	1000	32	7301	85	33733	184	2079	46	1250	35	631	25
B-3	61	2123	46	941	31	7344	86	33699	184	2038	45	1203	35	590	24
B-3	62	2114	46	956	31	7363	86	33224	182	1994	45	1230	35	613	25
B-3	63	2096	46	1008	32	7465	86	33440	183	2102	46	1257	35	585	24
B-3	64	2192	47	970	31	7483	87	33316	183	2087	46	1218	35	589	24
B-3	65	2188	47	952	31	7274	85	33674	184	2078	46	1287	36	581	24
B-3	66	2129	46	968	31	7326	86	33513	183	2057	45	1303	36	560	24
B-3	67	2079	46	958	31	7346	86	33304	182	2175	47	1260	36	612	25
B-3	68	2138	46	984	31	7434	86	33475	183	2071	46	1224	35	589	24
B-3	69	2123	46	966	31	7279	85	33796	184	2031	45	1199	35	598	24
B-3	70	2106	46	1005	32	7086	84	33757	184	2006	45	1244	35	556	24
B-3	71	2118	46	1010	32	7142	85	33480	183	2094	46	1239	35	572	24
B-3	72	2103	46	971	31	7095	84	33326	183	2092	46	1229	35	565	24
B-3	73	2089	46	980	31	7314	86	33635	183	2080	46	1227	35	566	24
B-3	74	2150	46	988	31	7402	86	33453	183	2048	45	1286	36	590	24
B-3	75	2072	46	1018	32	7349	86	33438	183	2024	45	1265	36	582	24
B-3	76	2098	46	917	30	7315	86	33350	183	2150	46	1343	37	608	25
B-3	77	2160	46	947	31	7326	86	33188	182	2160	46	1380	37	581	24
B-3	78	2111	46	1029	32	7487	87	32907	181	2160	46	1361	37	582	24
B-3	79	2219	47	1065	33	7447	86	33025	182	2162	47	1441	38	621	25
B-3	80	2165	47	1011	32	7620	87	33040	182	2077	46	1329	36	617	25
B-3	81	2109	46	969	31	7466	86	32935	181	2126	46	1313	36	619	25
B-3	82	2126	46	1041	32	7480	86	33353	183	2097	46	1386	37	601	25
B-3	83	2140	46	960	31	7577	87	33186	182	2035	45	1352	37	625	25
B-3	84	2182	47	1045	32	7647	87	32876	181	1993	45	1329	36	613	25
B-3	85	2036	45	976	31	7629	87	33583	183	2141	46	1423	38	611	25
B-3	86	2182	47	971	31	7512	87	33278	182	2010	45	1370	37	612	25
B-3	87	2190	47	992	32	7644	87	33101	182	2146	46	1366	37	599	24
B-3	88	2148	46	948	31	7651	87	33191	182	2052	45	1397	37	588	24
B-3	89	2132	46	977	31	7670	88	32934	181	2027	45	1383	37	606	25
B-3	90	2168	47	1033	32	7597	87	33043	182	2030	45	1441	38	635	25
B-3	91	2215	47	957	31	7682	88	33152	182	2092	46	1460	38	601	25
B-3	92	2218	47	964	31	7773	88	32991	182	2068	45	1332	37	603	25
B-3	93	2186	47	1027	32	7746	88	32509	180	2166	47	1469	38	629	25
B-3	94	2252	47	1036	32	7872	89	32840	181	2080	46	1502	39	618	25
B-3	95	2158	46	960	31	7918	89	32557	180	2053	45	1469	38	582	24
B-3	96	2156	46	995	32	7815	88	33245	182	2098	46	1459	38	607	25
B-3	97	2165	47	1014	32	7826	88	32686	181	2130	46	1463	38	590	24
B-3	98	2221	47	1030	32	7788	88	32755	181	2078	46	1370	37	582	24

B-3	99	2301	48	1016	32	7561	87	32951	182	1985	45	1402	37	610	25
B-3	100	2194	47	942	31	7612	87	32983	182	2067	45	1424	38	597	24
B-3	101	2174	47	1027	32	7880	89	32868	181	1970	44	1415	38	609	25
B-3	102	2203	47	1033	32	7791	88	33011	182	2087	46	1471	38	561	24
B-3	103	2112	46	1017	32	7662	88	33019	182	2081	46	1384	37	581	24
B-3	104	2261	48	1008	32	7869	89	32656	181	2088	46	1402	37	580	24
B-3	105	2167	47	1043	32	7588	87	33443	183	2094	46	1509	39	601	25
B-3	106	2110	46	1034	32	7663	88	32750	181	2000	45	1394	37	599	24
B-3	107	2150	46	992	32	7786	88	33066	182	2080	46	1458	38	600	24
B-3	108	2203	47	1007	32	7734	88	33365	183	2063	45	1386	37	600	24
B-3	109	2238	47	965	31	7657	88	32822	181	2099	46	1449	38	595	24
B-3	110	2190	47	973	31	7680	88	33136	182	2154	46	1430	38	573	24
B-3	111	2152	46	1030	32	7723	88	33162	182	2127	46	1490	39	570	24
B-3	112	2171	47	999	32	7727	88	32847	181	2077	46	1462	38	631	25
B-3	113	2250	47	996	32	7878	89	33158	182	2129	46	1341	37	609	25
B-3	114	2119	46	983	31	7781	88	32916	181	2082	46	1416	38	599	24
B-3	115	2193	47	980	31	7770	88	32750	181	2177	47	1327	36	630	25
B-3	116	2123	46	998	32	7834	89	32804	181	2139	46	1451	38	560	24
B-3	117	2153	46	919	30	7735	88	32769	181	2142	46	1419	38	616	25
B-3	118	2189	47	985	31	7888	89	33077	182	2196	47	1362	37	601	25
B-3	119	2236	47	942	31	7632	87	32725	181	2083	46	1417	38	582	24
B-3	120	2117	46	1016	32	7813	88	32702	181	2192	47	1416	38	579	24
B-3	121	2241	47	1052	32	7756	88	32836	181	2093	46	1420	38	600	24
B-3	122	2280	48	972	31	7572	87	33110	182	2199	47	1377	37	595	24
B-3	123	2213	47	1001	32	7868	89	33193	182	2181	47	1342	37	567	24
B-3	124	2159	46	995	32	7597	87	32810	181	2144	46	1444	38	585	24
B-3	125	2154	46	986	31	7826	88	33219	182	2235	47	1460	38	512	23
B-3	126	2214	47	991	31	7696	88	32857	181	2152	46	1489	39	568	24
B-3	127	2171	47	1029	32	7677	88	33021	182	2156	46	1366	37	564	24
B-3	128	2237	47	987	31	7655	87	33058	182	2167	47	1390	37	580	24
B-3	129	2234	47	940	31	7737	88	32864	181	2229	47	1523	39	586	24
B-3	130	2317	48	1049	32	7841	89	32832	181	2138	46	1496	39	608	25
B-3	131	2300	48	1129	34	7595	87	32745	181	2173	47	1508	39	615	25
B-3	132	2309	48	1002	32	7701	88	33145	182	2193	47	1565	40	566	24
B-3	133	2265	48	1030	32	7430	86	33141	182	2106	46	1555	39	620	25
B-3	134	2071	46	987	31	6951	83	33505	183	2199	47	1437	38	599	24
B-3	135	2162	47	988	31	6693	82	33882	184	2184	47	1418	38	592	24
B-3	136	2112	46	1024	32	6560	81	34048	185	2172	47	1402	37	593	24
B-3	137	2119	46	1047	32	6698	82	34119	185	2153	46	1367	37	670	26
B-3	138	2173	47	1021	32	6448	80	33718	184	2168	47	1442	38	582	24
B-3	139	2157	46	1021	32	6796	82	33742	184	2172	47	1448	38	607	25
B-3	140	2169	47	1056	33	6871	83	33360	183	2202	47	1520	39	662	26
B-3	141	2196	47	1099	33	7067	84	33452	183	2212	47	1526	39	609	25
B-3	142	2348	48	1030	32	7267	85	33115	182	2261	48	1516	39	617	25
B-3	143	2223	47	1068	33	7226	85	33001	182	2279	48	1548	39	581	24
B-3	144	2227	47	945	31	7601	87	32748	181	2279	48	1569	40	646	25
B-3	145	2305	48	1057	33	7733	88	32568	180	2242	47	1609	40	644	25
B-3	146	2369	49	1031	32	7878	89	32419	180	2303	48	1678	41	589	24
B-3	147	2330	48	1051	32	8126	90	32233	180	2376	49	1634	40	606	25
B-3	148	2414	49	1031	32	8019	90	32367	180	2314	48	1578	40	631	25
B-3	149	2405	49	977	31	8145	90	32199	179	2313	48	1646	41	584	24
B-3	150	2362	49	1083	33	8118	90	32070	179	2327	48	1556	39	620	25
B-3	151	2369	49	1014	32	8174	90	32211	179	2328	48	1591	40	588	24
B-3	152	2339	48	1016	32	8160	90	32385	180	2231	47	1522	39	555	24
B-3	153	2375	49	992	32	8264	91	31987	179	2322	48	1575	40	587	24
B-3	154	2379	49	1003	32	8220	91	32339	180	2330	48	1595	40	622	25
B-3	155	2399	49	1017	32	7989	89	31970	179	2320	48	1582	40	585	24
B-3	156	2440	49	983	31	8372	92	32056	179	2292	48	1560	40	557	24
B-3	157	2316	48	1030	32	8158	90	32337	180	2317	48	1524	39	590	24
B-3	158	2334	48	1002	32	8112	90	32160	179	2323	48	1607	40	582	24
B-3	159	2375	49	1010	32	8114	90	32214	179	2275	48	1520	39	571	24
B-3	160	2411	49	1042	32	8103	90	32257	180	2231	47	1563	40	597	24
B-3	161	2359	49	1011	32	8233	91	32373	180	2259	48	1585	40	551	23

B-3	162	2285	48	1079	33	8344	91	31889	179	2313	48	1514	39	601	25
B-3	163	2346	48	1071	33	8128	90	31907	179	2332	48	1484	39	581	24
B-3	164	2384	49	992	32	8211	91	32224	180	2281	48	1568	40	586	24
B-3	165	2300	48	1086	33	7986	89	32407	180	2325	48	1527	39	591	24
B-3	166	2341	48	1011	32	8168	90	32103	179	2379	49	1530	39	606	25
B-3	167	2368	49	1032	32	8303	91	32253	180	2238	47	1438	38	610	25
B-3	168	2329	48	1035	32	8213	91	32281	180	2226	47	1534	39	572	24
B-3	169	2347	48	1039	32	8223	91	32167	179	2230	47	1576	40	617	25
B-3	170	2305	48	1055	32	8313	91	32215	179	2278	48	1521	39	558	24
B-3	171	2274	48	1026	32	8363	91	32161	179	2326	48	1520	39	614	25
B-3	172	2422	49	1057	33	8108	90	32360	180	2343	48	1506	39	598	24
B-3	173	2353	49	1085	33	8154	90	32115	179	2236	47	1593	40	590	24
B-3	174	2282	48	964	31	8113	90	31985	179	2297	48	1490	39	605	25
B-3	175	2353	49	1036	32	8104	90	32081	179	2227	47	1596	40	622	25
B-3	176	2361	49	1010	32	8331	91	32232	180	2331	48	1439	38	570	24
B-3	177	2382	49	956	31	8310	91	31911	179	2184	47	1552	39	605	25
B-3	178	2264	48	1009	32	8198	91	32360	180	2232	47	1540	39	580	24
B-3	179	2334	48	1079	33	8356	91	32032	179	2339	48	1501	39	597	24
B-3	180	2380	49	956	31	8373	92	31958	179	2278	48	1552	39	602	25
B-3	181	2396	49	1065	33	8463	92	32079	179	2329	48	1455	38	591	24
B-3	182	2323	48	992	32	8354	91	31928	179	2297	48	1535	39	622	25
B-3	183	2346	48	1038	32	8616	93	31801	178	2183	47	1540	39	563	24
B-3	184	2378	49	1029	32	8435	92	31953	179	2239	47	1526	39	560	24
B-3	185	2337	48	993	32	8405	92	31792	178	2247	47	1571	40	573	24
B-3	186	2343	48	1020	32	8322	91	32056	179	2235	47	1488	39	602	25
B-3	187	2237	47	1003	32	8530	92	31776	178	2275	48	1542	39	639	25
B-3	188	2264	48	1067	33	8236	91	31869	179	2163	47	1561	40	607	25
B-3	189	2356	49	1023	32	8562	93	31701	178	2179	47	1538	39	593	24
B-3	190	2348	48	1107	33	8456	92	31945	179	2319	48	1547	39	639	25
B-3	191	2305	48	1060	33	8538	92	31551	178	2271	48	1552	39	664	26
B-3	192	2302	48	1023	32	8449	92	31972	179	2353	49	1504	39	573	24
B-3	193	2371	49	1021	32	8418	92	31805	178	2170	47	1571	40	623	25
B-3	194	2267	48	1034	32	8379	92	32161	179	2265	48	1511	39	652	26
B-3	195	2276	48	1000	32	8342	91	32086	179	2259	48	1537	39	592	24
B-3	196	2308	48	1080	33	8251	91	31844	178	2224	47	1451	38	615	25
B-3	197	2244	47	1057	33	8154	90	32240	180	2244	47	1473	38	584	24
B-3	198	2263	48	1001	32	8288	91	31899	179	2265	48	1473	38	604	25
B-3	199	2274	48	1039	32	8054	90	32625	181	2153	46	1439	38	589	24
B-3	200	2265	48	1002	32	8214	91	32182	179	2265	48	1460	38	617	25
B-3	201	2190	47	1031	32	8040	90	32180	179	2269	48	1407	38	599	24
B-3	202	2210	47	979	31	7888	89	32512	180	2243	47	1451	38	564	24
B-3	203	2134	46	978	31	8105	90	32584	181	2276	48	1411	38	627	25
B-3	204	2161	46	1010	32	7968	89	32843	181	2194	47	1486	39	608	25
B-3	205	2317	48	1021	32	7936	89	31956	179	2220	47	1361	37	561	24
B-3	206	2268	48	1026	32	7830	88	32682	181	2205	47	1400	37	592	24
B-3	207	2263	48	1013	32	7894	89	32626	181	2253	47	1475	38	579	24
B-3	208	2289	48	1011	32	7908	89	32763	181	2197	47	1394	37	574	24
B-3	209	2212	47	963	31	7929	89	32543	180	2201	47	1495	39	592	24
B-3	210	2209	47	984	31	8160	90	32586	181	2247	47	1346	37	614	25
B-3	211	2254	47	1076	33	8111	90	32443	180	2168	47	1465	38	601	25
B-3	212	2274	48	978	31	7974	89	32361	180	2211	47	1447	38	559	24
B-3	213	2290	48	1011	32	7982	89	32343	180	2176	47	1414	38	572	24
B-3	214	2226	47	959	31	7961	89	32768	181	2231	47	1392	37	616	25
B-3	215	2138	46	982	31	7972	89	32444	180	2134	46	1457	38	557	24
B-3	216	2159	46	1030	32	7869	89	32643	181	2148	46	1409	38	520	23
B-3	217	2289	48	987	31	8000	89	32396	180	2120	46	1425	38	592	24
B-3	218	2277	48	1029	32	7897	89	32607	181	2215	47	1347	37	527	23
B-3	219	2176	47	1003	32	8065	90	32611	181	2146	46	1389	37	550	23
B-3	220	2296	48	1050	32	8079	90	32295	180	2219	47	1358	37	571	24
B-3	221	2176	47	1005	32	8046	90	32600	181	2234	47	1410	38	603	25
B-3	222	2170	47	1049	32	7927	89	32528	180	2120	46	1419	38	621	25
B-3	223	2200	47	968	31	8125	90	32490	180	2212	47	1458	38	578	24
B-3	224	2251	47	1009	32	8094	90	32714	181	2092	46	1454	38	534	23

B-3	225	2220	47	1030	32	7971	89	32408	180	2229	47	1427	38	587	24
B-3	226	2243	47	1061	33	8104	90	32799	181	2198	47	1356	37	578	24
B-3	227	2202	47	1027	32	8097	90	32402	180	2249	47	1460	38	574	24
B-3	228	2250	47	1016	32	8129	90	32302	180	2201	47	1425	38	604	25
B-3	229	2195	47	1015	32	8014	90	32436	180	2256	48	1443	38	580	24
B-3	230	2239	47	951	31	8056	90	32454	180	2201	47	1466	38	547	23
B-3	231	2280	48	958	31	8065	90	32277	180	2226	47	1475	38	586	24
B-3	232	2156	46	1027	32	8126	90	32571	180	2078	46	1451	38	594	24
B-3	233	2172	47	1027	32	8353	91	32330	180	2172	47	1500	39	599	24
B-3	234	2169	47	973	31	7983	89	32450	180	2239	47	1450	38	609	25
B-3	235	2227	47	1004	32	8022	90	32472	180	2149	46	1457	38	577	24
B-3	236	2182	47	970	31	8181	90	32185	179	2265	48	1497	39	587	24
B-3	237	2245	47	1042	32	8190	91	31988	179	2189	47	1478	38	561	24
B-3	238	2257	48	1006	32	8156	90	32369	180	2111	46	1480	38	607	25
B-3	239	2193	47	987	31	8505	92	31752	178	2169	47	1547	39	588	24
B-3	240	2271	48	1050	32	8410	92	31320	177	2115	46	1512	39	604	25
B-3	241	2238	47	1028	32	8450	92	31565	178	2193	47	1538	39	626	25
B-3	242	2356	49	1041	32	8509	92	31747	178	2208	47	1593	40	613	25
B-3	243	2348	48	1032	32	8791	94	31637	178	2222	47	1668	41	565	24
B-3	244	2291	48	948	31	8511	92	31797	178	2232	47	1518	39	612	25
B-3	245	2328	48	1027	32	8768	94	31558	178	2117	46	1641	41	608	25
B-3	246	2208	47	1056	33	8609	93	31832	178	2165	47	1561	40	621	25
B-3	247	2238	47	1060	33	8598	93	31974	179	2240	47	1551	39	602	25
B-3	248	2276	48	987	31	8506	92	31954	179	2119	46	1565	40	601	25
B-3	249	2204	47	984	31	8530	92	31937	179	2222	47	1526	39	631	25
B-3	250	2278	48	983	31	8661	93	32197	179	2188	47	1480	38	581	24
B-3	251	2218	47	1031	32	8448	92	31873	179	2191	47	1578	40	630	25
B-3	252	2177	47	1006	32	8582	93	31826	178	2153	46	1565	40	604	25
B-3	253	2207	47	1074	33	8495	92	31425	177	2128	46	1532	39	602	25
B-3	254	2307	48	1038	32	8526	92	31697	178	2168	47	1540	39	586	24
B-3	255	2209	47	1028	32	8382	92	31502	177	2153	46	1556	39	613	25
B-3	256	2303	48	941	31	8379	92	31983	179	2152	46	1488	39	654	26
B-3	257	2367	49	1038	32	8348	91	32109	179	2134	46	1577	40	611	25
B-3	258	2295	48	1067	33	8464	92	32342	180	2115	46	1495	39	607	25
B-3	259	2240	47	1047	32	8332	91	32136	179	2161	46	1511	39	604	25
B-3	260	2183	47	1021	32	8296	91	32216	179	2130	46	1510	39	584	24
B-3	261	2285	48	1051	32	8289	91	32315	180	2095	46	1484	39	608	25
B-3	262	2268	48	1066	33	8206	91	31975	179	2137	46	1516	39	602	25
B-3	263	2243	47	1012	32	8170	90	32176	179	2126	46	1476	38	571	24
B-3	264	2214	47	1024	32	8079	90	32427	180	2197	47	1460	38	603	25
B-3	265	2255	47	1057	33	8235	91	32232	180	2155	46	1414	38	593	24
B-3	266	2195	47	979	31	8270	91	32192	179	2273	48	1526	39	578	24
B-3	267	2263	48	1000	32	8090	90	31897	179	2147	46	1423	38	583	24
B-3	268	2285	48	1002	32	8332	91	31902	179	2198	47	1509	39	572	24
B-3	269	2263	48	1035	32	8221	91	31793	178	2101	46	1499	39	545	23
B-3	270	2221	47	982	31	8466	92	31984	179	2088	46	1422	38	610	25
B-3	271	2232	47	1002	32	8406	92	31646	178	2168	47	1427	38	577	24
B-3	272	2296	48	1067	33	8649	93	31662	178	2189	47	1493	39	637	25
B-3	273	2328	48	1012	32	8850	94	31185	177	2127	46	1599	40	620	25
B-3	274	2334	48	1092	33	9065	95	31129	176	2225	47	1614	40	604	25
B-3	275	2376	49	1041	32	9040	95	31279	177	2259	48	1628	40	601	25
B-3	276	2337	48	982	31	9054	95	31284	177	2268	48	1617	40	617	25
B-3	277	2242	47	1018	32	8711	93	31509	178	2225	47	1463	38	664	26
B-3	278	2290	48	1048	32	8689	93	31370	177	2235	47	1466	38	574	24
B-3	279	2334	48	978	31	8266	91	32221	180	2216	47	1435	38	580	24
B-3	280	2238	47	975	31	8226	91	32093	179	2203	47	1381	37	610	25
B-3	281	2232	47	978	31	8197	91	32277	180	2192	47	1384	37	572	24
B-3	282	2222	47	953	31	8278	91	31767	178	2221	47	1360	37	591	24
B-3	283	2206	47	981	31	8240	91	32152	179	2325	48	1390	37	547	23
B-3	284	2319	48	959	31	8278	91	32109	179	2356	49	1316	36	602	25
B-3	285	2359	49	981	31	8401	92	32018	179	2223	47	1403	37	584	24
B-3	286	2278	48	1044	32	8289	91	32182	179	2313	48	1420	38	611	25
B-3	287	2310	48	1004	32	8392	92	31812	178	2270	48	1463	38	658	26

B-3	288	2367	49	998	32	8373	92	32050	179	2272	48	1419	38	604	25
B-3	289	2299	48	1053	32	8311	91	32188	179	2229	47	1369	37	607	25
B-3	290	2272	48	1074	33	8142	90	32386	180	2255	47	1500	39	559	24
B-3	291	2281	48	1065	33	7965	89	32495	180	2252	47	1403	37	582	24
B-3	292	2261	48	999	32	7903	89	32518	180	2250	47	1311	36	643	25
B-3	293	2330	48	1077	33	7985	89	32251	180	2280	48	1348	37	560	24
B-3	294	2292	48	980	31	7853	89	32412	180	2268	48	1350	37	615	25
B-3	295	2216	47	1054	32	7790	88	32404	180	2223	47	1422	38	610	25
B-3	296	2231	47	1053	32	7734	88	32863	181	2274	48	1310	36	560	24
B-3	297	2251	47	1033	32	7560	87	32729	181	2248	47	1324	36	654	26
B-3	298	2208	47	1029	32	7764	88	32332	180	2221	47	1353	37	594	24
B-3	299	2275	48	1085	33	7585	87	32655	181	2237	47	1352	37	637	25
B-3	300	2252	47	987	31	7766	88	32449	180	2246	47	1324	36	607	25
B-3	301	2321	48	1031	32	7940	89	32574	180	2330	48	1407	38	589	24
B-3	302	2362	49	1057	33	8152	90	32272	180	2333	48	1454	38	518	23
B-3	303	2403	49	1062	33	8157	90	31648	178	2266	48	1365	37	557	24
B-3	304	2384	49	1092	33	8336	91	31653	178	2360	49	1446	38	592	24
B-3	305	2406	49	1115	33	8233	91	31915	179	2334	48	1458	38	625	25
B-3	306	2353	49	1059	33	8163	90	31934	179	2331	48	1458	38	595	24
B-3	307	2294	48	1057	33	8121	90	31913	179	2261	48	1428	38	603	25
B-3	308	2266	48	1044	32	7737	88	32539	180	2274	48	1304	36	568	24
B-3	309	2373	49	959	31	7432	86	32989	182	2142	46	1285	36	585	24
B-3	310	2188	47	990	31	7012	84	33314	183	2274	48	1321	36	570	24
B-3	311	2169	47	961	31	6609	81	33969	184	2137	46	1249	35	580	24
B-3	312	1981	45	960	31	5707	76	34715	186	2163	47	1094	33	543	23
B-3	313	1902	44	963	31	5568	75	35560	189	2049	45	1075	33	526	23
B-3	314	1986	45	973	31	5428	74	35354	188	2100	46	1044	32	507	23
B-3	315	1917	44	944	31	5593	75	35431	188	1976	44	1109	33	482	22
B-3	316	1963	44	932	31	5686	75	34964	187	2063	45	1100	33	503	22
B-3	317	1951	44	987	31	5847	76	34954	187	2021	45	1096	33	546	23
B-3	318	2017	45	958	31	6074	78	34700	186	2136	46	1144	34	578	24
B-3	319	1999	45	993	32	6279	79	34581	186	2091	46	1224	35	555	24
B-3	320	2174	47	1011	32	6266	79	34617	186	2123	46	1184	34	576	24
B-3	321	2147	46	988	31	6524	81	33782	184	2209	47	1237	35	551	23
B-3	322	2135	46	992	32	6671	82	33829	184	2141	46	1214	35	582	24
B-3	323	2061	45	994	32	6869	83	33747	184	2242	47	1229	35	549	23
B-3	324	2151	46	1016	32	6923	83	33357	183	2161	46	1263	36	608	25
B-3	325	2191	47	1047	32	7045	84	33529	183	2227	47	1278	36	604	25
B-3	326	2257	48	1043	32	7082	84	33297	182	2217	47	1307	36	619	25
B-3	327	2160	46	1012	32	7112	84	33257	182	2181	47	1341	37	573	24
B-3	328	2219	47	1092	33	6974	84	33220	182	2216	47	1379	37	656	26
B-3	329	2211	47	1068	33	7282	85	32997	182	2260	48	1336	37	617	25
B-3	330	2278	48	1104	33	7411	86	32886	181	2191	47	1373	37	621	25
B-3	331	2291	48	1052	32	7356	86	32916	181	2269	48	1398	37	568	24
B-3	332	2163	47	1043	32	7311	86	32774	181	2227	47	1322	36	637	25
B-3	333	2269	48	1036	32	7539	87	32535	180	2162	47	1340	37	595	24
B-3	334	2244	47	1101	33	7586	87	32111	179	2256	48	1378	37	585	24
B-3	335	2224	47	1068	33	7504	87	32546	180	2249	47	1412	38	612	25
B-3	336	2272	48	1162	34	7731	88	32316	180	2245	47	1416	38	651	26
B-3	337	2367	49	1089	33	7768	88	32034	179	2204	47	1423	38	658	26
B-3	338	2261	48	1063	33	7787	88	32238	180	2296	48	1344	37	698	26
B-3	339	2218	47	1074	33	7735	88	31945	179	2262	48	1399	37	673	26
B-3	340	2289	48	1126	34	7805	88	32126	179	2174	47	1409	38	652	26
B-3	341	2283	48	1103	33	7790	88	32724	181	2307	48	1365	37	611	25
B-3	342	2268	48	1109	33	7716	88	32440	180	2269	48	1359	37	637	25
B-3	343	2185	47	1199	35	7729	88	32357	180	2362	49	1358	37	679	26
B-3	344	2191	47	1107	33	7619	87	32639	181	2217	47	1365	37	621	25
B-3	345	2253	47	1092	33	7860	89	32466	180	2240	47	1365	37	601	25
B-3	346	2316	48	1068	33	8024	90	32128	179	2347	48	1396	37	642	25
B-3	347	2361	49	1149	34	8111	90	32000	179	2435	49	1334	37	607	25
B-3	348	2303	48	1030	32	7963	89	31910	179	2294	48	1423	38	676	26
B-3	349	2282	48	1075	33	8327	91	31478	177	2235	47	1365	37	685	26
B-3	350	2323	48	1050	32	8326	91	31767	178	2355	49	1385	37	682	26

B-3	351	2267	48	1071	33	8260	91	31728	178	2407	49	1443	38	647	25
B-3	352	2243	47	1091	33	8122	90	31386	177	2342	48	1403	37	663	26
B-3	353	2343	48	1035	32	8234	91	31516	178	2298	48	1296	36	690	26
B-3	354	2307	48	1065	33	8280	91	31779	178	2301	48	1229	35	625	25
B-3	355	2339	48	1089	33	8186	90	31812	178	2292	48	1260	36	675	26
B-3	356	2288	48	1081	33	8119	90	31999	179	2267	48	1257	35	638	25
B-3	357	2314	48	1068	33	8249	91	31971	179	2310	48	1336	37	617	25
B-3	358	2247	47	1085	33	8180	90	31767	178	2383	49	1304	36	589	24
B-3	359	2363	49	1030	32	8170	90	31922	179	2358	49	1274	36	619	25
B-3	360	2251	47	1028	32	8246	91	31655	178	2385	49	1226	35	614	25
B-3	361	2335	48	976	31	8020	90	31887	179	2289	48	1147	34	623	25
B-3	362	2311	48	988	31	8298	91	31949	179	2313	48	1210	35	669	26
B-3	363	2314	48	980	31	8149	90	32146	179	2385	49	1225	35	650	26
B-3	364	2366	49	1034	32	8081	90	31871	179	2269	48	1181	34	570	24
B-3	365	2308	48	1094	33	8268	91	31693	178	2334	48	1243	35	610	25
B-3	366	2330	48	1053	32	8380	92	31795	178	2279	48	1224	35	619	25
B-3	367	2388	49	1040	32	8460	92	31384	177	2369	49	1319	36	646	25
B-3	368	2288	48	1040	32	8479	92	31255	177	2307	48	1310	36	659	26
B-3	369	2390	49	1007	32	8612	93	31295	177	2296	48	1228	35	651	26
B-3	370	2431	49	1064	33	8598	93	31129	176	2359	49	1292	36	652	26
B-3	371	2449	49	1072	33	8848	94	31138	176	2379	49	1286	36	661	26
B-3	372	2391	49	1083	33	8642	93	31321	177	2401	49	1305	36	666	26
B-3	373	2419	49	1064	33	8779	94	31096	176	2454	50	1309	36	632	25
B-3	374	2378	49	1025	32	8788	94	31135	176	2242	47	1309	36	654	26
B-3	375	2278	48	1058	33	8836	94	31139	176	2410	49	1314	36	678	26
B-3	376	2404	49	1039	32	8852	94	30834	176	2346	48	1280	36	645	25
B-3	377	2378	49	1134	34	8857	94	31183	177	2369	49	1300	36	661	26
B-3	378	2356	49	1083	33	8772	94	30970	176	2379	49	1303	36	665	26
B-3	379	2398	49	1125	34	8594	93	31194	177	2507	50	1209	35	732	27
B-3	380	2481	50	1007	32	8690	93	30871	176	2424	49	1229	35	624	25
B-3	381	2337	48	1074	33	8525	92	31297	177	2431	49	1255	35	672	26
B-3	382	2390	49	1097	33	8397	92	31289	177	2427	49	1253	35	609	25
B-3	383	2363	49	1098	33	8436	92	31167	177	2366	49	1210	35	628	25
B-3	384	2464	50	1040	32	8308	91	31463	177	2377	49	1221	35	621	25
B-3	385	2278	48	1031	32	8366	91	31629	178	2442	49	1161	34	594	24
B-3	386	2282	48	1033	32	8310	91	31739	178	2334	48	1162	34	598	24
B-3	387	2396	49	1054	32	8210	91	31672	178	2419	49	1148	34	607	25
B-3	388	2291	48	1016	32	7892	89	31888	179	2521	50	1124	34	605	25
B-3	389	2247	47	1011	32	8113	90	31535	178	2307	48	1049	32	573	24
B-3	390	2345	48	1057	33	8108	90	31821	178	2358	49	1096	33	587	24
B-3	391	2314	48	983	31	8071	90	31947	179	2379	49	1133	34	619	25
B-3	392	2254	47	1008	32	8000	89	31831	178	2286	48	1058	33	584	24
B-3	393	2265	48	917	30	8082	90	31937	179	2359	49	1093	33	580	24
B-3	394	2279	48	1004	32	7917	89	31961	179	2346	48	1072	33	609	25
B-3	395	2288	48	979	31	7988	89	31988	179	2415	49	1137	34	605	25
B-3	396	2349	48	978	31	7827	88	31866	179	2338	48	1036	32	565	24
B-3	397	2350	48	975	31	7908	89	32000	179	2347	48	1095	33	608	25
B-3	398	2233	47	935	31	8064	90	31825	178	2330	48	1103	33	617	25
B-3	399	2216	47	991	31	8040	90	32057	179	2347	48	1094	33	614	25
B-3	400	2258	48	989	31	7979	89	31432	177	2323	48	1071	33	595	24
B-3	401	2290	48	986	31	7987	89	31985	179	2358	49	1079	33	589	24
B-3	402	2319	48	1022	32	7948	89	32073	179	2329	48	1075	33	591	24
B-3	403	2282	48	981	31	7878	89	31740	178	2322	48	1138	34	608	25
B-3	404	2315	48	958	31	7883	89	32285	180	2294	48	1095	33	578	24
B-3	405	2302	48	961	31	7845	89	31844	178	2408	49	1074	33	551	23
B-3	406	2264	48	914	30	7793	88	32286	180	2273	48	1069	33	538	23
B-3	407	2284	48	965	31	7606	87	32003	179	2368	49	1086	33	589	24
B-3	408	2239	47	976	31	7628	87	32296	180	2367	49	1101	33	568	24
B-3	409	2204	47	986	31	7705	88	32034	179	2373	49	1107	33	613	25
B-3	410	2285	48	980	31	7692	88	31820	178	2267	48	1110	33	566	24
B-3	411	2283	48	952	31	7852	89	32553	180	2302	48	1096	33	587	24
B-3	412	2305	48	939	31	7841	89	32424	180	2362	49	1104	33	606	25
B-3	413	2372	49	977	31	7887	89	31805	178	2325	48	1102	33	590	24

B-3	414	2336	48	966	31	7774	88	32182	179	2413	49	1129	34	606	25
B-3	415	2275	48	984	31	7883	89	31694	178	2283	48	1160	34	580	24
B-3	416	2382	49	930	31	8007	89	31480	177	2326	48	1124	34	601	25
B-3	417	2299	48	942	31	7994	89	31922	179	2228	47	1164	34	633	25
B-3	418	2343	48	962	31	8120	90	31726	178	2325	48	1142	34	586	24
B-3	419	2338	48	1037	32	8979	95	30146	174	2332	48	1243	35	561	24
B-3	420	2331	48	1063	33	9423	97	29996	173	2258	48	1208	35	630	25
B-3	421	2392	49	1062	33	8093	90	31248	177	2353	49	1259	35	584	24
B-3	422	2395	49	1081	33	8120	90	31718	178	2358	49	1260	36	625	25
B-3	423	2344	48	1015	32	7938	89	31519	178	2292	48	1276	36	608	25
B-3	424	2362	49	1018	32	7870	89	31669	178	2293	48	1286	36	637	25
B-3	425	2357	49	1023	32	7948	89	31588	178	2278	48	1295	36	605	25
B-3	426	2300	48	1031	32	7640	87	31783	178	2277	48	1286	36	612	25
B-3	427	2297	48	996	32	7532	87	32015	179	2328	48	1202	35	597	24
B-3	428	2146	46	1036	32	7325	86	32335	180	2229	47	1214	35	596	24
B-3	429	2252	47	1045	32	7423	86	32402	180	2177	47	1147	34	592	24
B-3	430	2305	48	951	31	7282	85	32577	180	2236	47	1165	34	582	24
B-3	431	2205	47	1035	32	7189	85	32427	180	2224	47	1147	34	621	25
B-3	432	2174	47	986	31	7198	85	32175	179	2257	48	1181	34	600	24
B-3	433	2308	48	1004	32	7365	86	31899	179	2252	47	1254	35	598	24
B-3	434	2239	47	1046	32	7337	86	32272	180	2279	48	1260	36	569	24
B-3	435	2286	48	1007	32	7432	86	32248	180	2225	47	1210	35	548	23
B-3	436	2257	48	1002	32	7751	88	32173	179	2257	48	1322	36	623	25
B-3	437	2279	48	967	31	7699	88	32119	179	2233	47	1314	36	603	25
B-3	438	2295	48	1051	32	7819	88	31816	178	2195	47	1352	37	624	25
B-3	439	2427	49	1063	33	7878	89	31593	178	2237	47	1318	36	599	24
B-3	440	2347	48	1030	32	7633	87	31405	177	2305	48	1334	37	583	24
B-3	441	2356	49	1022	32	7870	89	31860	178	2278	48	1338	37	599	24
B-3	442	2349	48	1015	32	7889	89	31713	178	2306	48	1376	37	627	25
B-3	443	2346	48	1048	32	7702	88	31472	177	2265	48	1385	37	663	26
B-3	444	2241	47	1082	33	7882	89	31566	178	2309	48	1337	37	578	24
B-3	445	2352	49	1050	32	7886	89	31438	177	2372	49	1391	37	627	25
B-3	446	2182	47	1038	32	7678	88	31587	178	2275	48	1376	37	604	25
B-3	447	2300	48	1061	33	7770	88	31822	178	2286	48	1336	37	592	24
B-3	448	2339	48	1017	32	7641	87	32038	179	2313	48	1350	37	609	25
B-3	449	2278	48	1079	33	7492	87	32008	179	2275	48	1316	36	619	25
B-3	450	2339	48	1032	32	7662	88	32088	179	2292	48	1337	37	626	25
B-3	451	2150	46	1066	33	7481	86	32231	180	2176	47	1291	36	629	25
B-3	452	2275	48	989	31	7575	87	32278	180	2241	47	1342	37	561	24
B-3	453	2303	48	995	32	7505	87	32307	180	2290	48	1338	37	592	24
B-3	454	2258	48	975	31	7504	87	32105	179	2188	47	1282	36	591	24
B-3	455	2340	48	1064	33	7600	87	31933	179	2222	47	1395	37	580	24
B-3	456	2308	48	1110	33	7812	88	31817	178	2311	48	1381	37	615	25
B-3	457	2340	48	1046	32	7892	89	31216	177	2298	48	1385	37	588	24
B-3	458	2307	48	1044	32	8075	90	31227	177	2191	47	1412	38	583	24
B-3	459	2375	49	1081	33	8135	90	31630	178	2292	48	1407	38	603	25
B-3	460	2351	48	1084	33	8177	90	31446	177	2251	47	1371	37	627	25
B-3	461	2380	49	1070	33	8082	90	31306	177	2206	47	1381	37	600	24
B-3	462	2362	49	1047	32	7939	89	31715	178	2174	47	1437	38	595	24
B-3	463	2354	49	1027	32	7998	89	31753	178	2290	48	1405	37	603	25
B-3	464	2278	48	1033	32	7954	89	31834	178	2165	47	1436	38	597	24
B-3	465	2340	48	1066	33	8059	90	31821	178	2241	47	1409	38	626	25
B-3	466	2193	47	1036	32	7796	88	32061	179	2178	47	1393	37	579	24
B-3	467	2203	47	1033	32	7794	88	32313	180	2217	47	1383	37	593	24
B-3	468	2323	48	996	32	7678	88	31921	179	2270	48	1342	37	574	24
B-3	469	2243	47	994	32	7669	88	32251	180	2195	47	1401	37	600	24
B-3	470	2259	48	1008	32	7706	88	32330	180	2239	47	1410	38	613	25
B-3	471	2248	47	1012	32	7669	88	32255	180	2208	47	1319	36	628	25
B-3	472	2196	47	1011	32	7580	87	32215	179	2242	47	1312	36	592	24
B-3	473	2245	47	979	31	7713	88	31871	179	2221	47	1457	38	590	24
B-3	474	2188	47	994	32	7657	88	32277	180	2183	47	1314	36	654	26
B-3	475	2263	48	1008	32	7600	87	32169	179	2221	47	1388	37	598	24
B-3	476	2227	47	979	31	7554	87	32472	180	2219	47	1347	37	619	25

B-3	477	2249	47	991	31	7577	87	32309	180	2134	46	1417	38	597	24
B-3	478	2213	47	975	31	7624	87	32326	180	2286	48	1411	38	588	24
B-3	479	2207	47	989	31	7764	88	32220	180	2162	47	1391	37	632	25
B-3	480	2206	47	990	31	7548	87	32319	180	2220	47	1388	37	608	25
B-3	481	2175	47	1008	32	7683	88	32304	180	2224	47	1414	38	583	24
B-3	482	2281	48	996	32	7673	88	32214	179	2168	47	1400	37	615	25
B-3	483	2106	46	994	32	7706	88	32214	179	2184	47	1415	38	608	25
B-3	484	2242	47	980	31	7780	88	32209	179	2174	47	1399	37	636	25
B-3	485	2311	48	953	31	7838	89	31718	178	2193	47	1459	38	619	25
B-3	486	2262	48	1038	32	7951	89	31686	178	2186	47	1475	38	590	24
B-3	487	2292	48	1003	32	7930	89	31589	178	2142	46	1504	39	579	24
B-3	488	2200	47	996	32	8156	90	31508	178	2222	47	1477	38	593	24
B-3	489	2230	47	1017	32	8280	91	31579	178	2233	47	1487	39	594	24
B-3	490	2333	48	1023	32	8374	92	31414	177	2241	47	1433	38	626	25
B-3	491	2243	47	1071	33	8369	91	31350	177	2289	48	1492	39	572	24
B-3	492	2345	48	1030	32	8192	91	31569	178	2201	47	1525	39	563	24
B-3	493	2326	48	989	31	8271	91	31512	178	2181	47	1505	39	603	25
B-3	494	2405	49	1010	32	8327	91	31588	178	2230	47	1454	38	594	24
B-3	495	2246	47	985	31	8568	93	31496	177	2214	47	1517	39	566	24
B-3	496	2333	48	1010	32	8311	91	31383	177	2179	47	1438	38	604	25
B-3	497	2350	48	1035	32	8328	91	31109	176	2179	47	1473	38	596	24
B-3	498	2258	48	1038	32	8442	92	31333	177	2265	48	1485	39	584	24
B-3	499	2238	47	1016	32	8399	92	31619	178	2261	48	1542	39	622	25
B-3	500	2339	48	1039	32	8615	93	31352	177	2132	46	1480	38	607	25
B-3	501	2244	47	939	31	8559	93	31355	177	2245	47	1464	38	597	24
B-3	502	2215	47	977	31	8390	92	31321	177	2221	47	1492	39	555	24
B-3	503	2245	47	956	31	8313	91	31524	178	2192	47	1500	39	632	25
B-3	504	2296	48	1044	32	8374	92	31405	177	2125	46	1504	39	602	25
B-3	505	2317	48	952	31	8321	91	31568	178	2108	46	1412	38	573	24
B-3	506	2226	47	1040	32	8447	92	30884	176	2174	47	1556	39	564	24
B-3	507	2261	48	1028	32	8502	92	31316	177	2167	47	1494	39	600	24
B-3	508	2369	49	1040	32	8290	91	31555	178	2111	46	1461	38	611	25
B-3	509	2270	48	1013	32	8573	93	31440	177	2118	46	1534	39	601	25
B-3	510	2279	48	1041	32	8442	92	31378	177	2161	46	1539	39	592	24
B-3	511	2290	48	988	31	8419	92	31116	176	2092	46	1475	38	581	24
B-3	512	2272	48	1008	32	8619	93	31290	177	2171	47	1491	39	634	25
B-3	513	2281	48	1014	32	8614	93	31577	178	2216	47	1455	38	546	23
B-3	514	2234	47	1016	32	8281	91	31482	177	2128	46	1463	38	606	25
B-3	515	2201	47	1022	32	8460	92	31164	177	2190	47	1503	39	619	25
B-3	516	2364	49	1050	32	8510	92	31183	177	2193	47	1474	38	587	24
B-3	517	2296	48	1030	32	8633	93	31301	177	2199	47	1450	38	576	24
B-3	518	2176	47	1013	32	8511	92	31001	176	2193	47	1473	38	626	25
B-3	519	2299	48	980	31	8746	94	31247	177	2193	47	1400	37	590	24
B-3	520	2227	47	1050	32	8386	92	31581	178	2172	47	1459	38	580	24
B-3	521	2245	47	981	31	8402	92	31660	178	2115	46	1425	38	596	24
B-3	522	2235	47	1036	32	8439	92	31364	177	2201	47	1404	37	588	24
B-3	523	2255	47	995	32	8233	91	31566	178	2129	46	1452	38	610	25
B-3	524	2222	47	1002	32	8229	91	31654	178	2136	46	1508	39	591	24
B-3	525	2211	47	977	31	8298	91	31319	177	2178	47	1476	38	583	24
B-3	526	2196	47	1034	32	8277	91	31541	178	2177	47	1378	37	600	24
B-3	527	2170	47	1038	32	8172	90	31673	178	2188	47	1452	38	602	25
B-3	528	2251	47	1052	32	8236	91	31573	178	2132	46	1515	39	607	25
B-3	529	2161	46	963	31	8235	91	31564	178	2151	46	1476	38	614	25
B-3	530	2187	47	1012	32	8523	92	31642	178	2050	45	1392	37	541	23
B-3	531	2239	47	975	31	8412	92	31218	177	2119	46	1482	39	587	24
B-3	532	2318	48	995	32	8154	90	31765	178	2124	46	1406	38	609	25
B-3	533	2114	46	1030	32	8425	92	31214	177	2120	46	1508	39	587	24
B-3	534	2126	46	1046	32	8321	91	31322	177	2115	46	1414	38	575	24
B-3	535	2216	47	1029	32	8371	91	31358	177	2101	46	1535	39	591	24
B-3	536	2321	48	965	31	8363	91	31455	177	2153	46	1523	39	615	25
B-3	537	2333	48	982	31	8283	91	31345	177	2148	46	1518	39	598	24
B-3	538	2264	48	1073	33	8159	90	31305	177	2118	46	1474	38	627	25
B-3	539	2182	47	986	31	8380	92	31320	177	2153	46	1476	38	615	25

B-3	540	2199	47	984	31	8423	92	31150	176	2144	46	1376	37	613	25
B-3	541	2294	48	1003	32	8234	91	31385	177	2150	46	1463	38	617	25
B-3	542	2220	47	1019	32	8318	91	31453	177	2144	46	1516	39	617	25
B-3	543	2239	47	1059	33	8225	91	31597	178	2119	46	1470	38	605	25
B-3	544	2271	48	1051	32	8250	91	31386	177	2168	47	1486	39	600	24
B-3	545	2231	47	1022	32	8169	90	31376	177	2126	46	1549	39	541	23
B-3	546	2183	47	1053	32	8025	90	31629	178	2121	46	1491	39	609	25
B-3	547	2228	47	1054	32	8169	90	31486	177	2106	46	1566	40	622	25
B-3	548	2262	48	1008	32	8302	91	31720	178	2071	46	1501	39	582	24
B-3	549	2237	47	939	31	8189	90	31461	177	2213	47	1444	38	636	25
B-3	550	2164	47	950	31	8155	90	31741	178	2075	46	1449	38	586	24
B-3	551	2223	47	1009	32	8122	90	31319	177	2142	46	1502	39	649	25
B-3	552	2249	47	995	32	8191	91	31320	177	2092	46	1437	38	593	24
B-3	553	2182	47	1008	32	8130	90	31409	177	2156	46	1509	39	667	26
B-3	554	2301	48	1028	32	8107	90	31604	178	2179	47	1449	38	559	24
B-3	555	2227	47	980	31	8186	90	31802	178	2190	47	1457	38	634	25
B-3	556	2130	46	1013	32	8166	90	31660	178	2125	46	1412	38	597	24
B-3	557	2258	48	969	31	7977	89	31644	178	2120	46	1445	38	616	25
B-3	558	2194	47	996	32	7900	89	31770	178	2135	46	1416	38	594	24
B-3	559	2280	48	928	30	7652	87	32066	179	2185	47	1412	38	586	24
B-3	560	2190	47	985	31	7621	87	32125	179	2143	46	1327	36	583	24
B-3	561	2124	46	997	32	7504	87	32245	180	2223	47	1362	37	577	24
B-3	562	2061	45	988	31	7400	86	32147	179	2195	47	1350	37	614	25
B-3	563	2137	46	1015	32	7341	86	32578	180	2065	45	1286	36	619	25
B-3	564	2066	45	1001	32	7305	85	32796	181	2168	47	1372	37	558	24
B-3	565	2210	47	987	31	7394	86	32519	180	2099	46	1295	36	579	24
B-3	566	2188	47	974	31	7584	87	32323	180	2189	47	1378	37	583	24
B-3	567	2167	47	1005	32	7773	88	32326	180	2139	46	1330	36	602	25
B-3	568	2217	47	990	31	7795	88	31970	179	2229	47	1379	37	618	25
B-3	569	2291	48	1038	32	7649	87	31785	178	2171	47	1388	37	616	25
B-3	570	2292	48	1029	32	7884	89	31665	178	2193	47	1409	38	651	26
B-3	571	2157	46	1064	33	7714	88	31841	178	2247	47	1405	37	644	25
B-3	572	2180	47	1002	32	7788	88	31662	178	2213	47	1453	38	624	25
B-3	573	2250	47	959	31	7818	88	31918	179	2228	47	1409	38	583	24
B-3	574	2167	47	977	31	7834	89	31569	178	2312	48	1469	38	633	25
B-3	575	2288	48	1071	33	7628	87	32012	179	2265	48	1394	37	588	24
B-3	576	2188	47	981	31	7678	88	32320	180	2310	48	1392	37	607	25
B-3	577	2321	48	1009	32	7548	87	32029	179	2210	47	1417	38	591	24
B-3	578	2315	48	1020	32	7471	86	32393	180	2098	46	1348	37	589	24
B-3	579	2162	47	986	31	7442	86	32307	180	2261	48	1409	38	588	24
B-3	580	2214	47	1085	33	7244	85	32120	179	2347	48	1443	38	644	25
B-3	581	2084	46	1036	32	7285	85	32059	179	2212	47	1412	38	651	26
B-3	582	2165	47	1070	33	7395	86	32207	179	2224	47	1448	38	672	26
B-3	583	2299	48	971	31	7377	86	32019	179	2276	48	1392	37	615	25
B-3	584	2190	47	1010	32	7371	86	32589	181	2288	48	1304	36	562	24
B-3	585	2215	47	951	31	7430	86	32186	179	2221	47	1232	35	576	24
B-3	586	2214	47	1002	32	7495	87	32488	180	2216	47	1339	37	590	24
B-3	587	2232	47	1045	32	7640	87	32160	179	2258	48	1215	35	570	24
B-3	588	2204	47	989	31	7624	87	32452	180	2179	47	1270	36	582	24
B-3	589	2219	47	1036	32	7404	86	32453	180	2203	47	1242	35	583	24
B-3	590	2206	47	935	31	7491	87	32238	180	2196	47	1172	34	626	25
B-3	591	2139	46	986	31	7401	86	32141	179	2303	48	1203	35	567	24
B-3	592	2256	48	1010	32	7405	86	32690	181	2221	47	1205	35	552	23
B-3	593	2226	47	960	31	7258	85	32592	181	2221	47	1164	34	584	24
B-3	594	2192	47	997	32	7285	85	32588	181	2145	46	1231	35	588	24
B-3	595	2204	47	996	32	7432	86	31972	179	2255	47	1199	35	572	24
B-3	596	2199	47	973	31	7602	87	31729	178	2281	48	1185	34	568	24
B-3	597	2233	47	992	32	7450	86	32064	179	2270	48	1187	34	612	25
B-3	598	2217	47	937	31	7276	85	32357	180	2253	47	1171	34	606	25
B-3	599	2161	46	928	30	7329	86	32502	180	2255	47	1157	34	560	24
B-3	600	2212	47	936	31	7339	86	32268	180	2260	48	1208	35	616	25
B-3	601	2203	47	911	30	7186	85	32745	181	2276	48	1231	35	594	24
B-3	602	2236	47	935	31	7341	86	32280	180	2270	48	1217	35	611	25

B-3	603	2213	47	927	30	7134	84	32323	180	2251	47	1172	34	603	25
B-3	604	2257	48	933	31	7191	85	32229	180	2268	48	1136	34	587	24
B-3	605	2240	47	985	31	7375	86	32374	180	2248	47	1126	34	570	24
B-3	606	2225	47	965	31	7340	86	32408	180	2237	47	1215	35	537	23
B-3	607	2224	47	929	30	7402	86	31937	179	2271	48	1178	34	604	25
B-3	608	2393	49	948	31	7354	86	32397	180	2369	49	1180	34	590	24
C-1	1	5840	76	2302	48	13095	114	58173	241	4856	70	2700	52	1278	36
C-1	2	5662	75	2288	48	13208	115	59332	244	5121	72	2753	52	1291	36
C-1	3	5759	76	2269	48	13407	116	60197	245	5165	72	2750	52	1228	35
C-1	4	5665	75	2185	47	13483	116	60982	247	4993	71	2695	52	1184	34
C-1	5	5584	75	2196	47	13328	115	61629	248	5126	72	2663	52	1254	35
C-1	6	5482	74	2163	47	13572	117	61864	249	5006	71	2647	51	1210	35
C-1	7	5488	74	2120	46	13523	116	61993	249	5100	71	2571	51	1188	34
C-1	8	5243	72	2158	46	13491	116	62475	250	5112	72	2393	49	1171	34
C-1	9	5355	73	2163	47	13950	118	63234	251	5163	72	2501	50	1140	34
C-1	10	5255	72	2085	46	14002	118	62313	250	5210	72	2460	50	1197	35
C-1	11	5186	72	2115	46	14190	119	62882	251	5097	71	2414	49	1121	33
C-1	12	5260	73	2082	46	14299	120	63007	251	5223	72	2382	49	1171	34
C-1	13	5302	73	2050	45	14403	120	62750	251	5236	72	2400	49	1142	34
C-1	14	5152	72	2059	45	14633	121	62782	251	5229	72	2472	50	1219	35
C-1	15	5220	72	1954	44	14910	122	62546	250	5321	73	2403	49	1237	35
C-1	16	5115	72	2103	46	15032	123	63009	251	5142	72	2433	49	1185	34
C-1	17	5207	72	2042	45	15273	124	63142	251	5240	72	2466	50	1149	34
C-1	18	5125	72	2081	46	15444	124	63216	251	5194	72	2467	50	1152	34
C-1	19	5132	72	2052	45	15354	124	63386	252	5164	72	2471	50	1152	34
C-1	20	5074	71	2106	46	15605	125	63260	252	5256	73	2451	50	1133	34
C-1	21	5080	71	2033	45	15678	125	63336	252	5211	72	2471	50	1173	34
C-1	22	5020	71	2088	46	15618	125	63301	252	5202	72	2429	49	1124	34
C-1	23	4838	70	2115	46	15843	126	62915	251	5287	73	2483	50	1154	34
C-1	24	5104	71	2062	45	15927	126	62958	251	5320	73	2457	50	1173	34
C-1	25	4919	70	2067	45	15954	126	63044	251	5187	72	2411	49	1136	34
C-1	26	4778	69	2020	45	15866	126	63236	251	5174	72	2534	50	1145	34
C-1	27	4847	70	2048	45	16050	127	63621	252	5156	72	2376	49	1110	33
C-1	28	4877	70	2042	45	16054	127	63491	252	5167	72	2506	50	1195	35
C-1	29	4754	69	2036	45	15937	126	63419	252	5097	71	2546	50	1176	34
C-1	30	4776	69	2063	45	16038	127	63301	252	4996	71	2525	50	1168	34
C-1	31	4774	69	2064	45	15953	126	63394	252	4998	71	2503	50	1166	34
C-1	32	4705	69	2035	45	16172	127	63738	252	4953	70	2569	51	1188	34
C-1	33	4731	69	2064	45	16264	128	63984	253	5086	71	2574	51	1159	34
C-1	34	4795	69	2110	46	16147	127	63688	252	5047	71	2506	50	1168	34
C-1	35	4817	69	2073	46	16137	127	63433	252	4987	71	2516	50	1224	35
C-1	36	4639	68	2105	46	16110	127	63853	253	5012	71	2451	50	1222	35
C-1	37	4660	68	2143	46	15934	126	64145	253	4882	70	2428	49	1255	35
C-1	38	4707	69	2116	46	15924	126	64141	253	4921	70	2491	50	1207	35
C-1	39	4678	68	2116	46	16227	127	63794	253	4968	70	2484	50	1163	34
C-1	40	4546	67	2118	46	16169	127	63952	253	4869	70	2561	51	1174	34
C-1	41	4600	68	2094	46	16184	127	63894	253	4919	70	2474	50	1244	35
C-1	42	4596	68	2033	45	16166	127	63845	253	4993	71	2519	50	1228	35
C-1	43	4554	67	2107	46	16154	127	63971	253	4998	71	2598	51	1253	35
C-1	44	4579	68	2043	45	16269	128	64390	254	4841	70	2562	51	1211	35
C-1	45	4540	67	2103	46	16306	128	63913	253	4763	69	2599	51	1216	35
C-1	46	4574	68	2149	46	16267	128	64194	253	4929	70	2470	50	1177	34
C-1	47	4476	67	2103	46	16180	127	63994	253	4787	69	2500	50	1220	35
C-1	48	4627	68	2044	45	16023	127	64367	254	4799	69	2389	49	1198	35
C-1	49	4405	66	2063	45	16341	128	64425	254	4616	68	2607	51	1321	36
C-1	50	4550	67	2076	46	16533	129	64540	254	4791	69	2485	50	1235	35
C-1	51	4469	67	2100	46	16097	127	64352	254	4781	69	2541	50	1250	35
C-1	52	4476	67	2039	45	16088	127	64525	254	4800	69	2558	51	1196	35
C-1	53	4529	67	2055	45	16240	127	64416	254	4644	68	2538	50	1220	35
C-1	54	4461	67	2115	46	16068	127	64328	254	4777	69	2552	51	1230	35
C-1	55	4405	66	2058	45	16126	127	64381	254	4865	70	2512	50	1261	36
C-1	56	4319	66	2073	46	15994	126	64751	254	4708	69	2444	49	1225	35
C-1	57	4432	67	2012	45	16226	127	64939	255	4706	69	2560	51	1187	34

C-1	58	4475	67	2094	46	16161	127	64799	255	4665	68	2565	51	1216	35
C-1	59	4464	67	2097	46	16041	127	64522	254	4641	68	2582	51	1176	34
C-1	60	4399	66	2015	45	16134	127	65011	255	4762	69	2530	50	1203	35
C-1	61	4481	67	2081	46	16279	128	65221	255	4573	68	2592	51	1256	35
C-1	62	4510	67	2123	46	16046	127	64665	254	4510	67	2546	50	1226	35
C-1	63	4255	65	2071	46	16228	127	65025	255	4522	67	2563	51	1215	35
C-1	64	4400	66	2081	46	16205	127	65255	255	4493	67	2624	51	1246	35
C-1	65	4368	66	2015	45	16253	127	64710	254	4517	67	2590	51	1180	34
C-1	66	4423	67	2131	46	16250	127	65116	255	4491	67	2540	50	1235	35
C-1	67	4284	65	2078	46	16264	128	64892	255	4637	68	2560	51	1225	35
C-1	68	4319	66	2088	46	15973	126	65056	255	4693	69	2483	50	1209	35
C-1	69	4352	66	2076	46	16137	127	64620	254	4453	67	2604	51	1198	35
C-1	70	4242	65	2164	47	16261	128	64937	255	4377	66	2629	51	1226	35
C-1	71	4322	66	2174	47	16289	128	64612	254	4619	68	2734	52	1228	35
C-1	72	4347	66	2161	46	16119	127	65236	255	4427	67	2670	52	1181	34
C-1	73	4285	65	2161	46	16468	128	65257	255	4551	67	2607	51	1202	35
C-1	74	4308	66	2023	45	16080	127	64730	254	4531	67	2655	52	1190	35
C-1	75	4384	66	2085	46	16176	127	64961	255	4433	67	2646	51	1167	34
C-1	76	4334	66	2034	45	16363	128	64778	255	4517	67	2664	52	1267	36
C-1	77	4388	66	2099	46	16466	128	64664	254	4527	67	2682	52	1201	35
C-1	78	4413	66	2151	46	16497	128	64712	254	4388	66	2562	51	1308	36
C-1	79	4318	66	2080	46	16212	127	64597	254	4564	68	2635	51	1250	35
C-1	80	4245	65	2146	46	16141	127	64695	254	4445	67	2650	51	1264	36
C-1	81	4308	66	2207	47	16711	129	64850	255	4522	67	2665	52	1232	35
C-1	82	4354	66	2043	45	16379	128	64628	254	4611	68	2666	52	1274	36
C-1	83	4359	66	2126	46	16534	129	64704	254	4492	67	2721	52	1226	35
C-1	84	4393	66	2070	46	16529	129	64543	254	4532	67	2730	52	1230	35
C-1	85	4379	66	2079	46	16510	128	64350	254	4402	66	2758	53	1211	35
C-1	86	4215	65	2122	46	16765	129	64839	255	4417	66	2683	52	1209	35
C-1	87	4252	65	2096	46	16332	128	64573	254	4449	67	2766	53	1202	35
C-1	88	4376	66	2022	45	16506	128	64508	254	4453	67	2748	52	1168	34
C-1	89	4262	65	2028	45	16653	129	64324	254	4476	67	2684	52	1221	35
C-1	90	4256	65	2126	46	16587	129	64721	254	4534	67	2817	53	1275	36
C-1	91	4270	65	2133	46	16749	129	64749	254	4437	67	2890	54	1267	36
C-1	92	4259	65	2083	46	16834	130	64384	254	4486	67	2728	52	1243	35
C-1	93	4140	64	2098	46	16709	129	64402	254	4340	66	2800	53	1307	36
C-1	94	4278	65	2059	45	16776	130	64705	254	4308	66	2751	52	1255	35
C-1	95	4271	65	2115	46	16815	130	64375	254	4414	66	2842	53	1208	35
C-1	96	4351	66	2134	46	16694	129	64140	253	4473	67	2805	53	1239	35
C-1	97	4296	66	2064	45	16922	130	64755	254	4372	66	2820	53	1279	36
C-1	98	4326	66	2098	46	16792	130	64219	253	4221	65	2841	53	1304	36
C-1	99	4344	66	2051	45	16631	129	64386	254	4363	66	2734	52	1215	35
C-1	100	4342	66	2127	46	16911	130	64581	254	4434	67	2760	53	1205	35
C-1	101	4258	65	2012	45	16942	130	64146	253	4307	66	2812	53	1249	35
C-1	102	4233	65	2118	46	16726	129	64132	253	4465	67	2969	54	1193	35
C-1	103	4277	65	2157	46	17010	130	64034	253	4425	67	2819	53	1279	36
C-1	104	4299	66	2112	46	16814	130	63791	253	4399	66	2823	53	1244	35
C-1	105	4236	65	2143	46	16940	130	64609	254	4437	67	2832	53	1181	34
C-1	106	4143	64	2105	46	17025	130	64172	253	4404	66	2824	53	1208	35
C-1	107	4208	65	2130	46	16712	129	64644	254	4491	67	2804	53	1202	35
C-1	108	4362	66	2067	45	17016	130	64346	254	4361	66	2739	52	1196	35
C-1	109	4298	66	2136	46	16864	130	64082	253	4387	66	2862	54	1264	36
C-1	110	4301	66	2031	45	16813	130	64371	254	4351	66	2808	53	1210	35
C-1	111	4160	65	2134	46	16936	130	64940	255	4420	66	2768	53	1256	35
C-1	112	4332	66	2191	47	16890	130	64584	254	4476	67	2852	53	1181	34
C-1	113	4265	65	2159	46	16945	130	64276	254	4423	67	2769	53	1325	36
C-1	114	4155	64	2051	45	16961	130	64124	253	4471	67	2740	52	1291	36
C-1	115	4351	66	2074	46	17071	131	64421	254	4458	67	2914	54	1244	35
C-1	116	4287	65	2115	46	17104	131	63701	252	4476	67	2831	53	1207	35
C-1	117	4408	66	2142	46	17113	131	64377	254	4310	66	2919	54	1229	35
C-1	118	4298	66	2159	46	17194	131	63905	253	4454	67	2923	54	1219	35
C-1	119	4466	67	2132	46	17317	132	64015	253	4494	67	2898	54	1322	36
C-1	120	4325	66	2232	47	17259	131	64034	253	4408	66	2825	53	1231	35

C-1	121	4147	64	2042	45	17194	131	63768	253	4443	67	2906	54	1259	35
C-1	122	4302	66	2178	47	17298	132	63847	253	4346	66	3018	55	1339	37
C-1	123	4332	66	2255	47	17581	133	64363	254	4456	67	2917	54	1238	35
C-1	124	4287	65	2077	46	17444	132	63784	253	4429	67	2904	54	1243	35
C-1	125	4235	65	2088	46	17420	132	63473	252	4475	67	2746	52	1321	36
C-1	126	4412	66	2151	46	17210	131	63910	253	4320	66	2920	54	1293	36
C-1	127	4470	67	2181	47	17432	132	63753	252	4395	66	2966	54	1226	35
C-1	128	4359	66	2137	46	17470	132	63194	251	4443	67	2880	54	1318	36
C-1	129	4459	67	2096	46	17725	133	63313	252	4429	67	2812	53	1268	36
C-1	130	4365	66	2143	46	17560	133	63245	251	4443	67	2946	54	1275	36
C-1	131	4376	66	2236	47	17583	133	62981	251	4363	66	2841	53	1275	36
C-1	132	4391	66	2113	46	17430	132	63326	252	4513	67	2924	54	1278	36
C-1	133	4343	66	2210	47	17625	133	63460	252	4398	66	2894	54	1314	36
C-1	134	4304	66	2079	46	17744	133	63615	252	4506	67	2864	54	1275	36
C-1	135	4392	66	2159	46	17474	132	63014	251	4652	68	2897	54	1263	36
C-1	136	4327	66	2144	46	17648	133	63110	251	4481	67	2918	54	1303	36
C-1	137	4358	66	2132	46	17525	132	63322	252	4506	67	2887	54	1304	36
C-1	138	4219	65	2197	47	17472	132	63923	253	4632	68	2828	53	1296	36
C-1	139	4277	65	2134	46	17445	132	63413	252	4374	66	2900	54	1264	36
C-1	140	4333	66	2193	47	17243	131	63676	252	4506	67	2746	52	1344	37
C-1	141	4270	65	2113	46	17103	131	64307	254	4541	67	2774	53	1286	36
C-1	142	4320	66	2052	45	17095	131	64039	253	4504	67	2719	52	1250	35
C-1	143	4352	66	2222	47	17158	131	64197	253	4600	68	2818	53	1310	36
C-1	144	4332	66	2126	46	17080	131	63527	252	4514	67	2753	52	1232	35
C-1	145	4251	65	2212	47	17265	131	64193	253	4603	68	2858	53	1266	36
C-1	146	4290	66	2095	46	16707	129	64224	253	4579	68	2790	53	1269	36
C-1	147	4390	66	2180	47	16798	130	64611	254	4511	67	2741	52	1236	35
C-1	148	4262	65	2165	47	16917	130	64903	255	4496	67	2663	52	1275	36
C-1	149	4271	65	2122	46	16650	129	64355	254	4648	68	2630	51	1177	34
C-1	150	4283	65	2099	46	16436	128	64108	253	4581	68	2679	52	1296	36
C-1	151	4288	65	2049	45	16546	129	64755	254	4741	69	2623	51	1293	36
C-1	152	4260	65	2088	46	16470	128	65055	255	4627	68	2651	51	1215	35
C-1	153	4255	65	2147	46	16721	129	64633	254	4750	69	2506	50	1258	35
C-1	154	4364	66	2110	46	16307	128	64848	255	4643	68	2747	52	1229	35
C-1	155	4305	66	2229	47	16396	128	64357	254	4708	69	2677	52	1288	36
C-1	156	4304	66	2137	46	16165	127	64452	254	4846	70	2611	51	1234	35
C-1	157	4458	67	2123	46	16337	128	64618	254	4616	68	2717	52	1228	35
C-1	158	4345	66	2117	46	16320	128	64751	254	4663	68	2632	51	1293	36
C-1	159	4426	67	2178	47	16371	128	64925	255	4720	69	2620	51	1195	35
C-1	160	4428	67	2097	46	16215	127	64925	255	4666	68	2574	51	1279	36
C-1	161	4359	66	2142	46	16239	127	64876	255	4804	69	2627	51	1243	35
C-1	162	4360	66	2092	46	16207	127	64686	254	4767	69	2566	51	1203	35
C-1	163	4546	67	2176	47	16125	127	64795	255	4867	70	2601	51	1190	35
C-1	164	4336	66	2161	46	16136	127	64561	254	4935	70	2519	50	1213	35
C-1	165	4372	66	2072	46	16189	127	64858	255	4795	69	2591	51	1213	35
C-1	166	4495	67	1967	44	16186	127	65045	255	4873	70	2602	51	1182	34
C-1	167	4342	66	2036	45	16064	127	65066	255	4950	70	2531	50	1213	35
C-1	168	4410	66	2106	46	16089	127	64954	255	5033	71	2568	51	1200	35
C-1	169	4391	66	2095	46	16081	127	64914	255	5011	71	2632	51	1245	35
C-1	170	4416	66	2156	46	16048	127	64769	255	5119	72	2618	51	1189	34
C-1	171	4466	67	2162	47	15953	126	64667	254	5042	71	2514	50	1256	35
C-1	172	4502	67	2123	46	16100	127	64495	254	5023	71	2528	50	1183	34
C-1	173	4513	67	2111	46	15958	126	64768	255	5213	72	2628	51	1289	36
C-1	174	4630	68	2062	45	16117	127	65228	255	5158	72	2536	50	1259	35
C-1	175	4493	67	2073	46	15837	126	64854	255	5362	73	2359	49	1255	35
C-1	176	4603	68	2058	45	16102	127	64753	254	5204	72	2533	50	1202	35
C-1	177	4639	68	2118	46	15776	126	64872	255	5159	72	2434	49	1214	35
C-1	178	4500	67	2089	46	16234	127	64744	254	5268	73	2505	50	1215	35
C-1	179	4651	68	2073	46	16052	127	64498	254	5332	73	2567	51	1161	34
C-1	180	4661	68	2076	46	16067	127	64434	254	5390	73	2495	50	1234	35
C-1	181	4828	69	2150	46	16048	127	64334	254	5413	74	2424	49	1159	34
C-1	182	4829	69	2047	45	15713	125	65354	256	5368	73	2527	50	1177	34
C-1	183	4770	69	2071	46	15947	126	64322	254	5464	74	2475	50	1198	35

C-1	184	4858	70	2054	45	15919	126	64494	254	5543	74	2475	50	1208	35
C-1	185	4948	70	2001	45	15925	126	64550	254	5541	74	2540	50	1231	35
C-1	186	5014	71	2043	45	15960	126	64484	254	5709	76	2454	50	1239	35
C-1	187	4957	70	1996	45	15903	126	64477	254	5576	75	2495	50	1212	35
C-1	188	5074	71	2060	45	15535	125	65109	255	5713	76	2654	52	1195	35
C-1	189	5136	72	2028	45	15200	123	64500	254	5696	75	2449	49	1222	35
C-1	190	4976	71	2109	46	15106	123	64976	255	5758	76	2619	51	1258	35
C-1	191	5188	72	2059	45	14965	122	65335	256	5768	76	2596	51	1184	34
C-1	192	5116	72	2123	46	14523	121	64958	255	5685	75	2663	52	1271	36
C-1	193	5184	72	2123	46	14133	119	65115	255	5811	76	2536	50	1253	35
C-1	194	5450	74	2154	46	14294	120	65347	256	5756	76	2649	51	1283	36
C-1	195	5615	75	2035	45	14164	119	65057	255	5755	76	2596	51	1269	36
C-1	196	5697	75	2271	48	14232	119	65486	256	5790	76	2770	53	1323	36
C-1	197	5944	77	2202	47	13704	117	64667	254	5900	77	2717	52	1341	37
C-1	198	5926	77	2178	47	12572	112	65549	256	6032	78	2930	54	1478	38
C-1	199	5753	76	2146	46	9672	98	68454	262	5221	72	3204	57	1696	41
C-1	200	5652	75	2051	45	9351	97	69718	264	5314	73	2662	52	1379	37
C-1	201	5940	77	1872	43	10199	101	69903	264	5375	73	2538	50	1343	37
C-1	202	6056	78	1945	44	10297	101	68980	263	5477	74	2542	50	1283	36
C-1	203	6178	79	2023	45	11074	105	68421	262	5605	75	2461	50	1234	35
C-1	204	6427	80	1877	43	11960	109	67200	259	5771	76	2428	49	1219	35
C-1	205	6419	80	1887	43	12843	113	66602	258	5813	76	2389	49	1151	34
C-1	206	6634	81	1886	43	13506	116	65747	256	6032	78	2471	50	1100	33
C-1	207	6708	82	1851	43	13709	117	65149	255	5933	77	2356	49	1093	33
C-1	208	6408	80	1856	43	14077	119	65585	256	5999	77	2504	50	1088	33
C-1	209	6542	81	1885	43	13812	118	64832	255	6224	79	2424	49	1074	33
C-1	210	6541	81	1904	44	13983	118	65028	255	6009	78	2458	50	1144	34
C-1	211	6617	81	1859	43	13977	118	65496	256	6006	78	2287	48	1110	33
C-1	212	6506	81	1908	44	13924	118	64629	254	6011	78	2306	48	1077	33
C-1	213	6499	81	1880	43	14063	119	65303	256	6093	78	2326	48	1096	33
C-1	214	6419	80	1897	44	14037	118	65219	255	6128	78	2380	49	1114	33
C-1	215	6400	80	1836	43	14239	119	64719	254	6061	78	2367	49	1104	33
C-1	216	6526	81	1978	44	14155	119	65214	255	5943	77	2439	49	1139	34
C-1	217	6372	80	1961	44	14229	119	65117	255	6022	78	2359	49	1091	33
C-1	218	6404	80	1814	43	14335	120	64318	254	5912	77	2359	49	1077	33
C-2	1	3990	63	1903	44	12526	112	62825	251	3873	62	1953	44	972	31
C-2	2	3866	62	1910	44	12853	113	63224	251	3861	62	2129	46	1008	32
C-2	3	3789	62	1849	43	13032	114	64262	254	3861	62	2260	48	977	31
C-2	4	3848	62	1970	44	13121	115	63625	252	3725	61	2341	48	1039	32
C-2	5	3762	61	1938	44	13478	116	64016	253	3796	62	2495	50	1048	32
C-2	6	3709	61	1967	44	13712	117	64065	253	3787	62	2617	51	1108	33
C-2	7	3816	62	1957	44	13720	117	63767	253	3745	61	2642	51	1157	34
C-2	8	3733	61	1954	44	14119	119	64014	253	3843	62	2631	51	1109	33
C-2	9	3703	61	1969	44	13968	118	64123	253	3728	61	2655	52	1127	34
C-2	10	3812	62	1871	43	14209	119	64069	253	3916	63	2703	52	1160	34
C-2	11	3812	62	1991	45	14398	120	63982	253	3762	61	2713	52	1095	33
C-2	12	3855	62	1967	44	14405	120	63918	253	3841	62	2760	53	1122	34
C-2	13	3798	62	1980	45	14685	121	64228	253	3750	61	2704	52	1099	33
C-2	14	3953	63	1991	45	14633	121	64447	254	3858	62	2853	53	1208	35
C-2	15	3845	62	2006	45	14587	121	64314	254	3855	62	2779	53	1189	34
C-2	16	3926	63	2022	45	14809	122	64651	254	3848	62	2715	52	1116	33
C-2	17	3817	62	1958	44	14808	122	64643	254	3909	63	2707	52	1200	35
C-2	18	3925	63	2068	45	14865	122	64485	254	3934	63	2785	53	1124	34
C-2	19	3912	63	2022	45	15019	123	64272	254	3835	62	2791	53	1210	35
C-2	20	3860	62	1937	44	14936	122	64483	254	4003	63	2767	53	1127	34
C-2	21	3834	62	1967	44	15080	123	64139	253	3879	62	2912	54	1164	34
C-2	22	3885	62	1958	44	15141	123	64377	254	3874	62	2881	54	1165	34
C-2	23	3982	63	2048	45	15273	124	64556	254	3881	62	2968	54	1185	34
C-2	24	3873	62	1983	45	15501	125	64442	254	4065	64	2936	54	1138	34
C-2	25	4031	63	2002	45	15382	124	64204	253	3943	63	2916	54	1199	35
C-2	26	3761	61	2098	46	15581	125	64369	254	3990	63	2982	55	1192	35
C-2	27	3941	63	1978	44	15578	125	63822	253	3938	63	2987	55	1171	34
C-2	28	3921	63	2044	45	15409	124	64406	254	3957	63	2889	54	1133	34

C-2	29	3955	63	2059	45	15650	125	64393	254	4043	64	2835	53	1139	34
C-2	30	3882	62	2078	46	16060	127	64104	253	4073	64	2880	54	1159	34
C-2	31	3885	62	2035	45	15894	126	64248	253	4067	64	2998	55	1203	35
C-2	32	3970	63	2012	45	15686	125	64080	253	3976	63	2977	55	1192	35
C-2	33	3921	63	1944	44	15896	126	64366	254	4008	63	2953	54	1166	34
C-2	34	3897	62	2002	45	15939	126	64491	254	4011	63	2928	54	1232	35
C-2	35	3975	63	2033	45	15781	126	64485	254	3931	63	2970	55	1194	35
C-2	36	3923	63	2084	46	16144	127	64564	254	3958	63	2998	55	1216	35
C-2	37	3990	63	2077	46	15962	126	64328	254	4016	63	2956	54	1171	34
C-2	38	3979	63	2053	45	15851	126	63702	252	4040	64	2955	54	1164	34
C-2	39	3946	63	2113	46	16027	127	64311	254	3999	63	2979	55	1196	35
C-2	40	3867	62	2056	45	15940	126	64154	253	4020	63	2957	54	1239	35
C-2	41	3858	62	2095	46	16281	128	64505	254	3951	63	2971	55	1188	34
C-2	42	3966	63	1977	44	16117	127	64320	254	3970	63	3003	55	1188	34
C-2	43	4034	64	2028	45	15955	126	63962	253	3994	63	2979	55	1305	36
C-2	44	3937	63	2031	45	15780	126	64191	253	4066	64	3036	55	1184	34
C-2	45	3986	63	1973	44	15887	126	64751	254	3938	63	3003	55	1151	34
C-2	46	3968	63	2012	45	16156	127	64664	254	4081	64	3018	55	1226	35
C-2	47	3922	63	2074	46	15842	126	64605	254	3968	63	2953	54	1129	34
C-2	48	3832	62	2053	45	16006	127	64880	255	3917	63	2964	54	1203	35
C-2	49	3962	63	2154	46	15971	126	64688	254	3973	63	2949	54	1217	35
C-2	50	3903	62	2072	46	15770	126	64967	255	4038	64	2887	54	1180	34
C-2	51	3983	63	1992	45	15741	125	65049	255	4064	64	3002	55	1222	35
C-2	52	3910	63	2126	46	15936	126	64929	255	3995	63	3058	55	1219	35
C-2	53	3979	63	2020	45	15755	126	64599	254	3974	63	2920	54	1158	34
C-2	54	3777	61	2043	45	15850	126	65275	255	3964	63	2837	53	1189	34
C-2	55	3878	62	2078	46	15482	124	65418	256	3949	63	3006	55	1245	35
C-2	56	3830	62	2067	45	15624	125	65047	255	4067	64	2970	55	1172	34
C-2	57	3848	62	2016	45	15787	126	65041	255	4060	64	2947	54	1175	34
C-2	58	3784	62	2025	45	15713	125	65412	256	4081	64	2951	54	1149	34
C-2	59	3914	63	2058	45	15637	125	64780	255	4041	64	2884	54	1174	34
C-2	60	3807	62	2046	45	15569	125	65238	255	3975	63	2948	54	1216	35
C-2	61	3858	62	2033	45	15658	125	65246	255	4063	64	2986	55	1203	35
C-2	62	3894	62	1998	45	15796	126	65281	256	3946	63	3034	55	1203	35
C-2	63	3866	62	2001	45	15687	125	65098	255	4000	63	2994	55	1213	35
C-2	64	3854	62	2025	45	15557	125	65363	256	4000	63	2873	54	1226	35
C-2	65	3938	63	2093	46	15625	125	65155	255	4035	64	2844	53	1246	35
C-2	66	3831	62	2049	45	15709	125	65455	256	4028	63	3017	55	1190	35
C-2	67	3837	62	1972	44	15705	125	64823	255	4004	63	2977	55	1173	34
C-2	68	3793	62	1978	44	15399	124	65784	256	3997	63	3029	55	1144	34
C-2	69	3714	61	1985	45	15583	125	65555	256	3981	63	2979	55	1219	35
C-2	70	3862	62	2015	45	15819	126	65704	256	3966	63	2962	54	1153	34
C-2	71	3871	62	2038	45	15917	126	65399	256	4013	63	2987	55	1207	35
C-2	72	3841	62	2030	45	15924	126	65380	256	3939	63	2940	54	1176	34
C-2	73	3917	63	2044	45	15725	125	65453	256	4024	63	2870	54	1171	34
C-2	74	3840	62	2097	46	15616	125	65038	255	4008	63	2966	54	1172	34
C-2	75	3876	62	2016	45	15679	125	65641	256	3990	63	2940	54	1266	36
C-2	76	3835	62	2069	45	15483	124	65084	255	4017	63	3010	55	1180	34
C-2	77	3875	62	2084	46	15622	125	65645	256	3923	63	2966	54	1259	35
C-2	78	3918	63	2067	45	15656	125	64872	255	4140	64	2995	55	1245	35
C-2	79	3826	62	2117	46	15500	125	65339	256	4043	64	2889	54	1187	34
C-2	80	3933	63	2102	46	15547	125	65176	255	4041	64	2905	54	1253	35
C-2	81	3854	62	2037	45	15617	125	65314	256	3989	63	2787	53	1091	33
C-2	82	3717	61	2014	45	15682	125	65578	256	4117	64	2933	54	1225	35
C-2	83	3855	62	2089	46	15462	124	65266	255	4046	64	2891	54	1183	34
C-2	84	3873	62	1968	44	15552	125	65053	255	3948	63	2899	54	1209	35
C-2	85	3854	62	2019	45	15409	124	64960	255	4050	64	2884	54	1155	34
C-2	86	3839	62	2095	46	15672	125	65697	256	4002	63	2933	54	1197	35
C-2	87	3898	62	2059	45	15721	125	65577	256	3953	63	2898	54	1229	35
C-2	88	3800	62	2003	45	15583	125	65173	255	3965	63	2956	54	1201	35
C-2	89	3974	63	1989	45	15685	125	65344	256	4091	64	2936	54	1201	35
C-2	90	3919	63	2029	45	15426	124	65527	256	3949	63	2973	55	1199	35
C-2	91	3817	62	2060	45	15761	126	65082	255	3983	63	2895	54	1187	34

C-2	92	3841	62	2084	46	15316	124	65842	257	4044	64	2905	54	1218	35
C-2	93	3756	61	2021	45	15353	124	65521	256	3960	63	2971	55	1172	34
C-2	94	3865	62	2018	45	15335	124	65600	256	3926	63	2907	54	1114	33
C-2	95	3868	62	2021	45	15336	124	65459	256	3978	63	2941	54	1202	35
C-2	96	3815	62	2033	45	15349	124	65654	256	3990	63	2934	54	1193	35
C-2	97	3742	61	2043	45	15507	125	65444	256	4002	63	2919	54	1232	35
C-2	98	3854	62	2048	45	15360	124	65592	256	4069	64	2934	54	1208	35
C-2	99	3887	62	2065	45	15254	124	65710	256	4005	63	2906	54	1236	35
C-2	100	3795	62	1964	44	15415	124	65907	257	3844	62	2858	53	1167	34
C-2	101	3917	63	2022	45	15256	124	65860	257	4001	63	2953	54	1183	34
C-2	102	3808	62	2017	45	15432	124	65653	256	4048	64	2936	54	1213	35
C-2	103	3766	61	2063	45	15389	124	65888	257	4135	64	2853	53	1201	35
C-2	104	3850	62	1992	45	15421	124	65821	257	4003	63	2954	54	1163	34
C-2	105	3856	62	2046	45	15403	124	65905	257	3982	63	2928	54	1181	34
C-2	106	3794	62	2032	45	15220	123	65739	256	4127	64	2893	54	1163	34
C-2	107	3822	62	2021	45	15443	124	65870	257	4118	64	2937	54	1161	34
C-2	108	3773	61	1947	44	15230	123	66082	257	4018	63	2863	54	1238	35
C-2	109	3795	62	2062	45	15215	123	65754	256	4125	64	2925	54	1186	34
C-2	110	3930	63	2015	45	15263	124	66051	257	3918	63	2890	54	1178	34
C-2	111	3707	61	2073	46	15438	124	65416	256	3930	63	2902	54	1192	35
C-2	112	3713	61	1969	44	15297	124	65493	256	4059	64	2874	54	1208	35
C-2	113	3739	61	2044	45	14979	122	66118	257	4067	64	2858	53	1138	34
C-2	114	3811	62	2048	45	15326	124	66068	257	3946	63	2918	54	1229	35
C-2	115	3700	61	1973	44	15073	123	65925	257	4027	63	2897	54	1163	34
C-2	116	3863	62	1984	45	15426	124	65673	256	3990	63	2927	54	1153	34
C-2	117	3741	61	2020	45	15239	123	66054	257	4011	63	2893	54	1141	34
C-2	118	3777	61	1972	44	15413	124	65858	257	3841	62	2789	53	1168	34
C-2	119	3889	62	1974	44	15440	124	65701	256	3971	63	2854	53	1157	34
C-2	120	3770	61	1934	44	15183	123	65721	256	4002	63	2954	54	1147	34
C-2	121	3878	62	1959	44	15157	123	66114	257	4059	64	2897	54	1184	34
C-2	122	3711	61	2009	45	15231	123	65540	256	4034	64	2850	53	1131	34
C-2	123	3807	62	2013	45	14973	122	66248	257	4055	64	2913	54	1220	35
C-2	124	3805	62	1963	44	15228	123	66293	257	4032	64	2859	53	1196	35
C-2	125	3839	62	1979	44	15142	123	65994	257	3914	63	2950	54	1228	35
C-2	126	3804	62	1928	44	15113	123	66446	258	4100	64	2843	53	1169	34
C-2	127	3788	62	1966	44	15184	123	65609	256	3979	63	2866	54	1220	35
C-2	128	3760	61	1916	44	14961	122	65556	256	3953	63	2842	53	1231	35
C-2	129	3857	62	2045	45	14938	122	65869	257	3950	63	2807	53	1165	34
C-2	130	3835	62	1998	45	15102	123	65791	257	4030	63	2953	54	1173	34
C-2	131	3673	61	1984	45	15165	123	66005	257	4043	64	2750	52	1155	34
C-2	132	3797	62	1962	44	15313	124	65761	256	4084	64	2823	53	1174	34
C-2	133	3808	62	2014	45	14699	121	65834	257	3891	62	2958	54	1246	35
C-2	134	3784	62	2000	45	15070	123	66151	257	4061	64	2848	53	1232	35
C-2	135	3846	62	2080	46	14789	122	65870	257	3933	63	2862	54	1194	35
C-2	136	3803	62	1944	44	15323	124	66256	257	4019	63	2923	54	1134	34
C-2	137	3751	61	2073	46	15000	122	66133	257	4139	64	2904	54	1180	34
C-2	138	3856	62	1959	44	15277	124	65688	256	3930	63	2862	54	1149	34
C-2	139	3792	62	2023	45	15282	124	65511	256	3979	63	2933	54	1175	34
C-2	140	3801	62	2049	45	15140	123	66175	257	3978	63	2804	53	1225	35
C-2	141	3735	61	2017	45	15168	123	65886	257	3974	63	2884	54	1220	35
C-2	142	3691	61	2010	45	15141	123	65961	257	4055	64	2789	53	1160	34
C-2	143	3795	62	1992	45	14911	122	65855	257	4011	63	2943	54	1195	35
C-2	144	3781	61	1979	44	15088	123	65912	257	4062	64	2946	54	1198	35
C-2	145	3711	61	2037	45	15292	124	65509	256	4095	64	2898	54	1179	34
C-2	146	3844	62	1959	44	15216	123	65683	256	4143	64	2908	54	1211	35
C-2	147	3810	62	1988	45	15366	124	65729	256	3918	63	2891	54	1203	35
C-2	148	3797	62	2054	45	15072	123	65914	257	3982	63	2830	53	1185	34
C-2	149	3933	63	2008	45	15181	123	65886	257	3965	63	2901	54	1091	33
C-2	150	3885	62	2041	45	15030	123	65944	257	4096	64	2852	53	1159	34
C-2	151	3697	61	2064	45	15256	124	65983	257	4067	64	2785	53	1169	34
C-2	152	3790	62	2080	46	15333	124	66015	257	4096	64	2910	54	1244	35
C-2	153	3830	62	1961	44	15213	123	65950	257	4021	63	2895	54	1210	35
C-2	154	3820	62	2015	45	15307	124	65697	256	3986	63	2881	54	1202	35

C-2	155	3715	61	1986	45	15290	124	65928	257	4039	64	2853	53	1184	34
C-2	156	3835	62	1972	44	14976	122	66118	257	4092	64	2853	53	1215	35
C-2	157	3827	62	2014	45	15195	123	65930	257	3953	63	2848	53	1160	34
C-2	158	3818	62	2026	45	14959	122	65591	256	4014	63	2836	53	1190	35
C-2	159	3770	61	2132	46	15308	124	65831	257	4077	64	2853	53	1172	34
C-2	160	3769	61	1950	44	15145	123	65726	256	4064	64	2868	54	1156	34
C-2	161	3780	61	2043	45	15078	123	65362	256	4140	64	2815	53	1202	35
C-2	162	3742	61	2050	45	15087	123	66145	257	3998	63	2775	53	1180	34
C-2	163	3824	62	1991	45	15155	123	66229	257	4108	64	2893	54	1206	35
C-2	164	3667	61	2027	45	15121	123	65787	256	3994	63	2875	54	1210	35
C-2	165	3807	62	2008	45	15178	123	65970	257	4077	64	2809	53	1190	35
C-2	166	3773	61	1966	44	14799	122	65913	257	4039	64	2837	53	1179	34
C-2	167	3794	62	1930	44	15041	123	66007	257	4027	63	2791	53	1226	35
C-2	168	3796	62	2012	45	15076	123	66060	257	4186	65	2832	53	1205	35
C-2	169	3659	60	1930	44	15109	123	65783	256	4111	64	2860	53	1165	34
C-2	170	3758	61	1999	45	15095	123	65697	256	3949	63	2859	53	1225	35
C-2	171	3828	62	2020	45	15007	123	65684	256	4062	64	2788	53	1189	34
C-2	172	3895	62	2045	45	15115	123	65855	257	4086	64	2910	54	1187	34
C-2	173	3817	62	2021	45	15034	123	65631	256	3943	63	2876	54	1164	34
C-2	174	3790	62	2033	45	15232	123	65894	257	3950	63	2793	53	1206	35
C-2	175	3795	62	2010	45	15141	123	65552	256	4013	63	2826	53	1210	35
C-2	176	3696	61	1999	45	15067	123	65834	257	4099	64	2801	53	1192	35
C-2	177	3745	61	1953	44	15123	123	65915	257	4078	64	2777	53	1219	35
C-2	178	3831	62	2012	45	14977	122	66224	257	4109	64	2809	53	1155	34
C-2	179	3873	62	1989	45	14918	122	66009	257	4137	64	2904	54	1203	35
C-2	180	3679	61	2008	45	14904	122	65437	256	4158	64	2862	54	1232	35
C-2	181	3835	62	1993	45	15004	122	66117	257	4006	63	2857	53	1198	35
C-2	182	3630	60	2037	45	14933	122	66164	257	4010	63	2900	54	1207	35
C-2	183	3732	61	2066	45	14603	121	66041	257	4167	65	2869	54	1140	34
C-2	184	3747	61	2020	45	14739	121	66074	257	3992	63	2820	53	1109	33
C-2	185	3751	61	1902	44	14740	121	66024	257	4084	64	2831	53	1194	35
C-2	186	3619	60	1972	44	14739	121	66399	258	4162	65	2812	53	1139	34
C-2	187	3633	60	1996	45	14538	121	66864	259	4032	64	2612	51	1191	35
C-2	188	3625	60	1921	44	14411	120	66652	258	4204	65	2802	53	1190	35
C-2	189	3522	59	2036	45	14069	119	66596	258	4100	64	2628	51	1109	33
C-2	190	3483	59	2054	45	13956	118	67545	260	4148	64	2565	51	1181	34
C-2	191	3623	60	1985	45	13705	117	67232	259	4282	65	2533	50	1106	33
C-2	192	3412	58	1918	44	13328	115	68150	261	4284	65	2420	49	1092	33
C-2	193	3597	60	1941	44	13099	114	68432	262	4345	66	2296	48	1079	33
C-2	194	3696	61	1928	44	12918	114	68387	262	4585	68	1959	44	1073	33
C-2	195	3822	62	1877	43	12831	113	68669	262	4927	70	1899	44	1069	33
C-2	196	4360	66	1887	43	12589	112	69048	263	5158	72	1884	43	981	31
C-2	197	4844	70	1821	43	11257	106	68746	262	5042	71	2246	47	1056	33
C-2	198	4982	71	1780	42	7649	87	71259	267	4567	68	2780	53	1555	39
C-2	199	4849	70	1690	41	7281	85	71271	267	4492	67	2398	49	1629	40
C-2	200	5016	71	1729	42	7802	88	71316	267	4735	69	2135	46	1593	40
C-2	201	5237	72	1644	41	9030	95	70015	265	4859	70	1912	44	1545	39
C-2	202	5434	74	1683	41	9960	100	69294	263	5089	71	1782	42	1457	38
C-2	203	5435	74	1794	42	10365	102	69212	263	5160	72	1791	42	1478	38
C-2	204	5453	74	1732	42	10577	103	69118	263	5112	72	1774	42	1532	39
C-2	205	5586	75	1693	41	11009	105	68103	261	5222	72	1773	42	1503	39
C-2	206	5669	75	1781	42	11028	105	68168	261	5251	72	1703	41	1457	38
C-2	207	5441	74	1738	42	11259	106	67971	261	5374	73	1690	41	1471	38
C-2	208	5472	74	1754	42	11782	109	67560	260	5468	74	1672	41	1407	38
C-2	209	5458	74	1647	41	11927	109	67314	259	5546	74	1699	41	1352	37
C-2	210	5339	73	1687	41	12462	112	66621	258	5557	75	1602	40	1360	37
C-2	211	5540	74	1567	40	12631	112	66807	258	5548	74	1596	40	1214	35
C-2	212	5476	74	1619	40	12835	113	66680	258	5574	75	1633	40	1257	35
C-2	213	5379	73	1626	40	13143	115	67116	259	5644	75	1636	40	1230	35
C-2	214	5341	73	1638	40	13072	114	66751	258	5613	75	1590	40	1281	36
C-2	215	5360	73	1647	41	12854	113	66827	259	5506	74	1540	39	1230	35
C-2	216	5245	72	1664	41	12384	111	67634	260	5380	73	1472	38	1257	35
C-2	217	5305	73	1569	40	12056	110	67391	260	5362	73	1550	39	1258	35

C-3	1	6468	80	2526	50	7811	88	35512	188	3482	59	2264	48	1029	32
C-3	2	8081	90	2226	47	10251	101	56537	238	5249	72	3001	55	1316	36
C-3	3	7552	87	2156	46	11180	106	61599	248	5624	75	3208	57	1311	36
C-3	4	7266	85	2224	47	11470	107	63200	251	5734	76	3296	57	1318	36
C-3	5	7151	85	2168	47	11781	109	63521	252	5679	75	3177	56	1308	36
C-3	6	6963	83	2134	46	11623	108	64695	254	5774	76	3009	55	1318	36
C-3	7	6882	83	2102	46	11690	108	64782	255	5773	76	2941	54	1260	36
C-3	8	6912	83	2194	47	12151	110	64839	255	5734	76	2902	54	1229	35
C-3	9	6881	83	2065	45	11890	109	64591	254	5712	76	2826	53	1179	34
C-3	10	6741	82	2103	46	12162	110	65380	256	5639	75	2768	53	1206	35
C-3	11	6460	80	2061	45	12387	111	65750	256	5724	76	2640	51	1113	33
C-3	12	6541	81	2015	45	12519	112	65580	256	5910	77	2601	51	1181	34
C-3	13	6482	81	1923	44	12716	113	66306	258	5888	77	2565	51	1076	33
C-3	14	6402	80	1929	44	12889	114	66014	257	5794	76	2475	50	1099	33
C-3	15	6305	79	1951	44	12911	114	66399	258	5863	77	2577	51	1053	32
C-3	16	6291	79	1902	44	13214	115	65995	257	5912	77	2464	50	1090	33
C-3	17	6121	78	1945	44	13404	116	65835	257	5887	77	2551	51	1046	32
C-3	18	6057	78	1952	44	13266	115	66112	257	5980	77	2419	49	1056	33
C-3	19	6123	78	1994	45	13515	116	66463	258	5987	77	2412	49	1053	32
C-3	20	6053	78	1983	45	13770	117	66152	257	5924	77	2422	49	1073	33
C-3	21	5944	77	1937	44	13896	118	66272	257	5798	76	2410	49	1038	32
C-3	22	5973	77	1932	44	13752	117	66171	257	5849	76	2343	48	1051	32
C-3	23	5921	77	1966	44	13951	118	66052	257	5991	77	2320	48	1077	33
C-3	24	6007	78	1980	45	14146	119	65791	257	6001	77	2397	49	1078	33
C-3	25	5936	77	1915	44	14165	119	66372	258	5871	77	2445	49	1008	32
C-3	26	5943	77	1999	45	14134	119	65998	257	6035	78	2365	49	1096	33
C-3	27	5787	76	1907	44	14410	120	65858	257	5998	77	2276	48	1111	33
C-3	28	5793	76	2002	45	14213	119	65935	257	6021	78	2314	48	1107	33
C-3	29	5845	76	2013	45	14329	120	65817	257	5982	77	2320	48	1025	32
C-3	30	5807	76	1949	44	14177	119	65985	257	5929	77	2319	48	1109	33
C-3	31	5718	76	1958	44	14381	120	66439	258	5965	77	2446	49	1091	33
C-3	32	5970	77	1939	44	14609	121	66020	257	6020	78	2363	49	1125	34
C-3	33	5735	76	1954	44	14230	119	66396	258	6035	78	2348	48	1067	33
C-3	34	5710	76	1956	44	14498	120	65655	256	6056	78	2395	49	1095	33
C-3	35	5713	76	1934	44	14539	121	66558	258	5951	77	2329	48	1109	33
C-3	36	5690	75	1845	43	14441	120	65852	257	5987	77	2411	49	1109	33
C-3	37	5759	76	1907	44	14553	121	65807	257	5904	77	2414	49	1062	33
C-3	38	5775	76	1993	45	14612	121	66053	257	5964	77	2514	50	1097	33
C-3	39	5623	75	1967	44	14397	120	66235	257	5987	77	2393	49	1108	33
C-3	40	5620	75	1893	44	14439	120	65938	257	5990	77	2273	48	1045	32
C-3	41	5724	76	1980	45	14645	121	66420	258	6000	77	2380	49	1059	33
C-3	42	5763	76	1999	45	14411	120	66630	258	5900	77	2400	49	1064	33
C-3	43	5634	75	1935	44	14504	120	66308	258	5947	77	2292	48	1108	33
C-3	44	5803	76	1911	44	14260	119	66292	257	5909	77	2415	49	1152	34
C-3	45	5674	75	1990	45	14396	120	67147	259	6034	78	2401	49	1107	33
C-3	46	5650	75	1953	44	14137	119	66643	258	5948	77	2438	49	1121	33
C-3	47	5575	75	1959	44	14336	120	66296	257	5978	77	2434	49	1085	33
C-3	48	5562	75	1965	44	14441	120	66045	257	6094	78	2355	49	1093	33
C-3	49	5656	75	2029	45	14561	121	66717	258	5905	77	2444	49	1160	34
C-3	50	5655	75	2007	45	14440	120	66601	258	6012	78	2323	48	1123	34
C-3	51	5665	75	2000	45	14454	120	67003	259	5873	77	2473	50	1090	33
C-3	52	5483	74	1959	44	14520	121	66767	258	5854	77	2433	49	1153	34
C-3	53	5712	76	1960	44	14374	120	66498	258	5960	77	2434	49	1113	33
C-3	54	5773	76	1875	43	14310	120	66071	257	5986	77	2466	50	1138	34
C-3	55	5827	76	1963	44	14295	120	66345	258	6038	78	2492	50	1078	33
C-3	56	5756	76	2006	45	14355	120	66749	258	5994	77	2439	49	1074	33
C-3	57	5903	77	2006	45	14226	119	66645	258	5942	77	2314	48	1088	33
C-3	58	5781	76	1961	44	14297	120	66903	259	6122	78	2487	50	1166	34
C-3	59	5861	77	2049	45	14056	119	66417	258	5902	77	2430	49	1159	34
C-3	60	5688	75	1962	44	13949	118	66630	258	6078	78	2508	50	1153	34
C-3	61	5776	76	2081	46	14227	119	66996	259	6060	78	2440	49	1137	34
C-3	62	5802	76	1939	44	13854	118	66828	259	5870	77	2506	50	1139	34
C-3	63	5944	77	2036	45	14097	119	66245	257	5873	77	2500	50	1114	33

C-3	64	5790	76	1962	44	13872	118	67123	259	6034	78	2624	51	1175	34
C-3	65	5881	77	1966	44	13902	118	66395	258	6240	79	2620	51	1165	34
C-3	66	5761	76	2011	45	13859	118	66573	258	5931	77	2538	50	1124	34
C-3	67	5864	77	2027	45	13702	117	66887	259	6124	78	2516	50	1176	34
C-3	68	5883	77	2032	45	13902	118	67190	259	5977	77	2584	51	1168	34
C-3	69	5882	77	1995	45	13643	117	67217	259	5979	77	2512	50	1142	34
C-3	70	5796	76	1958	44	13779	117	66917	259	6105	78	2560	51	1173	34
C-3	71	5831	76	2067	45	13819	118	67048	259	5960	77	2591	51	1126	34
C-3	72	5826	76	1953	44	13664	117	66711	258	5979	77	2670	52	1098	33
C-3	73	5862	77	2025	45	13729	117	67018	259	5980	77	2669	52	1238	35
C-3	74	5957	77	2018	45	13771	117	66910	259	6022	78	2707	52	1139	34
C-3	75	5874	77	1969	44	13748	117	66914	259	6001	77	2574	51	1150	34
C-3	76	5950	77	1993	45	13935	118	66944	259	5920	77	2593	51	1114	33
C-3	77	5929	77	1978	44	13972	118	66924	259	6065	78	2598	51	1074	33
C-3	78	5846	76	1982	45	13977	118	66849	259	5848	76	2652	52	1185	34
C-3	79	6049	78	1968	44	14025	118	66995	259	6006	78	2618	51	1128	34
C-3	80	5875	77	2006	45	14114	119	66828	259	6038	78	2565	51	1153	34
C-3	81	6031	78	2044	45	14026	118	66568	258	6024	78	2557	51	1154	34
C-3	82	5893	77	1943	44	13922	118	66981	259	6136	78	2546	50	1142	34
C-3	83	5978	77	1980	45	13969	118	66729	258	6156	78	2535	50	1130	34
C-3	84	6045	78	1990	45	13997	118	66719	258	5989	77	2522	50	1136	34
C-3	85	6010	78	1880	43	14385	120	66293	257	6098	78	2559	51	1100	33
C-3	86	6112	78	1979	44	14308	120	66544	258	6159	78	2512	50	1147	34
C-3	87	6056	78	2111	46	14286	120	66579	258	6042	78	2533	50	1160	34
C-3	88	6272	79	1976	44	14513	120	66662	258	6146	78	2518	50	1057	33
C-3	89	6164	79	1957	44	14399	120	66188	257	5987	77	2589	51	1146	34
C-3	90	6367	80	1985	45	14364	120	65942	257	6031	78	2635	51	1141	34
C-3	91	6230	79	1991	45	14359	120	65902	257	6063	78	2660	52	1105	33
C-3	92	6500	81	2037	45	13999	118	66386	258	6100	78	2702	52	1160	34
C-3	93	6442	80	2064	45	13953	118	66267	257	5968	77	2653	52	1182	34
C-3	94	6301	79	2017	45	13949	118	66344	258	5924	77	2787	53	1155	34
C-3	95	6380	80	2122	46	13660	117	65898	257	5869	77	2974	55	1225	35
C-3	96	6529	81	2136	46	13341	116	65900	257	5805	76	3122	56	1139	34
C-3	97	6462	80	2030	45	13339	115	65674	256	5778	76	3236	57	1377	37
C-3	98	6159	78	2067	45	12906	114	66026	257	5753	76	3120	56	1441	38
C-3	99	5790	76	2184	47	11490	107	67913	261	5547	74	3259	57	1626	40
C-3	100	5431	74	2225	47	10561	103	69078	263	5302	73	2865	54	1553	39
C-3	101	5489	74	2090	46	13166	115	67564	260	5669	75	2613	51	1280	36
C-3	102	5287	73	2007	45	14705	121	66375	258	5902	77	2513	50	1284	36
C-3	103	5121	72	2024	45	14965	122	66474	258	5609	75	2357	49	1204	35
C-3	104	4933	70	2045	45	14680	121	66402	258	5579	75	2230	47	1155	34
C-3	105	4609	68	2040	45	15172	123	66745	258	5549	74	2362	49	1196	35
C-3	106	4667	68	2043	45	15586	125	66364	258	5425	74	2309	48	1212	35
C-3	107	4690	68	2034	45	16065	127	65464	256	5510	74	2392	49	1269	36
C-3	108	4523	67	2112	46	16244	127	65540	256	5501	74	2314	48	1226	35
D-1	1	3403	58	1871	43	12962	114	60900	247	4188	65	1999	45	1139	34
D-1	2	4246	65	2034	45	13656	117	59319	244	4948	70	1985	45	1110	33
D-1	3	4413	66	2037	45	13668	117	58817	243	4869	70	1884	43	1125	34
D-1	4	4544	67	2031	45	13837	118	59153	243	4864	70	1766	42	1197	35
D-1	5	4278	65	2039	45	14032	118	58762	242	4666	68	1888	43	1241	35
D-1	6	4230	65	1973	44	13951	118	58331	242	4941	70	1917	44	1111	33
D-1	7	4089	64	2045	45	14029	118	58962	243	4763	69	1880	43	1198	35
D-1	8	4124	64	2052	45	14016	118	58624	242	4790	69	1892	44	1201	35
D-1	9	4041	64	1998	45	13970	118	58734	242	4801	69	1837	43	1180	34
D-1	10	4091	64	2083	46	13975	118	58747	242	4706	69	2011	45	1178	34
D-1	11	3953	63	1919	44	14051	119	58721	242	4637	68	1986	45	1165	34
D-1	12	3874	62	2043	45	14122	119	58381	242	4708	69	2026	45	1146	34
D-1	13	3897	62	2016	45	14266	119	58044	241	4637	68	2054	45	1215	35
D-1	14	3875	62	1991	45	13849	118	58282	241	4627	68	1983	45	1194	35
D-1	15	3773	61	1928	44	14283	120	58773	242	4652	68	2031	45	1156	34
D-1	16	3752	61	1930	44	14263	119	59149	243	4601	68	1990	45	1172	34
D-1	17	3829	62	1931	44	13924	118	58819	243	4783	69	2053	45	1210	35
D-1	18	3893	62	1941	44	14167	119	58424	242	4649	68	1949	44	1178	34

D-1	19	3779	61	1990	45	14115	119	58649	242	4626	68	1964	44	1185	34
D-1	20	3817	62	1943	44	14210	119	58701	242	4581	68	1938	44	1177	34
D-1	21	3748	61	1836	43	13855	118	58490	242	4485	67	1913	44	1215	35
D-1	22	3719	61	1780	42	13960	118	58903	243	4538	67	2044	45	1178	34
D-1	23	3688	61	1880	43	14374	120	58833	243	4510	67	1996	45	1181	34
D-1	24	3764	61	1852	43	14217	119	58923	243	4625	68	1957	44	1125	34
D-1	25	3784	62	1879	43	14010	118	59023	243	4551	67	1944	44	1074	33
D-1	26	3764	61	1901	44	14194	119	59244	243	4597	68	1902	44	1136	34
D-1	27	3691	61	1822	43	13962	118	58885	243	4577	68	1855	43	1123	34
D-1	28	3706	61	1933	44	14091	119	59229	243	4612	68	1943	44	1119	33
D-1	29	3692	61	1992	45	14085	119	58557	242	4639	68	1899	44	1136	34
D-1	30	3727	61	1919	44	14048	119	58829	243	4575	68	1899	44	1124	34
D-1	31	3665	61	1827	43	13875	118	59166	243	4616	68	1914	44	1111	33
D-1	32	3560	60	1940	44	13866	118	58526	242	4594	68	1889	43	1122	34
D-1	33	3601	60	1804	42	13905	118	58311	241	4641	68	1774	42	1137	34
D-1	34	3585	60	1830	43	13978	118	59244	243	4570	68	1851	43	1140	34
D-1	35	3693	61	1950	44	13939	118	59555	244	4544	67	1827	43	1111	33
D-1	36	3675	61	1809	43	13997	118	59744	244	4500	67	1880	43	1080	33
D-1	37	3548	60	1820	43	13892	118	59548	244	4527	67	1830	43	1109	33
D-1	38	3527	59	1773	42	13998	118	59393	244	4542	67	1909	44	1089	33
D-1	39	3672	61	1787	42	13911	118	59727	244	4501	67	1871	43	1055	32
D-1	40	3595	60	1806	43	13808	118	60322	246	4492	67	1811	43	1118	33
D-1	41	3709	61	1854	43	13613	117	60017	245	4488	67	1747	42	1079	33
D-1	42	3586	60	1862	43	13698	117	59406	244	4497	67	1793	42	1096	33
D-1	43	3631	60	1830	43	13747	117	60124	245	4426	67	1838	43	1087	33
D-1	44	3504	59	1858	43	13581	117	60329	246	4453	67	1829	43	1115	33
D-1	45	3537	59	1782	42	13758	117	60335	246	4512	67	1781	42	1029	32
D-1	46	3503	59	1781	42	13598	117	59959	245	4454	67	1705	41	1041	32
D-1	47	3550	60	1749	42	13418	116	59792	245	4461	67	1767	42	1019	32
D-1	48	3482	59	1786	42	13422	116	60641	246	4342	66	1801	42	1051	32
D-1	49	3521	59	1716	41	13315	115	60511	246	4422	67	1700	41	1012	32
D-1	50	3415	58	1818	43	13316	115	60104	245	4446	67	1734	42	1015	32
D-1	51	3360	58	1733	42	13298	115	60419	246	4366	66	1675	41	1122	34
D-1	52	3363	58	1809	43	13503	116	60567	246	4385	66	1720	41	1045	32
D-1	53	3436	59	1787	42	13447	116	60505	246	4409	66	1729	42	999	32
D-1	54	3448	59	1761	42	13106	114	60037	245	4277	65	1764	42	1059	33
D-1	55	3325	58	1730	42	13115	115	60730	246	4409	66	1722	42	1048	32
D-1	56	3443	59	1740	42	13388	116	60503	246	4357	66	1724	42	1015	32
D-1	57	3426	59	1783	42	13188	115	60742	246	4360	66	1640	41	1016	32
D-1	58	3344	58	1831	43	13316	115	60926	247	4173	65	1702	41	1068	33
D-1	59	3359	58	1788	42	13020	114	60693	246	4277	65	1746	42	1042	32
D-1	60	3218	57	1756	42	13226	115	60619	246	4184	65	1674	41	993	32
D-1	61	3307	58	1721	41	13118	115	60139	245	4192	65	1680	41	1016	32
D-1	62	3289	57	1840	43	13068	114	60383	246	4254	65	1697	41	1094	33
D-1	63	3319	58	1794	42	13237	115	60568	246	4392	66	1674	41	1050	32
D-1	64	3344	58	1836	43	13041	114	60335	246	4195	65	1756	42	1021	32
D-1	65	3318	58	1802	42	13171	115	60503	246	4273	65	1696	41	1042	32
D-1	66	3204	57	1774	42	13202	115	61003	247	4247	65	1722	42	1002	32
D-1	67	3224	57	1759	42	13087	114	60111	245	4087	64	1814	43	1020	32
D-1	68	3281	57	1819	43	13235	115	60412	246	4146	64	1760	42	977	31
D-1	69	3435	59	1744	42	13078	114	59620	244	4290	66	1739	42	1033	32
D-1	70	3272	57	1702	41	13231	115	60023	245	4166	65	1721	41	1051	32
D-1	71	3178	56	1877	43	13112	115	59910	245	4190	65	1745	42	999	32
D-1	72	3204	57	1800	42	12985	114	60219	245	4129	64	1687	41	1075	33
D-1	73	3058	55	1782	42	13009	114	60152	245	4145	64	1729	42	1043	32
D-1	74	3173	56	1772	42	13013	114	60261	245	4142	64	1682	41	1024	32
D-1	75	3193	57	1861	43	13020	114	60182	245	4085	64	1729	42	1042	32
D-1	76	3163	56	1738	42	12875	113	60796	247	4050	64	1800	42	1053	32
D-1	77	3167	56	1683	41	12793	113	60396	246	3956	63	1668	41	1012	32
D-1	78	3208	57	1853	43	12897	114	60930	247	4098	64	1626	40	977	31
D-1	79	3174	56	1721	41	12532	112	60832	247	4182	65	1652	41	1043	32
D-1	80	3179	56	1756	42	12357	111	60979	247	3987	63	1659	41	973	31
D-1	81	3154	56	1722	42	12505	112	61180	247	4179	65	1658	41	1035	32

D-1	82	3181	56	1705	41	12659	113	61036	247	4037	64	1712	41	1047	32
D-1	83	3168	56	1768	42	12730	113	60862	247	4070	64	1696	41	1036	32
D-1	84	3175	56	1777	42	12874	113	60403	246	4026	63	1720	41	985	31
D-1	85	3215	57	1764	42	13066	114	60573	246	4066	64	1728	42	982	31
D-1	86	3360	58	1813	43	13010	114	60192	245	4071	64	1709	41	1043	32
D-1	87	3196	57	1769	42	13222	115	59576	244	4366	66	1723	42	1043	32
D-1	88	3278	57	1803	42	13422	116	59301	244	4038	64	1687	41	1042	32
D-1	89	3273	57	1772	42	13521	116	58808	243	4131	64	1748	42	1032	32
D-1	90	3276	57	1853	43	13605	117	58859	243	4148	64	1778	42	1084	33
D-1	91	3275	57	1746	42	13931	118	59056	243	4159	64	1734	42	1001	32
D-1	92	3328	58	1875	43	13846	118	58869	243	4071	64	1764	42	1046	32
D-1	93	3380	58	1816	43	13800	117	58322	242	4120	64	1791	42	1071	33
D-1	94	3341	58	1824	43	13985	118	58635	242	4184	65	1851	43	1080	33
D-1	95	3348	58	1858	43	14074	119	58524	242	4104	64	1772	42	1118	33
D-1	96	3365	58	1870	43	14037	118	58503	242	4018	63	1864	43	1038	32
D-1	97	3347	58	1860	43	14007	118	58453	242	4069	64	1830	43	1070	33
D-1	98	3344	58	1858	43	14103	119	58400	242	4056	64	1939	44	1078	33
D-1	99	3387	58	1847	43	14284	120	58564	242	4151	64	1801	42	1092	33
D-1	100	3288	57	1853	43	14139	119	58048	241	4253	65	1792	42	1122	34
D-1	101	3359	58	1856	43	14264	119	58481	242	4170	65	1885	43	1125	34
D-1	102	3338	58	1774	42	14177	119	58269	241	4134	64	1841	43	1087	33
D-1	103	3300	57	1800	42	14008	118	58114	241	4148	64	1911	44	1103	33
D-1	104	3263	57	1788	42	14282	120	57950	241	4085	64	1915	44	1120	33
D-1	105	3204	57	1863	43	14187	119	58316	241	4226	65	1769	42	1083	33
D-1	106	3395	58	1854	43	13946	118	58122	241	4124	64	1845	43	1080	33
D-1	107	3351	58	1933	44	14136	119	57584	240	4198	65	1836	43	1087	33
D-1	108	3443	59	1857	43	14255	119	58252	241	4096	64	1894	44	1109	33
D-1	109	3394	58	1914	44	14186	119	57675	240	4136	64	1892	44	1146	34
D-1	110	3329	58	1879	43	14343	120	58114	241	4127	64	1869	43	1113	33
D-1	111	3406	58	1962	44	14329	120	57942	241	4017	63	1952	44	1129	34
D-1	112	3383	58	1835	43	14407	120	58100	241	4127	64	1901	44	1042	32
D-1	113	3340	58	1984	45	14557	121	57296	239	4120	64	1851	43	1119	33
D-1	114	3348	58	1778	42	14151	119	57891	241	4103	64	1795	42	1090	33
D-1	115	3417	58	1883	43	14272	119	57662	240	4095	64	1843	43	1098	33
D-1	116	3537	59	1873	43	14298	120	57437	240	4149	64	1928	44	1090	33
D-1	117	3457	59	1882	43	14408	120	57603	240	4234	65	1866	43	1089	33
D-1	118	3428	59	1895	44	14468	120	57937	241	4187	65	1903	44	1048	32
D-1	119	3459	59	1865	43	14469	120	57794	240	4165	65	1866	43	1056	33
D-1	120	3498	59	1918	44	14476	120	57729	240	4128	64	1811	43	1056	33
D-1	121	3314	58	1784	42	14457	120	57942	241	4168	65	1839	43	1141	34
D-1	122	3438	59	1959	44	14526	121	57268	239	4124	64	1832	43	1121	33
D-1	123	3418	58	1882	43	14365	120	57417	240	4174	65	1828	43	1068	33
D-1	124	3471	59	1877	43	14590	121	57887	241	4170	65	1795	42	1070	33
D-1	125	3432	59	1894	44	14561	121	58125	241	4059	64	1840	43	1063	33
D-1	126	3455	59	1848	43	14334	120	57755	240	4169	65	1882	43	1153	34
D-1	127	3465	59	1869	43	14522	121	57704	240	4067	64	1878	43	1095	33
D-1	128	3499	59	1844	43	14501	120	57925	241	4132	64	1765	42	1127	34
D-1	129	3467	59	1932	44	14491	120	57856	241	4133	64	1864	43	1126	34
D-1	130	3541	60	1851	43	14461	120	57550	240	4067	64	1739	42	1053	32
D-1	131	3500	59	1842	43	14259	119	58066	241	4093	64	1858	43	1078	33
D-1	132	3496	59	1849	43	14283	120	58575	242	4200	65	1760	42	1047	32
D-1	133	3480	59	1899	44	14310	120	58338	242	4150	64	1792	42	1042	32
D-1	134	3480	59	1889	43	14428	120	58027	241	4113	64	1794	42	1147	34
D-1	135	3515	59	1849	43	14271	119	58029	241	4134	64	1701	41	1093	33
D-1	136	3479	59	1900	44	14282	120	58388	242	4173	65	1849	43	1039	32
D-1	137	3569	60	1864	43	14237	119	58215	241	4130	64	1795	42	1076	33
D-1	138	3588	60	1851	43	14239	119	58057	241	4088	64	1727	42	1068	33
D-1	139	3561	60	1856	43	14312	120	58278	241	4253	65	1739	42	1087	33
D-1	140	3414	58	1895	44	14024	118	58446	242	4145	64	1771	42	1063	33
D-1	141	3526	59	1876	43	14063	119	57856	241	4250	65	1728	42	1068	33
D-1	142	3504	59	1856	43	13914	118	58685	242	4044	64	1742	42	1069	33
D-1	143	3435	59	1822	43	14039	118	57990	241	4137	64	1827	43	1082	33
D-1	144	3531	59	1870	43	14242	119	58724	242	4113	64	1746	42	1041	32

D-1	145	3404	58	1884	43	14086	119	58508	242	4131	64	1762	42	999	32
D-1	146	3509	59	1820	43	14090	119	58332	242	4190	65	1759	42	1106	33
D-1	147	3508	59	1815	43	14035	118	58318	241	4334	66	1767	42	1063	33
D-1	148	3498	59	1917	44	14007	118	57881	241	4116	64	1773	42	1107	33
D-1	149	3478	59	1947	44	14078	119	57741	240	4171	65	1772	42	1041	32
D-1	150	3530	59	1861	43	13966	118	58449	242	4257	65	1744	42	1029	32
D-1	151	3452	59	1927	44	14049	119	58231	241	4246	65	1661	41	1057	33
D-1	152	3351	58	1844	43	13847	118	58307	241	4142	64	1734	42	1133	34
D-1	153	3512	59	1806	43	13734	117	58141	241	4169	65	1722	42	1022	32
D-1	154	3426	59	1876	43	13919	118	58067	241	4273	65	1753	42	1037	32
D-1	155	3398	58	1817	43	14117	119	58039	241	4125	64	1734	42	1002	32
D-1	156	3503	59	1851	43	13841	118	57535	240	4222	65	1763	42	1009	32
D-1	157	3505	59	1884	43	14087	119	57511	240	4258	65	1667	41	1063	33
D-1	158	3518	59	1851	43	14037	118	57888	241	4290	66	1647	41	1045	32
D-1	159	3506	59	1833	43	14363	120	57762	240	4273	65	1722	42	1036	32
D-1	160	3539	59	1825	43	14246	119	57299	239	4185	65	1776	42	1028	32
D-1	161	3563	60	1826	43	14461	120	56944	239	4286	65	1720	41	996	32
D-1	162	3651	60	1860	43	14365	120	56294	237	4351	66	1747	42	1031	32
D-1	163	3630	60	1842	43	14917	122	56882	239	4398	66	1736	42	1090	33
D-1	164	3722	61	1890	43	14916	122	56518	238	4381	66	1823	43	1093	33
D-1	165	3699	61	1847	43	15060	123	56339	237	4500	67	1732	42	1026	32
D-1	166	3754	61	1766	42	15125	123	55801	236	4467	67	1797	42	1068	33
D-1	167	3791	62	1856	43	15216	123	55856	236	4300	66	1783	42	1012	32
D-1	168	3784	62	1926	44	15435	124	55650	236	4310	66	1871	43	1061	33
D-1	169	3734	61	1849	43	15031	123	55748	236	4514	67	1791	42	981	31
D-1	170	3752	61	1769	42	14970	122	56458	238	4364	66	1782	42	1035	32
D-1	171	3677	61	1737	42	14495	120	56778	238	4477	67	1722	42	997	32
D-1	172	3645	60	1778	42	14109	119	57716	240	4267	65	1723	42	964	31
D-1	173	3481	59	1745	42	13508	116	57932	241	4254	65	1800	42	992	32
D-1	174	3579	60	1703	41	13017	114	59055	243	4270	65	1674	41	971	31
D-1	175	3448	59	1815	43	12784	113	58890	243	4253	65	1710	41	1063	33
D-1	176	3351	58	1690	41	12172	110	59226	243	4073	64	1795	42	1070	33
D-1	177	3345	58	1789	42	11765	108	59969	245	4194	65	1700	41	1108	33
D-1	178	3303	57	1851	43	11974	109	59105	243	4113	64	1797	42	1169	34
D-1	179	3522	59	1766	42	13431	116	56927	239	4350	66	2028	45	1253	35
D-1	180	3611	60	1780	42	13726	117	56791	238	4348	66	1951	44	1092	33
D-1	181	3659	60	1783	42	13925	118	56582	238	4364	66	1855	43	1045	32
D-1	182	3602	60	1729	42	13715	117	58023	241	4409	66	1808	43	1012	32
D-1	183	3477	59	1674	41	13890	118	57420	240	4277	65	1653	41	1077	33
D-1	184	3408	58	1741	42	14085	119	57516	240	4324	66	1695	41	1050	32
D-1	185	3587	60	1707	41	14243	119	57577	240	4304	66	1704	41	1052	32
D-1	186	3599	60	1847	43	14266	119	57162	239	4223	65	1766	42	1076	33
D-1	187	3585	60	1899	44	14355	120	56787	238	4287	65	1804	42	1079	33
D-1	188	3598	60	1799	42	14493	120	56809	238	4262	65	1713	41	1083	33
D-1	189	3436	59	1834	43	14760	121	55592	236	4224	65	1919	44	1107	33
D-1	190	3566	60	1837	43	14794	122	55877	236	4347	66	1836	43	1184	34
D-1	191	3481	59	1865	43	14558	121	55684	236	4270	65	1947	44	1133	34
D-1	192	3570	60	1801	42	14977	122	55511	236	4114	64	1940	44	1147	34
D-1	193	3522	59	1821	43	14957	122	56105	237	4118	64	1879	43	1129	34
D-1	194	3415	58	1867	43	14507	120	55778	236	4204	65	1944	44	1190	35
D-1	195	3425	59	1892	44	14550	121	55961	237	4178	65	1810	43	1256	35
D-1	196	3458	59	1858	43	14674	121	55796	236	4121	64	1957	44	1247	35
D-1	197	3348	58	1799	42	14632	121	56234	237	4026	63	1893	44	1175	34
D-1	198	3317	58	1861	43	14517	120	56270	237	4081	64	1888	43	1153	34
D-1	199	3342	58	1810	43	14338	120	55994	237	4052	64	1872	43	1145	34
D-1	200	3341	58	1841	43	14434	120	56300	237	4138	64	1915	44	1140	34
D-1	201	3291	57	1787	42	13976	118	57528	240	4066	64	1718	41	1064	33
D-1	202	3240	57	1727	42	14120	119	57698	240	4016	63	1708	41	1134	34
D-1	203	3175	56	1762	42	13911	118	57254	239	4023	63	1758	42	1075	33
D-1	204	3296	57	1781	42	13992	118	57277	239	4050	64	1823	43	1152	34
D-1	205	3391	58	1773	42	14337	120	57067	239	3998	63	1778	42	1101	33
D-1	206	3283	57	1724	42	14065	119	56818	238	3953	63	1804	42	1109	33
D-1	207	3329	58	1841	43	14561	121	56482	238	3881	62	1784	42	1157	34

D-1	208	3303	57	1805	42	14296	120	57292	239	4074	64	1780	42	1062	33
D-1	209	3314	58	1802	42	14425	120	56700	238	4029	63	1825	43	1049	32
D-1	210	3292	57	1789	42	14369	120	56901	239	4123	64	1806	43	1144	34
D-1	211	3269	57	1850	43	14374	120	56431	238	3971	63	1935	44	1052	32
D-1	212	3249	57	1756	42	14381	120	57116	239	3985	63	1776	42	1083	33
D-1	213	3238	57	1731	42	14246	119	57074	239	3966	63	1867	43	1061	33
D-1	214	3246	57	1733	42	14283	120	57067	239	3897	62	1775	42	1085	33
D-1	215	3222	57	1738	42	14162	119	57213	239	3955	63	1722	42	1184	34
D-1	216	3179	56	1770	42	14040	118	57125	239	3967	63	1837	43	1068	33
D-1	217	3236	57	1777	42	13951	118	56863	238	3856	62	1731	42	1086	33
D-1	218	3277	57	1772	42	14016	118	57565	240	4006	63	1765	42	1122	34
D-1	219	3294	57	1724	42	13960	118	57364	240	3927	63	1778	42	1096	33
D-1	220	3103	56	1707	41	13731	117	57741	240	4015	63	1751	42	1074	33
D-1	221	3122	56	1724	42	13570	116	58374	242	3939	63	1702	41	1043	32
D-1	222	3077	55	1689	41	13440	116	58326	242	3898	62	1715	41	1052	32
D-1	223	3072	55	1673	41	13316	115	58494	242	3921	63	1698	41	1095	33
D-1	224	3128	56	1797	42	13011	114	58206	241	4052	64	1715	41	1108	33
D-1	225	3065	55	1642	41	13459	116	58419	242	3913	63	1708	41	1149	34
D-1	226	3209	57	1769	42	13336	115	58097	241	4059	64	1710	41	1135	34
D-1	227	3066	55	1644	41	13530	116	57852	241	3983	63	1812	43	1155	34
D-1	228	3025	55	1724	42	13732	117	57896	241	3937	63	1867	43	1132	34
D-1	229	3149	56	1719	41	13891	118	57406	240	3901	62	1814	43	1166	34
D-1	230	3227	57	1710	41	13924	118	57011	239	3925	63	1863	43	1126	34
D-1	231	3219	57	1626	40	14167	119	56365	237	3813	62	1840	43	1134	34
D-1	232	3148	56	1735	42	13911	118	57150	239	3887	62	1919	44	1221	35
D-1	233	3219	57	1732	42	13969	118	57167	239	3943	63	1842	43	1193	35
D-1	234	3073	55	1624	40	13915	118	57158	239	3910	63	1884	43	1197	35
D-1	235	3204	57	1639	40	13504	116	58227	241	3909	63	1757	42	1159	34
D-1	236	2974	55	1674	41	13125	115	58187	241	3890	62	1655	41	1164	34
D-1	237	2959	54	1578	40	13214	115	58734	242	4042	64	1732	42	1152	34
D-1	238	2927	54	1530	39	13088	114	58092	241	3901	62	1682	41	1167	34
D-1	239	2978	55	1621	40	12911	114	58614	242	3948	63	1620	40	1159	34
D-1	240	2974	55	1536	39	12760	113	58639	242	3903	62	1681	41	1161	34
D-1	241	3023	55	1567	40	12981	114	58793	242	3889	62	1659	41	1133	34
D-1	242	3009	55	1508	39	12906	114	58640	242	3881	62	1671	41	1140	34
D-1	243	2931	54	1556	39	12835	113	59073	243	3829	62	1661	41	1145	34
D-1	244	2977	55	1505	39	12744	113	58677	242	3945	63	1632	40	1147	34
D-1	245	2954	54	1474	38	12891	114	58557	242	3837	62	1658	41	1189	34
D-1	246	3005	55	1461	38	13008	114	58821	243	3844	62	1705	41	1154	34
D-1	247	3000	55	1527	39	13229	115	58290	241	3849	62	1658	41	1165	34
D-1	248	3036	55	1497	39	13057	114	58764	242	3850	62	1702	41	1160	34
D-1	249	3082	56	1476	38	13301	115	57950	241	3796	62	1715	41	1166	34
D-1	250	3031	55	1484	39	13161	115	58216	241	3835	62	1705	41	1191	35
D-1	251	3084	56	1547	39	13135	115	58293	241	4029	63	1705	41	1173	34
D-1	252	2961	54	1568	40	13220	115	58040	241	3790	62	1731	42	1174	34
D-1	253	3014	55	1610	40	13058	114	58166	241	3842	62	1679	41	1205	35
D-1	254	2957	54	1564	40	13234	115	58149	241	3937	63	1698	41	1226	35
D-1	255	3079	55	1542	39	13284	115	57913	241	3953	63	1732	42	1177	34
D-1	256	3075	55	1527	39	13093	114	57686	240	3761	61	1731	42	1142	34
D-1	257	3104	56	1565	40	13152	115	58116	241	3792	62	1757	42	1202	35
D-1	258	3059	55	1562	40	13261	115	57917	241	3832	62	1724	42	1129	34
D-1	259	3092	56	1608	40	13337	115	57800	240	3860	62	1804	42	1149	34
D-1	260	3081	56	1601	40	13186	115	58338	242	3847	62	1733	42	1154	34
D-1	261	3071	55	1529	39	13189	115	58071	241	3894	62	1729	42	1127	34
D-1	262	2973	55	1603	40	12942	114	58461	242	3883	62	1705	41	1133	34
D-1	263	3004	55	1604	40	12967	114	58464	242	3785	62	1738	42	1117	33
D-1	264	3058	55	1552	39	12977	114	58518	242	3900	62	1748	42	1143	34
D-1	265	2953	54	1583	40	13000	114	58576	242	3917	63	1774	42	1146	34
D-1	266	2937	54	1536	39	12747	113	58543	242	3992	63	1721	41	1101	33
D-1	267	3062	55	1627	40	13141	115	58354	242	3845	62	1775	42	1119	33
D-1	268	3032	55	1627	40	12776	113	58798	242	3907	63	1742	42	1148	34
D-1	269	3094	56	1682	41	13062	114	58295	241	3836	62	1788	42	1141	34
D-1	270	3026	55	1667	41	12929	114	58434	242	3971	63	1802	42	1159	34

D-1	271	3131	56	1610	40	13181	115	57938	241	3901	62	1800	42	1120	33
D-1	272	2964	54	1619	40	13366	116	58457	242	3922	63	1831	43	1100	33
D-1	273	3063	55	1660	41	13279	115	57788	240	3877	62	1799	42	1054	32
D-1	274	3092	56	1614	40	13355	116	57384	240	3907	63	1839	43	1129	34
D-1	275	3026	55	1671	41	13691	117	57566	240	3914	63	1870	43	1092	33
D-1	276	3089	56	1698	41	13576	117	56965	239	3940	63	1888	43	1149	34
D-1	277	3092	56	1733	42	13554	116	57881	241	3865	62	1931	44	1147	34
D-1	278	3024	55	1724	42	13682	117	57539	240	3824	62	1886	43	1113	33
D-1	279	3072	55	1729	42	13549	116	57001	239	3896	62	1845	43	1129	34
D-1	280	3012	55	1736	42	13585	117	57515	240	3902	62	1815	43	1128	34
D-1	281	3126	56	1633	40	13472	116	57653	240	3921	63	1935	44	1161	34
D-1	282	3158	56	1775	42	13734	117	56860	238	3874	62	1820	43	1149	34
D-1	283	3083	56	1704	41	13721	117	56575	238	3922	63	1936	44	1124	34
D-1	284	3208	57	1773	42	13710	117	56720	238	3929	63	1995	45	1112	33
D-1	285	3264	57	1723	42	13966	118	56545	238	3852	62	1931	44	1144	34
D-1	286	3086	56	1708	41	14010	118	56721	238	3892	62	1941	44	1187	34
D-1	287	3147	56	1768	42	13719	117	57073	239	3963	63	1930	44	1146	34
E-1	1	5450	74	1705	41	10036	100	57093	239	5435	74	1907	44	1126	34
E-1	2	5477	74	1644	41	10711	103	56275	237	5695	75	1816	43	1013	32
E-1	3	5208	72	1490	39	12337	111	53904	232	5645	75	1688	41	1028	32
E-1	4	4991	71	1595	40	13559	116	51905	228	5852	77	1613	40	1042	32
E-1	5	5156	72	1577	40	13798	117	54340	233	5929	77	1539	39	974	31
E-1	6	4933	70	1664	41	13454	116	54971	234	5943	77	1519	39	969	31
E-1	7	4957	70	1684	41	13867	118	55251	235	5885	77	1483	39	950	31
E-1	8	4835	70	1634	40	13963	118	55163	235	5859	77	1467	38	964	31
E-1	9	4693	69	1646	41	14180	119	55476	236	5732	76	1518	39	942	31
E-1	10	4582	68	1657	41	14352	120	55302	235	5743	76	1491	39	984	31
E-1	11	4712	69	1710	41	14466	120	55374	235	5673	75	1449	38	984	31
E-1	12	4095	64	1584	40	13917	118	52471	229	5289	73	1477	38	950	31
E-1	13	4606	68	1696	41	14388	120	55087	235	5556	75	1517	39	891	30
E-1	14	4515	67	1670	41	14489	120	55680	236	5616	75	1424	38	972	31
E-1	15	4325	66	1718	41	14430	120	55378	235	5641	75	1434	38	958	31
E-1	16	4293	66	1713	41	14313	120	56087	237	5437	74	1455	38	990	31
E-1	17	4195	65	1671	41	14300	120	56301	237	5345	73	1465	38	1006	32
E-1	18	4075	64	1683	41	14269	119	56023	237	5264	73	1489	39	1066	33
E-1	19	4098	64	1700	41	14254	119	56370	237	5269	73	1477	38	991	31
E-1	20	4012	63	1749	42	14517	120	56004	237	5392	73	1551	39	993	32
E-1	21	3965	63	1777	42	14408	120	56139	237	5221	72	1456	38	1035	32
E-1	22	3873	62	1740	42	14199	119	56176	237	5249	72	1516	39	1026	32
E-1	23	3929	63	1739	42	14034	118	56899	239	5188	72	1516	39	1022	32
E-1	24	3705	61	1698	41	13413	116	57452	240	4937	70	1500	39	1062	33
E-1	25	3762	61	1679	41	13290	115	58193	241	4997	71	1498	39	1028	32
E-1	26	3623	60	1634	40	13160	115	58329	242	4854	70	1473	38	1013	32
E-1	27	3717	61	1672	41	13162	115	58010	241	4879	70	1536	39	1011	32
E-1	28	3699	61	1727	42	13632	117	57523	240	5003	71	1521	39	1033	32
E-1	29	3754	61	1679	41	13661	117	57465	240	4936	70	1549	39	1038	32
E-1	30	3763	61	1658	41	13777	117	57379	240	5000	71	1499	39	1060	33
E-1	31	3707	61	1704	41	13864	118	57376	240	4874	70	1565	40	1033	32
E-1	32	3753	61	1742	42	13798	117	57663	240	4778	69	1558	39	1050	32
E-1	33	3733	61	1780	42	13840	118	56858	238	4733	69	1553	39	1047	32
E-1	34	3574	60	1764	42	14137	119	57115	239	4673	68	1613	40	1090	33
E-1	35	3689	61	1694	41	14710	121	56832	238	4688	68	1599	40	1053	32
E-1	36	3780	61	1781	42	14615	121	56588	238	4733	69	1602	40	1079	33
E-1	37	3728	61	1825	43	14666	121	56065	237	4576	68	1598	40	1105	33
E-1	38	3807	62	1809	43	14830	122	56076	237	4579	68	1583	40	1035	32
E-1	39	3639	60	1764	42	14143	119	55540	236	4585	68	1520	39	1036	32
E-1	40	3506	59	1770	42	14284	120	55790	236	4651	68	1521	39	1100	33
E-1	41	3775	61	1764	42	14393	120	56681	238	4611	68	1524	39	1058	33
E-1	42	3546	60	1702	41	14263	119	57004	239	4667	68	1496	39	1045	32
E-1	43	3641	60	1803	42	14340	120	57604	240	4613	68	1499	39	1086	33
E-1	44	3505	59	1795	42	14349	120	57155	239	4632	68	1516	39	1069	33
E-1	45	3563	60	1821	43	14466	120	56728	238	4474	67	1477	38	1133	34
E-1	46	3516	59	1872	43	14788	122	56408	238	4520	67	1497	39	1101	33

E-1	47	3458	59	1796	42	14367	120	57073	239	4615	68	1510	39	1095	33
E-1	48	3384	58	1713	41	14207	119	57655	240	4457	67	1439	38	1052	32
E-1	49	3268	57	1728	42	13699	117	58260	241	4488	67	1439	38	1078	33
E-1	50	3405	58	1727	42	13789	117	58365	242	4407	66	1385	37	1051	32
E-1	51	3268	57	1714	41	13636	117	57802	240	4475	67	1473	38	1041	32
E-1	52	3237	57	1741	42	13854	118	58314	241	4411	66	1432	38	1020	32
E-1	53	3240	57	1791	42	14160	119	57440	240	4379	66	1388	37	1087	33
E-1	54	3277	57	1734	42	14128	119	57765	240	4416	66	1448	38	1046	32
E-1	55	3431	59	1782	42	14187	119	57563	240	4303	66	1477	38	1069	33
E-1	56	3373	58	1766	42	14139	119	57472	240	4345	66	1459	38	1069	33
E-1	57	3340	58	1787	42	14255	119	57431	240	4358	66	1377	37	1078	33
E-1	58	3411	58	1817	43	14362	120	56958	239	4243	65	1535	39	1088	33
E-1	59	3379	58	1879	43	14820	122	56236	237	4343	66	1504	39	1104	33
E-1	60	3370	58	1882	43	14825	122	56534	238	4379	66	1511	39	1075	33
E-1	61	3309	58	1866	43	14895	122	56794	238	4260	65	1540	39	1184	34
E-1	62	3391	58	1885	43	14997	122	56567	238	4184	65	1556	39	1153	34
E-1	63	3334	58	1808	43	14628	121	56789	238	4280	65	1564	40	1109	33
E-1	64	3340	58	1832	43	14447	120	57329	239	4322	66	1517	39	1144	34
E-1	65	3334	58	1812	43	14143	119	57642	240	4192	65	1503	39	1126	34
E-1	66	3390	58	1861	43	14017	118	58354	242	4369	66	1489	39	1017	32
E-1	67	3286	57	1808	43	13771	117	57929	241	4190	65	1493	39	1012	32
E-1	68	3234	57	1788	42	13998	118	57935	241	4319	66	1555	39	1093	33
E-1	69	3310	58	1689	41	14054	119	57774	240	4134	64	1478	38	1057	33
E-1	70	3327	58	1741	42	14088	119	57946	241	4165	65	1493	39	1062	33
E-1	71	3254	57	1780	42	14050	119	57426	240	4232	65	1559	39	1102	33
E-1	72	3366	58	1820	43	14302	120	57651	240	4197	65	1506	39	1059	33
E-1	73	3400	58	1870	43	14818	122	56716	238	4190	65	1568	40	1144	34
E-1	74	3418	58	1917	44	14841	122	56962	239	4220	65	1529	39	1107	33
E-1	75	3379	58	1908	44	14746	121	56368	237	4284	65	1553	39	1125	34
E-1	76	3363	58	1908	44	14983	122	55676	236	4180	65	1603	40	1089	33
E-1	77	3436	59	1801	42	14964	122	56485	238	4184	65	1583	40	1117	33
E-1	78	3446	59	1802	42	15093	123	55963	237	4178	65	1654	41	1124	34
E-1	79	3360	58	1844	43	14952	122	56432	238	4154	64	1585	40	1194	35
E-1	80	3335	58	1840	43	14811	122	56498	238	4095	64	1530	39	1123	34
E-1	81	3310	58	1793	42	15041	123	56790	238	4214	65	1575	40	1115	33
E-1	82	3302	57	1948	44	14850	122	56303	237	4086	64	1623	40	1116	33
E-1	83	3343	58	1848	43	14693	121	56656	238	4249	65	1480	38	1105	33
E-1	84	3265	57	1871	43	14613	121	56633	238	4250	65	1557	39	1126	34
E-1	85	3385	58	1878	43	14947	122	56322	237	4218	65	1605	40	1105	33
E-1	86	3397	58	1870	43	14793	122	56402	237	4190	65	1542	39	1134	34
E-1	87	3373	58	1896	44	14981	122	56315	237	4165	65	1600	40	1099	33
E-1	88	3427	59	1871	43	14753	121	56863	238	4111	64	1521	39	1099	33
E-1	89	3327	58	1812	43	14517	120	57274	239	4184	65	1455	38	1087	33
E-1	90	3407	58	1844	43	14264	119	56930	239	4098	64	1527	39	1113	33
E-1	91	3335	58	1848	43	14404	120	57592	240	4090	64	1545	39	1052	32
E-1	92	3292	57	1842	43	14305	120	57241	239	4214	65	1440	38	1099	33
E-1	93	3319	58	1865	43	14567	121	56749	238	4202	65	1446	38	1092	33
E-1	94	3350	58	1813	43	14728	121	56659	238	4175	65	1615	40	1095	33
E-1	95	3307	58	1757	42	14697	121	57138	239	4202	65	1570	40	1122	34
E-1	96	3377	58	1823	43	14625	121	56536	238	4095	64	1572	40	1153	34
E-1	97	3341	58	1818	43	14380	120	57333	239	4180	65	1534	39	1147	34
E-1	98	3283	57	1840	43	14102	119	57742	240	4066	64	1505	39	1070	33
E-1	99	3202	57	1819	43	14211	119	57451	240	4122	64	1561	40	1069	33
E-1	100	3278	57	1764	42	14123	119	58311	241	4146	64	1506	39	1038	32
E-1	101	3211	57	1805	42	14094	119	58070	241	4030	63	1528	39	1144	34
E-1	102	3328	58	1860	43	14166	119	57808	240	4066	64	1446	38	1069	33
E-1	103	3190	56	1780	42	14043	119	57615	240	4169	65	1556	39	1118	33
E-1	104	3208	57	1897	44	14580	121	57287	239	4190	65	1463	38	1132	34
E-1	105	3252	57	1845	43	14748	121	56954	239	4156	64	1596	40	1106	33
E-1	106	3413	58	1865	43	14834	122	56645	238	4203	65	1585	40	1194	35
E-1	107	3313	58	1923	44	15021	123	56068	237	4220	65	1551	39	1166	34
E-1	108	3349	58	1910	44	14897	122	56325	237	4172	65	1604	40	1135	34
E-1	109	3390	58	1778	42	15003	122	56251	237	4206	65	1587	40	1190	35

E-1	110	3346	58	1827	43	15263	124	55966	237	4029	63	1577	40	1157	34
E-1	111	3260	57	1833	43	15147	123	55959	237	4072	64	1644	41	1114	33
E-1	112	3315	58	1845	43	15002	122	55970	237	4119	64	1598	40	1104	33
E-1	113	3333	58	1859	43	14964	122	56723	238	4157	64	1561	40	1080	33
E-1	114	3308	58	1869	43	14857	122	56360	237	4202	65	1589	40	1148	34
E-1	115	3372	58	1910	44	14668	121	56964	239	4133	64	1550	39	1149	34
E-1	116	3415	58	1875	43	14975	122	56613	238	4093	64	1595	40	1163	34
E-1	117	3318	58	1853	43	14886	122	56167	237	4132	64	1573	40	1154	34
E-1	118	3356	58	1916	44	14903	122	56586	238	4200	65	1608	40	1064	33
E-1	119	3319	58	1834	43	14799	122	56288	237	4036	64	1574	40	1142	34
E-1	120	3350	58	1877	43	14758	121	56877	238	4132	64	1605	40	1214	35
E-1	121	3383	58	1861	43	14776	122	56297	237	4150	64	1615	40	1114	33
E-1	122	3276	57	1839	43	14885	122	56799	238	4142	64	1561	40	1106	33
E-1	123	3366	58	1820	43	14753	121	56956	239	4185	65	1559	39	1137	34
E-1	124	3411	58	1890	43	15056	123	56795	238	4047	64	1631	40	1075	33
E-1	125	3397	58	1857	43	14774	122	56277	237	4199	65	1656	41	1118	33
E-1	126	3346	58	1936	44	14987	122	56422	238	4157	64	1544	39	1146	34
E-1	127	3327	58	1874	43	14739	121	56339	237	4258	65	1596	40	1160	34
E-1	128	3313	58	1839	43	15050	123	56517	238	4193	65	1544	39	1139	34
E-1	129	3457	59	1875	43	14741	121	56326	237	4296	66	1561	40	1149	34
E-1	130	3298	57	1853	43	14915	122	56603	238	4233	65	1605	40	1081	33
E-1	131	3426	59	1867	43	14923	122	56678	238	4126	64	1552	39	1126	34
E-1	132	3319	58	1802	42	15001	122	56908	239	4099	64	1523	39	1151	34
E-1	133	3412	58	1889	43	14608	121	56542	238	4361	66	1579	40	1119	33
E-1	134	3382	58	1885	43	14724	121	56818	238	4322	66	1511	39	1069	33
E-1	135	3337	58	1818	43	14480	120	56918	239	4279	65	1475	38	1090	33
E-1	136	3296	57	1788	42	14658	121	56859	238	4392	66	1525	39	1093	33
E-1	137	3420	58	1932	44	14552	121	56674	238	4446	67	1495	39	1103	33
E-1	138	3454	59	1787	42	14748	121	56566	238	4334	66	1561	40	1074	33
E-1	139	3443	59	1847	43	14657	121	56669	238	4340	66	1546	39	1055	32
E-1	140	3374	58	1840	43	14770	122	56409	238	4430	67	1528	39	1122	34
E-1	141	3479	59	1936	44	14900	122	56702	238	4443	67	1599	40	1103	33
E-1	142	3511	59	1781	42	14852	122	56578	238	4431	67	1531	39	1058	33
E-1	143	3501	59	1885	43	14917	122	56023	237	4490	67	1498	39	1043	32
E-1	144	3492	59	1798	42	14922	122	56255	237	4513	67	1490	39	1058	33
E-1	145	3619	60	1880	43	14945	122	55496	236	4511	67	1498	39	1153	34
E-1	146	3589	60	1885	43	14953	122	55978	237	4607	68	1495	39	1109	33
E-1	147	3653	60	1843	43	14981	122	56382	237	4634	68	1448	38	1093	33
E-1	148	3676	61	1772	42	14965	122	56060	237	4688	68	1448	38	1089	33
E-1	149	3707	61	1785	42	14741	121	56025	237	4600	68	1489	39	1127	34
E-1	150	3751	61	1796	42	14652	121	56189	237	4823	69	1430	38	1088	33
E-1	151	3714	61	1787	42	14732	121	56009	237	4928	70	1368	37	1045	32
E-1	152	4024	63	1780	42	14847	122	56249	237	4742	69	1378	37	1053	32
E-1	153	3923	63	1755	42	14844	122	55492	236	4992	71	1410	38	1041	32
E-1	154	3981	63	1837	43	14698	121	55992	237	4988	71	1404	37	1009	32
E-1	155	4139	64	1780	42	14947	122	55735	236	5087	71	1389	37	970	31
E-1	156	4256	65	1786	42	14571	121	55443	235	5190	72	1403	37	1036	32
E-1	157	4436	67	1785	42	14474	120	55578	236	5306	73	1426	38	995	32
E-1	158	4472	67	1736	42	14387	120	55273	235	5412	74	1482	39	988	31
E-1	159	4858	70	1663	41	14348	120	55324	235	5336	73	1460	38	943	31
E-1	160	4879	70	1704	41	14216	119	54898	234	5278	73	1563	40	970	31
E-1	161	5159	72	1797	42	13654	117	55176	235	5411	74	1584	40	1058	33
E-1	162	5056	71	1784	42	13474	116	55070	235	5379	73	1703	41	1055	32
E-1	163	5329	73	1770	42	13385	116	55021	235	5249	72	1784	42	1110	33
E-1	164	5283	73	1826	43	13608	117	54843	234	5249	72	1802	42	1059	33
E-1	165	5441	74	1808	43	13545	116	55018	235	5268	73	1889	43	1005	32
E-1	166	5386	73	1786	42	13388	116	55310	235	5249	72	1944	44	950	31
E-1	167	5207	72	1818	43	13001	114	55545	236	5307	73	1889	43	946	31
E-1	168	4787	69	1880	43	10570	103	57517	240	4928	70	1969	44	1329	36
E-1	169	4425	67	1909	44	9369	97	58524	242	4556	68	2016	45	1455	38
E-1	170	4423	67	1852	43	10616	103	57979	241	4843	70	1951	44	1382	37
E-1	171	4403	66	1795	42	11798	109	57640	240	4950	70	1746	42	1273	36
E-1	172	4360	66	1799	42	12231	111	57311	239	4970	71	1635	40	1229	35

E-1	173	4047	64	1733	42	11752	108	58433	242	4809	69	1506	39	1167	34
E-1	174	3677	61	1763	42	11329	106	59713	244	4623	68	1382	37	1146	34
E-1	175	3592	60	1766	42	11690	108	58993	243	4635	68	1470	38	1041	32
E-1	176	3676	61	1745	42	12655	112	58334	242	4803	69	1502	39	1132	34
E-1	177	3769	61	1841	43	13242	115	57099	239	4649	68	1506	39	1097	33
E-1	178	3833	62	1845	43	13881	118	56699	238	4607	68	1619	40	1094	33
E-1	179	3714	61	1753	42	13974	118	56626	238	4686	68	1520	39	1113	33
E-1	180	3814	62	1825	43	14057	119	56703	238	4662	68	1522	39	1072	33
E-1	181	3674	61	1879	43	13965	118	57159	239	4610	68	1600	40	1075	33
E-1	182	3686	61	1747	42	14019	118	56990	239	4526	67	1608	40	1047	32
E-1	183	3739	61	1801	42	13925	118	57124	239	4387	66	1514	39	1032	32
E-1	184	3569	60	1793	42	13508	116	57037	239	4365	66	1589	40	1018	32
E-1	185	3533	59	1724	42	13451	116	57934	241	4383	66	1573	40	1019	32
E-1	186	3622	60	1733	42	13053	114	58466	242	4326	66	1504	39	1006	32
E-1	187	3434	59	1739	42	13142	115	58565	242	4471	67	1584	40	1022	32
E-1	188	3592	60	1804	42	13680	117	57560	240	4298	66	1631	40	1083	33
E-1	189	3550	60	1925	44	13901	118	57091	239	4297	66	1650	41	1101	33
E-1	190	3469	59	1842	43	13778	117	56908	239	4238	65	1800	42	1142	34
E-1	191	3529	59	1872	43	13909	118	56835	238	4285	65	1800	42	1122	34
E-1	192	3569	60	1764	42	13820	118	57095	239	4207	65	1734	42	1118	33
E-1	193	3533	59	1725	42	13745	117	57062	239	4204	65	1701	41	1124	34
E-1	194	3473	59	1886	43	13816	118	56995	239	4123	64	1821	43	1170	34
E-1	195	3554	60	1802	42	13987	118	57415	240	4093	64	1781	42	1168	34
E-1	196	3503	59	1889	43	13543	116	56870	238	4031	63	1820	43	1153	34
E-1	197	3495	59	1831	43	13560	116	57216	239	4117	64	1834	43	1163	34
E-1	198	3449	59	1839	43	13612	117	57400	240	4076	64	1742	42	1152	34

Appendix B

EPMA dataset

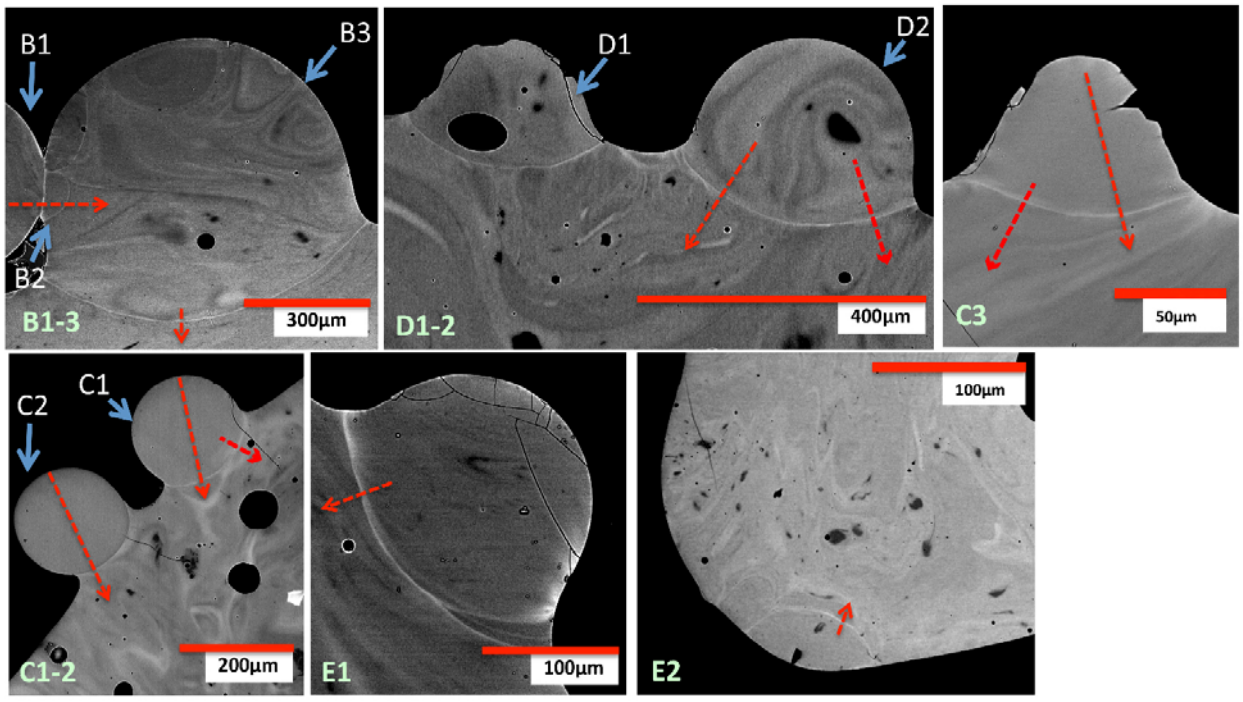

Figure B.1: BSE images of samples and objects, with the locations of sequential EPMA spot analyses indicated by red, dashed arrows.

Table B.1: Electron probe microanalysis spots across interfaces for 9 agglomerated aerodynamic fallout glass samples, presented as major element oxides

Sample	Spot	A_2O_3	MnO	Na_2O	K_2O	SiO_2	FeO	MgO	CaO	TiO_2
B-1	1	11.14±0.06	0.09±0.01	2.41±0.04	3.91±0.03	75.27±0.35	2.22±0.08	0.42±0.01	1.69±0.02	0.2±0.01
B-1	2	11.42±0.06	0.10±0.01	1.59±0.03	4.01±0.03	74.94±0.34	2.29±0.08	0.46±0.01	1.80±0.02	0.21±0.01
B-1	3	11.54±0.06	0.09±0.01	1.48±0.03	4.01±0.03	74.69±0.35	2.36±0.08	0.43±0.01	1.83±0.02	0.21±0.01
B-1	4	12.17±0.07	0.09±0.01	1.59±0.03	4.10±0.03	74.05±0.35	2.47±0.09	0.47±0.01	1.89±0.02	0.23±0.01
B-1	5	12.40±0.07	0.09±0.01	1.55±0.03	4.06±0.03	72.20±0.35	2.44±0.09	0.45±0.01	1.97±0.02	0.24±0.01
B-1	6	12.79±0.07	0.07±0.01	1.68±0.03	4.03±0.03	72.52±0.34	2.20±0.08	0.49±0.01	2.06±0.02	0.24±0.01
B-1	7	13.01±0.07	0.08±0.01	1.84±0.03	4.11±0.03	72.42±0.34	2.40±0.09	0.49±0.01	2.08±0.02	0.28±0.01

B-1	8	13.15±0.07	0.08±0.01	1.68±0.03	4.02±0.03	71.91±0.35	2.49±0.09	0.49±0.01	2.12±0.02	0.25±0.01
B-1	9	13.39±0.07	0.11±0.01	1.66±0.03	4.04±0.03	72.26±0.35	2.33±0.08	0.56±0.01	2.10±0.02	0.26±0.01
B-1	10	13.29±0.07	0.11±0.01	1.57±0.03	4.10±0.03	72.33±0.35	2.44±0.09	0.54±0.01	2.10±0.02	0.24±0.01
B-1	11	13.06±0.07	0.09±0.01	1.52±0.03	4.04±0.03	73.37±0.34	2.51±0.09	0.5±0.01	2.03±0.02	0.23±0.01
B-1	12	12.44±0.07	0.10±0.01	1.53±0.03	4.02±0.03	73.51±0.35	2.42±0.09	0.51±0.01	1.88±0.02	0.23±0.01
B-1	13	11.54±0.06	0.07±0.01	1.43±0.03	3.97±0.03	75.21±0.35	2.29±0.08	0.5±0.01	1.71±0.02	0.21±0.01
B-1	14	8.94±0.06	0.06±0.01	1.03±0.02	3.51±0.03	79.54±0.36	2.16±0.08	0.36±0.01	1.11±0.02	0.15±0.01
B-1	15	8.93±0.06	0.07±0.01	1.08±0.02	3.52±0.03	78.79±0.35	2.07±0.08	0.35±0.01	1.12±0.02	0.18±0.01
B-1	16	10.02±0.06	0.07±0.01	1.24±0.03	3.70±0.03	78.24±0.35	2.32±0.08	0.34±0.01	1.22±0.02	0.19±0.01
B-1	17	11.37±0.06	0.10±0.02	1.36±0.03	3.86±0.03	75.59±0.35	2.39±0.09	0.38±0.02	1.41±0.02	0.21±0.02
B-1	18	12.72±0.07	0.10±0.01	1.21±0.02	4.01±0.03	74.06±0.35	2.52±0.09	0.36±0.01	1.56±0.02	0.23±0.01
B-1	19	13.15±0.07	0.12±0.01	1.39±0.03	4.06±0.03	73.4±0.34	2.51±0.09	0.43±0.01	1.60±0.02	0.25±0.01
B-1	20	13.37±0.07	0.11±0.01	1.38±0.03	4.01±0.03	73.21±0.34	2.67±0.09	0.44±0.01	1.62±0.02	0.24±0.01
B-1	21	13.29±0.07	0.08±0.01	1.19±0.02	4.08±0.03	73.13±0.34	2.51±0.09	0.41±0.01	1.51±0.02	0.21±0.01
B-1	22	12.81±0.07	0.09±0.01	1.30±0.03	3.98±0.03	74.40±0.35	2.40±0.09	0.37±0.01	1.44±0.02	0.24±0.01
B-1	23	12.25±0.07	0.11±0.01	1.30±0.03	3.94±0.03	75.01±0.35	2.43±0.09	0.38±0.01	1.36±0.02	0.22±0.01
B-1	24	11.92±0.06	0.10±0.01	1.38±0.03	3.89±0.03	75.14±0.35	2.33±0.08	0.43±0.01	1.29±0.02	0.24±0.01
B-1	25	11.71±0.06	0.12±0.01	1.41±0.03	3.81±0.03	74.91±0.35	2.36±0.09	0.39±0.01	1.32±0.02	0.22±0.01
B-1	26	11.96±0.06	0.07±0.01	1.27±0.03	3.81±0.03	75.4±0.35	2.51±0.09	0.46±0.01	1.38±0.02	0.23±0.01
B-1	27	11.81±0.06	0.11±0.01	1.29±0.03	3.81±0.03	75.61±0.35	2.46±0.09	0.42±0.01	1.41±0.02	0.23±0.01
B-1	28	12.11±0.07	0.11±0.01	1.17±0.02	3.90±0.03	74.97±0.35	2.47±0.09	0.45±0.01	1.44±0.02	0.24±0.01
B-1	29	12.17±0.07	0.10±0.01	1.25±0.03	3.83±0.03	75.03±0.35	2.39±0.09	0.45±0.01	1.44±0.02	0.26±0.01
B-1	30	11.94±0.06	0.10±0.01	1.35±0.03	3.86±0.03	75.15±0.35	2.43±0.09	0.45±0.01	1.36±0.02	0.25±0.01
B-1	31	11.90±0.06	0.10±0.01	1.23±0.03	3.81±0.03	75.53±0.35	2.48±0.09	0.47±0.01	1.32±0.02	0.25±0.01
B-1	32	12.18±0.07	0.06±0.01	1.18±0.02	3.83±0.03	74.82±0.35	2.31±0.08	0.47±0.01	1.33±0.02	0.25±0.01
B-1	33	12.30±0.07	0.08±0.01	1.13±0.02	3.84±0.03	74.90±0.35	2.42±0.09	0.46±0.01	1.35±0.02	0.26±0.01
B-1	34	12.57±0.07	0.09±0.01	1.24±0.03	3.83±0.03	74.51±0.35	2.41±0.09	0.49±0.01	1.41±0.02	0.25±0.01
B-1	35	13.04±0.07	0.08±0.01	1.48±0.03	3.82±0.03	73.51±0.35	2.36±0.09	0.48±0.01	1.41±0.02	0.25±0.01
B-1	36	13.63±0.07	0.09±0.01	1.46±0.03	3.92±0.03	73.12±0.34	2.49±0.09	0.51±0.01	1.46±0.02	0.26±0.01
B-1	37	13.86±0.07	0.08±0.01	1.48±0.03	3.91±0.03	72.49±0.35	2.40±0.09	0.54±0.01	1.52±0.02	0.26±0.01
B-1	38	14.30±0.07	0.10±0.01	1.33±0.03	3.89±0.03	72.47±0.35	2.82±0.09	0.5±0.01	1.53±0.02	0.23±0.01
B-1	39	14.52±0.07	0.11±0.01	1.33±0.03	3.94±0.03	72.22±0.35	2.72±0.09	0.53±0.01	1.58±0.02	0.25±0.01
B-1	40	14.50±0.07	0.07±0.01	1.37±0.03	3.88±0.03	72.75±0.35	2.47±0.09	0.57±0.01	1.55±0.02	0.29±0.01
B-1	41	14.36±0.07	0.09±0.01	1.56±0.03	3.94±0.03	72.17±0.35	2.47±0.09	0.53±0.01	1.51±0.02	0.27±0.01
B-1	42	14.35±0.07	0.11±0.01	1.39±0.03	3.93±0.03	72.18±0.35	2.23±0.08	0.55±0.01	1.48±0.02	0.25±0.01
B-1	43	14.22±0.07	0.08±0.01	1.45±0.03	3.92±0.03	73.07±0.34	2.54±0.09	0.54±0.01	1.40±0.02	0.26±0.01
B-1	44	13.95±0.07	0.06±0.01	1.35±0.03	3.88±0.03	73.49±0.35	2.39±0.09	0.52±0.01	1.30±0.02	0.23±0.01
B-1	45	13.73±0.07	0.10±0.01	1.20±0.02	3.91±0.03	73.84±0.35	2.39±0.09	0.55±0.01	1.31±0.02	0.26±0.01
B-1	46	13.58±0.07	0.11±0.01	1.19±0.02	3.95±0.03	73.41±0.35	2.22±0.08	0.53±0.01	1.29±0.02	0.25±0.01
B-1	47	13.10±0.07	0.08±0.01	1.30±0.03	3.91±0.03	73.66±0.35	2.45±0.09	0.49±0.01	1.23±0.02	0.25±0.01
B-1	48	13.39±0.07	0.12±0.01	1.30±0.03	3.92±0.03	74.43±0.35	2.27±0.08	0.54±0.01	1.20±0.02	0.26±0.01
B-1	49	13.43±0.07	0.07±0.01	1.41±0.03	3.98±0.03	74.21±0.35	2.33±0.08	0.53±0.01	1.22±0.02	0.25±0.01
B-1	50	13.45±0.07	0.09±0.01	1.40±0.03	3.95±0.03	73.28±0.34	2.35±0.09	0.55±0.01	1.23±0.02	0.29±0.01
B-1	51	13.75±0.07	0.06±0.01	1.34±0.03	3.97±0.03	73.74±0.35	2.33±0.08	0.51±0.01	1.21±0.02	0.29±0.01
B-1	52	13.77±0.07	0.07±0.01	1.27±0.03	3.90±0.03	73.49±0.35	2.40±0.09	0.52±0.01	1.28±0.02	0.29±0.01
B-1	53	14.12±0.07	0.08±0.01	1.35±0.03	4.01±0.03	72.21±0.35	2.24±0.08	0.53±0.01	1.32±0.02	0.3±0.01
B-1	54	14.26±0.07	0.11±0.01	1.41±0.03	4.00±0.03	73.21±0.34	2.43±0.09	0.56±0.01	1.37±0.02	0.3±0.01
B-1	55	14.10±0.07	0.06±0.01	1.54±0.03	4.04±0.03	72.17±0.35	2.25±0.08	0.54±0.01	1.34±0.02	0.29±0.01
B-1	56	14.44±0.07	0.07±0.01	1.52±0.03	4.04±0.03	71.72±0.34	2.43±0.09	0.55±0.01	1.36±0.02	0.32±0.01
B-1	57	14.50±0.07	0.10±0.01	1.46±0.03	4.07±0.03	72.28±0.35	2.17±0.08	0.58±0.01	1.38±0.02	0.29±0.01
B-1	58	14.49±0.07	0.08±0.01	1.39±0.03	4.13±0.03	72.41±0.35	2.39±0.09	0.56±0.01	1.40±0.02	0.32±0.01
B-1	59	14.60±0.07	0.11±0.01	1.32±0.03	4.12±0.03	72.38±0.35	2.48±0.09	0.55±0.01	1.37±0.02	0.28±0.01
B-1	60	14.36±0.07	0.10±0.01	1.40±0.03	4.10±0.03	72.21±0.35	2.37±0.09	0.61±0.01	1.40±0.02	0.32±0.01
B-1	61	14.05±0.07	0.07±0.01	1.56±0.03	4.12±0.03	71.62±0.34	2.41±0.09	0.51±0.01	1.44±0.02	0.34±0.01
B-1	62	14.45±0.07	0.11±0.01	1.55±0.03	4.15±0.03	71.63±0.34	2.46±0.09	0.56±0.01	1.48±0.02	0.33±0.01
B-1	63	14.25±0.07	0.07±0.01	1.54±0.03	4.20±0.03	71.82±0.34	2.56±0.09	0.56±0.01	1.46±0.02	0.35±0.01
B-1	64	13.71±0.07	0.08±0.01	1.56±0.03	4.18±0.03	72.44±0.35	2.31±0.08	0.59±0.01	1.47±0.02	0.31±0.01
B-1	65	13.61±0.07	0.08±0.02	1.39±0.03	4.22±0.03	72.51±0.35	2.39±0.09	0.56±0.02	1.48±0.02	0.32±0.02
B-1	66	13.33±0.07	0.09±0.01	1.14±0.02	4.15±0.03	72.97±0.34	2.36±0.08	0.51±0.01	1.50±0.02	0.34±0.01
B-1	67	12.87±0.07	0.08±0.01	1.47±0.03	4.15±0.03	74.12±0.35	2.22±0.08	0.53±0.01	1.50±0.02	0.31±0.01
B-1	68	12.24±0.07	0.05±0.01	1.45±0.03	4.05±0.03	74.41±0.35	2.28±0.08	0.52±0.01	1.54±0.02	0.31±0.01
B-1	69	11.53±0.06	0.08±0.01	1.56±0.03	4.01±0.03	75.10±0.35	2.39±0.09	0.52±0.01	1.58±0.02	0.3±0.01
B-1	70	11.60±0.06	0.09±0.01	1.54±0.03	3.98±0.03	75.29±0.35	2.53±0.09	0.53±0.01	1.80±0.02	0.27±0.01
B-1	71	12.34±0.07	0.11±0.01	1.46±0.03	4.04±0.03	72.99±0.34	2.72±0.09	0.57±0.01	2.03±0.02	0.25±0.01
B-1	72	12.92±0.07	0.11±0.01	1.35±0.03	4.14±0.03	73.52±0.35	2.51±0.09	0.51±0.01	1.95±0.02	0.28±0.01
B-1	73	13.15±0.07	0.08±0.01	1.37±0.03	4.16±0.03	73.43±0.35	2.31±0.08	0.49±0.01	1.85±0.02	0.27±0.01
B-1	74	13.10±0.07	0.09±0.01	1.47±0.03	4.13±0.03	73.63±0.35	2.31±0.08	0.52±0.01	1.75±0.02	0.29±0.01
B-1	75	13.15±0.07	0.10±0.01	1.63±0.03	4.09±0.03	72.82±0.34	2.31±0.08	0.51±0.01	1.83±0.02	0.27±0.01
B-1	76	13.21±0.07	0.09±0.01	1.72±0.03	4.09±0.03	73.13±0.34	2.64±0.09	0.56±0.01	1.88±0.02	0.28±0.01
B-1	77	13.62±0.07	0.09±0.01	1.65±0.03	4.04±0.03	72.53±0.35	2.40±0.09	0.58±0.01	1.92±0.02	0.29±0.01
B-1	78	13.45±0.07	0.11±0.01	1.51±0.03	4.06±0.03	72.45±0.35	2.49±0.09	0.49±0.01	1.87±0.02	0.31±0.01
B-1	79	13.33±0.07	0.10±0.01	1.43±0.03	4.10±0.03	72.58±0.34	2.35±0.08	0.53±0.01	1.82±0.02	0.3±0.01
B-1	80	13.02±0.07	0.08±0.01	1.43±0.03	4.08±0.03	73.84±0.35	2.45±0.09	0.48±0.01	1.69±0.02	0.26±0.01
B-1	81	12.88±0.07	0.07±0.01	1.55±0.03	4.08±0.03	74.17±0.35	2.37±0.09	0.48±0.01	1.70±0.02	0.27±0.01
B-1	82	13.27±0.07	0.09±0.01	1.64±0.03	4.12±0.03	72.75±0.34	2.19±0.08	0.47±0.01	1.71±0.02	0.28±0.01
B-1	83	13.02±0.07	0.08±0.01	1.49±0.03	4.11±0.03	73.14±0.34	2.33±0.08	0.48±0.01	1.78±0.02	0.26±0.01
B-1	84	12.91±0.07	0.07±0.01	1.48±0.03	4.08±0.03	73.53±0.35	2.36±0.09	0.48±0.01	1.79±0.02	0.25±0.01
B-1	85	12.48±0.07	0.07±0.01	1.38±0.03	4.08±0.03	73.72±0.35	2.39±0.09	0.47±0.01	1.83±0.02	0.27±0.01
B-1	86	12.66±0.07	0.09±0.01	1.29±0.03	4.11±0.03	73.58±0.35	2.25±0.08	0.48±0.01	1.85±0.02	0.27±0.01
B-1	87	12.78±0.07	0.09±0.01	1.39±0.03	4.00±0.03	74.20±0.35	2.40±0.09	0.49±0.01	1.86±0.02	0.26±0.01
B-1	88	12.82±0.07	0.10±0.01	1.54±0.03	4.06±0.03	73.45±0.35	2.38±0.09	0.48±0.01	1.91±0.02	0.24±0.01
B-1	89	12.86±0.07	0.08±0.01	1.57±0.03	4.00±0.03	73.71±0.35	2.45±0.09	0.44±0.01	1.95±0.02	0.25±0.01
B-1	90	14.30±0.07	0.06±0.01	2.53±0.04	3.91±0.03	71.76±0.34	2.49±0.09	0.49±0.01	2.40±0.02	0.29±0.01
B-1	91	13.84±0.07	0.09±0.01	1.55±0.03	3.91±0.03	72.15±0.35	2.52±0.09	0.52±0.01	2.37±0.02	0.32±0.01
B-1	92	13.55±0.07	0.08±0.01	1.53±0.03	3.82±0.03	72.83±0.34	2.34±0.08	0.55±0.01	2.39±0.02	0.3±0.01

B-1	93	13.53±0.07	0.08±0.01	1.38±0.03	3.88±0.03	73.13±0.34	2.40±0.09	0.51±0.01	2.35±0.02	0.32±0.01
B-1	94	13.49±0.07	0.10±0.01	1.54±0.03	3.90±0.03	73.02±0.34	2.57±0.09	0.53±0.01	2.32±0.02	0.3±0.01
B-1	95	13.49±0.07	0.10±0.01	1.35±0.03	3.89±0.03	72.55±0.34	2.29±0.08	0.52±0.01	2.32±0.02	0.3±0.01
B-1	96	13.20±0.07	0.08±0.01	1.28±0.03	3.86±0.03	73.13±0.34	2.25±0.08	0.52±0.01	2.25±0.02	0.3±0.01
B-1	97	13.08±0.07	0.08±0.01	1.41±0.03	3.88±0.03	73.89±0.35	2.26±0.08	0.5±0.01	2.26±0.02	0.28±0.01
B-1	98	13.52±0.07	0.08±0.01	1.22±0.03	3.88±0.03	73.09±0.34	2.37±0.09	0.5±0.01	2.24±0.02	0.3±0.01
B-1	99	13.47±0.07	0.10±0.01	1.45±0.03	3.94±0.03	72.63±0.34	2.23±0.08	0.48±0.01	2.23±0.02	0.29±0.01
B-1	100	13.55±0.07	0.08±0.01	1.37±0.03	3.96±0.03	73.66±0.35	2.40±0.09	0.48±0.01	2.25±0.02	0.29±0.01
B-1	101	13.55±0.07	0.11±0.01	1.34±0.03	3.99±0.03	73.29±0.34	2.27±0.08	0.5±0.01	2.29±0.02	0.26±0.01
B-1	102	13.35±0.07	0.08±0.01	1.68±0.03	3.99±0.03	71.23±0.34	2.23±0.08	0.49±0.01	2.33±0.02	0.28±0.01
B-1	103	13.87±0.07	0.09±0.01	1.41±0.03	3.95±0.03	73.00±0.34	2.27±0.08	0.51±0.01	2.34±0.02	0.27±0.01
B-1	104	14.04±0.07	0.08±0.01	1.70±0.03	4.03±0.03	71.94±0.35	2.38±0.09	0.52±0.01	2.38±0.02	0.29±0.01
B-1	105	14.10±0.07	0.07±0.01	1.48±0.03	3.99±0.03	72.52±0.35	2.33±0.08	0.47±0.01	2.36±0.02	0.26±0.01
B-1	106	13.87±0.07	0.07±0.01	1.70±0.03	4.04±0.03	72.14±0.35	2.31±0.08	0.48±0.01	2.31±0.02	0.28±0.01
B-1	107	13.87±0.07	0.06±0.01	1.42±0.03	4.06±0.03	72.36±0.35	2.35±0.08	0.51±0.01	2.28±0.02	0.27±0.01
B-1	108	13.60±0.07	0.08±0.01	1.30±0.03	4.07±0.03	72.58±0.34	2.39±0.09	0.5±0.01	2.17±0.02	0.27±0.01
B-1	109	13.63±0.07	0.08±0.01	1.63±0.03	4.15±0.03	72.75±0.34	2.50±0.09	0.45±0.01	2.28±0.02	0.27±0.01
B-1	110	13.69±0.07	0.07±0.01	1.42±0.03	4.03±0.03	71.72±0.34	2.39±0.09	0.5±0.01	2.33±0.02	0.27±0.01
B-1	111	13.97±0.07	0.07±0.01	1.55±0.03	4.10±0.03	71.59±0.34	2.36±0.08	0.53±0.01	2.41±0.02	0.3±0.01
B-1	112	13.96±0.07	0.10±0.01	1.50±0.03	4.14±0.03	70.29±0.34	2.27±0.08	0.49±0.01	2.44±0.02	0.3±0.01
B-1	113	14.03±0.07	0.09±0.01	1.75±0.03	4.14±0.03	71.07±0.34	2.36±0.08	0.49±0.01	2.42±0.02	0.3±0.01
B-1	114	14.13±0.07	0.10±0.01	1.41±0.03	4.08±0.03	72.4±0.35	2.44±0.09	0.49±0.01	2.42±0.02	0.31±0.01
B-1	115	13.95±0.07	0.09±0.02	1.51±0.03	4.11±0.03	72.14±0.35	2.34±0.10	0.43±0.02	2.39±0.03	0.28±0.02
B-1	116	13.76±0.07	0.05±0.01	1.32±0.03	4.13±0.03	72.26±0.35	2.26±0.08	0.46±0.01	2.36±0.02	0.3±0.01
B-1	117	12.85±0.07	0.09±0.01	1.49±0.03	4.12±0.03	71.87±0.34	2.39±0.08	0.44±0.01	2.26±0.02	0.3±0.01
B-1	118	12.93±0.07	0.08±0.01	1.62±0.03	4.13±0.03	73.36±0.34	2.11±0.08	0.4±0.01	2.08±0.02	0.27±0.01
B-1	119	12.53±0.07	0.07±0.01	1.28±0.03	4.11±0.03	74.42±0.35	2.27±0.08	0.46±0.01	2.00±0.02	0.28±0.01
B-1	120	11.82±0.07	0.08±0.01	1.53±0.03	4.12±0.03	75.34±0.35	2.30±0.08	0.41±0.01	1.83±0.02	0.24±0.01
B-1	121	11.87±0.06	0.07±0.01	1.35±0.03	4.14±0.03	74.49±0.35	2.13±0.08	0.41±0.01	1.77±0.02	0.24±0.01
B-1	122	11.81±0.06	0.06±0.01	1.32±0.03	4.07±0.03	75.28±0.35	2.01±0.08	0.4±0.01	1.74±0.02	0.25±0.01
B-1	123	11.83±0.07	0.05±0.01	1.47±0.03	4.16±0.03	74.87±0.35	2.25±0.08	0.43±0.01	1.75±0.02	0.23±0.01
B-1	124	11.83±0.07	0.05±0.01	1.49±0.03	4.23±0.03	74.76±0.35	2.13±0.08	0.43±0.01	1.74±0.02	0.25±0.01
B-1	125	11.75±0.06	0.03±0.01	1.44±0.03	4.19±0.03	75.03±0.35	2.00±0.08	0.46±0.01	1.72±0.02	0.26±0.01
B-1	126	11.85±0.07	0.04±0.01	1.36±0.03	4.16±0.03	75.07±0.35	2.19±0.08	0.45±0.01	1.72±0.02	0.28±0.01
B-1	127	11.61±0.06	0.10±0.01	1.38±0.03	4.28±0.03	75.09±0.35	2.18±0.08	0.47±0.01	1.73±0.02	0.26±0.01
B-1	128	12.22±0.07	0.06±0.01	1.55±0.03	4.36±0.03	74.16±0.35	2.28±0.08	0.52±0.01	1.72±0.02	0.29±0.01
B-1	129	11.99±0.06	0.06±0.01	1.38±0.03	4.36±0.03	73.81±0.35	2.18±0.08	0.53±0.01	1.73±0.02	0.3±0.01
B-1	130	11.85±0.07	0.07±0.01	1.48±0.03	4.41±0.03	74.44±0.35	2.21±0.08	0.57±0.01	1.78±0.02	0.29±0.01
B-1	131	11.62±0.06	0.06±0.01	1.35±0.03	4.38±0.03	74.06±0.35	2.54±0.09	0.6±0.01	2.11±0.02	0.27±0.01
B-1	132	11.75±0.06	0.10±0.01	1.93±0.03	4.40±0.03	71.99±0.35	3.13±0.10	0.71±0.01	3.07±0.03	0.26±0.01
B-1	133	12.86±0.07	0.06±0.01	2.09±0.03	4.50±0.03	71.42±0.34	1.99±0.08	0.48±0.01	3.04±0.03	0.24±0.01
B-2	1	13.05±0.07	0.06±0.01	2.30±0.04	4.55±0.03	72.49±0.34	1.80±0.07	0.4±0.01	2.72±0.03	0.25±0.01
B-2	2	13.06±0.07	0.08±0.01	2.09±0.03	4.59±0.03	72.44±0.34	1.98±0.08	0.39±0.01	2.51±0.02	0.26±0.01
B-2	3	13.21±0.07	0.05±0.01	2.30±0.04	4.67±0.03	71.55±0.34	1.87±0.07	0.42±0.01	2.30±0.02	0.27±0.01
B-2	4	13.40±0.07	0.06±0.01	1.99±0.03	4.65±0.03	72.55±0.34	1.98±0.08	0.45±0.01	2.27±0.02	0.25±0.01
B-2	5	13.63±0.07	0.07±0.01	2.21±0.03	4.69±0.03	71.18±0.34	1.99±0.08	0.45±0.01	2.19±0.02	0.27±0.01
B-2	6	13.75±0.07	0.04±0.01	1.96±0.03	4.60±0.03	71.62±0.34	2.03±0.08	0.44±0.01	2.21±0.02	0.25±0.01
B-2	7	13.97±0.07	0.09±0.01	1.57±0.03	4.52±0.03	72.25±0.35	2.24±0.08	0.44±0.01	2.22±0.02	0.28±0.01
B-2	8	14.05±0.07	0.06±0.01	1.99±0.03	4.56±0.03	71.02±0.34	2.14±0.08	0.45±0.01	2.17±0.02	0.27±0.01
B-2	9	13.96±0.07	0.08±0.01	1.77±0.03	4.46±0.03	71.59±0.34	2.06±0.08	0.47±0.01	2.22±0.02	0.26±0.01
B-2	10	14.18±0.07	0.09±0.01	1.98±0.03	4.51±0.03	71.34±0.34	2.13±0.08	0.49±0.01	2.26±0.02	0.28±0.01
B-2	11	14.16±0.07	0.09±0.01	1.83±0.03	4.37±0.03	71.29±0.34	1.99±0.08	0.44±0.01	2.25±0.02	0.27±0.01
B-2	12	14.30±0.07	0.07±0.01	1.68±0.03	4.37±0.03	71.63±0.34	2.07±0.08	0.47±0.01	2.29±0.02	0.29±0.01
B-2	13	14.31±0.07	0.07±0.01	1.65±0.03	4.32±0.03	71.61±0.34	2.34±0.08	0.48±0.01	2.31±0.02	0.28±0.01
B-2	14	14.36±0.07	0.09±0.01	1.68±0.03	4.35±0.03	72.12±0.35	2.21±0.08	0.46±0.01	2.33±0.02	0.27±0.01
B-2	15	14.43±0.07	0.06±0.01	1.79±0.03	4.29±0.03	72.15±0.35	2.10±0.08	0.47±0.01	2.32±0.02	0.27±0.01
B-2	16	14.13±0.07	0.06±0.01	1.70±0.03	4.23±0.03	72.08±0.35	2.21±0.08	0.47±0.01	2.33±0.02	0.25±0.01
B-2	17	14.51±0.07	0.07±0.01	1.76±0.03	4.28±0.03	71.73±0.34	2.19±0.08	0.5±0.01	2.34±0.02	0.27±0.01
B-2	18	14.24±0.07	0.05±0.01	1.57±0.03	4.25±0.03	71.46±0.34	2.13±0.08	0.48±0.01	2.31±0.02	0.26±0.01
B-2	19	14.54±0.07	0.07±0.01	1.48±0.03	4.24±0.03	71.67±0.34	2.14±0.08	0.46±0.01	2.32±0.02	0.27±0.01
B-2	20	14.51±0.07	0.05±0.01	1.88±0.03	4.25±0.03	70.08±0.34	2.17±0.08	0.46±0.01	2.35±0.02	0.27±0.01
B-2	21	14.35±0.07	0.06±0.01	1.73±0.03	4.28±0.03	71.61±0.34	2.11±0.08	0.5±0.01	2.32±0.02	0.26±0.01
B-2	22	14.34±0.07	0.08±0.01	1.86±0.03	4.30±0.03	71.87±0.34	1.97±0.08	0.47±0.01	2.29±0.02	0.27±0.01
B-2	23	14.37±0.07	0.07±0.01	1.56±0.03	4.32±0.03	71.59±0.34	1.94±0.08	0.45±0.01	2.27±0.02	0.26±0.01
B-2	24	14.34±0.07	0.06±0.01	1.94±0.03	4.35±0.03	71.07±0.34	2.25±0.08	0.49±0.01	2.29±0.02	0.28±0.01
B-2	25	14.04±0.07	0.06±0.01	1.80±0.03	4.33±0.03	71.63±0.34	1.96±0.08	0.44±0.01	2.35±0.02	0.24±0.01
B-2	26	14.09±0.07	0.07±0.01	1.71±0.03	4.41±0.03	71.78±0.34	2.01±0.08	0.42±0.01	2.40±0.02	0.28±0.01
B-2	27	13.95±0.07	0.06±0.01	1.94±0.03	4.36±0.03	71.83±0.34	2.07±0.08	0.43±0.01	2.49±0.02	0.26±0.01
B-2	28	13.65±0.07	0.06±0.01	1.52±0.03	4.32±0.03	72.57±0.34	1.95±0.08	0.4±0.01	2.54±0.02	0.26±0.01
B-2	29	13.17±0.07	0.06±0.01	1.80±0.03	4.28±0.03	72.48±0.34	1.99±0.08	0.47±0.01	2.67±0.03	0.24±0.01
B-2	30	11.79±0.07	0.10±0.01	1.65±0.03	4.11±0.03	73.45±0.34	2.55±0.08	0.55±0.01	2.90±0.03	0.22±0.01
B-2	31	11.27±0.07	0.10±0.02	1.28±0.04	4.00±0.03	74.44±0.35	2.14±0.10	0.52±0.02	2.66±0.03	0.19±0.02
B-2	32	12.69±0.06	0.11±0.01	1.65±0.03	4.18±0.03	72.52±0.35	2.24±0.08	0.46±0.01	2.84±0.03	0.23±0.01
B-2	33	11.32±0.06	0.08±0.01	1.41±0.03	4.06±0.03	73.97±0.35	2.18±0.08	0.48±0.01	2.39±0.02	0.22±0.01
B-2	34	11.94±0.06	0.05±0.01	1.69±0.03	4.24±0.03	74.5±0.35	2.10±0.08	0.41±0.01	2.23±0.02	0.21±0.01
B-2	35	11.94±0.06	0.10±0.01	1.54±0.03	4.20±0.03	73.35±0.34	2.03±0.08	0.46±0.01	2.31±0.02	0.21±0.01
B-2	36	12.66±0.07	0.07±0.01	1.83±0.03	4.25±0.03	73.14±0.34	2.08±0.08	0.46±0.01	2.28±0.02	0.25±0.01
B-2	37	12.76±0.07	0.08±0.01	1.58±0.03	4.34±0.03	72.86±0.34	2.30±0.08	0.46±0.01	2.30±0.02	0.22±0.01
B-2	38	12.96±0.07	0.05±0.01	1.73±0.03	4.24±0.03	72.78±0.34	2.05±0.08	0.49±0.01	2.35±0.02	0.24±0.01
B-2	39	12.91±0.07	0.08±0.01	1.43±0.03	4.20±0.03	72.52±0.34	2.07±0.08	0.45±0.01	2.37±0.02	0.24±0.01
B-2	40	13.01±0.07	0.08±0.01	1.50±0.03	4.23±0.03	72.43±0.34	2.10±0.08	0.47±0.01	2.33±0.02	0.25±0.01
B-2	41	13.10±0.07	0.06±0.01	1.63±0.03	4.26±0.03	72.97±0.34	2.12±0.08	0.53±0.01	2.36±0.02	0.25±0.01
B-2	42	13.06±0.07	0.08±0.01	1.55±0.03	4.22±0.03	71.46±0.34	2.13±0.08	0.45±0.01	2.37±0.02	0.23±0.01
B-2	43	13.08±0.07	0.05±0.01	1.68±0.03	4.24±0.03	72.85±0.34	2.11±0.08	0.47±0.01	2.34±0.02	0.21±0.01
B-2	44	12.87±0.07	0.07±0.01	1.56±0.03	4.18±0.03	72.45±0.34	2.20±0.08	0.48±0.01	2.37±0.02	0.25±0.01

B-2	45	13.10±0.07	0.08±0.01	1.57±0.03	4.18±0.03	72.52±0.34	2.15±0.08	0.49±0.01	2.34±0.02	0.24±0.01
B-2	46	13.09±0.07	0.10±0.01	1.45±0.03	4.24±0.03	72.79±0.34	2.17±0.08	0.5±0.01	2.36±0.02	0.23±0.01
B-2	47	13.18±0.07	0.08±0.01	1.43±0.03	4.21±0.03	72.38±0.34	2.03±0.08	0.5±0.01	2.35±0.02	0.24±0.01
B-2	48	13.16±0.07	0.10±0.01	1.77±0.03	4.21±0.03	71.50±0.34	2.30±0.08	0.48±0.01	2.35±0.02	0.23±0.01
B-2	49	13.18±0.07	0.09±0.01	1.52±0.03	4.20±0.03	72.27±0.35	2.24±0.08	0.52±0.01	2.37±0.02	0.26±0.01
B-3	1	14.44±0.07	0.06±0.01	2.39±0.04	3.52±0.03	71.30±0.34	2.61±0.09	0.53±0.01	2.59±0.03	0.26±0.01
B-3	2	14.46±0.07	0.06±0.01	1.74±0.03	3.58±0.03	71.99±0.35	2.37±0.08	0.51±0.01	2.71±0.03	0.28±0.01
B-3	3	14.42±0.07	0.08±0.01	1.56±0.03	3.61±0.03	71.68±0.34	2.48±0.09	0.52±0.01	2.68±0.03	0.26±0.01
B-3	4	14.49±0.07	0.09±0.01	1.59±0.03	3.58±0.03	71.94±0.35	2.15±0.08	0.5±0.01	2.71±0.03	0.27±0.01
B-3	5	14.51±0.07	0.10±0.01	1.65±0.03	3.58±0.03	71.73±0.34	2.50±0.09	0.51±0.01	2.71±0.03	0.26±0.01
B-3	6	14.70±0.07	0.09±0.01	1.71±0.03	3.57±0.03	71.39±0.34	2.62±0.09	0.51±0.01	2.81±0.03	0.31±0.01
B-3	7	14.77±0.07	0.09±0.01	1.46±0.03	3.57±0.03	71.25±0.34	2.55±0.09	0.49±0.01	2.74±0.03	0.3±0.01
B-3	8	14.49±0.07	0.10±0.01	1.79±0.03	3.57±0.03	72.34±0.35	2.30±0.08	0.48±0.01	2.67±0.03	0.27±0.01
B-3	9	14.35±0.07	0.09±0.01	1.68±0.03	3.61±0.03	71.94±0.35	2.44±0.09	0.47±0.01	2.64±0.03	0.28±0.01
B-3	10	14.34±0.07	0.08±0.01	1.62±0.03	3.56±0.03	72.5±0.35	2.71±0.09	0.54±0.01	2.64±0.03	0.26±0.01
B-3	11	13.34±0.07	0.10±0.01	1.50±0.03	3.62±0.03	72.72±0.34	2.53±0.09	0.47±0.01	2.56±0.02	0.27±0.01
B-3	12	13.56±0.07	0.09±0.01	1.58±0.03	3.62±0.03	73.83±0.35	2.45±0.09	0.49±0.01	2.42±0.02	0.25±0.01
B-3	13	13.07±0.07	0.05±0.01	1.54±0.03	3.60±0.03	73.93±0.35	2.36±0.08	0.49±0.01	2.23±0.02	0.24±0.01
B-3	14	12.73±0.07	0.07±0.01	1.34±0.03	3.60±0.03	74.56±0.35	2.37±0.08	0.47±0.01	2.17±0.02	0.25±0.01
B-3	15	12.52±0.07	0.08±0.01	1.60±0.03	3.68±0.03	73.32±0.34	2.34±0.08	0.41±0.01	2.12±0.02	0.27±0.01
B-3	16	12.82±0.07	0.05±0.01	1.60±0.03	3.70±0.03	73.74±0.35	2.48±0.09	0.48±0.01	2.17±0.02	0.28±0.01
B-3	17	13.21±0.07	0.07±0.01	1.54±0.03	3.74±0.03	74.12±0.35	2.44±0.09	0.49±0.01	2.26±0.02	0.3±0.01
B-3	18	13.54±0.07	0.08±0.01	1.44±0.03	3.75±0.03	73.27±0.34	2.57±0.09	0.48±0.01	2.30±0.02	0.3±0.01
B-3	19	13.53±0.07	0.09±0.01	1.59±0.03	3.77±0.03	72.97±0.34	2.42±0.08	0.52±0.01	2.35±0.02	0.33±0.01
B-3	20	13.76±0.07	0.09±0.01	1.64±0.03	3.78±0.03	71.24±0.34	2.56±0.09	0.52±0.01	2.47±0.02	0.34±0.01
B-3	21	13.82±0.07	0.08±0.01	1.48±0.03	3.87±0.03	72.3±0.35	2.49±0.09	0.52±0.01	2.43±0.02	0.35±0.01
B-3	22	13.43±0.07	0.07±0.01	1.75±0.03	3.83±0.03	73.02±0.34	2.57±0.09	0.54±0.01	2.40±0.02	0.35±0.01
B-3	23	13.04±0.07	0.09±0.01	1.69±0.03	3.87±0.03	73.31±0.34	2.39±0.08	0.5±0.01	2.40±0.02	0.31±0.01
B-3	24	12.79±0.07	0.11±0.01	1.59±0.03	3.79±0.03	72.87±0.34	2.80±0.09	0.54±0.01	2.51±0.02	0.32±0.01
B-3	25	12.67±0.07	0.09±0.01	1.58±0.03	3.75±0.03	72.73±0.34	3.17±0.10	0.65±0.01	2.67±0.03	0.29±0.01
B-3	26	12.84±0.07	0.11±0.01	1.38±0.03	3.79±0.03	73.22±0.34	2.84±0.09	0.54±0.01	2.47±0.02	0.25±0.01
B-3	27	13.00±0.07	0.09±0.01	1.65±0.03	3.95±0.03	73.94±0.35	2.37±0.08	0.5±0.01	2.14±0.02	0.3±0.01
B-3	28	13.18±0.07	0.08±0.01	1.74±0.03	3.95±0.03	73.56±0.35	2.47±0.09	0.52±0.01	2.05±0.02	0.28±0.01
B-3	29	12.98±0.07	0.04±0.01	1.68±0.03	3.96±0.03	74.81±0.35	2.17±0.08	0.49±0.01	1.97±0.02	0.28±0.01
B-3	30	12.99±0.07	0.05±0.01	1.60±0.03	3.92±0.03	74.37±0.35	2.66±0.09	0.48±0.01	1.92±0.02	0.25±0.01
B-3	31	12.95±0.07	0.09±0.02	1.57±0.03	3.95±0.03	74.06±0.35	2.27±0.09	0.5±0.02	1.89±0.02	0.3±0.02
B-3	32	12.93±0.07	0.08±0.01	1.25±0.03	3.89±0.03	73.91±0.35	2.43±0.09	0.53±0.01	1.94±0.02	0.26±0.01
B-3	33	13.07±0.07	0.09±0.01	1.36±0.03	3.96±0.03	73.96±0.35	2.60±0.09	0.48±0.01	1.86±0.02	0.26±0.01
B-3	34	12.72±0.07	0.10±0.01	1.61±0.03	3.95±0.03	74.15±0.35	2.54±0.09	0.47±0.01	1.86±0.02	0.28±0.01
B-3	35	12.76±0.07	0.10±0.01	1.72±0.03	3.95±0.03	74.27±0.35	2.34±0.08	0.46±0.01	1.86±0.02	0.26±0.01
B-3	36	12.99±0.07	0.08±0.01	1.65±0.03	3.94±0.03	74.67±0.35	2.46±0.09	0.41±0.01	1.76±0.02	0.25±0.01
B-3	37	12.60±0.07	0.10±0.01	1.54±0.03	3.95±0.03	74.04±0.35	2.39±0.09	0.42±0.01	1.64±0.02	0.26±0.01
B-3	38	12.50±0.07	0.07±0.01	1.49±0.03	3.99±0.03	73.99±0.35	2.61±0.09	0.42±0.01	1.70±0.02	0.28±0.01
B-3	39	12.52±0.07	0.06±0.01	1.39±0.03	3.96±0.03	74.60±0.35	2.43±0.09	0.43±0.01	1.74±0.02	0.24±0.01
B-3	40	12.90±0.07	0.09±0.01	1.67±0.03	4.02±0.03	74.62±0.35	2.45±0.09	0.45±0.01	1.83±0.02	0.26±0.01
B-3	41	12.64±0.07	0.08±0.01	1.71±0.03	4.02±0.03	73.49±0.35	2.43±0.09	0.42±0.01	1.88±0.02	0.25±0.01
B-3	42	12.84±0.07	0.09±0.01	1.82±0.03	4.06±0.03	73.84±0.35	2.44±0.09	0.44±0.01	1.93±0.02	0.24±0.01
B-3	43	13.02±0.07	0.11±0.01	1.80±0.03	4.01±0.03	73.60±0.35	2.45±0.09	0.49±0.01	2.07±0.02	0.24±0.01
B-3	44	13.09±0.07	0.12±0.01	1.75±0.03	4.02±0.03	73.63±0.35	2.64±0.09	0.5±0.01	2.11±0.02	0.27±0.01
B-3	45	12.99±0.07	0.10±0.01	1.67±0.03	4.06±0.03	73.85±0.35	2.33±0.08	0.51±0.01	2.09±0.02	0.26±0.01
B-3	46	13.06±0.07	0.13±0.01	1.47±0.03	4.11±0.03	73.71±0.35	2.41±0.09	0.5±0.01	2.10±0.02	0.28±0.01
B-3	47	13.00±0.07	0.08±0.01	1.76±0.03	4.10±0.03	74.22±0.35	2.37±0.09	0.48±0.01	2.09±0.02	0.27±0.01
B-3	48	12.81±0.07	0.10±0.01	1.83±0.03	4.08±0.03	73.53±0.35	2.48±0.09	0.52±0.01	2.10±0.02	0.26±0.01
B-3	49	12.93±0.07	0.10±0.01	2.03±0.03	4.13±0.03	73.97±0.35	2.59±0.09	0.51±0.01	2.13±0.02	0.27±0.01
B-3	50	13.04±0.07	0.15±0.01	1.95±0.03	4.20±0.03	73.93±0.35	2.51±0.09	0.49±0.01	2.19±0.02	0.25±0.01
B-3	51	12.73±0.07	0.08±0.01	1.94±0.03	4.48±0.03	72.06±0.35	2.57±0.09	0.58±0.01	2.09±0.02	0.27±0.01
B-3	52	12.28±0.07	0.08±0.01	1.90±0.03	4.30±0.03	72.61±0.34	2.48±0.09	0.55±0.01	1.94±0.02	0.24±0.01
B-3	53	11.97±0.06	0.09±0.01	1.81±0.03	4.32±0.03	73.3±0.34	2.25±0.08	0.5±0.01	1.80±0.02	0.25±0.01
B-3	54	11.82±0.07	0.07±0.01	1.66±0.03	4.25±0.03	73.97±0.35	2.15±0.08	0.45±0.01	1.75±0.02	0.27±0.01
B-3	55	12.21±0.07	0.09±0.01	1.35±0.03	4.21±0.03	73.77±0.35	2.18±0.08	0.46±0.01	1.70±0.02	0.26±0.01
B-3	56	11.95±0.06	0.06±0.01	1.65±0.03	4.11±0.03	73.77±0.35	2.14±0.08	0.48±0.01	1.66±0.02	0.24±0.01
B-3	57	12.36±0.07	0.05±0.01	1.45±0.03	4.06±0.03	74.58±0.35	2.17±0.08	0.47±0.01	1.71±0.02	0.29±0.01
B-3	58	12.42±0.07	0.07±0.01	1.58±0.03	4.07±0.03	73.52±0.35	2.39±0.09	0.52±0.01	1.69±0.02	0.26±0.01
B-3	59	12.64±0.07	0.08±0.01	1.68±0.03	4.02±0.03	73.27±0.34	2.18±0.08	0.51±0.01	1.68±0.02	0.29±0.01
B-3	60	12.66±0.07	0.06±0.01	1.46±0.03	3.94±0.03	74.40±0.35	2.15±0.08	0.51±0.01	1.70±0.02	0.28±0.01
B-3	61	12.74±0.07	0.08±0.01	1.53±0.03	3.96±0.03	74.04±0.35	2.28±0.08	0.47±0.01	1.71±0.02	0.27±0.01
B-3	62	12.84±0.07	0.08±0.01	1.37±0.03	3.91±0.03	74.39±0.35	2.37±0.09	0.45±0.01	1.74±0.02	0.25±0.01
B-3	63	12.82±0.07	0.05±0.01	1.48±0.03	3.86±0.03	73.78±0.35	2.28±0.08	0.49±0.01	1.73±0.02	0.28±0.01
B-3	64	12.78±0.07	0.07±0.01	1.50±0.03	3.85±0.03	74.11±0.35	2.13±0.08	0.45±0.01	1.74±0.02	0.27±0.01
B-3	65	12.72±0.07	0.07±0.01	1.23±0.03	3.76±0.03	73.98±0.35	2.32±0.08	0.49±0.01	1.76±0.02	0.29±0.01
B-3	66	12.72±0.07	0.12±0.01	1.47±0.03	3.75±0.03	73.61±0.35	2.29±0.08	0.49±0.01	1.78±0.02	0.25±0.01
B-3	67	12.80±0.07	0.07±0.01	1.39±0.03	3.68±0.03	74.57±0.35	2.39±0.09	0.51±0.01	1.78±0.02	0.25±0.01
B-3	68	12.74±0.07	0.12±0.01	1.43±0.03	3.73±0.03	74.50±0.35	2.23±0.08	0.47±0.01	1.80±0.02	0.26±0.01
B-3	69	12.71±0.07	0.09±0.01	1.24±0.03	3.69±0.03	73.58±0.35	2.29±0.08	0.5±0.01	1.81±0.02	0.26±0.01
B-3	70	12.57±0.07	0.11±0.01	1.30±0.03	3.68±0.03	74.56±0.35	2.28±0.08	0.48±0.01	1.79±0.02	0.26±0.01
B-3	71	12.63±0.07	0.10±0.01	1.47±0.03	3.64±0.03	74.85±0.35	2.30±0.08	0.5±0.01	1.79±0.02	0.26±0.01
B-3	72	12.63±0.07	0.10±0.01	1.43±0.03	3.64±0.03	74.75±0.35	2.30±0.08	0.48±0.01	1.79±0.02	0.28±0.01
B-3	73	12.38±0.07	0.10±0.02	1.51±0.03	3.56±0.03	75.69±0.35	2.28±0.09	0.49±0.02	1.82±0.02	0.26±0.02
B-3	74	12.65±0.07	0.11±0.01	0.8±0.02	3.58±0.03	75.69±0.35	2.44±0.09	0.5±0.01	1.83±0.02	0.25±0.01
C-1 1	1	11.44±0.07	0.12±0.02	2.88±0.04	4.64±0.03	73.33±0.35	2.76±0.10	0.51±0.02	2.02±0.04	0.32±0.02
C-1 1	2	11.72±0.08	0.11±0.02	1.40±0.03	4.53±0.03	74.19±0.35	3.03±0.11	0.53±0.02	2.04±0.04	0.28±0.02
C-1 1	3	11.71±0.07	0.07±0.02	1.55±0.03	4.61±0.03	74.05±0.35	2.97±0.11	0.53±0.02	1.96±0.04	0.31±0.02
C-1 1	4	11.76±0.08	0.10±0.02	1.46±0.03	4.58±0.03	73.23±0.35	2.83±0.10	0.53±0.02	2.11±0.04	0.3±0.02
C-1 1	5	11.50±0.07	0.10±0.02	1.69±0.04	4.73±0.04	74.62±0.35	2.78±0.10	0.51±0.02	2.06±0.04	0.32±0.02
C-1 1	6	11.34±0.07	0.06±0.02	1.38±0.03	4.73±0.04	74.24±0.35	2.81±0.10	0.52±0.02	1.98±0.04	0.29±0.02

C-1 1	7	11.33±0.07	0.07±0.02	1.34±0.03	4.74±0.04	74.15±0.35	2.85±0.10	0.57±0.02	2.08±0.04	0.28±0.02
C-1 1	8	11.29±0.07	0.11±0.02	1.28±0.03	4.76±0.04	74.04±0.35	2.94±0.10	0.5±0.02	2.10±0.04	0.27±0.02
C-1 1	9	11.22±0.07	0.04±0.02	1.37±0.03	4.79±0.04	72.91±0.35	3.02±0.11	0.54±0.02	2.04±0.04	0.28±0.02
C-1 1	10	11.15±0.07	0.08±0.02	1.66±0.04	4.95±0.04	73.43±0.35	2.73±0.10	0.48±0.02	2.08±0.04	0.27±0.02
C-1 1	11	11.09±0.07	0.11±0.02	1.68±0.04	4.96±0.04	72.55±0.35	3.00±0.11	0.57±0.02	2.15±0.04	0.25±0.02
C-1 1	12	10.94±0.07	0.12±0.02	1.64±0.04	5.00±0.04	73.23±0.35	2.73±0.10	0.55±0.02	2.19±0.04	0.25±0.02
C-1 1	13	10.82±0.07	0.11±0.02	1.45±0.03	4.97±0.04	74.22±0.35	2.76±0.10	0.5±0.02	2.21±0.04	0.27±0.02
C-1 1	14	10.50±0.07	0.11±0.02	1.57±0.03	4.97±0.04	73.98±0.35	2.86±0.10	0.53±0.02	2.28±0.04	0.29±0.02
C-1 1	15	9.96±0.07	0.08±0.02	1.97±0.04	5.17±0.04	74.21±0.35	3.01±0.10	0.57±0.02	2.36±0.04	0.24±0.02
C-1 1	16	9.81±0.07	0.15±0.02	1.66±0.04	5.08±0.04	74.06±0.35	3.04±0.11	0.59±0.02	2.48±0.04	0.24±0.02
C-1 1	17	9.47±0.07	0.12±0.02	2.24±0.04	5.17±0.04	73.28±0.35	3.65±0.11	0.64±0.02	2.60±0.04	0.21±0.02
C-1 1	18	7.79±0.06	0.09±0.02	2.20±0.04	4.75±0.04	75.28±0.35	3.83±0.12	0.58±0.02	2.93±0.04	0.2±0.02
C-1 1	19	5.37±0.05	0.12±0.02	1.92±0.04	4.52±0.03	77.90±0.36	4.20±0.12	0.67±0.02	2.75±0.04	0.23±0.02
C-1 1	20	6.06±0.06	0.07±0.02	1.73±0.04	4.64±0.03	77.02±0.35	4.21±0.12	0.72±0.02	2.42±0.04	0.22±0.02
C-1 1	21	7.14±0.06	0.10±0.02	2.18±0.04	4.90±0.04	76.69±0.35	3.52±0.11	0.73±0.02	2.20±0.04	0.19±0.02
C-1 1	22	8.20±0.06	0.06±0.02	2.15±0.04	5.11±0.04	75.05±0.35	3.18±0.11	0.69±0.02	1.94±0.04	0.2±0.02
C-1 1	23	9.24±0.07	0.08±0.02	1.97±0.04	5.12±0.04	74.75±0.35	3.22±0.11	0.69±0.02	1.91±0.04	0.23±0.02
C-1 1	24	10.10±0.07	0.09±0.02	1.48±0.03	4.96±0.04	74.32±0.35	3.32±0.11	0.75±0.02	1.93±0.04	0.22±0.02
C-1 1	25	10.77±0.07	0.12±0.02	1.45±0.03	4.85±0.04	73.38±0.35	3.12±0.11	0.74±0.02	1.96±0.04	0.22±0.02
C-1 1	26	11.60±0.08	0.08±0.02	1.55±0.03	4.97±0.04	71.41±0.35	3.08±0.11	0.8±0.02	2.10±0.04	0.24±0.02
C-1 1	27	12.31±0.08	0.05±0.02	1.82±0.04	5.03±0.04	70.80±0.35	3.17±0.11	0.77±0.03	2.07±0.04	0.3±0.02
C-1 1	28	12.97±0.08	0.09±0.02	2.13±0.04	5.32±0.04	69.71±0.34	3.20±0.11	0.83±0.03	2.18±0.04	0.32±0.02
C-1 1	29	12.96±0.08	0.09±0.02	1.99±0.04	5.26±0.04	69.79±0.34	3.27±0.11	0.82±0.03	2.09±0.04	0.3±0.02
C-1 1	30	12.62±0.08	0.08±0.02	1.95±0.04	5.22±0.04	69.62±0.34	3.53±0.11	0.87±0.03	2.16±0.04	0.3±0.02
C-1 1	31	12.64±0.08	0.11±0.02	1.31±0.03	4.84±0.04	70.61±0.35	3.39±0.11	0.83±0.03	2.14±0.04	0.35±0.02
C-1 1	32	12.47±0.08	0.09±0.02	1.72±0.04	5.00±0.04	71.44±0.35	3.44±0.11	0.82±0.03	2.08±0.04	0.36±0.02
C-1 1	33	11.74±0.08	0.09±0.02	1.70±0.04	5.04±0.04	71.99±0.35	3.16±0.11	0.78±0.03	1.85±0.04	0.35±0.02
C-1 1	34	10.79±0.07	0.11±0.02	1.32±0.03	4.85±0.04	74.86±0.35	2.82±0.10	0.73±0.02	1.58±0.03	0.28±0.02
C-1 1	35	10.12±0.07	0.06±0.02	1.17±0.03	4.67±0.04	76.08±0.36	2.78±0.10	0.68±0.02	1.47±0.03	0.28±0.02
C-1 1	36	10.03±0.07	0.01±0.02	1.15±0.03	4.55±0.03	76.09±0.36	2.59±0.10	0.59±0.02	1.38±0.03	0.25±0.02
C-1 1	37	10.92±0.07	0.07±0.02	1.18±0.03	4.61±0.04	74.76±0.35	2.76±0.10	0.67±0.02	1.38±0.03	0.25±0.02
C-1 1	38	11.83±0.08	0.07±0.02	1.29±0.03	4.80±0.04	73.74±0.35	2.71±0.10	0.68±0.02	1.47±0.03	0.31±0.02
C-1 1	39	12.57±0.08	0.13±0.02	1.60±0.04	4.77±0.04	71.86±0.34	2.90±0.11	0.66±0.02	1.62±0.03	0.32±0.02
C-1 1	40	13.10±0.08	0.07±0.02	1.18±0.03	4.70±0.04	71.51±0.35	3.02±0.11	0.7±0.02	1.62±0.03	0.36±0.02
C-1 1	41	13.07±0.08	0.09±0.02	1.36±0.03	4.74±0.04	71.43±0.35	3.11±0.11	0.72±0.02	1.59±0.03	0.38±0.02
C-1 1	42	13.22±0.08	0.12±0.02	1.45±0.03	4.72±0.03	71.17±0.35	3.02±0.11	0.75±0.02	1.64±0.03	0.38±0.02
C-1 1	43	12.87±0.08	0.09±0.02	1.22±0.03	4.66±0.03	71.80±0.34	3.04±0.11	0.73±0.02	1.52±0.03	0.33±0.02
C-1 1	44	12.53±0.08	0.07±0.02	1.17±0.03	4.68±0.04	73.23±0.35	2.98±0.10	0.71±0.02	1.43±0.03	0.33±0.02
C-2	1	12.45±0.08	0.05±0.02	0.9±0.03	3.32±0.03	77.03±0.36	2.14±0.09	0.25±0.02	1.33±0.03	0.21±0.02
C-2	2	12.95±0.08	0.11±0.02	0.83±0.03	3.74±0.03	79.61±0.37	2.38±0.09	0.34±0.02	1.30±0.03	0.23±0.02
C-2	3	12.88±0.08	0.08±0.02	0.89±0.03	3.47±0.03	79.26±0.36	2.46±0.10	0.39±0.02	1.83±0.04	0.22±0.02
C-2	4	13.10±0.08	0.10±0.02	0.72±0.03	3.38±0.03	78.51±0.36	2.56±0.10	0.42±0.02	2.06±0.04	0.22±0.02
C-2	5	13.60±0.08	0.05±0.02	0.81±0.03	3.35±0.03	77.94±0.36	2.99±0.10	0.41±0.02	2.20±0.04	0.24±0.02
C-2	6	14.50±0.08	0.10±0.02	0.69±0.03	3.31±0.03	76.51±0.36	2.99±0.11	0.47±0.02	2.36±0.04	0.25±0.02
C-2	7	13.90±0.08	0.14±0.02	0.89±0.03	3.36±0.03	76.38±0.36	3.11±0.11	0.47±0.02	2.43±0.04	0.25±0.02
C-2	8	13.86±0.08	0.09±0.02	0.99±0.03	3.34±0.03	75.64±0.36	2.90±0.10	0.47±0.02	2.46±0.04	0.26±0.02
C-2	9	13.92±0.08	0.14±0.02	0.94±0.03	3.30±0.03	76.31±0.36	2.95±0.10	0.42±0.02	2.48±0.04	0.3±0.02
C-2	10	13.90±0.08	0.11±0.02	1.06±0.03	3.34±0.03	76.27±0.36	2.82±0.10	0.49±0.02	2.62±0.04	0.26±0.02
C-2	11	14.15±0.08	0.10±0.02	0.91±0.03	3.34±0.03	76.16±0.36	2.81±0.10	0.51±0.02	2.61±0.04	0.26±0.02
C-2	12	14.23±0.08	0.10±0.02	0.84±0.03	3.28±0.03	76.05±0.36	2.94±0.10	0.43±0.02	2.54±0.04	0.25±0.02
C-2	13	14.02±0.08	0.10±0.02	0.9±0.03	3.32±0.03	76.47±0.36	3.02±0.11	0.46±0.02	2.64±0.04	0.26±0.02
C-2	14	14.17±0.08	0.09±0.02	1.07±0.03	3.38±0.03	74.72±0.35	3.03±0.11	0.48±0.02	2.65±0.04	0.25±0.02
C-2	15	14.20±0.08	0.10±0.02	1.10±0.03	3.38±0.03	74.68±0.36	2.93±0.10	0.45±0.02	2.59±0.04	0.24±0.02
C-2	16	14.36±0.08	0.11±0.02	0.87±0.03	3.36±0.03	75.28±0.35	3.23±0.11	0.46±0.02	2.63±0.04	0.29±0.02
C-2	17	14.29±0.08	0.15±0.02	1.11±0.03	3.39±0.03	75.65±0.36	2.84±0.10	0.5±0.02	2.65±0.04	0.27±0.02
C-2	18	14.15±0.08	0.13±0.02	1.17±0.03	3.37±0.03	72.25±0.35	2.95±0.10	0.49±0.02	2.57±0.04	0.27±0.02
C-2	19	14.30±0.08	0.15±0.02	1.00±0.03	3.44±0.03	74.14±0.36	3.05±0.11	0.51±0.02	2.69±0.04	0.28±0.02
C-2	20	14.28±0.08	0.14±0.02	1.03±0.03	3.44±0.03	75.06±0.35	2.95±0.10	0.51±0.02	2.61±0.04	0.26±0.02
C-2	21	14.25±0.08	0.07±0.02	1.16±0.03	3.44±0.03	74.64±0.35	2.98±0.10	0.5±0.02	2.58±0.04	0.3±0.02
C-2	22	14.30±0.08	0.07±0.02	1.29±0.03	3.41±0.03	73.19±0.35	3.08±0.11	0.5±0.02	2.60±0.04	0.28±0.02
C-2	23	14.42±0.08	0.10±0.02	1.14±0.03	3.48±0.03	74.01±0.36	3.10±0.11	0.53±0.02	2.71±0.04	0.28±0.02
C-2	24	14.30±0.08	0.12±0.02	1.08±0.03	3.48±0.03	74.60±0.36	2.91±0.10	0.5±0.02	2.60±0.04	0.27±0.02
C-2	25	14.28±0.08	0.14±0.02	1.08±0.03	3.41±0.03	75.33±0.35	3.01±0.11	0.49±0.02	2.62±0.04	0.27±0.02
C-2	26	14.32±0.08	0.10±0.02	0.91±0.03	3.40±0.03	74.46±0.36	2.82±0.10	0.51±0.02	2.70±0.04	0.27±0.02
C-2	27	14.29±0.08	0.12±0.02	1.10±0.03	3.44±0.03	74.84±0.35	2.96±0.11	0.5±0.02	2.63±0.04	0.27±0.02
C-2	28	14.08±0.08	0.07±0.02	1.02±0.03	3.41±0.03	73.98±0.36	2.87±0.11	0.51±0.02	2.64±0.04	0.27±0.02
C-2	29	14.08±0.08	0.08±0.02	1.06±0.03	3.38±0.03	74.19±0.36	2.89±0.10	0.52±0.02	2.70±0.04	0.27±0.02
C-2	30	14.10±0.08	0.07±0.02	1.34±0.03	3.43±0.03	74.36±0.36	3.02±0.11	0.53±0.02	2.59±0.04	0.26±0.02
C-2	31	13.91±0.08	0.10±0.02	1.22±0.03	3.36±0.03	75.11±0.35	2.88±0.10	0.54±0.02	2.63±0.04	0.25±0.02
C-2	32	13.91±0.08	0.09±0.02	1.14±0.03	3.46±0.03	75.78±0.36	2.90±0.10	0.5±0.02	2.62±0.04	0.28±0.02
C-2	33	13.85±0.08	0.09±0.02	0.96±0.03	3.43±0.03	74.72±0.35	3.09±0.11	0.53±0.02	2.66±0.04	0.26±0.02
C-2	34	13.80±0.08	0.07±0.02	1.11±0.03	3.47±0.03	74.66±0.35	2.85±0.10	0.51±0.02	2.60±0.04	0.27±0.02
C-2	35	13.62±0.08	0.09±0.02	1.20±0.03	3.45±0.03	71.93±0.35	2.91±0.10	0.51±0.02	2.62±0.04	0.29±0.02
C-2	36	13.64±0.08	0.12±0.02	1.03±0.03	3.43±0.03	74.11±0.36	2.94±0.10	0.53±0.02	2.62±0.04	0.27±0.02
C-2	37	13.67±0.08	0.08±0.02	1.19±0.03	3.40±0.03	74.62±0.35	3.13±0.11	0.55±0.02	2.59±0.04	0.29±0.02
C-2	38	13.52±0.08	0.11±0.02	1.09±0.03	3.46±0.03	73.55±0.35	2.77±0.10	0.53±0.02	2.61±0.04	0.24±0.02
C-2	39	13.64±0.08	0.11±0.02	0.94±0.03	3.41±0.03	74.24±0.36	3.03±0.11	0.52±0.02	2.55±0.04	0.27±0.02
C-2	40	13.71±0.08	0.10±0.02	0.87±0.03	3.41±0.03	73.64±0.35	2.96±0.11	0.54±0.02	2.63±0.04	0.31±0.02
C-2	41	13.50±0.08	0.05±0.02	1.01±0.03	3.41±0.03	75.34±0.35	2.85±0.10	0.53±0.02	2.62±0.04	0.26±0.02
C-2	42	13.50±0.08	0.07±0.02	1.05±0.03	3.45±0.03	75.24±0.35	2.82±0.10	0.49±0.02	2.57±0.04	0.27±0.02
C-2	43	13.49±0.08	0.11±0.02	1.13±0.03	3.34±0.03	74.59±0.35	2.91±0.10	0.52±0.02	2.58±0.04	0.27±0.02
C-2	44	13.53±0.08	0.09±0.02	1.22±0.03	3.41±0.03	73.69±0.35	3.08±0.11	0.53±0.02	2.60±0.04	0.29±0.02
C-2	45	13.54±0.08	0.12±0.02	1.05±0.03	3.38±0.03	74.35±0.36	2.91±0.10	0.52±0.02	2.58±0.04	0.25±0.02
C-2	46	13.48±0.08	0.12±0.02	0.94±0.03	3.42±0.03	72.10±0.35	3.03±0.11	0.52±0.02	2.57±0.04	0.28±0.02
C-2	47	13.30±0.08	0.06±0.02	1.11±0.03	3.44±0.03	74.76±0.35	2.87±0.10	0.53±0.02	2.62±0.04	0.26±0.02

C-2	48	13.37±0.08	0.12±0.02	1.06±0.03	3.45±0.03	75.23±0.35	3.18±0.11	0.47±0.02	2.56±0.04	0.25±0.02
C-2	49	13.27±0.08	0.09±0.02	1.26±0.03	3.45±0.03	73.22±0.35	2.86±0.10	0.5±0.02	2.53±0.04	0.28±0.02
C-2	50	13.37±0.08	0.11±0.02	1.19±0.03	3.37±0.03	74.80±0.35	2.78±0.10	0.54±0.02	2.58±0.04	0.26±0.02
C-2	51	13.44±0.08	0.11±0.02	1.12±0.03	3.39±0.03	75.20±0.35	2.97±0.10	0.51±0.02	2.54±0.04	0.26±0.02
C-2	52	13.46±0.08	0.08±0.02	0.87±0.03	3.38±0.03	73.46±0.35	2.80±0.10	0.49±0.02	2.51±0.04	0.29±0.02
C-2	53	13.40±0.08	0.10±0.02	0.96±0.03	3.41±0.03	74.25±0.36	2.89±0.10	0.5±0.02	2.53±0.04	0.27±0.02
C-2	54	13.36±0.08	0.10±0.02	0.97±0.03	3.47±0.03	74.74±0.35	2.73±0.10	0.48±0.02	2.53±0.04	0.26±0.02
C-2	55	13.38±0.08	0.10±0.02	1.15±0.03	3.44±0.03	74.67±0.35	2.86±0.11	0.49±0.02	2.51±0.04	0.27±0.02
C-2	56	13.28±0.08	0.06±0.02	1.06±0.03	3.42±0.03	74.85±0.35	2.93±0.11	0.48±0.02	2.61±0.04	0.29±0.02
C-2	57	13.39±0.08	0.06±0.02	1.23±0.03	3.38±0.03	74.87±0.35	2.91±0.10	0.5±0.02	2.52±0.04	0.28±0.02
C-2	58	13.30±0.08	0.09±0.02	1.20±0.03	3.42±0.03	74.44±0.36	2.96±0.11	0.49±0.02	2.59±0.04	0.25±0.02
C-2	59	13.14±0.08	0.10±0.02	1.18±0.03	3.38±0.03	74.80±0.35	3.03±0.11	0.5±0.02	2.55±0.04	0.3±0.02
C-2	60	13.41±0.08	0.10±0.02	0.99±0.03	3.38±0.03	73.51±0.35	2.91±0.10	0.49±0.02	2.59±0.04	0.27±0.02
C-2	61	13.36±0.08	0.10±0.02	1.10±0.03	3.42±0.03	75.41±0.35	2.81±0.10	0.48±0.02	2.58±0.04	0.25±0.02
C-2	62	13.38±0.08	0.09±0.02	1.17±0.03	3.38±0.03	73.11±0.35	2.95±0.11	0.53±0.02	2.58±0.04	0.26±0.02
C-2	63	13.34±0.08	0.11±0.02	1.06±0.03	3.43±0.03	74.33±0.36	2.98±0.11	0.51±0.02	2.49±0.04	0.24±0.02
C-2	64	13.33±0.08	0.14±0.02	0.94±0.03	3.44±0.03	74.51±0.35	2.80±0.10	0.46±0.02	2.56±0.04	0.26±0.02
C-2	65	13.25±0.08	0.09±0.02	1.06±0.03	3.42±0.03	74.14±0.36	2.83±0.10	0.49±0.02	2.60±0.04	0.25±0.02
C-2	66	13.29±0.08	0.12±0.02	1.10±0.03	3.43±0.03	74.54±0.36	2.78±0.10	0.53±0.02	2.61±0.04	0.22±0.02
C-2	67	13.21±0.08	0.12±0.02	0.94±0.03	3.40±0.03	75.63±0.36	2.89±0.10	0.5±0.02	2.54±0.04	0.27±0.02
C-2	68	13.11±0.08	0.09±0.02	1.01±0.03	3.40±0.03	74.56±0.36	2.88±0.10	0.45±0.02	2.46±0.04	0.26±0.02
C-2	69	13.10±0.08	0.08±0.02	1.16±0.03	3.43±0.03	75.21±0.35	2.94±0.10	0.47±0.02	2.50±0.04	0.26±0.02
C-2	70	13.10±0.08	0.09±0.02	1.10±0.03	3.41±0.03	75.06±0.35	3.15±0.11	0.48±0.02	2.51±0.04	0.27±0.02
C-2	71	13.12±0.08	0.07±0.02	1.10±0.03	3.33±0.03	74.46±0.36	3.09±0.11	0.5±0.02	2.59±0.04	0.24±0.02
C-2	72	13.07±0.08	0.10±0.02	1.20±0.03	3.40±0.03	73.30±0.35	2.88±0.10	0.51±0.02	2.56±0.04	0.25±0.02
C-2	73	13.28±0.08	0.12±0.02	1.01±0.03	3.40±0.03	75.01±0.35	2.83±0.10	0.51±0.02	2.48±0.04	0.29±0.02
C-2	74	13.03±0.08	0.10±0.02	1.03±0.03	3.39±0.03	72.93±0.35	2.83±0.10	0.48±0.02	2.61±0.04	0.29±0.02
C-2	75	13.23±0.08	0.04±0.02	1.09±0.03	3.42±0.03	73.74±0.35	2.75±0.10	0.51±0.02	2.57±0.04	0.26±0.02
C-2	76	13.07±0.08	0.13±0.02	1.02±0.03	3.38±0.03	75.03±0.35	2.95±0.10	0.56±0.02	2.55±0.04	0.29±0.02
C-2	77	13.36±0.08	0.11±0.02	1.12±0.03	3.43±0.03	74.22±0.36	2.91±0.10	0.51±0.02	2.54±0.04	0.26±0.02
C-2	78	13.27±0.08	0.11±0.02	1.20±0.03	3.43±0.03	74.22±0.36	2.97±0.10	0.49±0.02	2.52±0.04	0.3±0.02
C-2	79	13.32±0.08	0.12±0.02	1.09±0.03	3.40±0.03	75.10±0.35	2.82±0.10	0.53±0.02	2.53±0.04	0.28±0.02
C-2	80	13.43±0.08	0.08±0.02	0.93±0.03	3.43±0.03	74.43±0.35	2.90±0.10	0.5±0.02	2.53±0.04	0.28±0.02
C-2	81	13.22±0.08	0.10±0.02	1.09±0.03	3.37±0.03	74.71±0.35	2.91±0.11	0.51±0.02	2.58±0.04	0.29±0.02
C-2	82	13.18±0.08	0.09±0.02	1.10±0.03	3.43±0.03	74.13±0.36	2.85±0.10	0.48±0.02	2.61±0.04	0.26±0.02
C-2	83	13.25±0.08	0.11±0.02	1.22±0.03	3.43±0.03	74.90±0.35	2.68±0.10	0.52±0.02	2.55±0.04	0.25±0.02
C-2	84	13.32±0.08	0.06±0.02	1.12±0.03	3.37±0.03	73.10±0.35	2.83±0.10	0.52±0.02	2.58±0.04	0.24±0.02
C-2	85	13.20±0.08	0.07±0.02	1.16±0.03	3.41±0.03	73.55±0.35	2.73±0.10	0.48±0.02	2.55±0.04	0.28±0.02
C-2	86	13.07±0.08	0.08±0.02	1.26±0.03	3.47±0.03	74.17±0.36	2.88±0.10	0.5±0.02	2.48±0.04	0.26±0.02
C-2	87	13.23±0.08	0.08±0.02	0.96±0.03	3.39±0.03	73.40±0.35	2.96±0.10	0.51±0.02	2.64±0.04	0.25±0.02
C-2	88	13.20±0.08	0.07±0.02	0.92±0.03	3.45±0.03	74.82±0.35	3.05±0.11	0.51±0.02	2.56±0.04	0.29±0.02
C-2	89	13.24±0.08	0.12±0.02	1.06±0.03	3.39±0.03	74.49±0.35	3.21±0.11	0.49±0.02	2.59±0.04	0.26±0.02
C-2	90	13.12±0.08	0.13±0.02	1.17±0.03	3.39±0.03	74.28±0.36	2.94±0.10	0.51±0.02	2.55±0.04	0.25±0.02
C-2	91	13.10±0.08	0.05±0.02	1.17±0.03	3.44±0.03	73.18±0.35	2.98±0.11	0.48±0.02	2.58±0.04	0.29±0.02
C-2	92	13.09±0.08	0.12±0.02	1.20±0.03	3.42±0.03	74.95±0.35	3.02±0.11	0.51±0.02	2.56±0.04	0.27±0.02
C-2	93	12.97±0.08	0.10±0.02	1.13±0.03	3.36±0.03	75.18±0.35	2.78±0.10	0.52±0.02	2.52±0.04	0.27±0.02
C-2	94	13.07±0.08	0.13±0.02	0.92±0.03	3.39±0.03	73.82±0.35	2.96±0.10	0.46±0.02	2.52±0.04	0.28±0.02
C-2	95	12.96±0.08	0.12±0.02	0.96±0.03	3.38±0.03	75.21±0.35	2.89±0.10	0.5±0.02	2.51±0.04	0.29±0.02
C-2	96	12.95±0.08	0.12±0.02	1.12±0.03	3.44±0.03	73.70±0.35	2.94±0.10	0.49±0.02	2.47±0.04	0.27±0.02
C-2	97	12.91±0.08	0.12±0.02	1.07±0.03	3.35±0.03	74.72±0.35	2.77±0.10	0.51±0.02	2.52±0.04	0.28±0.02
C-2	98	12.86±0.08	0.11±0.02	1.14±0.03	3.43±0.03	75.09±0.35	3.02±0.11	0.47±0.02	2.64±0.04	0.25±0.02
C-2	99	12.92±0.08	0.12±0.02	1.25±0.03	3.40±0.03	75.06±0.35	2.85±0.10	0.45±0.02	2.46±0.04	0.25±0.02
C-2	100	12.94±0.08	0.10±0.02	0.82±0.03	3.41±0.03	74.86±0.35	2.86±0.10	0.5±0.02	2.47±0.04	0.28±0.02
C-2	101	12.87±0.08	0.07±0.02	1.01±0.03	3.47±0.03	75.19±0.35	2.74±0.10	0.43±0.02	2.50±0.04	0.24±0.02
C-2	102	12.81±0.08	0.10±0.02	1.03±0.03	3.47±0.03	75.42±0.35	2.88±0.10	0.47±0.02	2.49±0.04	0.26±0.02
C-2	103	12.71±0.08	0.13±0.02	1.09±0.03	3.44±0.03	75.78±0.36	2.89±0.10	0.49±0.02	2.43±0.04	0.26±0.02
C-2	104	12.74±0.08	0.12±0.02	1.13±0.03	3.39±0.03	75.74±0.36	2.92±0.10	0.48±0.02	2.48±0.04	0.27±0.02
C-2	105	12.51±0.08	0.11±0.02	1.11±0.03	3.43±0.03	75.15±0.35	2.84±0.10	0.46±0.02	2.46±0.04	0.26±0.02
C-2	106	12.57±0.08	0.07±0.02	1.19±0.03	3.41±0.03	75.68±0.36	2.83±0.10	0.43±0.02	2.42±0.04	0.27±0.02
C-2	107	12.59±0.08	0.12±0.02	0.93±0.03	3.39±0.03	76.30±0.36	2.93±0.11	0.47±0.02	2.48±0.04	0.25±0.02
C-2	108	12.59±0.08	0.11±0.02	0.93±0.03	3.48±0.03	75.20±0.35	2.94±0.10	0.48±0.02	2.42±0.04	0.24±0.02
C-2	109	12.56±0.08	0.12±0.02	1.07±0.03	3.44±0.03	75.61±0.36	2.88±0.10	0.47±0.02	2.36±0.04	0.25±0.02
C-2	110	12.52±0.08	0.15±0.02	1.14±0.03	3.41±0.03	75.36±0.35	2.99±0.11	0.48±0.02	2.44±0.04	0.24±0.02
C-2	111	12.44±0.08	0.08±0.02	1.07±0.03	3.37±0.03	73.67±0.35	2.87±0.10	0.51±0.02	2.43±0.04	0.25±0.02
C-2	112	12.51±0.08	0.06±0.02	1.14±0.03	3.40±0.03	75.99±0.36	2.90±0.10	0.48±0.02	2.45±0.04	0.25±0.02
C-2	113	12.39±0.08	0.10±0.02	0.91±0.03	3.44±0.03	76.29±0.36	2.72±0.10	0.47±0.02	2.41±0.04	0.25±0.02
C-2	114	12.50±0.08	0.08±0.02	1.02±0.03	3.39±0.03	74.01±0.36	2.82±0.10	0.48±0.02	2.36±0.04	0.26±0.02
C-2	115	12.26±0.08	0.08±0.02	1.04±0.03	3.47±0.03	75.85±0.36	2.92±0.10	0.45±0.02	2.44±0.04	0.27±0.02
C-2	116	12.40±0.08	0.08±0.02	1.04±0.03	3.42±0.03	74.77±0.35	2.79±0.10	0.47±0.02	2.39±0.04	0.23±0.02
C-2	117	12.55±0.08	0.11±0.02	1.07±0.03	3.46±0.03	74.54±0.35	2.87±0.10	0.43±0.02	2.46±0.04	0.26±0.02
C-2	118	12.49±0.08	0.13±0.02	1.25±0.03	3.48±0.03	74.80±0.35	2.82±0.10	0.47±0.02	2.31±0.04	0.25±0.02
C-2	119	12.44±0.08	0.08±0.02	1.03±0.03	3.43±0.03	74.73±0.35	2.88±0.10	0.49±0.02	2.43±0.04	0.25±0.02
C-2	120	12.42±0.08	0.07±0.02	0.88±0.03	3.47±0.03	75.13±0.35	2.99±0.11	0.49±0.02	2.56±0.04	0.28±0.02
C-2	121	12.56±0.08	0.12±0.02	0.89±0.03	3.47±0.03	74.38±0.36	3.12±0.11	0.52±0.02	2.53±0.04	0.25±0.02
C-2	122	12.38±0.08	0.09±0.02	0.99±0.03	3.46±0.03	74.76±0.35	2.88±0.10	0.48±0.02	2.39±0.04	0.22±0.02
C-2	123	12.32±0.08	0.11±0.02	0.97±0.03	3.43±0.03	75.05±0.35	2.83±0.10	0.5±0.02	2.43±0.04	0.22±0.02
C-2	124	12.26±0.08	0.07±0.02	0.89±0.03	3.49±0.03	75.01±0.35	2.80±0.10	0.48±0.02	2.46±0.04	0.25±0.02
C-2	125	12.04±0.08	0.06±0.02	1.08±0.03	3.50±0.03	74.80±0.35	2.83±0.10	0.47±0.02	2.41±0.04	0.26±0.02
C-2	126	11.93±0.08	0.11±0.02	0.97±0.03	3.58±0.03	75.92±0.36	2.95±0.11	0.46±0.02	2.35±0.04	0.24±0.02
C-2	127	11.54±0.08	0.12±0.02	0.91±0.03	3.63±0.03	76.83±0.36	2.80±0.10	0.52±0.02	2.21±0.04	0.22±0.02
C-2	128	11.22±0.07	0.14±0.02	0.87±0.03	3.70±0.03	76.55±0.36	2.86±0.10	0.46±0.02	2.05±0.04	0.26±0.02
C-2	129	11.01±0.07	0.07±0.02	1.00±0.03	3.94±0.03	76.90±0.36	2.47±0.10	0.46±0.02	1.68±0.03	0.23±0.02
C-2	130	10.84±0.07	0.07±0.02	1.11±0.03	4.29±0.03	77.23±0.36	2.47±0.10	0.43±0.02	1.32±0.03	0.22±0.02
C-2	131	10.09±0.07	0.09±0.02	1.76±0.04	4.84±0.04	77.34±0.36	2.29±0.09	0.35±0.02	1.17±0.03	0.21±0.02
C-2	132	7.75±0.06	0.10±0.02	2.03±0.04	4.58±0.03	77.32±0.36	3.51±0.11	0.34±0.02	1.76±0.04	0.19±0.02

C-2	133	7.05±0.06	0.11±0.02	1.49±0.03	4.54±0.03	77.01±0.35	3.99±0.12	0.33±0.02	1.62±0.03	0.15±0.02
C-2	134	8.02±0.06	0.11±0.02	1.56±0.03	4.66±0.03	77.61±0.36	4.10±0.12	0.28±0.02	1.17±0.03	0.19±0.02
C-2	135	8.86±0.07	0.12±0.02	1.79±0.04	4.71±0.04	76.58±0.36	3.77±0.12	0.3±0.02	0.86±0.03	0.25±0.02
C-2	136	9.45±0.07	0.15±0.02	1.30±0.03	4.16±0.03	77.70±0.36	3.88±0.12	0.3±0.02	0.82±0.03	0.24±0.02
C-2	137	10.12±0.07	0.18±0.02	1.46±0.03	4.33±0.03	76.39±0.36	3.42±0.11	0.29±0.02	0.75±0.03	0.25±0.02
C-2	138	10.48±0.07	0.13±0.02	2.26±0.04	5.24±0.04	72.72±0.35	3.29±0.11	0.27±0.02	0.73±0.02	0.25±0.02
C-2	139	10.79±0.07	0.12±0.02	2.25±0.04	5.13±0.04	73.97±0.36	3.26±0.11	0.26±0.02	0.66±0.02	0.22±0.02
C-2	140	10.88±0.07	0.17±0.02	1.59±0.03	4.53±0.03	76.03±0.36	3.28±0.11	0.28±0.02	0.67±0.02	0.17±0.02
C-2	141	11.26±0.07	0.13±0.02	1.63±0.04	4.59±0.03	76.23±0.36	3.27±0.11	0.28±0.02	0.69±0.02	0.23±0.02
C-2	142	11.38±0.07	0.14±0.02	1.84±0.04	4.84±0.04	75.74±0.36	3.39±0.11	0.23±0.02	0.64±0.02	0.18±0.02
C-2	143	11.11±0.07	0.12±0.02	2.22±0.04	5.15±0.04	75.45±0.35	3.24±0.11	0.26±0.02	0.66±0.02	0.22±0.02
C-1 2	1	13.64±0.08	0.11±0.02	3.88±0.05	4.99±0.04	71.83±0.35	3.72±0.12	0.71±0.03	2.37±0.04	0.27±0.02
C-1 2	2	12.92±0.08	0.09±0.02	2.26±0.04	5.08±0.04	73.34±0.35	3.80±0.12	0.75±0.03	2.50±0.04	0.32±0.02
C-1 2	3	12.97±0.08	0.06±0.02	1.46±0.03	5.00±0.04	75.04±0.35	3.91±0.12	0.68±0.03	2.43±0.04	0.27±0.02
C-1 2	4	12.68±0.08	0.10±0.02	2.47±0.04	5.18±0.04	73.64±0.35	3.40±0.11	0.64±0.02	2.29±0.04	0.29±0.02
C-1 2	5	12.76±0.08	0.11±0.02	1.71±0.04	5.08±0.04	74.47±0.35	3.35±0.11	0.64±0.02	2.17±0.04	0.29±0.02
C-1 2	6	12.58±0.08	0.09±0.02	2.10±0.04	5.10±0.04	74.27±0.36	3.20±0.11	0.58±0.02	2.10±0.04	0.33±0.02
C-1 2	7	12.85±0.08	0.06±0.02	1.83±0.04	5.05±0.04	73.17±0.35	3.16±0.11	0.54±0.02	1.94±0.04	0.29±0.02
C-1 2	8	12.90±0.08	0.08±0.02	1.80±0.04	5.06±0.04	75.45±0.35	3.10±0.11	0.54±0.02	1.95±0.04	0.28±0.02
C-1 2	9	13.01±0.08	0.09±0.02	1.62±0.03	5.05±0.04	74.79±0.35	2.70±0.10	0.55±0.02	1.98±0.04	0.29±0.02
C-1 2	10	13.24±0.08	0.10±0.02	1.79±0.04	5.11±0.04	74.07±0.36	2.90±0.10	0.54±0.02	1.94±0.04	0.28±0.02
C-1 2	11	13.34±0.08	0.12±0.02	1.94±0.04	5.12±0.04	74.30±0.36	2.87±0.10	0.53±0.02	1.92±0.04	0.33±0.02
C-1 2	12	13.53±0.08	0.06±0.02	2.15±0.04	5.09±0.04	72.02±0.35	2.89±0.10	0.54±0.02	1.85±0.04	0.33±0.02
C-1 2	13	13.84±0.08	0.10±0.02	1.67±0.04	5.06±0.04	73.96±0.36	2.84±0.10	0.48±0.02	1.83±0.04	0.33±0.02
C-1 2	14	13.75±0.08	0.11±0.02	1.67±0.04	4.96±0.04	73.02±0.35	2.96±0.11	0.53±0.02	1.79±0.04	0.31±0.02
C-1 2	15	13.82±0.08	0.11±0.02	1.50±0.03	5.00±0.04	71.86±0.35	3.02±0.11	0.52±0.02	1.82±0.04	0.3±0.02
C-1 2	16	13.86±0.08	0.08±0.02	1.63±0.03	4.88±0.04	73.17±0.35	2.90±0.10	0.51±0.02	1.84±0.04	0.31±0.02
C-1 2	17	13.90±0.08	0.09±0.02	1.47±0.03	4.93±0.04	72.87±0.35	2.91±0.10	0.57±0.02	1.85±0.04	0.34±0.02
C-1 2	18	13.99±0.08	0.12±0.02	1.71±0.04	4.91±0.04	72.79±0.35	3.02±0.11	0.61±0.02	1.90±0.04	0.34±0.02
C-1 2	19	13.74±0.08	0.10±0.02	1.95±0.04	4.84±0.04	72.60±0.35	2.88±0.10	0.53±0.02	1.85±0.04	0.31±0.02
C-1 2	20	14.02±0.08	0.13±0.02	1.37±0.03	4.78±0.04	73.69±0.35	3.01±0.11	0.53±0.02	1.88±0.04	0.3±0.02
C-1 2	21	14.05±0.08	0.13±0.02	1.73±0.04	4.78±0.04	73.39±0.35	3.06±0.11	0.55±0.02	1.94±0.04	0.33±0.02
C-1 2	22	14.03±0.08	0.11±0.02	1.31±0.03	4.74±0.04	73.02±0.35	3.00±0.11	0.53±0.02	1.81±0.04	0.33±0.02
C-1 2	23	14.06±0.08	0.09±0.02	1.57±0.03	4.67±0.04	73.00±0.35	2.81±0.10	0.57±0.02	1.93±0.04	0.33±0.02
C-1 2	24	13.96±0.08	0.06±0.02	1.46±0.03	4.70±0.04	72.81±0.35	2.93±0.11	0.6±0.02	1.90±0.04	0.31±0.02
C-1 2	25	13.90±0.08	0.09±0.02	1.59±0.04	4.64±0.03	72.56±0.35	2.87±0.10	0.56±0.02	1.87±0.04	0.3±0.02
C-1 2	26	14.05±0.08	0.09±0.02	1.83±0.04	4.61±0.04	72.89±0.35	3.15±0.11	0.56±0.02	1.89±0.04	0.33±0.02
C-1 2	27	14.11±0.08	0.09±0.02	1.33±0.03	4.53±0.03	73.50±0.35	2.95±0.11	0.59±0.02	1.91±0.04	0.3±0.02
C-1 2	28	14.09±0.08	0.10±0.02	1.79±0.04	4.58±0.03	72.92±0.35	3.02±0.11	0.52±0.02	1.90±0.04	0.35±0.02
C-1 2	29	14.33±0.08	0.14±0.02	1.16±0.03	4.39±0.03	73.6±0.35	3.11±0.11	0.56±0.02	1.92±0.04	0.28±0.02
C-1 2	30	14.10±0.08	0.13±0.02	1.66±0.04	4.47±0.03	70.72±0.35	2.88±0.10	0.55±0.02	1.98±0.04	0.31±0.02
C-1 2	31	13.98±0.08	0.11±0.02	1.12±0.03	4.43±0.03	72.53±0.35	3.00±0.11	0.54±0.02	1.89±0.04	0.32±0.02
C-1 2	32	13.95±0.08	0.07±0.02	1.51±0.03	4.36±0.03	73.00±0.35	2.83±0.10	0.55±0.02	2.02±0.04	0.37±0.02
C-1 2	33	13.85±0.08	0.09±0.02	1.50±0.03	4.39±0.03	73.63±0.35	2.97±0.11	0.58±0.02	1.95±0.04	0.31±0.02
C-1 2	34	13.93±0.08	0.07±0.02	1.35±0.03	4.26±0.03	73.22±0.35	2.90±0.10	0.59±0.02	2.01±0.04	0.3±0.02
C-1 2	35	13.84±0.08	0.10±0.02	1.78±0.04	4.33±0.03	73.41±0.35	2.90±0.10	0.57±0.02	1.95±0.04	0.32±0.02
C-1 2	36	14.17±0.08	0.09±0.02	1.18±0.03	4.26±0.03	74.15±0.36	2.91±0.11	0.58±0.02	1.93±0.04	0.31±0.02
C-1 2	37	13.93±0.08	0.11±0.02	1.69±0.04	4.26±0.03	71.33±0.35	3.08±0.11	0.59±0.02	1.97±0.04	0.32±0.02
C-1 2	38	13.89±0.08	0.07±0.02	1.05±0.03	4.20±0.03	73.72±0.35	3.00±0.11	0.58±0.02	2.07±0.04	0.35±0.02
C-1 2	39	13.90±0.08	0.11±0.02	1.60±0.03	4.22±0.03	73.96±0.36	2.85±0.10	0.57±0.02	2.07±0.04	0.29±0.02
C-1 2	40	13.87±0.08	0.08±0.02	1.53±0.03	4.15±0.03	72.74±0.35	3.11±0.11	0.59±0.02	1.97±0.04	0.33±0.02
C-1 2	41	13.91±0.08	0.06±0.02	1.33±0.03	4.20±0.03	73.92±0.35	3.00±0.11	0.58±0.02	1.93±0.04	0.3±0.02
C-1 2	42	13.98±0.08	0.10±0.02	1.39±0.03	4.11±0.03	72.98±0.35	3.05±0.11	0.59±0.02	1.97±0.04	0.27±0.02
C-1 2	43	13.82±0.08	0.10±0.02	1.40±0.03	4.12±0.03	72.22±0.35	3.05±0.11	0.6±0.02	2.04±0.04	0.31±0.02
C-1 2	44	13.87±0.08	0.09±0.02	1.52±0.03	4.11±0.03	73.12±0.35	3.07±0.11	0.56±0.02	2.03±0.04	0.3±0.02
C-1 2	45	13.89±0.08	0.09±0.02	0.99±0.03	4.05±0.03	73.55±0.35	3.20±0.11	0.56±0.02	2.11±0.04	0.32±0.02
C-1 2	46	13.83±0.08	0.12±0.02	1.36±0.03	4.03±0.03	74.32±0.36	2.92±0.11	0.56±0.02	2.04±0.04	0.31±0.02
C-1 2	47	13.76±0.08	0.04±0.02	1.29±0.03	4.04±0.03	71.24±0.35	3.08±0.11	0.56±0.02	2.10±0.04	0.32±0.02
C-1 2	48	13.77±0.08	0.09±0.02	1.27±0.03	4.01±0.03	73.63±0.35	3.06±0.11	0.54±0.02	2.10±0.04	0.29±0.02
C-1 2	49	13.94±0.08	0.09±0.02	1.35±0.03	3.98±0.03	73.02±0.35	2.83±0.10	0.55±0.02	2.12±0.04	0.28±0.02
C-1 2	50	13.78±0.08	0.12±0.02	1.27±0.03	3.98±0.03	73.07±0.35	2.90±0.10	0.58±0.02	2.12±0.04	0.29±0.02
C-1 2	51	13.92±0.08	0.10±0.02	1.52±0.03	3.99±0.03	73.24±0.35	3.10±0.11	0.55±0.02	2.15±0.04	0.3±0.02
C-1 2	52	13.96±0.08	0.09±0.02	1.53±0.03	3.91±0.03	72.93±0.35	3.06±0.11	0.57±0.02	2.10±0.04	0.3±0.02
C-1 2	53	13.97±0.08	0.10±0.02	1.12±0.03	3.95±0.03	72.90±0.35	2.94±0.10	0.59±0.02	2.17±0.04	0.31±0.02
C-1 2	54	14.00±0.08	0.10±0.02	1.50±0.03	3.94±0.03	73.36±0.35	2.90±0.10	0.57±0.02	2.16±0.04	0.25±0.02
C-1 2	55	13.99±0.08	0.17±0.02	1.25±0.03	3.89±0.03	72.41±0.35	2.90±0.10	0.58±0.02	2.18±0.04	0.28±0.02
C-1 2	56	14.03±0.08	0.11±0.02	1.43±0.03	3.88±0.03	73.24±0.35	2.99±0.11	0.56±0.02	2.23±0.04	0.31±0.02
C-1 2	57	13.85±0.08	0.11±0.02	1.40±0.03	3.92±0.03	73.39±0.35	3.20±0.11	0.6±0.02	2.22±0.04	0.29±0.02
C-1 2	58	14.01±0.08	0.08±0.02	1.49±0.03	3.93±0.03	72.73±0.35	2.92±0.10	0.58±0.02	2.28±0.04	0.29±0.02
C-1 2	59	14.06±0.08	0.09±0.02	1.63±0.03	3.85±0.03	72.15±0.35	2.94±0.10	0.54±0.02	2.28±0.04	0.26±0.02
C-1 2	60	14.19±0.08	0.09±0.02	1.10±0.03	3.80±0.03	72.77±0.35	3.06±0.11	0.59±0.02	2.24±0.04	0.28±0.02
C-1 2	61	14.29±0.08	0.13±0.02	1.45±0.03	3.86±0.03	72.31±0.35	3.02±0.11	0.6±0.02	2.28±0.04	0.26±0.02
C-1 2	62	14.23±0.08	0.07±0.02	1.03±0.03	3.81±0.03	72.87±0.35	2.80±0.10	0.53±0.02	2.39±0.04	0.3±0.02
C-1 2	63	14.25±0.08	0.10±0.02	1.41±0.03	3.84±0.03	72.33±0.35	3.11±0.11	0.58±0.02	2.29±0.04	0.3±0.02
C-1 2	64	14.34±0.08	0.12±0.02	1.09±0.03	3.82±0.03	73.07±0.35	3.04±0.11	0.57±0.02	2.31±0.04	0.27±0.02
C-1 2	65	14.32±0.08	0.07±0.02	1.60±0.04	3.80±0.03	72.14±0.35	3.11±0.11	0.59±0.02	2.38±0.04	0.24±0.02
C-1 2	66	14.27±0.08	0.09±0.02	1.70±0.04	3.88±0.03	72.77±0.35	3.12±0.11	0.59±0.02	2.34±0.04	0.29±0.02
C-1 2	67	14.34±0.08	0.09±0.02	1.26±0.03	3.84±0.03	73.13±0.35	3.24±0.11	0.55±0.02	2.36±0.04	0.3±0.02
C-1 2	68	14.36±0.08	0.08±0.02	1.56±0.04	3.77±0.03	72.75±0.35	3.19±0.11	0.56±0.02	2.34±0.04	0.29±0.02
C-1 2	69	14.56±0.08	0.05±0.02	1.14±0.03	3.77±0.03	72.87±0.35	2.87±0.10	0.55±0.02	2.36±0.04	0.27±0.02
C-1 2	70	14.48±0.08	0.09±0.02	1.41±0.03	3.78±0.03	72.74±0.35	2.97±0.11	0.57±0.02	2.43±0.04	0.27±0.02
C-1 2	71	14.39±0.08	0.12±0.02	1.00±0.03	3.76±0.03	73.54±0.35	3.13±0.11	0.54±0.02	2.38±0.04	0.27±0.02
C-1 2	72	14.37±0.08	0.07±0.02	1.57±0.03	3.78±0.03	70.96±0.35	2.99±0.11	0.59±0.02	2.45±0.04	0.29±0.02
C-1 2	73	14.31±0.08	0.07±0.02	1.47±0.03	3.82±0.03	72.90±0.35	2.97±0.11	0.58±0.02	2.44±0.04	0.28±0.02
C-1 2	74	14.30±0.08	0.08±0.02	1.37±0.03	3.79±0.03	73.37±0.35	3.05±0.11	0.6±0.02	2.35±0.04	0.3±0.02

C-1 2	75	14.55±0.08	0.10±0.02	1.38±0.03	3.78±0.03	71.90±0.35	3.16±0.11	0.54±0.02	2.37±0.04	0.28±0.02
C-1 2	76	14.25±0.08	0.13±0.02	1.25±0.03	3.79±0.03	73.15±0.35	2.97±0.10	0.56±0.02	2.40±0.04	0.28±0.02
C-1 2	77	14.51±0.08	0.06±0.02	1.53±0.03	3.83±0.03	72.51±0.35	3.25±0.11	0.62±0.02	2.44±0.04	0.27±0.02
C-1 2	78	14.54±0.08	0.06±0.02	1.14±0.03	3.76±0.03	71.93±0.35	3.06±0.11	0.56±0.02	2.41±0.04	0.26±0.02
C-1 2	79	14.40±0.08	0.08±0.02	1.43±0.03	3.80±0.03	72.46±0.35	2.99±0.10	0.58±0.02	2.35±0.04	0.29±0.02
C-1 2	80	14.42±0.08	0.10±0.02	1.50±0.03	3.82±0.03	72.45±0.35	3.10±0.11	0.6±0.02	2.43±0.04	0.27±0.02
C-1 2	81	14.51±0.08	0.13±0.02	1.53±0.03	3.77±0.03	72.30±0.35	3.05±0.11	0.61±0.02	2.51±0.04	0.31±0.02
C-1 2	82	14.58±0.08	0.10±0.02	1.45±0.03	3.76±0.03	72.34±0.35	2.91±0.11	0.57±0.02	2.46±0.04	0.3±0.02
C-1 2	83	14.63±0.08	0.14±0.02	1.34±0.03	3.85±0.03	72.38±0.35	3.09±0.11	0.58±0.02	2.44±0.04	0.28±0.02
C-1 2	84	14.82±0.08	0.15±0.02	1.39±0.03	3.77±0.03	72.33±0.35	3.00±0.11	0.6±0.02	2.50±0.04	0.3±0.02
C-1 2	85	14.78±0.08	0.07±0.02	1.58±0.04	3.84±0.03	71.73±0.35	3.22±0.11	0.61±0.02	2.48±0.04	0.31±0.02
C-1 2	86	14.64±0.08	0.12±0.02	1.16±0.03	3.77±0.03	71.44±0.35	3.03±0.11	0.62±0.02	2.47±0.04	0.29±0.02
C-1 2	87	14.79±0.08	0.08±0.02	1.60±0.03	3.84±0.03	72.05±0.35	3.09±0.11	0.57±0.02	2.47±0.04	0.28±0.02
C-1 2	88	14.87±0.08	0.14±0.02	1.49±0.03	3.84±0.03	70.23±0.34	3.22±0.11	0.6±0.02	2.44±0.04	0.31±0.02
C-1 2	89	14.88±0.08	0.12±0.02	1.54±0.03	3.84±0.03	71.08±0.35	3.07±0.11	0.62±0.02	2.35±0.04	0.31±0.02
C-1 2	90	14.86±0.08	0.09±0.02	1.42±0.03	3.89±0.03	70.59±0.35	3.15±0.11	0.58±0.02	2.37±0.04	0.28±0.02
C-1 2	91	14.75±0.08	0.12±0.02	1.32±0.03	3.87±0.03	71.92±0.35	3.21±0.11	0.63±0.02	2.38±0.04	0.31±0.02
C-1 2	92	14.71±0.08	0.11±0.02	1.54±0.03	3.93±0.03	72.36±0.35	3.16±0.11	0.61±0.02	2.39±0.04	0.29±0.02
C-1 2	93	14.78±0.08	0.10±0.02	1.13±0.03	3.84±0.03	72.24±0.35	3.15±0.11	0.63±0.02	2.35±0.04	0.29±0.02
C-1 2	94	14.62±0.08	0.08±0.02	1.50±0.03	3.91±0.03	70.40±0.34	3.16±0.11	0.61±0.02	2.35±0.04	0.31±0.02
C-1 2	95	14.54±0.08	0.13±0.02	1.00±0.03	3.99±0.03	71.44±0.35	3.24±0.11	0.65±0.02	2.38±0.04	0.3±0.02
C-1 2	96	14.52±0.08	0.12±0.02	1.71±0.04	3.93±0.03	72.42±0.35	3.02±0.11	0.6±0.02	2.31±0.04	0.3±0.02
C-1 2	97	14.35±0.08	0.09±0.02	1.27±0.03	3.92±0.03	70.91±0.35	3.41±0.11	0.6±0.02	2.26±0.04	0.32±0.02
C-1 2	98	14.28±0.08	0.07±0.02	1.46±0.03	3.96±0.03	72.28±0.35	3.01±0.11	0.57±0.02	2.22±0.04	0.32±0.02
C-1 2	99	14.17±0.08	0.07±0.02	1.55±0.03	4.03±0.03	72.92±0.35	2.96±0.10	0.61±0.02	2.18±0.04	0.27±0.02
C-1 2	100	14.15±0.08	0.10±0.02	1.08±0.03	3.97±0.03	72.43±0.35	3.07±0.11	0.58±0.02	2.18±0.04	0.29±0.02
C-1 2	101	14.13±0.08	0.12±0.02	1.40±0.03	4.10±0.03	73.04±0.35	3.03±0.11	0.59±0.02	2.16±0.04	0.3±0.02
C-1 2	102	14.00±0.08	0.11±0.02	1.08±0.03	4.08±0.03	72.89±0.35	3.15±0.11	0.56±0.02	2.17±0.04	0.29±0.02
C-1 2	103	14.11±0.08	0.12±0.02	1.60±0.04	4.13±0.03	72.39±0.35	3.18±0.11	0.58±0.02	2.15±0.04	0.32±0.02
C-1 2	104	13.92±0.08	0.11±0.02	1.25±0.03	4.08±0.03	72.84±0.35	3.12±0.11	0.6±0.02	2.04±0.04	0.28±0.02
C-1 2	105	14.00±0.08	0.09±0.02	1.52±0.03	4.20±0.03	70.43±0.35	3.13±0.11	0.63±0.02	2.01±0.04	0.3±0.02
C-1 2	106	13.94±0.08	0.07±0.02	1.42±0.03	4.20±0.03	71.93±0.35	2.91±0.11	0.59±0.02	2.01±0.04	0.34±0.02
C-1 2	107	13.94±0.08	0.06±0.02	1.33±0.03	4.20±0.03	72.46±0.35	3.00±0.11	0.59±0.02	2.02±0.04	0.34±0.02
C-1 2	108	14.01±0.08	0.09±0.02	1.32±0.03	4.34±0.03	72.07±0.35	3.18±0.11	0.58±0.02	2.01±0.04	0.3±0.02
C-1 2	109	13.95±0.08	0.10±0.02	1.35±0.03	4.33±0.03	73.26±0.35	3.03±0.11	0.58±0.02	2.03±0.04	0.31±0.02
C-1 2	110	13.91±0.08	0.08±0.02	1.64±0.04	4.41±0.03	70.67±0.35	2.94±0.11	0.58±0.02	2.04±0.04	0.34±0.02
C-1 2	111	13.90±0.08	0.12±0.02	1.11±0.03	4.35±0.03	72.48±0.35	2.77±0.10	0.56±0.02	1.98±0.04	0.31±0.02
C-1 2	112	13.79±0.08	0.11±0.02	1.75±0.04	4.50±0.03	71.45±0.35	3.09±0.11	0.59±0.02	1.92±0.04	0.36±0.02
C-1 2	113	13.88±0.08	0.08±0.02	1.66±0.04	4.56±0.03	71.37±0.35	3.18±0.11	0.59±0.02	1.95±0.04	0.31±0.02
C-1 2	114	13.97±0.08	0.05±0.02	1.45±0.03	4.59±0.03	72.72±0.35	2.77±0.10	0.57±0.02	1.84±0.04	0.31±0.02
C-1 2	115	13.84±0.08	0.16±0.02	1.43±0.03	4.60±0.03	72.96±0.35	2.91±0.10	0.57±0.02	1.93±0.04	0.33±0.02
C-1 2	116	13.79±0.08	0.06±0.02	1.46±0.03	4.73±0.04	72.65±0.35	2.98±0.11	0.58±0.02	1.87±0.04	0.34±0.02
C-1 2	117	14.05±0.08	0.12±0.02	1.47±0.03	4.72±0.04	70.98±0.35	3.07±0.10	0.53±0.02	1.89±0.04	0.32±0.02
C-1 2	118	13.92±0.08	0.09±0.02	1.61±0.04	4.86±0.04	73.29±0.35	3.00±0.11	0.55±0.02	1.79±0.04	0.34±0.02
C-1 2	119	13.92±0.08	0.14±0.02	1.93±0.04	4.87±0.04	72.06±0.35	3.30±0.11	0.52±0.02	1.83±0.04	0.29±0.02
C-1 2	120	13.99±0.08	0.10±0.02	1.83±0.04	5.04±0.04	71.45±0.35	3.10±0.11	0.56±0.02	1.82±0.04	0.32±0.02
C-1 2	121	14.03±0.08	0.08±0.02	1.65±0.04	5.04±0.04	71.85±0.35	2.91±0.10	0.59±0.02	1.80±0.04	0.34±0.02
C-1 2	122	14.00±0.08	0.10±0.02	1.81±0.04	5.14±0.04	72.78±0.35	2.90±0.11	0.54±0.02	1.83±0.04	0.33±0.02
C-1 2	123	14.00±0.08	0.12±0.02	1.62±0.04	5.16±0.04	72.00±0.35	2.82±0.10	0.52±0.02	1.88±0.04	0.34±0.02
C-1 2	124	13.84±0.08	0.07±0.02	1.47±0.03	5.20±0.04	71.84±0.35	2.80±0.10	0.54±0.02	1.90±0.04	0.35±0.02
C-1 2	125	13.75±0.08	0.11±0.02	1.94±0.04	5.33±0.04	72.95±0.35	2.92±0.10	0.54±0.02	1.90±0.04	0.33±0.02
C-1 2	126	13.63±0.08	0.08±0.02	1.56±0.03	5.19±0.04	72.53±0.35	2.87±0.10	0.57±0.02	1.87±0.04	0.34±0.02
C-1 2	127	13.23±0.08	0.06±0.02	2.36±0.04	5.52±0.04	72.18±0.35	3.07±0.11	0.52±0.02	1.88±0.04	0.29±0.02
C-1 2	128	12.98±0.08	0.09±0.02	1.91±0.04	5.47±0.04	73.11±0.35	3.11±0.11	0.55±0.02	1.95±0.04	0.34±0.02
C-1 2	129	12.17±0.08	0.03±0.02	2.62±0.04	5.52±0.04	71.95±0.35	3.01±0.11	0.61±0.02	1.94±0.04	0.29±0.02
C-1 2	130	11.88±0.08	0.14±0.02	2.43±0.04	5.54±0.04	72.24±0.35	3.23±0.11	0.66±0.02	2.07±0.04	0.28±0.02
C-1 2	131	11.47±0.08	0.11±0.02	2.38±0.04	5.45±0.04	72.97±0.35	3.50±0.11	0.62±0.02	2.23±0.04	0.28±0.02
C-1 2	132	9.62±0.07	0.14±0.02	2.83±0.05	5.22±0.04	71.21±0.35	4.16±0.12	0.62±0.02	2.83±0.04	0.24±0.02
C-1 2	133	8.20±0.06	0.14±0.02	1.89±0.04	4.84±0.04	74.80±0.35	4.03±0.12	0.6±0.02	3.04±0.05	0.19±0.02
C-1 2	134	8.15±0.06	0.09±0.02	3.03±0.05	5.18±0.04	74.57±0.35	3.02±0.11	0.52±0.02	2.81±0.04	0.22±0.02
C-1 2	135	9.04±0.07	0.07±0.02	1.99±0.04	5.15±0.04	75.94±0.36	2.84±0.10	0.46±0.02	2.40±0.04	0.21±0.02
C-1 2	136	10.40±0.07	0.07±0.02	3.29±0.05	5.70±0.04	74.01±0.36	2.73±0.10	0.42±0.02	1.78±0.04	0.22±0.02
C-1 2	137	10.80±0.07	0.08±0.02	1.93±0.04	5.12±0.04	74.75±0.35	2.61±0.10	0.4±0.02	1.73±0.04	0.26±0.02
C-1 2	138	10.72±0.07	0.08±0.02	2.40±0.04	5.39±0.04	74.42±0.36	2.71±0.10	0.43±0.02	1.73±0.04	0.25±0.02
C-1 2	139	10.72±0.07	0.08±0.02	2.42±0.04	5.14±0.04	73.98±0.36	2.76±0.10	0.49±0.02	1.80±0.04	0.22±0.02
C-1 2	140	10.69±0.07	0.08±0.02	2.18±0.04	5.19±0.04	74.14±0.36	2.74±0.10	0.48±0.02	1.84±0.04	0.22±0.02
C-1 2	141	10.49±0.07	0.10±0.02	3.10±0.05	5.62±0.04	73.17±0.35	2.71±0.10	0.48±0.02	1.91±0.04	0.24±0.02
C-1 2	142	10.68±0.07	0.08±0.02	1.90±0.04	5.07±0.04	73.44±0.35	2.93±0.10	0.5±0.02	1.89±0.04	0.24±0.02
C-1 2	143	10.46±0.07	0.08±0.02	3.28±0.05	5.59±0.04	74.18±0.36	2.89±0.10	0.49±0.02	1.91±0.04	0.25±0.02
C-1 2	144	10.76±0.07	0.15±0.02	2.05±0.04	5.14±0.04	74.36±0.35	2.72±0.10	0.52±0.02	1.97±0.04	0.24±0.02
C-1 2	145	10.68±0.07	0.11±0.02	2.97±0.05	5.55±0.04	74.19±0.36	2.55±0.10	0.46±0.02	1.93±0.04	0.23±0.02
C-1 2	146	11.02±0.07	0.08±0.02	2.47±0.04	5.35±0.04	75.31±0.35	2.69±0.10	0.48±0.02	1.86±0.04	0.23±0.02
C-1 2	147	11.19±0.07	0.07±0.02	2.04±0.04	5.28±0.04	74.31±0.36	2.66±0.10	0.48±0.02	1.76±0.04	0.22±0.02
C-1 2	148	11.38±0.08	0.10±0.02	2.20±0.04	5.26±0.04	73.67±0.35	2.59±0.10	0.46±0.02	1.80±0.04	0.28±0.02
C-1 2	149	11.42±0.07	0.07±0.02	1.96±0.04	5.18±0.04	74.52±0.35	2.79±0.10	0.48±0.02	1.71±0.04	0.26±0.02
C-1 2	150	11.31±0.07	0.10±0.02	2.25±0.04	5.29±0.04	73.58±0.35	3.01±0.11	0.49±0.02	1.60±0.03	0.28±0.02
C-1 2	151	11.01±0.07	0.10±0.02	2.03±0.04	5.18±0.04	74.16±0.36	3.19±0.11	0.54±0.02	1.55±0.03	0.3±0.02
C-1 2	152	10.48±0.07	0.12±0.02	2.14±0.04	5.42±0.04	74.17±0.36	3.80±0.12	0.51±0.02	1.48±0.03	0.27±0.02
C-1 2	153	10.29±0.07	0.11±0.02	1.65±0.04	5.25±0.04	74.51±0.35	4.28±0.12	0.57±0.02	1.50±0.03	0.38±0.02
C-3 1	1	11.87±0.13	0.12±0.03	4.92±0.06	5.83±0.04	72.99±0.34	2.75±0.10	0.54±0.02	2.13±0.04	0.22±0.02
C-3 1	2	12.33±0.13	0.11±0.03	2.57±0.04	5.73±0.04	72.63±0.33	2.70±0.10	0.53±0.02	2.11±0.04	0.19±0.02
C-3 1	3	12.49±0.14	0.13±0.02	2.99±0.05	5.85±0.04	73.05±0.34	2.75±0.10	0.53±0.02	2.00±0.04	0.2±0.02
C-3 1	4	12.66±0.14	0.11±0.02	3.13±0.05	5.87±0.04	74.21±0.34	2.61±0.10	0.53±0.02	1.89±0.04	0.2±0.02
C-3 1	5	12.82±0.14	0.09±0.02	3.22±0.05	5.92±0.04	71.42±0.34	2.56±0.09	0.46±0.02	1.82±0.03	0.22±0.02
C-3 1	6	13.06±0.14	0.06±0.02	2.85±0.04	5.85±0.04	74.26±0.34	2.31±0.09	0.46±0.02	1.80±0.03	0.25±0.02

C-3 1	7	13.26±0.14	0.06±0.02	2.61±0.04	5.82±0.04	72.66±0.33	2.26±0.09	0.44±0.02	1.73±0.03	0.24±0.02
C-3 1	8	13.71±0.14	0.09±0.02	2.30±0.04	5.66±0.04	74.44±0.34	2.33±0.09	0.43±0.02	1.70±0.03	0.23±0.02
C-3 1	9	13.57±0.14	0.09±0.02	2.48±0.04	5.84±0.04	73.60±0.34	2.41±0.09	0.44±0.02	1.68±0.03	0.24±0.02
C-3 1	10	13.55±0.14	0.08±0.02	2.68±0.04	5.87±0.04	73.28±0.34	2.18±0.09	0.43±0.02	1.64±0.03	0.25±0.02
C-3 1	11	13.40±0.14	0.07±0.02	2.91±0.04	5.92±0.04	72.77±0.33	2.45±0.09	0.45±0.02	1.57±0.03	0.25±0.02
C-3 1	12	14.01±0.14	0.11±0.02	1.90±0.04	5.41±0.04	73.29±0.34	2.29±0.09	0.44±0.02	1.67±0.03	0.24±0.02
C-3 1	13	13.79±0.14	0.16±0.02	2.53±0.04	5.91±0.04	73.09±0.34	2.48±0.09	0.44±0.02	1.55±0.03	0.25±0.02
C-3 1	14	14.08±0.14	0.11±0.02	2.42±0.04	5.74±0.04	73.22±0.34	2.25±0.09	0.45±0.02	1.58±0.03	0.25±0.02
C-3 1	15	14.17±0.14	0.09±0.02	2.32±0.04	5.73±0.04	72.84±0.34	2.41±0.09	0.4±0.02	1.64±0.03	0.23±0.02
C-3 1	16	14.06±0.14	0.09±0.02	2.40±0.04	5.80±0.04	72.02±0.34	2.46±0.09	0.44±0.02	1.59±0.03	0.24±0.02
C-3 1	17	14.14±0.14	0.12±0.02	3.01±0.04	5.90±0.04	72.82±0.33	2.45±0.09	0.46±0.02	1.67±0.03	0.24±0.02
C-3 1	18	13.93±0.14	0.08±0.02	2.70±0.04	5.87±0.04	71.72±0.34	2.38±0.09	0.45±0.02	1.61±0.03	0.26±0.02
C-3 1	19	14.10±0.14	0.09±0.02	2.84±0.04	5.84±0.04	73.42±0.34	2.40±0.09	0.43±0.02	1.67±0.03	0.23±0.02
C-3 1	20	14.08±0.14	0.06±0.02	2.84±0.04	5.86±0.04	73.29±0.34	2.41±0.09	0.42±0.02	1.59±0.03	0.24±0.02
C-3 1	21	14.27±0.14	0.07±0.02	2.56±0.04	5.81±0.04	73.13±0.34	2.27±0.09	0.41±0.02	1.56±0.03	0.24±0.02
C-3 1	22	14.09±0.14	0.08±0.02	2.08±0.04	5.48±0.04	74.36±0.34	2.46±0.09	0.44±0.02	1.64±0.03	0.23±0.02
C-3 1	23	14.29±0.14	0.06±0.02	1.74±0.04	5.38±0.04	73.72±0.34	2.29±0.09	0.42±0.02	1.60±0.03	0.23±0.02
C-3 1	24	14.13±0.14	0.06±0.02	2.61±0.04	5.87±0.04	73.42±0.34	2.56±0.10	0.42±0.02	1.61±0.03	0.27±0.02
C-3 1	25	14.02±0.14	0.09±0.02	3.09±0.05	5.95±0.04	72.32±0.34	2.45±0.09	0.46±0.02	1.66±0.03	0.23±0.02
C-3 1	26	13.75±0.14	0.08±0.02	2.98±0.04	5.86±0.04	72.99±0.34	2.52±0.09	0.44±0.02	1.69±0.03	0.21±0.02
C-3 1	27	13.78±0.14	0.08±0.02	2.77±0.04	5.80±0.04	73.54±0.34	2.49±0.09	0.45±0.02	1.63±0.03	0.24±0.02
C-3 1	28	13.78±0.14	0.13±0.02	2.58±0.04	5.81±0.04	73.66±0.34	2.38±0.09	0.47±0.02	1.64±0.03	0.24±0.02
C-3 1	29	13.73±0.14	0.06±0.02	2.56±0.04	5.68±0.04	73.39±0.34	2.47±0.09	0.42±0.02	1.62±0.03	0.25±0.02
C-3 1	30	13.60±0.14	0.08±0.02	2.79±0.04	5.85±0.04	73.37±0.34	2.44±0.09	0.44±0.02	1.75±0.03	0.22±0.02
C-3 1	31	13.45±0.14	0.12±0.03	3.02±0.05	5.87±0.04	72.74±0.33	2.43±0.09	0.45±0.02	1.65±0.03	0.2±0.02
C-3 1	32	13.53±0.14	0.04±0.02	3.13±0.05	5.85±0.04	72.91±0.34	2.63±0.10	0.41±0.02	1.65±0.03	0.22±0.02
C-3 1	33	13.50±0.14	0.10±0.02	2.70±0.04	5.78±0.04	73.10±0.34	2.40±0.09	0.41±0.02	1.75±0.03	0.23±0.02
C-3 1	34	13.61±0.14	0.08±0.02	2.00±0.04	5.49±0.04	73.22±0.34	2.37±0.09	0.45±0.02	1.75±0.03	0.24±0.02
C-3 1	35	13.66±0.14	0.05±0.02	2.22±0.04	5.57±0.04	73.28±0.34	2.57±0.09	0.41±0.02	1.71±0.03	0.25±0.02
C-3 1	36	13.40±0.14	0.11±0.03	2.58±0.04	5.73±0.04	72.42±0.34	2.51±0.09	0.4±0.02	1.75±0.03	0.25±0.02
C-3 1	37	13.26±0.14	0.08±0.02	2.53±0.04	5.74±0.04	73.81±0.34	2.45±0.09	0.47±0.02	1.71±0.03	0.26±0.02
C-3 1	38	12.91±0.14	0.08±0.02	3.08±0.05	5.91±0.04	73.06±0.34	2.52±0.09	0.44±0.02	1.72±0.03	0.23±0.02
C-3 1	39	13.00±0.14	0.11±0.02	3.29±0.05	5.87±0.04	72.11±0.34	2.53±0.09	0.46±0.02	1.70±0.03	0.21±0.02
C-3 1	40	13.24±0.14	0.06±0.02	3.08±0.05	5.97±0.04	73.27±0.34	2.35±0.09	0.48±0.02	1.70±0.03	0.24±0.02
C-3 1	41	12.96±0.14	0.11±0.02	2.98±0.04	5.91±0.04	71.89±0.34	2.44±0.09	0.45±0.02	1.84±0.03	0.23±0.02
C-3 1	42	13.26±0.14	0.09±0.02	2.66±0.04	5.78±0.04	73.01±0.34	2.52±0.09	0.46±0.02	1.82±0.03	0.24±0.02
C-3 1	43	13.13±0.14	0.09±0.02	2.68±0.04	5.81±0.04	72.56±0.34	2.67±0.10	0.5±0.02	1.85±0.03	0.19±0.02
C-3 1	44	13.20±0.14	0.11±0.02	3.32±0.05	5.90±0.04	73.51±0.34	2.46±0.09	0.44±0.02	1.80±0.03	0.18±0.02
C-3 1	45	13.02±0.14	0.10±0.02	2.23±0.04	5.49±0.04	73.35±0.34	2.47±0.09	0.47±0.02	1.85±0.04	0.21±0.02
C-3 1	46	12.82±0.14	0.08±0.02	3.08±0.05	5.82±0.04	73.76±0.34	2.72±0.10	0.44±0.02	1.87±0.03	0.21±0.02
C-3 1	47	12.61±0.13	0.09±0.02	3.22±0.05	5.90±0.04	72.72±0.33	2.67±0.10	0.49±0.02	1.92±0.04	0.17±0.02
C-3 1	48	12.88±0.14	0.07±0.02	2.85±0.04	5.84±0.04	72.31±0.34	2.73±0.10	0.52±0.02	1.87±0.04	0.2±0.02
C-3 1	49	13.09±0.14	0.06±0.02	2.54±0.04	5.70±0.04	73.14±0.34	2.75±0.10	0.49±0.02	1.95±0.04	0.22±0.02
C-3 1	50	12.71±0.14	0.08±0.02	2.75±0.04	5.76±0.04	72.21±0.34	2.67±0.10	0.45±0.02	1.94±0.04	0.22±0.02
C-3 1	51	12.73±0.14	0.11±0.02	2.88±0.04	5.82±0.04	72.75±0.33	2.58±0.10	0.51±0.02	1.91±0.04	0.21±0.02
C-3 1	52	12.71±0.14	0.08±0.02	3.39±0.05	5.92±0.04	72.91±0.34	2.52±0.09	0.52±0.02	1.84±0.03	0.19±0.02
C-3 1	53	12.93±0.14	0.04±0.02	3.55±0.05	5.89±0.04	72.42±0.34	2.73±0.10	0.48±0.02	1.78±0.03	0.19±0.02
C-3 1	54	12.91±0.14	0.09±0.02	3.17±0.05	5.89±0.04	73.13±0.34	2.61±0.10	0.52±0.02	1.80±0.03	0.24±0.02
C-3 1	55	13.07±0.14	0.11±0.02	3.12±0.05	5.89±0.04	72.62±0.33	2.70±0.10	0.48±0.02	1.86±0.03	0.23±0.02
C-3 1	56	12.72±0.14	0.12±0.02	2.17±0.04	5.38±0.04	73.56±0.34	2.82±0.10	0.5±0.02	1.88±0.04	0.19±0.02
C-3 1	57	12.73±0.14	0.11±0.02	2.56±0.04	5.57±0.04	73.51±0.34	2.52±0.10	0.5±0.02	1.84±0.03	0.24±0.02
C-3 1	58	12.68±0.14	0.07±0.02	3.13±0.05	5.72±0.04	72.72±0.33	2.61±0.10	0.48±0.02	1.94±0.04	0.23±0.02
C-3 1	59	12.54±0.14	0.14±0.02	3.47±0.05	5.75±0.04	72.32±0.34	2.66±0.10	0.51±0.02	2.07±0.04	0.23±0.02
C-3 1	60	12.71±0.14	0.09±0.02	3.31±0.05	5.81±0.04	72.31±0.34	2.83±0.10	0.57±0.02	2.26±0.04	0.22±0.02
C-3 1	61	12.76±0.14	0.11±0.02	2.94±0.04	5.60±0.04	70.74±0.33	3.01±0.10	0.57±0.02	2.48±0.04	0.22±0.02
C-3 1	62	12.18±0.13	0.19±0.03	2.63±0.04	5.40±0.04	71.84±0.34	3.93±0.12	0.67±0.02	2.82±0.04	0.22±0.02
C-3 1	63	10.12±0.12	0.19±0.03	2.29±0.04	5.15±0.04	72.33±0.33	4.29±0.12	0.68±0.02	2.72±0.04	0.24±0.02
C-3 1	64	13.11±0.14	0.11±0.02	2.27±0.04	5.58±0.04	71.69±0.34	3.55±0.11	0.58±0.02	2.01±0.04	0.24±0.02
C-3 1	65	14.23±0.14	0.10±0.03	2.33±0.04	5.60±0.04	71.72±0.34	2.88±0.10	0.54±0.02	1.52±0.03	0.29±0.02
C-3 1	66	15.12±0.15	0.11±0.03	2.16±0.04	5.47±0.04	72.42±0.34	2.97±0.10	0.59±0.02	1.22±0.03	0.27±0.02
C-3 1	67	15.36±0.15	0.13±0.02	1.88±0.04	5.26±0.04	72.84±0.34	2.85±0.10	0.64±0.02	1.12±0.03	0.29±0.02
C-3 1	68	16.36±0.15	0.12±0.02	1.30±0.03	5.00±0.04	72.25±0.34	3.03±0.10	0.74±0.02	1.19±0.03	0.34±0.02
C-3 1	69	18.74±0.16	0.06±0.02	1.88±0.04	5.07±0.04	68.13±0.33	3.41±0.11	0.92±0.03	1.57±0.03	0.46±0.02
C-3 1	70	19.19±0.16	0.14±0.03	1.79±0.04	4.95±0.04	68.13±0.33	3.41±0.11	0.93±0.03	1.57±0.03	0.46±0.02
C-3 1	71	19.54±0.16	0.14±0.03	1.68±0.04	4.91±0.03	66.24±0.32	3.41±0.11	0.94±0.03	1.63±0.03	0.44±0.02
C-3 1	72	19.47±0.17	0.10±0.02	2.07±0.04	4.79±0.03	67.87±0.33	3.52±0.11	1.06±0.03	1.71±0.03	0.44±0.02
C-3 1	73	19.54±0.17	0.12±0.02	1.91±0.04	4.65±0.03	66.80±0.33	3.65±0.11	1.05±0.03	1.78±0.03	0.46±0.02
C-3 1	74	19.83±0.17	0.12±0.03	1.99±0.04	4.56±0.03	67.20±0.33	3.76±0.11	1.03±0.03	1.94±0.04	0.53±0.02
C-3 1	75	20.09±0.17	0.16±0.03	1.73±0.04	4.41±0.03	67.79±0.33	3.71±0.11	1.02±0.03	2.00±0.04	0.5±0.02
C-3 1	76	19.41±0.16	0.11±0.02	1.64±0.03	4.49±0.03	68.28±0.33	3.48±0.11	0.93±0.03	1.92±0.04	0.45±0.02
C-3 1	77	19.32±0.16	0.06±0.02	1.66±0.03	4.53±0.03	68.11±0.33	3.49±0.11	0.88±0.03	1.94±0.04	0.43±0.02
C-3 1	78	19.43±0.17	0.18±0.02	1.79±0.04	4.52±0.03	68.28±0.33	3.14±0.10	0.8±0.03	1.98±0.04	0.37±0.02
C-3 1	79	19.58±0.16	0.12±0.02	1.52±0.03	4.54±0.03	69.21±0.33	3.17±0.10	0.79±0.03	1.97±0.04	0.34±0.02
C-3 1	80	19.27±0.16	0.11±0.03	1.98±0.04	4.48±0.03	68.01±0.33	3.00±0.10	0.72±0.02	2.03±0.04	0.34±0.02
C-3 1	81	19.53±0.16	0.12±0.02	1.95±0.04	4.30±0.03	67.63±0.33	3.08±0.10	0.74±0.02	2.21±0.04	0.35±0.02
C-3 1	82	19.13±0.16	0.16±0.02	2.03±0.04	4.28±0.03	68.76±0.33	3.10±0.10	0.71±0.02	2.16±0.04	0.34±0.02
C-3 1	83	18.36±0.16	0.15±0.02	1.64±0.03	4.29±0.03	69.68±0.33	3.01±0.10	0.64±0.02	1.95±0.04	0.32±0.02
C-3 1	84	16.34±0.15	0.09±0.02	1.40±0.03	4.36±0.03	72.18±0.34	2.67±0.10	0.54±0.02	1.72±0.03	0.3±0.02
C-3 2	1	13.42±0.14	0.12±0.02	4.88±0.06	5.93±0.04	70.51±0.33	2.55±0.09	0.49±0.02	1.84±0.03	0.21±0.02
C-3 2	2	13.38±0.14	0.07±0.02	3.12±0.05	5.94±0.04	71.67±0.34	2.63±0.10	0.49±0.02	1.94±0.04	0.23±0.02
C-3 2	3	13.90±0.14	0.12±0.02	2.30±0.04	5.59±0.04	71.14±0.33	2.71±0.10	0.49±0.02	1.97±0.04	0.25±0.02
C-3 2	4	13.76±0.14	0.10±0.02	2.16±0.04	5.45±0.04	71.32±0.34	2.53±0.09	0.5±0.02	1.95±0.04	0.24±0.02
C-3 2	5	13.70±0.14	0.12±0.02	2.90±0.04	5.77±0.04	72.19±0.34	2.60±0.10	0.48±0.02	2.01±0.04	0.2±0.02
C-3 2	6	13.84±0.14	0.07±0.02	1.77±0.04	5.03±0.04	72.74±0.34	2.75±0.10	0.5±0.02	2.09±0.04	0.24±0.02
C-3 2	7	13.49±0.14	0.11±0.03	2.22±0.04	5.44±0.04	72.55±0.34	2.78±0.10	0.5±0.02	1.97±0.04	0.25±0.02

C-3 2	8	12.90±0.14	0.12±0.02	3.11±0.05	5.84±0.04	72.40±0.34	2.99±0.10	0.53±0.02	2.11±0.04	0.22±0.02
C-3 2	9	13.36±0.14	0.08±0.02	2.51±0.04	5.58±0.04	72.13±0.34	2.72±0.10	0.55±0.02	2.14±0.04	0.22±0.02
C-3 2	10	13.57±0.14	0.09±0.03	2.60±0.04	5.61±0.04	72.21±0.34	2.91±0.10	0.6±0.02	2.33±0.04	0.22±0.02
C-3 2	11	12.57±0.14	0.13±0.03	3.00±0.05	5.66±0.04	70.83±0.33	3.66±0.11	0.66±0.02	2.68±0.04	0.23±0.02
C-3 2	12	11.49±0.13	0.16±0.03	2.06±0.04	5.02±0.04	72.39±0.34	4.19±0.12	0.72±0.02	2.74±0.04	0.25±0.02
C-3 2	13	9.19±0.12	0.17±0.03	1.84±0.04	4.82±0.03	74.04±0.34	4.49±0.12	0.73±0.02	2.43±0.04	0.23±0.02
C-3 2	14	11.70±0.13	0.19±0.03	2.00±0.04	5.36±0.04	74.17±0.34	3.37±0.11	0.52±0.02	1.79±0.03	0.25±0.02
C-3 2	15	14.76±0.14	0.06±0.02	1.65±0.03	5.40±0.04	73.78±0.34	2.66±0.10	0.51±0.02	1.50±0.03	0.3±0.02
C-3 2	16	14.71±0.15	0.10±0.02	1.57±0.03	5.24±0.04	71.81±0.34	2.53±0.10	0.5±0.02	1.41±0.03	0.3±0.02
C-3 2	17	15.12±0.15	0.10±0.02	1.82±0.04	5.29±0.04	72.66±0.34	2.53±0.09	0.51±0.02	1.35±0.03	0.3±0.02
C-3 2	18	15.15±0.15	0.11±0.02	1.59±0.03	5.18±0.04	72.31±0.34	2.81±0.10	0.58±0.02	1.34±0.03	0.3±0.02
C-3 2	19	15.93±0.15	0.11±0.02	1.60±0.03	5.08±0.04	76.60±0.33	2.86±0.10	0.53±0.02	1.54±0.03	0.36±0.02
C-3 2	20	15.98±0.15	0.11±0.02	1.76±0.04	4.86±0.03	71.88±0.34	2.98±0.10	0.56±0.02	1.56±0.03	0.33±0.02
C-3 2	21	15.73±0.15	0.17±0.03	1.51±0.03	4.79±0.03	71.47±0.34	2.92±0.10	0.58±0.02	1.72±0.03	0.3±0.02
C-3 2	22	16.11±0.15	0.10±0.03	0.97±0.03	4.64±0.03	72.14±0.34	3.19±0.11	0.58±0.02	1.60±0.03	0.32±0.02
C-3 2	23	15.98±0.15	0.12±0.02	1.50±0.03	4.69±0.03	71.55±0.34	2.98±0.10	0.59±0.02	1.72±0.03	0.31±0.02
C-3 2	24	15.94±0.15	0.11±0.02	1.17±0.03	4.55±0.03	71.26±0.33	3.17±0.10	0.59±0.02	1.70±0.03	0.33±0.02
C-3 2	25	16.11±0.15	0.13±0.03	1.26±0.03	4.54±0.03	70.99±0.33	3.28±0.11	0.58±0.02	1.67±0.03	0.34±0.02
C-3 2	26	16.02±0.15	0.11±0.02	1.40±0.03	4.46±0.03	71.95±0.34	3.14±0.10	0.61±0.02	1.69±0.03	0.32±0.02
C-3 2	27	16.16±0.15	0.11±0.02	1.23±0.03	4.32±0.03	71.97±0.34	3.28±0.11	0.67±0.02	1.74±0.03	0.32±0.02
C-3 2	28	15.96±0.15	0.12±0.02	1.33±0.03	4.39±0.03	71.21±0.33	3.28±0.11	0.62±0.02	1.64±0.03	0.32±0.02
C-3 2	29	16.26±0.15	0.11±0.03	1.33±0.03	4.30±0.03	72.16±0.34	3.09±0.10	0.65±0.02	1.60±0.03	0.34±0.02
C-3 2	30	15.94±0.15	0.15±0.02	1.33±0.03	4.28±0.03	72.26±0.34	3.16±0.11	0.65±0.02	1.56±0.03	0.33±0.02
C-3 2	31	15.74±0.15	0.16±0.03	1.34±0.03	4.26±0.03	72.97±0.34	3.03±0.10	0.66±0.02	1.48±0.03	0.3±0.02
C-3 2	32	15.36±0.15	0.09±0.03	1.20±0.03	4.18±0.03	72.96±0.34	2.99±0.10	0.65±0.02	1.43±0.03	0.32±0.02
D-2	1	17.00±0.16	0.11±0.02	2.57±0.04	3.71±0.03	67.59±0.34	3.43±0.11	0.95±0.03	2.20±0.04	0.45±0.02
D-2	2	17.70±0.16	0.09±0.03	1.25±0.03	3.72±0.03	67.47±0.34	3.46±0.11	0.98±0.03	2.23±0.04	0.47±0.02
D-2	3	17.31±0.16	0.11±0.03	1.04±0.03	3.68±0.03	67.40±0.34	3.50±0.11	0.96±0.03	2.26±0.04	0.49±0.02
D-2	4	17.69±0.16	0.13±0.03	1.44±0.03	3.73±0.03	67.44±0.34	3.50±0.11	0.95±0.03	2.27±0.04	0.46±0.02
D-2	5	17.84±0.16	0.15±0.03	1.29±0.03	3.69±0.03	67.06±0.34	3.68±0.12	0.99±0.03	2.27±0.04	0.47±0.02
D-2	6	17.75±0.16	0.15±0.03	1.14±0.03	3.62±0.03	67.28±0.34	3.65±0.11	1.01±0.03	2.32±0.04	0.47±0.02
D-2	7	18.04±0.16	0.12±0.03	1.34±0.03	3.68±0.03	67.27±0.34	3.55±0.11	0.92±0.03	2.25±0.04	0.44±0.02
D-2	8	17.53±0.16	0.09±0.03	1.39±0.03	3.72±0.03	67.65±0.34	3.46±0.11	0.96±0.03	2.26±0.04	0.47±0.02
D-2	9	17.34±0.16	0.19±0.03	1.31±0.03	3.73±0.03	67.67±0.34	3.44±0.11	0.97±0.03	2.27±0.04	0.49±0.02
D-2	10	17.17±0.16	0.09±0.03	1.09±0.03	3.69±0.03	67.20±0.34	3.56±0.11	0.95±0.03	2.18±0.04	0.49±0.02
D-2	11	17.07±0.16	0.10±0.03	1.38±0.03	3.75±0.03	67.93±0.34	3.39±0.11	0.89±0.03	2.15±0.04	0.46±0.02
D-2	12	16.91±0.16	0.16±0.03	1.23±0.03	3.73±0.03	68.06±0.34	3.40±0.11	0.94±0.03	2.09±0.04	0.48±0.02
D-2	13	16.91±0.16	0.13±0.03	0.99±0.03	3.75±0.03	68.11±0.34	3.53±0.11	0.93±0.03	2.14±0.04	0.47±0.02
D-2	14	16.71±0.16	0.12±0.03	1.23±0.03	3.73±0.03	68.39±0.34	3.36±0.11	0.97±0.03	2.08±0.04	0.47±0.02
D-2	15	16.75±0.16	0.15±0.03	1.13±0.03	3.72±0.03	66.58±0.34	3.73±0.12	0.94±0.03	2.08±0.04	0.46±0.02
D-2	16	17.05±0.16	0.11±0.03	1.13±0.03	3.74±0.03	68.92±0.34	3.42±0.12	0.92±0.03	2.03±0.04	0.42±0.02
D-2	17	16.82±0.16	0.14±0.03	0.93±0.03	3.74±0.03	68.50±0.34	3.67±0.12	0.92±0.03	2.08±0.04	0.44±0.02
D-2	18	16.73±0.16	0.18±0.03	1.39±0.03	3.74±0.03	68.75±0.34	3.36±0.11	0.91±0.03	2.02±0.04	0.46±0.02
D-2	19	16.99±0.16	0.13±0.03	1.26±0.03	3.77±0.03	68.89±0.34	3.50±0.11	0.87±0.03	2.05±0.04	0.46±0.02
D-2	20	16.60±0.16	0.16±0.03	1.06±0.03	3.76±0.03	68.11±0.35	3.45±0.11	0.9±0.03	2.06±0.04	0.46±0.02
D-2	21	17.06±0.16	0.12±0.03	1.41±0.03	3.78±0.03	68.31±0.35	3.41±0.11	0.88±0.03	2.04±0.04	0.47±0.02
D-2	22	17.06±0.16	0.16±0.03	1.25±0.03	3.71±0.03	68.30±0.35	3.49±0.11	0.91±0.03	2.03±0.04	0.46±0.02
D-2	23	16.73±0.16	0.09±0.03	1.28±0.03	3.75±0.03	68.36±0.35	3.39±0.11	0.89±0.03	1.98±0.04	0.49±0.02
D-2	24	16.85±0.16	0.13±0.03	1.26±0.03	3.72±0.03	68.70±0.35	3.54±0.12	0.92±0.03	2.08±0.04	0.46±0.02
D-2	25	16.91±0.16	0.14±0.03	1.21±0.03	3.71±0.03	68.48±0.35	3.45±0.11	0.95±0.03	2.09±0.04	0.45±0.02
D-2	26	16.89±0.16	0.13±0.03	1.16±0.03	3.75±0.03	68.24±0.35	3.55±0.12	0.98±0.03	2.04±0.04	0.45±0.02
D-2	27	17.10±0.16	0.19±0.03	1.21±0.03	3.74±0.03	67.24±0.34	3.54±0.12	0.95±0.03	2.05±0.04	0.47±0.02
D-2	28	16.85±0.16	0.14±0.03	1.13±0.03	3.78±0.03	68.63±0.35	3.47±0.12	0.93±0.03	1.91±0.04	0.46±0.02
D-2	29	17.14±0.16	0.16±0.03	1.12±0.03	3.76±0.03	67.82±0.35	3.54±0.12	0.94±0.03	2.06±0.04	0.45±0.02
D-2	30	17.11±0.16	0.18±0.03	1.17±0.03	3.76±0.03	68.71±0.35	3.62±0.12	0.93±0.03	2.02±0.04	0.44±0.02
D-2	31	17.19±0.16	0.06±0.03	1.13±0.03	3.76±0.03	68.65±0.35	3.67±0.12	0.94±0.03	1.96±0.04	0.48±0.02
D-2	32	17.11±0.16	0.10±0.03	1.20±0.03	3.80±0.03	68.38±0.35	3.64±0.12	0.92±0.03	2.02±0.04	0.43±0.02
D-2	33	17.27±0.16	0.10±0.03	1.32±0.03	3.68±0.03	68.10±0.35	3.63±0.12	1.00±0.03	2.03±0.04	0.46±0.02
D-2	34	17.01±0.16	0.13±0.03	1.48±0.04	3.79±0.03	67.63±0.35	3.59±0.12	0.93±0.03	2.14±0.04	0.46±0.02
D-2	35	17.37±0.17	0.12±0.03	1.12±0.03	3.79±0.03	68.14±0.35	3.50±0.12	0.98±0.03	2.03±0.04	0.47±0.02
D-2	36	17.62±0.17	0.13±0.03	1.26±0.03	3.75±0.03	66.99±0.35	3.84±0.12	0.96±0.03	2.01±0.04	0.48±0.02
D-2	37	17.67±0.17	0.18±0.03	1.35±0.03	3.81±0.03	67.30±0.35	3.68±0.12	0.94±0.03	1.99±0.04	0.48±0.02
D-2	38	17.63±0.16	0.14±0.03	1.39±0.03	3.85±0.03	67.75±0.34	3.68±0.12	0.94±0.03	2.01±0.04	0.45±0.02
D-2	39	17.68±0.16	0.13±0.02	1.39±0.03	3.81±0.03	66.99±0.33	3.77±0.12	0.96±0.03	1.98±0.04	0.46±0.02
D-2	40	17.70±0.16	0.10±0.03	1.32±0.03	3.84±0.03	67.23±0.34	3.73±0.12	1.00±0.03	2.01±0.04	0.48±0.02
D-2	41	17.80±0.16	0.14±0.03	1.50±0.03	3.82±0.03	66.45±0.33	3.88±0.12	0.97±0.03	2.04±0.04	0.48±0.02
D-2	42	17.68±0.16	0.13±0.03	1.09±0.03	3.85±0.03	66.46±0.33	3.56±0.11	0.92±0.03	1.92±0.04	0.49±0.02
D-2	43	17.54±0.16	0.14±0.03	1.20±0.03	3.84±0.03	67.39±0.34	3.57±0.11	0.94±0.03	1.91±0.04	0.48±0.02
D-2	44	17.27±0.16	0.14±0.03	1.36±0.03	3.93±0.03	67.27±0.34	3.61±0.11	0.91±0.03	1.87±0.04	0.49±0.02
D-2	45	17.02±0.16	0.12±0.03	1.01±0.03	3.91±0.03	67.76±0.34	3.56±0.11	0.91±0.03	1.87±0.04	0.47±0.02
D-2	46	16.98±0.16	0.18±0.03	1.22±0.03	3.97±0.03	68.03±0.34	3.62±0.11	0.87±0.03	1.73±0.03	0.44±0.02
D-2	47	16.86±0.16	0.12±0.03	1.52±0.04	4.03±0.03	68.97±0.34	3.65±0.12	0.88±0.03	1.79±0.04	0.41±0.02
D-2	48	16.92±0.16	0.11±0.02	1.03±0.03	3.96±0.03	68.75±0.34	3.64±0.12	0.88±0.03	1.73±0.03	0.46±0.02
D-2	49	16.90±0.16	0.14±0.03	1.27±0.03	3.98±0.03	68.11±0.34	3.42±0.11	0.87±0.03	1.70±0.03	0.44±0.02
D-2	50	16.70±0.16	0.11±0.03	1.56±0.04	4.06±0.03	68.07±0.34	3.42±0.11	0.83±0.03	1.68±0.03	0.47±0.02
D-2	51	16.82±0.16	0.12±0.03	1.18±0.03	4.06±0.03	68.89±0.34	3.61±0.12	0.89±0.03	1.73±0.03	0.45±0.02
D-2	52	16.92±0.16	0.14±0.03	1.27±0.03	4.19±0.03	69.03±0.35	3.52±0.11	0.86±0.03	1.66±0.03	0.47±0.02
D-2	53	16.30±0.16	0.11±0.03	1.52±0.04	4.19±0.03	68.71±0.34	3.45±0.11	0.85±0.03	1.64±0.03	0.44±0.02
D-2	54	16.50±0.16	0.17±0.03	1.26±0.03	4.21±0.03	69.4±0.35	3.46±0.12	0.83±0.03	1.58±0.03	0.44±0.02
D-2	55	16.42±0.16	0.14±0.03	1.01±0.03	4.17±0.03	69.27±0.35	3.27±0.11	0.75±0.03	1.71±0.04	0.47±0.02
D-2	56	16.10±0.16	0.11±0.03	1.20±0.03	4.22±0.03	68.81±0.34	3.35±0.11	0.83±0.03	1.55±0.03	0.41±0.02
D-2	57	15.80±0.16	0.11±0.03	1.39±0.03	4.33±0.03	69.63±0.35	3.32±0.11	0.79±0.03	1.58±0.03	0.39±0.02
D-2	58	15.39±0.15	0.15±0.03	0.86±0.03	4.35±0.03	70.50±0.35	3.17±0.11	0.73±0.03	1.44±0.03	0.42±0.02
D-2	59	15.01±0.15	0.09±0.03	1.40±0.03	4.49±0.04	69.95±0.35	3.14±0.11	0.73±0.03	1.55±0.03	0.39±0.02
D-2	60	15.02±0.15	0.12±0.03	1.00±0.03	4.45±0.04	70.41±0.35	3.40±0.11	0.73±0.03	1.62±0.03	0.4±0.02

D-2	61	15.00±0.15	0.15±0.03	1.55±0.04	4.52±0.04	69.30±0.35	3.49±0.12	0.78±0.03	1.90±0.04	0.4±0.02
D-2	62	14.18±0.15	0.18±0.03	1.32±0.03	4.43±0.03	70.46±0.35	3.83±0.12	0.82±0.03	2.08±0.04	0.35±0.02
D-2	63	13.08±0.14	0.15±0.03	1.29±0.03	4.27±0.03	70.44±0.35	4.10±0.12	0.79±0.03	2.21±0.04	0.3±0.02
D-2	64	12.57±0.14	0.09±0.03	1.05±0.03	4.25±0.03	71.14±0.35	4.24±0.13	0.73±0.03	2.19±0.04	0.3±0.02
D-2	65	13.02±0.14	0.09±0.03	1.47±0.04	4.34±0.03	70.54±0.35	3.72±0.12	0.7±0.03	2.21±0.04	0.29±0.02
D-2	66	14.10±0.15	0.08±0.02	1.43±0.03	4.36±0.03	70.40±0.34	3.70±0.12	0.64±0.02	2.19±0.04	0.3±0.02
D-2	67	14.03±0.15	0.17±0.03	1.06±0.03	4.43±0.03	70.42±0.35	3.08±0.11	0.55±0.02	2.09±0.04	0.33±0.02
D-2	68	14.02±0.15	0.12±0.03	1.49±0.04	4.49±0.04	70.95±0.35	3.00±0.11	0.45±0.02	1.82±0.04	0.33±0.02
D-2	69	14.94±0.15	0.11±0.03	1.21±0.03	4.35±0.03	71.16±0.35	3.27±0.11	0.51±0.02	1.74±0.04	0.31±0.02
D-2	70	14.72±0.15	0.16±0.03	1.25±0.03	4.33±0.03	70.70±0.35	3.13±0.11	0.54±0.02	1.79±0.04	0.29±0.02
D-2	71	14.81±0.15	0.12±0.02	1.12±0.03	4.26±0.03	70.24±0.34	3.27±0.11	0.56±0.02	1.74±0.04	0.32±0.02
D-2	72	14.70±0.15	0.09±0.03	1.19±0.03	4.30±0.03	71.09±0.35	3.34±0.11	0.55±0.02	1.76±0.04	0.32±0.02
D-2	73	14.61±0.15	0.12±0.03	0.92±0.03	4.16±0.03	71.47±0.35	3.19±0.11	0.55±0.02	1.70±0.04	0.29±0.02
D-2	74	14.44±0.15	0.06±0.03	1.37±0.03	4.18±0.03	71.90±0.35	3.21±0.11	0.58±0.02	1.73±0.04	0.31±0.02
D-2	75	14.41±0.15	0.13±0.03	1.16±0.03	4.12±0.03	70.99±0.35	3.08±0.11	0.59±0.02	1.76±0.04	0.34±0.02
D-2	76	14.21±0.15	0.14±0.03	1.21±0.03	4.05±0.03	71.18±0.35	3.35±0.11	0.58±0.02	1.77±0.04	0.3±0.02
D-2	77	14.22±0.15	0.15±0.03	1.16±0.03	4.03±0.03	71.23±0.35	3.20±0.11	0.58±0.02	1.83±0.04	0.34±0.02
D-2	78	14.09±0.15	0.13±0.03	1.15±0.03	4.00±0.03	71.38±0.34	3.29±0.11	0.63±0.02	1.82±0.04	0.32±0.02
D-2	79	14.12±0.15	0.14±0.03	1.26±0.03	4.02±0.03	69.21±0.34	3.18±0.11	0.62±0.02	1.82±0.04	0.32±0.02
D-2	80	14.19±0.15	0.15±0.03	1.62±0.04	4.01±0.03	70.86±0.35	3.31±0.11	0.64±0.02	1.84±0.04	0.33±0.02
D-2	81	14.12±0.15	0.15±0.03	1.08±0.03	3.95±0.03	69.18±0.35	3.30±0.11	0.63±0.02	1.83±0.04	0.33±0.02
D-2	82	13.80±0.15	0.11±0.03	1.40±0.03	4.00±0.03	71.39±0.36	3.23±0.11	0.62±0.02	1.86±0.04	0.28±0.02
D-2	83	13.93±0.15	0.12±0.03	1.31±0.03	3.94±0.03	71.44±0.36	3.04±0.11	0.59±0.02	1.82±0.04	0.36±0.02
D-2	84	13.68±0.15	0.12±0.03	1.19±0.03	3.91±0.03	71.62±0.36	2.91±0.11	0.55±0.02	1.78±0.04	0.32±0.02
D-2	85	13.36±0.14	0.09±0.03	1.19±0.03	3.90±0.03	72.04±0.35	3.06±0.11	0.56±0.02	1.80±0.03	0.31±0.02
D-2	86	13.66±0.14	0.13±0.02	1.28±0.03	3.94±0.03	70.77±0.34	3.08±0.11	0.54±0.02	1.80±0.04	0.29±0.02
D-2	87	13.57±0.14	0.14±0.03	1.45±0.03	3.94±0.03	71.08±0.35	3.11±0.11	0.58±0.02	1.88±0.04	0.29±0.02
D-2	88	13.78±0.15	0.12±0.03	1.07±0.03	3.92±0.03	71.28±0.35	3.23±0.11	0.59±0.02	1.82±0.04	0.33±0.02
D-2	89	14.00±0.15	0.15±0.03	1.35±0.03	3.97±0.03	71.69±0.35	3.37±0.11	0.64±0.02	1.88±0.04	0.35±0.02
D-2	90	13.87±0.15	0.08±0.03	1.44±0.03	3.83±0.03	71.74±0.35	3.05±0.11	0.56±0.02	1.86±0.04	0.26±0.02
D-2	91	13.89±0.15	0.13±0.03	1.07±0.03	3.92±0.03	68.88±0.34	3.05±0.11	0.59±0.02	1.88±0.04	0.29±0.02
D-2	92	13.58±0.15	0.03±0.03	1.50±0.03	3.90±0.03	71.70±0.35	3.43±0.11	0.59±0.02	1.87±0.04	0.31±0.02
D-2	93	13.94±0.15	0.19±0.03	1.36±0.03	3.89±0.03	71.33±0.35	3.22±0.11	0.62±0.02	1.88±0.04	0.3±0.02
D-2	94	13.69±0.15	0.12±0.03	1.45±0.03	3.92±0.03	71.84±0.35	3.30±0.11	0.6±0.02	1.91±0.04	0.3±0.02
D-2	95	14.06±0.15	0.07±0.03	1.19±0.03	3.95±0.03	71.83±0.35	3.63±0.12	0.59±0.02	1.98±0.04	0.29±0.02
D-2	96	13.75±0.15	0.10±0.03	1.23±0.03	3.95±0.03	70.92±0.35	3.57±0.11	0.64±0.02	1.90±0.04	0.28±0.02
D-2	97	13.50±0.14	0.15±0.03	1.45±0.03	3.92±0.03	71.88±0.35	3.51±0.11	0.6±0.02	1.89±0.04	0.3±0.02
D-2	98	13.56±0.15	0.08±0.03	1.08±0.03	3.97±0.03	72.32±0.35	3.28±0.11	0.55±0.02	1.80±0.04	0.31±0.02
D-2	99	13.29±0.14	0.13±0.03	1.25±0.03	4.01±0.03	72.55±0.35	3.19±0.11	0.56±0.02	1.85±0.04	0.27±0.02
D-2	100	15.76±0.15	0.16±0.03	2.22±0.04	3.85±0.03	69.39±0.35	3.63±0.12	0.78±0.03	1.29±0.03	0.37±0.02
D-2	101	15.65±0.15	0.18±0.03	0.93±0.03	3.82±0.03	70.44±0.35	3.40±0.11	0.72±0.03	1.31±0.03	0.36±0.02
D-2	102	15.92±0.16	0.14±0.03	0.98±0.03	3.81±0.03	70.58±0.35	3.53±0.11	0.69±0.02	1.28±0.03	0.38±0.02
D-2	103	16.00±0.16	0.14±0.03	0.71±0.03	3.91±0.03	70.43±0.35	3.56±0.11	0.69±0.03	1.24±0.03	0.39±0.02
D-2	104	15.74±0.15	0.13±0.03	0.88±0.03	3.84±0.03	69.78±0.34	3.38±0.11	0.74±0.03	1.20±0.03	0.32±0.02
D-2	105	15.64±0.15	0.09±0.03	0.89±0.03	3.81±0.03	69.89±0.35	3.53±0.11	0.7±0.03	1.25±0.03	0.35±0.02
D-2	106	15.66±0.16	0.11±0.03	0.98±0.03	3.90±0.03	70.40±0.35	3.42±0.11	0.7±0.03	1.21±0.03	0.35±0.02
D-2	107	15.91±0.16	0.12±0.03	0.77±0.03	3.87±0.03	70.56±0.35	3.41±0.11	0.74±0.03	1.30±0.03	0.34±0.02
D-2	108	15.61±0.16	0.15±0.03	0.99±0.03	3.85±0.03	70.05±0.35	3.25±0.11	0.69±0.03	1.33±0.03	0.32±0.02
D-2	109	15.94±0.16	0.12±0.03	0.7±0.03	3.81±0.03	68.33±0.35	3.39±0.12	0.67±0.02	1.28±0.03	0.37±0.02
D-2	110	16.01±0.16	0.14±0.03	0.92±0.03	3.88±0.03	69.9±0.36	3.39±0.12	0.71±0.03	1.34±0.03	0.37±0.02
D-2	111	15.96±0.16	0.15±0.03	1.05±0.03	3.89±0.03	69.49±0.35	3.38±0.11	0.72±0.03	1.37±0.03	0.4±0.02
D-2	112	16.24±0.16	0.17±0.03	0.83±0.03	3.90±0.03	69.16±0.35	3.26±0.11	0.71±0.03	1.41±0.03	0.41±0.02
D-2	113	16.63±0.16	0.12±0.03	1.09±0.03	3.97±0.03	69.65±0.36	3.46±0.12	0.67±0.03	1.48±0.03	0.38±0.02
D-2	114	16.50±0.16	0.13±0.03	0.8±0.03	3.89±0.03	69.13±0.35	3.34±0.11	0.69±0.03	1.55±0.03	0.4±0.02
D-2	115	16.54±0.16	0.10±0.03	1.10±0.03	3.94±0.03	68.76±0.35	3.15±0.11	0.68±0.03	1.55±0.03	0.37±0.02
D-2	116	16.29±0.16	0.18±0.03	1.25±0.03	4.01±0.03	69.57±0.35	3.14±0.11	0.71±0.03	1.61±0.04	0.37±0.02
D-2	117	16.19±0.16	0.09±0.03	0.96±0.03	3.97±0.03	69.81±0.36	3.08±0.11	0.65±0.03	1.60±0.03	0.35±0.02
D-2	118	15.68±0.16	0.15±0.03	1.03±0.03	3.98±0.03	71.14±0.36	3.06±0.11	0.64±0.02	1.54±0.03	0.33±0.02
D-2	119	15.66±0.16	0.15±0.03	0.8±0.03	3.94±0.03	72.09±0.36	2.95±0.11	0.61±0.02	1.58±0.04	0.32±0.02
D-2	120	14.95±0.16	0.14±0.03	1.03±0.03	4.06±0.03	71.84±0.36	2.96±0.11	0.58±0.02	1.54±0.03	0.3±0.02
D-2	121	14.78±0.16	0.13±0.03	0.78±0.03	3.97±0.03	71.79±0.36	2.87±0.11	0.55±0.02	1.56±0.03	0.29±0.02
D-2	122	14.52±0.15	0.13±0.03	0.98±0.03	4.00±0.03	73.07±0.35	2.93±0.10	0.56±0.02	1.62±0.03	0.24±0.02
D-2	123	14.47±0.15	0.06±0.02	1.00±0.03	4.10±0.03	72.08±0.35	2.70±0.10	0.57±0.02	1.61±0.03	0.23±0.02
D-2	124	13.83±0.15	0.06±0.03	1.05±0.03	4.05±0.03	72.26±0.35	2.57±0.10	0.59±0.02	1.84±0.04	0.24±0.02
D-2	125	13.71±0.15	0.07±0.03	0.88±0.03	3.92±0.03	71.91±0.35	3.00±0.11	0.58±0.02	1.78±0.04	0.25±0.02
D-2	126	13.69±0.15	0.07±0.03	1.17±0.03	4.02±0.03	71.74±0.36	2.94±0.11	0.61±0.02	1.86±0.04	0.28±0.02
D-2	127	13.56±0.15	0.13±0.03	1.29±0.03	4.12±0.03	71.50±0.36	2.83±0.11	0.68±0.03	2.04±0.04	0.23±0.02
D-2	128	13.92±0.15	0.11±0.03	1.01±0.03	4.06±0.03	71.69±0.36	3.29±0.11	0.66±0.03	2.14±0.04	0.28±0.02
D-2	129	13.92±0.14	0.10±0.03	1.25±0.03	4.15±0.03	71.08±0.34	3.18±0.11	0.71±0.02	2.19±0.04	0.28±0.02
D-2	130	13.20±0.14	0.11±0.03	1.20±0.03	4.22±0.03	72.31±0.35	2.95±0.11	0.67±0.02	2.03±0.04	0.28±0.02
D-2	131	13.77±0.14	0.15±0.03	1.38±0.03	4.38±0.03	71.54±0.34	2.76±0.10	0.63±0.02	1.98±0.04	0.29±0.02
D-2	132	14.05±0.15	0.16±0.02	1.32±0.03	4.49±0.03	70.39±0.34	2.57±0.10	0.6±0.02	2.29±0.04	0.28±0.02
D-2	133	13.71±0.15	0.15±0.03	0.92±0.03	4.30±0.03	71.76±0.35	2.71±0.10	0.61±0.02	2.28±0.04	0.27±0.02
D-2	134	12.53±0.14	0.12±0.03	1.13±0.03	4.27±0.03	70.28±0.34	3.40±0.11	0.64±0.02	2.24±0.04	0.26±0.02
D-2	135	12.43±0.14	0.11±0.03	0.89±0.03	4.31±0.03	71.80±0.35	3.50±0.11	0.69±0.03	2.47±0.04	0.23±0.02
D-2	136	14.15±0.15	0.18±0.03	1.56±0.03	4.62±0.03	68.68±0.34	3.57±0.11	0.78±0.03	2.58±0.04	0.32±0.02
D-2	137	14.19±0.14	0.11±0.02	1.62±0.03	4.75±0.03	69.92±0.34	3.37±0.11	0.68±0.02	2.29±0.04	0.34±0.02
D-2	138	15.10±0.15	0.10±0.03	0.95±0.03	4.56±0.03	70.80±0.34	2.70±0.10	0.58±0.02	1.72±0.03	0.31±0.02
D-2	139	14.83±0.15	0.16±0.02	1.15±0.03	4.57±0.03	70.99±0.34	2.92±0.10	0.56±0.02	1.69±0.03	0.32±0.02
D-2	140	14.81±0.15	0.13±0.02	1.17±0.03	4.57±0.03	70.32±0.34	3.17±0.11	0.62±0.02	1.66±0.03	0.34±0.02
D-2	141	14.89±0.15	0.10±0.03	1.10±0.03	4.48±0.04	70.58±0.35	3.03±0.11	0.66±0.02	1.68±0.04	0.33±0.02
D-2	142	15.36±0.14	0.07±0.02	0.78±0.02	4.27±0.03	70.52±0.32	2.77±0.09	0.61±0.02	1.67±0.03	0.34±0.02
D-2	143	15.67±0.15	0.11±0.03	1.07±0.03	4.31±0.03	71.50±0.33	2.99±0.10	0.67±0.02	1.81±0.03	0.37±0.02
D-2	144	15.23±0.15	0.13±0.03	1.07±0.03	4.26±0.03	70.12±0.34	3.09±0.10	0.63±0.02	1.79±0.03	0.33±0.02
D-2	145	15.53±0.15	0.16±0.03	0.93±0.03	4.14±0.03	69.88±0.34	2.94±0.10	0.6±0.02	1.81±0.03	0.34±0.02

D-2	146	15.04±0.15	0.08±0.02	1.06±0.03	4.21±0.03	70.48±0.34	2.86±0.10	0.62±0.02	1.90±0.04	0.34±0.02
D-2	147	15.11±0.15	0.11±0.03	0.86±0.03	4.14±0.03	71.41±0.34	2.96±0.10	0.63±0.02	1.70±0.03	0.31±0.02
D-2	148	14.56±0.14	0.11±0.02	1.03±0.03	4.16±0.03	71.01±0.33	2.82±0.10	0.56±0.02	1.76±0.03	0.33±0.02
D-2	149	15.21±0.15	0.12±0.02	0.82±0.03	4.07±0.03	70.89±0.33	2.71±0.10	0.58±0.02	1.82±0.03	0.3±0.02
D-2	150	15.39±0.15	0.09±0.02	0.93±0.03	3.95±0.03	70.51±0.33	2.95±0.10	0.58±0.02	1.84±0.03	0.32±0.02
D-2	151	15.34±0.15	0.10±0.02	1.26±0.03	4.14±0.03	70.52±0.33	2.93±0.10	0.63±0.02	1.87±0.03	0.31±0.02
D-2	152	15.91±0.15	0.10±0.02	0.99±0.03	4.00±0.03	69.18±0.33	2.93±0.10	0.63±0.02	2.02±0.04	0.32±0.02
D-2	153	16.12±0.15	0.11±0.02	0.97±0.03	4.00±0.03	68.81±0.33	3.17±0.10	0.62±0.02	2.00±0.04	0.32±0.02
D-2	154	16.21±0.15	0.12±0.02	1.07±0.03	3.95±0.03	68.92±0.33	3.09±0.10	0.64±0.02	2.06±0.04	0.35±0.02
D-2	155	16.42±0.16	0.14±0.03	0.92±0.03	3.87±0.03	69.66±0.35	3.15±0.11	0.64±0.02	2.24±0.04	0.36±0.02
D-2	156	15.87±0.15	0.11±0.03	0.98±0.03	3.99±0.03	69.91±0.34	3.14±0.11	0.65±0.02	1.95±0.04	0.35±0.02
D-2	157	15.75±0.15	0.11±0.02	1.00±0.03	3.94±0.03	69.66±0.33	3.03±0.10	0.65±0.02	2.01±0.04	0.39±0.02
D-2	158	15.66±0.15	0.12±0.02	1.10±0.03	3.92±0.03	70.23±0.34	3.13±0.10	0.61±0.02	1.93±0.04	0.39±0.02
D-2	159	15.21±0.15	0.07±0.02	1.08±0.03	3.96±0.03	70.53±0.34	2.91±0.10	0.64±0.02	1.95±0.04	0.33±0.02
D-2	160	15.21±0.15	0.07±0.03	1.04±0.03	4.00±0.03	70.54±0.34	2.96±0.10	0.61±0.02	1.95±0.04	0.32±0.02
D-2	161	15.39±0.15	0.11±0.03	0.78±0.03	3.85±0.03	71.14±0.33	3.00±0.10	0.61±0.02	1.94±0.04	0.31±0.02
D-2	162	14.90±0.15	0.12±0.02	1.12±0.03	4.02±0.03	70.70±0.33	3.08±0.10	0.6±0.02	1.86±0.04	0.33±0.02
E-1	1	14.23±0.07	0.10±0.02	2.66±0.04	4.86±0.04	71.53±0.34	2.31±0.09	0.54±0.02	1.11±0.02	0.3±0.02
E-1	2	14.09±0.07	0.09±0.01	1.71±0.03	4.95±0.03	72.09±0.35	2.28±0.08	0.56±0.01	1.15±0.02	0.31±0.01
E-1	3	13.91±0.07	0.05±0.01	1.63±0.03	5.02±0.04	71.95±0.35	2.39±0.09	0.53±0.01	1.12±0.02	0.33±0.01
E-1	4	14.47±0.07	0.10±0.01	1.88±0.03	5.11±0.04	71.38±0.34	2.29±0.08	0.53±0.01	1.13±0.02	0.32±0.01
E-1	5	14.42±0.07	0.08±0.01	2.08±0.03	5.18±0.04	71.83±0.34	2.21±0.08	0.51±0.01	1.12±0.02	0.32±0.01
E-1	6	14.65±0.07	0.10±0.01	2.04±0.03	5.26±0.04	71.34±0.34	2.28±0.08	0.53±0.01	1.16±0.02	0.33±0.01
E-1	7	14.37±0.07	0.07±0.01	2.00±0.03	5.31±0.04	71.82±0.34	2.33±0.08	0.55±0.01	1.18±0.02	0.33±0.01
E-1	8	14.39±0.07	0.08±0.01	1.89±0.03	5.35±0.04	71.19±0.34	2.35±0.08	0.56±0.01	1.18±0.02	0.33±0.01
E-1	9	14.12±0.07	0.07±0.01	2.27±0.04	5.45±0.04	71.10±0.34	2.28±0.08	0.53±0.01	1.17±0.02	0.3±0.01
E-1	10	14.12±0.07	0.08±0.01	2.46±0.04	5.52±0.04	71.86±0.34	2.24±0.08	0.55±0.01	1.15±0.02	0.34±0.01
E-1	11	14.05±0.07	0.05±0.01	2.73±0.04	5.63±0.04	70.73±0.34	2.15±0.08	0.54±0.01	1.19±0.02	0.32±0.01
E-1	12	13.78±0.07	0.08±0.01	2.42±0.04	5.66±0.04	70.7±0.34	2.31±0.08	0.53±0.01	1.18±0.02	0.3±0.01
E-1	13	13.42±0.07	0.11±0.01	2.47±0.04	5.68±0.04	70.97±0.34	2.39±0.09	0.55±0.01	1.19±0.02	0.31±0.01
E-1	14	13.50±0.07	0.06±0.01	2.29±0.04	5.71±0.04	71.66±0.34	2.43±0.09	0.54±0.01	1.22±0.02	0.3±0.01
E-1	15	13.45±0.07	0.06±0.01	2.93±0.04	5.76±0.04	70.68±0.34	2.55±0.09	0.59±0.01	1.32±0.02	0.29±0.01
E-1	16	13.45±0.07	0.09±0.01	3.21±0.04	5.72±0.04	69.43±0.34	2.41±0.09	0.6±0.01	1.54±0.02	0.31±0.01
E-1	17	13.08±0.07	0.12±0.01	3.37±0.04	5.78±0.04	68.97±0.34	2.91±0.09	0.71±0.01	1.88±0.02	0.3±0.01
E-1	18	12.12±0.07	0.12±0.01	3.61±0.05	5.57±0.04	69.06±0.34	3.41±0.10	0.77±0.02	2.29±0.02	0.26±0.01
E-1	19	10.61±0.06	0.18±0.01	2.51±0.04	5.31±0.04	70.75±0.34	3.85±0.11	0.79±0.02	2.37±0.02	0.28±0.01
E-1	20	9.00±0.06	0.13±0.01	2.30±0.04	5.10±0.04	74.77±0.34	3.16±0.10	0.56±0.01	1.68±0.02	0.21±0.01
E-1	21	9.40±0.06	0.09±0.01	2.19±0.03	5.17±0.04	76.39±0.35	2.28±0.08	0.31±0.01	1.12±0.02	0.22±0.01
E-1	22	10.06±0.06	0.08±0.01	2.06±0.03	5.12±0.04	75.48±0.35	2.37±0.09	0.28±0.01	0.92±0.01	0.23±0.01
E-1	23	11.17±0.06	0.09±0.01	2.03±0.03	5.20±0.04	75.39±0.35	2.34±0.08	0.26±0.01	0.86±0.01	0.23±0.01
E-1	24	11.37±0.06	0.11±0.01	2.00±0.03	5.18±0.04	74.35±0.35	2.31±0.08	0.31±0.01	0.81±0.01	0.2±0.01
E-1	25	11.92±0.06	0.11±0.01	1.79±0.03	5.06±0.04	74.35±0.35	2.72±0.09	0.33±0.01	0.81±0.01	0.23±0.01
E-1	26	11.91±0.06	0.08±0.01	1.72±0.03	5.03±0.04	74.49±0.35	2.59±0.09	0.36±0.01	0.81±0.01	0.26±0.01
E-1	27	12.04±0.07	0.04±0.01	1.51±0.03	4.92±0.03	74.39±0.35	2.51±0.09	0.42±0.01	0.79±0.01	0.28±0.01
E-1	28	12.16±0.07	0.10±0.01	1.58±0.03	4.85±0.03	74.05±0.35	2.69±0.09	0.44±0.01	0.81±0.01	0.29±0.01
E-1	29	12.76±0.07	0.11±0.01	1.55±0.03	4.75±0.03	73.38±0.34	2.90±0.09	0.51±0.01	0.87±0.01	0.31±0.01
E-1	30	13.54±0.07	0.08±0.01	1.66±0.03	4.75±0.03	72.42±0.35	2.97±0.10	0.54±0.01	0.94±0.01	0.34±0.01
E-1	31	13.98±0.07	0.09±0.01	1.55±0.03	4.66±0.03	72.95±0.34	2.83±0.09	0.58±0.01	1.00±0.02	0.4±0.01
E-1	32	13.66±0.07	0.12±0.01	1.71±0.03	4.67±0.03	71.76±0.34	2.77±0.09	0.56±0.01	1.00±0.02	0.37±0.01
E-1	33	13.89±0.07	0.12±0.01	1.52±0.03	4.60±0.03	71.78±0.34	2.70±0.09	0.62±0.01	0.98±0.01	0.33±0.01
E-1	34	14.01±0.07	0.06±0.01	1.51±0.03	4.55±0.03	71.74±0.34	2.67±0.09	0.58±0.01	1.00±0.02	0.34±0.01
E-1	35	14.11±0.07	0.11±0.01	1.32±0.03	4.51±0.03	72.34±0.35	2.77±0.09	0.58±0.01	1.04±0.02	0.34±0.01
E-1	36	14.27±0.07	0.10±0.01	1.65±0.03	4.54±0.03	72.80±0.35	3.00±0.10	0.63±0.01	1.04±0.02	0.33±0.01
E-1	37	14.24±0.07	0.08±0.01	1.78±0.03	4.42±0.03	72.29±0.35	2.63±0.09	0.66±0.01	1.08±0.02	0.33±0.01
E-2	1	14.54±0.07	0.10±0.01	2.56±0.04	4.10±0.03	72.80±0.35	2.61±0.09	0.57±0.01	1.34±0.02	0.31±0.01
E-2	2	14.55±0.07	0.06±0.01	1.70±0.03	4.12±0.03	72.19±0.35	2.75±0.09	0.56±0.01	1.30±0.02	0.32±0.01
E-2	3	14.46±0.07	0.08±0.01	2.06±0.03	4.29±0.03	73.50±0.35	2.65±0.09	0.53±0.01	1.30±0.02	0.29±0.01
E-2	4	14.29±0.07	0.07±0.01	1.80±0.03	4.34±0.03	73.07±0.34	2.63±0.09	0.53±0.01	1.25±0.02	0.28±0.01
E-2	5	13.99±0.07	0.06±0.01	1.96±0.03	4.42±0.03	72.96±0.34	2.68±0.09	0.52±0.01	1.34±0.02	0.3±0.01
E-2	6	13.82±0.07	0.07±0.01	1.93±0.03	4.50±0.03	72.49±0.35	2.54±0.09	0.5±0.01	1.42±0.02	0.3±0.01
E-2	7	13.51±0.07	0.08±0.01	1.90±0.03	4.49±0.03	73.15±0.34	2.55±0.09	0.57±0.01	1.42±0.02	0.29±0.01
E-2	8	12.59±0.07	0.06±0.01	2.05±0.03	4.47±0.03	74.11±0.35	2.73±0.09	0.55±0.01	1.43±0.02	0.28±0.01
E-2	9	12.53±0.07	0.08±0.01	1.92±0.03	4.55±0.03	73.50±0.35	2.88±0.09	0.61±0.01	1.50±0.02	0.3±0.01
E-2	10	13.19±0.07	0.08±0.01	2.27±0.04	4.68±0.03	71.81±0.34	3.00±0.10	0.63±0.01	1.58±0.02	0.29±0.01
E-2	11	13.82±0.07	0.10±0.01	2.23±0.04	4.77±0.03	71.72±0.34	2.60±0.09	0.58±0.01	1.64±0.02	0.3±0.01
E-2	12	13.94±0.07	0.08±0.01	2.77±0.04	4.84±0.03	71.29±0.34	2.33±0.08	0.58±0.01	1.60±0.02	0.31±0.01
E-2	13	13.96±0.07	0.05±0.01	2.34±0.04	4.98±0.03	71.71±0.34	2.46±0.09	0.54±0.01	1.56±0.02	0.32±0.01
E-2	14	13.91±0.07	0.10±0.02	2.50±0.04	5.01±0.04	71.22±0.34	2.35±0.09	0.56±0.02	1.57±0.02	0.32±0.02
E-2	15	14.09±0.07	0.10±0.01	2.41±0.04	5.05±0.04	70.79±0.34	2.24±0.08	0.57±0.01	1.66±0.02	0.31±0.01
E-2	16	13.99±0.07	0.09±0.01	2.73±0.04	5.07±0.03	71.18±0.34	2.46±0.09	0.58±0.01	1.75±0.02	0.32±0.01
E-2	17	13.54±0.07	0.12±0.01	3.02±0.04	5.02±0.04	70.62±0.34	2.31±0.08	0.64±0.01	1.96±0.02	0.32±0.01
E-2	18	13.27±0.07	0.12±0.01	2.81±0.04	4.91±0.03	70.79±0.34	2.58±0.09	0.65±0.01	2.27±0.02	0.32±0.01
E-2	19	12.63±0.07	0.16±0.01	2.47±0.04	4.73±0.03	70.33±0.34	3.08±0.10	0.74±0.02	2.61±0.03	0.3±0.01
E-2	20	12.23±0.07	0.15±0.01	2.97±0.04	4.65±0.03	69.87±0.34	3.68±0.11	0.87±0.02	3.07±0.03	0.3±0.01
E-2	21	11.89±0.07	0.17±0.01	2.48±0.04	4.48±0.03	69.00±0.34	3.71±0.11	0.93±0.02	3.11±0.03	0.29±0.01
E-2	22	11.39±0.06	0.16±0.01	2.66±0.04	4.48±0.03	70.43±0.34	3.62±0.11	0.84±0.02	2.97±0.03	0.27±0.01
E-2	23	11.85±0.07	0.14±0.01	2.24±0.04	4.58±0.03	71.77±0.34	3.10±0.10	0.66±0.01	2.58±0.03	0.25±0.01
E-2	24	12.51±0.07	0.15±0.01	2.65±0.04	4.73±0.03	71.93±0.35	2.45±0.09	0.49±0.01	2.09±0.02	0.24±0.01
E-2	25	12.47±0.07	0.08±0.01	2.29±0.04	4.68±0.03	72.89±0.34	2.19±0.08	0.45±0.01	1.85±0.02	0.25±0.01
E-2	26	12.37±0.07	0.11±0.01	2.16±0.03	4.64±0.03	73.93±0.35	2.12±0.08	0.44±0.01	1.70±0.02	0.23±0.01
E-2	27	12.75±0.07	0.08±0.01	2.30±0.04	4.49±0.03	73.20±0.34	2.24±0.08	0.48±0.01	1.66±0.02	0.24±0.01
E-2	28	12.71±0.07	0.11±0.01	1.77±0.03	4.41±0.03	74.55±0.35	2.23±0.08	0.44±0.01	1.66±0.02	0.24±0.01
E-2	29	12.61±0.07	0.10±0.01	1.97±0.03	4.34±0.03	73.75±0.35	2.31±0.08	0.44±0.01	1.73±0.02	0.23±0.01
E-2	30	12.83±0.07	0.11±0.01	1.65±0.03	4.21±0.03	73.99±0.35	2.35±0.08	0.46±0.01	1.71±0.02	0.26±0.01
E-2	31	13.05±0.07	0.11±0.01	1.54±0.03	4.10±0.03	73.52±0.35	2.40±0.09	0.43±0.01	1.86±0.02	0.25±0.01

E-2	32	13.08±0.07	0.11±0.01	1.72±0.03	4.00±0.03	74.05±0.35	2.36±0.08	0.46±0.01	1.92±0.02	0.25±0.01
E-2	33	12.59±0.07	0.14±0.01	1.57±0.03	3.89±0.03	74.60±0.35	2.30±0.08	0.44±0.01	1.95±0.02	0.27±0.01
E-2	34	12.88±0.07	0.13±0.01	1.74±0.03	3.82±0.03	74.04±0.35	2.41±0.09	0.47±0.01	2.01±0.02	0.24±0.01
E-2	35	12.98±0.07	0.12±0.01	1.67±0.03	3.73±0.03	73.92±0.35	2.35±0.08	0.49±0.01	2.07±0.02	0.26±0.01
E-2	36	12.79±0.07	0.10±0.01	1.76±0.03	3.69±0.03	73.75±0.35	2.54±0.09	0.48±0.01	2.12±0.02	0.25±0.01
E-2	37	12.93±0.07	0.11±0.01	1.47±0.03	3.60±0.03	74.33±0.35	2.28±0.08	0.48±0.01	2.17±0.02	0.23±0.01
E-2	38	12.93±0.07	0.12±0.01	1.29±0.03	3.57±0.03	74.28±0.35	2.49±0.09	0.46±0.01	2.15±0.02	0.25±0.01
E-2	39	12.65±0.07	0.09±0.01	1.66±0.03	3.58±0.03	74.93±0.35	2.35±0.08	0.49±0.01	2.25±0.02	0.25±0.01
E-2	40	12.86±0.07	0.12±0.01	1.45±0.03	3.47±0.03	75.34±0.35	2.27±0.08	0.48±0.01	2.23±0.02	0.29±0.01

Appendix C

NanoSIMS Dataset

Table C.1: Isotope ratios from interface traverse across Sample A1 as determined from NanoSIMS ion image, with 1σ uncertainties

Distance (μm)	$^{44}Ca/^{30}Si$	1σ	$^{56}Fe/^{30}Si$	1σ	$^{235}U/^{30}Si$	1σ	$^{235}U/^{238}U$	1σ
0.00	0.0899	0.0001	1.8267	0.0005	0.000212	0.000003	8.80	0.27
0.71	0.0947	0.0001	1.8676	0.0005	0.000215	0.000003	8.48	0.28
1.42	0.0959	0.0001	1.8565	0.0005	0.000199	0.000003	9.25	0.33
2.14	0.0951	0.0001	1.8774	0.0005	0.000198	0.000003	8.96	0.32
2.85	0.0952	0.0001	1.9616	0.0006	0.000188	0.000003	7.84	0.28
3.56	0.0961	0.0001	2.0816	0.0006	0.000206	0.000003	8.04	0.27
4.27	0.1023	0.0001	2.3120	0.0007	0.000206	0.000003	8.50	0.30
4.99	0.1043	0.0001	2.6335	0.0007	0.000158	0.000003	7.64	0.30
5.70	0.0994	0.0001	2.8486	0.0008	0.000121	0.000003	8.60	0.40
6.41	0.0953	0.0001	2.7419	0.0008	0.000129	0.000003	7.13	0.30
7.12	0.0900	0.0001	2.4656	0.0007	0.000196	0.000003	9.51	0.36
7.84	0.0869	0.0001	2.1681	0.0006	0.000198	0.000003	9.16	0.34
8.55	0.0938	0.0001	2.0243	0.0006	0.000215	0.000004	8.82	0.32
9.26	0.0939	0.0001	1.8646	0.0005	0.000220	0.000004	9.58	0.34

Table C.2: Isotope ratios from interface traverse across Sample B1 as determined from NanoSIMS ion image, with 1σ uncertainties

Distance (μm)	$^{44}Ca/^{30}Si$	1σ	$^{54}Fe/^{30}Si$	1σ	$^{235}U/^{30}Si$	1σ	$^{235}U/^{238}U$	1σ	U Conc*	1σ
0	0.1375	0.0001	0.0765	0.0001	0.000067	0.000002	6.73	0.64	11	7
0.59	0.1360	0.0001	0.0731	0.0001	0.000058	0.000002	3.87	0.33	11	6
1.18	0.1354	0.0001	0.0708	0.0001	0.000054	0.000002	3.7	0.31	10	6
1.77	0.1355	0.0001	0.0692	0.0001	0.000054	0.000002	3.39	0.28	10	6
2.36	0.1367	0.0001	0.0683	0.0001	0.000057	0.000002	7.44	0.81	9	6
2.95	0.1390	0.0001	0.0669	0.0001	0.000045	0.000002	4.74	0.5	8	5
3.54	0.1410	0.0001	0.0656	0.0001	0.000062	0.000002	5.29	0.48	11	6
4.13	0.1459	0.0001	0.0644	0.0001	0.000056	0.000002	7.1	0.8	9	5
4.72	0.1512	0.0001	0.0645	0.0001	0.000049	0.000002	4.51	0.43	9	5
5.31	0.1567	0.0001	0.0645	0.0001	0.000045	0.000002	3.6	0.34	8	5
5.89	0.1631	0.0001	0.0648	0.0001	0.000049	0.000002	4.37	0.42	9	5
6.48	0.1716	0.0001	0.0657	0.0001	0.000055	0.000002	7.4	0.88	9	5
7.07	0.1821	0.0001	0.0689	0.0001	0.000046	0.000002	4.34	0.44	8	5
7.66	0.1957	0.0001	0.0736	0.0001	0.000057	0.000002	4.53	0.44	10	6
8.25	0.2165	0.0002	0.0805	0.0001	0.000072	0.000003	5.27	0.49	13	7
8.84	0.2402	0.0002	0.0923	0.0001	0.000091	0.000003	4.36	0.34	16	10
9.43	0.2660	0.0002	0.1077	0.0001	0.000172	0.000004	4.25	0.23	31	18
10.02	0.2668	0.0002	0.1168	0.0001	0.000202	0.000005	5.23	0.3	35	21
10.61	0.2061	0.0002	0.1101	0.0001	0.000128	0.000004	4.68	0.31	23	13
11.2	0.1358	0.0001	0.0928	0.0001	0.000072	0.000003	3.86	0.3	13	8
11.79	0.1012	0.0001	0.0771	0.0001	0.000052	0.000002	5.89	0.61	9	5
12.38	0.0900	0.0001	0.0680	0.0001	0.000050	0.000002	4.22	0.4	9	5
12.97	0.0889	0.0001	0.0641	0.0001	0.000059	0.000002	8.16	0.91	10	6
13.56	0.0909	0.0001	0.0624	0.0001	0.000055	0.000002	5.62	0.57	9	6
14.15	0.0941	0.0001	0.0611	0.0001	0.000083	0.000003	6.17	0.53	14	8
14.74	0.0979	0.0001	0.0611	0.0001	0.000089	0.000003	5.58	0.43	15	9
15.33	0.1028	0.0001	0.0622	0.0001	0.000089	0.000003	6.42	0.53	15	9
15.92	0.1058	0.0001	0.0620	0.0001	0.000099	0.000003	5.96	0.47	17	10
16.51	0.1079	0.0001	0.0618	0.0001	0.000099	0.000003	7.24	0.63	16	10
17.09	0.1095	0.0001	0.0626	0.0001	0.000092	0.000003	5.54	0.44	16	9
17.68	0.1097	0.0001	0.0628	0.0001	0.000092	0.000003	5.3	0.4	16	9
18.27	0.1091	0.0001	0.0626	0.0001	0.000098	0.000003	6.16	0.5	17	10
18.86	0.1088	0.0001	0.0631	0.0001	0.000101	0.000003	6.88	0.58	17	10

* U concentration is in ppm.

Table C.3: Isotope ratios from interface traverse across Sample B2 as determined from NanoSIMS ion image, with 1σ uncertainties

Distance (μm)	$^{44}Ca/^{30}Si$	1σ	$^{54}Fe/^{30}Si$	1σ	$^{235}U/^{30}Si$	1σ	$^{235}U/^{238}U$	1σ	U Conc*	1σ
0	0.1165	0.0001	0.083	0.0001	0.000175	0.000002	6.16	0.21	30	18
0.77	0.1135	0.0001	0.0813	0.0001	0.000167	0.000002	5.93	0.21	29	17
1.54	0.1113	0.0001	0.0793	0.0001	0.000178	0.000002	6.03	0.21	31	18
2.32	0.1096	0.0001	0.0776	0.0001	0.00019	0.000002	6.47	0.23	33	19
3.09	0.1102	0.0001	0.076	0.0001	0.000171	0.000002	6.07	0.22	30	17
3.86	0.1124	0.0001	0.0744	0.0001	0.000175	0.000002	6.48	0.23	30	17
4.63	0.1156	0.0001	0.0735	0.0001	0.000146	0.000002	6.22	0.25	25	15
5.4	0.1214	0.0001	0.0749	0.0001	0.000132	0.000002	6.21	0.26	23	13
6.17	0.1307	0.0001	0.0806	0.0001	0.000099	0.000002	5.12	0.23	18	10
6.95	0.1462	0.0001	0.0865	0.0001	0.000069	0.000002	4.08	0.2	13	7
7.72	0.1604	0.0001	0.0891	0.0001	0.000053	0.000001	4.77	0.28	10	6
8.49	0.1598	0.0001	0.0861	0.0001	0.000052	0.000001	4.07	0.23	10	6
9.26	0.1519	0.0001	0.0797	0.0001	0.000053	0.000001	3.93	0.22	10	6
10.03	0.1451	0.0001	0.0744	0.0001	0.00005	0.000001	5.16	0.33	9	5
10.81	0.1401	0.0001	0.0716	0.0001	0.000045	0.000001	3.59	0.2	9	5
11.58	0.1369	0.0001	0.0707	0.0001	0.000052	0.000001	4.02	0.22	10	6
12.35	0.1341	0.0001	0.0707	0.0001	0.000051	0.000001	4.64	0.26	9	5
13.12	0.1322	0.0001	0.0718	0.0001	0.000057	0.000001	4.26	0.23	10	6
13.89	0.1289	0.0001	0.072	0.0001	0.000055	0.000001	5.24	0.31	10	6
14.66	0.1272	0.0001	0.0726	0.0001	0.000055	0.000001	4.22	0.22	10	6

* U concentration is in ppm.

Table C.4: Isotope ratios from interface traverse across Sample B3 as determined from NanoSIMS ion image, with 1σ uncertainties

Distance (μm)	$^{44}Ca/^{30}Si$	1σ	$^{54}Fe/^{30}Si$	1σ	$^{235}U/^{30}Si$	1σ	$^{235}U/^{238}U$	1σ	U conc*	1σ
0	0.0751	0.0001	0.0811	0.0001	0.000075	0.000003	3.8	0.33	14	8
0.76	0.0716	0.0001	0.0774	0.0001	0.000076	0.000003	3.11	0.24	15	9
1.52	0.0707	0.0001	0.0746	0.0001	0.000061	0.000002	2.5	0.18	13	7
2.29	0.0729	0.0001	0.0748	0.0001	0.000057	0.000002	2.88	0.22	11	7
3.05	0.0747	0.0001	0.0744	0.0001	0.000043	0.000002	2.87	0.26	9	5
3.81	0.0743	0.0001	0.0735	0.0001	0.000048	0.000002	3.21	0.29	9	5
4.57	0.0751	0.0001	0.0732	0.0001	0.000052	0.000002	2.97	0.26	10	6
5.33	0.0711	0.0001	0.0703	0.0001	0.000048	0.000002	4.12	0.45	9	5
6.1	0.0684	0.0001	0.0686	0.0001	0.000039	0.000002	1.8	0.16	9	5
6.86	0.0711	0.0001	0.0683	0.0001	0.000049	0.000002	2.08	0.16	11	6
7.62	0.0772	0.0001	0.0694	0.0001	0.000075	0.000003	4.07	0.33	14	8
8.38	0.0806	0.0001	0.0691	0.0001	0.000069	0.000003	4.17	0.35	13	7
9.15	0.0791	0.0001	0.0677	0.0001	0.000054	0.000002	2.65	0.21	11	6
9.91	0.0797	0.0001	0.0704	0.0001	0.000044	0.000002	2.95	0.28	9	5
10.67	0.1039	0.0001	0.0831	0.0001	0.000059	0.000003	4.42	0.46	11	6
11.43	0.1122	0.0001	0.0862	0.0001	0.000052	0.000003	4.51	0.51	9	5
12.19	0.114	0.0001	0.078	0.0001	0.000045	0.000002	5.32	0.64	8	5
12.96	0.1109	0.0001	0.068	0.0001	0.000063	0.000002	6.63	0.72	11	6
13.72	0.1134	0.0001	0.0653	0.0001	0.000073	0.000003	5.11	0.46	13	7
14.48	0.1134	0.0001	0.0643	0.0001	0.00005	0.000002	4.62	0.48	9	5
15.24	0.1122	0.0001	0.065	0.0001	0.000066	0.000003	5.31	0.53	11	7
16	0.1106	0.0001	0.0667	0.0001	0.000059	0.000003	4.69	0.5	10	6
16.77	0.109	0.0001	0.0676	0.0001	0.000065	0.000003	5.41	0.58	11	7
17.53	0.1058	0.0001	0.0678	0.0001	0.000068	0.000003	4.61	0.42	12	7
18.29	0.1032	0.0001	0.0673	0.0001	0.000071	0.000003	5.96	0.57	12	7
19.05	0.1044	0.0001	0.0688	0.0001	0.000086	0.000003	4.11	0.3	16	9
19.82	0.1051	0.0001	0.0696	0.0001	0.000094	0.000003	6.8	0.59	16	9
20.58	0.1064	0.0001	0.0716	0.0001	0.000096	0.000003	5.2	0.4	17	10
21.34	0.1089	0.0001	0.0737	0.0001	0.0001	0.000003	4.87	0.37	18	10

* U concentration is in ppm.

Table C.5: Isotope ratios from interface traverse across Sample C1 as determined from NanoSIMS ion image, with 1σ uncertainties

Distance (μm)	$^{44}Ca/^{30}Si$	1σ	$^{54}Fe/^{30}Si$	1σ	$^{235}U/^{30}Si$	1σ	$^{235}U/^{238}U$	1σ	U conc*	1σ
0	0.0989	0.0001	0.1318	0.0001	0.000117	0.000003	6.44	0.35	19	11
0.78	0.0994	0.0001	0.1286	0.0001	0.00014	0.000003	6.88	0.32	23	13
1.56	0.0971	0.0001	0.1236	0.0001	0.000132	0.000003	6.36	0.3	22	13
2.33	0.094	0.0001	0.1186	0.0001	0.000135	0.000003	6.66	0.31	22	13
3.11	0.0914	0.0001	0.115	0.0001	0.000127	0.000003	6.52	0.3	21	12
3.89	0.0891	0.0001	0.1128	0.0001	0.000132	0.000003	5.97	0.26	22	13
4.67	0.0872	0.0001	0.1111	0.0001	0.000132	0.000003	7.49	0.35	21	13
5.45	0.0866	0.0001	0.111	0.0001	0.000136	0.000003	6.14	0.27	23	13
6.22	0.0909	0.0001	0.1183	0.0001	0.000212	0.000004	6.68	0.24	35	20
7	0.1009	0.0001	0.138	0.0001	0.000411	0.000006	7.14	0.19	67	39
7.78	0.1164	0.0001	0.1701	0.0001	0.000811	0.000008	7.73	0.15	132	77
8.56	0.1251	0.0001	0.191	0.0001	0.000943	0.000009	7.25	0.13	154	90
9.34	0.1098	0.0001	0.1688	0.0001	0.000543	0.000007	6.74	0.16	90	52
10.11	0.0997	0.0001	0.1476	0.0001	0.000367	0.000005	6.35	0.18	61	36
10.89	0.0905	0.0001	0.1299	0.0001	0.000303	0.000005	6.81	0.21	50	29
11.67	0.081	0.0001	0.1114	0.0001	0.000227	0.000004	6.58	0.24	38	22
12.45	0.0757	0.0001	0.0983	0.0001	0.00017	0.000004	6.6	0.28	28	16
13.23	0.0736	0.0001	0.0928	0.0001	0.000142	0.000003	5.77	0.26	24	14
14	0.0742	0.0001	0.0918	0.0001	0.000125	0.000003	6.12	0.28	21	12
14.78	0.0759	0.0001	0.0934	0.0001	0.00012	0.000003	5.29	0.23	20	12

* U concentration is in ppm.

Table C.6: Isotope ratios from interface traverse across Sample C2 as determined from NanoSIMS ion image, with 1σ uncertainties

Distance (μm)	$^{44}Ca/^{30}Si$	1σ	$^{54}Fe/^{30}Si$	1σ	$^{235}U/^{30}Si$	1σ	$^{235}U/^{238}U$	1σ	U conc*	1σ
0	0.099	0.0001	0.113	0.0001	0.000127	0.000003	7.14	0.28	23	13
0.65	0.0965	0.0001	0.1118	0.0001	0.000128	0.000002	6.25	0.23	23	14
1.29	0.09	0.0001	0.1096	0.0001	0.000113	0.000002	5.3	0.2	21	12
1.94	0.0814	0.0001	0.1052	0.0001	0.000112	0.000002	6.19	0.24	20	12
2.59	0.0707	0.0001	0.1	0.0001	0.000099	0.000002	6.23	0.27	18	10
3.23	0.0606	0.0001	0.0953	0.0001	0.000103	0.000002	6.59	0.27	19	11
3.88	0.0516	0.0001	0.0911	0.0001	0.00008	0.000002	5.73	0.26	15	9
4.53	0.0462	0.0001	0.0869	0.0001	0.00008	0.000002	8.71	0.49	14	8
5.17	0.0474	0.0001	0.0831	0.0001	0.000071	0.000002	5.62	0.29	13	8
5.82	0.0567	0.0001	0.0856	0.0001	0.000078	0.000002	6.77	0.33	14	8
6.47	0.0768	0.0001	0.1071	0.0001	0.000168	0.000003	7.09	0.24	30	18
7.11	0.1019	0.0001	0.1458	0.0001	0.000313	0.000004	7.42	0.2	56	32
7.76	0.1138	0.0001	0.1762	0.0001	0.000411	0.000005	6.99	0.15	74	43
8.4	0.111	0.0001	0.1868	0.0001	0.000453	0.000005	6.68	0.15	82	48
9.05	0.1034	0.0001	0.1873	0.0001	0.00045	0.000005	6.83	0.14	81	47
9.7	0.0935	0.0001	0.1838	0.0001	0.000408	0.000005	6.45	0.15	74	43
10.34	0.0858	0.0001	0.1812	0.0001	0.000369	0.000004	6.9	0.16	66	39
10.99	0.0792	0.0001	0.1791	0.0001	0.000351	0.000004	6.63	0.16	63	37
11.64	0.075	0.0001	0.1791	0.0001	0.000338	0.000005	6.98	0.18	60	35
12.28	0.0711	0.0001	0.1791	0.0001	0.000299	0.000004	6.91	0.19	54	31
12.93	0.0672	0.0001	0.1795	0.0001	0.000303	0.000004	7.08	0.19	54	32

* U concentration is in ppm.

Table C.7: Isotope ratios from interface traverse across Sample D1 as determined from NanoSIMS ion image, with 1σ uncertainties

Distance (μm)	$^{44}Ca/^{30}Si$	1σ	$^{54}Fe/^{30}Si$	1σ	$^{235}U/^{30}Si$	1σ	$^{235}U/^{238}U$	1σ
0.00	0.0720	0.0001	0.1080	0.0001	0.000176	0.000003	5.56	0.27
1.20	0.0698	0.0000	0.0995	0.0001	0.000193	0.000002	6.98	0.25
2.41	0.0661	0.0000	0.0922	0.0001	0.000166	0.000002	6.62	0.23
3.61	0.0659	0.0000	0.0906	0.0001	0.000167	0.000002	7.44	0.28
4.81	0.0662	0.0000	0.0907	0.0001	0.000160	0.000002	6.42	0.23
6.01	0.0657	0.0000	0.0900	0.0001	0.000153	0.000002	5.40	0.19
7.22	0.0692	0.0000	0.0971	0.0001	0.000144	0.000002	5.29	0.19
8.42	0.0670	0.0001	0.0962	0.0001	0.000130	0.000002	5.25	0.22
9.62	0.0645	0.0000	0.1028	0.0001	0.000122	0.000002	4.67	0.19
10.82	0.0726	0.0000	0.1166	0.0001	0.000120	0.000002	5.51	0.23
12.03	0.0927	0.0001	0.1143	0.0001	0.000154	0.000002	6.39	0.25
13.23	0.0815	0.0001	0.0988	0.0001	0.000142	0.000002	6.35	0.26
14.43	0.0702	0.0000	0.0932	0.0001	0.000139	0.000002	5.79	0.23
15.63	0.0629	0.0000	0.0935	0.0001	0.000120	0.000002	6.57	0.30
16.84	0.0613	0.0000	0.1021	0.0001	0.000132	0.000002	6.63	0.31
18.04	0.0585	0.0000	0.1044	0.0001	0.000117	0.000002	7.33	0.38
19.24	0.0574	0.0000	0.1085	0.0001	0.000104	0.000002	6.84	0.34
20.45	0.0574	0.0000	0.1153	0.0001	0.000096	0.000002	5.71	0.26
21.65	0.0594	0.0000	0.1191	0.0001	0.000075	0.000001	5.51	0.28
22.85	0.0630	0.0000	0.1219	0.0001	0.000074	0.000001	6.11	0.32
24.05	0.0676	0.0000	0.1275	0.0001	0.000082	0.000002	5.78	0.29

Table C.8: Isotope ratios from interface traverse across Sample D2 as determined from NanoSIMS ion image, with 1σ uncertainties

Distance (μm)	$^{44}Ca/^{30}Si$	1σ	$^{54}Fe/^{30}Si$	1σ	$^{235}U/^{30}Si$	1σ	$^{235}U/^{238}U$	1σ	U conc*	1σ
0	0.0495	0.0001	0.0593	0.0001	0.000075	0.000002	8.61	0.64	12	7
0.86	0.0473	0.0001	0.0563	0.0001	0.000073	0.000002	5.14	0.31	13	7
1.72	0.0466	0.0001	0.0562	0.0001	0.000075	0.000002	6.03	0.38	13	7
2.57	0.0453	0.0001	0.0555	0.0001	0.000065	0.000002	5.15	0.33	11	6
3.43	0.0436	0.0001	0.0546	0.0001	0.000066	0.000002	5.47	0.35	11	7
4.29	0.0419	0.0001	0.0539	0.0001	0.000067	0.000002	5.35	0.34	11	7
5.15	0.0417	0.0001	0.0547	0.0001	0.000078	0.000002	8.02	0.56	13	7
6	0.0408	0.0001	0.0546	0.0001	0.000074	0.000002	5.89	0.37	12	7
6.86	0.0392	0.0001	0.053	0.0001	0.000059	0.000002	8.05	0.65	10	6
7.72	0.0388	0.0001	0.0529	0.0001	0.000072	0.000002	5.77	0.36	12	7
8.58	0.0395	0.0001	0.06	0.0001	0.000084	0.000002	7.87	0.51	14	8
9.43	0.0503	0.0001	0.0788	0.0001	0.000136	0.000002	8.19	0.43	22	13
10.29	0.0664	0.0001	0.0821	0.0001	0.000171	0.000003	10.61	0.59	27	16
11.15	0.0722	0.0001	0.0762	0.0001	0.000149	0.000003	10.64	0.64	23	14
12.01	0.065	0.0001	0.0649	0.0001	0.000079	0.000002	6.53	0.43	13	8
12.87	0.0613	0.0001	0.059	0.0001	0.000068	0.000002	5.65	0.37	11	7
13.72	0.0603	0.0001	0.0588	0.0001	0.000081	0.000002	8.51	0.6	13	8
14.58	0.0604	0.0001	0.0614	0.0001	0.000091	0.000002	8.64	0.58	15	8
15.44	0.0607	0.0001	0.0645	0.0001	0.000081	0.000002	8.82	0.62	13	8
16.3	0.0626	0.0001	0.0687	0.0001	0.000082	0.000002	6.82	0.42	13	8
17.15	0.0639	0.0001	0.0742	0.0001	0.000127	0.000002	7.02	0.35	21	12

* U concentration is in ppm.

Table C.9: Isotope ratios from interface traverse across Sample E1 as determined from NanoSIMS ion image, with 1σ uncertainties

Distance (μm)	$^{44}Ca/^{30}Si$	1σ	$^{54}Fe/^{30}Si$	1σ	$^{235}U/^{30}Si$	1σ	$^{235}U/^{238}U$	1σ	U conc*	1σ
0	0.0624	0.0001	0.0948	0.0001	0.000114	0.000002	8.17	0.5	18	11
0.9	0.068	0.0001	0.0939	0.0001	0.000149	0.000002	6.21	0.23	25	14
1.79	0.0694	0.0001	0.0906	0.0001	0.000162	0.000002	7.18	0.28	26	15
2.69	0.0712	0.0001	0.0896	0.0001	0.000197	0.000002	7.45	0.25	32	19
3.59	0.0755	0.0001	0.0927	0.0001	0.000223	0.000003	7.97	0.27	36	21
4.48	0.079	0.0001	0.093	0.0001	0.000242	0.000003	7.37	0.23	39	23
5.38	0.0822	0.0001	0.0933	0.0001	0.000281	0.000003	7.57	0.21	45	26
6.27	0.0912	0.0001	0.1091	0.0001	0.000287	0.000003	8.27	0.25	46	27
7.17	0.1225	0.0001	0.1405	0.0001	0.000313	0.000003	7.78	0.22	50	29
8.07	0.1542	0.0001	0.1494	0.0001	0.000279	0.000003	8.22	0.27	45	26
8.96	0.1714	0.0001	0.1551	0.0001	0.000272	0.000003	8.91	0.3	43	25
9.86	0.1628	0.0001	0.1465	0.0001	0.000243	0.000003	8.51	0.31	39	23
10.76	0.1499	0.0001	0.1362	0.0001	0.000217	0.000003	7.16	0.25	35	21
11.65	0.1319	0.0001	0.1262	0.0001	0.000194	0.000002	7.94	0.3	31	18
12.55	0.1167	0.0001	0.1169	0.0001	0.000166	0.000002	7.66	0.31	27	16
13.45	0.1072	0.0001	0.1134	0.0001	0.000166	0.000002	8.3	0.33	27	15
14.34	0.0965	0.0001	0.108	0.0001	0.000159	0.000002	8.14	0.34	25	15
15.24	0.0872	0.0001	0.1051	0.0001	0.000157	0.000002	10.07	0.44	25	14
16.13	0.0809	0.0001	0.104	0.0001	0.000155	0.000002	6.49	0.24	26	15
17.03	0.0775	0.0001	0.105	0.0001	0.000156	0.000002	6.49	0.23	26	15

* U concentration is in ppm.

Appendix D

Diffusion Couple Dataset

Table D.1: Uranium X-ray counts measured by EPMA on diffusion couple Run 1 (2023 K, 14400 s), with 1σ uncertainties

Distance (mm)	Counts U	1σ Uncertainty
0.011	12979	114
0.033	12281	111
0.044	12632	112
0.063	12318	111
0.077	12913	114
0.121	12777	113
0.118	12850	113
0.167	12713	113
0.175	12365	111
0.198	12716	113
0.214	12891	114
0.211	12578	112
0.233	12755	113
0.244	12476	112
0.258	12616	112
0.271	12338	111
0.291	12689	113
0.324	12691	113
0.345	12413	111
0.359	12589	112
0.392	12416	111
0.406	12662	113
0.409	12735	113
0.422	12352	111
0.444	12738	113
0.466	12495	112
0.496	11798	109
0.507	12358	111
0.532	12499	112
0.556	12361	111
0.584	12433	112
0.614	12260	111
0.639	12332	111
0.639	12161	110
0.671	11988	109
0.696	12165	110
0.732	12097	110
0.746	12413	111
0.74	11512	107
0.751	11234	106
0.776	11410	107
0.841	11170	106
0.858	11346	107
0.874	11102	105
0.907	11210	106
0.951	11038	105
0.97	10795	104
0.986	11040	105
0.986	10869	104
1.071	10631	103
1.085	10736	104
1.11	10494	102
1.137	10635	103
1.151	10392	102
1.175	10568	103
1.192	10430	102
1.219	10571	103
1.23	10327	102
1.249	10434	102

1.264	6068	78
1.279	10296	101
1.293	10437	102
1.329	10090	100
1.343	10545	103
1.361	9498	97
1.375	10303	102
1.4	10444	102
1.449	10482	102
1.468	10274	101
1.49	10485	102
1.531	10314	102
1.551	10245	101
1.575	10247	101
1.6	10388	102
1.625	10320	102
1.644	10077	100
1.671	10184	101
1.699	10081	100
1.715	10222	101
1.734	10188	101
1.778	10401	102
1.819	10264	101
1.844	10091	100
1.868	9219	96
1.885	10129	101
1.904	10409	102
1.926	10201	101
1.962	10239	101
1.986	10345	102
2.011	10277	101
2.038	10384	102
2.074	10212	101
2.096	10178	101
2.123	10355	102
2.145	10426	102
2.173	10498	102

Table D.2: Uranium X-ray counts measured by EPMA on diffusion couple Run 2 (1923 K, 28800 s), with 1σ uncertainties

Distance (mm)	Counts U	1σ Uncertainty
0.016	9808	99
0.038	9982	100
0.063	9946	100
0.082	9807	99
0.104	9598	98
0.121	9771	99
0.143	9701	98
0.157	9909	100
0.170	9561	98
0.209	10047	100
0.234	9873	99
0.269	10046	100
0.286	9698	98
0.299	9941	100
0.313	9662	98
0.338	10010	100
0.363	10009	100
0.390	9800	99
0.423	9729	99
0.451	9555	98
0.467	9937	100
0.486	10041	100
0.519	10075	100
0.533	9622	98
0.544	9900	100
0.585	9586	98
0.604	9725	99
0.646	9724	99
0.676	9932	100
0.712	9827	99
0.750	9757	99
0.797	9964	100
0.813	9477	97
0.835	9929	100
0.879	10067	100
0.879	9892	99
0.907	9822	99
0.929	10065	100
0.967	10238	101
0.992	10167	101
0.992	10097	100
1.006	10375	102
1.028	10409	102
1.047	10305	102
1.074	10547	103
1.110	10581	103
1.140	10372	102
1.140	10510	103
1.170	10892	104
1.198	10787	104
1.234	11030	105
1.234	10959	105
1.250	11272	106
1.250	10680	103
1.283	11375	107
1.313	11374	107
1.327	11652	108
1.352	11478	107
1.368	11790	109

1.398	11824	109
1.442	11615	108
1.467	12136	110
1.508	12274	111
1.511	11959	109
1.544	12063	110
1.574	12236	111
1.618	11818	109
1.629	12061	110
1.648	12130	110
1.687	12234	111
1.712	12129	110
1.714	12232	111
1.750	12405	111
1.764	12196	110
1.797	12578	112
1.802	12369	111
1.887	12471	112
1.937	12574	112
1.973	12399	111
1.973	12779	113
1.973	12499	112
1.995	12533	112
2.008	12846	113
2.017	12637	112

Table D.3: Uranium X-ray counts measured by EPMA on diffusion couple Run 3 (1823 K, 86400 s), with 1σ uncertainties

Distance (mm)	Counts U	1σ Uncertainty
0.015	12724	113
0.038	12434	112
0.071	12652	112
0.074	12543	112
0.104	12724	113
0.121	12507	112
0.154	13158	115
0.154	13412	116
0.201	12941	114
0.216	13158	115
0.237	13122	115
0.254	12941	114
0.281	12905	114
0.284	12652	112
0.314	12688	113
0.343	12833	113
0.367	12977	114
0.402	13050	114
0.441	12941	114
0.468	13050	114
0.488	13086	114
0.488	13231	115
0.503	12977	114
0.530	13014	114
0.559	12869	113
0.589	12833	113
0.618	12905	114
0.645	13014	114
0.692	12724	113
0.716	12688	113
0.743	12507	112
0.766	12507	112
0.767	12471	112
0.790	12181	110
0.799	12507	112
0.817	12217	111
0.840	12362	111
0.840	12181	110
0.873	12072	110
0.885	11819	109
0.920	11928	109
0.923	11819	109
0.935	11529	107
0.950	11710	108
0.971	11348	107
1.006	11131	106
1.018	11348	107
1.045	11059	105
1.068	10914	104
1.104	11023	105
1.107	10371	102
1.133	9756	99
1.157	10335	102
1.181	10190	101
1.216	10009	100
1.243	10009	100
1.249	9900	100
1.284	9756	99
1.290	9575	98

1.293	9683	98
1.326	9756	99
1.341	9357	97
1.367	9538	98
1.388	9249	96
1.423	9176	96
1.462	9213	96
1.491	8995	95
1.509	9213	96
1.533	9140	96
1.565	9213	96
1.595	9104	95
1.604	9430	97
1.631	9068	95
1.633	8887	94
1.663	8923	94
1.687	8633	93
1.716	8851	94
1.752	8923	94
1.773	8670	93
1.811	8742	93
1.847	8670	93
1.879	8923	94
1.906	8814	94
1.909	8633	93
1.920	8271	91
1.926	8851	94
1.959	8706	93
1.983	8814	94
2.006	8851	94
2.024	8597	93
2.062	9032	95
2.092	8923	94
2.095	8923	94
2.116	8995	95

Table D.4: Uranium X-ray counts measured by EPMA on diffusion couple Run 4 (1723 K, 100800 s), with 1σ uncertainties

Distance (mm)	Counts U	1σ Uncertainty
0.013	12652	112
0.036	12977	114
0.016	12109	110
0.027	11566	108
0.042	12941	114
0.054	12724	113
0.068	12869	113
0.094	12869	113
0.094	12579	112
0.094	13050	114
0.132	12760	113
0.158	12833	113
0.158	12905	114
0.187	12905	114
0.187	12977	114
0.230	13122	115
0.262	12869	113
0.273	13231	115
0.288	13158	115
0.305	12941	114
0.311	13231	115
0.331	13050	114
0.354	13376	116
0.389	12977	114
0.404	13267	115
0.429	13086	114
0.441	13303	115
0.461	13267	115
0.487	12941	114
0.487	13158	115
0.493	13122	115
0.513	13303	115
0.528	13158	115
0.560	13158	115
0.560	13267	115
0.577	13086	114
0.594	13339	115
0.623	13195	115
0.626	12977	114
0.661	12977	114
0.664	12796	113
0.721	12652	112
0.730	12398	111
0.768	12362	111
0.771	11855	109
0.782	11348	107
0.808	11855	109
0.817	11348	107
0.848	11312	106
0.883	11131	106
0.903	10950	105
0.909	10878	104
0.926	10335	102
0.941	10842	104
0.967	10552	103
0.970	10624	103
0.995	10009	100
1.016	10443	102
1.047	10262	101

1.079	10081	100
1.082	10081	100
1.108	9466	97
1.117	9828	99
1.151	9719	99
1.194	9357	97
1.226	9575	98
1.249	9756	99
1.267	9538	98
1.296	9756	99
1.330	9575	98
1.354	9864	99
1.354	9683	98
1.406	9792	99
1.446	9756	99
1.472	9430	97
1.495	9719	99
1.527	9647	98
1.559	9611	98
1.594	9683	98
1.622	9719	99
1.625	9647	98
1.677	10009	100
1.703	9538	98
1.727	9937	100
1.767	9864	99
1.802	9937	100
1.839	10045	100
1.871	9611	98
1.886	10009	100
1.920	10262	101